ASME
SETTING THE STANDARD

Transactions of the ASME, Journal of Turbomachinery (ISSN 0889-504X) is published quarterly (Jan., Apr., July, Oct.) by The American Society of Mechanical Engineers, Three Park Avenue, New York, NY 10016. Periodicals postage paid at New York, NY and additional mailing offices.
POSTMASTER: Send address changes to Transactions of the ASME, Journal of Turbomachinery, c/o THE AMERICAN SOCIETY OF MECHANICAL ENGINEERS, 22 Law Drive, Box 2300, Fairfield, NJ 07007-2300.
CHANGES OF ADDRESS must be received at Society headquarters seven weeks before they are to be effective. Please send old label and new address.

Journal of Turbomachinery

Published Quarterly by ASME

VOLUME 128 • NUMBER 3 • JULY 2006

TECHNICAL PAPERS

(Contents continued on inside back cover)

This journal is printed on acid-free paper, which exceeds the ANSI Z39.48-1992 specification for permanence of paper and library materials. ♾™
♻ 85% recycled content, including 10% post-consumer fibers.

Journal of Turbomachinery Volume 128, Number 3 JULY 2006

TECHNICAL BRIEF

The ASME Journal of Turbomachinery is abstracted and indexed in the following:

Aluminum Industry Abstracts, Aquatic Science and Fisheries Abstracts, Ceramics Abstracts, Chemical Abstracts, Civil Engineering Abstracts, Compendex (The electronic equivalent of Engineering Index), Corrosion Abstracts, Current Contents, Ei EncompassLit, Electronics & Communications Abstracts, Energy Information Abstracts, Engineered Materials Abstracts, Engineering Index, Environmental Science and Pollution Management, Excerpta Medica, Fluidex, Fuel and Energy Abstracts, INSPEC, Index to Scientific Reviews, Materials Science Citation Index, Mechanical & Transportation Engineering Abstracts, Mechanical Engineering Abstracts, METADEX (The electronic equivalent of Metals Abstracts and Alloys Index), Metals Abstracts, Oceanic Abstracts, Pollution Abstracts, Referativnyi Zhurnal, Shock & Vibration Digest, Steels Alert

F. R. Menter
e-mail: florian.menter@ansys.com

R. B. Langtry
e-mail: robin.langtry@ansys.com

ANSYS CFX Germany,
12 Staudenfeldweg,
Otterfing, Bavaria 83624,
Germany

S. R. Likki
Department of Mechanical Engineering,
University of Kentucky,
216A RGAN Building,
Lexington, KY 40502–0503
e-mail: srinivas@engr.uky.edu

Y. B. Suzen
Department of Mechanical Engineering,
North Dakota State University,
Dolve Hall 111,
P.O. Box 5285,
Fargo, ND 58105
e-mail: bora.suzen@ndsu.edu

P. G. Huang
Department of Mechanical Engineering,
University of Kentucky,
216A RGAN Building,
Lexington, KY 40502-0503
e-mail: ghuang@engr.uky.edu

S. Völker
General Electric Company,
One Research Circle,
ES-221, Niskayuna, NY 12309
e-mail: voelker@crd.ge.com

A Correlation-Based Transition Model Using Local Variables—Part I: Model Formulation

*A new correlation-based transition model has been developed, which is based strictly on local variables. As a result, the transition model is compatible with modern computational fluid dynamics (CFD) approaches, such as unstructured grids and massive parallel execution. The model is based on two transport equations, one for intermittency and one for the transition onset criteria in terms of momentum thickness Reynolds number. The proposed transport equations do not attempt to model the physics of the transition process (unlike, e.g., turbulence models) but form a framework for the implementation of correlation-based models into general-purpose CFD methods. Part I (this part) of this paper gives a detailed description of the mathematical formulation of the model and some of the basic test cases used for model validation, including a two-dimensional turbine blade. Part II (Langtry, R. B., Menter, F. R., Likki, S. R., Suzen, Y. B., Huang, P. G., and Völker, S., 2006, ASME J. Turbomach., **128**(3), pp. 423–434) of the paper details a significant number of test cases that have been used to validate the transition model for turbomachinery and aerodynamic applications. The authors believe that the current formulation is a significant step forward in engineering transition modeling, as it allows the combination of correlation-based transition models with general purpose CFD codes.* [DOI: 10.1115/1.2184352]

1 Introduction

Engineering transition predictions are based mainly on two modeling concepts. The first is the use of low-Reynolds (Re) number turbulence models, where the wall damping functions of the underlying turbulence model trigger the transition onset. This concept is attractive, as it is based on transport equations and can therefore be implemented without much effort into available CFD codes. However, experience has shown that this approach is not capable of reliably capturing the influence of the many different factors that affect transition [1–3], such as:

- freestream turbulence
- pressure gradients and separation
- Mach number effects
- turbulent length scale influence
- wall roughness
- streamline curvature

This is not surprising, as the ability of a low-Re model to predict transition seems coincidental. There is no inherent reason, why damping functions, which have been optimized to damp the turbulence in the viscous sublayer, should reliably predict an entirely different and complex physical process. Low-Re models are therefore not widely used in industrial computational fluid dynamics (CFD) simulations. Some low-Re models have been developed that explicitly contain information on the transition mechanism. Examples are the model of Wilcox [4] and Langtry and Sjolander [5]. While some of these models result in significant predictive improvements, they still suffer from the restriction that their transition calibration is linked to the viscous sublayer formulation. An independent calibration of both effects is therefore not possible.

The second approach, which is favored by industry over low-Re models, is the use of experimental correlations. The correlations usually relate the turbulence intensity Tu in the freestream to the momentum-thickness Reynolds number $Re_{\theta t}$ at transition onset. A typical example is the Abu-Ghannam and Shaw [6] correlation,

Contributed by the International Gas Turbine Institute (IGTI) of ASME for publication in the JOURNAL OF TURBOMACHINARY. Manuscript received October 1, 2003; final manuscript received March 1, 2004. IGTI Review Chair: A. J. Strazisar. Paper presented at the International Gas Turbine and Aeroegine Congress and Exhibition, Vienna, Austria, June 13–17, 2004, Paper No. 2004-GT-53452.

which is based on a large number of experimental observations. Although this method proves sufficiently accurate, it poses numerical and programming challenges in Navier-Stokes codes. For classical correlation-based transition models, it is necessary to compare the actual momentum-thickness Reynolds numbers Re_θ to the transition value from the correlation, $\mathrm{Re}_{\theta t}$. This is not an easy task in a Navier-Stokes environment because the boundary layer edge is not well defined and the integration will therefore depend on the implementation of a search algorithm. The difficulties associated with nonlocal formulations are exaggerated by modern CFD methods that are based on unstructured grids and massive parallel execution. Unstructured grids do not easily provide the infrastructure needed to integrate global boundary layer parameters because the grid lines normal to the surface cannot be easily identified. In the case of a general parallelized CFD code, the boundary layer can be split between different CPUs making the integration even harder to perform. The use of correlation-based transition criteria is therefore incompatible with modern CFD codes. As a result, these models are typically only available in specialized in-house CFD codes for specific applications and geometries. Correlation-based models are frequently linked to an intermittency transport equation, such as that developed by Suzen et al. [7] (or more complex formulations as proposed by Steelant and Dick [8]). Nevertheless, all these models require nonlocal information to trigger the production term in the intermittency equation. The predictive capability of the transport equations themselves is therefore limited, as the main input is provided by the experimental correlation, even though physical argumentation is used in their derivation.

A novel approach to avoid the need for nonlocal information in correlation-based models has been introduced by Menter et al. [9]. In this formulation, only local information is used to activate the production term in the intermittency equation. The link between the correlation and the intermittency equation is achieved through the use of the vorticity Reynolds number. The model given by Menter et al. [9] did not satisfy the requirements of an industrial-strength transition model, both in terms of its numerical behavior and in terms of its calibration. It is the goal of the present paper to present a transition model built on the same concepts, which avoids the deficiencies of the original formulation, and is calibrated over a wide range of flow conditions.

The proposed formulation is based on two transport equations. The first is an intermittency equation used to trigger the transition process. The equation is similar to the model given by Menter et al. [9], with numerous enhancements and generalizations. In addition, a second transport equation is formulated for avoiding additional nonlocal operations introduced by the quantities used in the experimental correlations. Correlations are typically based on freestream values, like the turbulence intensity or the pressure gradient outside the boundary layer. The additional equation is formulated in terms of the transition onset Reynolds number $\mathrm{Re}_{\theta t}$. Outside the boundary layer, the transport variable is forced to follow the value of $\mathrm{Re}_{\theta t}$ provided by the experimental correlation. This information is then diffused into the boundary layer by a standard diffusion term. By this mechanism, the strong variations of the turbulence intensity and the pressure gradient, which are typically observed in industrial flows, can be taken into account.

It should be stressed that the proposed transport equations do not attempt to model the physics of the transition process (unlike, e.g., turbulence models) but form a framework for the implementation of correlation-based models into general-purpose CFD methods. The physics of the transition process is contained entirely in the experimental correlations provided to the model. The formulation is therefore not limited to one specific transition mechanism, such as bypass transition, but can be used for all mechanisms, as long as appropriate correlations can be provided. The current correlations have been formulated to cover standard bypass transition as well as flows in low freestream turbulence environments.

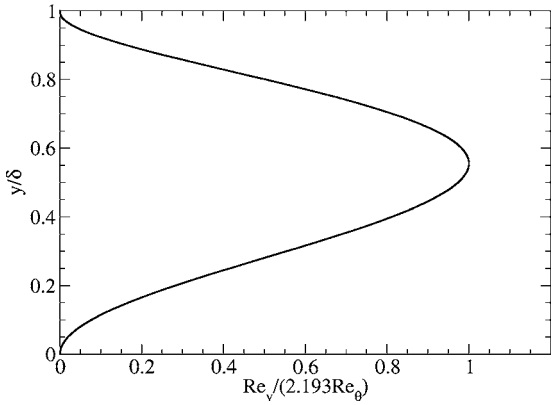

Fig. 1 Scaled vorticity Reynolds number (Re_v) profile in a Blasius boundary layer

In the present paper, all details of the formulation of the model framework will be given. Some of the correlations used in the simulations are based on internal information and are therefore proprietary. However, the framework is generally applicable and can be combined with standard [10,6,7] or in-house correlations.

As the current model will be the basis for future developments by the authors and will most likely be used by other groups, it is necessary to introduce a proper naming convention and version numbering. The basic model framework (transport equations without the correlations) will be called γ-Re_θ model. The version number of the current formulation and the correlations used is CFX-v-1.0. The proper identifier of the current model is, therefore, γ-Re_θ model, CFX-v-1.0. The entire concept behind the present approach is referred to as local correlation-based transition modeling (LCTM).

2 Vorticity Reynolds Number

Instead of using the momentum thickness Reynolds number to trigger the onset of transition, the current model is based on the vorticity Reynolds number Re_v, [11,9]

$$\mathrm{Re}_v = \frac{\rho y^2}{\mu}\frac{\partial u}{\partial y} = \frac{\rho y^2}{\mu}\Omega \tag{1}$$

where y is the distance from the nearest wall. Since the vorticity Reynolds number depends only on density, viscosity, wall distance, and the vorticity (or shear strain rate), it is a local property and can be easily computed at each grid point in an unstructured, parallel Navier-Stokes code.

A scaled profile of the vorticity Reynolds number is shown in Fig. 1 for a Blasius boundary layer. The scaling is chosen in order to have a maximum of one inside the boundary layer. This is achieved by dividing the profile by the corresponding momentum thickness Reynolds number and a constant of 2.193. In other words, the maximum of the profile is proportional to the momentum thickness Reynolds number and can therefore be related to transition correlations [4,9] as follows:

$$\mathrm{Re}_\theta = \frac{\mathrm{Re}_{v\ \max}}{2.193} \tag{2}$$

Based on this observation, a general framework can be built that can serve as a local environment for correlation-based transition models.

When the laminar boundary layer is subjected to strong pressure gradients, the relationship between momentum thickness and vorticity Reynolds number described by Eq. (2) changes due to the change in the shape of the profile. The relative error between momentum thickness and vorticity Reynolds number, as a function of shape factor (H), is shown in Fig. 2. For moderate pressure

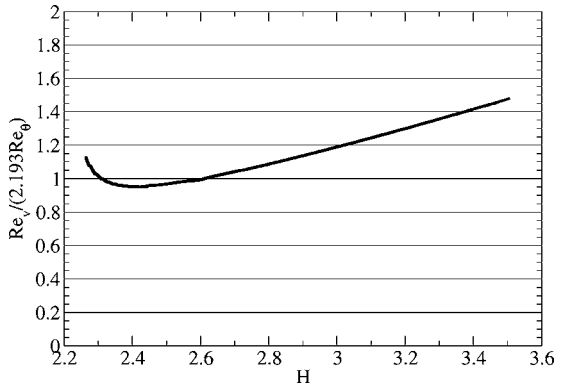

Fig. 2 Relative error between vorticity Reynolds number (Re_v) and the momentum thickness Reynolds number (Re_θ) as a function of boundary layer shape factor (H)

gradients ($2.3 < H < 2.9$) the difference between the actual momentum thickness Reynolds number and the maximum of the vorticity Reynolds number is $<10\%$. Based on boundary layer analysis, a shape factor of 2.3 corresponds to a pressure gradient parameter (λ_θ) of ~ 0.06. Since the majority of experimental data on transition in favorable pressure gradients falls within that range (see, for example, [6]), the relative error between momentum thickness and vorticity Reynolds number is not of great concern under those conditions.

For strong adverse pressure gradients, the difference between the momentum thickness and vorticity Reynolds number can become significant, particularly near separation ($H=3.5$). However, the correct trend with experiments is that adverse pressure gradients reduce the transition momentum thickness Reynolds number. In practice, if a constant transition momentum thickness Reynolds number is specified, the transition model is not very sensitive to adverse pressure gradients and an empirical correlation, such as that of Abu-Ghannam and Shaw [6] is necessary in order to predict adverse pressure gradient transition accurately. It will also be shown in this paper that the increase in vorticity Reynolds number with increasing shape factor can actually be used to predict separation-induced transition. This is one of the main advantages to the present approach because the standard definition of momentum thickness Reynolds number is not suitable in separated flows.

3 Model Formulation

The main requirement for the transition model development was that only local variables and gradients, as well as the wall distance could be used in the equations. The wall distance can be computed from a Poisson equation and does therefore not break the paradigm of modern CFD methods. The present formulation avoids another very severe shortcoming of the correlation-based models, namely, their limitation to two-dimensional (2D) flows. Already the definition of a momentum-thickness is strictly a 2D concept. It cannot be computed in general three-dimensional (3D) flows, such as a turbine blade sidewall boundary layer, which is usually highly three-dimensional. The current formulation avoids this shortcoming and allows the simulation of 3D flows originating from different walls.

In the following, a transport equation for the intermittency γ model will be described, in detail, that can be used to trigger transition locally. The intermittency function is coupled with the SST k-ω based turbulence model [12]. It is used to turn on the production term of the turbulent kinetic energy downstream of the transition point. The formulation of the intermittency equation has also been extended to account for the rapid onset of transition caused by separation of the laminar boundary layer. As well, the model can be fully calibrated with proprietary transition onset and transition length correlations. The correlations can also be extended to flows at low freestream turbulence intensity or to flows with cross-flow instability.

In addition to the transport equation for the intermittency, a second transport equation is solved in terms of the transition onset momentum-thickness Reynolds number ($\tilde{\mathrm{Re}}_{\theta t}$). This is necessary in order to capture the nonlocal influence of the turbulence intensity, which changes due to the decay of the turbulence kinetic energy in the freestream, as well as due to changes in the freestream velocity outside the boundary layer. This additional transport equation is an essential part of the model as it ties the empirical correlation to the onset criteria in the intermittency equation and allows the models use in general geometries and over multiple blades, without interaction from the user.

The present transition model formulation is described in five sections. Section 3.1 gives the formulation of the intermittency transport equation used to trigger the transition onset. Section 3.2 describes the new transport equation for the transition momentum thickness Reynolds number $\tilde{\mathrm{Re}}_{\theta t}$, which is used to capture the non-local effect of freestream turbulence intensity and pressure gradient at the boundary layer edge. Section 3.3 describes a modification that is used to improve the predictions for separated flow transition. Section 3.4 describes the link between the transition model and the shear stress transport (SST) model. Section 3.5 describes a new empirical correlation that has been designed by the present authors to improve on the standard Abu-Ghannam and Shaw [6] correlation.

3.1 Transport Equation for Intermittency. A new transport equation for the intermittency γ has been developed that corrects most of the deficiencies that were observed with the baseline intermittency equation proposed by Menter et al. [9]. The principle deficiencies with this equation were that the transition length was too short and the distance between the specified critical momentum thickness $\mathrm{Re}_{\theta c}$, and the actual transition Reynolds number $\mathrm{Re}_{\theta t}$ was too long. In addition, since the source term for the production of intermittency was based on the strain rate, the model suffered from excessive production of intermittency in stagnation regions. As a result, for a turbine blade, the large values of intermittency produced in the stagnation region convected around the blade and resulted in a fully turbulent boundary layer on the surface of the blade. The intermittency equation described in this paper has been modified specifically to allow for a good prediction of the transitional region while avoiding the problem of early transition due to a stagnation point.

A significant change to the formulation given by Menter et al. [9] is that the intermittency is now set to be equal to one in the freestream, instead of a small value as in the original model. This has several advantages, especially in stagnation regions and near the boundary layer edge, where the original formulation did interfere with the turbulence model. The concept of a nonzero freestream intermittency is not new and has been employed by Steelant and Dick [8] in their intermittency transport equation. Although physics arguments can be made for this modification (at least for bypass transition, where the turbulence is diffused into the boundary layer from high freestream levels), it is mainly used here to extend the applicability and robustness of the current method.

The intermittency equation is formulated as follows:

$$\frac{\partial(\rho\gamma)}{\partial t} + \frac{\partial(\rho U_j \gamma)}{\partial x_j} = P_{\gamma 1} - E_{\gamma 1} + P_{\gamma 2} - E_{\gamma 2} + \frac{\partial}{\partial x_j}\left[\left(\mu + \frac{\mu_t}{\sigma_f}\right)\frac{\partial \gamma}{\partial x_j}\right] \tag{3}$$

The transition sources are defined as

$$P_{\gamma 1} = F_{\mathrm{length}} \rho S [\gamma F_{\mathrm{onset}}]^{c_{a1}} \tag{4}$$

$$E_{\gamma 1} = c_{e1} P_{\gamma 1} \gamma \tag{5}$$

where S is the strain rate magnitude.

The main difference to other intermittency models lies in the formulation of the function F_{onset}, which is used to trigger the intermittency production. It is formulated as a function of the vorticity (in this case strain rate) Reynolds number

$$\text{Re}_V = \frac{\rho y^2 S}{\mu} \tag{6}$$

$$F_{\text{onset }1} = \frac{\text{Re}_v}{2.193\,\text{Re}_{\theta c}} \tag{7}$$

$$F_{\text{onset }2} = \min[\max(F_{\text{onset }1}, F^4_{\text{onset }1}), 2.0] \tag{8}$$

$$R_T = \frac{\rho k}{\mu \omega} \tag{9}$$

$$F_{\text{onset }3} = \max\left[1 - \left(\frac{R_T}{2.5}\right)^3, 0\right] \tag{10}$$

$$F_{\text{onset}} = \max(F_{\text{onset }2} - F_{\text{onset }3}, 0) \tag{11}$$

$\text{Re}_{\theta c}$ in Eq. (7) is the critical Reynolds number where the intermittency first starts to increase in the boundary layer. This occurs upstream of the transition Reynolds number $\text{Re}_{\theta t}$. The connection between the two can be obtained from an empirical correlation, where

$$\text{Re}_{\theta c} = f(\tilde{\text{Re}}_{\theta t}) \tag{12}$$

This correlation is determined based on a series of numerical experiments on a flat plate. $\tilde{\text{Re}}_{\theta t}$ comes from the transport equation given by Eq. (17).

F_{length} in Eq. (4) is an empirical correlation that controls the length of the transition region. It is based on a significant amount of numerical experimentation whereby a series of flat plate experiments where reproduced and a curve fitting program was used to develop a correlation that resulted in the correct prediction of the transition length as compared to experimental data. The correlations can be exchanged according to the experimental information available to the institution. At present, both the $\text{Re}_{\theta c}$ and F_{length} correlations are proprietary and for this reason their formulation is not given in this paper.

The destruction/relaminarization sources are defined as follows:

$$P_{\gamma 2} = c_{a2} \rho \Omega \gamma F_{\text{turb}} \tag{13}$$

$$E_{\gamma 2} = c_{e2} P_{\gamma 2} \gamma \tag{14}$$

where Ω is the vorticity magnitude. These terms ensure that the intermittency remains zero in the laminar boundary layer (it is one in the freestream) and also enables the model to predict relaminarization.

F_{turb} is used to disable the destruction/relaminarization sources outside of a laminar boundary layer or in the viscous sublayer. It is defined as follows:

$$F_{\text{turb}} = e^{-(R_T/4)^4} \tag{15}$$

The constants for the intermittency equation are

$$c_{e1} = 1.0; \quad c_{a1} = 0.5$$

$$c_{e2} = 50; \quad c_{a2} = 0.03; \quad \sigma_f = 1.0$$

The boundary condition for γ at a wall is zero normal flux while at an inlet γ is equal to 1. In order to capture the laminar and transitional boundary layers correctly, the grid must have a y^+ of ~ 1. If the y^+ is too large (i.e., >5), then the transition onset location moves upstream with increasing y^+. It has also been determined that the transition onset location is very sensitive to the advection scheme used for the turbulence and transition model equations. For this reason, all equations were solved with a bounded second-order upwind scheme. This resulted in grid independent solutions on reasonable sized grids (e.g., for a blade, 200 nodes around the blade, y^+ of 1 with a wall normal grid expansion ratio of 1.1).

3.2 Transport Equation for Transition Momentum Thickness Reynolds Number. Experimental correlations relate the Reynolds number of transition onset, $\text{Re}_{\theta t}$, to the turbulence intensity Tu, and other quantities in the freestream, where

$$\text{Re}_{\theta t} = f(\text{Tu}, \ldots)_{\text{freestream}} \tag{16}$$

This is a nonlocal operation, as the value of $\text{Re}_{\theta t}$ is required by the intermittency equation inside the boundary layer. Note that the turbulence intensity can change strongly in a domain and that one global value over the entire flowfield is therefore not acceptable. Examples of such flows are highly loaded transonic turbomachinery or unsteady rotor-stator interactions. Since the main requirement for the current transition model is that only local quantities can be used, there must be a means of passing the information about the freestream conditions into the boundary layer.

The following transport equation can be used to resolve this issue using only a local formulation. The basic concept is to treat the transition momentum thickness Reynolds number $\text{Re}_{\theta t}$, as a scalar transported quantity. One way to do this is to use an empirical correlation to calculate $\text{Re}_{\theta t}$ in the freestream and then allow the freestream value to diffuse into the boundary layer. Since the empirical correlations are defined as $\text{Re}_{\theta t} = f(\text{Tu}, dp/ds)$, and since Tu and dp/ds are defined in the freestream, $\text{Re}_{\theta t}$ is the only unknown quantity in the equation.

The transport equation for the transition momentum thickness Reynolds number $\tilde{\text{Re}}_{\theta t}$ is defined as follows:

$$\frac{\partial(\rho \tilde{\text{Re}}_{\theta t})}{\partial t} + \frac{\partial(\rho U_j \tilde{\text{Re}}_{\theta t})}{\partial x_j} = P_{\theta t} + \frac{\partial}{\partial x_j}\left[\sigma_{\theta t}(\mu + \mu_t)\frac{\partial \tilde{\text{Re}}_{\theta t}}{\partial x_j}\right] \tag{17}$$

The source term $\text{P}_{\theta t}$ is designed to force the transported scalar $\tilde{\text{Re}}_{\theta t}$ to match the local value of $\text{Re}_{\theta t}$ calculated from an empirical correlation outside the boundary layer. The source term is defined as follows:

$$P_{\theta t} = c_{\theta t}\frac{\rho}{t}(\text{Re}_{\theta t} - \tilde{\text{Re}}_{\theta t})(1.0 - F_{\theta t}) \tag{18}$$

$$t = \frac{500\mu}{\rho U^2} \tag{19}$$

where t is a time scale that is present for dimensional reasons. The blending function $F_{\theta t}$ is used to turn off the source term in the boundary layer and allow the transported scalar $\tilde{\text{Re}}_{\theta t}$ to diffuse in from the freestream. $F_{\theta t}$ is equal to zero in the freestream and one in the boundary layer. It is defined as follows:

$$F_{\theta t} = \min\left\{\max\left[F_{\text{wake}} e^{-(y/\delta)^4}, \quad 1.0 - \left(\frac{\gamma - 1/c_{e2}}{1.0 - 1/c_{e2}}\right)^2\right], \quad 1.0\right\} \tag{20}$$

$$\theta_{BL} = \frac{\tilde{\text{Re}}_{\theta t}\mu}{\rho U} \quad \delta_{BL} = \frac{15}{2}\theta_{BL} \quad \delta = \frac{50\Omega y}{U}\delta_{BL} \tag{21}$$

$$\text{Re}_\omega = \frac{\rho \omega y^2}{\mu} \tag{22}$$

$$F_{\text{wake}} = e^{-[\text{Re}_\omega/(1E+5)]^2} \tag{23}$$

The boundary condition for $\tilde{\text{Re}}_{\theta t}$ at a wall is zero flux. The boundary condition for $\tilde{\text{Re}}_{\theta t}$ at an inlet should be calculated from the

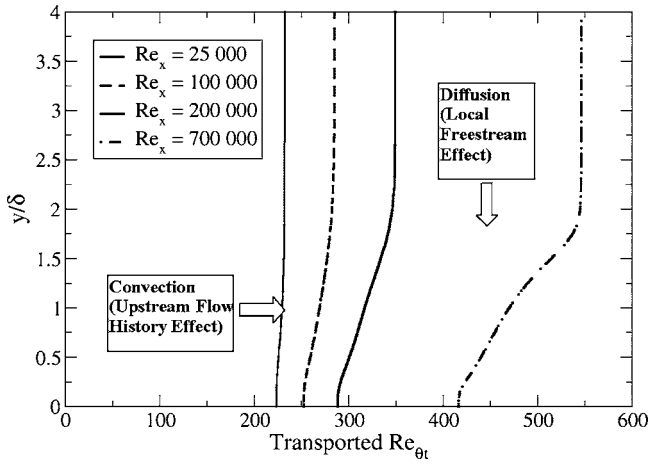

Fig. 3 Profiles of the transported scalar $\tilde{Re}_{\theta t}$ for a flat plate with a rapidly decaying freestream turbulence intensity (T3A test case)

empirical correlation based on the inlet turbulence intensity.

The model constants for the transport equation are as follows, where $c_{\theta t}$ controls the magnitude of the source term and $\sigma_{\theta t}$ controls the diffusion coefficient:

$$c_{\theta t} = 0.03$$

$$\sigma_{\theta t} = 10.0$$

The profiles of the transported scalar $\tilde{\mathrm{Re}}_{\theta t}$ for a flat plate case with rapidly decreasing freestream turbulence intensity (and, hence, increasing $\tilde{\mathrm{Re}}_{\theta t}$) are shown in Fig. 3. There is some lag between changes in the freestream value of $\tilde{\mathrm{Re}}_{\theta t}$ and that inside the boundary layer. The lag is desirable, as according to Abu-Ghannam and Shaw [6] the onset of transition is primarily affected by the past history of pressure gradient and turbulence intensity and not the local value at transition. The lag between the local value of $\tilde{\mathrm{Re}}_{\theta t}$ in the boundary layer and that in the freestream can be controlled by the diffusion coefficient $\sigma_{\theta t}$.

The present value of $\sigma_{\theta t}=10$ was obtained based on flat plate transition experiments were the freestream turbulence intensity was rapidly decaying. The contour plot of the local value of the transition momentum thickness Reynolds number from the new empirical correlation $\mathrm{Re}_{\theta t}$ and from the solution of the transport equation $\tilde{\mathrm{Re}}_{\theta t}$ is shown in Fig. 4. The two are virtually identical except in the boundary layer regions as desired. Of particular interest is the large increase in $\mathrm{Re}_{\theta t}$ at the blade leading edge due to the strong acceleration and the large decrease in the wake region due to the large levels of turbulence intensity.

3.3 Separation-Induced Transition. It became apparent during the development of the present transition model that whenever a laminar boundary layer separation occurred, the model consistently predicted the turbulent reattachment location too far downstream. Based on experimental results for a low-pressure turbine blade (see part II [13] of this paper for further details) the agreement with experiment tended to decrease as the freestream turbulence intensity was lowered. Presumably this is because the turbulent kinetic energy k in the separating shear layer is smaller at lower freestream turbulence intensities. As a result, it takes longer for k to grow to large enough values that would cause the boundary layer to reattach. This is the case even if the onset of transition is predicted at or near the separation point.

To correct this deficiency, a modification to the transition model is introduced that allows k to grow rapidly once the laminar boundary layer separates. The modification has been formulated

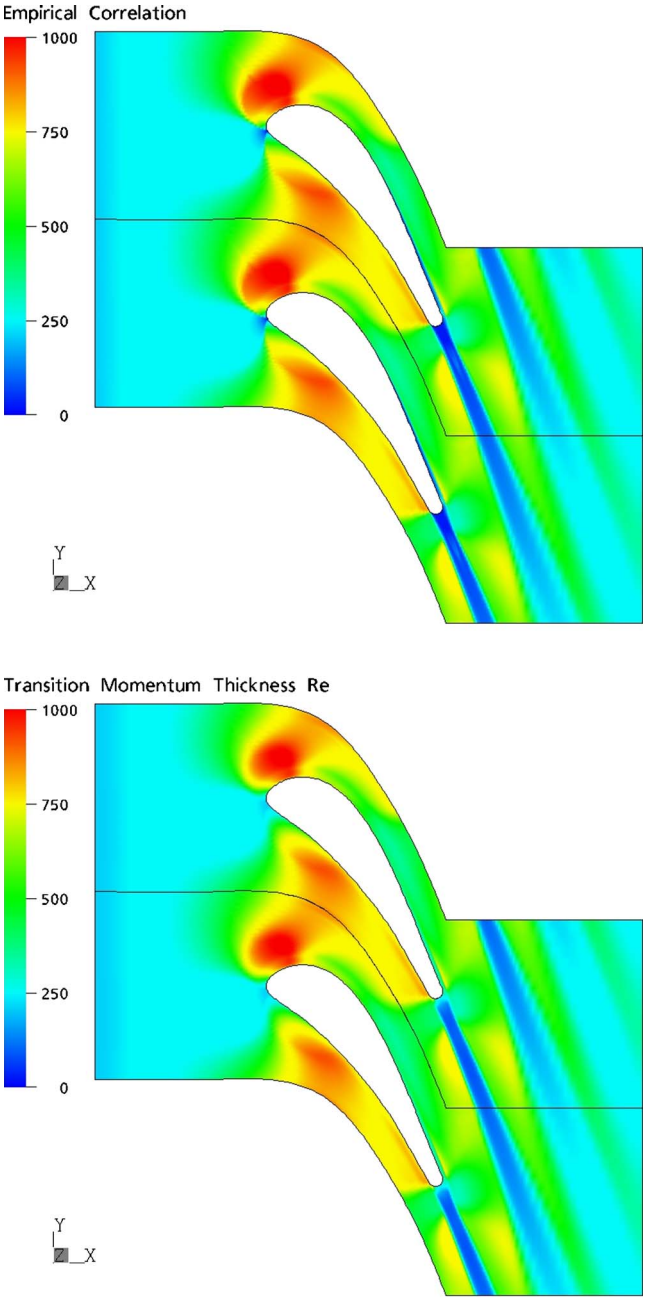

Fig. 4 Contours of transition onset momentum thickness Reynolds number from the empirical correlation ($\mathrm{Re}_{\theta t}$, top) and the transport equation ($\tilde{Re}_{\theta t}$, bottom) for the Genoa turbine blade

so that it has a negligible effect on the predictions for attached transition. The main idea behind the separated flow correction is to allow the local intermittency to exceed 1 whenever the laminar boundary layer separates. This will result in a large production of k, which, in turn, will cause earlier reattachment. The means for accomplishing this is based on the fact that for a laminar separation the vorticity Reynolds number Re_v significantly exceeds the critical momentum thickness Reynolds number $\mathrm{Re}_{\theta c}$. As a result, the ratio between the two can be thought of as a measure of the size of the laminar separation and can therefore be used to increase the production of turbulent kinetic energy. The modification for separation-induced transition is given by

$$\gamma_{\text{sep}} = \min\left\{ s_1 \max\left[\left(\frac{\text{Re}_v}{2.193\,\text{Re}_{\theta c}} \right) - 1{,}0 \right] F_{\text{reattach}}, 5 \right\} F_{\theta t} \quad s_1 = 8 \tag{24}$$

$$F_{\text{reattach}} = e^{-(R_T/15)^4} \tag{25}$$

$$\gamma_{\text{eff}} = \max(\gamma, \gamma_{\text{sep}}) \tag{26}$$

The size of the separation bubble can be controlled with the constant s_1. F_{reattach} disables the modification once the viscosity ratio is large enough to cause reattachment. $F_{\theta t}$ is the blending function from the $\widetilde{\text{R}}e_{\theta t}$ equation (Eq. (17)) and confines the modification to boundary-layer-type flows. The destruction term in the k equation is now limited so that it can never exceed the fully turbulent value. The ability to include such a complex effect in such a simple way into the model shows the flexibility of the current approach.

3.4 Coupling With the Turbulence Model. The new transition model has been calibrated for use with the SST turbulence model Menter [12]. The transition model is coupled with the turbulence model as follows:

$$\frac{\partial}{\partial t}(\rho k) + \frac{\partial}{\partial x_j}(\rho u_j k) = \widetilde{P}_k - \widetilde{D}_k + \frac{\partial}{\partial x_j}\left[(\mu + \sigma_k \mu_t) \frac{\partial k}{\partial x_j} \right] \tag{27}$$

$$\frac{\partial}{\partial t}(\rho \omega) + \frac{\partial}{\partial x_j}(\rho u_j \omega) = \alpha \frac{P_k}{v_t} - D_\omega + Cd_\omega + \frac{\partial}{\partial x_j}\left[(\mu + \sigma_k \mu_t) \frac{\partial \omega}{\partial x_j} \right] \tag{28}$$

$$\widetilde{P}_k = \gamma_{\text{eff}} P_k \tag{29}$$

$$\widetilde{D}_k = \min[\max(\gamma_{\text{eff}}, 0.1), 1.0] D_k \tag{30}$$

where P_k and D_k are the production and destruction terms from the turbulent kinetic energy equation in the original SST turbulence model and γ_{eff} is the effective intermittency obtained from Eqs. (24)–(26).

The final modification to the SST model is a change in the blending function F_1 responsible for switching between the k-ω and k-ε models. It was found that in the center of the laminar boundary layer F_1 could potentially switch from 1.0 to 0.0. This is not desirable, as the k-ω model must be active in the laminar and transitional boundary layers. The deficiency in the blending function is not surprising as the equations used to define F_1 were intended solely for use in turbulent boundary layers. The solution is to redefine F_1 in terms of a blending function that will always be equal to 1.0 in a laminar boundary layer. The modified blending function is defined as follows:

$$R_y = \frac{\rho y \sqrt{k}}{\mu} \tag{31}$$

$$F_3 = e^{-(R_y/120)^8} \tag{32}$$

$$F_1 = \max(F_{1\ \text{orig}}, F_3) \tag{33}$$

where $F_{1\ \text{orig}}$ is the original blending function from the SST turbulence model.

3.5 New Empirical Correlation. It has also been observed by Suzen et al. [7] that for a low-pressure turbine blade at high turbulence intensity the correlation of Abu-Ghannam and Shaw [6] results in transition onset being predicted before the laminar boundary layer separates. As a result, the separation bubble on the suction side of the blade is too small. The Abu-Ghannam and Shaw [6] correlation indicates that there is almost no change in the transition onset momentum thickness Reynolds number $\text{Re}_{\theta t}$ when the flow is strongly accelerated. As shown by Suzen et al. [7] this is not actually the case and strong accelerations can result in a significant increase in $\text{Re}_{\theta t}$. On the other hand, the Abu-Ghannam and Shaw [6] correlation does predict transition in zero and adverse pressure gradient flows well. It would therefore be desirable to have an empirical correlation that behaves similar to Abu-Ghannam and Shaw's in adverse pressure gradients, yet incorporates the desirable aspects of the Suzen and Huang [7] correlation as well. In this paper an attempt has been made to develop an empirical correlation that should retain the favorable aspects of both correlations.

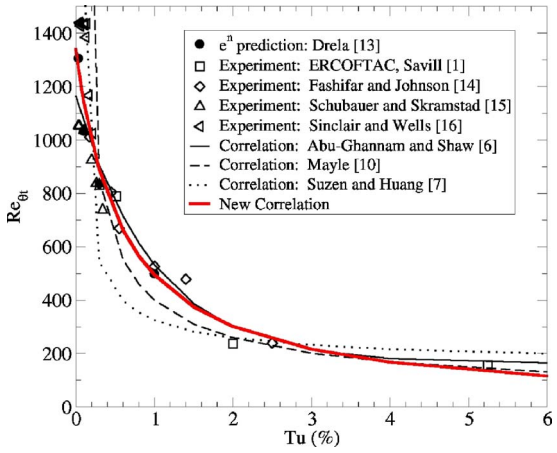

Fig. 5 Transition onset momentum thickness Reynolds number ($\text{Re}_{\theta t}$) predicted by the new correlation as a function of turbulence intensity (Tu) for a flat plate with zero pressure gradient

The new formulation is shown in Figs. 5 and 6. For zero pressure gradients (Fig. 5), the new correlation behaves similar to the Mayle [10] correlation at high freestream turbulence intensities ($\text{Tu} > 3.0$) and is comparable to the Abu-Ghannam and Shaw [6] correlation at moderate turbulence intensities ($1.0 < \text{Tu} < 3.0$). At low turbulence intensity ($\text{Tu} < 1.0$) the new correlation has been curve fit to agree with zero pressure gradient results from Drela's [14] e^n-type model. In adverse pressure gradients (see Fig. 6), the new correlation has been curve fit to match the correlation of Abu-Ghannam and Shaw [6]. This results in very good agreement with the transition onset data from Fashifar and Johnson [15]. At

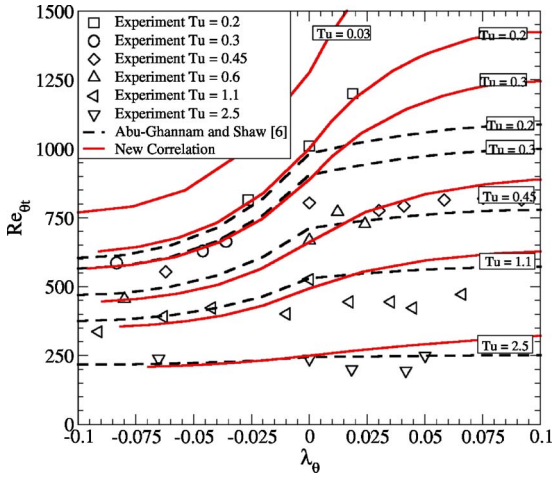

Fig. 6 Transition onset momentum thickness Reynolds number ($\text{Re}_{\theta t}$) predicted by the new correlation as a function of pressure gradient parameter (λ_θ) for constant values of turbulence intensity (Tu). Experimental data are from Fashifar and Johnson [15].

Table 1 Summary of all test case inlet conditions

Case	U inlet (m/s)	FSTI (%) inlet	μ_t/μ	ρ (kg/m^3)	μ (kg/ms)
T3A	5.4	3.5	13.3	1.2	1.8×10^{-5}
T3B	9.4	6.5	100.0	1.2	1.8×10^{-5}
T3A-	19.8	0.874	8.72	1.2	1.8×10^{-5}
Schubauer and Klebanof	50.1	0.18	5.0	1.2	1.8×10^{-5}
T3C4	1.37	3.0	8	1.2	1.8×10^{-5}
Genoa	26.8	3.0	1.0	1.2	1.8×10^{-5}

low turbulence intensities, the new correlation has been designed to predict a large increase in $\mathrm{Re}_{\theta t}$ whenever a favorable pressure gradient is present. This is based on Drela's [14] e^n model, which indicates that small favorable pressure gradients will cause a large increase in $\mathrm{Re}_{\theta t}$. Based on the Fashifar and Johnson [15] data, the effect appears to be reduced as the freestream turbulence intensity increases and the new correlation is designed to reflect this. The new empirical correlation is defined as follows:

$$\lambda_\theta = (\theta^2/v)dU/ds \tag{34}$$

$$K = (v/U^2)dU/ds \tag{35}$$

where dU/ds is the acceleration along in the streamwise direction and can be computed by taking the derivative of the velocity (U) in the x, y, and z directions and then summing the contribution of these derivatives along the streamwise flow direction as follows:

$$U = (u^2 + v^2 + w^2)^{1/2} \tag{36}$$

$$\frac{dU}{dx} = \frac{1}{2}(u^2+v^2+w^2)^{-(1/2)}\left[2u\frac{du}{dx} + 2v\frac{dv}{dx} + 2w\frac{dw}{dx}\right] \tag{37}$$

$$\frac{dU}{dy} = \frac{1}{2}(u^2+v^2+w^2)^{-(1/2)}\left[2u\frac{du}{dy} + 2v\frac{dv}{dy} + 2w\frac{dw}{dy}\right] \tag{38}$$

$$\frac{dU}{dz} = \frac{1}{2}(u^2+v^2+w^2)^{-(1/2)}\left[2u\frac{du}{dz} + 2v\frac{dv}{dz} + 2w\frac{dw}{dz}\right] \tag{39}$$

$$\frac{dU}{ds} = (u/U)\frac{dU}{dx} + (v/U)\frac{dU}{dy} + (w/U)\frac{dU}{dz} \tag{40}$$

The empirical correlation is defined as

$$\mathrm{Re}_{\theta t} = 803.73[\mathrm{Tu} + 0.6067]^{-1.027}F(\lambda_\theta, K) \tag{41}$$

$$F(\lambda_\theta, K) = 1 - [-10.32\lambda_\theta - 89.47\lambda_\theta^2 - 265.51\lambda_\theta^3]e^{[-\mathrm{Tu}/3.0]}, \quad \lambda_\theta \leq 0 \tag{42}$$

$$F(\lambda_\theta, K) = 1 + [0.0962[K10^6] + 0.148[K10^6]^2 + 0.0141[K10^6]^3] \times (1 - e^{[-\mathrm{Tu}/1.5]}) + 0.556[1 - e^{[-23.9\lambda_\theta]}]e^{[-\mathrm{Tu}/1.5]}, \quad \lambda_\theta > 0 \tag{43}$$

where Tu is the local turbulence intensity (in percent) as defined in the nomenclature. For numerical robustness the acceleration parameters and the empirical correlation should be limited as follows:

$$-0.1 \leq \lambda_\theta \leq 0.1 \tag{44}$$

$$-3\times10^{-6} \leq K \leq 3\times10^{-6} \tag{45}$$

$$\mathrm{Re}_{\theta t} \geq 20 \tag{46}$$

Note that the use of the streamline direction is not Galilean invariant. This deficiency is inherent to correlation-based models, as their main variable, the turbulence intensity is already based on the local freestream velocity and therefore does violate Galilean invariance. This is not problematic, as the correlations are defined with respect to a wall boundary layer and all velocities are therefore relative to the wall. However, multiple moving walls in one domain will require additional information. It should also be stressed that the empirical correlation is used only in the source term (Eq. (18)) of the transport equation for transition onset momentum thickness Reynolds number. Finally, because the momentum thickness (θ_t) is present in the pressure gradient parameter (λ_θ), Eqs. (41)–(43) must be solved iteratively. In the present work, an initial guess for the local value of θ_t was obtained based on the zero pressure gradient solution of Eq. (41) and the local value of U, ρ, and μ. With this initial guess, Eqs. (41)–(43) were solved by iterating on the value of θ_t and convergence was obtained in less then ten iterations.

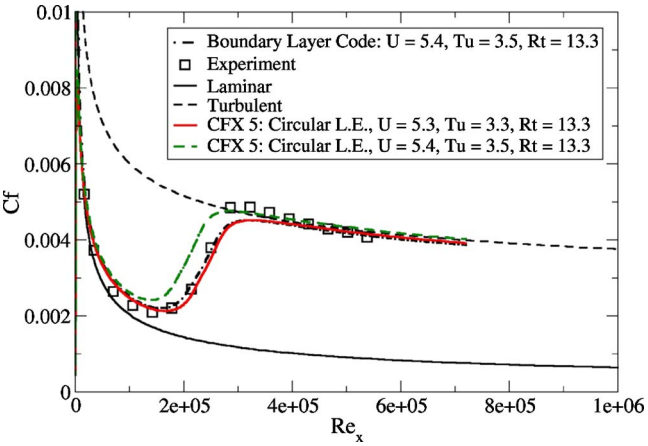

Fig. 7 Skin friction (*Cf*) for the T3A test case (FSTI=3.5%)

4 Results and Discussion

Test cases presented in this paper include the ERCOFTAC [1,2] T3 series of flat plate experiments and the well-known Schubauer and Klebanof [18] flat plate experiment, all of which are commonly used as benchmarks for transition models. The first three cases (T3A-, T3A, and T3B) have zero pressure gradient with free-stream turbulence levels of 1%, 3% and 6% that correspond to transition in the bypass regime. The Schubauer and Klebanof [18] test case has a low free-stream turbulence intensity and corresponds to natural transition. The T3C4 test case consists of a flat plate with a favorable and adverse pressure gradient imposed by

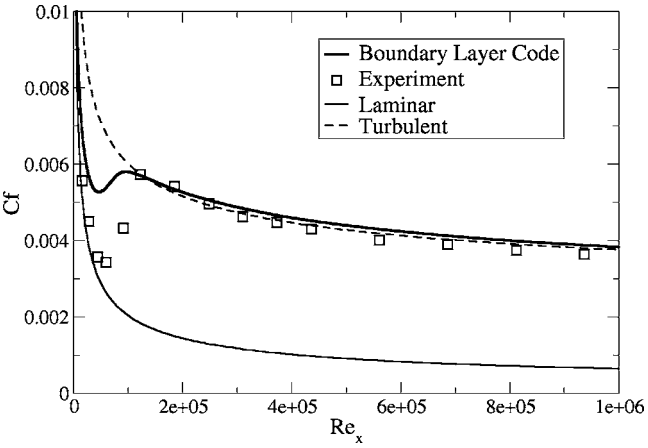

Fig. 8 Skin friction (*Cf*) for the T3B test case (FSTI=6.5%)

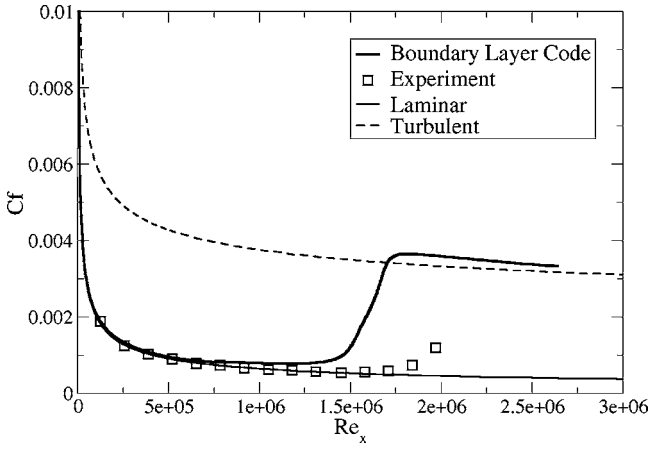

Fig. 9 Skin friction (*Cf*) for the T3A-test case (FSTI=0.87%)

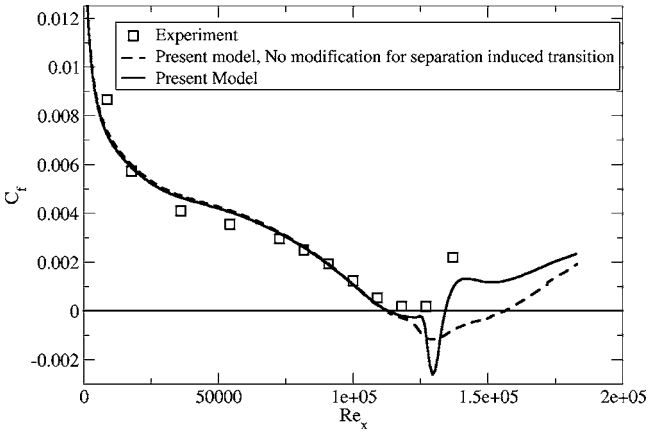

Fig. 11 Predicted skin friction (*Cf*) for the T3C4 test case with and without the modification for separated flow transition

the opposite converging/diverging wall. It is used to demonstrates the new transition models ability to predict separation-induced transition and the subsequent reattachment of the turbulent boundary layer. The final test case is the Genoa large-scale turbine blade [19]. This is used to demonstrate the predicative ability of the new transition model on an actual turbine blade. The inlet quantities for all the test cases computed are summarized in Table 1. It should be noted again, that deficiencies between simulations and experimental data can be reduced by the formulation of improved transition correlations in the future.

The T3A, T3B, T3A-, and Schubauer and Klebanof [17] test cases predicted by the University of Kentucky boundary layer code are shown in Figs. 7–10. The T3A predictions from the boundary layer code and the Navier-Stokes code CFX 5 are compared to the experimentally measured skin friction in Fig. 7. There is a discrepancy between CFX-5 results and the boundary layer code transition onset location and this appears to be caused by the effect of a circular leading edge that was present in the CFX-5 simulation (and in the experiment). When the inlet conditions for the CFX 5 case are adjusted to better match the boundary layer edge conditions (i.e., velocity U and turbulence intensity Tu) observed with the boundary layer code the agreement between the two codes is good. Computations performed by the University of Kentucky authors indicate that at the grid independent limit with a sharp leading edge, the predictions from the parabolic boundary layer code and an elliptic Navier-Stokes code are identical. With the exception of the T3A- test case, all the flat plate cases are in good agreement with the experimentally measured skin friction.

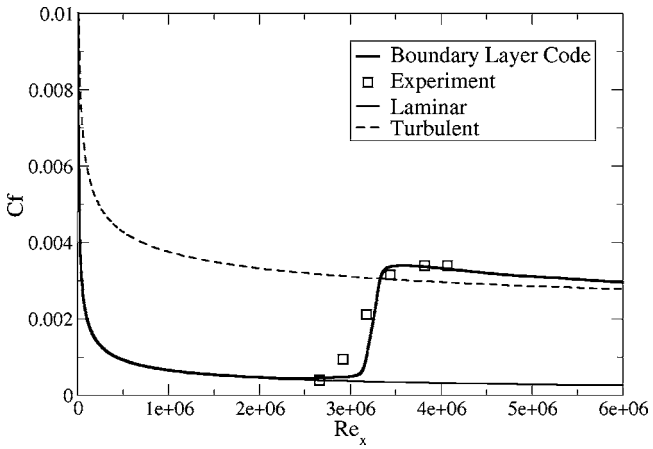

Fig. 10 Skin friction (*Cf*) for the Schubauer and Klebanof [18] test case (FSTI=0.18%)

The difference between the prediction and the experiment for the T3A- test is attributed to the effect of freestream turbulence length scale, which at present is not accounted for in the empirical correlations.

The remaining test cases in this paper have all been computed with the Navier-Stokes code CFX-5. The predicted skin friction for the T3C4 test case is shown in Fig. 11. This test case was used to calibrate the modification for separation-induced transition. The predicted skin friction with and without the modification is compared to the experimentally measured value. With the separation-induced transition modification the predicted boundary layer reattachment location is in good agreement with the experiment.

Figure 12 illustrates the contours of intermittency (γ), effective intermittency (γ_{eff}—Eq. (24)) and turbulence intensity Tu for the T3C4 test case near the laminar separation bubble. The effective intermittency is equal to the intermittency from the transport equation everywhere except in the laminar separation bubble where it is allowed to increase above one. This, in turn, results in excess production of turbulent kinetic energy, which forces the boundary layer to reattach. Through the s_1 constant, the reattachment location can be controlled. The larger the value of s_1 the shorter the reattachment length.

The normalized suction-side friction velocity for the Genoa test case is shown in Fig. 13. The onset of transition is predicted slightly early. Note however, that the two different measurements indicate also some experimental uncertainty in the location of transition onset. For this test case, the pressure side of the blade was completely laminar both in the experiment and the prediction.

5 Summary

A new framework for a correlation-based transition model has been developed that is built strictly on local variables and is thereby compatible with modern CFD methods. It utilizes transport equations for intermittency and momentum thickness Reynolds number. Part I [13] of this paper gave a detailed description of the mathematical formulation of the model and some of the basic test cases used for model validation including a 2D turbine blade. Part II details the validation studies that have been performed for a number of turbomachinery and aerodynamic test cases. In all cases, the agreement with the experiments was good and the authors believe that the current model is a significant step forward in engineering transition modeling. The present model formulation is very likely a starting point for the inclusion of numerous additional effects and flow regimes such as roughness, freestream turbulent length scale, streamline curvature, cross-flow transition, and Mach number effects.

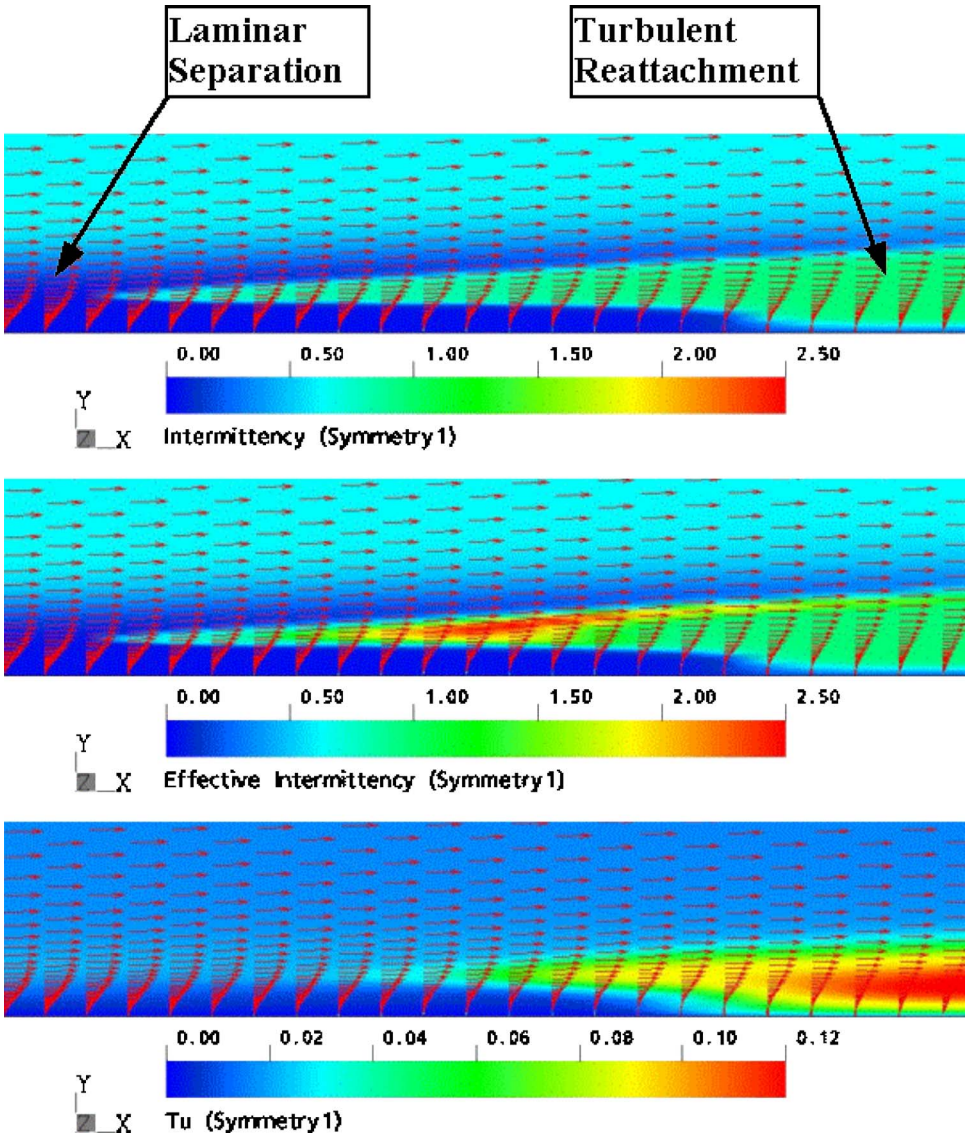

Fig. 12 Intermittency (γ, top), effective intermittency (γ_{eff}, middle), and turbulence intensity (Tu, bottom) for the T3C4 test case

Acknowledgment

The authors would like to acknowledge the support and technical contributions from Dr. William Solomon at GE Aircraft Engines. The model development and validation at ANSYS CFX was funded by GE Aircraft Engines and GE Global Research. The authors, Y. B. Suzen and P. G. Huang, are supported by NASA Glenn Research Center under Grant No. NCC3-590 and followed by Grant No. NCC3-1040. Additional support to the University of Kentucky was provided through a research grant from GE Global Research.

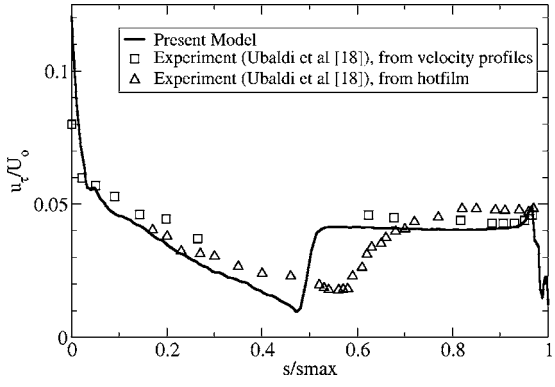

Fig. 13 Normalized wall friction velocity distributions (u_τ/U_o) on the suction side of the Genoa cascade Ubaldi [19]

Nomenclature

C_f = skin friction coefficient, $\tau/(0.5\rho U_{\text{ref}}^2)$
FSTI = freestream turbulence intensity (%), $100(2k/3)^{1/2}/U_{\text{ref}}$
k = turbulent kinetic energy
K = flow acceleration parameter
L = axial reference length
Re_x = Reynolds number, $\rho L U_{\text{ref}}/\mu$
Re_θ = momentum thickness Reynolds number, $\rho\theta U_0/\mu$
$\text{Re}_{\theta t}$ = transition onset momentum thickness Reynolds number (based on freestream conditions), $\rho\theta_t U_0/\mu$

$\tilde{\mathrm{Re}}_{\theta t}$ = local transition onset momentum thickness Reynolds number (obtained from a transport equation)
R_T = viscosity ratio
R_y = wall-distance based turbulent Reynolds number
R_v = vorticity Reynolds number
S = absolute value of strain rate, $(2S_{ij}S_{ij})^{1/2}$
S_{ij} = strain rate tensor, $0.5(\partial u_i/\partial x_j + \partial u_j/\partial x_i)$
Tu = turbulence intensity, $100(2k/3)^{1/2}/U$
U = local velocity
U_o = local freestream velocity
U_{ref} = inlet reference velocity
u' = local fluctuating streamwise velocity
$s/s_{\max}$ = arc length over total arc length
y = distance to nearest wall
y^+ = distance in wall coordinates, $\rho y \mu_\tau/\mu$
δ = boundary layer thickness
ε = turbulence dissipation rate
θ = momentum thickness
λ_θ = pressure gradient parameter, $(\rho\theta^2/\mu)(dU/ds)$
μ = molecular viscosity
μ_t = eddy viscosity
μ_τ = friction velocity
ρ = density
τ = wall shear stress
Ω = absolute value of vorticity, $(2\Omega_{ij}\Omega_{ij})^{1/2}$
Ω_{ij} = vorticity tensor, $0.5(\partial u_i/\partial x_j - \partial u_j/\partial x_i)$
ω = specific turbulence dissipation rate

Subscripts

t = transition onset
s = streamline

References

[1] Savill, A. M., 1993, "Some Recent Progress in the Turbulence Modelling of By-pass Transition," *Near-Wall Turbulent Flows*, R. M. C. So, C. G. Speziale, and B. E. Launder, eds. Elsevier, New York, p. 829.

[2] Savill, A. M., 1996, "One-Point Closures Applied to Transition," *Turbulence and Transition Modelling*, M. Hallbäck et al., eds., Kluwer, Dordrecht, pp. 233–268.

[3] Suzen, Y. B., Huang, P. G., Hultgren, L. S., and Ashpis, D. E., 2003, "Predictions of Separated and Transitional Boundary Layers Under Low-Pressure Turbine Airfoil Conditions Using an Intermittency Transport Equation," ASME J. Turbomach., **125**(3), pp. 455–464.

[4] Wilcox, D. C., 1993, *Turbulence Modeling for CFD*, DCW Industries, La Canada, CA.

[5] Langtry, R. B., and Sjolander, S. A., 2002, "Prediction of Transition for Attached and Separated Shear Layers in Turbomachinery," AIAA Paper No. AIAA-2002–3643.

[6] Abu-Ghannam, B. J., and Shaw, R., 1980, "Natural Transition of Boundary Layers-The Effects of Turbulence, Pressure Gradient, and Flow History," J. Mech. Eng. Sci., **22**(5), pp. 213–228.

[7] Suzen, Y. B., Xiong, G., and Huang, P. G., 2000, "Predictions of Transitional Flows in Low-Pressure Turbines Using an Intermittency Transport Equation," AIAA Paper No. AIAA-2000–2654.

[8] Steelant, J., and Dick, E., 2001, "Modeling of Laminar-Turbulent Transition for High Freestream Turbulence," ASME J. Fluids Eng., **123**, pp. 22–30.

[9] Menter, F. R., Esch, T., and Kubacki, S., 2002, "Transition Modelling Based on Local Variables," 5th International Symposium on Turbulence Modeling and Measurements, Mallorca, Spain.

[10] Mayle, R. E., 1991, "The Role of Laminar-Turbulent Transition in Gas Turbine Engines," ASME J. Turbomach., **113**, pp. 509–537.

[11] Van Driest, E. R., and Blumer, C. B., 1963, "Boundary Layer Transition: Freestream Turbulence and Pressure Gradient Effects," AIAA J., **1**(6), pp. 1303–1306.

[12] Menter, F. R., 1994, "Two-Equation Eddy-Viscosity Turbulence Models for Engineering Applications," AIAA J., **32**(8), pp. 1598–1605; 2002, AIAA J., **40**(2) pp. 254–266.

[13] Langtry, R. B., Menter, F. R., Likki, S. R., Suzen, Y. B., Huang, P. G., and Völker, S., 2006, "A Correlation-Based Transition Model Using Local Variables—Part II: Test Cases and Industrial Applications," ASME J. Turbomach., **128**(3), pp. 423–434.

[14] Drela, M., 1995, "MISES Implementation of Modified Abu-Ghannam and Shaw Transition Criteria," MIT Aero-Astro.

[15] Fashifar, A., and Johnson, M. W., 1992, "An Improved Boundary Layer Transition Correlation," ASME Paper No. ASME-92-GT-245.

[16] Schubauer, G. B., and Skramstad, H. K., 1948, "Laminar-Boundary-Layer Oscillations and Transition on a Flat Plate," NACA Report No. 909.

[17] Sinclair, C., and Wells, C. S., Jr., 1967, "Effects of Freestream Turbulence on Boundary-Layer Transition," AIAA J., **5**(1), pp. 172–174.

[18] Schubauer, G. B., and Klebanoff, P. S., 1955, "Contribution on the Mechanics of Boundary Layer Transition," NACA TN 3489.

[19] Ubaldi, M., Zunino, P., Campora, U., and Ghiglione, A., 1996, "Detailed Velocity and Turbulence Measurements of the Profile Boundary Layer in a Large Scale Turbine Cascade," ASME Paper No. ASME-96-GT-42.

R. B. Langtry
e-mail: robin.langtry@ansys.com

F. R. Menter
e-mail: florian.menter@ansys.com

ANSYS CFX Germany,
12 Staudenfeldweg,
Otterfing, Bavaria 83624,
Germany

S. R. Likki
Department of Mechanical Engineering,
University of Kentucky,
216A RGAN Building,
Lexington, KY 40502–0503
e-mail: srinivas@engr.uky.edu

Y. B. Suzen
Department of Mechanical Engineering,
North Dakota State University,
Dolve Hall 111,
P.O. Box 5285,
Fargo, ND 58105
e-mail: suzen@engr.uky.edu

P. G. Huang
Department of Mechanical Engineering,
University of Kentucky,
216A RGAN Building,
Lexington, kY 40502-0503
e-mail: ghuang@engr.uky.edu

S. Völker
General Electric Company,
One Research Circle, ES-221,
Niskayuna, NY 12309
e-mail: voelker@crd.ge.com

A Correlation-Based Transition Model Using Local Variables—Part II: Test Cases and Industrial Applications

A new correlation-based transition model has been developed, which is built strictly on local variables. As a result, the transition model is compatible with modern computational fluid dynamics (CFD) methods using unstructured grids and massive parallel execution. The model is based on two transport equations, one for the intermittency and one for the transition onset criteria in terms of momentum thickness Reynolds number. The proposed transport equations do not attempt to model the physics of the transition process (unlike, e.g., turbulence models), but form a framework for the implementation of correlation-based models into general-purpose CFD methods. Part I of this paper (Menter, F. R., Langtry, R. B., Likki, S. R., Suzen, Y. B., Huang, P. G., and Völker, S., 2006, ASME J. Turbomach., ***128****(3), pp. 413–422) gives a detailed description of the mathematical formulation of the model and some of the basic test cases used for model validation. Part II (this part) details a significant number of test cases that have been used to validate the transition model for turbomachinery and aerodynamic applications, including the drag crisis of a cylinder, separation-induced transition on a circular leading edge, and natural transition on a wind turbine airfoil. Turbomachinery test cases include a highly loaded compressor cascade, a low-pressure turbine blade, a transonic turbine guide vane, a 3D annular compressor cascade, and unsteady transition due to wake impingement. In addition, predictions are shown for an actual industrial application, namely, a GE low-pressure turbine vane. In all cases, good agreement with the experiments could be achieved and the authors believe that the current model is a significant step forward in engineering transition modeling.* [DOI: 10.1115/1.2184353]

Introduction

The location of the onset and extent of transition are of major importance in turbomachinery design applications, where the wall shear stress or wall heat transfer are of interest. In addition, blockage and loss, which are important criteria for assessing turbomachinery performance, are strongly affected by transition. Matters are further complicated by the fact that a number of fundamentally different transition mechanisms can be found in turbomachinery flows, including bypass transition, separation-induced transition, wake-induced transition, and shock-induced transition [1].

Turbomachinery blades typically operate at Reynolds numbers where the laminar boundary layer may extend significantly downstream from the leading edge. It has been observed that the boundary layers on the pressure side of turbine blades are often entirely laminar [1]. The transition process can also have a strong influence on the separation behavior of boundary layers. For example, compressor performance can be affected by separation-induced transition, where the laminar boundary layer separates and after transitioning, reattaches fully turbulent downstream of the separation point [2]. Rotor-stator interactions are an example for wake-induced transition, where the transition region of the downstream blade row becomes unsteady due to wake-passing effects [3]. In all of the above examples, a fully turbulent solution will overpredict the wall shear stress and heat transfer distributions. In addition, a fully turbulent solution will not predict blockage and loss correctly, which will lead to incorrect engine performance estimates.

Despite its obvious importance for predicting turbomachinery flows, transition is usually not accounted for in Reynolds-averaged Navier-Stokes (RANS) methods using statistical turbulence models. If transition is accounted for, additional information has to be supplied in order to simulate the transition process. Most commonly, the additional information consists of experimental transition correlations. These correlations typically relate flow parameters like turbulence intensity and pressure gradient coefficients to the momentum thickness Reynolds number at which

Contributed by the International Gas Turbine Institute (IGTI) of ASME for publication in the JOURNAL OF TURBOMACHINERY. Manuscript received October 1, 2003; final manuscript received March 1, 2004. IGTI Review Chair: A. J. Strazisar. Paper presented at the International Gas Turbine and Aeroengine Congress and Exhibition, VIenna, Austria, June 13–17, 2004, Paper No. 2004-GT-53434.

Table 1 Summary of all test case inlet conditions

Case	U inlet (m/s)	FSTI (%) Inlet / L.E.	μ_t/μ	ρ (kg/m^3)	μ (kg/ms)
Pak-B cascade	4.7, 7.05, 9.4	0.08/0.08	10, 10, 10	1.225	1.81×10^{-5}
Pak-B cascade	4.7, 7.05, 9.4	2.35/1.6	6.5, 9.75, 13	1.225	1.81×10^{-5}
Pak-B cascade	4.7, 7.05, 9.4	6.0/2.85	15, 22.5, 30	1.225	1.81×10^{-5}
Low-Tu airfoil	74	1.0/0.02	1	1.25	1.84×10^{-5}
Zierke (PSU), −1.5 deg	32.9	0.18/0.18	15.0	1.2	1.81×10^{-5}
VKI MUR 241	61.8	6.5/6.17	1000.0	2.69	2.388×10^{-5}
VKI MUR 116	61.8	1.0/0.9	11.0	2.69	2.388×10^{-5}
T3LB	5	0.64/0.63	1.09	1.2	1.8×10^{-5}
T3LC	5	2.39/2.06	3.4	1.2	1.8×10^{-5}
T3LD	5	5.64/5.34	18.92	1.2	1.8×10^{-5}
Drag crisis of a cylinder		0.45/0.3		1.2	1.8×10^{-5}
RGW	95.5	1.25/0.65	2	1.2	1.8×10^{-5}
T106 cascade unsteady wake/blade interaction	7.2	0.1/0.1	1	1.2	1.87×10^{-5}
GE LPT	172	5.0	31	1.53	1.44×10^{-3}

transition will occur. However, current correlation-based transition models are incompatible with modern computational fluid dynamics (CFD) methods as they rely on nonlocal variables, such as the momentum thickness Reynolds number, turbulence intensity at the edge of the boundary layer, or shape factors just to name a few [4,5]. These quantities are not readily available in modern CFD codes, particularly when unstructured grids and scalable parallelization are used. In addition, current correlation based methods are inherently two-dimensional. Important effects, such as endwall boundary layers or leakage flows, cannot be included. On the other hand, correlation-based methods are very attractive, as they allow the inclusion of experimental evidence.

The present paper describes a correlation-based transition model, which is built strictly on local variables and thereby compatible with modern CFD methods. It is based on transport equations for intermittency and momentum thickness Reynolds number. Part I of this paper [6] gives a detailed description of the mathematical formulation of the model and some of the basic test cases used for model validation. Part II will focus on the application of the transition model to turbomachinery test cases. This includes two-dimensional (2D) and three-dimensional (3D) test cases as well as actual industrial problems.

Model Formulation

In Part I [6], a transport equation for the intermittency γ, which can be used to trigger transition locally, has been described in detail. The intermittency function is coupled with the shear stress transport (SST) turbulence model [7]. It is used to turn on the production term of the turbulent kinetic energy downstream of the transition point. In addition to the transport equation for the intermittency, a second transport equation is solved in terms of the transition onset momentum-thickness Reynolds number $\tilde{\mathrm{Re}}_{\theta t}$. This is done in order to capture the nonlocal influence of the turbulence intensity, which changes due to the decay of the turbulence kinetic energy in the freestream, as well as due to changes in the freestream velocity outside the boundary layer. This additional transport equation is an essential part of the model as it ties the empirical correlation to the onset criteria in the intermittency equation and allows the models use in general geometries and over multiple blades, without interaction from the user.

The formulation of the intermittency equation has also been extended to account for the rapid onset of transition caused by separation of the laminar boundary layer. In addition, the model can be fully calibrated with internal or proprietary transition onset and transition length correlations. The correlations can also be extended to flows at low freestream turbulence intensity or to flows with cross-flow instability. The model formulation therefore offers a flexible environment for engineering transition predictions that is fully compatible with the infrastructure of modern CFD methods. The present transition model formulation is described very briefly for completeness, a detailed description can be found in the companion paper [6].

The transport equation for the intermittency γ reads

$$\frac{\partial(\rho\gamma)}{\partial t}+\frac{\partial(\rho U_j\gamma)}{\partial x_j}=P_{\gamma1}-E_{\gamma1}+P_{\gamma2}-E_{\gamma2}+\frac{\partial}{\partial x_j}\left[\left(\mu+\frac{\mu_t}{\sigma_f}\right)\frac{\partial\gamma}{\partial x_j}\right] \tag{1}$$

The transition sources are defined as follows:

$$P_{\gamma1}=F_{\text{length}}\rho S[\gamma F_{\text{onset}}]^{c_{a1}} \tag{2}$$

$$E_{\gamma1}=c_{e1}P_{\gamma1}\gamma \tag{3}$$

where S is the strain rate magnitude. F_{length} is an empirical correlation that controls the length of the transition region. The destruction/relaminarization sources are defined as follows:

$$P_{\gamma2}=c_{a2}\rho\Omega\gamma F_{\text{turb}} \tag{4}$$

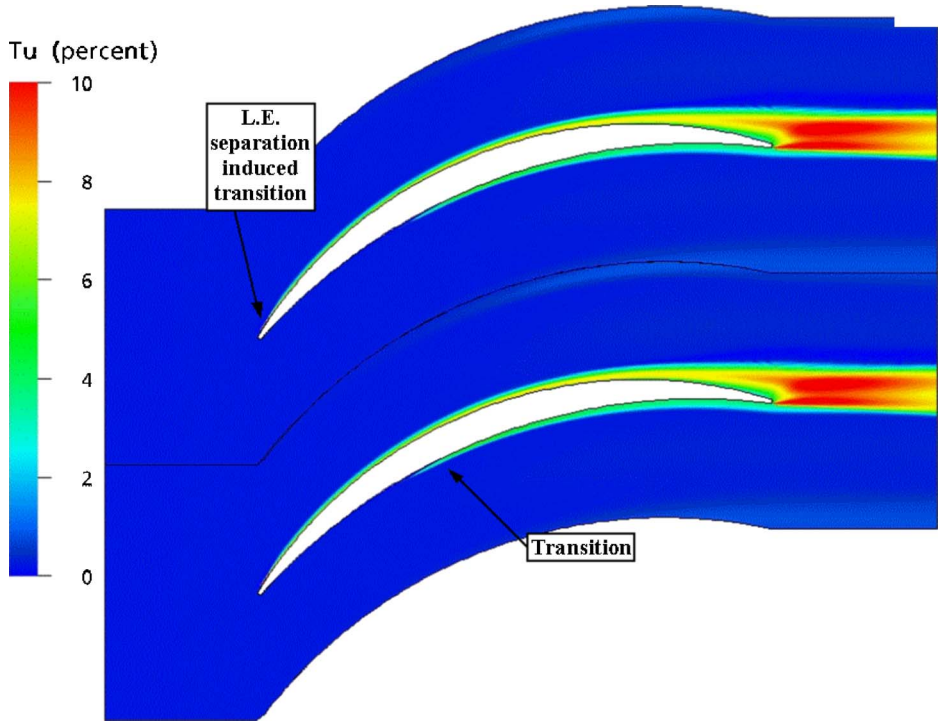

Fig. 1 Contours of turbulence intensity Tu for the Zierke (PSU) compressor

$$E_{\gamma 2} = c_{e2} P_{\gamma 2} \gamma \tag{5}$$

where Ω is the vorticity magnitude. The transition onset is controlled by the following functions:

$$\mathrm{Re}_V = \frac{\rho y^2 S}{\mu} \tag{6}$$

$$F_{\text{onset 1}} = \frac{\mathrm{Re}_v}{2.193\,\mathrm{Re}_{\theta c}} \tag{7}$$

$$F_{\text{onset 2}} = \min[\max(F_{\text{onset 1}}, F^4_{\text{onset 1}}), 2.0] \tag{8}$$

$$R_T = \frac{\rho k}{\mu \omega} \tag{9}$$

$$F_{\text{onset 3}} = \max\left[1 - \left(\frac{R_T}{2.5}\right)^3, 0\right] \tag{10}$$

$$F_{\text{onset}} = \max(F_{\text{onset 2}} - F_{\text{onset 3}}, 0) \tag{11}$$

$$F_{\text{turb}} = e^{-(R_T/4)^4} \tag{12}$$

$\mathrm{Re}_{\theta c}$ is the critical Reynolds number where the intermittency first starts to increase in the boundary layer. This occurs upstream of the transition Reynolds number, $\tilde{\mathrm{Re}}_{\theta t}$, and the difference between the two must be obtained from an empirical correlation. At the present time the F_{length} and $\mathrm{Re}_{\theta c}$ correlations are proprietary and are not given in this paper.

The constants for the intermittency equation are

$$c_{e1} = 1.0; \quad c_{a1} = 0.5$$

$$c_{e2} = 50; \quad c_{a2} = 0.03; \quad \sigma_f = 1.0$$

The modification for separation-induced transition is defined below.

$$\gamma_{\text{sep}} = \min\left(s_1 \max\left[\left(\frac{\mathrm{Re}_v}{2.193\,\mathrm{Re}_{\theta c}}\right) - 1, 0\right] F_{\text{reattach}}, 5\right) F_{\theta t} \quad s_1 = 8 \tag{13}$$

$$F_{\text{reattach}} = e^{-(R_T/15)^4} \tag{14}$$

$$\gamma_{\text{eff}} = \max(\gamma, \gamma_{\text{sep}}) \tag{15}$$

The boundary condition for γ at a wall is zero normal flux while for an inlet γ is equal to 1.0.

The transport equation for the transition momentum thickness Reynolds number $\tilde{\mathrm{Re}}_{\theta t}$ reads

$$\frac{\partial(\rho \tilde{\mathrm{Re}}_{\theta t})}{\partial t} + \frac{\partial(\rho U_j \tilde{\mathrm{Re}}_{\theta t})}{\partial x_j} = P_{\theta t} + \frac{\partial}{\partial x_j}\left[\sigma_{\theta t}(\mu + \mu_t)\frac{\partial \tilde{\mathrm{Re}}_{\theta t}}{\partial x_j}\right] \tag{16}$$

The source term is defined as follows:

$$P_{\theta t} = c_{\theta t}\frac{\rho}{t}(\mathrm{Re}_{\theta t} - \tilde{\mathrm{Re}}_{\theta t})(1.0 - F_{\theta t}) \tag{17}$$

$$t = \frac{500\mu}{\rho U^2} \tag{18}$$

$$F_{\theta t} = \min\left\{\max\left[F_{\text{wake}} e^{-(y/\delta)^4}, \; 1.0 - \left(\frac{\gamma - 1/c_{e2}}{1.0 - 1/c_{e2}}\right)^2\right], 1.0\right\} \tag{19}$$

$$\theta_{BL} = \frac{\tilde{\mathrm{Re}}_{\theta t}\mu}{\rho U} \quad \delta_{BL} = \frac{15}{2}\theta_{BL} \quad \delta = \frac{50\Omega y}{U}\delta_{BL} \tag{20}$$

$$\mathrm{Re}_\omega = \frac{\rho \omega y^2}{\mu} \tag{21}$$

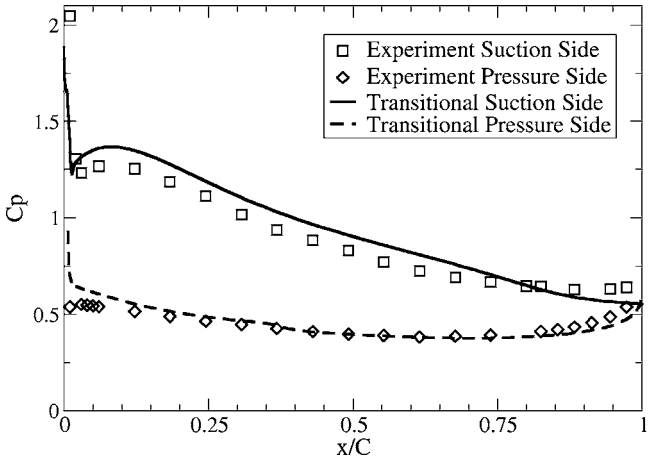

Fig. 2 *Cp* distribution for the Zierke (PSU) compressor

$$F_{\text{wake}} = e^{-[\text{Re}_\omega/(1E+5)]^2} \tag{22}$$

The model constants for the $\widetilde{\text{Re}}_{\theta t}$ equation are

$$c_{\theta t} = 0.03; \quad \sigma_{\theta t} = 10.0$$

The boundary condition for $\widetilde{\text{Re}}_{\theta t}$ at a wall is zero flux. The boundary condition for $\widetilde{\text{Re}}_{\theta t}$ at an inlet should be calculated from the empirical correlation based on the inlet turbulence intensity. The empirical correlation is defined as

$$\text{Re}_{\theta t} = 803.73[\text{Tu} + 0.6067]^{-1.027} F(\lambda_\theta, K) \tag{23}$$

$$F(\lambda_\theta, K) = 1 - [-10.32\lambda_\theta - 89.47\lambda_\theta^2 - 265.51\lambda_\theta^3]e^{-\text{Tu}/3.0}, \quad \lambda_\theta \leq 0 \tag{24}$$

$$F(\lambda_\theta, K) = 1 + [0.0962[K10^6] + 0.148[K10^6]^2 + 0.0141[K10^6]^3] \times (1 - e^{-\text{Tu}/1.5}) + 0.556[1 - e^{[-23.9\lambda_\theta]}]e^{-\text{Tu}/1.5}, \quad \lambda_\theta > 0 \tag{25}$$

The empirical correlation is a function of Thwaites' pressure gradient coefficient λ_θ and the pressure gradient coefficient K

$$\lambda_\theta = (\theta^2/v)dU/ds \tag{26}$$

$$K = (v/U^2)dU/ds \tag{27}$$

where dU/ds is the acceleration along in the streamwise direction

$$U = (u^2 + v^2 + w^2)^{1/2} \tag{28}$$

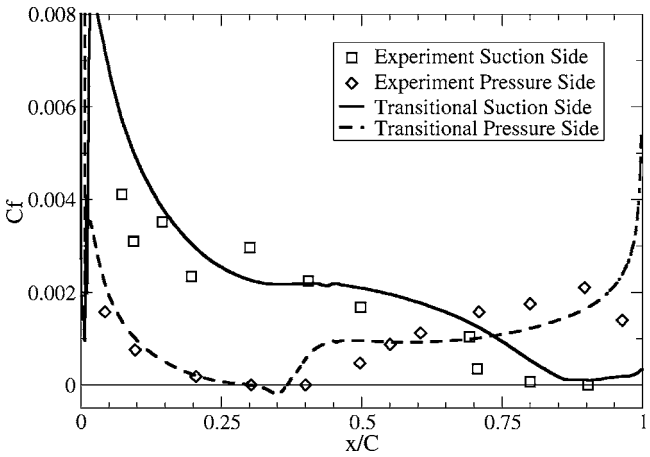

Fig. 3 *Cf* distribution for the Zierke (PSU) compressor

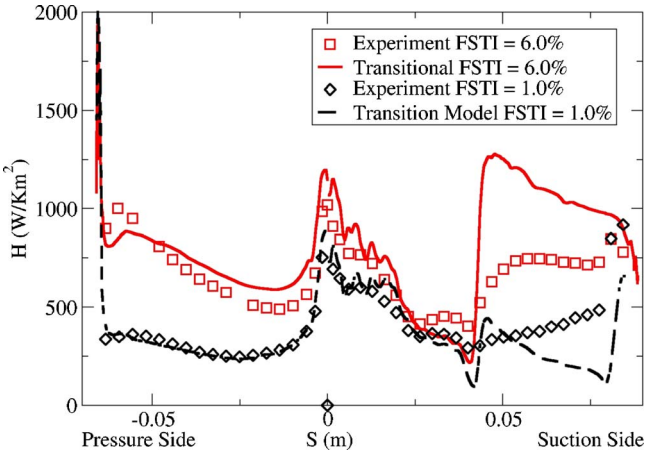

Fig. 4 Heat transfer for the VKI MUR241 (FSTI=6.0%) and MUR116 (FSTI=1.0%) test cases

$$\frac{dU}{ds} = (u/U)\frac{dU}{dx} + (v/U)\frac{dU}{dy} + (w/U)\frac{dU}{dz} \tag{29}$$

For numerical robustness, the acceleration parameters and the empirical correlation should be limited as follows:

$$-0.1 \leq \lambda_\theta \leq 0.1 \tag{30}$$

$$-3 \times 10^{-6} \leq K \leq 3 \times 10^{-6} \tag{31}$$

$$\text{Re}_{\theta t} \geq 20 \tag{32}$$

It should also be stressed that the empirical correlation is used only in the source term (Eq. (17)) of the transport equation for transition onset momentum thickness Reynolds number.

The transition model interacts with the turbulence model as follows:

$$\frac{\partial}{\partial t}(\rho k) + \frac{\partial}{\partial x_j}(\rho u_j k) = \tilde{P}_k - \tilde{D}_k + \frac{\partial}{\partial x_j}\left((\mu + \sigma_k \mu_t)\frac{\partial k}{\partial x_j}\right) \tag{33}$$

$$\frac{\partial}{\partial t}(\rho\omega) + \frac{\partial}{\partial x_j}(\rho u_j \omega) = \alpha\frac{P_k}{v_t} - D_\omega + Cd_\omega + \frac{\partial}{\partial x_j}\left((\mu + \sigma_k \mu_t)\frac{\partial \omega}{\partial x_j}\right) \tag{34}$$

$$\tilde{P}_k = \gamma_{\text{eff}} P_k \tag{35}$$

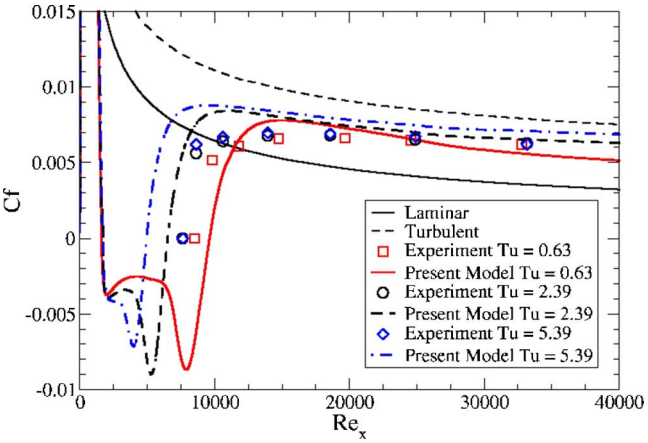

Fig. 5 Skin friction *Cf* for the T3LB, T3LC, and T3LD test cases (freestream turbulence intensity=0.63%, 2.39%, and 5.39%)

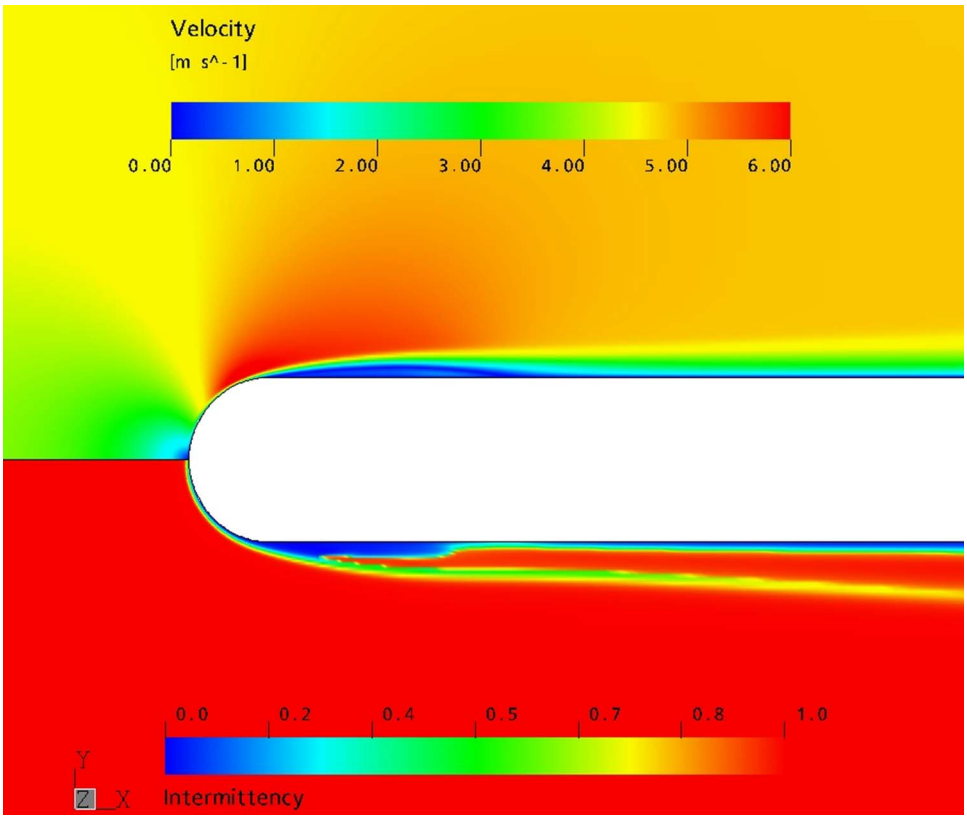

Fig. 6 Contours of velocity (top) and intermittency (bottom) due to separation induced transition on a circular leading edge for the T3LC test case

$$\tilde{D}_k = \min[\max(\gamma_{\text{eff}}, 0.1), 1.0] D_k \tag{36}$$

$$R_y = \frac{\rho y \sqrt{k}}{\mu} \tag{37}$$

$$F_3 = e^{-(R_y/120)^8} \tag{38}$$

$$F_1 = \max(F_{1\ \text{orig}}, F_3) \tag{39}$$

where P_k and D_k are the original production and destruction terms for the SST model and $F_{1\ \text{orig}}$ is the original SST blending function described in Menter [2].

In order to capture the laminar and transitional boundary layers correctly, the grid must have a y^+ of ~ 1. If the y^+ is too large (i.e., >5) than the transition onset location moves upstream with increasing y^+. All simulations have been performed with a bounded second-order upwind biased discretization for the mean flow, turbulence, and transition equations.

Results and Discussion

The rest of the paper describes the numerical results for a wide variety of validation test cases, including the drag crisis of a cylinder [8], separation-induced transition on a circular leading edge (T3L, [9]), and unsteady transition due to wake impingement (T106, [3]). In addition, the predicted transition onset location for an airfoil at very low freestream turbulence intensity is compared to experimental results and the XFOIL code that is often used to predict natural transition. Turbomachinery test cases include a highly loaded compressor cascade (PSU, [10]), a low-pressure turbine blade (Pak-B, [4]), a transonic turbine guide vane cascade (VKI MUR, [11]), and a 3D annular compressor cascade (RGW, [12]). As well, results are shown for an actual industrial application, namely, a GE low-pressure turbine (LPT). All simulations have been computed with CFX-5, except for the Pak-B and T106 cases, which where computed with an in house N-S code developed by the University of Kentucky authors. A summary of the inlet conditions for all the test cases described in this paper is given in Table 1. Where possible, the inlet viscosity ratio was specified in order to match the experimentally measured decay rate of freestream turbulence intensity (FSTI).

Zierke & Deutsch Compressor Cascade. Contours of turbulence intensity (Tu) for the Zierke (PSU) compressor are shown in Fig. 1. On the suction side, transition occurs at the leading edge due to a small leading edge separation bubble. On the pressure side, transition occurs at about midchord. The pressure *Cp* and skin friction *Cf* distribution are shown in Figs. 2 and 3. There appears to be a significant amount of scatter in the experimental data; however, in principal, the transition model is predicting the major flow features correctly (i.e., fully turbulent suction side, transition at midchord on the pressure side). One important issue to note is the effect of streamwise grid resolution on resolving the leading edge laminar separation and subsequent transition on the suction side. If the number of streamwise nodes clustered around the leading edge is too low, the model cannot resolve the rapid transition and a laminar boundary layer on the suction side is the result. For the present study, 60 streamwise nodes where used in between the leading edge and the x/C equal to 0.1 location.

Von Karman Institute Turbine Cascade. The surface heat transfer for the VKI MUR 241 (FSTI=6.0%) and MUR 116 (FSTI=1.0%) test cases is shown in Fig. 4. The strong acceleration on the suction side for the MUR 241 case keeps the flow laminar until a weak shock at midchord, whereas for the MUR 116 case the flow is laminar until right before the trailing edge. Downstream of transition there appears to be a significant amount of error between the predicted turbulent heat transfer and the mea-

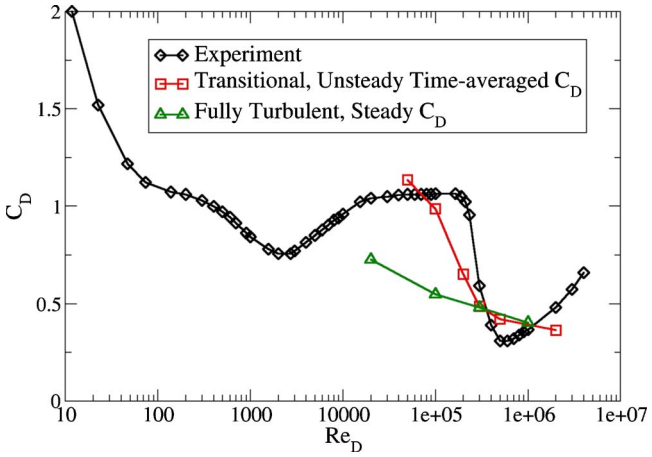

Fig. 7 Drag crisis of a cylinder in cross-flow

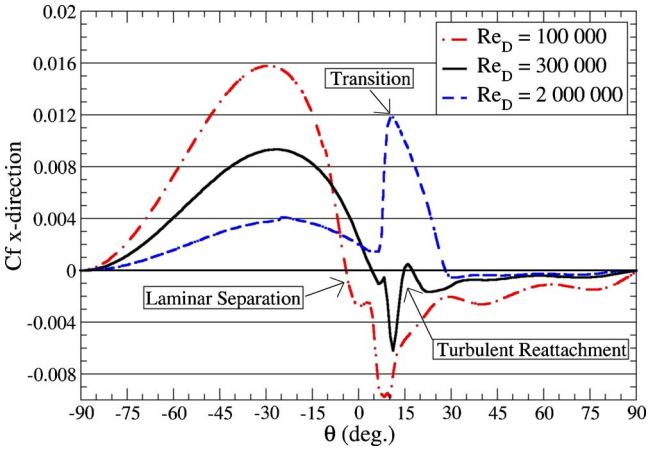

Fig. 8 Predicted instantaneous skin friction *Cf* for a cylinder in cross-flow at Reynolds numbers Re_D of 100,000, 300,000, and 2,000,000

sure value. It is possible that this is the result of a Mach number effect on the transition length [5]. At present, no attempt has been made to account for this effect in the model. It can be incorporated in future correlations, if found consistently important.

The pressure-side heat transfer is of particular interest for this case. For both cases, transition did not occur on the pressure side; however, the heat transfer was significantly increased for the high turbulence intensity case. It is believed that large freestream levels of turbulence can buffet the laminar boundary layer and increase the heat transfer and skin friction. From a modeling standpoint, the effect was caused by the large freestream viscosity ratio necessary for MUR 241 to keep the turbulence intensity from decaying below 6%, which is the freestream value quoted in the experiment [11]. The enhanced heat transfer on the pressure side was also present in the experiment and the effect appears to be physical.

Coupland Flat Plate. The T3L series of test cases are commonly used to validate a transition models ability to predict separation induced transition on a circular leading edge subjected to varying turbulence intensities. The results obtained with the present transition model are shown in Figs. 5 and 6 (note that no negative wall shear stresses could be measured in the experiments and these where manually set to zero based on the hotwire signal). In general, the predicted reattachment location is in reasonably good agreement with the location measured in the experiment. The model captured the size of the laminar separation bubble due to freestream turbulence intensities of 0.63% and 2.39%. For the freestream turbulence intensity of 5.39%, the predicted reattachment is too early; however, the error is difficult to quantify without an additional experimental point in the reattaching region.

A contour plot of velocity (top) and intermittency (bottom) is shown in Fig 6. Near the wall in the viscous sublayer, the intermittency is always small because the viscosity ratio is small and as a result the destruction terms (Eqs. (4) and (5)) of the intermittency equation are active. This has not been found to have any effect on the turbulent solution. For this case, there is also a region at the outer boundary layer edge where the intermittency is approximately equal to 0.5. This is caused by the large laminar separation upstream of the reattachment point. As the turbulent boundary layer thickness increases this artifact disappears downstream.

Cylinder in Cross-Flow. One of the most challenging applications for any turbulence closure level is the prediction of the drag crisis of a cylinder in crossflow (see LES results of [13]). Even on a RANS level, this simulation would require a fully unsteady simulation and most likely even a partial resolution of the 3D turbulent structures in the wake. In order to reduce the numerical effort, the current simulations with the transition model have been computed in unsteady mode on a 2D grid. Because of time constraints, the fully turbulent simulations have been obtained with symmetric steady-state simulations.

The predicted drag coefficient for a varying Reynolds number is shown in Fig. 7. Although the agreement with experiments is not perfect, it appears that the transition model can, in principle, predict the appropriate Reynolds number range at which the sepa-

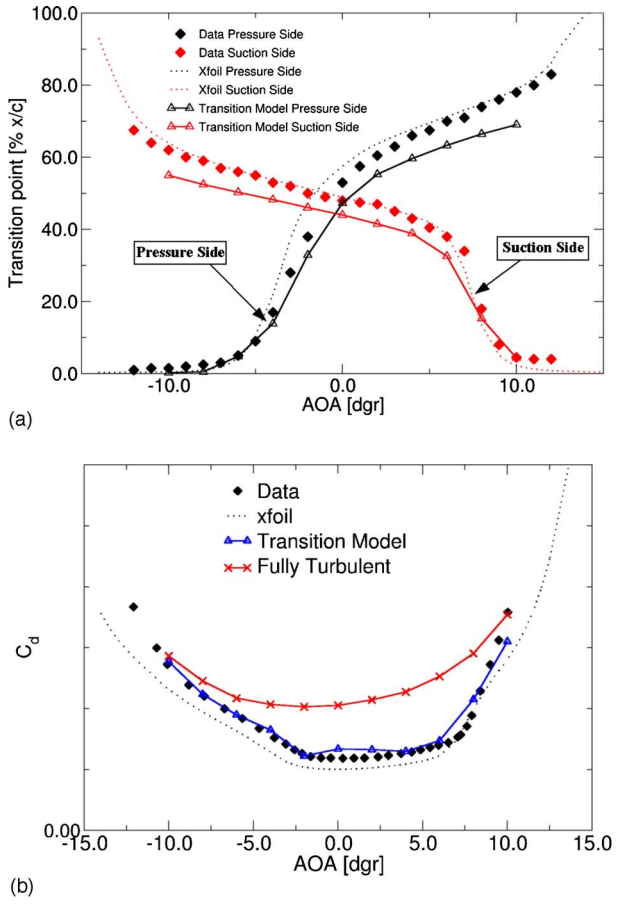

Fig. 9 Predicted transition location (*x/C*) and drag coefficient as a function of angle of attack for a wind turbine airfoil

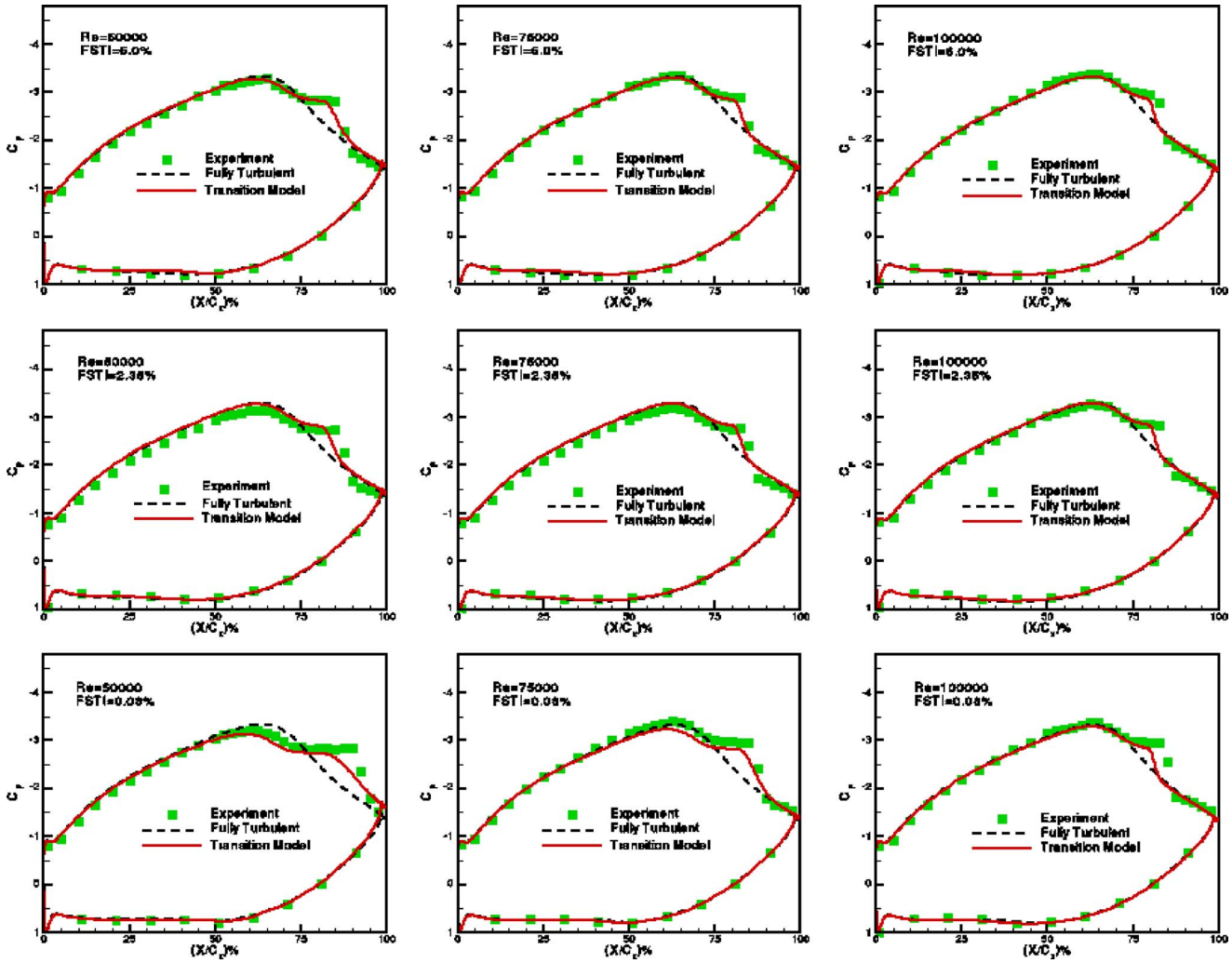

Fig. 10 Predicted blade loading for the Pak-B low-pressure turbine at various freestream turbulence intensities (FSTI) and Reynolds numbers

ration on the cylinder switches from a laminar separation to a turbulent one. For the present simulations, only about 30 time steps per vortex shedding period have been used in the unsteady simulations. It is possible that smaller time steps are required to properly capture the drag coefficient. Instantaneous skin friction distributions as predicted by the transition model for various Reynolds numbers are shown in Fig. 8. The results are for three different flow regimes, demonstrating laminar separation, laminar separation with turbulent reattachment, and finally, transition before the separation point. Note that these effects are beyond most engineering transition models used today.

Wind Turbine Airfoil. The testcase geometry is a 2D airfoil section, as typically used for GE wind-turbine blades. It operates in a low FSTI environment with a turbulence intensity of only around 0.02% at the leading edge, resulting in a natural transition process. As the correlations used in the current model asymptote properly to low-FSTI data, it is still possible to compute such cases. Transition locations versus angle of attack are shown in Fig. 9(*a*). Wind tunnel results and XFOIL (v6.8) predictions are plotted for comparison. The experimental data were obtained using a stethoscope method. In general, the transition model captures the dependence of the transition location on the angle of attack in good agreement with the data. Nevertheless, transition is predicted to occur slightly too far upstream for all angles of attack. One possible explanation for this behavior is that the transition model in its current form—including the underlying correlations—was developed mainly for internal turbomachinery. As such, little attention was paid to turbulence length-scale effects, which are likely to play an important role in predicting transition for low-speed external flows, such as wind turbine airfoils. Note that this issue can be addressed by enhancing the transition correlations for the current applications. Figure 9(*b*) shows the predicted drag coefficient as a function of angle of attack. Included are results from a transitional computation using the XFOIL code and from fully turbulent simulations. Clearly, the drag coefficient predictions from the transitional computation show significant improvements over the fully turbulent computation for all angles of attack.

Pak-B Cascade. Huang et al. [4] conducted experiments on the PAK-B blade cascade for a range of Reynolds numbers and turbulence intensities. Experiments were performed for Reynolds numbers of 50,000, 75,000, and 100,000 based on inlet velocity and axial chord length, with turbulence intensities of 0.08%, 2.35%, and 6.0% (which correspond to values of 0.08%, 1.6%, and 2.85% at the leading edge of the blade). The computed pressure coefficient distributions are compared to experimental data along with the fully turbulent computations in Fig. 10. In this figure, the comparisons are organized such that the horizontal axis denotes the Reynolds number, whereas the vertical axis corresponds to the freestream turbulence intensity. The most important feature of this testcase is the extent of the separation bubble on the

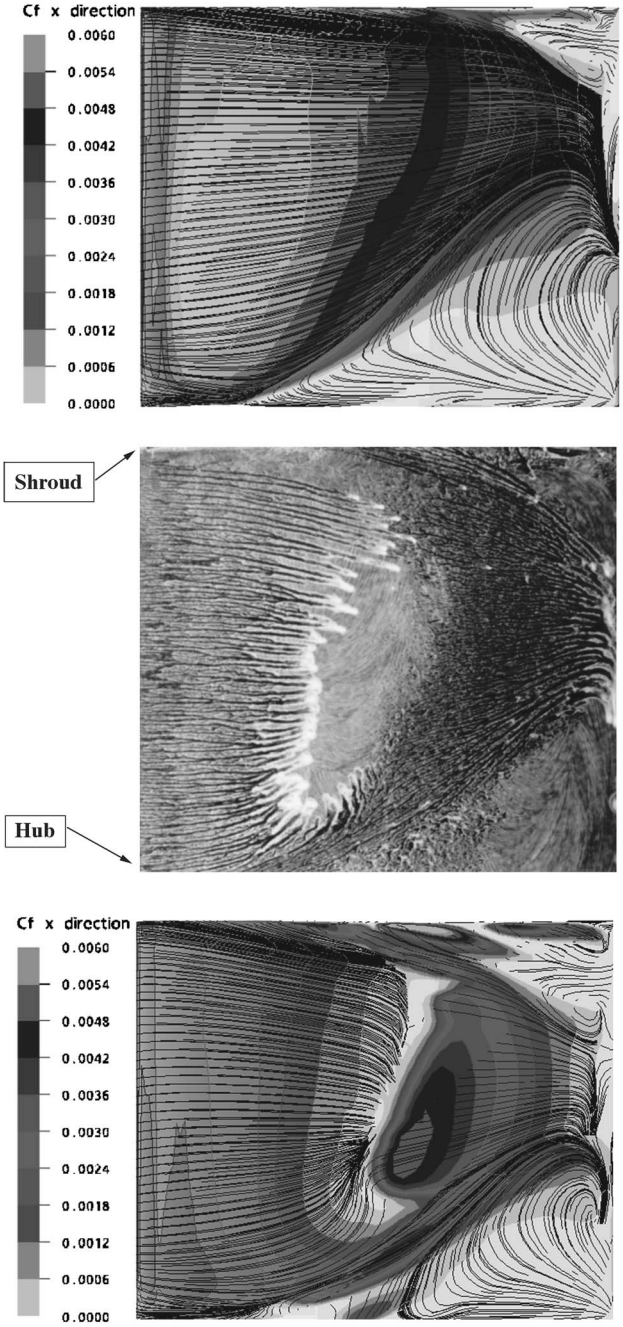

Fig. 11 Fully turbulent (top) and transitional (bottom) skin friction on the suction side of the 3D RGW compressor cascade compared to experimental oil flow visualization (middle, from Shulz and Galas [12], Institute of Jet Propulsion and Turbomachinery, RWTH Aachen University)

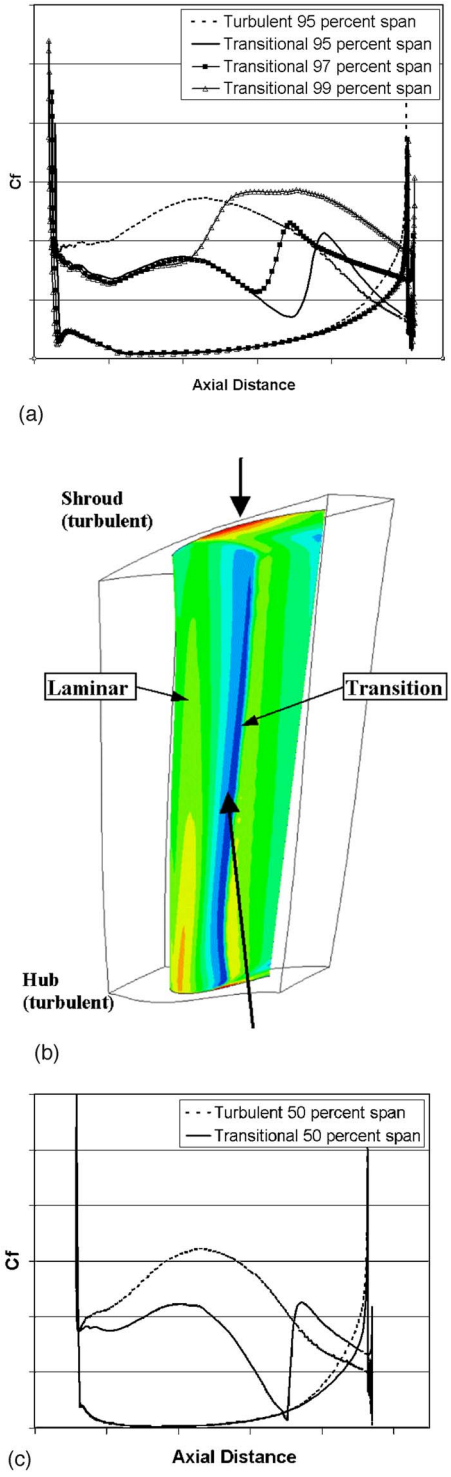

Fig. 12 Predicted skin friction (*Cf*) for the 3D GE low-pressure stator guide vane

suction side, characterized by the plateau in the pressure distribution. The size of the separation bubble is a complex function of the Re number and the FSTI value. The computations with the transition model compare well to the experimental data for all cases considered, illustrating the ability of the model to capture the effects of Reynolds number variations, FSTI, and flow separation on transition over a wide range of flow conditions.

RGW Compressor Cascade. The next test case is the RGW annular compressor [12]. It is a fully three-dimensional flow, including sidewall boundary layers originating upstream of the blade. This flow topology poses a major challenge to standard correlation-based transition models, as complex logic would be required to distinguish between the different boundary layers [2]. Figure 11 shows a comparison of the simulations on the suction side of the blade with an experimental oil-flow picture. For comparison, a fully turbulent flow simulation is also included. It can be seen that the transition model captures the complex flow topology of the experiments in good qualitative agreement with the data. A comparison between the transition model and the fully turbulent simulation shows the strong influence of the laminar

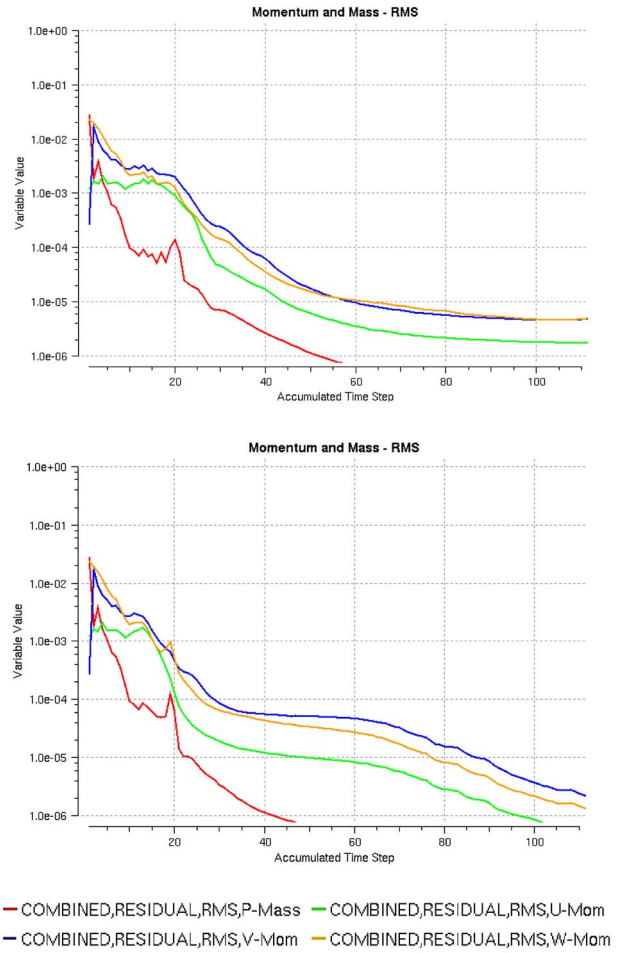

Fig. 13 Convergence history for the GE low-pressure stator vane for a fully turbulent (top) and transitional (bottom) computation

flow separation on the sidewall boundary layer separation. The flow separation on the shroud is significantly reduced by the displacement effect of the separation bubble in the transitional simulation. As a result, the loss coefficient Yp in the fully turbulent simulation of 0.19 is much higher than the experimental value of 0.097. The simulation with the transition model gives a value of 0.11 in much closer agreement with the experiment. The main difference between the simulations using the transition model and the experimental oil-flow lies in the reduced laminar separation zone observed in the simulations. It results from a downstream shift of the laminar separation line. Similar discrepancies have been observed by Thermann et al. [2] using an extended Mayle [1] criterion for transition. The main reason for the delayed laminar separation does not necessarily come from the transition model, as

Table 2 T106 cascade details

Chord	198 mm
Blade stagger	59.3 deg
Cascade pitch	158 mm
Inlet flow angle	37.7 deg
Design exit flow angle	63.2 deg
Bar diameter	2.05 mm
Axial distance: bars to LE	70 mm
Flow coefficient (U_{axial}/U_{bar})	0.83

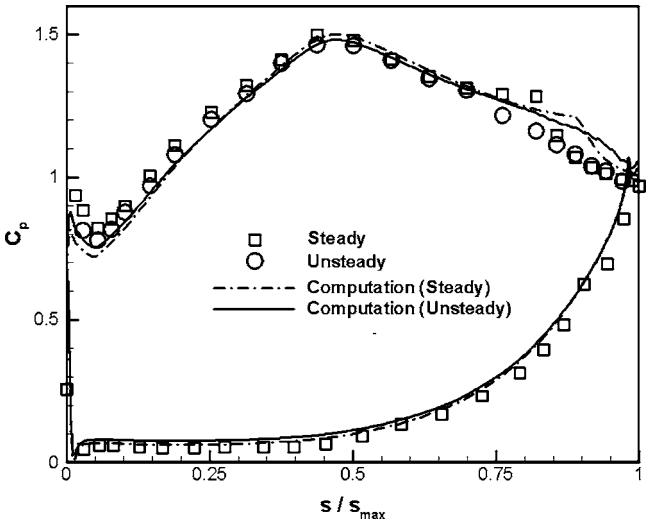

Fig. 14 Comparison of computed and experimental pressure coefficient distributions for T106 case

it is not activated until after the separation occurs. The flow exhibits a complex interaction between the turbulent separation on the sidewalls and the location of the laminar separation line. It appears that the turbulent separation zones on the hub and especially on the shroud are overestimated in the simulation. This results in an acceleration of the core flow, which, in turn, could be the cause of the delay in the laminar separation, as it reduced the strength of the adverse pressure gradient at the center of the blade.

GE Low Pressure Turbine Vane. This test case qualitatively investigates the behavior of the transition model in an actual 3D turbomachinery flow. In particular, the interaction of end-wall and vane boundary layers and the impact on the predicted transition location were of interest. Figure 12 shows wall-shear stress contours on the suction side of the vane and skin friction coefficients at various radial locations. The wall-shear contour plot (Fig. 12(*b*)) indicates that away from the end walls, the suction side flow is laminar up to about 70% chord, where it transitions right before separating. Figure 12(*c*) shows the friction coefficient at 50% span. For comparison, the friction coefficient from a fully turbulent computation is plotted as well. Figure 12(*a*) shows the

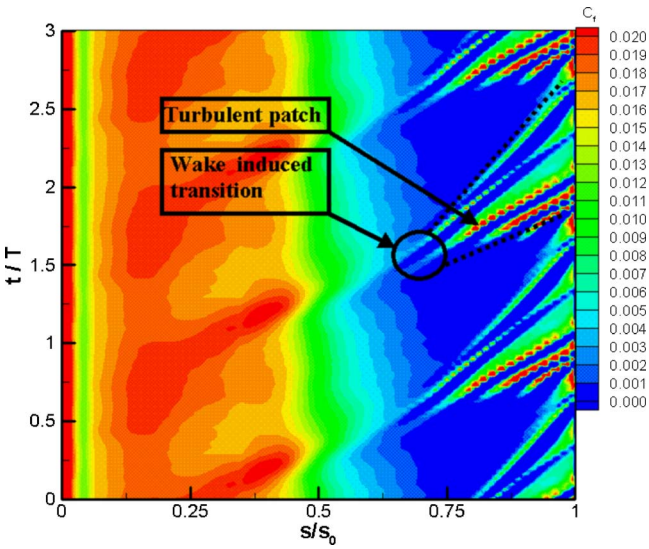

Fig. 15 Computed phase-averaged skin friction coefficient distribution on the suction surface of T106 blade

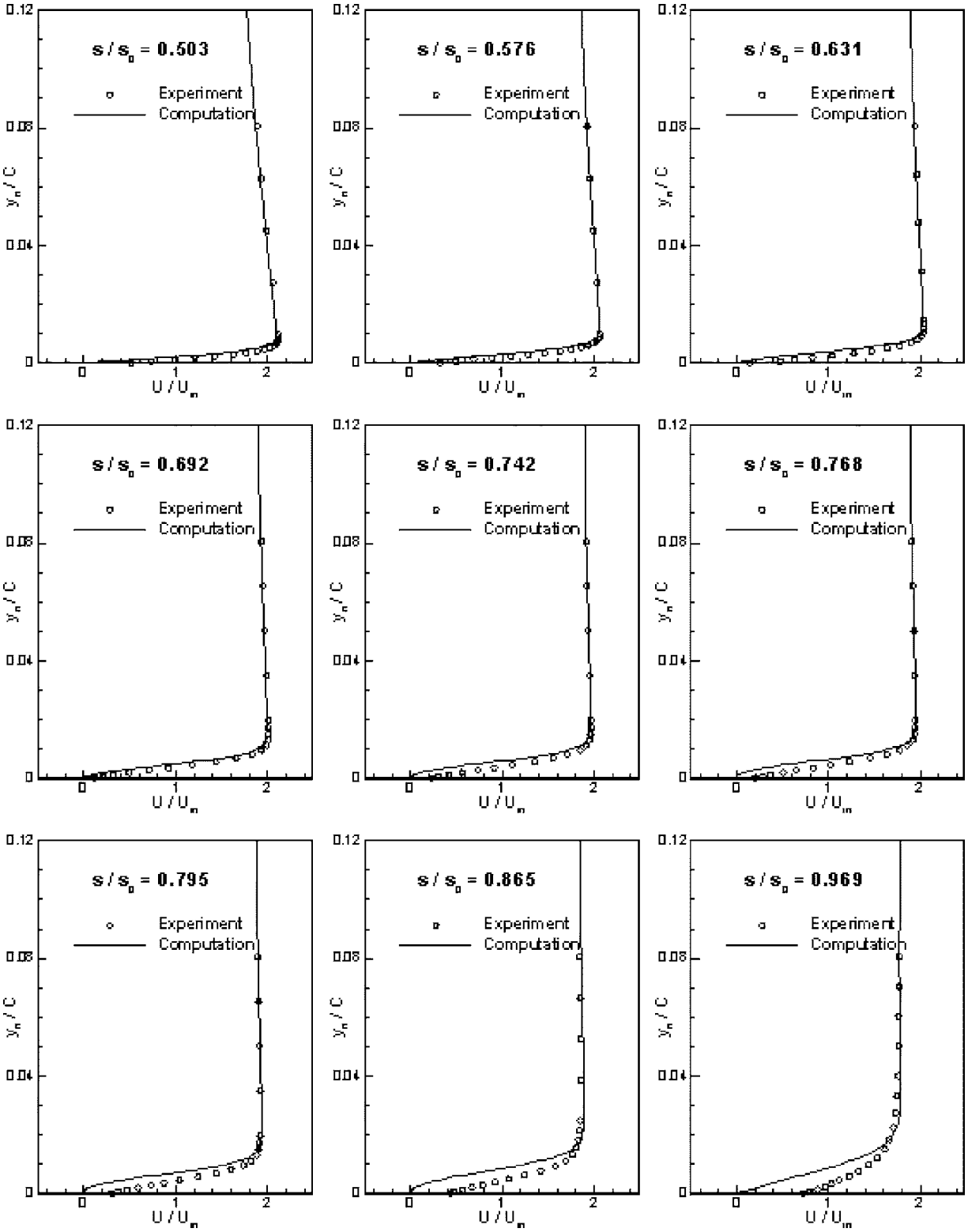

Fig. 16 Comparison of computed and experimental mean velocity profiles at various streamwise locations on the suction surface of T106 blade

effect of the end-wall boundary layer on the predicted transition location. Skin friction coefficients are plotted for 95, 97, and 99% span. With increasing span, the vane boundary layer interacts more strongly with the end-wall boundary layer, which is fully turbulent. As a result, the transition model sees higher levels of turbulence intensity outside the vane boundary layer and transition is triggered further upstream.

The convergence history for the fully turbulent and transitional computations is shown in Fig. 13. There is some additional effort required for the transitional computation because the laminar boundary layers must first be resolved before the turbulent boundary layer starts to develop downstream of transition. However,

overall the convergence with the transition model is very good. The transitional computation took ~17% more CPU time than the fully turbulent computation.

Unsteady Wake/Blade Interaction on T106 Blade Cascade. A computational investigation of the effects of unsteady wake/blade interaction on transition and separation in low-pressure turbines has been performed by numerical simulations of recent experiments of Stieger et al. [3]. These experiments were conducted in order to investigate the effects of periodically passing wakes on laminar-to-turbulent transition and separation in low-pressure turbines. The test section involved a T106 turbine blade cascade subjected to wake passing from a moving bar wake generator. The flow conditions correspond to Re_x=91,077 based on chord and inlet velocity and FSTI=0.1%. The details of the T106 cascade are summarized in Table 2.

The computed pressure coefficient distributions compared to experiment are shown Fig. 14. Both the wake-free (steady) computation and experiment are given along with the time-averaged pressure distributions from the unsteady experiments and computations. In the wake-free computation, the size of the predicted separation region is slightly larger than in the experiment. The time-averaged pressure distribution from unsteady experiments indicates that the laminar separation bubble on the suction side is completely suppressed due to the unsteady impinging wake. The computations predicted a partial suppression of the separation bubble as indicated from the pressure distribution shown in Fig. 14.

The time variation of the skin friction coefficient on the suction surface of the blade is shown in Fig. 15. From this figure it is evident that the flow is separated for a large portion of time over the aft part of the suction surface. However, at a wake passing time (t/T) of 0.5 early transition appears at the 70% chord location, which is approximately where the wake is located at that point in time. There also appears to be regions of reverse flow in the turbulent patch downstream of the transition location. Similar regions of reverse flow in the turbulent patch were also observed by Stieger et al. [3] in the experiment using a particle image velocimetry method.

The time-averaged velocity profiles at nine stations along the suction surface are compared to the experiment in Fig. 16. The simulations agree well with the experimental data except in the near-wall region of the last three stations where the computations indicate separated flow but the experiment indicates attached flow. Note that the current model already overpredicts the steady-state separation bubble. This might be the main reason why the unsteady simulations do not lead to a full time-averaged attached flow. It is possible that further adjustments to the separation-induced transition modification and to the diffusion coefficient ($\sigma_{\theta t}$) in the transition onset equation (to better account for flow history effects) is required in order to improve the predictions for unsteady blade-wake interactions.

Summary

A new correlation-based transition model has been developed, which is strictly formulated with local variables and thereby compatible with modern CFD methods. It is based on transport equations for intermittency and transition momentum thickness Reynolds number. Part I of this paper [6] gave a detailed description of the mathematical formulation of the model and some of the basic test cases used for model validation. Part II has validated the model for a number of turbomachinery and aerodynamic test cases. This includes transition in 2D and 3D test cases, an actual industrial turbine vane, and a turbine blade subjected to unsteady periodic impinging wakes. In all cases, the simulations agreed well with the experiments and the authors believe that the current model is a significant step forward in engineering transition modeling. The present model formulation is very likely a starting point for the inclusion of numerous additional effects and flow regimes such as roughness, freestream turbulent length scale, streamline curvature, cross-flow transition, and Mach number effects.

Acknowledgment

The authors would like to acknowledge the support and technical contribution of Dr. William Solomon at GE Aircraft Engines. The model development and validation at ANSYS CFX was funded by GE Aircraft Engines and GE Global Research. The second and third authors from University of Kentucky are supported by NASA Glenn Research Center under Grant No. NCC3-590 and followed by Grant No. NCC3-1040. Additional support to the University of Kentucky was provided through a research grant from GE Global Research.

Nomenclature

C_p = pressure coefficient, $p_{\mathrm{oinlet}}-p/(0.5\rho U_{\mathrm{ref}}^2)$
C_f = skin friction coefficient, $\tau/(0.5\rho U_{\mathrm{ref}}^2)$
FSTI = freestream turbulence intensity (percent), $100(2k/3)^{1/2}/U_{\mathrm{ref}}$
K = turbulent kinetic energy
K = flow acceleration parameter
L = axial reference length
P = local static pressure
p_{oinlet} = inlet total pressure
p_{ooutlet} = outlet total pressure
$P_{\mathrm{dynoutlet}}$ = outlet dynamic pressure
Re_x = Reynolds number, $\rho L U_{\mathrm{ref}}/\mu$
Re_θ = momentum thickness Reynolds number, $\rho\theta U_0/\mu$
$\mathrm{Re}_{\theta t}$ = transition onset momentum thickness Reynolds number (based on freestream conditions), $\rho\theta_t U_0/\mu$
$\widetilde{\mathrm{Re}}_{\theta t}$ = local transition onset momentum thickness Reynolds number (obtained from a transport equation)
R_T = viscosity ratio
R_y = wall-distance based turbulent Reynolds number
R_v = vorticity Reynolds number
S = absolute value of strain rate, $(2S_{ij}S_{ij})^{1/2}$
S_{ij} = strain rate tensor, $0.5(\partial u_i/\partial x_j+\partial u_j/\partial x_i)$
Tu = turbulence intensity, $100(2k/3)^{1/2}/U$
U = local velocity
U_o = local freestream velocity
U_{ref} = inlet reference velocity
u' = local fluctuating streamwise velocity
x/C = axial distance over axial chord
y = distance to nearest wall
Yp = loss coefficient, $(p_{\mathrm{oinlet}}-p_{\mathrm{ooutlet}})/p_{\mathrm{dynoutlet}}$
y^+ = distance in wall coordinates, $\rho y\mu_\tau/\mu$
δ = boundary layer thickness
θ = momentum thickness
λ_θ = pressure gradient parameter, $(\rho\theta^2/\mu)(dU/ds)$
μ = molecular viscosity
μ_t = eddy viscosity
μ_τ = friction velocity
ρ = density
τ = wall shear stress
Ω = absolute value of vorticity, $(2\Omega_{ij}\Omega_{ij})^{1/2}$
Ω_{ij} = vorticity tensor, $0.5(\partial u_i/\partial x_j-\partial u_j/\partial x_i)$
ω = specific turbulence dissipation rate

Subscripts

t = transition onset
s = streamline

References

[1] Mayle, R. E., (1991), "The Role of Laminar-Turbulent Transition in Gas Turbine Engines," ASME J. Turbomach., **113**, pp. 509–537.

[2] Thermann, H., Müller, M., and Niehuis, R., 2001, "Numerical Simulation of the Boundary Layer Transition in Turbomachinery Flows," ASME Paper No. 2001-GT-0475.

[3] Stieger, R., Hollis, D., and Hodson, H., 2003, "Unsteady Surface Pressures due to Wake Induced Transition in a Laminar Separation Bubble on a LP Turbine Cascade," ASME Paper No. ASME-GT2003-38303.

[4] Huang, J., Corke, T. C., and Thomas, F. O., 2003, "Plasma Actuators for Separation Control of Low Pressure Turbine Blades," AIAA Paper No. AIAA-2003-1027.

[5] Steelant, J., and Dick, E., 2001, "Modeling of Laminar-Turbulent Transition for High Freestream Turbulence," ASME J. Fluids Eng., **123**, pp. 22–30.

[6] Menter, F. R., Langtry, R. B., Likki, S. R., Suzen, Y. B., Huang, P. G., and Völker, S., 2004, "A Correlation Based Transition Model Using Local Variables Part I-Model Formulation," Vienna, ASME Paper No. ASME-GT2004-53452.

[7] Menter, F. R., 1994, "Two-Equation Eddy-Viscosity Turbulence Models for Engineering Applications," AIAA J., **32**(8), pp. 1598–1605.

[8] Achenbach, E., 1968, "Distribution of Local Pressure and Skin Friction Around a Circular Cylinder in Cross-Flow up to $Re=5\times10^6$," J. Fluid Mech., **34**, pp. 648–654.

[9] Coupland, J., "Separation and Transition Over a Semi-Circular Leading Edge: T3L Transition Cases," Rolls-Royce Applied Science Laboratory Data, ER-COFTAC Transition Modeling Special Interest Group, http://transition.imse.unige.it/cases/

[10] Zierke, W. C., and Deutsch, S., 1989, "The Measurement of Boundary Layers on a Compressor Blade in Cascade, Vols. 1 and 2," NASA CR 185118.

[11] Arts, T., Lambert de Rouvroit, M., and Rutherford, A. W., 1990, "Aero-Thermal Investigation of a Highly Loaded Transonic Linear Turbine Guide Vane Cascade," von Karman Institute for Fluid Dynamics, Technical Note 174.

[12] Schulz, H. D., and Gallus, H. D., (1988), "Experimental Investigation of the Three-Dimensional Flow in an Annular Compressor Cascade," ASME J. Turbomach., **110**, pp. 467–474.

[13] Wang, M., Catalano, P., and Iccarino, G., 2001, "Prediction of High Reynolds Number Flow Over a Circular Cylinder Using LES With Wall Modeling," Center for Turbulence Annual Research Briefs.

Performance and Flow Characteristics of an Optimized Supercritical Compressor Stator Cascade

Bo Song[1]

Wing F. Ng

Department of Mechanical Engineering,
Virginia Polytechnic Institute and State University,
Blacksburg, VA 24061

An experimental and numerical study was performed on an optimized compressor stator cascade designed to operate efficiently at high inlet Mach numbers (M_1) ranging from 0.83 to 0.93 (higher supercritical flow conditions). Linear cascade tests confirmed that low losses and high turning were achieved at normal supercritical flow conditions ($0.7 < M_1 < 0.8$), as well as higher supercritical flow conditions ($0.83 < M_1 < 0.93$), both at design and off-design incidences. The performance of this optimized stator cascade is better than those reported in the literature based on Double Circular Arc (DCA) and Controlled Diffusion Airfoil (CDA) blades, where losses increase rapidly for $M_1 > 0.83$. A two-dimensional (2D) Navier-Stokes solver was applied to the cascade to characterize the performance and flow behavior. Good agreement was obtained between the CFD and the experiment. Experimental loss characteristics, blade surface Mach numbers, shadowgraphs, along with CFD flowfield simulations, were presented to elucidate the flow physics. It is found that low losses are due to the well-controlled boundary layer, which is attributed to an optimum flow structure associated with the blade profile. The multishock pattern and the advantageous pressure gradient distribution on the blade are the key reasons of keeping the boundary layer from separating, which in turn accounts for the low losses at the higher supercritical flow conditions. [DOI: 10.1115/1.2183316]

Introduction

The trend towards more efficient and lighter gas turbine engines requires increasingly higher loading and higher speeds on the compressor blade components [1]. There is a pressing demand for advanced blades with minimum profile losses to improve machine efficiency [2,3]. The consequent challenge on the blade design necessitates the introduction of optimized blade profiles and an understanding of the associated flow physics. Such research was exemplified by two recently published works that proved the promise and advantage of the compressor blade design based on optimization techniques and CFD tools [4–7]. The increased research interest in the optimization approach for advanced compressor blade designs has also been seen from a large number of publications in recent years [8–11] (just to list a few). However, these papers only presented various optimization methods and design examples. The experimental verification and flow analysis on the optimized blades are not always available. In the open literature, there is an apparent lack of published cascade test results and flow analysis for newly designed optimized blades.

The trend of higher loading and higher speeds in modern compressor development requires elevated flow velocities relative to the blade rows, leading to transonic and supersonic speeds for rotor blades and supercritical flow conditions for stator blades [12]. Supercritical flow conditions are defined as those at which inlet Mach number (M_1) is high subsonic while transonic flow forms in the blade passage. A normal supercritical inlet Mach number is from 0.7 to 0.8. At a normal supercritical flow condition, flow in the blade forward portion accelerates beyond Mach number 1, and the supersonic patch is usually terminated by a passage shock. Afterward the flow is further diffused in the blade rear part within the subsonic regime. The adverse effect of the shock on the cascade performance lies in the shock loss and possible shock-induced boundary layer separation. Controlled diffusion airfoil (CDA) introduced in early 1980s marked a breakthrough for supercritical compressor cascades with its shock-free and controlled diffusion features, and the subsequent low losses (Hobbs and Weingold [13]). Hobbs's work demonstrated the superiority of CDA to conventional NACA 65 and Double Circular Arc (DCA) airfoils in that the critical inlet Mach number, at which losses increase abruptly, was extended to 0.82. Other published work on CDA blades also showed the advantage of the CDA design concept. However, to keep losses low for CDA blades, the inlet Mach numbers usually did not exceed 0.8 [14–17]). At more aggressive inlet Mach numbers (above 0.83), which can be referred to as "higher supercritical flow conditions," maintaining low losses has not shown to be possible from previous research. In particular, the simultaneous requirement of large turning angles on stator blades makes the design more difficult. Therefore, achieving low aerodynamic losses and high turning at higher supercritical flow conditions turns out to be one of the greatest design challenges for modern compressor stator blades. There is little information available on this topic. To the best of the authors' knowledge, only one prior work exists dealing with a high-turning supercritical compressor cascade composed of DCA blades [18]. The cascade was designed at an inlet Mach number of 0.85 with the blade camber angle of 56.8 deg. Tests of this cascade indicated that low losses were only achieved for inlet Mach numbers below 0.8.

This paper presents an experimental and numerical study of a compressor stator cascade at normal and higher supercritical flow conditions. The cascade geometry used in this study, is similar to the hub-section of a stator (exit guide vane) in a transonic fan stage, for an experimental small turbofan engine. The rotor total-pressure-ratio is about 1.8, leading to high subsonic inlet Mach

[1]Currently with Gardner Denver, Inc.

Contributed by the International Gas Turbine Institute (IGTI) of ASME for publication in the JOURNAL OF TURBOMACHINERY. Manuscript received October 1, 2004; final manuscript received February 1, 2005. IGTI Review Chair: K. C. Hall. Paper presented at the ASME Turbo Expo 2005: Land, Sea, and Air, Reno, NV, June 6–9, 2005, Paper No. GT2005-68569.

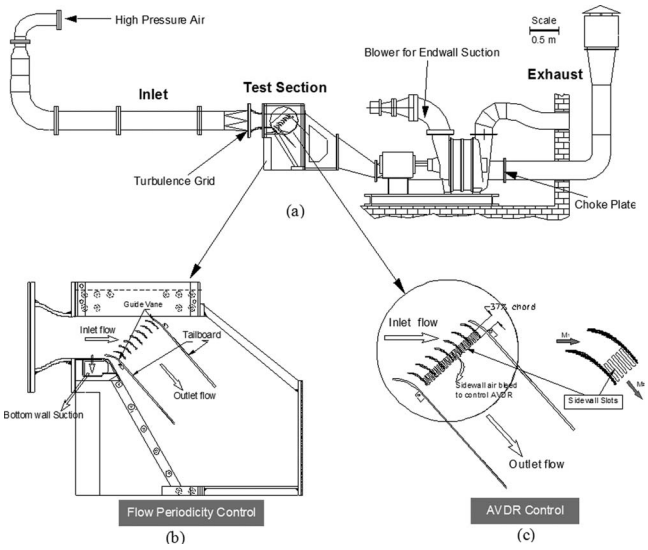

Fig. 1 The Virginia Tech High Speed Cascade Wind Tunnel

numbers for the stator. The Mach number, turning angle, and solidity are maximum at the hub-section. As such, the current cascade has a high solidity of 2 and the blades are highly cambered (54 deg). A state-of-the-art optimization approach, based on multi-objective genetic algorithm (MOGA), was employed in the design in an attempt to obtain low losses and high flow turning at the aggressive design inlet Mach number of 0.87. Detailed description of the design/optimization process was given by Yamaguchi and Arima [19]. The current work focused on the cascade test performance and flow characteristics.

Experimental Setup and Procedure

The experiments were conducted in the Virginia Tech High Speed Cascade Wind Tunnel (see Fig. 1(*a*)). The wind tunnel was a blowdown type. High speed steady flow was maintained for a short time span by a feedback control scheme. The inlet flow freestream turbulence level was increased by using a turbulence grid upstream of the test section. The facility allowed the control of flow periodicity [20] and axial velocity density ratio (AVDR) [21]. The control of flow periodicity was achieved by employing a pair of guide vanes and tailboards, as well as bottom wall suction

Table 1 Cascade geometry

Blade chord (C)	86 mm
Aspect ratio (AR=L/C)	1.77
Solidity (σ=C/S)	2
Stagger angle (γ)	16 deg
Camber angle (φ)	54 deg
L.E. circle radius	1 mm

(see Fig. 1(*b*)). The control of AVDR was achieved by using slotted sidewalls. The slots were made in the rear part of the cascade passages, and were open to the ambient for air bleed (see Fig. 1(*c*)). Choke plates of different size were used in the exhaust to obtain different static pressure in the test section for each tunnel run, thus achieving different air bleed rates and the control of AVDR. For this experiment, facility limitation only allowed the AVDR to be adjusted within the range of $1.09 < \text{AVDR} < 1.16$. Testing with solid sidewalls corresponded to the highest AVDR. This method led to the variation of Reynolds number, but only within a narrow range from 1.4×10^6 to 1.9×10^6 based on the blade chord and inlet conditions. The Reynolds number variation with changing inlet Mach number was also limited to a range of 1.2×10^6 to 1.8×10^6. The Reynolds number was well beyond the critical Reynolds number (order of 10^5) [22] and its effect on the experiments should be negligible.

Figure 2 shows the blade profile and illustrates the cascade nomenclature used in the current study. Cascade geometry is listed in Table 1. It is noticed that the optimized blade has a gradual turning along the whole chord with the highest camber occurred at about 40% chord. It has a rather uniform thickness distribution with gradual sharpening towards the L.E. and T.E., which is a desired feature from the perspective of blade strength. This feature was obtained by adding a mechanical constraint (blade thickness) to the optimization function [19]. The design condition of the cascade is: $M_1=0.87$, $\alpha_1=48.4$ deg (corresponding to $I=0$ deg), DF=0.55, $\text{Re}=1.5\times10^6$. The optimization objective was to achieve low losses and high flow turning.

In the experiments, inlet total temperature was measured using a type *K* thermocouple total temperature probe located upstream of the test section. The cascade consisted of seven blades, numbered 1–7, as shown in Fig. 3. Aerodynamic measurements were taken in the mid-span plane. Inlet total pressure was measured 87% chord upstream of Blade 2 using a total pressure probe. Inlet

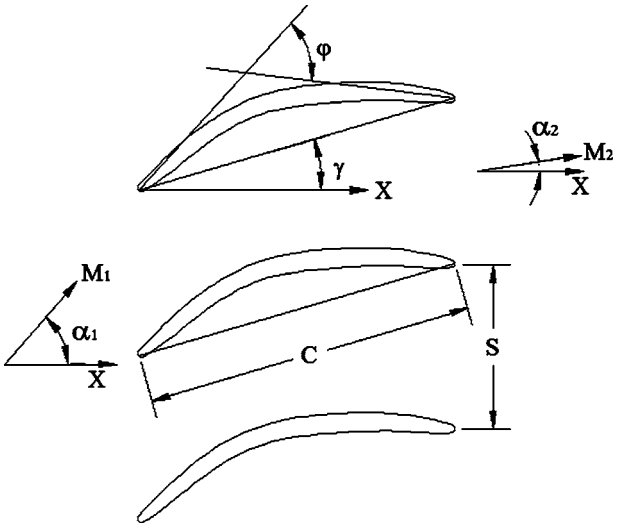

Fig. 2 Blade profile and cascade nomenclature

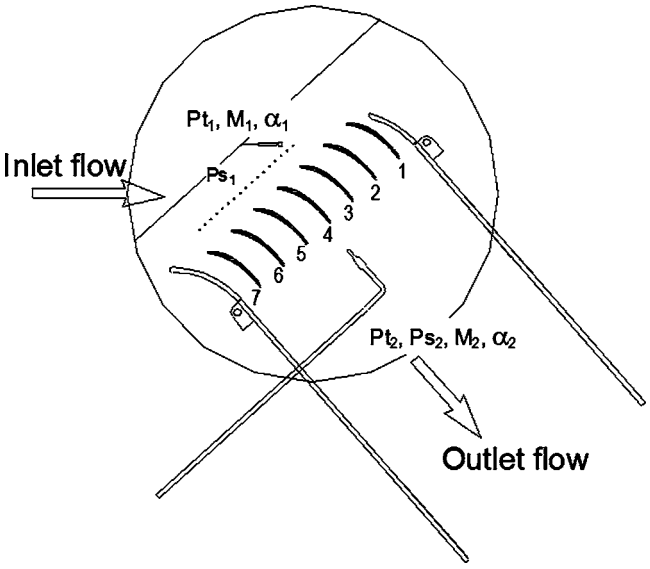

Fig. 3 Aerodynamic measurements

Table 2 Experimental conditions and uncertainty

Parameter	Value	Uncertainty
M_1	0.61–0.95	±0.005
α_1	44.4 deg–50.4 deg	±0.5 deg
AVDR	1.09–1.16	±0.01
Re	$1.2–1.9\times10^6$	$\pm0.02\times10^6$
Tu	1.2–1.6%	±0.05%
ω	0.061–0.356	±0.005

flow angle was checked 42% chord upstream of the cascade for different pitchwise locations using a three-hole angle probe. Seventeen sidewall pressure taps were evenly spaced in the pitchwise direction 29% chord upstream of the cascade, covering the middle four passages. All of these seventeen locations were used to monitor the inlet flow uniformity/periodicity, and some of them were specifically chosen for determining the inlet Mach number. Another three-hole angle probe was traversed 50% chord downstream of the cascade to measure outlet total pressure, Mach number and flow angle. Overall aerodynamic parameters were averaged for the middle two passages (from Blades 3 to 5). Blade 3 was instrumented on the pressure side while Blade 4 was instrumented on the suction side for blade surface pressure measurements. Blade surface flow visualization was performed on the suction surface of Blade 4. Shadowgraphs were taken for the passage between Blades 3 and 4. The experimental uncertainty was estimated based on flow aperiodicity, tunnel unsteadiness, and instrumentation error. Table 2 summarizes the experimental conditions and uncertainty.

Numerical Method

A two-dimensional, steady, Navier-Stokes solver was used to calculate the flow in the cascade at various conditions. The numerical simulation was intended to help characterize the cascade performance and understand the flow. The solver utilized a finite-volume, four-stage Runge-Kutta time-marching numerical procedure in conjunction with a flexible multiple grid block geometric representation to permit detailed aerodynamic simulations to be performed for complex configurations. The one-equation Spalart-Allmaras turbulence model was employed in the computations. More detailed information of the solver can be found in Song [23]. The H–O–H grid system was used in the calculations. As shown in Fig. 4, using the multiple-block grid system allowed a fine mesh around the blade passage. Near the blade surface, an even finer mesh was used. All these mesh characteristics led to improved resolution of the boundary layer and a successful capture of shocks. After trials and errors, the grid size was chosen to be 49×45 for the inlet region, 461×45 for the blade region, and 49×57 for the outlet region. Computations conducted with a finer grid offered the same solutions. Therefore, the current grid size was demonstrated to be sufficient.

For each simulation run, inlet flow conditions (Pt_1, Tt_1, α_1) were specified to match experimental conditions. Outlet static pressure was chosen through trial and error to achieve the desired inlet Mach number. Periodic boundary condition was used in the pitchwise direction. All simulation runs had stable convergence history. After 4000 iterations, the RMS residue reduced to the order of 10^{-7}, and the difference between the inlet and outlet mass flow rate was within 0.04%.

Cascade Performance

Performance Versus Inlet Mach Number. Experimental results of cascade performance at the design inlet flow angle (α_1 =48.4 deg) are shown in Fig. 5, along with the comparison to 2D CFD calculations. In general, good agreement is obtained between experiment and CFD, although CFD slightly over-predicted the

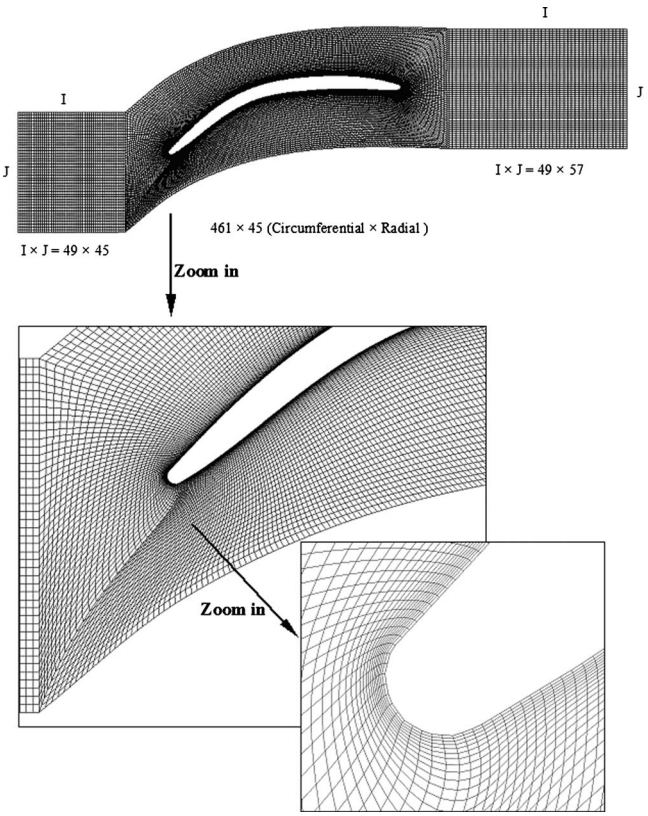

Fig. 4 Computation domain and grid

performance parameter values. It is seen that low losses are maintained for a wide high inlet Mach number range (0.83–0.93), which provides a robust envelope around the design condition (M_1=0.87). In contrast to conventional blades, on which low losses can only be maintained up to an inlet Mach number of about 0.8, the current optimized blade is able to sustain low losses ($\omega<0.07$) up to M_1=0.93. In addition, it is noteworthy that the

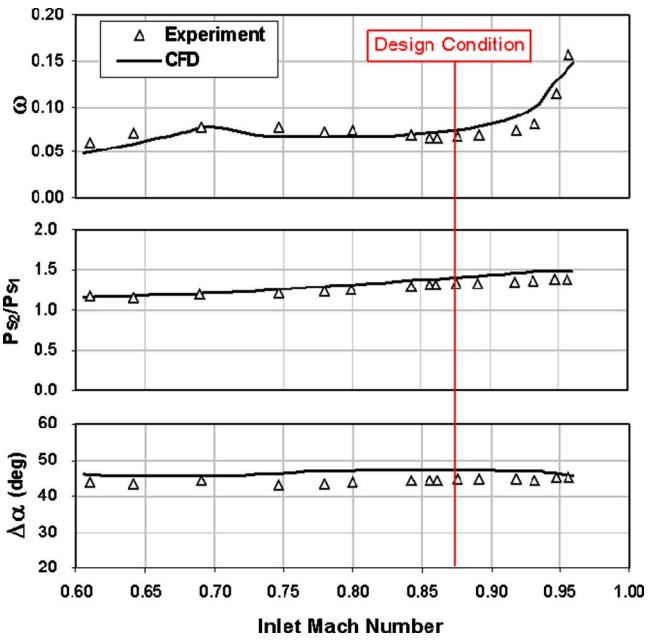

Fig. 5 Cascade performance at the design inlet flow angle (α_1=48.4 deg)

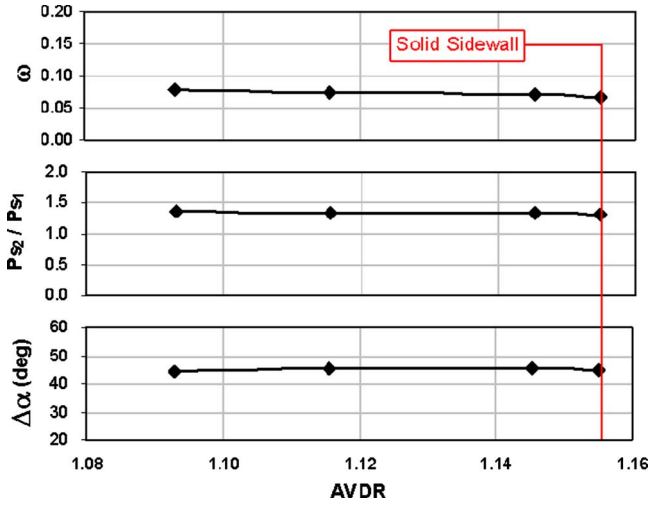

Fig. 6 Tested cascade performance with AVDR control at the design condition (M_1=0.87, α_1=48.4 deg)

current cascade performance remains good for low inlet Mach numbers (0.6–0.8), despite the fact that it was optimized at M_1 =0.87. The static pressure ratio is seen to gradually increase from 1.2 to 1.4 with increasing inlet Mach number. After reaching M_1 =0.93, the static pressure ratio increases very little due to flow separation. A high flow turning of about 45 deg is achieved and stays relatively constant for the entire inlet Mach number range.

The experimental results in Fig. 5 are based on solid sidewall cascade tests. The CFD results are two-dimensional with AVDR =1. The agreement between experiment and CFD suggests that, for the conditions tested in this experiment, the AVDR effect on the cascade performance is not significant. To further verify this, slotted sidewall tests with AVDR control were conducted for the design condition. The results are shown in Fig. 6. The data at the highest AVDR (1.155) corresponds to the solid sidewall test. It is seen that the AVDR effect on performance of this cascade is small. For more detailed discussion of the AVDR effect on cascade performance and the validity of solid sidewall tests, refer to [21]. The following experimental results presented are all based on solid sidewall tests.

Loss Versus Inlet Flow Angle. To fully characterize the cascade performance, 2D CFD simulations were performed for a wide range of inlet flow angles to cover the choke and stall conditions. The "loss bucket" (loss-incidence characteristic) was obtained. Figure 7 shows the loss bucket at three typical inlet Mach numbers (M_1=0.61, 0.78, and 0.87), which represents normal subsonic flow, normal supercritical flow and higher supercritical flow,

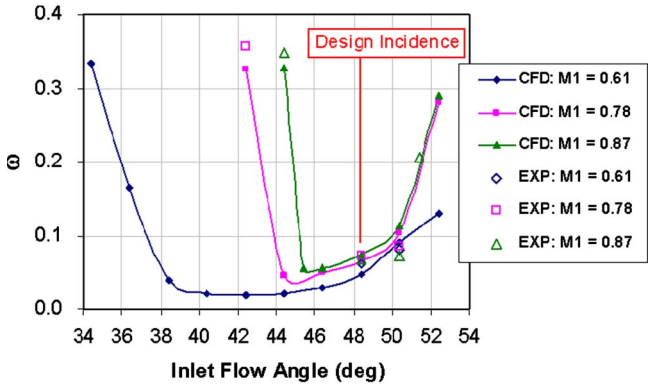

Fig. 7 Loss-incidence characteristics

Table 3 Incidence robustness

M_1	Effective incidence range (deg)	Incidence robustness (deg)
0.61	37–51	14
0.78	44–51	7
0.87	45–50	5

respectively. The available experimental data is included in the plot for reference. Although there is some quantitative discrepancy between experiment and CFD, the CFD prediction of the cascade performance is reasonably acceptable. If choosing loss coefficient ω=0.1 (twice as much as the minimum losses for M_1 =0.87) as the criterion to define the cascade effective operating incidence range, the incidence robustness can be quantified for the three inlet Mach numbers, as summarized in Table 3. It is seen that the effective incidence range decreases with increasing inlet Mach number, indicating the increasing design challenge of maintaining low losses for high turning stator blades at higher supercritical flow conditions. The reduction of the effective incidence range from M_1=0.61 to M_1=0.87 is due to the increase of the choke incidence angle while the stall incidence angle stays nearly the same. At the design inlet Mach number (M_1=0.87), the optimized cascade maintains an incidence robustness of 5 deg. In contrast, it has been shown by experimental and numerical investigations that a CDA cascade has a "zero" incidence robustness at M_1=0.87 [23]. At off-design inlet Mach numbers (M_1=0.61 and 0.78), the optimized cascade maintains a wide effective incidence range. It should be pointed out again that the optimized cascade does not sacrifice performance at low inlet Mach numbers and off-design inlet flow angles. Therefore, it can be concluded that the optimized cascade performs better than CDA cascades.

Blade Loading. Figure 8 shows the results of blade surface isentropic Mach number at the design inlet flow angle (α_1 =48.4 deg). Unlike a typical CDA cascade that has a "ski-jump" shape of suction surface Mach number and nearly constant subsonic Mach number on the pressure surface [13], the surface Mach number of the optimized cascade varies on the pressure surfaces, with a big depression around 40% chord due to the highest blade camber there. This distribution results in more even loading compared to the front-loaded characteristic of the CDA blades. For the current optimized blade, there is a strong L.E. acceleration due to the relatively sharp leading edge. At higher supercritical flow conditions (M_1=0.84, 0.87, and 0.91), a favorable pressure gradient (M_1=0.84 and 0.87) or nearly zero pressure gradient (M_1=0.91) at 20–30% chord on the S.S. occurs after the passage shock, making the next diffusion start at a more downstream location (30% chord), away from the shock (20% chord). As such, there is no shock-induced boundary layer separation, and hence losses are not high. The passage shock moves more downstream only when M_1 increasing to a higher value of 0.95. It is followed immediately by the diffusion process, causing boundary layer separation and the consequent higher losses (refer to Fig. 5).

Figure 9 shows the results of blade surface isentropic Mach number at the off-design inlet flow angle (α_1=45.4 deg). The difference between this inlet flow angle and the design inlet flow angle (Fig. 8) is basically the stronger L.E. acceleration and the deeper diffusion that follows. At normal supercritical flow conditions (M_1=0.70, 0.76, and 0.82), a favorable pattern of gradual acceleration and diffusion occurs on the S.S. (with the hump at 30% chord), achieving the diffusion process without boundary layer separation. At M_1=0.87, two passage shocks possibly occurs at 10% and 30% chord on the S.S. and no boundary layer separation is induced. The flow/shock pattern of 45.4 deg could be more advantageous than that of the design inlet flow angle. This explains the decrease of losses from 50 to 45 deg as seen in Fig. 7. The CFD flowfield characterization in the next section will pro-

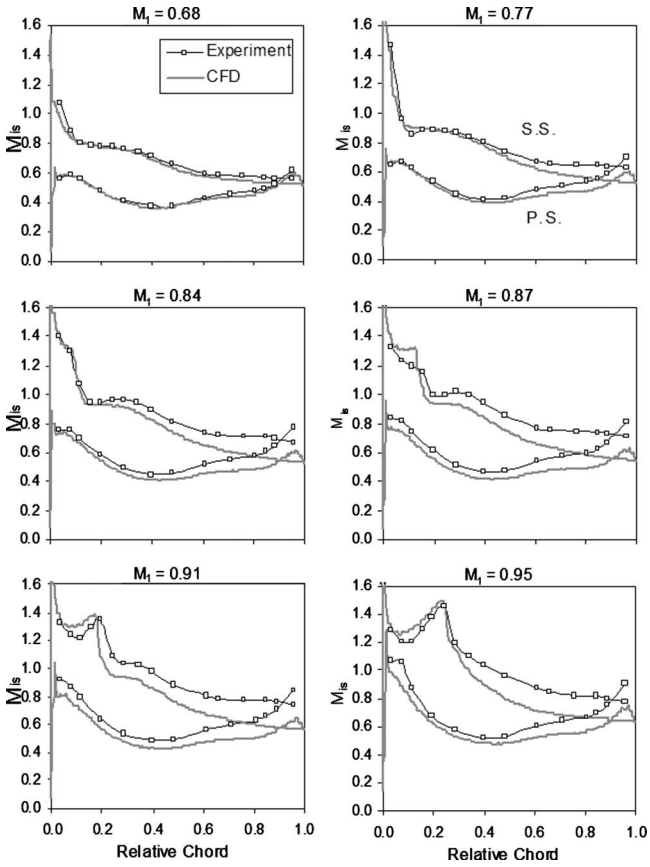

Fig. 8 Blade surface isentropic Mach number at the design inlet flow angle (α_1=48.4 deg)

vide more insight into the flow/shock pattern.

General agreement between CFD and experiment can be seen in Figs. 8 and 9. The agreement is particularly good at low M_1, with the discrepancy gradually increasing as M_1 increases. This is attributed to the increased AVDR effect. The upward shift of experimental results compared to CFD curves, at the aft portion of the blade, is an understandable fact. Since solid sidewall was used in the experiment, the flow in the cascade converged at the aft/exit section (AVDR$>$1), leading to the upward shift in the blade surface Mach number. Based on the agreement between CFD and experiment on the blade surface Mach number, as well as other cascade performance parameters (such as that shown in Fig. 5), the current CFD simulation is considered to be sufficiently acceptable for the purpose of understanding some of the flow physics in this cascade.

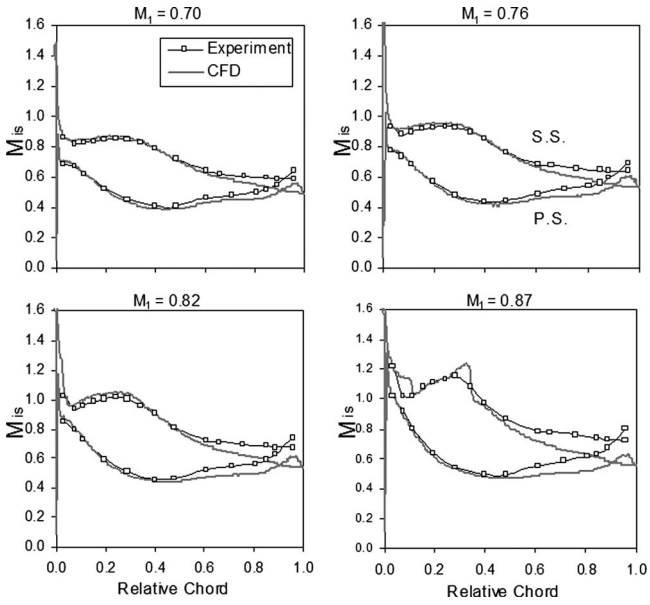

Fig. 9 Blade surface isentropic Mach number at the off-design inlet flow angle (α_1=45.4 deg)

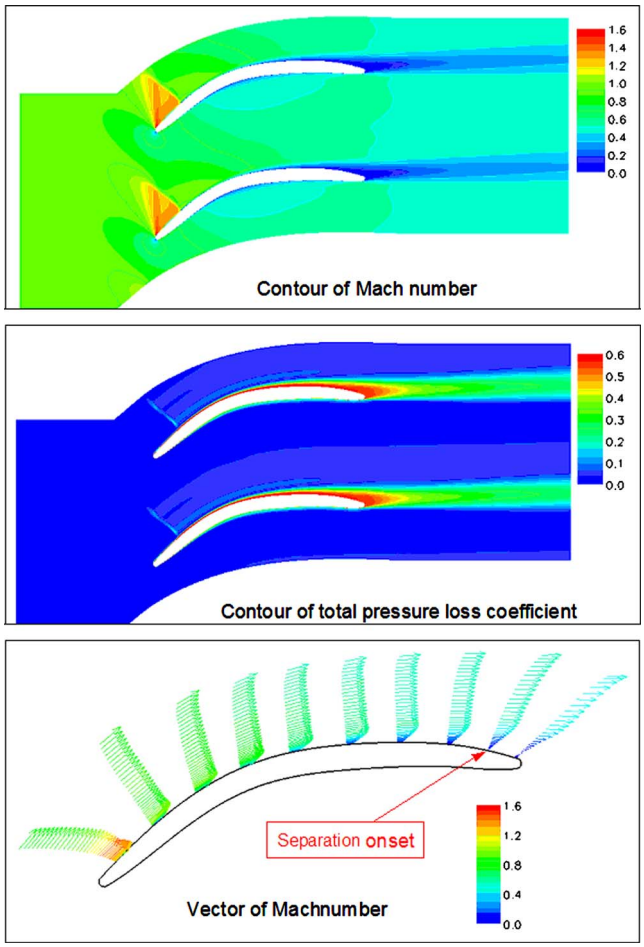

Fig. 10 Flowfield at the design condition (M_1=0.87, α_1 =48.4 deg)

Flow Characteristics

To understand the flow physics underlying the cascade performance, CFD simulations of the flowfield are presented in the following. The flow is interpreted using contours of Mach number, loss coefficient, and pressure gradient.

Flow Structure at the Design Condition. Figure 10 shows contours of Mach number, total pressure loss coefficient and vectors of Mach number at the design condition (M_1=0.87, α_1 =48.4 deg), which exhibit the flow structure, loss generation and transport, and boundary layer development, respectively. It is seen that a typical supersonic patch of a supercritical compressor cascade occurs at the blade forward section on the suction side, terminated by a passage shock at about 20% chord. After the passage shock, flow remains attached without separation. The boundary layer starts to thicken at the aft section and a slight separation commences near the trailing edge. Experimental blade surface oil flow visualization indicated no reversed flow on the blade suction

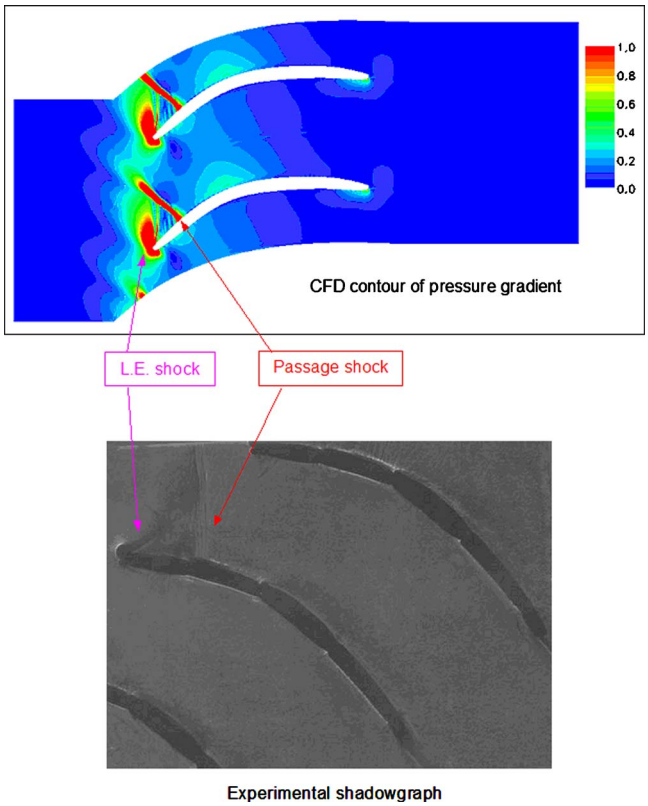

Fig. 11 Shock pattern at the design condition (M_1=0.87, α_1 =48.4 deg)

surface. The reason for no shock-induced boundary layer separation is that after the strong acceleration around the leading edge, the flow decelerates before the passage shock, thus the shock strength is reduced. Moreover, downstream of the shock, the flow accelerates before the final diffusion (refer to Fig. 8: M_1=0.87). It is also seen that the shock loss is smeared out in the downstream, contributing to a very small percentage to the overall losses.

Figure 11 shows the shock pattern at the design condition. The experimental Shadowgraph confirmed the CFD prediction. The flow structure is characterized by a strong L.E. acceleration, a L.E. shock, a passage shock at 20% chord, and an acceleration-deceleration process at 30–40% chord.

Flow Development With Inlet Mach Number. Figures 12 shows the flow development with increasing inlet Mach number at the design inlet flow angle (α_1=48.4 deg), providing an understanding of the loss development characteristic shown in Fig. 5. At M_1=0.68, typical subsonic flow prevails throughout the passage. However, the high adverse pressure gradient due to the deep diffusion caused by the strong L.E. acceleration initiates the thickening of the boundary layer, which accounts for the relatively high losses (refer to Fig. 5 for the small hump of the loss curve at this inlet Mach number). It is seen that there is a small trade-off in the performance at a lower speed of M_1=0.68, as the cascade was optimized at a higher supercritical speed (M_1=0.87).

At M_1=0.84, the typical supersonic patch at the blade front part forms and is terminated by a passage shock. The flow pattern is very similar to that of the design condition, except that the shock occurs farther upstream and with less strength. The overall loss level is about the same as that of the design condition (M_1 =0.87). This suggests that the overall losses are indeed primarily attributed to the viscous/mixing losses from the boundary layer and the ensuing wake downstream of the cascade, and the shock loss is of secondary importance. It is interesting to observe that losses at M_1=0.84 and 0.87 are lower than the losses at M_1 =0.68 (refer to Fig. 5), although the former has shock but the latter does not. The explanation may come from a closer look at the blade surface Mach number shown in Fig. 8 at M_1=0.84 and 0.87. The shock makes the front diffusion occur in two steps: The deceleration after the leading edge and the deceleration by the shock. In addition, the zero or favorable pressure gradient following the shock is advantageous in keeping the boundary layer from

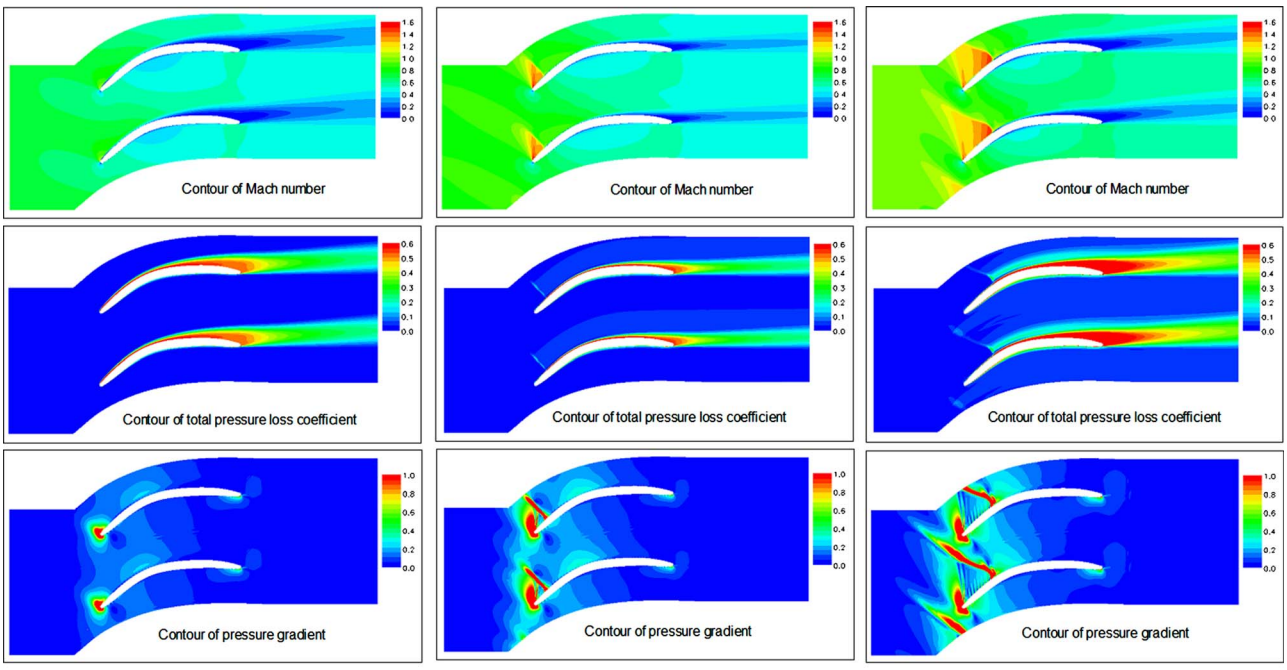

Fig. 12 Flow development with M_1 at α_1=48.4 deg

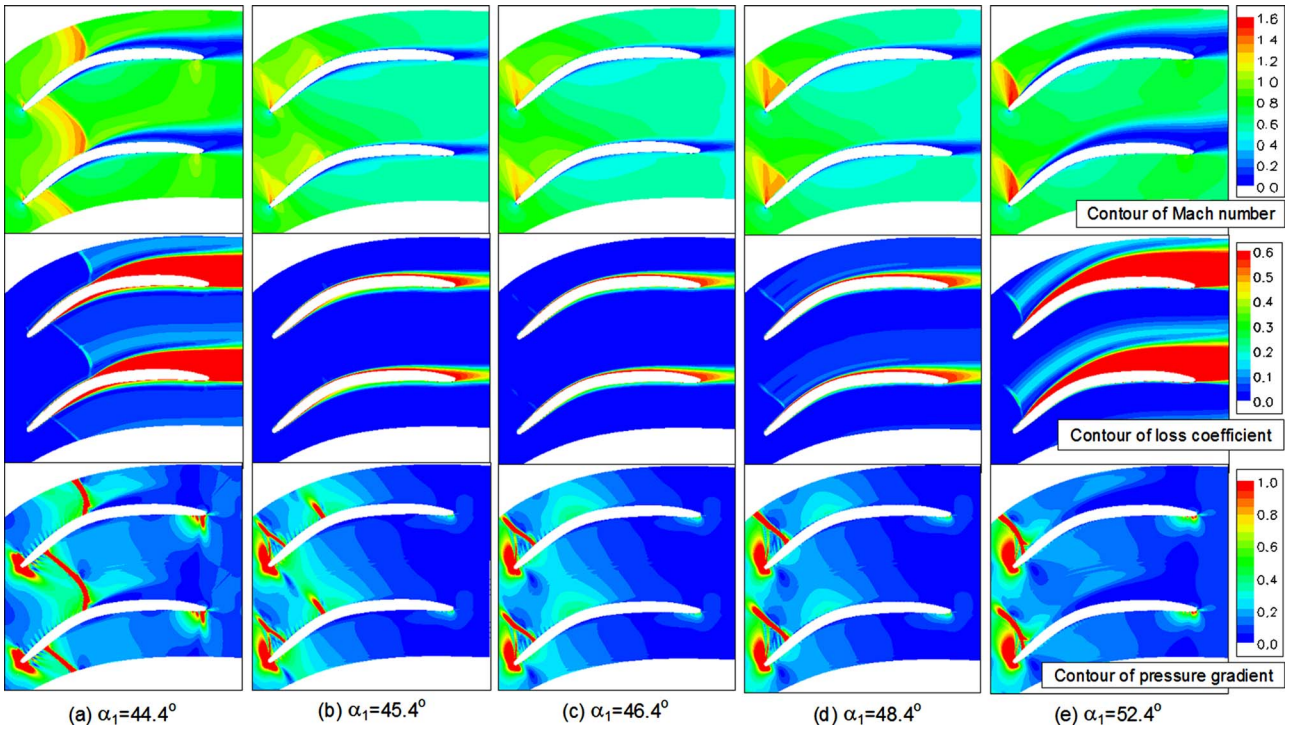

Fig. 13 Flow variation with incidence at $M_1=0.87$

separating. It is seen that the optimized cascade offers a better flow structure (thus no flow separation) for a higher supercritical flow condition ($M_1>0.83$).

At $M_1=0.95$, the supersonic patch grows, and the size and strength of the passage shock increase significantly. The boundary layer thickens after the shock and separates at the blade aft section and losses increase considerably compared to the design condition. In this case the shock loss contributes more to the overall losses. However, even at $M_1=0.95$, the flow has not separated as severely as the choke and stall flows (choke and stall flows will be discussed in the next section). The loss coefficient of this condition is 0.156 (Fig. 5), only half of the choke and stall flow values (Fig. 7). It is seen that the optimized cascade has good resistance to shock-induced separation due to advantageous velocity development through the passage: L.E. acceleration → deceleration → shock → re-acceleration → final diffusion.

Flow Variation With Incidence. Figure 13 shows the flow variation with incidence angle at the design inlet Mach number, corresponding to the loss bucket of $M_1=0.87$ shown in Fig. 7. Figures 13(*a*) and 13(*e*) on the two sides show the flow patterns at the choke and stall incidence angle, respectively. At the choke incidence ($\alpha_1=44.4$ deg, $I=-4$ deg), a strong passage shock crosses the entire passage and the flow is choked. After the shock, severe boundary layer separation occurs on the suction surface, resulting in the loss cliff on the left hand side in Fig. 7. At the stall incidence ($\alpha_1=52.4$ deg, $I=4$ deg), the supersonic patch at the blade forward section moves upstream close to the leading edge and results in a strong passage shock. Right after the passage shock, there is significant boundary layer separation, leading to the loss cliff on the right hand side in Fig. 7. At this incidence, the boundary layer separation is not only driven by the shock, but also by the larger incidence. For lower Mach numbers such as $M_1=0.61$, there is no shock generated, but losses are much elevated at $\alpha_1=52.4$ deg (see Fig. 7). This is due to the suction surface boundary layer separation (the results are not shown here), which is caused solely by the larger incidence.

Figure 7 shows the minimum losses at the negative incidence $I=-3$ deg ($\alpha_1=45.4$ deg) at $M_1=0.87$. This can be interpreted with comparing the flow patterns at $\alpha_1=45.4$, 46.4, and 48.4 deg, as shown in Figs. 13(*b*)–13(*d*). When the flow angle changes from the design incidence towards negative incidences ($\alpha_1=48.4$ deg → 46.4 deg → 45.4 deg), the supersonic patch at the blade forward section shrinks to the leading edge while the Mach number decreases. Consequently, the passage shock (the first one for 45.4 deg) weakens and the shock loss decreases. From the three contours of loss coefficient at the three incidence angles, the shock loss is barely visible for 46.4 deg and not visible for 45.4 deg given the same display scale as for 48.4 deg. In addition, the boundary layer of 48.4 deg is slightly thicker than the other two incidences. Therefore, overall losses are reduced when incidence approaches 45.4 deg.

Some other interesting observations are obtained from Fig. 13. At 45.4 deg, with the shrinking of the supersonic patch at the blade front part, the flow afterwards accelerates more to form the second supersonic patch, which terminates at the second passage shock. Both passage shocks of this incidence are weaker than the passage shock of 48.4 deg. Theoretically, for the same degree of deceleration of a supersonic flow, two steps by two shocks cause less loss than a single shock (taking it to the extreme, unlimited compression waves achieve the deceleration without loss). In this sense, the L.E. shock is favored for the low-loss blade design. Between the shocks, compression/expansion waves originate from the suction surface (as shown in the pressure gradient contours), which bridge the flow development between shocks, thus completing a mechanism for the multishock pattern. Experimental confirmation of the multishock pattern by Shadowgraph is shown in Fig. 14. The above flow analysis indicated a promising concept of achieving low losses and high turning at higher supercritical speeds. The current optimized blade, which is responsible for the flow characteristics, demonstrated a progress in blade profile generation.

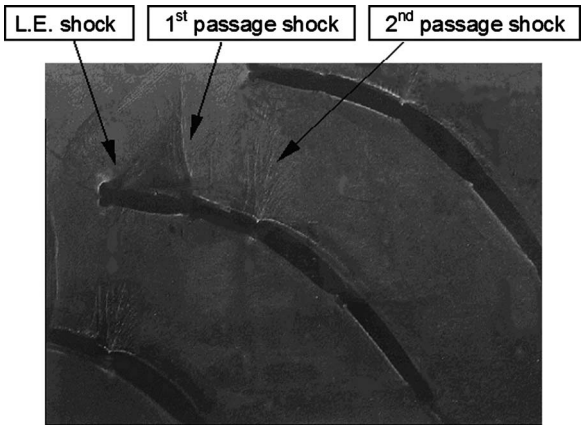

Fig. 14 Shadowgraph at $M_1=0.87$, $\alpha_1=45.4$ deg

Conclusions

Cascade tests confirmed that low losses were achieved on an optimized high turning compressor stator cascade at normal supercritical flow conditions (M_1 ranging from 0.61 to 0.83). In addition, low losses were extended to higher supercritical flow conditions (M_1 ranging from 0.83 to 0.93). This achievement demonstrated the superiority of the current cascade to those composed of conventional blades such as Double Circular Arc or Controlled Diffusion Airfoil. Neither DCA nor CDA cascade could maintain low losses when M_1 exceeded 0.83. The optimized cascade is able to operate with a low-loss incidence range of 5 deg at the aggressive design inlet Mach number ($M_1=0.87$), with the minimum losses at the incidence of −3 deg. The cascade is also able to maintain a wide low-loss incidence range at subsonic or normal supercritical flow speeds ($M_1=0.6-0.8$) as a CDA cascade did. At the design inlet flow angle, high flow turning of about 45 deg was obtained. In contrast to highly front-loaded CDA cascades, the blade loading of the optimized cascade shifts downstream to make a more uniform loading distribution. It is concluded that the optimized cascade has better performance compared to conventional cascades, particularly at higher supercritical flow conditions ($M_1>0.83$).

Flow analysis indicates that the superior performance of the optimized cascade is due to the avoidance of boundary layer separation, despite the presence of shocks. This is attributed to an optimum flow structure. The multishock pattern, along with the advantageous acceleration and deceleration flow pattern, allows the flow to overcome the adverse pressure gradient step by step and without separation, and finally achieve high pressure-ratio diffusion and high flow turning. The flow understanding obtained from the current work, although based on a specific cascade, can be of some guidance for the design of low-loss and high-turning compressor blades at higher supercritical flow conditions. The presented flow characteristics filled the deficiency of information on high-turning compressor cascades at higher supercritical speeds in the open literature. Future research on 3D flow of this type of blade will be an interesting pursuit.

Acknowledgment

This research was sponsored by Honda R&D Co., Ltd. The authors would like to thank the company for permission to publish the work. The support from Dr. Toyotaka Sonoda and Dr. Toshiyuki Arima as the project monitors is especially appreciated. The authors are indebted to Dr. Xingmin Gui, Dr. Shiming Li, and Mr. Hans Raven for their help on the experiments and Mrs. Sarah Stitzel for her help on the CFD work.

Nomenclature

AVDR = axial velocity density ratio $=(\rho_2 V_2 \cos\alpha_2)/(\rho_1 V_1 \cos\alpha_1)$
AR = aspect ratio $=L/C$
C = blade chord
DF = diffusion factor $=1-V_2/V_1+(V_1\sin\alpha_1-V_2\sin\alpha_2)/(2\sigma V_1)$
I = incidence angle
L = blade span
L.E. = leading edge
M = Mach number
P.S. = pressure surface
Ps = static pressure
Pt = total pressure
Re = Reynolds number
S = blade spacing
S.S. = suction surface
T.E. = trailing edge
Tt = total temperature
Tu = freestream turbulence intensity
V = flow velocity
X = distance in axial direction
α = flow angle (with respect to axial direction)
$\Delta\alpha$ = flow turning $=(\alpha_1-\alpha_2)$
γ = stagger angle
φ = camber angle
ρ = density
σ = solidity $=C/S$
ω = loss coefficient $=(Pt_1-Pt_2)/(Pt_1-Ps_1)$

Subscripts

1 = inlet plane
2 = outlet plane
is = isentropic

References

[1] Wennerstrom, A. J., 1990, "Highly Loaded Axial Flow Compressors: History and Current Developments," ASME J. Turbomach., **112**, pp. 567–578.
[2] Denton, J. D., 1993, "Loss Mechanism in Turbomachines," ASME J. Turbomach., **115**, pp. 621–656.
[3] Dunham, J., 1996, "Aerodynamic Losses in Turbomachines," AGARD-CP-571, Loss Mechanism and Unsteady Flows in Turbomachines, K1–K13.
[4] Köller, U., Mönig, R., Küsters, B., and Schreiber, H., 2000, "Development of Advanced Compressor Airfoils for Heavy-Duty Gas Turbines-Part I: Design and Optimization," ASME J. Turbomach., **122**, pp. 397–405.
[5] Küsters, B., Schreiber, H., Köller, U., and Mönig, R., 2000, "Development of Advanced Compressor Airfoils for Heavy-Duty Gas Turbines-Part II: Experimental and Theoretical Analysis," ASME J. Turbomach., **122**, pp. 406–415.
[6] Sonoda, T., Yamaguchi, Y., Arima, T., Olhofer, M., Sendhoff, B., and Schreiber, H., 2004, "Advanced High Turning Compressor Airfoils for Low Reynolds Number Condition-Part I: Design and Optimization," ASME J. Turbomach., **126**(3), pp. 350–359.
[7] Schreiber, H., Steinert, W., Sonoda, T., and Arima, T., 2004, "Advanced High Turning Compressor Airfoils for Low Reynolds Number Condition-Part II: Experimental and Numerical Analysis," ASME J. Turbomach., **126**(4), pp. 482–492.
[8] Benini, E., and Toffolo, A., 2002, "Development of High-Performance Airfoils for Axial Flow Compressors Using Evolutionary Computation," J. Propul. Power, **18**(3), pp. 544–554.
[9] Xu, C., and Amano, R. S., 2002, "A Turbomachinery Blade Design and Optimization Procedure," ASME Paper No. GT-2002-30541.
[10] Rai, M., and Madavan, N., 2001, "Application of Artificial Neural Networks to Design of Turbomachinery Airfoils," J. Propul. Power, **17**(1), pp. 176–183.
[11] Yiu, K. F. C., and Zangeneh, M., 2000, "Three-Dimensional Automatic Optimization Method for Turbomachinery Blade Design," J. Propul. Power, **16**(6), pp. 1174–1181.
[12] Dunker, R. J., 1987, "A Shock Loss Model for Supercritical Subsonic Flows in Transonic Axial Flow Compressors," Transonic and Supersonic Phenomena in Turbomachines, pp. 27.1–27.15, AGARD-CP-401.
[13] Hobbs, D. E., and Weingold, H. D., 1984, "Development of Controlled Diffusion Airfoils for Multistage Compressor Application," J. Eng. Gas Turbines Power, **106**, pp. 271–278.
[14] Steinert, W., Eisenberg, B., and Starken, H., 1991, "Design and Testing of a Controlled Diffusion Airfoil Cascade for Industrial Axial Flow Compressor Application," ASME J. Turbomach., **113**, pp. 583–590.

[15] Steinert, W., and Starken, H., 1994, "Off-Design Transition and Separation Behavior of a CDA Cascade," ASME Paper No. 94-GT-214.
[16] Dunker, R., Rechter, H., Starken, H., and Weyer, H., 1984, "Redesign and Performance Analysis of a Transonic Axial Compressor Stator and Equivalent Plane Cascades With Subsonic Controlled Diffusion Blades," J. Eng. Gas Turbines Power, **106**, pp. 279–287.
[17] Niederdrenk, P., Sobieczky, H., and Dulikravich, G. S., 1987, "Supercritical Cascade Flow Analysis With Shock-Boundary Layer Interaction and Shock-Free Redesign," ASME J. Turbomach., **109**, pp. 413–419.
[18] Hoheisel, H., and Seyb, N. J., 1987, "The Boundary Layer Behavior of Highly Loaded Compressor Cascade at Transonic Flow Conditions," Transonic and Supersonic Phenomena in Turbomachines, pp. 4.1–4.17, AGARD-CP-401.
[19] Yamaguchi, Y., and Arima, T., 2000, "Multi-Objective Optimization for the Transonic Compressor Stator Blade," 8th AIAA/USAF/NASA/ISSMO Symposium on Multidisciplinary Analysis and Optimization, Long Beach, CA, Paper No. AIAA-2000-4909.
[20] Song, B., Gui, X., Li, S.-M., Douglas, J., and Ng, W., 2002, "Flow periodicity improvement in a High Speed Compressor Cascade with a Large Turning-Angle," 38th AIAA/ASME/SAE/ASEE Joint Propulsion Conference & Exhibit, Indianapolis, Indiana, Paper No. AIAA 2002-3539.
[21] Song, B., and Ng, W., 2004, "Influence of Axial Velocity Density Ratio in Cascade Testing of Supercritical Compressor Blades," 40th AIAA/ASME/SAE/ASEE Joint Propulsion Conference & Exhibit, Fort Lauderdale, FL, Paper No. AIAA-2004-3414.
[22] Johnsen, I. A., and Bullock, R. O., 1965, "Aerodynamic Design of Axial-Flow Compressors," revised version, NASA SP-36.
[23] Song, B., 2003, "Experimental and Numerical Investigations of Optimized High-Turning Supercritical Compressor Blades," Ph.D. dissertation, Virginia Polytechnic Institute and State University, Blacksburg VA.

Simulation of Compressor Transient Behavior Through Recurrent Neural Network Models

M. Venturini
ENDIF—University of Ferrara,
Via Saragat, 1,
44100 Ferrara,
Italy

In the paper, self-adapting models capable of reproducing time-dependent data with high computational speed are investigated. The considered models are recurrent feed-forward neural networks (RNNs) with one feedback loop in a recursive computational structure, trained by using a back-propagation learning algorithm. The data used for both training and testing the RNNs have been generated by means of a nonlinear physics-based model for compressor dynamic simulation, which was calibrated on a multistage axial-centrifugal small size compressor. The first step of the analysis is the selection of the compressor maneuver to be used for optimizing RNN training. The subsequent step consists in evaluating the most appropriate RNN structure (optimal number of neurons in the hidden layer and number of outputs) and RNN proper delay time. Then, the robustness of the model response towards measurement uncertainty is ascertained, by comparing the performance of RNNs trained on data uncorrupted or corrupted with measurement errors with respect to the simulation of data corrupted with measurement errors. Finally, the best RNN model is tested on field data taken on the axial-centrifugal compressor on which the physics-based model was calibrated, by comparing physics-based model and RNN predictions against measured data. The comparison between RNN predictions and measured data shows that the agreement can be considered acceptable for inlet pressure, outlet pressure and outlet temperature, while errors are significant for inlet mass flow rate. [DOI: 10.1115/1.2183315]

Introduction

In the last years, increasing attention has been paid to evaluating the transient behavior of turbomachines and of the facilities in which they operate [1–7]. In fact, transient behavior analysis of energy systems finds useful application in the power plants design phase [8] and to set up plant control systems [9], in particular for aircraft engines that usually operate in unsteady state conditions [10]. Furthermore, transient response analysis has proven effective in investigating gas turbine component behavior under critical operating conditions [11,12] and in the presence of unsteady phenomena, such as stall or surge [13–16]. Another field of application of dynamic analysis is the study of integration between compressors and pipelines, especially when a rapid deceleration or a shutdown takes place [6,17]. Finally, transient data appear to provide significant diagnostic content, i.e., some faults may be more easily detectable from unsteady data analysis, since fault effects are magnified under transient conditions [18,19]. For this latter application, the availability of a dynamic simulation code is particularly required, since the experimental activity for obtaining real data would be expensive in terms of labor and cost. In fact, the employment of simulation codes allows a database of a great number of faults (different in type and severity) to be created, together with the analysis of their effects on measurable variables.

The mathematical model for developing a dynamic simulation code can be built through the laws of conservation (mass, momentum, energy, and moment of momentum) and heat balances, written in differential form, and by using the performance maps of the considered machine [1,3,4,7,9,12–14,17]. Since the physics-based approach requires knowledge of the phenomena taking place in the considered machine, it is possible to correctly understand both the physics of the processes and the way each malfunction may manifest itself. On the other hand, the development of physics-based dynamic simulation models presents some problems:

- The system to simulate may be complex, i.e., the number of equations to be solved could be high. Such complexity usually leads to computational times which may limit the use of the model in on-line applications. In order to simplify the system equation and thus to obtain advantages in terms of computational times, physics-based model transfer functions can be simplified [20]. Another solution is given by the method of characteristics which represents a relatively easy way to implement transient one-dimensional codes for complex systems, as made in [21];
- the capability of the model in reproducing the real machine is affected by the quality of the calibration process, i.e., it depends on the choice of the values of the physical parameters, such as volume, friction factors, or heat transfer coefficients, which define system response and which can be difficult to determine. Such parameters are usually estimated [7,17]. Moreover, the calibration of a physics-based model also requires the knowledge of machine performance maps which are not always available.

For these reasons, a good solution for overcoming these problems is the implementation of *black box* models which:

- Do not require knowledge of the physics of the problem under investigation, because of their self-adapting nature;
- usually have high mapping capabilities and guarantee a good generalization even with a reduced set of identification data. Moreover, they are robust in the presence of poor and/or noisy input data. For a discussion about this aspect, the reader is referred to [22];
- are characterized by high computational speed. This feature proves crucial mainly when *black box* models are used for real-time simulations.

Contributed by the International Gas Turbine Institute (IGTI) of ASME for publication in the JOURNAL OF TURBOMACHINERY. Manuscript received October 1, 2004; final manuscript received February 1, 2005. IGTI Review Chair: K. C. Hall. Paper presented at the ASME Turbo Expo 2005: Land, Sea, and Air, Reno, NV, June 6–9, 2005, Paper No. GT2005-68030.

On the other hand, the main limit of these models is high prediction error when they operate outside the field in which they were trained, i.e., they are not able to extrapolate. Among the various black box models, neural networks (NNs) have proved to be flexible and robust in simulating the behavior of energy systems in unsteady conditions [23–25].

In the paper, NN models (feed-forward NNs with a single hidden layer, trained by using a back-propagation learning algorithm) for the simulation of compressor behavior under unsteady conditions are studied and developed. In particular, the data used for both training and testing the NNs were obtained by means of a nonlinear modular model for compressor dynamic simulation [7]. The nonlinear model, developed through a physics-based approach and implemented through the MATLAB® Simulink tool, was calibrated on a multistage axial-centrifugal small size compressor running in the test facility of the University of Ferrara [26] and validated through experimental data measured on the compressor in different transient operating regimes [7].

In order to develop a NN model capable of reproducing time-dependent data, recurrent neural networks with one feedback loop in a recursive computational structure are investigated [27–29]. The first step of the analysis is the selection of the compressor maneuver which has to be used for optimizing RNN training. In this phase, different operating condition variations (i.e., different trajectories of compressor rotational speed, which is the input variable) are considered and tested for training, with respect to different compressor maneuvers (accelerations and decelerations) used for RNN testing. The subsequent step consists in evaluating the most suitable RNN structure (optimal number of neurons in the hidden layer and number of outputs). Then, an analysis is conducted for evaluating the most appropriate RNN total delay time. Moreover, the robustness of the model response towards measurement uncertainty is ascertained by comparing the performance of RNNs trained on data uncorrupted or corrupted with measurement errors with respect to the simulation of data corrupted with measurement errors. Finally, the best RNN model is tested on field data taken on the axial-centrifugal compressor on which the physics-based model was calibrated, by comparing physics-based model and RNN predictions against measured data.

Recurrent Neural Networks

Artificial neural networks (NNs) are mathematical structures which are able to link, in a nonlinear way through several interconnected simple units (the artificial neurons) in which data are processed in parallel, a multidimensional input space with a multidimensional output space, allowing very high computational speed. A detailed description of NN features and capabilities is beyond the scope of the paper: Further information can be found in specific literature, such as, among others, [27,28], and in papers illustrating NN applications to different fields [23–25,29–32]. For this reason, only the assumptions adopted in the paper for the NN model set up will be outlined below, with particular reference to the development of recurrent neural networks.

The problem of developing a NN model capable of reproducing time-dependent data consists in the fact that the neural network has to take into account the time variable by means of a memory process. This can be done through NN architectures characterized by feedback connections among the neurons. A brief, but exhaustive review of different NN dynamic models structures can be found in [24,28,29].

In the paper, according to [24,29], recurrent neural networks (RNNs) with one feedback loop in a recursive computational structure are considered. The input layer of the RNN consists of a data window made up by present and past values of *exogenous* inputs (i.e., originating from outside the network) and by delayed values of the outputs (in such a way, model outputs are *regressed*). Thus the recurrent network is also referred to as a *nonlinear autoregressive with exogenous inputs* model (NARX). The basic topology of a recurrent neural network is shown in Fig. 1, where Δt is the time delay unit.

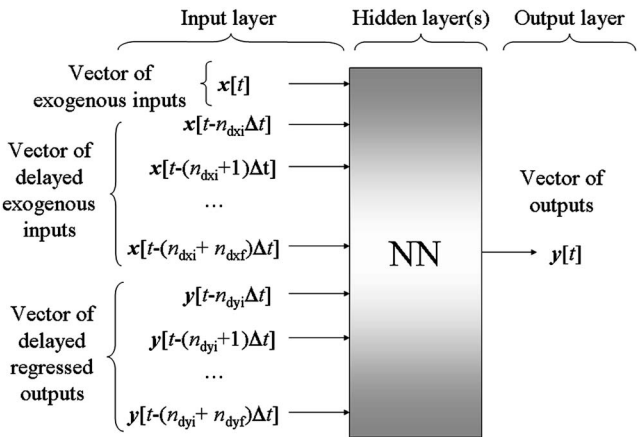

Fig. 1 Scheme of a recurrent neural network (RNN) model

From the scheme reported in Fig. 1, it can be observed that:

- The kernel of the model is the "classical" neural network, the only conceptual difference being (i) the presence of delayed values of the inputs and (ii) the regression of the outputs;
- the vector of exogenous inputs is evaluated at time t (the same as output vector $\mathbf{y}$). This condition is not necessary, since RNNs in which the output vector is ahead of the input vector by at least one time unit are presented in [27,28,33,34];
- the total delay time of the vector of delayed exogenous inputs is $(n_{dxi}+n_{dxf})\Delta t$, starting from time $n_{dxi}\Delta t$, and, similarly, the total delay time of the vector of delayed regressed outputs is $(n_{dyi}+n_{dyf})\Delta t$, starting from time $n_{dyi}\Delta t$. The delayed values of the outputs to be used as RNN inputs can be either taken from outside the RNN (for example, measured data or data estimated through a different model) or estimated through the RNN itself at antecedent time steps: In the paper, the first solution was adopted.

Owing to the above-mentioned considerations, the dynamic behavior of the NARX model is described by the following equation, where F is a nonlinear function of its arguments:

$$\mathbf{y}(t) = F[\mathbf{x}(t), \mathbf{x}(t - n_{dxi}\Delta t), \ldots, \mathbf{x}(t - n_{dxi}\Delta t - n_{dxf}\Delta t), \mathbf{y}(t - n_{dyi}\Delta t), \ldots, \mathbf{y}(t - n_{dyi}\Delta t - n_{dyf}\Delta t)] \quad (1)$$

The transfer function F depends on the chosen activation function (in this paper, sigmoidal) and on the network parameters (i.e., number of inputs, number of neurons in the hidden layers, and connection weights among the neurons). In particular, the proper connection weights can be identified through the optimization of the training process, which in the paper is always performed off-line. Thus, according to Eq. (1), the RNN model implicitly takes into consideration the time variable by means of the dependence-with-time of all variables, as in [28,29], and differently from [23], in which the time variable is one of the inputs.

The chosen NN architecture is the typical *feed-forward multilayer perceptron*. In particular, NNs with one hidden layer and a continuous sigmoid activation function are used, since it has been shown that this type of NN architecture is able to represent any type of multidimensional nonlinear function, if a suitable number of neurons of the hidden layer is chosen [28,35]. The use of multiple hidden layers usually requires a great computational effort, while it only allows a small improvement of performance [28], and so architectures with only one hidden layer are usually adopted in practice [24,32,34].

For the NN training, a *back-propagation* algorithm was used

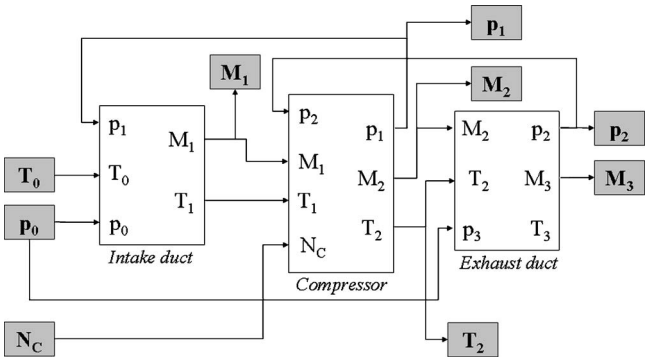

Fig. 2 Implementation of the physics-based model for compressor dynamic simulation through the Simulink tool

and the *TRAINSCG* algorithm (available in the MATLAB Neural Network toolbox) was adopted: In fact, this appeared to be very effective with a low computational effort [22,32,34].

The adopted stopping criterion for the NN training phase is the minimization of a performance function which was chosen to be the mean square error (*MSE*) on the whole training set between the target outputs and the corresponding NN computed outputs:

$$MSE = \frac{1}{n_o \cdot n_{\text{patt}}} \sum_{j=1}^{n_o} \sum_{i=1}^{n_{\text{patt}}} [t_{ij} - y_{ij}]^2 \tag{2}$$

where n_o is the number of NN outputs, n_{patt} is the number of patterns used for the NN training, t_{ij} are the target outputs, and y_{ij} the NN computed outputs.

The above-mentioned assumptions have already proved effective in many fields of NN application for the simulation of steady [30,32] and unsteady [23,24,29,34] data.

The Compressor Under Investigation

Test Rig. The test facility under consideration [7,26], which was set up in the laboratories of the University of Ferrara, consists of an asynchronous reversible electric motor/brake bench, operated by an inverter. The motor can give a maximum power of 87 kW at 5000 rpm.

Compressor. The compressor, which is part of the Allison 250-C18 turbo-shaft engine, is composed of six axial stages and one centrifugal stage. The compressor operates in an open circuit: The inlet section (an orifice plate used to perform the inlet mass flow measurement) is followed by a pipe; then, after flowing through the axial and centrifugal stages, the air exits through two semivolutes and is fed to a common cylinder in which a butterfly valve is inserted for compressor mass flow rate control.

A step-up gearbox with a gear ratio equal to 5.83 (which was part of the original gas turbine) is included in the test setup to analyze a range of compressor rotational speeds up to nearly 30,000 rpm.

Compressor Physics-Based Dynamic Model. For the above-described compressor, a nonlinear modular model for dynamic simulation was setup and implemented in MATLAB® environment through the Simulink tool [7]. A modular structure was adopted, by identifying three subsystems (*intake duct, compressor*, and *exhaust duct*), which are sketched in Fig. 2.

The model was developed through a physics-based approach by using the laws of conservation (mass and momentum) and heat balances, and by using the performance maps of the considered compressor. In particular, rises in pressure and temperature in steady-state conditions along the compressor are taken into account by means of machine performance maps, while balance equations are used in order to consider mass storage and thermal exchange phenomena. Mass storage effects in the suction and discharge piping systems are also taken into account through the *intake* and *exhaust duct* modules, while thermal exchange in both modules is assumed negligible.

The module inputs are ambient pressure p_0 and temperature T_0 and compressor rotational speed N_C (which is fed directly to *compressor* module), while the calculated outputs are:

- Compressor inlet: Mass flow rate M_1 and pressure p_1;
- compressor outlet: Mass flow rate M_2, pressure p_2, and temperature T_2;
- exhaust duct outlet: Mass flow rate M_3 and temperature T_3.

The physics-based dynamic model was calibrated on a multistage axial-centrifugal small size compressor [26] and validated through experimental data measured in different compressor transient operating regimes [7].

Data for NN Training and Testing

Data Generation. The physics-based dynamic model has been used to generate eleven different transients ($TR_1, TR_2, \ldots, TR_{11}$), which can be considered representative of the compressor behavior: TR_1–TR_6 are used for RNN training, while TR_7–TR_{11} are used to verify the generalization capabilities of the trained RNNs. All the simulated maneuvers reproduce accelerations and decelerations at ISO conditions (T_0=15 °C; p_0=101.3 kPa).

In Fig. 3, the time trajectory of the compressor rotational speed (which is the only input for the compressor dynamic model, once ambient conditions T_0 and p_0 are fixed) is plotted for a time interval of 100 s for each transient TR. All the considered curves cover a range of variation for compressor rotational speed from about 5000 up to 30,000 rpm, which is also the range of variation of the rotational speed for the compressor on which the physics-based model was calibrated.

As regards RNN training, the transients can be divided into triangular-shaped (TR_1, TR_2, and TR_3) and trapezoidal-shaped (TR_4, TR_5, and TR_6), which are reported in Figs. 3(*a*) and 3(*b*), respectively. Moreover, in each group, one curve is symmetrical with respect to the total time interval (TR_1 and TR_4), while the others are not symmetrical. Finally, it has to be observed that all the six curves are characterized by a stationary phase, whose duration is 10 s, both at the beginning and at the end of the transient.

The curves used for RNN testing (TR_7–TR_{11}) differ from each other, since compressor rotational speed varies:

- Quite slowly and symmetrically with respect to the total time interval (TR_7–TR_9 in Fig. 3(*c*));
- quite rapidly, as a fast ramp-shaped curve, and in an asymmetrical fashion (TR_{10} and TR_{11} in Fig. 3(*d*)).

Finally, it should be specified that for all the generated data, the sampling time was equal to 0.1 s: This means that (i) the time delay unit Δt reported in Eq. (1) is also considered equal to 0.1 s and (ii) each curve contains 1000 data patterns. Furthermore, since some transients are used for RNN training (TR_1–TR_6), while the rest (TR_7–TR_{11}) are used for RNN testing, the developed RNNs have all been tested on patterns not including the patterns used for training.

Measurement Errors. To take into account the presence of measurement errors, the generated data were corrupted with random errors included in the measurement uncertainty intervals reported in Table 1. The estimation of the absolute uncertainties for the measured quantities, reported in the second column of Table 1, was performed by using the results of the uncertainty analysis conducted in [26]. The percentage uncertainty values (fourth column of Table 1) were then calculated with respect to the values of the quantities in correspondence to the rotational speed (i.e., 28,948 rpm) for which the uncertainty analysis was conducted.

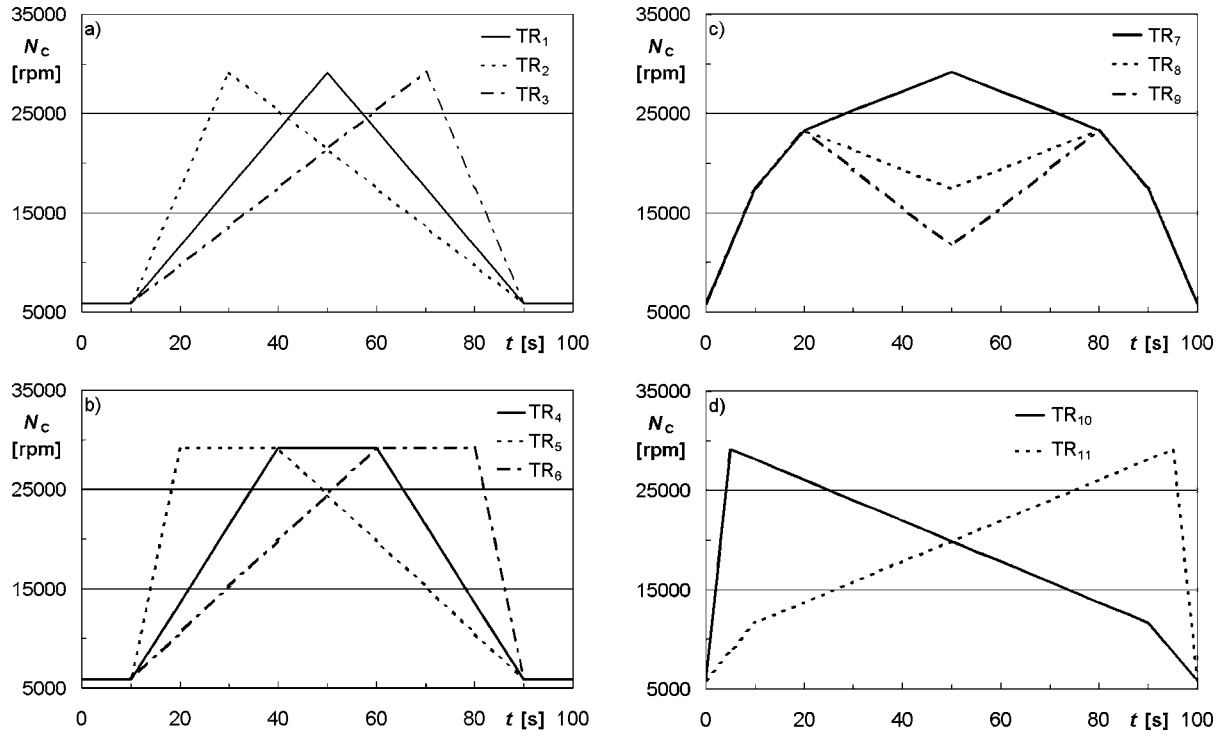

Fig. 3 Compressor rotational speed versus time for transients TR_i (simulated data) used for RNN training ((*a*) and (*b*)) and testing ((*c*) and (*d*))

Normalization of Data Patterns. Before the generated data are supplied to the RNNs, they have to be normalized to be comparable with each other. The normalization was performed with respect to the maximum and minimum value of the data set generated for each variable so that normalized values lie in the range $[-1;1]$.

RNN Model Identification

The developed RNN models are characterized by a single exogenous input (compressor rotational speed N_C) and four outputs (compressor inlet and outlet pressure p_1 and p_2, compressor inlet mass flow rate M_1 and compressor outlet temperature T_2). Thus, the exogenous input vector $\boldsymbol{x}$ is composed of only one element (i.e., $\boldsymbol{x}[t]=(N_C[t])$, and, so, the dimension of the vector is $d_x=1$), while the output vector $\boldsymbol{y}$ is made up of four elements, i.e., $\boldsymbol{y}[t]=(p_1[t],p_2[t],M_1[t],T_2[t])$ and thus $d_y=4$. In the interests of simplicity, dependence-with-time for all variables will be omitted in the notation throughout the paper.

As regards the choice of the delay time, for all the developed RNNs, it was assumed that (i) $n_{dxi}=n_{dyi}=n_{di}$ and (ii) $n_{dxf}=n_{dyf}=n_{df}$: for this reason, we will refer to n_{di} and to n_{df}, without specifying whether it is referred to input vector $\boldsymbol{x}$ or output vector $\boldsymbol{y}$. Then, two different types of RNNs are developed from the general scheme presented in Fig. 1 and are sketched in Fig. 4:

Table 1 Measurement uncertainty values

Quantity	Absolute uncertainty	Value @ N_C=28,948 rpm	Percentage uncertainty [%]
N_C	30.0 rpm	28948.0 rpm	0.10
p_1	0.636 kPa	98.36 kPa	0.65
p_2	1.817 kPa	165.83 kPa	1.10
M_0	0.012 kg/s	0.526 kg/s	2.28
T_2	1.0 K	374.3 K	0.27

- "Intermediate delayed" RNN: The number of initial delay units is put equal to one ($n_{di}=1$) and inputs and outputs are regressed to the RNN input layer for all intermediate time steps up to the time $n_{df}\Delta t$. Thus, the total number of inputs is $n_i=d_x+n_{df}(d_x+d_y)$.
- "one-time delayed" RNN: The number of initial delay units is put equal to the number of final delay units ($n_{di}=n_{df}$), so that the values of exogenous inputs and of the regressed outputs are both supplied to the RNN input layer only delayed of time $n_{df}\Delta t$. Thus, the total number of inputs is $n_i=(2d_x+d_y)$, i.e., six.

The choice of the most appropriate delay time $n_{df}\Delta t$ and RNN architecture is one of the main purposes of the paper: For this reason, intermediate delayed RNNs with $n_{df}=5$ or $n_{df}=10$ (i.e., total delay time equal to 0.5 s with $n_i=26$ or total delay time equal

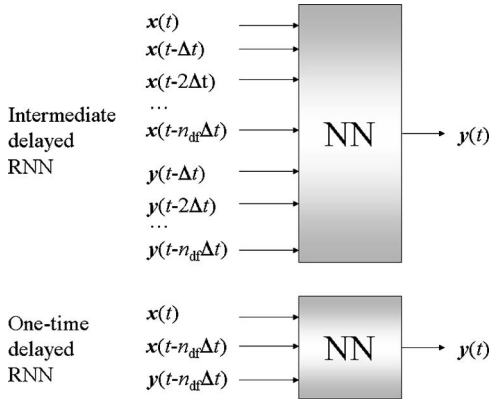

Fig. 4 Scheme of the recurrent neural network models adopted in the paper

to 1.0 s with $n_i=51$) and one-time delayed RNNs with $n_{df}=1,5,10,20$ (i.e., total delay time from 0.1 s up to 2.0 s) are developed and tested.

Analysis of RNN Configuration Parameters

The first step of the performed analyses is the selection of the compressor maneuver to be used for optimizing RNN training. For this purpose, different compressor rotational speed variations are considered and tested (TR_1–TR_6).

Then, in order to identify the most appropriate RNN structure, a sensitivity analysis is carried out with respect to the main RNN configuration parameters:

- Most appropriate RNN structure:
  - optimal number of neurons in the hidden layer (varied in the range 5–90);
  - proper number of RNN outputs, i.e., Multi-Input Multi-Output (MIMO) and Multi-Input Single-Output (MISO) network architectures are tested;
- most appropriate total delay time (from 0.1 s up to 2.0 s).

Finally, the RNN model robustness towards measurement uncertainty is ascertained, through the comparison with expected values corrupted with measurement errors.

The first parameter used for the comparison of the developed RNNs is the root mean square error (RMSE) made by the RNN on the whole set of test data in the calculation of each jth output (p_1, p_2, M_1, and T_2) for any given kth transient used for RNN testing (TR_7–TR_{11}):

$$\left(\mathrm{RMSE}=\sqrt{\frac{1}{n_{\mathrm{patt}}}\sum_{i=1}^{n_{\mathrm{patt}}}\left(\frac{t_i-y_i}{t_i}\right)^2}\right)_{jk},\quad j=1,\ldots,n_o,\quad k=1,\ldots,n_{\mathrm{TR}} \tag{3}$$

where t_i are the target outputs, y_i are the computed outputs, n_{patt} is the number of patterns for each transient used for RNN testing (i.e., 1000), n_o is the number of RNN outputs (i.e., one or four for MISO or MIMO networks, respectively) and n_{TR} is the number of transients used for RNN testing (i.e., five).

Two different concise indices are then derived:

- RMSE_{ov}, which represents the overall RMSE made by the RNN on all outputs for each transient used for RNN testing, and is defined as:

$$\left(\mathrm{RMSE}_{ov}=\sqrt{\frac{1}{n_o}\sum_{j=1}^{n_o}(\mathrm{RMSE})_j^2}\right)_k,\quad k=1,\ldots,n_{\mathrm{TR}} \tag{4}$$

- RMSE_m, which represents the RMSE made by the RNN on all transients used for testing. In this case, the "mean" value is calculated with respect to all transients, and thus the parameter can be calculated for any jth single output (Eq. (5)) and also as an overall value (Eq. (6)) as:

$$\left(\mathrm{RMSE}_m=\sqrt{\frac{1}{n_{\mathrm{TR}}}\sum_{k=1}^{n_{\mathrm{TR}}}(\mathrm{RMSE})_k^2}\right)_j,\quad j=1,\ldots,n_o \tag{5}$$

$$(\mathrm{RMSE}_m)_{ov}=\sqrt{\frac{1}{n_o}\sum_{j=1}^{n_o}(\mathrm{RMSE}_m)_j^2} \tag{6}$$

The second parameter used for the comparison of the different RNNs is the success rate (SR). It is considered that a success in the simulation of a computed output y_j is achieved when it results that:

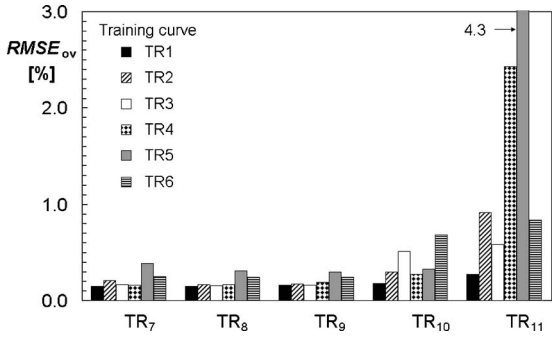

Fig. 5 Influence of the choice of the compressor maneuver used for training (one-time delayed RNNs, delay time=0.5 s, $n_{\mathrm{HLN}}=15$)

$$|t-y|_j \leq u_j,\quad j=1,\ldots,n_o \tag{7}$$

where u_j is the absolute measurement uncertainty of the jth output (p_1, p_2, M_1, and T_2) reported in Table 1.

Thus, it is possible to calculate the success rate for each RNN output, defined as the percentage ratio between the number of successes and the number of test patterns n_{patt}. According to formula (7), the success rate represents the ratio between the number of predicted values lying within measurement uncertainty (i.e., which do not deviate from the corresponding expected values more than the absolute measurement uncertainty) and the total number of predicted values. Such a parameter was also adopted for validating the physics-based compressor dynamic model [7]. The three parameters $(\mathrm{SR}_{ov})_k(k=1,\ldots,n_{\mathrm{TR}})$, $(\mathrm{SR}_m)_j(j=1,\ldots,n_o)$ and $(\mathrm{SR}_m)_{ov}$ can be then derived as previously done for the RMSE.

A large number of simulations have been performed in order to take into account the mutual influences of the configuration parameters on RNN performance: The most interesting results are reported below.

Optimal Compressor Maneuver for RNN Training. The influence of the choice of the compressor maneuver used for RNN training was established, by developing different one-time delayed RNN models (further in the paper, they prove to be the best RNN configuration). In particular, the number of time delay units n_{df} was assumed to be five, i.e., the exogenous inputs and the regressed outputs are delayed by 0.5 s, while the number of neurons in the hidden layer was assumed to be 15.

The results, which can be seen in Fig. 5, highlight the fact that the optimal maneuver for RNN training is TR_1, independently of the considered test maneuver (TR_7–TR_{11}), since lower RMSE_{ov} values are obtained. The reason can be attributed to the fact that TR_1 is triangular-shaped and symmetrical with respect to the total time interval (as most of the test curves are), so that all test curves can be reproduced with an acceptable error. Moreover, it can be observed that the most critical curve is TR_{11} (strongly asymmetrical), while the curves which are reproduced more accurately are TR_7, TR_8, and TR_9, since they are the most similar to all the training curves.

Curve TR_1 was confirmed as the optimal maneuver for RNN training even if different values of the total delay time (1.0 s or 2.0 s) were adopted. The results of this latter analysis are omitted in the current paragraph since the influence of the delay time is analyzed separately further in the paper.

Finally, the influence of the stationary phase at the beginning and at the end of the transients used for training was evaluated. The results of this latter analysis, not reported in the paper, showed that the presence of such a stationary phase is beneficial for improving RNN performance, i.e., lower RMSE_{ov} values are

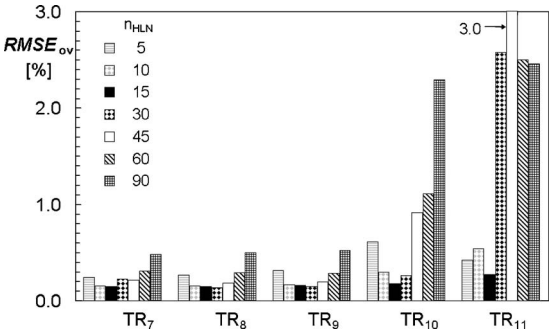

Fig. 6 Influence of the number of neurons in the hidden layer (one-time delayed RNNs with total delay time=0.5 s)

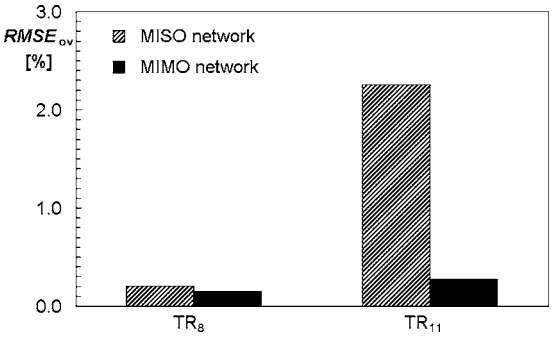

Fig. 7 Influence of the number of outputs for testing transients TR_8 and TR_{11} (one-time delayed RNNs; total delay time =0.5 s; n_{HLN}=15)

obtained if the training curves include a stationary phase rather than only time-dependent trajectories are considered. This effect proved particularly evident for TR_{11} curve.

Number of Neurons in the Hidden Layer. The influence of the number of neurons in the hidden layer on the RNN simulation error was evaluated by comparing the response of different one-time delayed RNNs with different values of n_{HLN} (varied in the range 5–90) and total delay time equal to 0.5 s.

All the developed RNNs were trained by using TR_1 curve (as a result of the analysis conducted in the previous paragraph), while the $RMSE_{ov}$ was evaluated by running each RNN in order to reproduce the curves used for testing (TR_7–TR_{11}).

The analysis of the results, presented in Fig. 6, shows that the best solution is represented by the RNN with a number of neurons in the hidden layer n_{HLN} equal to 15. This is not in agreement with the results presented in [32] for the development of a neural network trained on uncorrupted stationary data, for which the increase of the number of neurons in the hidden layer allowed the reduction of the error on test patterns. So, it is possible to conclude that for a recurrent neural network the overparametrization of the structure leads to a loss of generalization capability. On the other hand, a too low value for n_{HLN} (for instance, n_{HLN}=5) is also not to be recommended. This second remark is in agreement with a rule of thumb (theoretically demonstrated in [36]) used for NNs in steady-state applications, which states that the number of neurons in the hidden layer should be assumed to be higher than twice the number of inputs. Since in the case under investigation (one-time delayed RNN models) the number of inputs is six, the minimum number of neurons in the hidden layer (among the considered ones) which is in agreement with the rule of thumb is 15.

Moreover, the use of a reduced number of neurons in the hidden layer has a beneficial effect on the reduction of the computational time required for the training phase, since the number of epochs falls from 100,000 for n_{HLN}=60 to 12,000 for n_{HLN}=15.

Finally, this analysis also confirms curve TR_{11} as the most difficult to be simulated.

Number of RNN Outputs. The influence of the choice of the number of outputs on RNN performance was established by comparing RNNs with a Multi-Input Multi-Output (MIMO, i.e., calculating all the outputs) and a Multi-Input Single-Output (MISO, i.e., each one calculating a single output) structure.

The analysis was performed by adopting one-time delayed RNNs with total delay time equal to 0.5 s and with 15 neurons in the hidden layer, and testing them on two curves: The first one, which proved to be reproduced accurately (TR_8), and the second one, which on the contrary was identified as "critical" (TR_{11}). It can be seen from Fig. 7 that in both cases the Multi-Output (MIMO) structure is preferable with respect to the Single-Output (MISO) structure.

Delay Time. The influence of the choice of the proper delay time on RNN performance was established by comparing the response of six different RNN models: Two so-called "intermediate delayed" RNNs (n_{df}=5 or n_{df}=10, i.e., total delay time equal to 0.5 s or 1.0 s, respectively) and four so-called "one-time delayed" RNNs (n_{df}=1,5,10,20, i.e., total delay time from 0.1 up to 2.0 s).

All the developed RNNs were trained by adopting the solutions which proved preferable from the analyses performed in the previous sections (i.e., use of TR_1 curve for training, 15 neurons in the hidden layer, MIMO architecture) and then compared by means of the parameter $RMSE_m$.

The results, reported in Fig. 8, highlight that it is preferable, independent of the considered output (and so this fact also reflects on the overall value), to adopt:

- One-time delayed RNNs with respect to intermediate delayed RNNs for any assigned total delay time (except the cases of p_2 for a delay time of 0.5 s and T_2 for a delay time of 0.5 and 1.0 s). This means that the higher amount of information which is contained in the intermediate delayed RNNs is probably "excessive" and so damages RNN performance. This justifies the validity of the analyses which have been conducted in the previous sections through one-time delayed RNNs;
- one-time delayed RNNs with as reduced as possible total delay time (in the paper, 0.1 s): This allows $RMSE_m$ overall values of about 0.1%;
- the most critical quantity is the inlet compressor mass flow rate M_1, for which errors can be particularly high if a proper delay time is not adopted.

The influence of the delay time for different numbers of neurons in the hidden layer was evaluated and the results are reported in Fig. 9 where the $(RMSE_m)_{ov}$ is plotted against the number of neurons in the hidden layer normalized with respect to the number of inputs n_i. It can be observed that (i) it is confirmed that one-

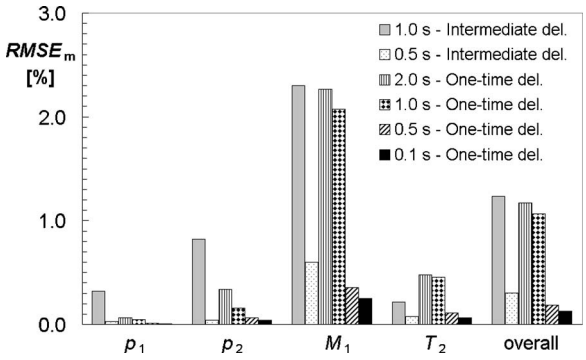

Fig. 8 Influence of the delay time (n_{HLN}=15)

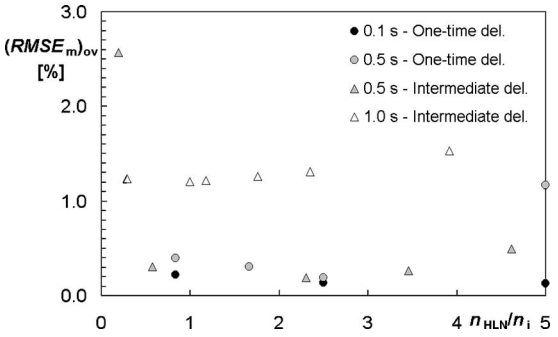

Fig. 9 Influence of the delay time with respect to the number of neurons in the hidden layer normalized with the number of inputs

time delayed RNNs are preferable to intermediate delayed RNNs, though these latter show a good performance if a low delay time is adopted (i.e., 0.5 s) and (ii) both intermediate delayed and one-time delayed RNNs reach the lowest values of $(\mathrm{RMSE}_m)_{ov}$ when the number of neurons in the hidden layer is slightly higher than the twice the number of inputs, being in agreement with the above-cited rule of thumb.

Measurement Uncertainty. In order to assess the RNN robustness towards measurement uncertainty, different one-time delayed RNNs (all with 15 neurons in the hidden layer and trained by using TR_1 curve) were considered. The analyses have been focused on the evaluation of the influence of the presence of measurement errors, reported in Table 1, for different values of the delay time (one-time delayed RNNs with total delay time equal to 0.1, 0.5, or 1.0 s). Two situations were investigated:

- Presence of measurement errors only in the test patterns, i.e., training patterns are not corrupted with measurement errors, while test patterns are corrupted with measurement errors (case Tr U, Ts C);
- presence of measurement errors both in training and test patterns, i.e., both training and test patterns are corrupted with measurement errors (case Tr C, Ts C).

The results, reported in Fig. 10, show that:

- RMSE_m values are noticeably higher than in the previous cases due to the presence of measurement uncertainty. In particular, inlet compressor mass flow rate M_1 is confirmed as the most critical quantity;
- independent of the considered delay time, RNNs trained on data corrupted with measurement errors (Tr C, Ts C) reach lower overall RMSE_m values (except p_1 which is almost constant and T_2 for a delay time of 0.1 s) and higher overall SR values (reported in Table 2) than the corresponding RNNs trained by using data not corrupted with measurement errors (Tr U, Ts C). This is in agreement with similar analyses performed in literature, as, among others, in [31,32]. Such a benefit is particularly evident when a high delay time is considered;
- in the case of RNNs trained on data corrupted with measurement errors (Tr C, Ts C), RMSE_m values decrease (especially the overall value) as the delay time passes from 0.1 to 0.5 s, while it remains quite constant from 0.5 to 1.0 s. This may seem in disagreement with the results presented in the previous section, but the analysis of the overall success rate values (see Table 2) confirms that the choice of adopting a low delay time is still confirmed: In fact, higher $(SR_m)_{ov}$ values can be obtained, though the improvement is small (from 60 to 65% if the delay time is decreased from 1.0 to 0.1 s in the case Tr C, Ts C).

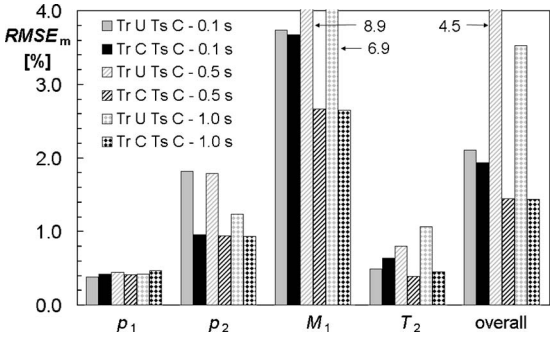

Fig. 10 Influence of the delay time (0.1, 0.5, 1.0 s) for one-time delayed RNNs in the presence of measurement uncertainty

Table 2 Overall success rate for RNNs (delay time =0.1, 0.5, 1.0 s) trained with data uncorrupted and corrupted with measurement errors in the simulation of data corrupted with measurement errors

	$(SR_m)_{ov}$ [%]		
Delay time [s]	0.1	0.5	1.0
Tr U, Ts C	23	12	14
Tr C, Ts C	65	61	60

The analysis of the influence of the delay time for different numbers of neurons in the hidden layer in the case of both training and test patterns corrupted with measurement errors (case Tr C, Ts C) substantially confirmed the results obtained in the previous section for uncorrupted data. In fact, for both intermediate delayed and one-time delayed RNNs, it was found (the results are not reported in the paper for the sake of brevity) that it is still advisable to adopt a number of neurons in the hidden layer slightly higher than twice the number of inputs, though, in the case of corrupted data, the lowest $(\mathrm{RMSE}_m)_{ov}$ value is about 1.4% instead of 0.1% obtainable in the case of uncorrupted data (reported in Fig. 9).

RNN Validation Against Experimental Data

The best RNN model, as derived from the analyses performed in the previous paragraphs, was also tested against measured values taken on the compressor under investigation and then compared with the response of the physics-based model developed in [7]. So, the RNN model which was adopted in this section presents the following features:

- Use of TR_1 curve data, corrupted with measurement errors reported in Table 1, for RNN training;
- "one-time delayed" configuration, with the as low as possible total delay time (i.e., 0.1 s);
- 15 neurons in the hidden layer and MIMO architecture.

Two test cases (TC1 and TC2) were considered, both measured at quasi-ISO conditions ($T_0 \approx 17\,^\circ\mathrm{C}$; $p_0 \approx 102$ kPa) and representing acceleration and deceleration maneuvers for the compressor on which the physics-based model was validated [7]. The two curves are reported in Fig. 11 and differ from each other since TC1 curve covers a wide range of variation for compressor rotational speed (N_C ranges from about 13,000 up to 23,000 rpm), while TC2 curve covers a more restricted region of N_C values (from about 20,000 up to 26,000 rpm). In any case, the range of variation for compressor rotational speed N_C lies within the range of variation of compressor rotational speed values in the data used for RNN

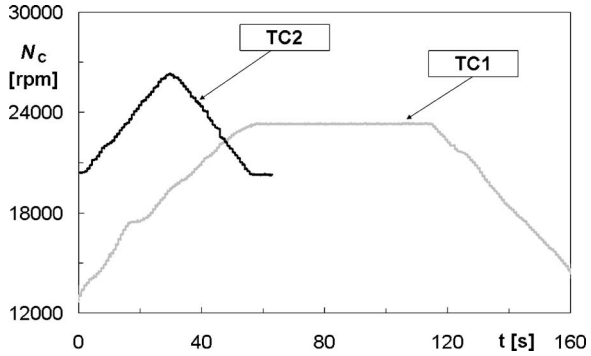

Fig. 11 Rotational speed profile versus time for the two test cases (measured data)

training (assumed to be in the range 5000–30,000 rpm). Finally, it can be noticed that the rotational speed gradient is comparable for both curves (i.e., about 200 rpm per second).

The at-a-glance results of the comparison between measured and predicted values is shown in Fig. 12 in terms of RMSE values and in Table 3 in terms of success rate values, where the corresponding results obtained in [7] through the physics-based model are reported for comparison purposes only. It can be observed that:

- Errors for inlet compressor pressure (maximum error for p_1 about 1.0%), for outlet compressor pressure (maximum error for p_2 about 1.6%) and for outlet compressor temperature T_2 (errors less than 0.7%) can be considered acceptable. This cannot be said for the inlet mass flow rate, whose maximum error is 5.9%. Thus, as also verified by using the physics-based model, this quantity is again confirmed as the most critical quantity to be simulated;
- for all quantities (except the case of p_2 and T_2 for TC1 curve), RMSE values obtained through the RNN are higher than the corresponding values obtained through the physics-based model, and so *SR* values are lower (except the case of T_2 for TC2 curve). In fact, the overall RMSE values for the RNN model are higher than RMSE values for the physics-based model by about 1.5 times. This reflects the fact that the RNN was trained by using data generated by means of the physics-based model and, so, the RNN is affected both by physics-based model approximations with respect to the real system (see [7]) and by the error due to the RNN training on generated data. Such a second source of error leads to RMSE values comparable to those obtained in the previous sections, though the overall error against field data is rather high (3.0% for TC1 curve and 1.4% for TC2 curve);

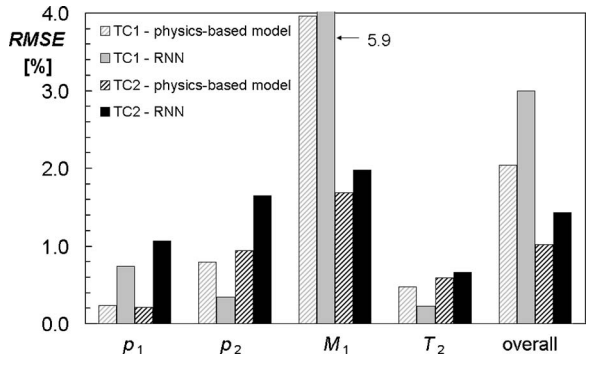

Fig. 12 Comparison between predictions (calculated through both the physics-based model and through the RNN) and measured values

Table 3 Success rate for the physics-based and for the RNN model against measured values

	Success rate [%]			
	Physics-based		RNN	
	TC1	TC2	TC1	TC2
p_1	100	100	55	42
p_2	98	86	88	62
M_1	50	90	34	86
T_2	46	30	37	37

- the decrease in the success rate for RNN model with respect to the physics-based model (see Table 3) is significant only for p_1, while it is small for the other quantities. In any case, such values depend on measurement uncertainty values (reported in Table 1) adopted as the threshold for success rate determination.

Finally, the trends over time of the four outputs are presented in Figs. 13 and 14 for TC1 and TC2 curves, respectively. In the figures, the trend of predictions obtained through the physics-based model is also reported for comparison purposes only and the discussion of the results obtained through this model can be found in [7]. As regards the trend of predictions obtained through the RNN model, it can be observed that:

- p_1 is always underestimated and shows a noticeable scatter even with respect to real data. In particular, this effect is more evident in Fig. 14(*a*);
- p_2 is underestimated for high values of the rotational speed, mainly in the case of TC2 curve (Fig. 14(*b*)). This deviation was also observed for predictions obtained through the physics-based model;
- the error in predicting the mass flow rate is more evident in the steady-state phase of TC1 curve (Fig. 13(*c*)), as can be also observed for the physics-based model, while in TC2 curve, which is characterized only by transient regime, this effect is not detectable (Fig. 14(*c*)). Although the qualitative analysis of the trend of predictions obtained through the physics-based model and through the RNN model may suggest that the results of the two models substantially agree, the RMSE values in Fig. 12 highlight that the difference is considerable (in particular for TC1 curve), as previously outlined;
- T_2 is reproduced quite accurately in both curves, though *SR* values for this quantity are very low (37%). In any case, this fact was also observed by using the physics-based model (*SR* values equal to 46% or 30%).

In conclusion, the agreement of the trends over time of the predicted values with measured values can be considered generally acceptable, except for the inlet mass flow rate, which presents significant errors (mainly for TC1 curve), and for the inlet compressor pressure, which on the contrary was simulated almost perfectly through the physics-based model.

In any case, although RNN's predictive performance is lower than that of the physics-based model, *black-box* self-adapting models represent an easy-to-implement way of modeling an even very complex system, and, in particular, are characterized by high computational speed, which allows real-time simulations. Moreover, a substantial improvement of RNN performance can be reasonably expected by training RNN models directly on experimental data rather than on simulated data, so that a significant source of errors can be eliminated.

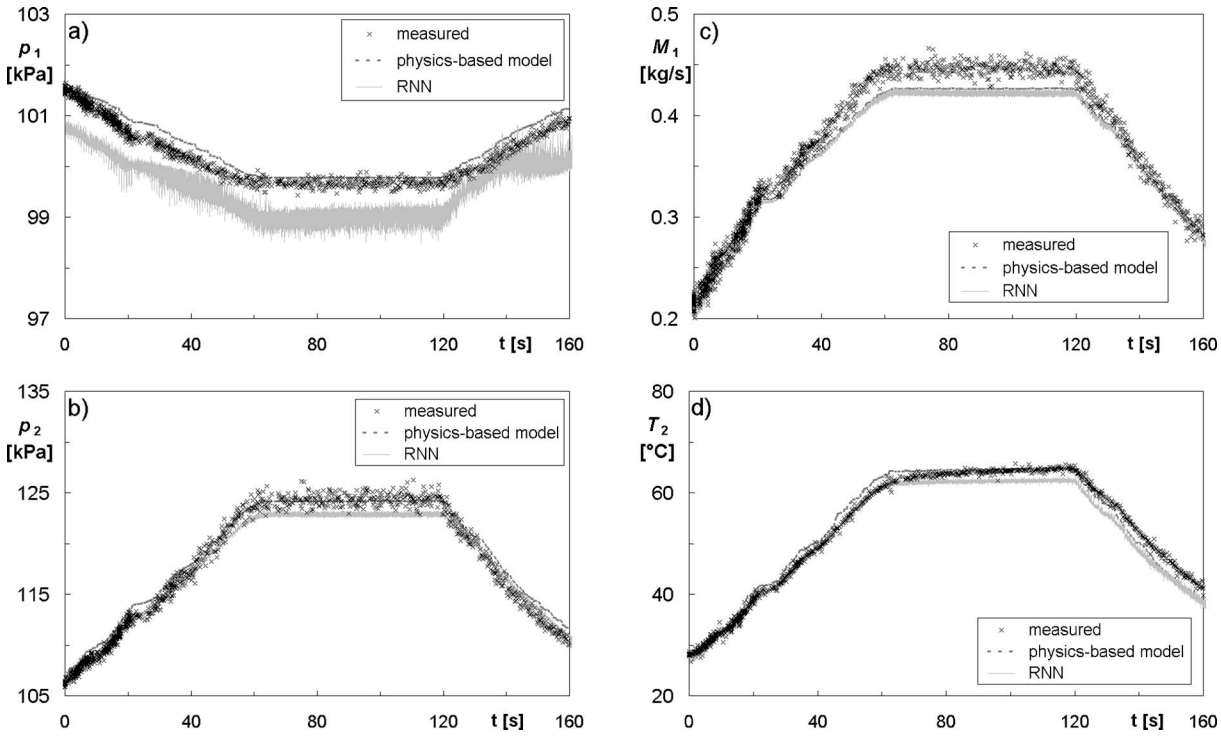

Fig. 13 Comparison of measured values and predictions (obtained through the physics-based model and the RNN) for TC1 curve

Conclusions

In the paper, recurrent feed-forward neural networks (RNNs) with one feedback loop were set up and tested in order to evaluate their capability in reproducing time-dependent data. The data used for developing an influence analysis on RNN configuration parameters were obtained by means of a nonlinear physics-based model for compressor dynamic simulation, which was validated on a multistage axial-centrifugal small size compressor.

The analysis allowed some general conclusions to be derived for the choice (i) of the compressor maneuver to be used for

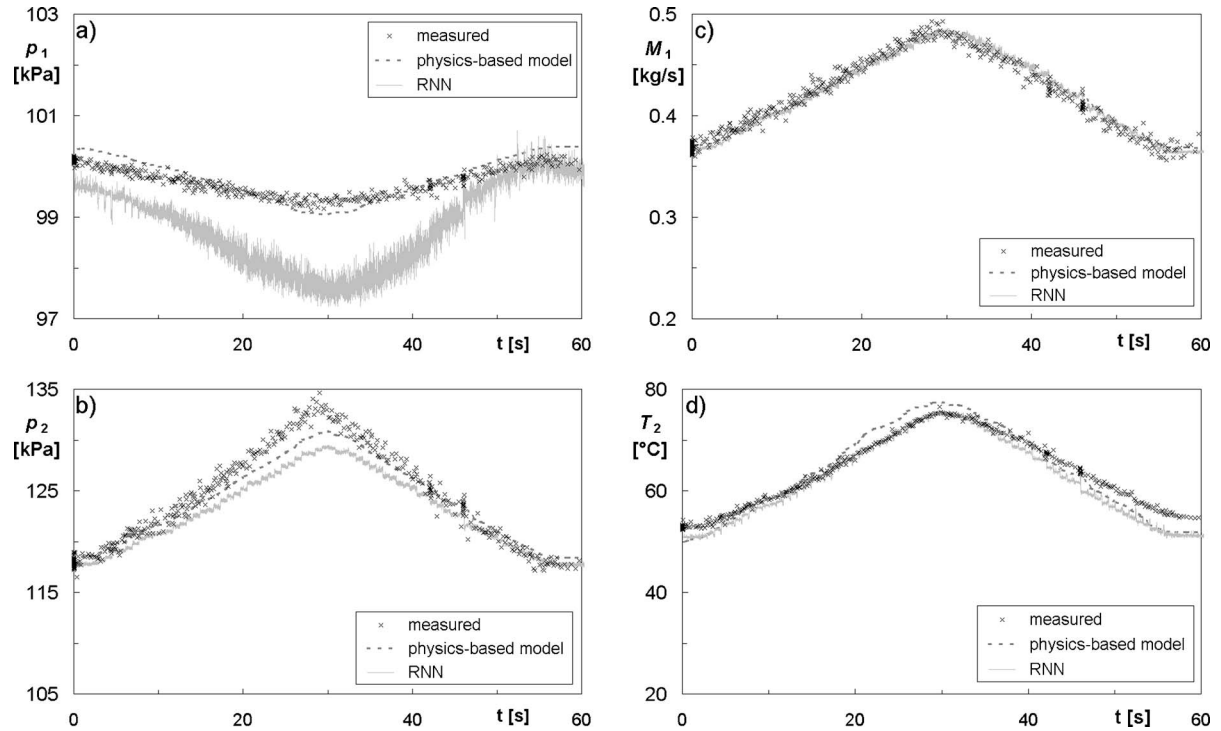

Fig. 14 Comparison of measured values and predictions (obtained through the physics-based model and the RNN) for TC2 curve

optimizing RNN training (triangular-shaped, symmetrical with respect to the total time interval with a stationary phase at the beginning and at the end), (ii) of the proper delay time (as low as possible, in the so-called "one-time delayed" configuration), and (iii) of the most appropriate RNN structure (multi-output architecture with a number of neurons in the hidden layer slightly higher than twice the number of inputs). Furthermore, the robustness of the model response towards measurement uncertainty was found to improve if the RNN is trained on data corrupted with measurement errors.

Finally, the best RNN model was tested on field data measured on the axial-centrifugal compressor on which the physics-based model was validated. The comparison between RNN predictions and measured data showed that the agreement with experimental data can be considered acceptable for inlet pressure, outlet pressure, and outlet temperature (though success rate values are rather low), while errors are significant for inlet mass flow rate. The overall RMSE values for RNN are higher than RMSE values for the physics-based model by about 1.5 times, mainly due to the fact that the RNN was trained by using data generated by means of the physics-based model and not by using field data.

In order to improve RNN performance, future developments of the present study will be aimed at evaluating the choice of different RNN parameters (for instance, use of a lower time delay unit and determination of the proper number of training patterns), at properly selecting RNN inputs (analysis of the influence of each input on RNN response) and, finally, at training the RNN models directly on field operating data.

Acknowledgment

The work was carried out with the support of the M.U.R.S.T. (Italian Ministry of University and Scientific and Technological Research). The author gratefully acknowledges Professor Roberto Bettocchi, Professor Pier Ruggero Spina, and Michele Pinelli, PhD for their suggestions and Dr. Federica Faccini for her precious support in performing the simulations.

Nomenclature

d = vector dimension
M = mass flow rate
MIMO = multi-input multi-output
MISO = multi-input single-output
MSE = mean square error
n_{d} = number of time delay units
n_{HLN} = number of neurons in the hidden layer
n_i = number of inputs
n_o = number of outputs
n_{patt} = number of patterns
n_{TR} = number of transients used for RNN testing
N_C = compressor rotational speed
p = pressure
RMSE = root mean square error
SR = success rate
t = time, expected target output
T = temperature
TC = test case curve (field data)
TR = transient curve (simulated data)
u = absolute measurement uncertainty
y = computed output
Δt = time delay unit

Subscripts and Superscripts

0, 1, 2, 3 = compressor physics-based model sections
f = final
i = initial
m = mean on all transients used for testing
min = minimum
max = maximum
ov = overall
x = input vector x
y = output vector y

References

[1] Blotemberg, W., 1993, "A Model for the Dynamic Simulation of a Two-Shaft Industrial Gas Turbine With Dry Low Nox Combustor," ASME Paper No. 93-GT-355.
[2] Schobeiri, M. T., Attia, M., and Lippe, C., 1994, "GETRAN: A Generic, Modularly Structured Computer Code for Simulation of Dynamic Behavior of Aero- and Power Generation Gas Turbine Engines," ASME J. Eng. Gas Turbines Power, **116**, pp. 483–494.
[3] Bettocchi, R., Spina, P. R., and Fabbri, F., 1996, "Dynamic Modeling of Single-Shaft Industrial Gas Turbine," ASME Paper No. 96-GT-332.
[4] Bianchi, M., Peretto, A., and Spina, P. R., 1998, "Modular Dynamic Model of Multi-Shaft Gas Turbine and Validation Test," *Proc. of "The Winter Annual Meeting of ASME*," AES-38, pp. 73–81.
[5] Traverso, A., Calzolari, F., and Massardo, A., 2003, "Transient Analysis and Control System for Advanced Cycles based on Micro Gas Turbine Technology," ASME Paper No. GT2003-38269.
[6] Pfeifer, U., and Warnack, D., 2003, "Simulation of Non-Steady and Non-Linear Flow Phenomena in Complex Piping Systems of Gas Turbines," ASME Paper No. GT2003-38056.
[7] Venturini, M., 2005, "Development and Experimental Validation of a Compressor Dynamic Model," ASME J. Turbomach., **127**(3), pp. 599–608.
[8] De Mello, F. P., 1994, "Dynamic Models for Combined Cycle Plants in Power System Studies," IEEE Trans. Power Syst., **9**(3), pp. 1698–1708.
[9] Camporeale, S. M., Fortunato, B., and Mastrovito, M., 2002, "A High-Fidelity Real-Time Simulation Code of Gas Turbine Dynamics for Control Applications," ASME Paper No. GT-2002-30039.
[10] Sampath, S., Li, Y. G., Ogaji, S. O. T., and Singh, R., 2003, "Fault Diagnosis of a Two-Spool Turbo-Fan Engine Using Transient Data: A Genetic Algorithm Approach," ASME Paper No. GT2003-38300.
[11] Botros, K. K., Jungowski, W. M., and Richards, D. J., 1996, "Compressor Station Recycle System Dynamics During Emergency Shutdown," ASME J. Eng. Gas Turbines Power, **118**, pp. 641–653.
[12] Theotokatos, G., and Kyrtatos, N. P., 2001, "Diesel Engine Transient Operation With Turbocharger Compressor Surging," ASME Paper No. 2001-01-1241.
[13] Moore, F. K., and Greitzer, E. M., 1986, "A Theory of Post-Stall Transients in Axial Compression Systems: Part I—Development of Equations," ASME J. Eng. Gas Turbines Power, **108**, pp. 68–76.
[14] Fink, D. A., Cumpsty, N. A., and Greitzer, E. M., 1992, "Surge Dynamics in a Free-Spool Centrifugal Compressor System," ASME J. Turbomach., **114**, pp. 321–332.
[15] Baojie, L., Hongwei, W., Huoxing, L., Hongjun, Y., Haokang, J., and Maozhang, C., 2003, "Experimental Investigation of Unsteady Flow Field in the Tip Region of an Axial Compressor Rotor Passage at Near Stall Condition with SPIV," ASME Paper No. GT2003-38185.
[16] Botha, B. W., Du Toit, B., and Rousseau, P. G., 2003, "Development of a Mathematical Compressor Model to Predict Surge in a Close Loop Brayton Cycle," ASME Paper No. GT2003-38795.
[17] Bakken, L. E., Bjorge, T., Bradley, T. M., and Smith, N., 2002, "Validation of Compressor Transient Behavior," ASME Paper No. GT-2002-30279.
[18] Dedoussis, V., Mathioudakis, K., and Papailiou, K. D., 1997, "Numerical Simulation of Blade Fault Signatures From Unsteady Wall Pressure Signals," ASME J. Eng. Gas Turbines Power, **119**, pp. 362–369.
[19] Aretakis, N., Mathioudakis, K., and Stamatis, A., 1998, "Blade Fault Recognition Based on Signal Processing and Adaptive Fluid Dynamic Modeling," ASME J. Eng. Gas Turbines Power, **120**, pp. 543–549.
[20] Bozzi, L., Crosa, G., and Trucco, A., 2003, "Simplified Simulation Block Diagram of Twin-Shaft Gas Turbines," ASME Paper No. GT-2003-38679.
[21] Ohanian, S., and Kurz, R., 2001, "Series or Parallel Arrangement in a Two-Unit Compressor Station," ASME J. Eng. Gas Turbines Power, **124**, pp. 936–941.
[22] Bettocchi, R., Pinelli, M., Spina, P. R., Venturini, M., and Zanetta, G. A., 2006, "Assessment of the Robustness of Gas Turbine Diagnostics Tools Based on Neural Networks," ASME Paper No. GT2006-90118.
[23] Desideri, U., Fantozzi, F., Bidini, G., and Mathieu, P., 1997, "Use of Artificial Neural Networks for the Simulation of Combined Cycles Transients," ASME Paper No. 97-GT-442.
[24] Chiras, N., Evans, C., and Rees, D., 2002, "Nonlinear Gas Turbine Modeling Using Feedforward Neural Networks," ASME Paper No. GT-2002-30035.
[25] Ogaji, S. O. T., Li, Y. G., Sampath, S., and Singh, R., 2003, "Gas Path Fault Diagnosis of a Turbofan Engine From Transient Data Using Artificial Neural Networks," ASME Paper No. GT2003-38423.
[26] Bettocchi, R., Pinelli, M., and Spina, P. R., 2005, "A MultiStage Compressor Test Facility: Uncertainty Analysis and Preliminary Test Results," ASME J. Eng. Gas Turbines Power, **127**(1), pp. 170–177.
[27] Faussett, L., 1994, *Fundamentals of Neural Networks-Architectures, Algorithms and Applications*, Prentice-Hall, Englewood Cliffs, NJ.
[28] Haykin, S., 1999, *Neural Networks-A Comprehensive Foundation*, 2nd ed., Prentice-Hall, Englewood Cliffs, NJ.
[29] Arsie, I., Pianese, C., and Sorrentino, M., 2002, "Recurrent Neural Network

Based Air-Fuel Ratio Observer for SI Internal Combustion Engines," *Proc. of ESDA 2002*, ESDA2002/APM038 ACC008.
[30] Simani, S., Fantuzzi, C., and Spina, P. R., 1998, "Application of a Neural Network in Gas Turbine Control Sensor Fault Detection," *Proc. of the 1998 IEEE International Conference on Control Applications*, Trieste, Italy.
[31] Romessis, C., Stamatis, A., and Mathioudakis, K., 2001, "A Parametric Investigation of the Diagnostic Ability of Probabilistic Neural Networks on Turbofan Engines," ASME Paper No. 2001-GT-0011.
[32] Bettocchi, R., Pinelli, M., Spina, P. R., Venturini, M., and Burgio, M., 2004, "Setup of a Robust Neural Network for Gas Turbine Simulation," ASME Paper No. GT2004-53421.
[33] Parlos, A., G., Rais, O. T., and Atiya, A. F., 2000, "Multi-Step-Ahead Prediction in Complex Systems Using Dynamic Recurrent Neural Networks," Neural Networks, **13**(7), pp. 765–786.
[34] Venturini, M., 2006, "Optimization of a Real-Time Simulator Based on Recurrent Neural Networks for Compressor Transient Behavior Prediction," ASME Paper No. GT2006-90117.
[35] Cybenko, G., 1989, "Approximation by Superimposition of a Sigmoidal Function," Math. Control, Signals, Syst., **2**, pp. 303–314.
[36] Kolmogorov, A. N., 1965, "On the Representation of Continuos Functions of Many Variables by Superposition of Continuous Functions of One Variable and Addition," Am. Math. Soc. Transl., **28**, pp. 55–59.

Unsteady Flow in a Turbocharger Centrifugal Compressor: Three-Dimensional Computational Fluid Dynamics Simulation and Numerical and Experimental Analysis of Impeller Blade Vibration

Hans-Peter Dickmann
e-mail: hans-peter.dickmann@ch.abb.com

Thomas Secall Wimmel
e-mail: thomas.secallwimmel@ch.abb.com

Jaroslaw Szwedowicz
e-mail: jaroslaw.szwedowicz@ch.abb.com

Dietmar Filsinger
e-mail: dietmar.filsinger@ch.abb.com

Christian H. Roduner
e-mail: christian.roduner@ch.abb.com

ABB Turbo Systems Ltd,
CH-5401 Baden,
Switzerland

Experimental investigations on a single stage centrifugal compressor showed that measured blade vibration amplitudes vary considerably along a constant speed line from choke to surge. The unsteady flow has been analyzed to obtain detailed insight into the excitation mechanism. Therefore, a turbocharger compressor stage impeller has been modeled and simulated by means of computational fluid dynamics (CFD). Two operating points at off-design conditions were analyzed. One was close to choke and the second one close to the surge line. Transient CFD was employed, since only then a meaningful prediction of the blade excitation, caused by the unsteady flow situation, can be expected. Actually, it was observed that close to surge a steady state solution could not be obtained; only transient CFD could deliver a converged solution. The CFD results show the effect of the interaction between the inducer casing bleed system and the main flow. Additionally, the effect of the nonaxisymmetric components, such as the suction elbow and the discharge volute, was analyzed. The volute geometry itself had not been modeled. It turned out to be sufficient to impose a circumferentially asymmetric pressure distribution at the exit of the vaned diffuser to simulate the volute. Volute and suction elbow impose a circumferentially asymmetric flow field, which induces blade excitation. To understand the excitation mechanism, which causes the measured vibration behavior of the impeller, the time dependent pressure distribution on the impeller blades was transformed into the frequency domain by Fourier decomposition. The complex modal pressure data were imposed on the structure that was modeled by finite element methods (FEM). Following state-of-the-art calculations to analyze the free vibration behavior of the impeller, forced response calculations were carried out. Comparisons with the experimental results demonstrate that this employed methodology is capable of predicting the impeller's vibration behavior under real engine conditions. Integrating the procedure into the design of centrifugal compressors will enhance the quality of the design process. [DOI: 10.1115/1.2183317]

Introduction

Centrifugal compressors of turbochargers operate in a wide range of rotational speeds, which depends on the load of the supercharged (Diesel) engine. Consequently, there are, according to the Campbell diagram (Fig. 1), a number of possible intersections between the excitation and the natural frequencies of the impeller with the potential for resonant vibration. Therefore, it is of great importance for a safe design of centrifugal compressors, to determine the structure's vibration behavior so that it can be properly accounted for operation under resonance conditions.

Current designs of turbocharger compressors exhibit high efficiencies accompanied by high flow capacities [1]. Consequences of aerodynamic optimization are high mean stress values in the blades due to centrifugal loading as well as dynamic stresses due to blade vibrations. Blade vibrations in a turbocharger compressor are assumed to be predominantly excited by unsteady aerodynamic forces. These forces are caused by a variety of sources influencing the flow. Examples include the geometry of the flow channel, elbows, the diffuser vanes, or struts. Therefore, an understanding of the fluid—structure interaction is essential for further design optimization. The performance of a new turbocharger compressor has been tested in an early design phase and blade vibration measurements have been carried out as well. The results for a configuration with asymmetric suction elbow showed at part load along the speedline of the 4th Engine Order (EO) exciting the first eigenmode (Fig. 1) of the main blade, that the blade stress amplitudes at surge (Fig. 2, OpcS=Operating Point close to Surge) were three times higher than at choke (Fig. 2, OpcC=Operating Point close to Choke).

With respect to future designs, two questions arose:

(1) Can transient CFD-simulations model these off-design operating points at all?

Contributed by the International Gas Turbine Institute (IGTI) of ASME for publication in the JOURNAL OF TURBOMACHINERY. Manuscript received October 1, 2004; final manuscript received February 1, 2005. IGTI Review Chair: K. C. Hall. Paper presented at the ASME Turbo Expo 2005: Land, Sea, and Air, Reno, NV, June 6–9, 2005, Paper No. GT2005-68235.

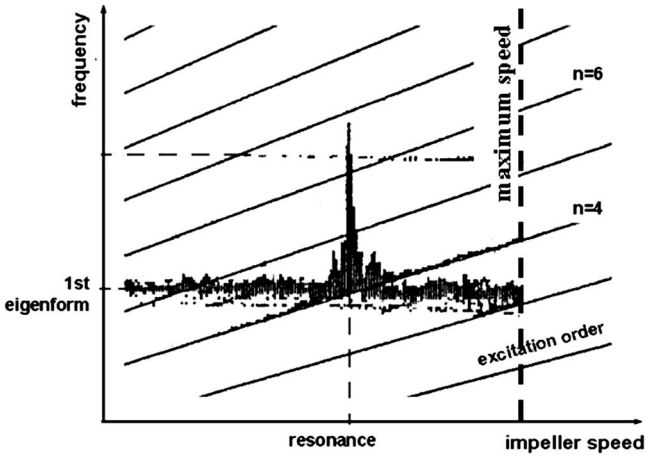

Fig. 1 Schematic of a Campbell diagram

(2) and if so—are the computed transient blade forces suitable to derive qualitatively the observed amplitudes during the tests?

Therefore, transient CFD simulations were performed to get insight of the main flow structure and the flow through the inducer casing bleed system at these operating points. The simulations provide data to validate a procedure to derive blade vibration amplitudes from transient CFD results at resonance.

Over the past 20 years, 3D-CFD simulations of flows through centrifugal compressor stages became standard for design and analysis. Usually just one pitch of the impeller and the vaned diffuser is used to represent the entire compressor. Typically components such as suction elbows and volutes which are asymmetric with respect to the circumference have been very rarely modeled and added upstream or downstream to the pure—bladed—stage [2–6]. These modeled stages were usually limited to one meridional blade length upstream and downstream maximum. Secondary flow paths like the one in the inducer casing bleed system have an additional impact on the main flow path and have to be taken into acount due to the need of broader performance maps and higher flow rates.

Today all these features can be integrated into the standard design procedure due to the growth in computer power and storage. For dedicated investigations, all devices mentioned above have indeed been occasionally added to the standard 3D-CFD design process for compressors and turbines at the original engine manufacturer (OEM) in the past five years [7–9]. But these calculations were restricted to steady state simulations only for compressors.

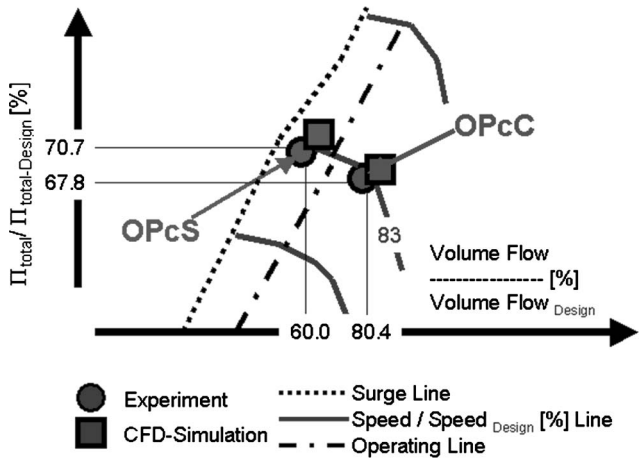

Fig. 2 Excerpt of the investigated compressor performance map

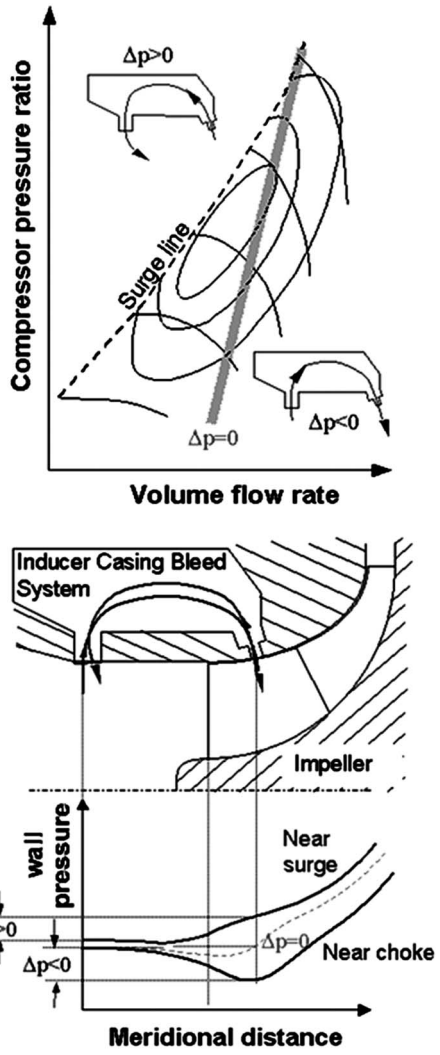

Fig. 3 Working principle of the inducer casing bleed system

Centrifugal Compressor Stage

The compressor stage belongs to a turbocharger, which supercharges a state-of-the-art 1100 kW Diesel engine. Investigations described here have been done on two off-design operating points on a speed line of 83% design speed (Fig. 2). OpcC corresponds to 80.4% of design volume flow, 67.8% design total pressure ratio and 103% of design efficiency. OpcS to 60.0%, 70.7%, and 100.0%, respectively. The compressor consists of an impeller with eight pairs of main and splitter blades and nine low solidity type diffuser vanes (LSD). The relative Mach numbers at the tip leading edge of the impeller are 1.50 for OpcC and 1.20 for OpcS. The absolute Mach numbers at the leading edges of the diffuser vanes are 0.65 for OPcC and 0.60 for OPcS. The investigated configuration is combined with a suction elbow at the inlet, an inducer casing bleed system and a volute at the outlet. The inducer casing bleed system allows a fraction of the main flow of the air to pass through a slot in the shroud that is downstream of the inducer inlet and circulate back to the impeller inlet and vice versa. It substantially enhances the surge margin and thereby broadens the compressor map width without sacrificing efficiency [10]. Figure 3 describes the principle: Depending on the position in the performance map, the flow in the bypass should travel either upstream

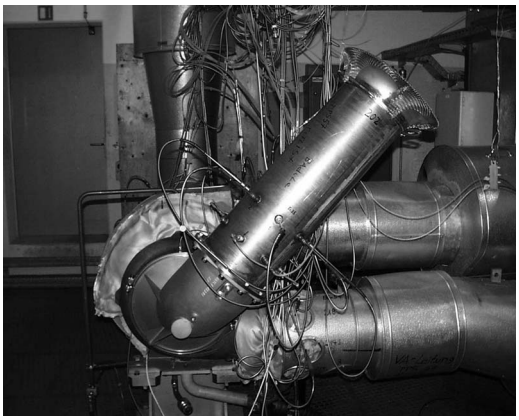

Fig. 4 Turbocharger test facility

or downstream to result in a stabilizing flow approaching the inducer and widening the stable operating volume rate range in the centrifugal compressor map. The stripe in the center is a theoretical assumption, where no flow at all exists ($\Delta p=0$). Principle and steady-state CFD simulations for different geometries of this recirculating system have been described in [7,8].

Test Facility

All measurements were performed on a turbocharger test rig at the Thermal Machinery Laboratory of the OEM. The test stand is equipped for mass flow, pressure and temperature measurements as well as for vibration measurements. It provides the means for a thorough thermodynamic evaluation of the turbocharger performance as well as measuring the relative contribution of the respective components, i.e., compressor and turbine. The measurement uncertainty of the mass flow is 1.0%. The uncertainty of the measured turbocharger efficiency is 0.4% or better depending on the operating point of the turbocharger. The test facility provides the operator with online monitoring of the operating conditions of the compressor and the turbine. For this purpose, the operating point of the compressor is presented in real-time in a compressor map on a monitor. The state-of-the-art test rig monitoring and control system enables the turbocharger to be operated under all possible conditions of a piston engine. Figure 4 shows a picture of the test facility and the tested turbocharger. The suction elbow can be seen in the foreground. In this test facility the turbocharger is operated like a gas turbine by the use of a combustion chamber.

Blade vibration measurements can be performed by means of an optical blade vibration (OBV) measurement system and verified by means of the strain gauge telemetry technique. The OBV measurement method will be described later. Summarizing all this, the test rig is equipped for performance map measurement as well as for blade vibration measurements.

CFD Model and Simulation

Geometry. The components/features of the test facility configuration

- suction elbow,
- inducer casing bleed system,
- impeller including tip gap,
- vaned diffuser, and
- volute

have been modeled with the exception of the volute. A typical pressure distribution at a vaned diffuser exit calculated for a different compressor, where the volute geometry had been modeled,

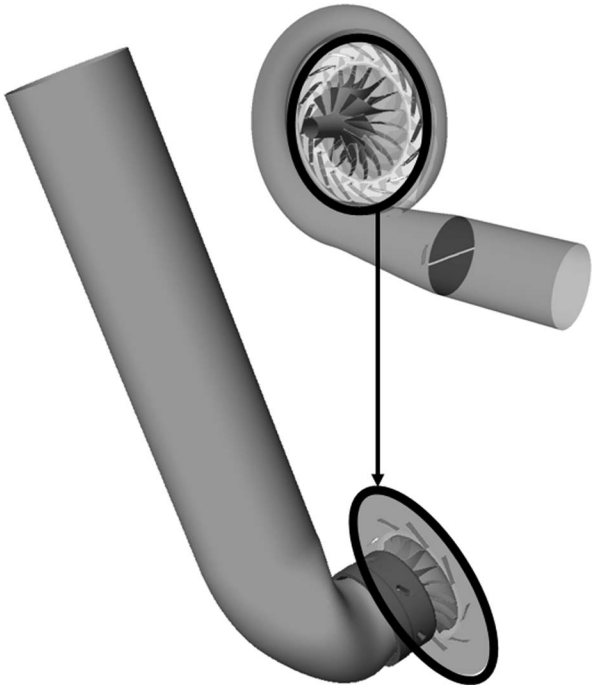

Fig. 5 CFD domain and principle of the outlet boundary condition

was available. This distribution was adjusted to the outlet of the setup of interest, meaning downstream of the vaned diffuser (Figs. 5 and 6). This has been done with respect to:

- The circumferential position of the tongue of the volute; and
- the average static outlet pressure of the relevant operating point.

This was necessary, because computation time and storage had to be saved since extensive simulation times were expected. As neither a measured nor a computed time-dependent outlet pressure distribution was available, this interpolated steady-state result had to be applied and it turned out that this approach was sufficient, which could be proven with the results later on. The length of the

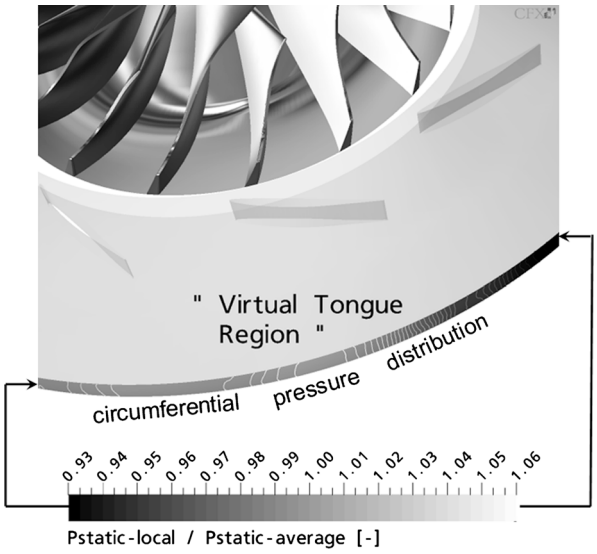

Fig. 6 Typical steady state pressure distribution at a volute inlet applied as outlet boundary condition for a compressor stage

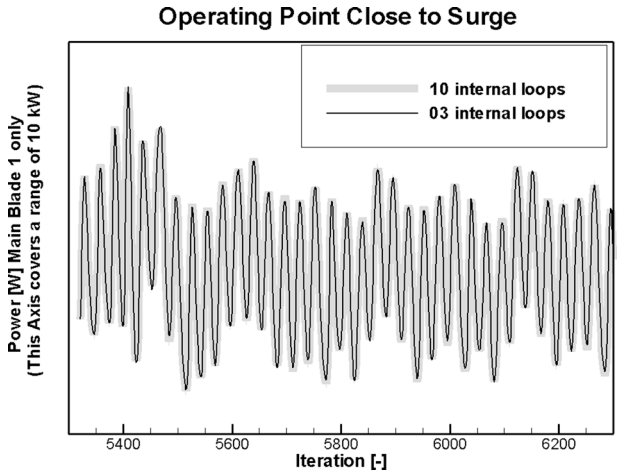

Fig. 7 Transient main blade power of blade 1 depending on different number of internal time steps

radial part in front of the elbow has been chosen due to the fact that a distance of 4.5 diameters of the radial intake channel in front of the elbow should guarantee a reasonable development of the flow at the beginning of the 90 deg-bend.

Discretization. The CFD simulations have been performed with the CFX5.7 code from ANSYS [11] using a grid with 730000 cells. This grid resolution is a compromise between expected results and numerical effort. High resolutions of boundary layers, very detailed secondary flows and very accurate captures of shocks cannot be expected with this mesh density. One impeller revolution has been resolved by $256=2^8$ time steps. 2^n time steps per revolution have to be chosen to be able to perform fast Fourier transformations (FFT) of the results considering the transformation into the frequency domain in the further procedure. The chosen number corresponds to 1.4 deg turning of the impeller per time step or a resolution of 16 states per pitch between a main and adjacent splitter blade of the impeller. Experience shows that this gives an appropriate resolution in time to catch the relevant effects which influence blade excitations.

The k-ε turbulence model with scalable wall functions has been applied. Second-order descritization in space has been used. For each time step all maximal residua are converged to 10^{-3} after 10 *internal* time step loops. These convergences of the maximal residua have to be regarded as sufficient concerning the data of interest, namely the online monitored main blade powers. Blade power is equivalent to blade torque times rotations per second. Blade torque is computed via the area integrals of pressures plus the area integrals of the corresponding shear stress components on the wetted surface of one main blade taking into account the distances to the axis of rotation. A test applied to the first 1000 time steps of OPcS even showed that there is no significant change of these data if only a number of 3 instead of the here applied 10 internal time steps was chosen. (Fig. 7). Each operating point needed about 20 revolutions of the impeller until the transient solutions of the main blade powers were periodic in time and the ratio of inlet to outlet mass flow remained at almost identical values for more than 4 revolutions: $\dot{m}_{\text{in}}/\dot{m}_{\text{out}}=1.0096$ for OPcC and 0.9787 for OPcS when the computations were stopped. These 20 revolutions were necessary due to the long distance between inlet boundary and impeller. For the presented case a pressure disturbance has to travel much longer between impeller and inlet as for set-ups without simulation of that long inlet casing, i.e., beginning close to the impeller inlet. The traveling time for one way to the inlet boundary is equivalent to 2.5–3 revolutions of the impeller. Due to reflecting boundary conditions at inlet and outlet of the computational domain these pressure waves have to travel several times from the impeller to inlet and outlet boundaries and back until a solution periodic in time has been established. The CFD simulations do not take into account any fluid structure interaction (FSI) and, therefore, they work without mesh deformations due to forces induced by the flow.

Boundary Conditions. Average values for total temperature and total pressure, a turbulence intensity of 5% and flow vertical to the inlet boundary have been applied to the inlet boundary. Figure 6 shows an excerpt of the static pressure distribution applied to the outlet boundary. The upstream circumferential bypass bleed slot has been treated as a general grid interface without one-to-one connections. The downstream slot and the interfaces "impeller/suction elbow" and "impeller/vaned diffuser" have been treated as transient "rotor/stator" interfaces.

Numerical Speed Line From OPcC to OPcS. A steady state result with a frozen rotor interface between impeller and vaned diffuser was used as initial solution for the operating point close to choke. This type of interface was appropriate to start a transient flow simulation because it does not produce any mixed state in front of or behind the impeller. The operating point close to surge was reached using a transient simulation while traveling up the speed line from OPcC to OPcS. It is remarkable that OPcS could be simulated transiently while it was impossible to simulate any steady-state result for it. Neither *frozen rotor* nor *stage=mixing-plane* interface applications allow significantly higher outlet pressures or lower mass flows while trying to travel from OPcC to OPcS. This is due to the much more "transient character" of OPcS and a very valuable experience for future simulations of operating points in these extreme regions of a compressor map. OPcS operates with 4% higher total pressure ratio and 25% less volume flow than OPcC. An operating point close to surge like OPcS is, therefore, characterized by small frequent blockages and recirculation areas. Comparing animations of the pressure fluctuations behind the impeller blades and diffuser vanes actually show that OPcS produces wakes which are more circumferentially asymmetric than those at OPcC and more significant pulsating wakes behind the diffuser vanes. These transient effects cannot be simulated as a converged steady state.

Centrifugal Compressor Flow Analysis

Flow Through the Entire Compressor. Figure 8 shows the overall absolute velocity distribution in the entire system for both operating points. Close to choke, the flow enters the diffuser with very high incidence angles at the LSD vanes' leading edges, which leads to flow separation and very low velocities on the pressure sides. The implemented volute outlet pressure causes a circumferentially different flow picture per vane. For both operating points, one can see that the vane close to the tongue works best. This is due to the fact that this vane is aligned to the virtual volute tongue position in the simulation and circumferentially fixed the same way to work together with the tongue as a type of tandem blade. In the inducer casing bleed system, the velocities in the two cuts at the center of the connecting slots to the main flow channel are much higher for OPcS than for OPcC, as expected based on the working principle of the bleed system.

Inducer Casing Bleed System. The principle of the inducer casing bleed system could be modeled for the steady state case for several operating points on two speed lines [7,8], but always for the direction opposite that of the main flow. Figure 9 shows the flow structures in the bleed system with the help of absolute velocity vectors. The flow direction in the bleed system is identical for both operating points. For OPcS the flow is almost "injected" into the system compared to OPcC (see also lower part of Fig. 8). The vortex systems in the meridional plane of the bleed system are slightly different. Animations show how the flow from the impeller into the bleed system is interrupted by the impeller main blades passing by resulting in alternating maxima and minima of

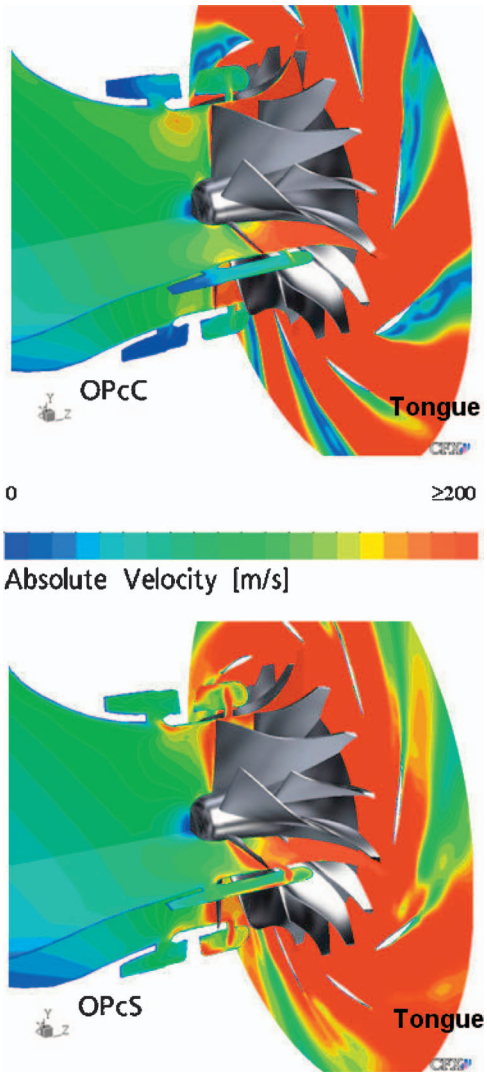

Fig. 8 Snapshot of absolute velocities in the entire system

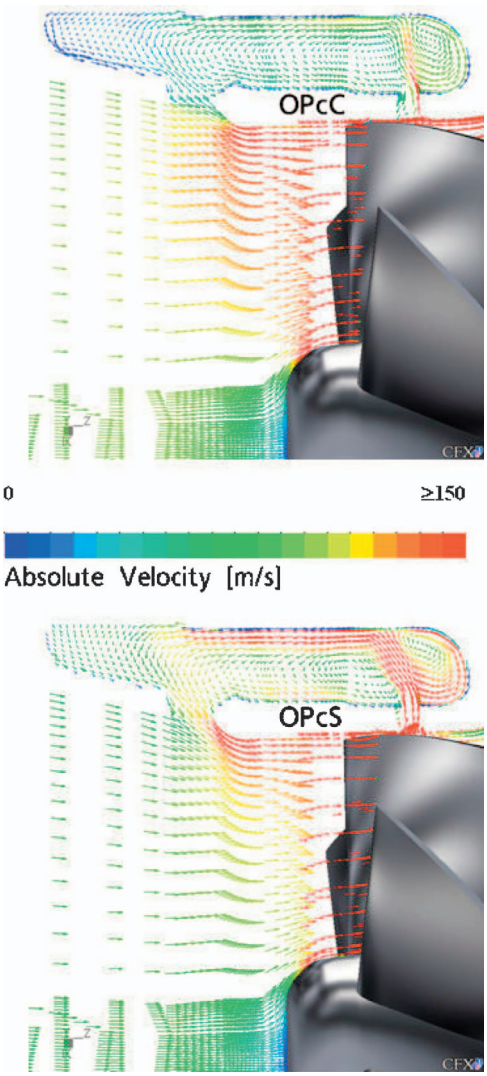

Fig. 9 Snapshot of velocity vectors in the inducer casing bleed system

pressure and velocity transporting the fluid to the upstream connection, from where it enters the main flow in front of the inducer leading edge tangentially to the casing wall. Although much lower velocities exist at the OPcC operation point, there is not a change in flow direction in the bleed channel compared to OPcS. Therefore, reversal in flow direction in the bleed chamber should occur at an operating point lower than OPcC (Fig. 3).

Effects of Asymmetry. Four planes with local pressure distributions have been chosen (Fig. 10) to show the influence of the circumferentially asymmetric devices, the suction elbow and the volute, on the impeller flow. Planes A and B illustrate the change of the flow pattern caused by the suction elbow. Plane B extends into the inducer casing bleed system and is located in the center of the upstream circumferential slot. Plane C is located in the center of the downstream circumferential slot while plane D represents the midspan plane of the vaned diffuser. Figure 11 shows representative snapshots of the transient simulation and no time-averaged states.

The flow is symmetric to the symmetry plane of the entire setup (plane A) upstream of the 90 deg bend with a pressure maximum at the bottom of the plane and two maxima close to the walls on the left and right side. The typical region of high pressure in the lower part downstream of the 90 deg bend (plane B as observed in [12]) proceeds into the impeller, where this pattern does not change qualitatively while the impeller rotates (plane C). The pattern is rotating due to the rotation of the impeller. Looking at the diffuser midspan pressure distribution, it is also obvious that the pressure distribution in the blade-to-blade pitches of the impeller is influenced as well by the higher pressures in the lower half of the modeled volute.

Close to surge the flow patterns in the annular part of the inducer casing bleed system (plane B) are dominated by six pressure maxima. They are induced by the struts which support the structure around the bleed system. Close to choke the flow is dominated by eight pressure maxima due to the number of main blades which periodically interrupt the incoming flow at the downstream slot.

The dependence of the flow structure in the casing bleed system upon the operating point is caused by the different relative mass flows. Close to surge, at OPcS, the mass flow passing the bleed channel is about 14% of the total mass flow, while close to choke, at OPcC, it amounts only to roughly 3%. This is due to the driving mechanism of the bleed system described earlier. Due to the high mass flow, close to surge, the downstream bleed slot is choked and consequently no pressure characteristics of the impeller main blades are transported upstream (OPcS Figs. 8 and 9). In this situation, the wakes of the struts are the dominant effect as shown in plane B of Fig. 11. Close to choke (OPcC in Figs. 8 and 9) the mass flow through the downstream slot is significantly smaller,

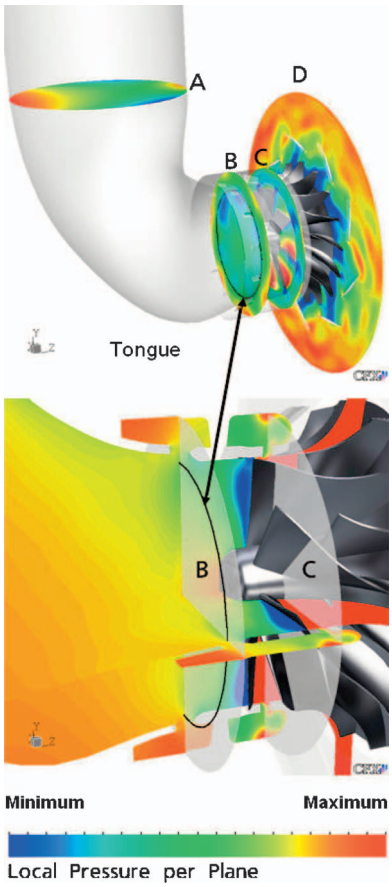

Fig. 10 Pressure distribution at rotor inlet and positions of planes in Fig. 11. Black circles in planes B mark the positions, where the FFT has been applied to the circumferential pressure distributions.

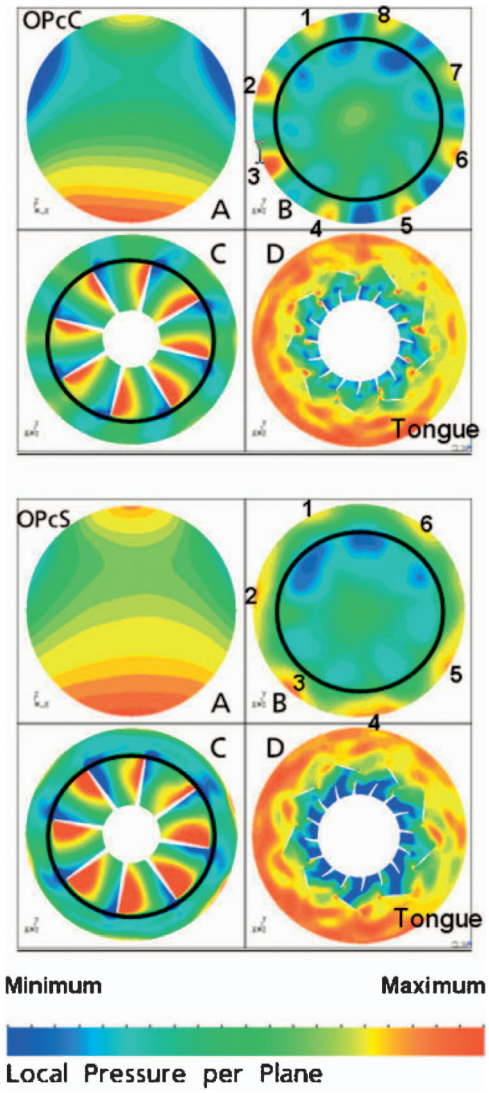

Fig. 11 *Local* pressure distributions at rotor inlet for 4 planes. Black circles mark borders to the impeller casing bleed system

therefore the pressure peaks of the eight main blade pressure sides dominate the instantaneous static pressure distribution at plane B (Fig. 11).

Because of the nonuniform circumferential distribution of flow pressure in the compressor inlet, the impeller blades are excited to vibration by entering into and moving out of zones of different flow pressure. This type of excitation is considered as a rotational harmonic excitation with a periodic excitation function with the period of $T=2\pi/\Omega$, where Ω indicates the angular speed of the compressor.

For the assessment of the excitation spectra for both operating conditions—OPcC and OPcS—an analysis using fast Fourier transformation was performed. The computed stationary flow pressure on plane B along the circumference of the inner radius within the compressor channel as indicated by a black circle in Fig. 10 was analyzed. The spectra in Fig. 12 are shown up to the 6th EO. Still, considering the associated speed of the turbocharger, the calculation is relevant and valid for the 4th EO only, since only for this EO resonance conditions—multiples of the TC speed match with an eigenfrequency of the structure—are fulfilled. The 4th EO is investigated since experience shows that the lowest EO in the operating range tends to be critical. The 3rd EO is not in the operating range. For the 5th and the 6th EO, resonance conditions would be fulfilled for much lower turbocharger speeds and, therefore, much lower power consumption. It can be seen, that the 4th EO excitation amplitude of OPcS is 3.4 times higher than the one of OPcC. This qualitative excitation assessment demonstrates the necessity for further forced vibration FE simulations to determine in detail the resonance von Mises stresses in relation to the allowable value for the infinite high cycle fatigue life (HCF) of an aluminium impeller.

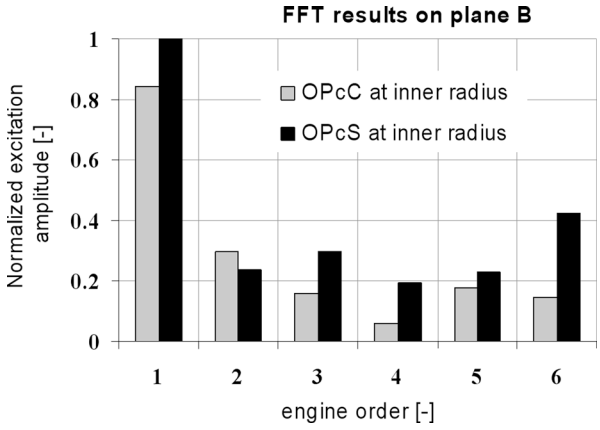

Fig. 12 Comparison of the resulting excitation spectra for operation points OPcC and OpcS (Figs. 10 and 11)

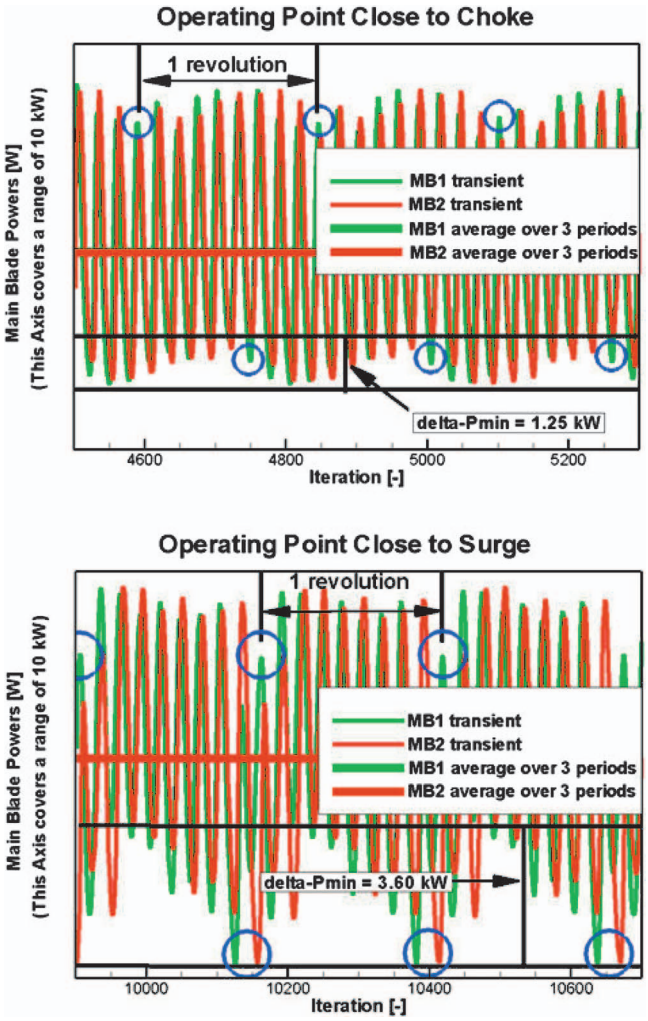

Fig. 13 Impeller main blade powers (3 revolutions)

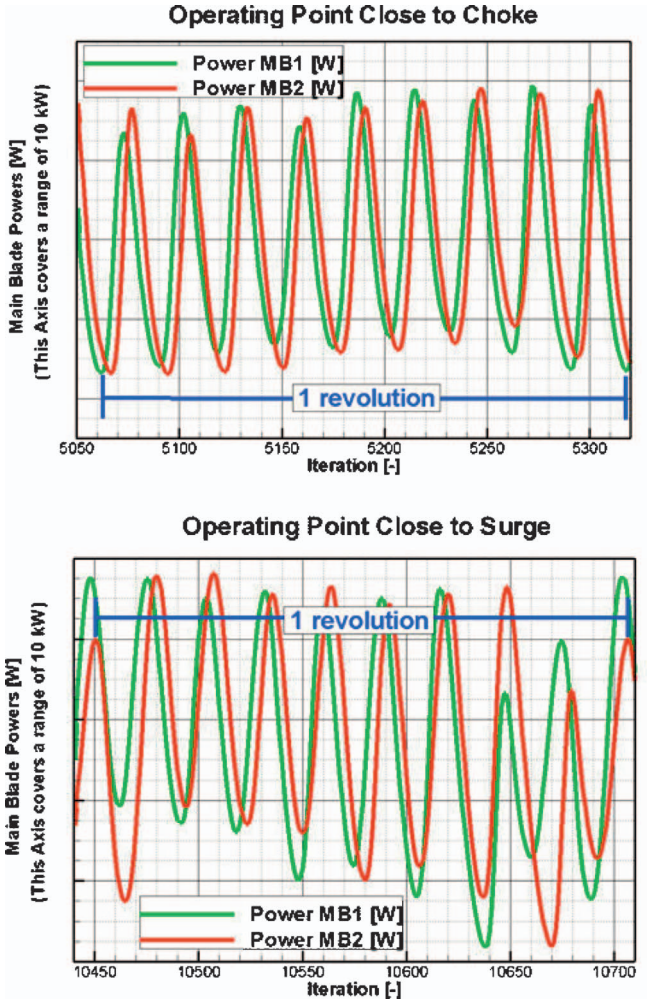

Fig. 14 Impeller main blade powers (1 revolution)

Main Blade Power. Figure 13 shows blade powers for two adjacent main blades of the impeller for the last three revolutions of each simulation. Blade power is equivalent to blade torque times rotations per second. It is periodic in time and has a phase shift of one diffuser vane pitch (Fig. 14). It can be seen that both simulations are periodic in time. Both ordinates cover a range of 10 kW, a fact which allows one to compare both plots directly. The time averaged value of the 2 single main blade powers of OPcS is 88.7% of the value of OPcC (see bold flat lines in Fig. 13). Due to higher pressure ratio and much lower mass flow circumferentially more asymmetric pressure distributions behind impeller and diffuser and periodically separating wakes behind the diffuser vanes can be observed in animations. These result in higher amplitude variations for main blade powers for OPcS than those for OPcC. As expected, amplitude variations for OPcS are much higher than those for OPcC. The variation of the minimum peak values have been computed to 1.25 kW for OPcC and 3.60 kW for OPcS.

As the volute was not geometrically modeled, it was of great interest whether or not the simplified distributed pressure approach could model the upstream effect of the volute tongue position on the impeller flow. In Fig. 15 four extreme positions of one main blade have been marked in the power amplitude plot: The one with the highest and lowest maximum and minimum peaks for the operating point close to surge. The corresponding circumferential main blade position covered by the vaned diffuser midspan pressure distribution shows clearly that:

a) The smallest value of blade power occurs always when the blade passes the circumferential (here virtual) volute tongue position and that;
b) the highest value of blade power occurs always when the blade is 180 deg from the volute tongue.

The analogue investigation for the operating point close to choke showed the same result: The lowest power occurs on *that* impeller blade which has just passed the volute tongue circumferential position. Similar behavior has been observed in [13] with static pressures at impeller exit (a distribution shape as the described outlet boundary condition *behind the vaned diffusers* here) and in [14] with total pressure ratios per blade passage for centrifugal compressors with *vaneless* diffusers. The stratification of circumferential pressure distribution at impeller exit caused by a vaned LSD downstream compared to a vaneless diffuser has been shown in [15]. The flow field is much more stratified as the one here, because double the number of LSD vanes have been applied there.

The CFD results suggest the usefulness of performing additional simulations in the future and to model the complex geometry either with a higher resolution in space or to invest in a geometric model of the volute. The advantage of a volute geometry is that it is possible to apply a more realistic outlet boundary condition behind the volute exit (=compressor exit). At this location, the flow is more of a steady state type than the one behind the vaned diffuser. Here the flow still "breathes" and this cannot be modeled with a steady state outlet boundary condition. Com-

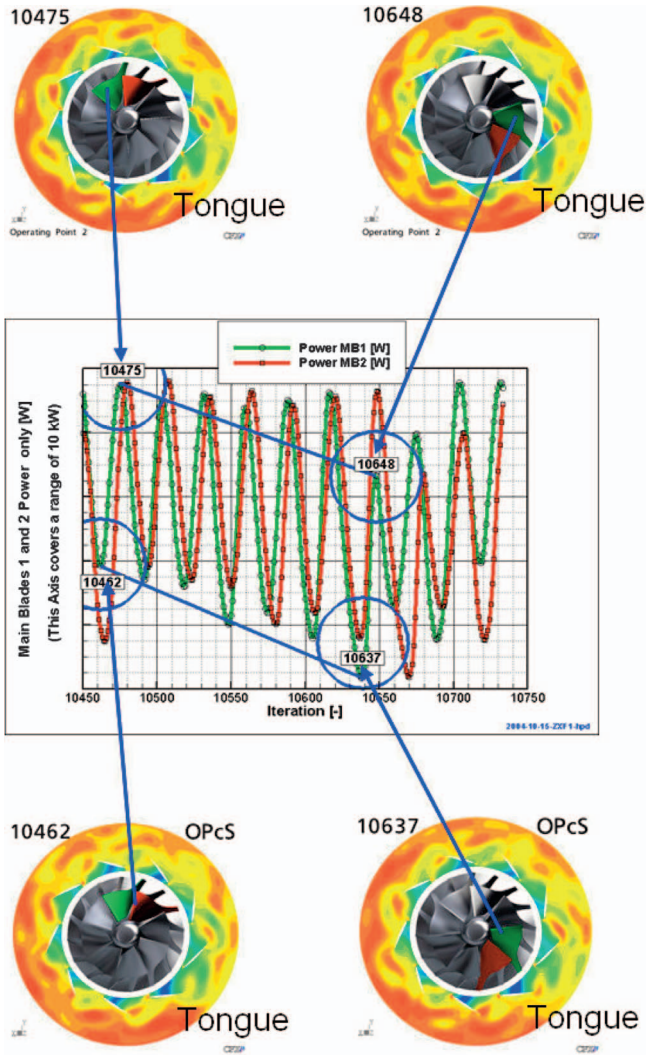

Fig. 15 Blade power vs time (iteration) and circumferential position of the main blades at closest and farest distance to the volute tongue

putation time saved by reduction of internal loops (Fig. 7) can then be invested in a geometric model of the volute.

Comparison of Measured and Calculated Operating Points

Figure 2 shows a section of the compressor performance map including the two mentioned operating points on a part load speed line. For OPcC the simulated total-to-total pressure ratio Π_{total} differs 2.5% and the mass flow 6% from the measured values. The simulated OPcS has 3.8% higher pressure ratio and 7.8% higher mass flow than measured on the test facility. Although this is not as good as for OPcC, it is a remarkable success, because no steady-state solution could be obtained at all for OPcS. The fact that very long computation times were expected due to the long distance between domain inlet and impeller also forced the authors to a moderate mesh resolution (730,000 cells). It was decided to perform these investigations limited to available resources and computation time in industry. With respect to this and the comparison of measured and computed blade vibration amplitudes in the following the authors think that measured and transiently computed locations of the two operating points match very well.

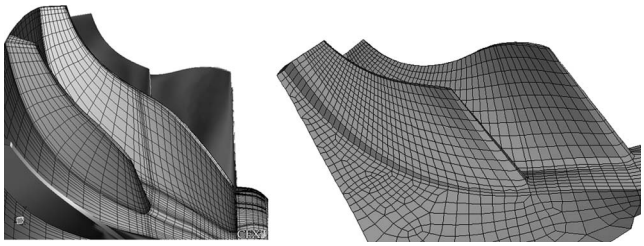

Fig. 16 Resolution of the CFD and FE meshes

Structural Resonance Analysis

In reality, the impeller is a system of N blades that differ slightly in their geometry due to manufacturing tolerances, resulting in the mistuning effect. Only the tuned impeller is taken into account in the design process when static and dynamic compressor behavior is assessed. The tuned impeller is then represented by a single hub sector of the FE model with a complex boundary condition imposed on the circumferential sides of the disc [16]. The sector model is built with parabolic brick and wedge finite elements as it is presented in Fig. 16(b). The static and dynamic analyses of the rotating impeller are performed using the commercial ABAQUS FE software [17].

The static and unsteady flow loads acting on the compressor contour are determined with the FFT of the computed unsteady pressure. Due to the revolution-periodicity of the unsteady CFD-pressure signal in form of 256 time increments, a complex Fourier decomposition was performed at each CFD-node, to get the static pressure and harmonic excitation amplitudes with respect to the rotational speed [18,19].

In literature, numerical tools for the interaction of CFD data with the FE mesh are well described for the axial turbine blades (e.g., [18–20]). For a radial 3D blade that has a more complicated geometry than an axial one, a computational process hardly can be found in literature (e.g., [21]). For the spatial extrapolation of the CFD data (Fig. 16(a)) onto the contour of the cyclic FE mesh of one sector of the radial impeller (Fig. 16(b)), the numerical formulation of the in-house FACET code [19] was generalized to be also used for radial disc assemblies. For the association of points of the CFD-mesh to a single element face on the FE contour, the weight function is defined using the distance tolerance based on the characteristic size of elemental dimensions modeling the blade and hub contour. More details about the CFD-FE interaction process can be found in [19]. As the result the FACET output gives the weighted CFD static and excitation amplitudes, which are associated with the appropriate elemental face of the FE mesh.

The FACET output uses the format of the standard FE-code ABAQUS and defines the static and complex excitation pressure distribution on FE-element faces. In the FE analysis, first the static deformation of the impeller is computed for the centrifugal load and static pressure (the aerodynamic pressure corresponding to the 0th harmonic of the Fourier decomposition) that correspond to the rotational speed of the measured resonance. In addition, the thermal static expansion of the impeller is calculated for the temperature distribution obtained from the stationary FE heat computation. In general, negligible changes in the static stress distribution and deformations of the impeller were found for the two operating points.

For the computed static deformation, the free vibration analysis is performed with respect to the nodal diameter number. For the analyzed rotational speed (identical for both operation points), the FE computed dispersion diagram of the impeller (Fig. 17) shows that the mode $i,n=1,4$ (i denotes the disc eigenfrequency and n the nodal diameter) can be excited by the 4th EO. For this mode only the main compressor blades vibrate (Fig. 18) [22]. The different mass flows and pressure distributions for both operation points have no additional stiffening effect on the structure.

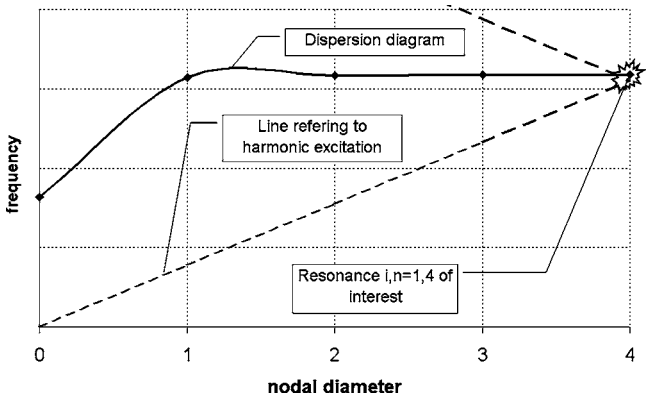

Fig. 17 Dispersion diagram for the first disc mode of the analyzed impeller at operating rotational speed

Finally a forced response calculation was performed by applying the complex excitation pressures for the 4th excitation order (Fig. 19) on the FE-mesh of the impeller. For the simulation the experimental damping ratio of 0.1% resulting from strain gauge measurements was applied. The resulting contour plot of the normalized dynamic equivalent stress (Fig. 20) shows higher stresses occurring for OPcS than for OPcC.

Verification of the Numerical Results With Experimental Data

All FE results were compared with the measured data obtained from the telemetry strain gauge (Fig. 1) and optical tip timing measurements (Figs. 21–23). All measurements were done on the compressor test rig under real operation conditions.

Optical tip timing measurement of blade vibrations was applied to validate the numerical results. This method consists of an arrangement of optical emitters that send light onto the rotating blade tips. Optical sensors register the time when light is reflected by the tips of passing blades (Fig. 21). In this way the relative motion between passing blades is determined and vibrations of the entire compressor hub are evaluated. An advantage of this experimental approach is that the motion of each blade is monitored independently and then the mistuning of the blades can be determined [23].

The calculated resonance frequency differs by less than 1% from the average of the measured values (Fig. 22). The experimental blade resonance frequencies differ maximally by 0.14% from the average of the measured values. This small variation among the blade eigenfrequencies indicates the weak mistuning effect in the measured impeller, which may generate an effect of mode localization in forced vibrations, which causes significant response amplification of only few blades in the stage. To determine the possible maximum forced response of this weakly mistuned impeller with $N=8$ cyclic sectors, the amplitude of the tuned system can be amplified by $a=1.9$ (where for N sectors in the disc assembly $a=(1+(N)^{1/2})/2$ as it is given in [24]).

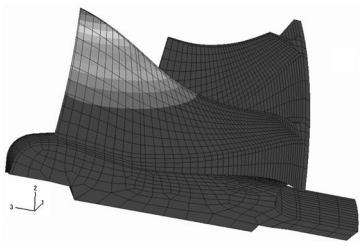

Fig. 18 Mode shape for the resonance $i,n=1,4$

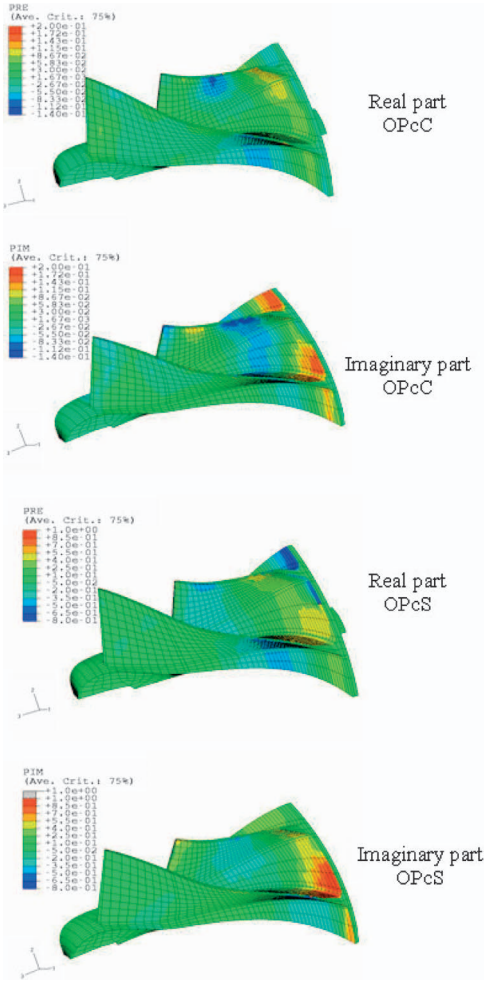

Fig. 19 Complex excitation pressures (normalized) on external FE faces of the impeller sector model for the EO 4 of interest

Figure 23 shows the measured blade vibration amplitudes, that are computed by FE-calculation of the tuned compressor disc. For both operating cases, the numerical resonance amplitudes of the tuned system are in very good agreement with the experimental results. By multiplying the tuned amplitudes with a factor of $a=1.9$ due to the localization effect of the mistuned system with $N=8$ sectors [24], the possible maximum resonance amplitudes of the weakly mistuned system are determined (dashed lines in Fig. 23). The measured resonance amplitudes of practically all blades are within the scatter band of the maximum resonance amplitudes obtained numerically for the tuned and mistuned compressor impeller.

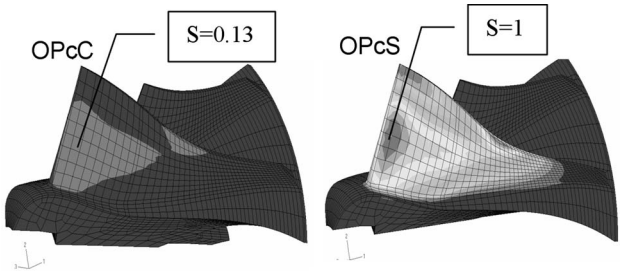

Fig. 20 Normalized dynamic equivalent stress in the impeller when exciting the mode $i,n=1,4$

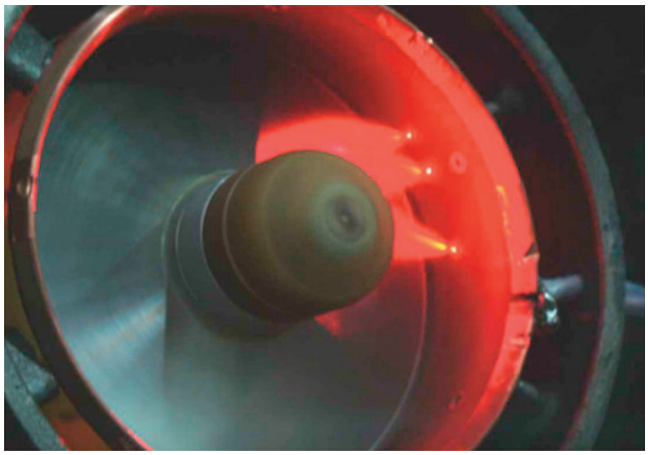

Fig. 21 Tip timing measurement of blade vibrations with optical emitters and sensors

Conclusions

- It is possible to simulate unsteady flows through complex centrifugal compressor geometries for off-design conditions, attaining a calculated volume flow and pressure ratio over the entire stage nearly equal to the measured values.
- It was impossible to simulate an initial steady state solution for the operating point close to surge.
- Snapshots, time-averaged data and CFD animations provide insight into the operation of the inducer casing bleed system. This is very hard or almost impossible to visualize by applying experimental techniques on compressors in operation.
- It was possible to compute the entire compressor stage flow field that is typical for a configuration with a volute by imposing a circumferentially asymmetric pressure distribution at the exit of the vaned diffuser.
- It was shown that the position of the tongue had a significant influence on the circumferential pressure distribution at the impeller exit, despite the damping effect of the vaned diffuser.
- For two different operating points, the difference between the calculated values of the blade stress amplitude qualitatively agreed with the difference in the measured values of the blade stress amplitude.
- It was demonstrated that other non-axisymmetrically positioned components, such as suction elbow, influence the circumferential pressure distribution of the rotating impeller.
- The difference in performance between individual diffuser vanes depending on their circumferential position and/or the operating point has been shown.

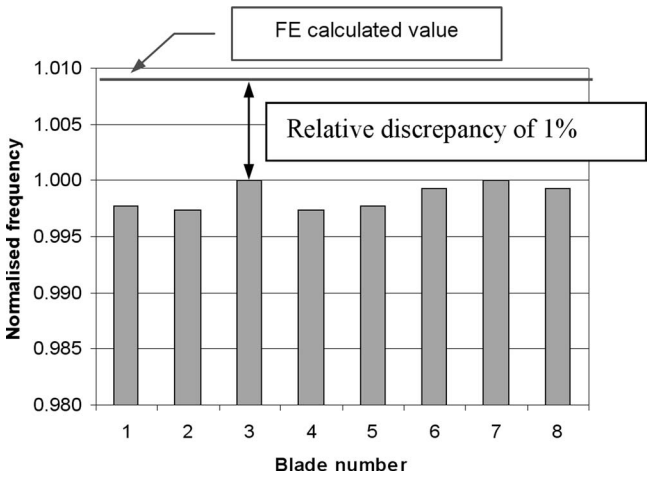

Fig. 22 Calculated eigenfrequency and measured eigenfrequency

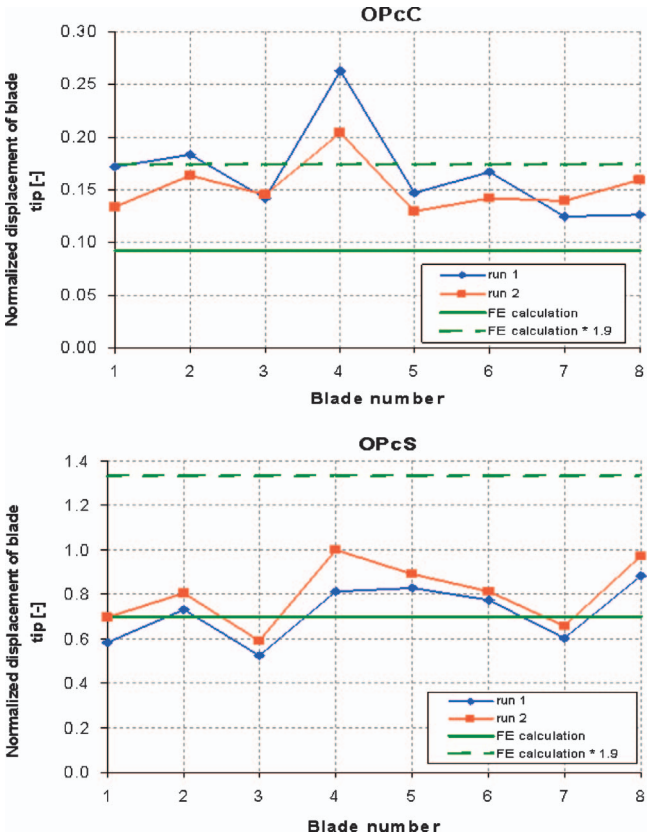

Fig. 23 Experimental results versus calculated blade amplitudes

Using the described numerical procedure, the simulation results satisfactorily reproduce the vibration measurement. This demonstrates that a coupled CFD-FE-simulation (here applied in series only and not simultaneously) is a useful tool for doing fluid and structural assessment of operation conditions of the analysed impeller. It allows the comparison of different systems with each other and the execution of parametric studies. Also the influence of different operation conditions on the impeller lifetime can be estimated and HCF assessments can be performed.

Acknowledgment

The authors would like to thank ABB Turbo Systems Ltd for the permission to publish this work. Several colleagues have contributed to the success of this project, particularly M. Schmitz, B. Klein, and O. Schäfer. We are thankful to D. Robinson for his final internal review, and to the ANSYS Germany Otterfing office for always providing very helpful support concerning the handling of the transient CFD simulations.

References

[1] Rodgers, C., 2003, "High Specific Speed, High Inducer Tip Mach Number, Centrifugal Compressor," ASME Paper No. GT2003-38949.
[2] Dawes, W. N., 1988, "Development of a 3D Navier Stokes Solver for Application to all Types of Turbomachinery," ASME Paper No. 88-GT-70.
[3] Dawes, W. N., 1993, "The Extension of a Solution Adaptive Three-Dimensional Navier-Stokes Solver Toward Geometries of Arbitrary Complexity," ASME J. Turbomach., **115**, pp. 283–295.
[4] Dawes, W. N., 1995, "A Simulation of the Unsteady Interaction of a Centrifugal Compressor With Its Vaned Diffuser: Flow Analysis," ASME J. Turbom-

ach., **117**, pp. 213–222.
[5] Domercq, O., and Thomas, R., 1997, "Unsteady Flow Investigation in a Transonic Centrifugal Compressor Stage," AIAA J.
[6] Walitt, L., Nguyen, and C., Nyquist, R., 1997, "Unsteady Analysis and Re-Design of a Centrifugal Compressor Stage Using a CFD Optimizer," AIAA J..
[7] Hunziker R., Dickmann, H.-P., and Emmrich, R., 2001, "Numerical and Experimental Investigation of a Centrifugal Compressor With an Inducer Casing Bleed System," ATI-CST-025/01, *Proceedings of 4th European Conference on Turbomachinery*, Florence, Italy, pp. 319–329.
[8] Hunziker, R., Jakoby, P., and Meier, A., "A New Series of New Turbochargers for High Flow Rates and High Pressure Ratios," *Proceedings of CIMAC Congress 2001*, Hamburg, Vol. 2, pp. 321–331.
[9] Filsinger, D., Szwedowicz, J., Schäfer, O., Dickmann, H.-P., "Pulse Charged Axial Turbocharger Turbines—A Challenge for Numerical Design Methods," *Proceedings of CIMAC Congress 2001*, Hamburg, Vol. 2, pp. 712–722.
[10] Fisher, F. B., 1988, "Application of Map Width Enhancement Devices to Turbocharger Compressor Stages," SAE Paper No. 880794.
[11] ANSYS, Inc. 2004, CFX-5.7 User Manual.
[12] Cui, M., 2004, "Unsteady Flow Around Suction Elbow and Inlet Guide Vane in a Centrifugal Compressor," ASME Paper No. GT2004-53273.
[13] Sorokes, J. M., Borer, C. J., and Koch, J. M., 1998, "Investigation of the Circumferential Static Pressure Non-Uniformity Caused by a Centrifugal Compressor Discharge Volute," ASME Paper No. 98-GT-326.
[14] Reunanen, A., Pitkänen, H., Siikonen, T., Heiska, H., Larjola, J., Esa, H., and Sallinen, P., 2000, "Computational and Experimental Comparison of Different Volute Geometries in a Radial Compressor," ASME Paper No. 2000-GT-469.
[15] Sorokes, J. M., and Koch, J., 2000, "The Influence of Low Solidity Vaned Diffusers on the Static Pressure Non-Uniformity by a Centrifugal Compressor Discharge Volute," ASME Paper No. 2000-GT-0454.
[16] Hagelstein, D., Hasemann, H., and Rautenberg, M., 1997, "Coupled Vibration of Unshrouded Centrifugal Compressor Impellers," *Proc. Of the 7th Int. Symp. On Transportation Phenomena and Dynamics of Rotating Machinery*, ISROMAC-7, pp. 1306–1317.
[17] ABAQUS User's manual Version 6.4, 2003, ABAQUS Inc., 1080 Main Street, Pawtucket, RI 02860-4847.
[18] Filsinger, D., Frank, Ch., and Schäfer, O., 2005, "Practical Use of Unsteady CFD and FEM Forced Response Calculation in the Design of Axial Turbocharger Turbines," ASME Paper No. GT2005-68439.
[19] Schmitz, M. B., Schäfer, O., Szwedowicz, J., Secall Wimmel, T., and Sommer, T. P., 2003, "Axial Turbine Blade Vibrations by Stator Flow—Comparison of Calculations and Experiment," 10th ISUAAAT, Durham, NC, 2003, Conf. Proc. on CD ROM.
[20] Moyroud, F., Cosme, N., Jöcker, M., Fransson, T. H., Lornage, D., and Jacquet-Richardet, G., 2000, "A Fluid-Structure Interfacing Technique of Computational Aeroelastic Simulations," 9th ISUAAAT, Lyon, France, Conference Proceedings pp. 721–738.
[21] Filsinger, D., Sekavcnik, M., Ihli, T., Schulz, A., and Wittig, S., 2002, "Vibration Characteristics of a Radial Turbocharger Impeller," *Proceedings of the 7th Int. Conference on Turbochargers and Turbocharging, London*, pp. 117–127.
[22] Senturier, E., Lombard, J.-P., Dumas, M., Dupont, C., Sharma, V., and Dupeux, J., 2004, "Forced Response Prediction Methodology for the Design of HP Compressors Bladed Disks," ASME Paper No. GT2004-53372.
[23] Schaber, U., 1997, "Non-Contact Vibration Measurements of Mistuned Coupled Blades," ASME Paper No. 97-GT-190.
[24] Whitehead, D. S., 1988, "The Maximum Factor by Which Forced Vibration of Blades Can Increase Due to Mistuning," J. Eng. Gas Turbines Power, **120**, pp. 115–119.

J. P. Ayers
D. M. Feiner
J. H. Griffin

Department of Mechanical Engineering,
Carnegie Mellon University,
5000 Forbes Avenue,
Pittsburgh, PA 15213

A Reduced-Order Model for Transient Analysis of Bladed Disk Forced Response

A method for predicting the vibratory response of bladed disks under high engine acceleration rates is developed. The method is based on the Fundamental Mistuning Model, an existing reduced order model for predicting the steady-state vibratory response. In addition, a criterion is developed for a critical engine acceleration rate, above which transient effects play a large role in the response. It is shown that military engines operate at acceleration rates above this critical value and therefore transient effects are important in practice. [DOI: 10.1115/1.2185675]

1 Introduction

Bladed disks are generally designed to be cyclically symmetric with each blade identical. However, due to imperfections in the manufacturing process as well as wear during operation, there are slight variations from blade to blade. These small differences have a large effect on the vibratory response of the disk, causing some blades to have significantly larger amplitudes than would be the case in the nominal system. This is referred to as the mistuning problem, and it has been studied extensively, as it contributes to high cycle fatigue and the failure of bladed disks in service. Srinivasan provides a thorough review of this topic in [1].

Significant work has gone towards efficiently predicting the vibratory response of mistuned bladed disks from a design perspective [2–4]. In addition, there have been several reduced order models developed to accurately predict the behavior, while limiting the degrees of freedom of the system and hence the computational complexity [5–11].

While transient behavior has been studied in other aspects of engine design [12–14], research on transient vibration of bladed disks has been limited. When high acceleration rates are used in engines, transient vibratory behavior is observed. An example of this type of behavior is shown in Fig. 1, which is data from a spin pit test of an integrally bladed rotor (IBR) measured at NASA Glenn [15]. In a test such as this, the steady state response of the IBR does not reflect its actual behavior. In order to correlate data such as this with predictions, a model that accounts for transient behavior is needed. The purpose of this research was to develop and validate such a transient model.

The transient model presented in this paper is based on the Fundamental Mistuning Model (FMM) [8]. FMM is a simple reduced order model of bladed disk vibration which was initially designed for use in low frequency modes, however it has since been shown to be applicable to a wider range of systems [16]. The previous FMM models were formulated for steady-state calculations, and needed to be reformulated to account for the transient nature of high engine accelerations.

This paper is organized as follows: Sec. 2 provides the theoretical basis for Transient FMM. In Sec. 3, we present two experimental benchmarks of the Transient FMM algorithm. Then, Sec. 4 discusses a sensitivity phenomenon that is unique to the transient solution. In Sec. 5 we define criteria for determining what acceleration rates will produce transient response. Finally, the key results are summarized in the Conclusions.

2 Theory

The transient simulation code is based on the FMM, an existing steady-state reduced order model [8]. The method is a simplification of the Subset of Nominal Modes theory (SNM) developed by Yang and Griffin [6] and is designed for use in isolated families of modes such as first bending and first torsion. One of the advantages of this approach is that it reduces the mistuning problem to its most basic elements. As a result, FMM requires a minimum number of input parameters, and it is extremely easy to use. This large simplification also makes FMM extremely efficient. When performing Monte Carlo simulations of steady-state forced response, FMM can simulate the response of about 200 disks per s on a 2 GHz PC. This makes the methodology ideal for transient calculations which require slower time integration solutions. The complete FMM formulation was presented in [8], and then later revised to allow for a more flexible disk in [17]. However, for completeness, a summary of the FMM formulation is included here.

Consider a mistuned, bladed disk in the absence of an excitation. By assuming a harmonic, undamped, steady state response, the equations of motion can be written as

$$[(\mathbf{K}^{\circ} + \Delta\mathbf{K}) - \omega_j^2(\mathbf{M}^{\circ} + \Delta\mathbf{M})]\boldsymbol{\phi}_j = 0 \tag{1}$$

where $\mathbf{K}^{\circ}$ and $\mathbf{M}^{\circ}$ are the tuned system mass and stiffness matrices. $\Delta\mathbf{K}$ and $\Delta\mathbf{M}$ are the variations in the stiffness and mass matrices due to mistuning. The vector $\boldsymbol{\phi}_j$ is the jth mistuned mode, and ω_j is its corresponding natural frequency.

In SNM, the mistuned modes are represented as a weighted sum of a limited number of nominal system modes [6], i.e.

$$\boldsymbol{\phi}_j = \sum_{m=0}^{N-1} \beta_{jm}\boldsymbol{\phi}_m^{\circ} \tag{2}$$

where β_{jm} is a weighting factor, and $\boldsymbol{\phi}_m^{\circ}$ is the mth nominal system mode normalized with respect to the tuned mass matrix. Alternatively, (2) may be expressed in matrix notation as

$$\boldsymbol{\phi}_j = \boldsymbol{\Phi}^{\circ}\boldsymbol{\beta}_j \tag{3}$$

where $\boldsymbol{\beta}_j$ is a vector of weighting factors, and $\boldsymbol{\Phi}^{\circ}$ is a matrix whose columns are the tuned system modes, i.e., $\boldsymbol{\Phi}^{\circ} = [\boldsymbol{\phi}_0^{\circ}\ \boldsymbol{\phi}_1^{\circ} \cdots \boldsymbol{\phi}_{N-1}^{\circ}]$. Substituting (3) into (1) and premultiplying by $\boldsymbol{\Phi}^{\circ H}$, where H is the Hermitian, yields the reduced order problem

Contributed by the International Gas Turbine Institute (IGTI) of ASME for publication in the JOURNAL OF TURBOMACHINERY. Manuscript received October 1, 2004; final manuscript received February 1, 2005. Assoc. Editor: K. C. Hall. Paper presented at the ASME Expo 2005: Land, Sea, and Air, Reno, NV, June 6–9, 2005, Paper No. GT2005-68128.

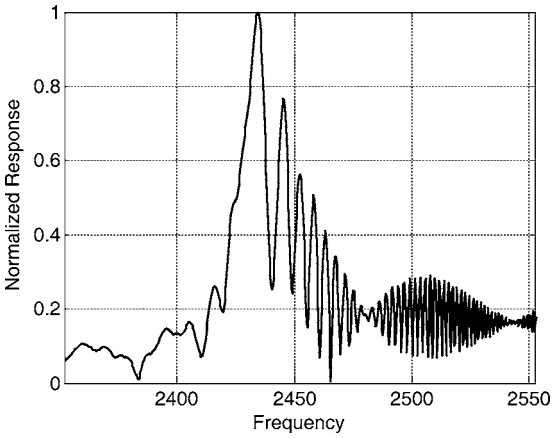

Fig. 1 Transient response from NASA spin pit test

$$[(\boldsymbol{\Omega}^{\circ 2} + \Delta\hat{\mathbf{K}}) - \omega_j^2(\mathbf{I} + \Delta\hat{\mathbf{M}})]\boldsymbol{\beta}_j = 0 \tag{4}$$

Physically, $\boldsymbol{\Omega}^{\circ 2}$ represents the modal stiffness matrix and $\mathbf{I}$ represents the modal mass matrix. However, since the modes are normalized with respect to the mass matrix, $\boldsymbol{\Omega}^{\circ 2}$ is simply a diagonal matrix of the tuned system eigenvalues,[1] and $\mathbf{I}$ is the identity matrix. $\Delta\hat{\mathbf{K}}$ and $\Delta\hat{\mathbf{M}}$ are the variations in the modal stiffness and modal mass matrices caused by stiffness and mass mistuning,

$$\Delta\hat{\mathbf{K}} = \boldsymbol{\Phi}^{\circ H}\Delta\mathbf{K}\boldsymbol{\Phi}^{\circ} \tag{5}$$

$$\Delta\hat{\mathbf{M}} = \boldsymbol{\Phi}^{\circ H}\Delta\mathbf{M}\boldsymbol{\Phi}^{\circ} \tag{6}$$

Equation (4) is the reduced order form of Eq. (1), and has only N degrees-of-freedom, where N is the number of tuned modes in the representation. This is the SNM formulation described by Yang and Griffin [6], and forms the basis of the FMM approach.

In FMM, Eq. (4) is further simplified by combining the mass and stiffness mistuning terms into a single mistuning matrix, $\hat{\mathbf{A}}$. This is accomplished by premultiplying the equation by $(\mathbf{I}+\Delta\hat{\mathbf{M}})^{-1}$ and keeping only first order terms. The expression simplifies to

$$(\boldsymbol{\Omega}^{\circ 2} + \hat{\mathbf{A}})\boldsymbol{\beta}_j = \omega_j^2\boldsymbol{\beta}_j \tag{7}$$

where

$$\hat{\mathbf{A}} = \Delta\hat{\mathbf{K}} - \Delta\hat{\mathbf{M}}\boldsymbol{\Omega}^{\circ 2} \tag{8}$$

The key to FMM's simplicity is that the mistuning matrix, $\hat{\mathbf{A}}$, can be related to the individual blade frequencies. Feiner and Griffin showed that when the subset of nominal mode representation in Eq. (2) contains only one family of nominal modes, that the individual elements of $\hat{\mathbf{A}}$ could be expressed as

$$\hat{\mathbf{A}}_{mn} = 2\omega_m^{\circ}\omega_n^{\circ}\left[\frac{1}{N}\sum_{s=0}^{N-1} e^{is(n-m)(2\pi/N)}\Delta\omega^{(s)}\right] \tag{9}$$

where $\Delta\omega^{(s)}$ is the fractional difference between the sth blade's frequency and the nominal blade frequency. This is an interesting relationship because it indicates that the dynamic response depends only on the blades frequency deviation and not on the physical cause of the mistuning.

Thus, to solve the FMM eigenvalue problem, Eq. (7), for the mistuned modes and natural frequencies, we need only know two sets of parameters: the natural frequencies of the tuned system, which compose the matrix $\boldsymbol{\Omega}^{\circ 2}$, and the blade frequency deviations, which define the mistuning matrix $\hat{\mathbf{A}}$ through Eq. (9). $\boldsymbol{\Omega}^{\circ 2}$ describes the nominal system, while $\hat{\mathbf{A}}$ characterizes the mistuning.

Equation (7) determines the modes and natural frequencies of the mistuned system. The system's forced response can then be calculated through a standard modal summation, i.e.

$$\boldsymbol{x}(t,\omega) = \sum_j a_j(t,\omega)\boldsymbol{\phi}_j \tag{10}$$

With the modes normalized to have a modal mass of one, the contribution of the jth mode is governed by the equation of motion,

$$\ddot{a}_j + 2\zeta_j\omega_{nj}\dot{a}_j + \omega_{nj}^2 a_j = f_j e^{i\omega t} \tag{11}$$

where ζ_j, ω_{nj}, and f_j are the modal damping, natural frequency, and modal force of the jth mode, respectively. In the case of the steady state response, Eq. (11) has a closed form solution which allows the system response to be readily calculated. However, in the case of transient solution to an engine accel excitation, the modal equation of motion, (11), becomes more complicated. In this case, the blades are excited harmonically, but the frequency of the excitation is a function of time. As a result, the forcing term in Eq. (11) takes the form

$$\ddot{a}_j + 2\zeta_j\omega_{nj}\dot{a}_j + \omega_{nj}^2 a_j = f_j e^{i\omega(t)\cdot t} \tag{12}$$

For purposes of discussion assume that the excitation frequency is a linear function of time, i.e., $\omega(t)=\omega_{\circ}+(\alpha/2)t$. When this expression is substituted into (12), a second order time term appears in the exponential. As there is no closed form solution to this equation, and it must be solved numerically.

The numerical integration was implemented in Matlab using an explicit time-domain numerical ODE solver. Similar techniques have been applied to other bladed disk response problems, such as friction damping [18] and coupled aerodynamic/structural response problems [19–21].

A subtle characteristic of the linear frequency sweep is that the instantaneous excitation frequency at any given time is not simply given by the frequency argument of the forcing term in Eq. (12). For instance, suppose we wish to determine the instantaneous excitation frequency at time t^*. At that instant, the excitation term in Eq. (12) will have a frequency argument of $\omega(t^*)$. However, the actual excitation frequency at time t^* is calculated by performing the change of variable $t=t^*+\Delta t$. With this substitution, the forcing term in Eq. (12) becomes to first order

$$f_j e^{i[\varphi+(\omega_{\circ}+\alpha t^*)\Delta t]} \tag{13}$$

where φ is a phase shift produced by the constant terms. Thus, the instantaneous excitation frequency at time t^* is actually given by $\omega_{\mathrm{ex}}(t^*)=\omega_{\circ}+\alpha t^*$, which differs from $\omega(t)=\omega_{\circ}+(\alpha/2)t$. This is a subtle distinction, but it is essential for correlating a predicted response with experimental measurements. Notice that α now has the physical interpretation as the acceleration rate of the excitation frequency in rad/s^2. α can be related to the change in engine speed by the expression $\alpha=2\pi E(\Delta\mathrm{RPM}/60\cdot T)$, where E is the engine order of the excitation, ΔRPM is the change in engine speed in revolutions per minute, and T is the acceleration time in s.

3 Experimental Application

In order to use transient FMM to predict the response of actual hardware, we must first obtain all the input parameters. Recall from Eqs. (7) and (9) that the input parameters to the FMM eigenvalue problem are the tuned system frequencies which describe the nominal system, and the blade frequency deviations which characterize the mistuning. These parameters can all be determined experimentally with FMM ID, a companion program to FMM which solves the inverse solution to the FMM eigenvalue

[1] An eigenvalue is equal to the square of the natural frequency of a mode.

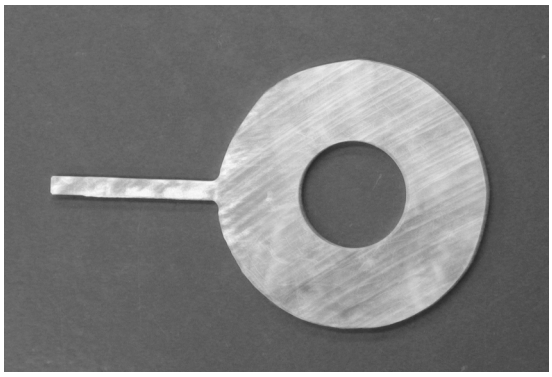

Fig. 2 Single blade rotor

problem [17,22]. FMM ID is based on the concept that small changes in blade frequencies can produce large changes in the mode shapes of a bladed disk system. Therefore, measurements of the mistuned modes shapes can be used as a mathematical "microscope" to precisely determine what mistuning must be present in the system. FMM ID requires measurements of the mistuned modes and natural frequencies, from which it can infer the structure's tuned system frequencies and mistuning. In practice, the mistuned system modes and frequencies are measured through standard modal testing techniques. This involves measuring a set of transfer functions, and then extracting modes with modal curve fitting software.

The final input parameter is the damping of the mistuned modes. In practice, aeroelastic predictions of damping could be used. However, for the purpose of our bench tests of a stationary IBR, we measured the damping experimentally. The two test pieces used in our benchmark studies are shown in Figs. 2 and 3. The first is a single blade IBR, which only has a single mode in the frequency range of interest. To measure its damping, we excited the structure with a speaker, and then we turned off the excitation and measured the blade's time response with a laser vibrometer as its amplitude decayed down, as shown in Fig. 4. The damping was then calculated from the exponential decay constant. The approach was slightly modified to calculate the damping in the second test piece. Since this IBR has 18 blades, multiple modes are excited in the frequency range of interest, and we must extract a separate damping value for each mode. This was accomplished by measuring the decay response of all 18 blades, and then decomposed that response into modal coordinates. Finally, each

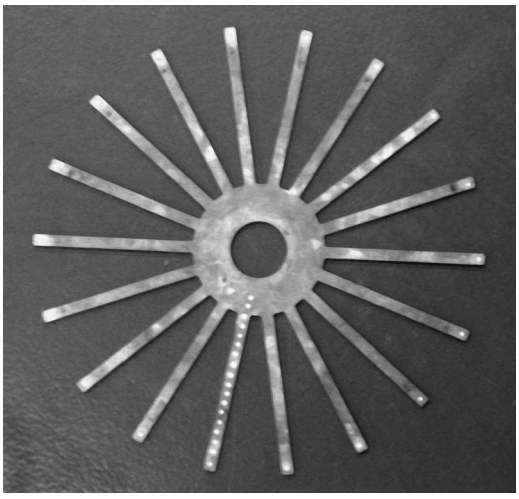

Fig. 3 Eighteen blade rotor

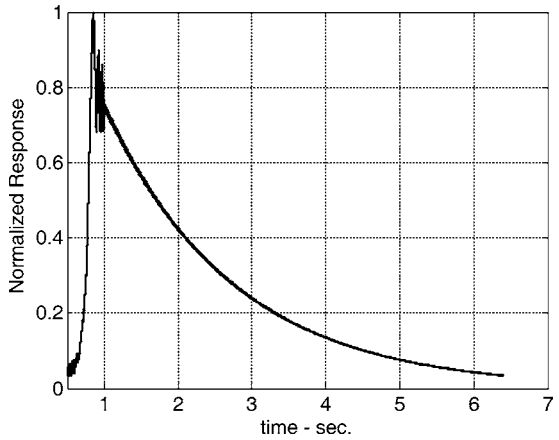

Fig. 4 Example of modal response used to calculate damping

individual modal damping value was determined from the decay constant of the corresponding modal response. It should be noted that the same modal analysis package that was used to determine the mode shapes also determines the modal damping. Although this is a simpler approach for measuring modal damping, our modal analysis software does not provide enough significant digits to provide a reasonable estimate of damping for these lightly damped parts.

This method was validated by comparing it with experiments on two separate disks, one with a single blade, and one with 18 blades.

3.1 Single-Blade Test Case. As an initial test of the Transient FMM algorithm, the method was applied to the simplest possible bladed disk; a disk with only one blade, Fig. 2. This disk only has one mode in the frequency range of interest, and therefore allows us to study transient response behavior without the added complexity of multiple mode interactions. The blade was excited acoustically with a two second sine sweep through the blade's first bending resonance. A laser vibrometer was used to measure and record the time history of the blade's response. A plot of this time history is shown in Fig. 5. Superimposed on this is a plot of the response envelope. For clarity, all subsequent response plots show only the response envelope.

It may be noted from this figure that there is a beating phenomenon present in the response. This occurs due to the interaction of the homogeneous solution of Eq. (12) and the particular solution. The homogeneous solution is harmonic and oscillates at the damped resonant frequency, i.e., $a_h=(e^{-\xi\omega_n t})e^{i\omega_{rj}t}$. The particular

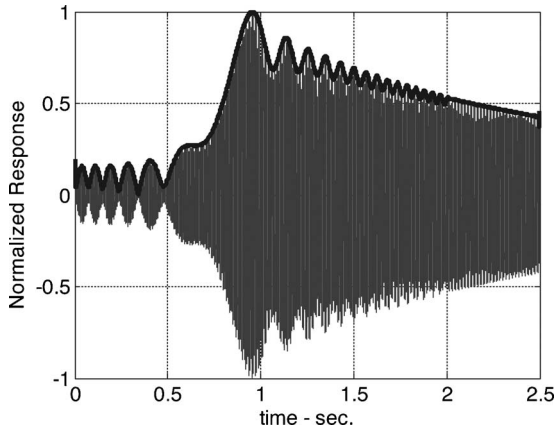

Fig. 5 Time response from single blade test case, with overlaid response envelope

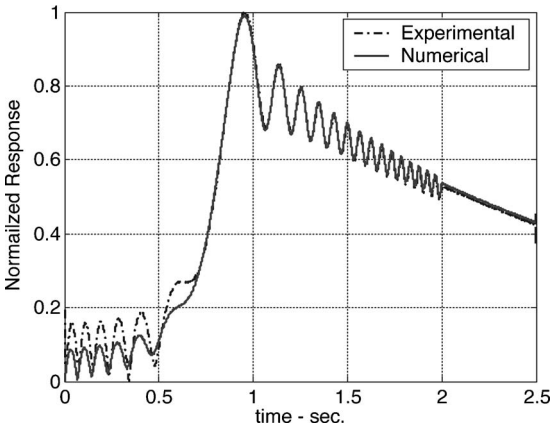

Fig. 6 Comparison of measurement with simulation for single blade

solution does not have a closed form, but is oscillatory and approximately follows the excitation frequency. Therefore, the interaction of the two solutions produces a beating effect when the excitation frequency is close to the damped resonant frequency. In beat theory, the frequency of the beat is related to the difference in the two interacting frequencies [23]. This gives rise to the increasing beat frequency seen in Fig. 5. Furthermore, notice that when the excitation is stopped after 2 s, only the homogeneous response remains and the beating stops. When multiple modes are summed this type of beating becomes very important in establishing the overall system response. Since the beating depends on the spacing of the natural frequencies, it will be shown that the transient response is sensitive to variations in the frequencies of the mistuned modes in quite a different manner than is the steady state response.

In the first experiment, standard modal testing was used to measure the natural frequency and damping of the blade's first bending mode. This information was then used as input into the transient simulation code to simulate the response. A comparison of the measured and simulated responses is shown in Fig. 6. The response has been normalized so that the peak amplitude has a value of 1. Note that it was not possible to directly measure the magnitude of the excitation force used in the experiments. Consequently, the value used in the simulation was chosen to minimize the error between the measured and simulated results. There is good agreement between the experimental and analytical results for the single blade case.

3.2 18-Blade Test Case. Next, an eighteen bladed disk was used to verify the prediction code in a more complex and realistic test involving multiple modes. For this test, we used a magnetic excitation source applied to a single blade, and did a two second sine sweep through the disk's first bending mode resonant frequencies. Again, a laser vibrometer was used to measure the response of each blade.

This rotor's response was then simulated using the transient code. FMM ID was used to determine the mistuning and tuned frequencies in the IBR and then FMM was used to calculate the system's mistuned modes and frequencies. Each mode's response was calculated and summed to get the overall system response.

A comparison of the results from two representative blades is shown in Fig. 7. The response has been normalized with respect to the peak blade amplitude on the entire disk. Again, the results match well, showing that the transient analysis correctly predicts the response of systems with multiple modes.

4 Transient Solution Sensitivity

A unique characteristic of transient behavior is the sensitivity of the blade response to small variations in the natural frequencies of

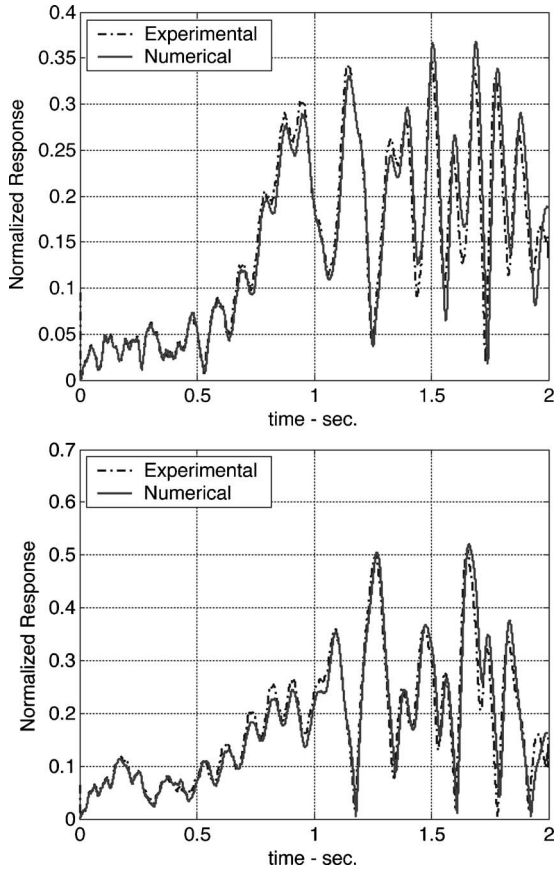

Fig. 7 Comparison of measurement with simulation for two representative blades from 18 blade test case

the mistuned system. To demonstrate this effect, we changed three of the natural frequencies from the 18 blade case in our numerical solution. Specifically, the frequencies of modes seven and nine were increased by 0.25%, and mode 8 was decreased by 0.25%. The mode shapes and damping were unchanged. The steady state frequency response of a representative blade is shown in Fig. 8, with the original and perturbed plots overlaid. Clearly, the change in frequencies had a negligible effect on the steady state response. In addition, the frequency changes had a relatively small effect on the transient responses of individual modes, refer to Fig. 9. However, consider the transient response of the blade shown in Fig. 10.

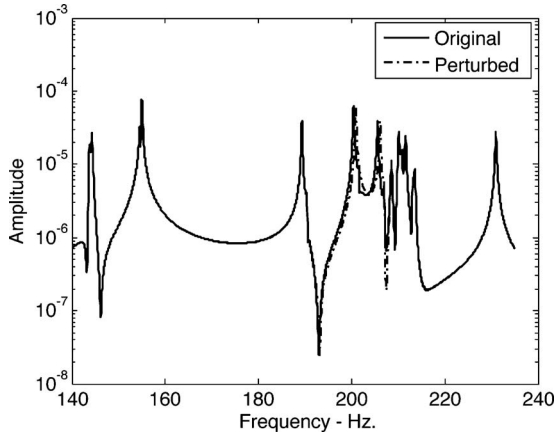

Fig. 8 Comparison of actual and perturbed steady-state response for 18 blade test case

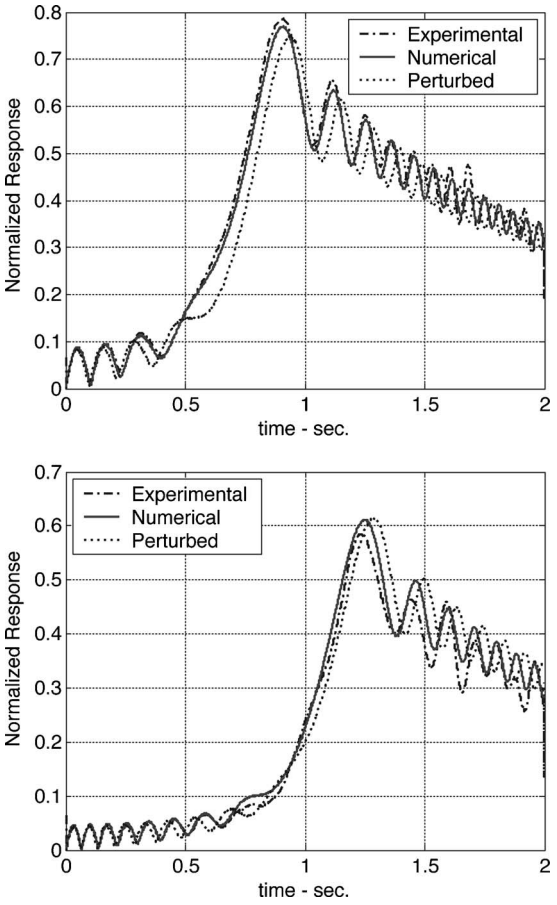

Fig. 9 Comparison of measured, simulated, and perturbed response for two representative modes from the 18 blade test case

There are three lines on this plot, one from the experiment, one from the original transient calculation, and one calculated with the perturbed natural frequencies. To understand this, note from the modal responses (Fig. 9) that each mode peaks at approximately 1 s after the excitation begins, i.e., the midpoint on the time scale. Until that time the perturbed response follows the original simulation fairly well. However, from one second on, the perturbed response looks markedly different. This is shown in Fig. 11, which expands to the second half of Fig. 10. The change is due to a shift

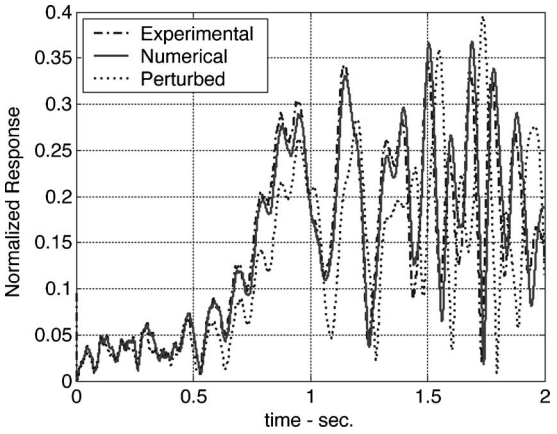

Fig. 10 Comparison of measured, simulated, and perturbed response for a representative blade from the 18 blade test case

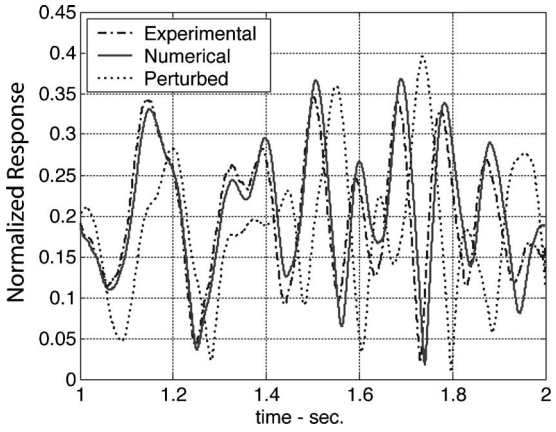

Fig. 11 Expanded view of a 1–2 s region of Fig. 10

in the phase of the beating of the three perturbed modes caused by the small changes in the natural frequencies. Although the change in each is small, when these modes are summed the phase changes produce a large change in the individual blade's response.

5 Acceleration Rates That Cause Large Transient Effects

Due to the added computational cost associated with the transient form of FMM, it is important to assess when a transient forced response analysis is required, and when a simpler steady-state calculation is sufficient. From experience, transient effects are most pronounced in lightly damped systems with high accel rates. They occur when the transient (homogeneous) part of the solution decays slowly relative to the time it takes to pass through resonance. However, quantitative guidelines are needed to predict when a system will be in the transient regime. We will define this in terms of a dimensionless critical accel rate which separates the boundary between the transient and steady-state regimes. Section 5.1 defines the critical accel rate for a given engine order harmonic. Then in Sec. 5.2 we describe how this result may be applied to the general case of multiple engine harmonics.

5.1 Critical Accel Rate. Consider the modal equation of motion (12). If we define a dimensionless time $\tau = t\omega_n$, Eq. (12) can be rewritten in a dimensionless form which has a characteristic response that is independent of the natural frequency,

$$\ddot{a}_j + 2\zeta_j \dot{a}_j + a_j = \left(\frac{f_j}{\omega_{nj}}\right) e^{i(\bar{\omega}_\circ + (\bar{\alpha}/2)\tau)\cdot\tau} \tag{14}$$

where $\bar{\omega}_o$ and $\bar{\alpha}$ are the dimensionless start frequency and acceleration rate defined as

$$\bar{\omega}_\circ \equiv \frac{\omega_\circ}{\omega_n} \tag{15a}$$

$$\bar{\alpha} \equiv \frac{\alpha}{\omega_n^2} \tag{15b}$$

The time this solution takes to pass through resonance can be approximated as the time required to accel through the steady-state half power bandwidth, i.e.,

$$\Delta\tau = \frac{\bar{\omega}_{\mathrm{bw}}}{\bar{\alpha}} = \frac{2\zeta}{\bar{\alpha}} \tag{16}$$

In this same time, the envelope of the homogeneous response will decay by a factor DF, given by

$$\mathrm{DF} = e^{-\zeta\omega_n(\Delta\tau)} \tag{17}$$

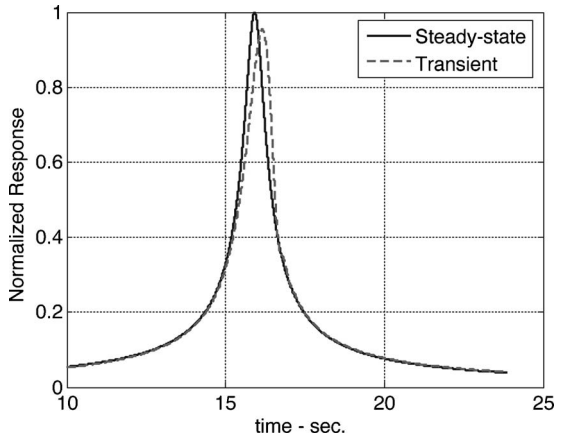

Fig. 12 Comparison of steady-state and transient response for a representative mode at critical acceleration rate

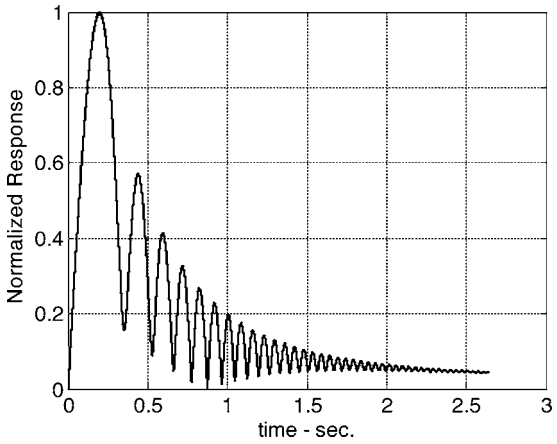

Fig. 13 Transient behavior with realistic acceleration rate and damping level

Equating the time span of these equations yields an expression for the dimensionless accel rate which will allow the homogeneous solution to decay by a factor DF in the time required to accel through the half-power bandwidth,

$$\bar{\alpha} = \frac{2\zeta^2}{\ln(\mathrm{DF})} \tag{18}$$

The issue is how rapidly the homogeneous response must decay over the half-power bandwidth for the system to be well approximated by a steady-state solution. Through simulation, we found that decay factors greater than 50 produce a response with negligible differences from the steady-state response, while smaller decay factors yield solutions with significant transient behavior. Thus, we can define a critical dimensionless accel rate as

$$\bar{\alpha}_c \equiv \frac{2\zeta^2}{\ln(50)} \simeq \frac{\zeta^2}{2} \tag{19}$$

This result compares well with those given by Ewins [24] and the ISO standard on shock and vibration [25] for frequency sweep rate in vibration testing. Figure 12 shows a comparison of the steady-state and transient responses of a representative mode at the critical acceleration rate. Notice that at this rate, the transient response is showing only subtle differences from the steady-state calculation.

A representative value of a fast acceleration rate used in a military engine is 6000 rpm in 4 s. If you assume a natural frequency of 500 Hz, and a third engine order excitation, this works out to a dimensionless acceleration rate of approximately 5×10^{-5}. Assuming a damping ratio of 0.2%, the critical acceleration rate would be 6.00×10^{-6}. Consequently, the actual acceleration rates that occur in military engines are significantly larger than that required to cause transient effects. Therefore, transient effects will be important in the response. To illustrate this point, a numerical simulation of the 18 bladed disk was performed in which the damping was changed to 0.2% and the dimensionless acceleration rate was set to 5×10^{-5}, in order to match representative engine conditions. The response of a representative mode is depicted in Fig. 13. Clearly, transient beating effects are very prominent in the response.

5.2 Transient Regimes for Generalized Excitations. Generally, the excitation forces in an engine are periodic in theta, the angular position around the disk. Therefore, even complicated forcing functions can be decomposed into a Fourier series. Since the equations of motion are linear, the system's response to each harmonic component can be considered separately. This is standard practice in the gas turbine industry, since each harmonic excites the structure at a distinct frequency given by the product of it harmonic number and the rotation speed. Typically, only a few engine order harmonics must be considered for a given frequency and speed range. Since the Fourier decomposition is performed in space as opposed to time, we would expect that same characteristics to hold in the transient regime as well. If so, than it would imply that we can assess the need for a transient or steady-state simulation on an individual basis for each harmonic.

To study this phenomenon, we performed transient FMM simulations. We simulated the response of the 18-bladed test piece rotating through a square wave forcing function. The square wave had a duty cycle of 10% and was designed to produce a dominant first engine-order harmonic. A plot of this excitation is shown in Fig. 14.

Because the disk is accelerating, the excitation is not periodic in time, however it is periodic in theta. Taking the Fourier decomposition of this function, you get the following result:

$$f(\theta) = f_\circ \frac{\Delta\theta}{\lambda} + \sum_{n=1}^{\infty} \frac{2f_\circ}{n\pi} \sin\frac{2\pi n\cdot\Delta\theta}{\lambda} \cos\frac{2\pi n\theta}{\lambda} \tag{20}$$

In this expression, theta is a function of time, $\theta=\omega_\circ t+(\alpha/2)t^2$, where $\omega_\circ$ is the initial rotational velocity of the disk and α is the acceleration rate. If you substitute this into Eq. (20), and replace λ with the actual wavelength, 2π, you get the following expression for the excitation force as a function of time:

$$f(t) = f_\circ \frac{\Delta\theta}{2\pi} + \sum_{n=1}^{\infty} \frac{2f_\circ}{n\pi} \sin(n\cdot\Delta\theta)\cos\left[n\left(\omega_\circ t + \frac{\alpha}{2}t^2\right)\right] \tag{21}$$

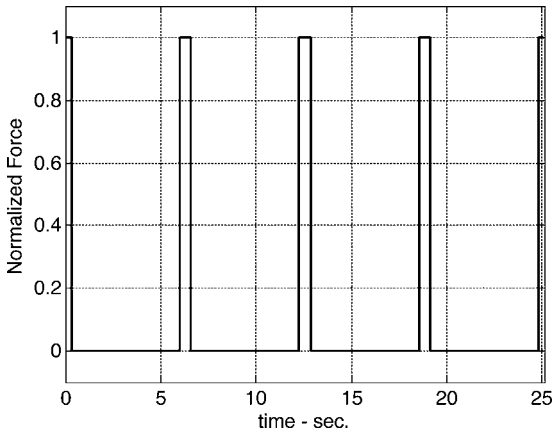

Fig. 14 Square wave excitation

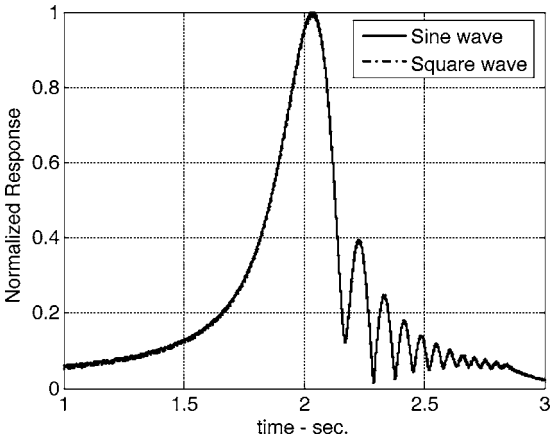

Fig. 15 Comparison of response to sine wave and square wave inputs

The system response was simulated using a square wave input and also with only the first harmonic of the square wave. It was found that the responses were virtually identical. See Fig. 15 for an example of the response to both a square wave and a 1E harmonic. This result indicates that even in the transient regime, each harmonic drives the structure at a distinct frequency and can be considered individually. Therefore, we can assess the need for a transient or steady-state simulation on an individual basis for each harmonic. If the acceleration rate for a particular harmonic is above the critical value, then a transient simulation will be necessary to model its response.

6 Conclusions

A method of predicting the transient response of bladed disks was developed to account for the transient effects of rapid engine accelerations. This method uses a numerical approach to integrate the modal equations of motion. As input data, it uses the frequency mistuning of the blades as well as the tuned system frequencies. The method was verified using two experimental test cases: a single blade system and an integrally bladed disk with 18 blades. In each case, the method was shown to accurately predict the forced response.

Transient FMM calculates a bladed disk's forced response through a two-step process. First, it calculates the modes and natural frequencies of the mistuned system. Then, it performs a transient modal summation to calculate the vibratory response. The first part of the process is done using the FMM algorithms that have been experimentally validated for real compressor and fan geometries [16,22,26]. The part of the transient FMM that is new is performing a transient modal analysis. Transient modal analysis is a widely used technique that is independent of the specific geometry of the structure. Consequently, the test results from the simplified IBR geometry used in this study provides an adequate validation that the transient modal analysis has been correctly integrated with FMM. As a result, it is clear that transient FMM can be used to predict the transient response of IBRs with more realistic geometries such as those studied in [16,22,26] and that qualitatively similar behavior will occur in those systems.

It was demonstrated that transient response is more sensitive to small errors in the system's natural frequencies than are the standard steady-state calculations. This occurs because the various homogeneous and particular components of the modal responses interact to produce a beat phenomenon. Small changes in the natural frequencies slightly shift the phase of the interacting waves, producing large changes in the forced response. It should be emphasized that this is a distinctly different phenomenon from the mistuning problem. Although both phenomena cause the blade amplitudes to be very sensitive to variations in frequency parameters, they are each caused by very different mechanisms.

Since the transient FMM algorithm uses numerical integration to solve the modal equations of motion, it is more time consuming than a corresponding steady-state response calculation. Therefore, it was necessary to establish guidelines to determine which engine acceleration conditions require transient forced response calculations. We developed an expression for a critical acceleration rate, above which transient effects become important. The expression showed that the critical acceleration rate for a particular mode is directly proportional to its damping ratio. Therefore, very lightly damped environments such as evacuated spin pits will readily produce transient response. In order to correlate forced response predictions with such tests, a transient response code is required. Furthermore, based on these guidelines it was shown that military engines operate in the transient regime. Therefore, transient versions of mistuned forced response algorithms such as transient FMM are important tools for high cycle fatigue mitigation.

Acknowledgment

The authors would like to acknowledge that this research was supported in part by the U.S. Air Force, Contract No. F33615-01-C-2186, under the direction of Dr. Charles Cross and by the GUIde Consortium. The POLYTEC scanning vibrometer used in the experiments was purchased through a DURIP grant sponsored by an AFOSR.

References

[1] Srinivasan, A. V., 1997, "Flutter and Resonant Vibration Characteristics of Engine Blades," ASME J. Eng. Gas Turbines Power, **119**(4), pp. 742–775.
[2] Seinturier, E., Lombard, J., Berthillier, M., and Sgarzi, O., 2002, "Turbine Mistuned Forced Response Prediction Comparison With Experimental Results," ASME Paper No. GT-2002–30424.
[3] Seinturier, E., Lombard, J., Dumas, M., Dupont, C., Sharma, V., and Dupeux, J., 2004, "Forced Response Prediction Methodology for the Design of HP Compressors Bladed Disks," ASME Paper No. GT2004–53372.
[4] Sextro, W., Panning, L., Gotting, F., and Popp, K., 2002, "Fast Calculation of the Statistics of the Forced Response of Mistuned Bladed Disk Assemblies With Friction Contacts," ASME Paper No. GT-2002–30427.
[5] Castanier, M. P., Ottarsson, G., and Pierre, C., 1997, "A Reduced Order Modeling Technique for Mistuned Bladed Disks," ASME J. Vibr. Acoust., **119**(3), pp. 439–447.
[6] Yang, M.-T., and Griffin, J. H., 2001, "A Reduced Order Model of Mistuning Using a Subset of Nominal Modes," ASME J. Eng. Gas Turbines Power, **123**(4), pp. 893–900.
[7] Petrov, E., Sanliturk, K., Ewins, D., and Elliott, R., 2000, "Quantitative Prediction of the Effects of Mistuning Arrangement on Resonant Response of a Practical Turbine Bladed Disk," 5th National Turbine Engine High Cycle Fatigue Conference, Chandler, AZ.
[8] Feiner, D. M., and Griffin, J. H., 2002, "A Fundamental Model of Mistuning for a Single Family of Modes," ASME J. Turbomach., **124**(4), pp. 597–605.
[9] Kruse, M. J., and Pierre, C., 1996, "Forced Response of Mistuned Bladed Disks Using Reduced-Order Modeling," *Proceedings of the 37th AIAA/ASME/ASCE/AHS/ASC Structures, Structural Dynamics, and Materials Conference*, Salt Lake City, Utah, 4, pp. 1938–1950.
[10] Bladh, R., Castanier, M. P., and Pierre, C., 2000, "Component-Mode-Based Reduced Order Modeling Techniques for Mistuned Bladed Disks, Part I: Theoretical Models," ASME Paper No. 2000-GT-0360.
[11] Bladh, R., Castanier, M. P., and Pierre, C., 2000, "Component-Mode-Based Reduced Order Modeling Techniques for Mistuned Bladed Disks, Part II: Application," ASME Paper No. 2000-GT-0361.
[12] Kim, J. H., Song, T. W., Kim, T. S., Ro, S. T., 2001, "Model Development and Simulation of Transient Behavior of Heavy Duty Gas Turbines," ASME J. Eng. Gas Turbines Power, **123**(3), pp. 589–594.
[13] Adams, M. L., 1980, "Nonlinear Dynamics of Flexible Multi-Bearing Rotors," J. Sound Vib., **71**(1), pp. 129–144.
[14] Chancey, V. C., Flowers, G. T., and Howard, C. L., 2003, "A Harmonic Wavelets Approach for Extracting Transient Patterns from Measured Rotor Vibration Data," ASME J. Eng. Gas Turbines Power, **125**(1), pp. 81–89.
[15] Mehmed, O., and Kurkov, A. P., 2002, personal communication.
[16] Feiner, D. M., and Griffin, J. H., 2004, "Exploring the Use of FMM ID for Engine Health Monitoring," *Proceedings of the 9th National High Cycle Fatigue Conference*, Pinehurst, NC.
[17] Feiner, D. M., and Griffin, J. H., 2003a, "Mistuning Identification of Bladed Disks Using a Fundamental Mistuning Model—Part I: Theory," ASME Journal of Turbomachinery, 126(1), pp. 150–158.
[18] Petrov, E. P., and Ewins, D. J., 2004, "Generic Friction Models for Time-Domain Vibration Analysis of Bladed Disks," ASME J. Turbomach., **126**(1), pp. 184–192.

[19] Breard, C., Vahdati, M., Sayma, A. I., and Imregun, M., 2000, "An Integrated Time-Domain Aeroelasticity Model for the Prediction of Fan Forced Response due to Inlet Distortion," ASME Paper No. 2000-GT-0373.
[20] Carstens, V., and Belz, J., 2000, "Numerical Investigation of Nonlinear Fluid-Structure Interaction in Vibrating Compressor Blades," ASME Paper No. 2000-GT-381.
[21] Marshall, J. G., and Green, J. S., 1998, "Application of a Time-Linearized Euler Method to Forced Response in a High-Pressure Turbine and Comparison with Engine Test Results," *Proceedings of the Third National High Cycle Fatigue Conference*, San Antonio, TX.
[22] Feiner, D. M., and Griffin, J. H., 2003b, "Mistuning Identification of Bladed Disks Using a Fundamental Mistuning Model—Part II: Application," ASME Journal of Turbomachinery, 126(1), pp. 159–165.
[23] Rao, S. S., 1995, *Mechanical Vibrations*, 3rd ed., Addison Wesley, Reading, MA.
[24] Ewins, D. J., 2000, *Modal Testing: Theory, Practice and Application*, Research Studies Press.
[25] International Organisation for Standardisation (ISO), "Vibration and shock—Experimental determination of mechanical mobility—Part 2: Measurements Using Single-Point Translation Excitation with an Attached Vibration Exciter."
[26] Feiner, D. M., Griffin, J. H., Jones, K. W., Kenyon, J. A., Mehmed, O., and Kurkov, A. P., 2003 "System Identification of Mistuned Bladed Disks from Traveling Wave Response Measurements," ASME Paper No. VIB-48448.

Unsteady Navier-Stokes Simulation of a Transonic Flutter Cascade Near-Stall Conditions Applying Algebraic Transition Models

Hans Thermann

Reinhard Niehuis

Institute of Jet Propulsion and Turbomachinery,
RWTH Aachen,
Templergraben 55,
52062 Aachen,
Germany

Due to the trend in the design of modern aeroengines to reduce weight and to realize high pressure ratios, fan and first-stage compressor blades are highly susceptible to flutter. At operating points with transonic flow velocities and high incidences, stall flutter might occur involving strong shock-boundary layer interactions, flow separation, and oscillating shocks. In this paper, results of unsteady Navier-Stokes flow calculations around an oscillating blade in a linear transonic compressor cascade at different operating points including near-stall conditions are presented. The nonlinear unsteady Reynolds-averaged Navier-Stokes equations are solved time accurately using implicit time integration. Different low-Reynolds-number turbulence models are used for closure. Furthermore, empirical algebraic transition models are applied to enhance the accuracy of prediction. Computations are performed two dimensionally as well as three dimensionally. It is shown that, for the steady calculations, the prediction of the boundary layer development and the blade loading can be substantially improved compared with fully turbulent computations when algebraic transition models are applied. Furthermore, it is shown that the prediction of the aerodynamic damping in the case of oscillating blades at near-stall conditions can be dependent on the applied transition models.
[DOI: 10.1115/1.2183313]

Introduction

Due to the trend in the design of modern aeroengines to reduce weight and to realize high pressure ratios fan and first-stage compressor blades are highly susceptible to flutter. At operating points with transonic flow velocities and high incidences, stall flutter might occur involving strong shock-boundary layer interactions, flow separation, and oscillating shocks. The precise prediction of the aerodynamic damping of oscillating blades at operating points at or near stall conditions is therefore a demanding task as the flow solver used must be capable of accurately predicting steady and unsteady turbulent and transitional flow phenomena.

With the progress of the available computer power computational fluid dynamics has become an important tool and computational methods have advanced from two-dimensional unsteady time-linearized inviscid to three-dimensional unsteady viscous analysis (e.g., [1–10]). Although time-linearized methods are still of great importance, especially in the aeroelastic design process, due to their robustness and low computational costs, physical phenomena such as large flow separations and the effects of large oscillation amplitudes can only be captured by time-accurate nonlinear Navier-Stokes computations. Thus, these computations can be useful to validate the time-linearized results on the one hand and to evaluate the influence of nonlinear and viscous effects on the other hand.

In the past, several authors (e.g., [11,12]) found that the laminar, transitional, and turbulent portions of the flow must be modeled properly in order to achieve a reasonable prediction of the steady and unsteady aerodynamic blade loading. It has been concluded that a successful prediction of the steady and unsteady boundary layer development is not always obtained by fully turbulent flow computations. Although many viscous flow solvers, often applying two-equation low-Reynolds-number turbulence models, have reached a high level of accuracy in simulating turbomachinery flows, deficits in the prediction of turbulent flow phenomena, and especially the transitional boundary layer development still exist [13,14]. Computational results can, however, be improved by using additional transition models. Recently, transition models for turbomachinery flow applications have been developed, e.g., by [15–17]. The approach that has been realized in the presented work is based on the intermittency concept originally proposed by [18], wherein an intermittency function is used to modify the turbulent viscosity [19].

The paper begins with a brief introduction of the numerical code and the turbulence and transition models used in this study. Two and three-dimensional, steady and unsteady computational results for a linear transonic compressor cascade at different incidence flow angles including near-stall conditions are presented. The results are analyzed with emphasis regarding the influence of transition modeling on the accuracy of prediction.

Numerical Method

Governing Equations, Discretization, and Boundary Conditions. The three-dimensional viscous flow solver PANTA, which was used for these computations, was developed at the Institute for Jet Propulsion and Turbomachinery of the RWTH Aachen by [12,20]. It is based on the compressible Reynolds and Favre-averaged Navier-Stokes equations using different low-Reynolds-number $k-\varepsilon$ turbulence models for closure. A cell-centered finite-volume method is used for the spatial discretization of the conservation equations. The inviscid fluxes are calculated

Contributed by the International Gas Turbine Institute (IGTI) of ASME for publication in the JOURNAL OF TURBOMACHINARY. Manuscript received October 1, 2004; final manuscript received February 1, 2005. IGTI Review Chair: K. C. Hall. Paper presented at the ASME Turbo Expo 2005: Land, Sea and Air, Reno, NV, June 6–9, 2005, Paper No. GT2005-68221.

with the upwind flux-difference splitting method of [21]. The MUSCL technique [22] is applied to achieve a spatial accuracy of second or third order. In regions with large gradients the order is limited by a TVD-limiter to avoid numerical instabilities. The interpolation technique of [23] is applied to calculate the viscous fluxes. The source terms are discretized by central differences. An implicit method is used for time integration. Since for an implicit scheme the state vector is unknown for the new time step, the nonlinear system is solved by Newton iterations. For steady computations, only one iteration per time step, is needed. For each Newton step, the system of equations is solved by a block-Jacobi iterative algorithm.

For steady computations the total pressure, total temperature, and flow angle are specified as boundary conditions at the inlet, the static pressure at the outlet. For unsteady computations, using the steady computations as start solutions, one-dimensional nonreflecting boundary conditions are applied at inlet and outlet. A no-slip boundary condition is used at solid walls.

In order to reduce computation time, the program has been parallelized using both shared memory (OpenMP) and distributed memory (MPI) techniques.

Turbulence Models. The turbulence models used in this study are the low-Reynolds-number $k-\varepsilon$ models by [24] (hereafter referred to as AB) and by [25] (hereafter referred to as CH). The main differences between the $k-\varepsilon$ models of AB and CH are the formulations of the near-wall damping functions of the turbulent fluctuations and the definition of the wall boundary condition for ε (see [24,25]).

The realizability concept proposed by [26] has been applied to overcome the well-known stagnation point anomaly of linear eddy-viscosity turbulence models. The overproduction of turbulent kinetic energy at stagnation points can be avoided by using a modified closure coefficient as an upper bound in the relation for the turbulent viscosity. The modified closure coefficient is calculated taking into account the time-scale realizability as proposed by [27].

Transition Models. The applied transition models are based on the intermittency concept originally proposed by [18], which defined the intermittency function γ as the probability of a flow being turbulent at a given position. With a constant turbulent spot propagation parameter σ, the intermittency function can be written as [28]:

$$\gamma = 1 - \exp\left[- \left. \frac{n\sigma}{u_\infty} \right|_{\mathrm{tr}} (x - x_{\mathrm{tr}})^2 \right] \tag{1}$$

where u_∞ is the freestream velocity and n the spot generation rate. n is defined as the number of turbulent spots produced per unit length and time at the position of transition onset x_{tr}. n is computed by transition models that correlate it to characteristic flow properties.

In [29] an intermittency function was introduced, taking into account the effect of changing freestream velocities on the convection velocity of the turbulent spots:

$$\gamma = 1 - \exp\left[- \left. n\sigma \right|_{\mathrm{tr}} (x - x_{\mathrm{tr}}) \int_{x_{\mathrm{tr}}}^{x} \frac{1}{u_\infty} dx \right] \tag{2}$$

This model was extented in [30] by defining the turbulent spot propagation parameter σ and the spot spreading half-angle α as a function of the local pressure gradient parameter λ_θ (see Appendix Eqs. (A1) and (A2)):

$$\gamma = 1 - \exp\left[- \left. n \right|_{\mathrm{tr}} \int_{x_{\mathrm{tr}}}^{x} \frac{\sigma}{u_\infty \tan \alpha} dx \int_{x_{\mathrm{tr}}}^{x} \tan \alpha dx \right] \tag{3}$$

For separated-flow transition it was found that the spot production rate is several orders higher than for attached boundary layers. The model of [29] was extended in [31] with a modified spot production rate to calculate the intermittency function. The definitions of n, σ, and α for the applied transition models are given in the Appendix.

The intermittency function as calculated by the described models is used to modify the turbulent viscosity, yielding:

$$\mu_t^\star = \gamma \cdot \mu_t \tag{4}$$

As the flow in the freestream is turbulent, the modification of μ_t is performed only within the boundary layer. At the interface, a switching function is applied and γ is set to unity outside the boundary layer. The boundary layer thickness is computed at each time step by the 99% criterion. Alternatively, the boundary layer thickness has been computed with the vorticity-based method proposed by [32]. However, results are almost identical for both methods. Nevertheless, it should be mentioned that the main uncertainty in the use of algebraic transition models consists of calculating the required boundary layer parameters.

In order to calculate the intermittency function with the models described above, the onset of transition has to be known. It is mainly a function of the turbulence intensity and the pressure gradient. Different approaches for the onset of transition were proposed by various researchers. For separated-flow transition in short bubbles, [33] defined the onset of transition as (without turbulence intensity extension):

$$(\mathrm{Re}_x)_{s-\mathrm{tr}} = 300\, \mathrm{Re}_{\theta,s}^{0.7} \tag{5}$$

where $(\mathrm{Re}_x)_{s-\mathrm{tr}}$ is the difference of the momentum thickness Reynolds number calculated at the separation point and at transition onset. $\mathrm{Re}_{\theta,s}$ is the Reynolds number calculated with the momentum thickness at the separation point.

For attached flow, [34] proposed the following correlation for the onset of transition:

$$\mathrm{Re}_{\theta,\mathrm{tr}} = \exp\left[5.094 - 25\left(\frac{\overline{Tu}}{100} \right)^{1.6} \right] - 400 \exp[-0.01(\overline{Tu} + 2.5)^4] + \exp\left[f(\lambda_\theta) - \frac{f(\lambda_\theta)}{6.91} \overline{Tu} \right] \tag{6}$$

where $\overline{Tu}$ is the average turbulence intensity calculated with the inflow velocity and the local velocity. The function $f(\lambda_\theta)$ is given in the appendix.

Since in complex turbomachinery flows both transitions modes can occur on the same airfoil at the same time, [19] introduced a method combining transition models and criteria for bypass transition and for separated-flow transition. This method has been applied for the transitional computations in this study (hereafter referred to as TRA). In the combined method, the model of [30] and the criterion of [34] are used for bypass transition, and the model of [31] and the criterion of [33] are used for separated-flow transition. For a detailed description of the combined method, see [19].

Flutter Computations. In the flutter computations, the blades are forced to oscillate at a constant amplitude and frequency according to the corresponding test case. The position of the oscillating profile is calculated at each time step by solving the corresponding equation of motion and the new grid points are then computed using an algebraic method.

Flutter computations are carried out as influence mode (IM) computations. In the IM, computations are run on five blade channels, with only the center blade oscillating while all other blades are at rest. A frozen state from the steady computations is specified at the outer periodic boundaries.

Results and Discussion

Experimental Data and Computational Setup. The test case that has been chosen for this study is a linear transonic compressor cascade. It has been experimentally investigated by [35]. Geometry and inlet aerodynamic data for this cascade are given in

Table 1 Geometry and inlet aerodynamic data

Number of Blades	9
Cascade Width [mm]	116.0
Cascade Height [mm]	79.0
Blade Pitch [mm]	25.67
Chord Length [mm]	41.192
Aspect Ratio	1.9
Stagger Angle [deg]	49.5
Turning Angle [deg]	13
Mach Number	0.88
Reynolds Number	8×10^5
Turbulence Intensity	2%
Incidence Angles [deg]	0, 4

Table 1.

Two operating points have been chosen for this study: one with a flow incidence angle of 0 deg and one with an incidence angle of 4 deg, which is at near stall conditions. While the flow is nearly two dimensional on the pressure side, the oil flow visualizations (Figs. 4–8, left) show relatively strong separations of the sidewall boundary layers on the suction side for both operating points. Additionally, a shock-induced separation can be found on the suction side, where transition occurs. This separation is shifted upstream for the 4 deg incidence case and covers large areas of the airfoil surface around midspan.

Previous investigations [12] found that the separation bubble on the suction side, especially for the 4 deg case, could not be resolved properly with fully turbulent computations using the turbulence model of [25]. Consequently, the pressure distribution, including a pressure plateau at midspan caused by the shock-induced separation, could not be predicted precisely. Therefore, computations with the turbulence model of [24], which is presumably more suitable for the prediction of transitional flow phenomena, as well as computations additionally applying algebraic transition models are carried out in this study in order to improve the quality of the results.

Computations are carried out two dimensionally and three dimensionally. In the two-dimensional computations, the sidewall boundary layers were not resolved in order to save computation time. However, to account for the acceleration at midspan, a channel divergence was applied at the sidewall boundaries, which simulates the streamline contraction. There is a linear contraction of the sidewall boundaries from the blade's leading edge to the trailing edge as proposed by [36]. The channel divergence was chosen so that the computed inflow static pressure matched the measured values. The best agreement was found using an overall channel divergence of 8%. A slip boundary condition is used at the sidewall boundaries.

It should be mentioned that the use of the channel contraction to some extent allows for the adjustment of the pressure distribution at midspan. Therefore, three-dimensional computations have been carried out in order to investigate the performance of the models under the influence of the sidewall separations. In the three-dimensional computations, the grid has been refined toward the sidewall in order to resolve the sidewall boundary layer.

Due to the lack of measured radial distributions, inlet boundary conditions where specified as block profiles. At the sidewall boundary layers a velocity correction according to the 1/7-law has been applied. The use of appropriate inlet boundary conditions certainly has an impact on the development of the sidewall boundary layers which should be investigated in future work.

The symmetry of the cascade could be used to reduce the number of grid points in spanwise direction: a symmetry boundary condition is applied at midspan for all computations.

Grid Dependency Study. Structured multiblock H-O-H grids with different resolutions have been generated. A grid dependency study has been conducted in order to assure that the solutions obtained with the grid consisting of 151×31 nodes in the main block are sufficiently grid independent, since this grid has been used for all further computations. The resolutions, the average dimensionless wall distance y^+ and the number of nodes within the boundary layer N_{BL} are given in Table 2 for all meshes. Figure 1 shows a blade-to-blade section and magnifications of the leading and trailing edges of the computational grid consisting of 151×31 nodes in the main block.

Figure 2 shows a comparison of the computed static profile pressures and the shear stress coefficients with the measurements for fully turbulent and for transitional computations with the model of CH. A significant grid dependency can only observed for the coarse grid, while the solutions obtained with the finer grids are almost identical for the fully turbulent as well as the transitional computations. It is interesting to note, however, that the transitional computation with the coarse mesh is less grid dependent than the fully turbulent one.

Steady Computations for 0 Deg Incidence. Figures 3(*a*) and 3(*c*) show a comparison of the measured and computed static profile pressure distribution at midspan for 0 deg incidence. While the overall agreement with the experiment is very good for all 2D computations, the shock is predicted a little too far upstream in the 2D fully turbulent computations. This is also the case in the 3D fully turbulent calculation with the model of CH, while the transitional calculation agrees excellently with the experimental results. In contrast to that, the pressure minimum on the suction side is predicted too high for both 3D computations with the model of AB. This is due to a slight overprediction of the sidewall separations. Furthermore, all fully turbulent computations fail to predict the pressure plateau at about 25% chord length on the suction side, which is caused by a shock-induced laminar separation bubble. The transitional computations, however, predict the laminar separation bubble, where transition occurs, and the corresponding pressure plateau. Except for the 3D computation with the model of AB, they agree very well with the experimental results.

A comparison of the computed shear stress coefficient along the profile's surface at midspan for all computations is outlined in Figs. 3(*b*) and 3(*d*) for the 0 deg incidence case. It can be seen that the computed shear stresses along the profile's surface are almost identical on the pressure side and downstream of about 50% chord length on the suction side for all computations. All computations reveal a small separation near the leading edge on the pressure side, which has also been detected experimentally

Table 2 Grid resolutions

	Inflow Block (H-type)	Main Block (O-type)	Outflow Block (H-type)	y^+	N_{BL}
2D Coarse	$17\times15\times3$	$101\times15\times3$	$19\times15\times3$	4	5
2D	$21\times15\times3$	$151\times31\times3$	$23\times15\times3$	1	15
2D Fine	$25\times15\times3$	$301\times61\times3$	$27\times15\times3$	0.25	35
3D	$21\times15\times81$	$151\times31\times81$	$23\times15\times81$	1	15

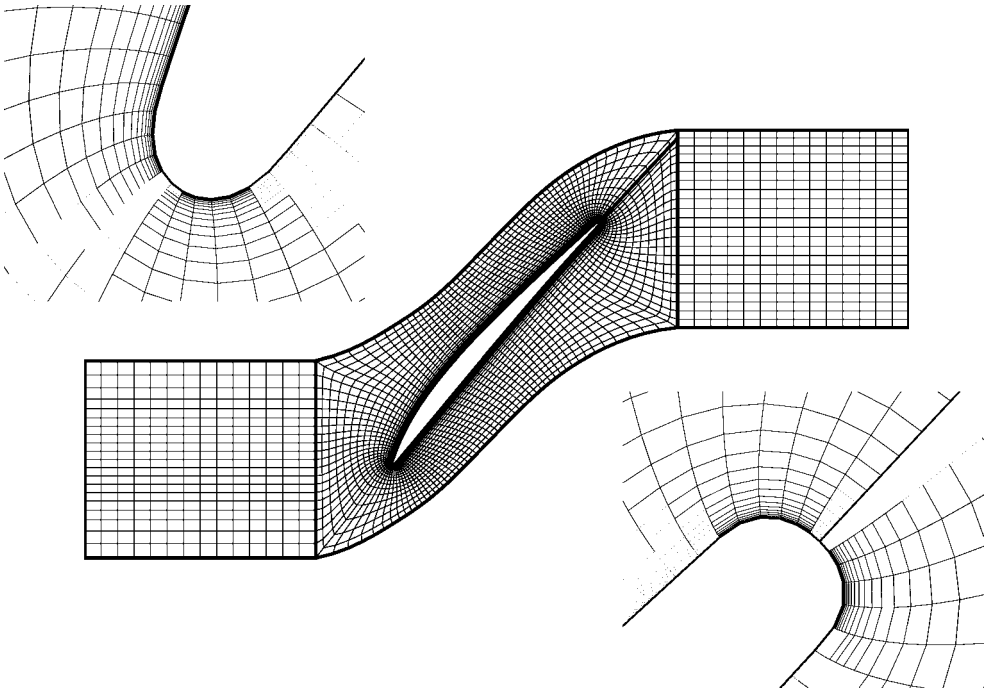

Fig. 1 Blade-to-blade section of the computational grid

(see [35]). On the suction side, the flow does not separate for the fully turbulent calculations, except for the 2D fully turbulent computation with the model of CH. However, the separation bubble (extending from about 29% to 32% chord length) is too small and located too far downstream as compared with the measurements. With the help of oil flow visualizations (Figs. 4 and 5, left) and hot film measurements at midspan the separation bubble could be detected experimentally between 22% and 31% chord length [35]. All transitional computations agree better with these experimental results. They predict separation bubbles extending between 24% and 34% chord length.

Figures 4 and 5 show comparisons of the oil flow visualization on the suction side with the calculated streamlines and shear stress coefficients of the 3D computations. As can be seen, both fully turbulent computations do not predict the laminar separation bubble at midspan, while the transitional computations do. In the

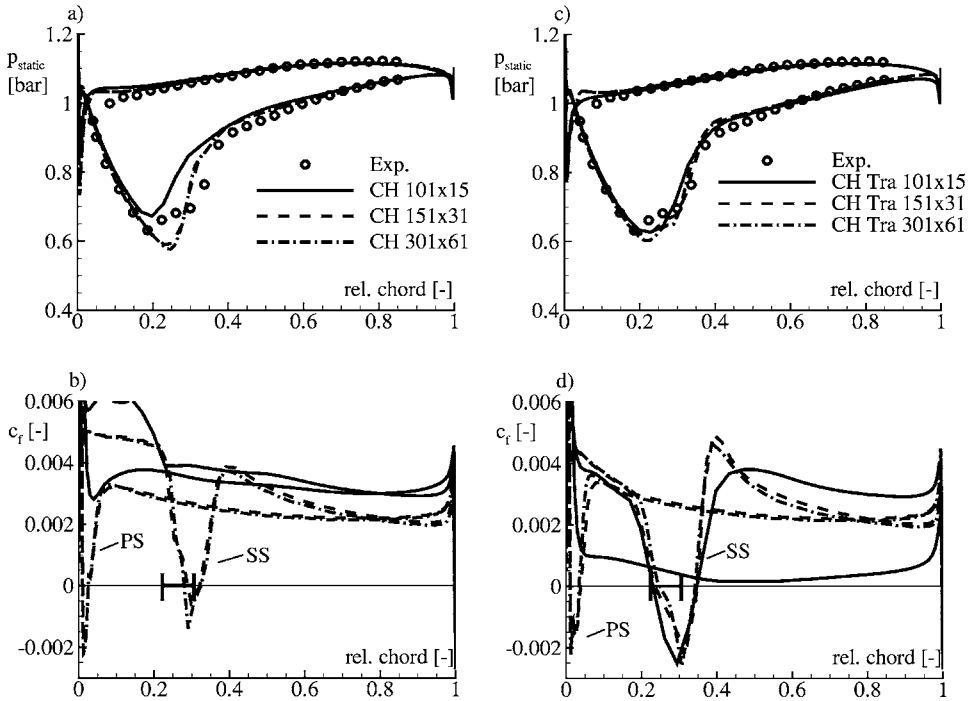

Fig. 2 Grid-dependency: steady computations for 0 deg incidence; upper: CH; lower: CH TRA; (*a*) and (*c*) static profile pressure; (*b*) and (*d*) shear stress coefficient

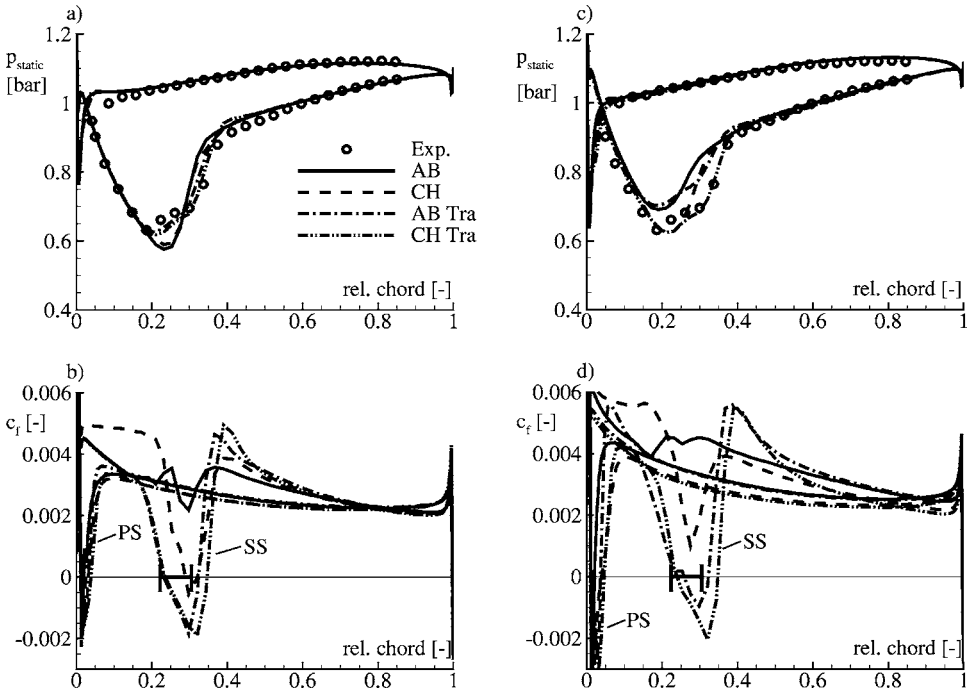

Fig. 3 Steady computations for 0 deg incidence; upper: 2D; lower: 3D; (*a*) and (*c*) static profile pressure; (*b*) and (*d*) shear stress coefficient

transitional computation with the model of CH, the spanwise extension of the laminar separation bubble is calculated in very good agreement with the measurements. In the transitional computation with the model of AB, the separation does not extend far enough toward the sidewalls. The predicted size of sidewall separations seems to agree well with the measurements for all models. However, although difficult to judge visually, in the computations with the model of AB, the sidewall separations are slightly overpredicted in the spanwise direction, thus influencing the pressure distribution at midspan (Fig. 3(*c*)).

The results show that the prediction of the boundary layer development and accordingly the pressure distribution can be improved compared with fully turbulent calculations when applying additional transition models. However, it also becomes obvious that the accurate simulation of the sidewall boundary layer separations is crucial for a precise prediction of the surface pressure at midspan in the 3D computations due to the blockage effect. Here, the model of AB clearly overpredicts the sidewall separations in both the fully turbulent and the transitional calculation.

Steady Computations for 4 Deg Incidence. For the case with an inlet incidence angle of 4 deg, which is at near-stall conditions, differences between the various models and between 2D and 3D computations are greater than for the 0 deg case due to the complexity of the flow field (see Figs. 6(*a*) and 6(*c*)). As can also be seen regarding the oil flow visualizations (Figs. 7 and 8, left) large flow separations exist on the suction side for the 4 deg incidence case. Due to the higher incidence, the flow separates further upstream at about 14% chord length. It remains unclear from the experimental results, however, whether the flow reattaches or not.

On the pressure side, the computed profile pressure distributions at midspan are very similar for all 2D computations. They

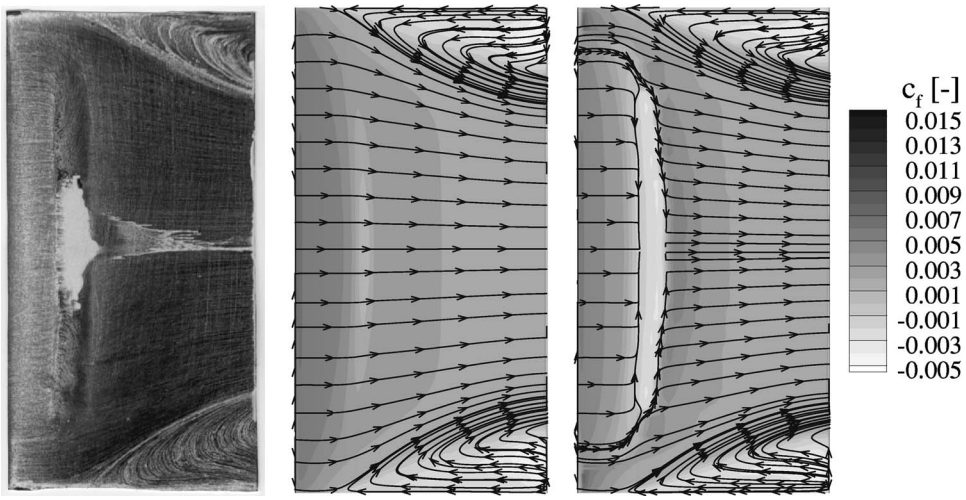

Fig. 4 Zero degree incidence; comparison of oil flow visualization (left) with streamlines and shear stress coefficients on the suction surface; middle: CH; right: CH TRA

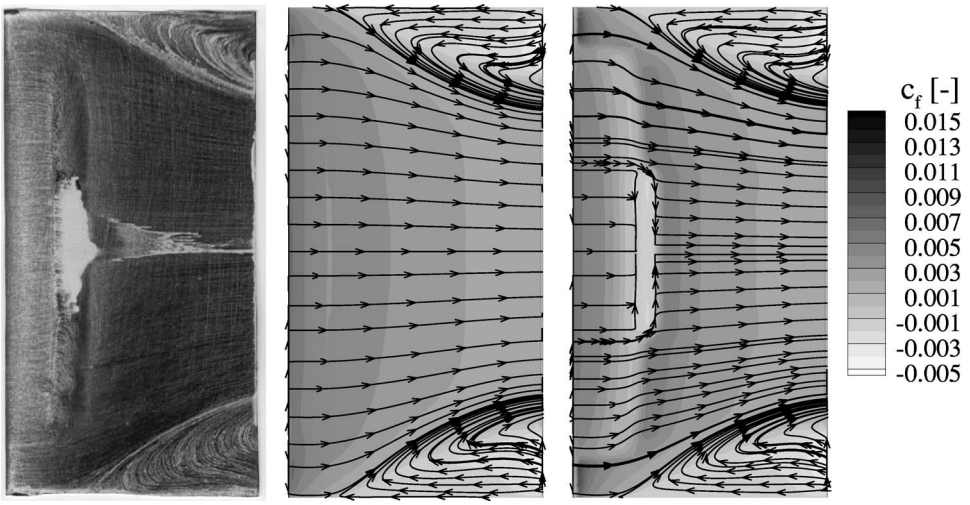

Fig. 5 Zero degree incidence; comparison of oil flow visualization (left) with streamlines and shear stress coefficients on the suction surface; middle: AB; right: AB TRA

agree well with the experiment except near the leading edge. Greater differences can again be found on the suction side, especially in the shock region. Here, the 2D fully turbulent computations both predict a pressure minimum that is too low and a shock that is much too strong compared with the experimental data. In contrast to the fully turbulent computations, the transitional computation with the model of CH predicts a pressure plateau upstream of the shock, which can also be detected in the measurements. However, the pressure minimum is still too low and the shock too strong. The pressure distribution predicted by the transitional computation with the model of AB agrees excellently with the measured values. In the transitional computations, transition occurs at about 25% chord length on the suction side.

As can be seen regarding the shear stress coefficient shown in Figs. 6(*b*) and 6(*d*), the 2D computations all predict separation bubbles with different extend. In all 2D calculations, the flow re-attaches. In the 3D computations, the separation bubbles are either short (AB TRA and CH) or the flow is completely separated (AB and CH TRA).

As can also be seen in Figs. 6(*b*) and 6(*d*), a laminar to turbulent transition occurs on the pressure side for both 2D transitional computations and for the 3D transitional computation with the model of CH at about 40% chord length, while the flow is fully turbulent on the pressure side in all other computations.

As a result of the under- or overpredicted separation bubbles, none of the predicted pressure distributions at midspan agree well with the experiments for the 3D computations. In the cases where the separation bubbles at midspan are too short, calculated pressures are too high on the pressure side and downstream of the shock location on the suction side. In the cases, where the flow is

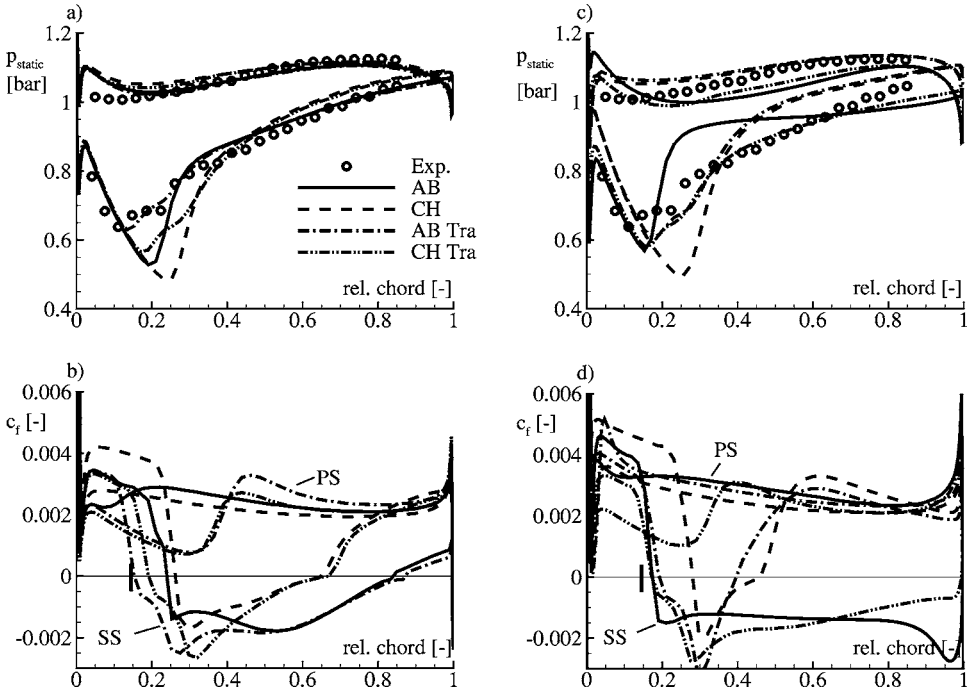

Fig. 6 Steady computations for 4 deg incidence; upper: 2D; lower 3D; (*a*) and (*c*) static profile pressure; (*b*) and (*d*) shear stress coefficient

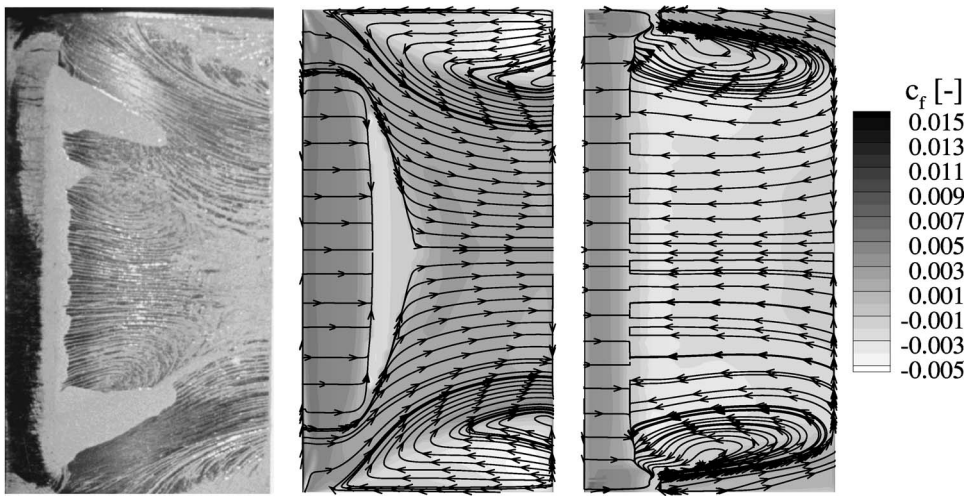

Fig. 7 Four degree incidence; comparison of oil flow visualization (left) with streamlines and shear stress coefficients on the suction surface; middle: CH; right: CH TRA

completely separated, the predicted profile pressures on the pressure side are too low. On the suction side, the pressure remains nearly constant downstream of the shock for the fully turbulent calculation with the model of AB due to the flow being completely separated. Furthermore, both fully turbulent computations clearly overestimate the shock strength. The best agreement is found for the transitional computation with the model of CH, although the flow is also completely separated. The predicted shear stress coefficient, however, shows a clear tendency to reattach toward the trailing edge.

Figures 7 and 8 show comparisons of the oil flow visualization on the suction side with the calculated streamlines and shear stress coefficients of the 3D computations. As can be seen, none of the computations is able to predict the highly complex flow patterns accurately. In the transitional computation with the model of CH and in the fully turbulent computation with the model of AB, the flow separates over the whole blade span downstream of about 19% chord length and does not re-attach. In the fully turbulent computation with the model of CH and in the transitional computation with the model of AB, the laminar separation bubbles extend only around midspan and not far enough toward the sidewalls. Compared with the measurements, they are also too short in the streamwise direction, while the sidewall separations are clearly overpredicted.

Since the best agreement with the experimental pressure distribution is found for the 2D transitional computations and to some extent for the 3D transitional computation with the model of CH, it might be concluded that the flow actually does re-attach at midspan on the suction side. Furthermore, the results show that in the 3D computations none of the modes is able to predict the highly complex flow patterns correctly at near-stall conditions. Similar to the 0 deg incidence case, the accurate prediction of the sidewall separations seems to have a great influence on the boundary layer development and consequently on the flow separations and the pressure distributions at midspan. Further improvements, e.g., higher-order turbulence models, seem to be necessary in order to yield a better prediction with regard to the 3D computations. However, especially the 2D results show that the pressure distribution at midspan can be predicted accurately even at near-stall conditions when additional transition models are applied.

Unsteady Computations for 0 Deg Incidence. Experimental flutter investigations have been carried out for the linear transonic compressor cascade by [35]. In the experiment, the center blade was forced to oscillate in a torsional motion with a frequency of 310 Hz and at an amplitude of 0.65 deg. The torsional axis is

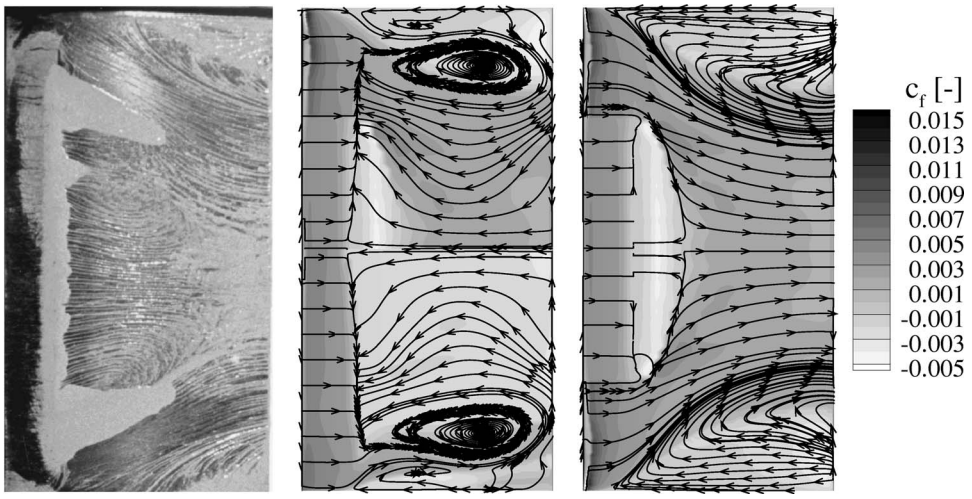

Fig. 8 Four degree incidence; comparison of oil flow visualization (left) with streamlines and shear stress coefficients on the suction surface; middle: AB; right: AB TRA

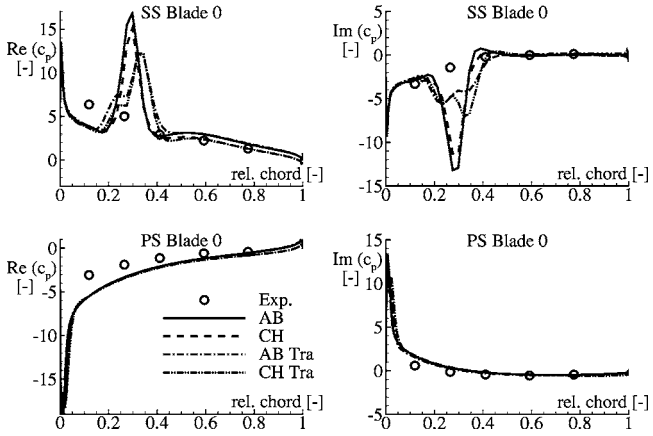

Fig. 9 2D unsteady computations for 0 deg incidence: real and imaginary parts of the first harmonic of the unsteady pressure coefficient on the oscillating blade

located at midchord. The reduced frequency based on chord length and inlet velocity for this case is 0.16. Using the results of the steady calculations presented in the previous section as starting solutions, unsteady flutter computations have been performed applying the same boundary conditions as in the experiment. Due to the long computation times and the better agreement of the steady 3D computations with the measurements, 3D unsteady computations have been carried out with the model of CH only. Computation time for an unsteady 3D computation on five blade channels, consisting of $\approx 2.16 \times 10^6$ grid points, is about one week using five Ultra-Sparc-III processors on a Sun Microsystems SMP-Cluster.

Figures 9 and 10 show a comparison of the measured and computed real and imaginary parts of the first harmonic of the unsteady profile pressure coefficient on the oscillating blade for the 0 deg incidence case for the 2D computations. Real and imaginary parts were preferred here over amplitude and phase since the imaginary part is out of phase with the blade motion and thus represents the energetically meaningful part of the unsteady surface pressure. A negative imaginary part on the suction side upstream of the torsional axis, which is located at midchord corresponds to aerodynamic damping.

As can be seen in Figs. 9 and 10, all computational results are nearly identical and in good agreement with the experiment on the pressure side of the oscillating blade regarding both real and imaginary part of the unsteady pressure coefficient. The level of the measured pressure fluctuations on the pressure side is low; however, the computations show large values toward the leading edge. These have not been detected experimentally as the first unsteady pressure transducer is located at 12% chord length.

Table 3 Zero degree incidence: aerodynamic work per oscillation cycle

	AB [mJ]	CH [mJ]	AB TRA [mJ]	CH TRA [mJ]
2D	−0.064	−0.065	−0.059	−0.064
3D	—	−0.319	—	−0.296

On the suction side, the calculated real and imaginary parts again are very similar for all computations and agree well with the measurements except for the shock region. Here, all models predict a shock impulse which has not been detected experimentally. In the 2D computations, the strength of the shock impulse corresponds to the steady shock strength. In both 3D computations, the shock impulse is predicted much weaker as in the 2D computations. This might be due to the sidewall separations. While the channel contraction is fixed in the 2D computations, the size of the sidewall separations changes due to changing incidence and is thus influencing the unsteady pressure distribution at midspan.

All models predict a damping influence of the shock impulse. The overall aerodynamic work on the oscillating blade, summarized in Table 3, is also very similar for all models in the 2D calculations and in the 3D calculations. All models predict a global damping of the oscillating blade due to the unsteady aerodynamic forces.

Unsteady Computations for 4 Deg Incidence. For the 4 deg incidence case, all computational results are again nearly identical and in good agreement with the experiment on the pressure side of the oscillating blade regarding both real and imaginary part of the unsteady pressure coefficient (Figs. 11 and 12). Differences exist mainly for the imaginary part toward the leading edge, where the computations with the model of AB and the 3D fully turbulent computation with the model of CH predict negative and thus exciting values, while the experiments show positive and thus damping values.

In contrast to the 0 deg incidence case, a shock impulse is detected experimentally for the 4 deg case on the suction side. The shock impulse, which is now exciting the blade motion, is predicted by all models. All models agree qualitatively well with the measured unsteady pressure coefficients. The 2D fully turbulent computation with the model of AB clearly overpredicts this

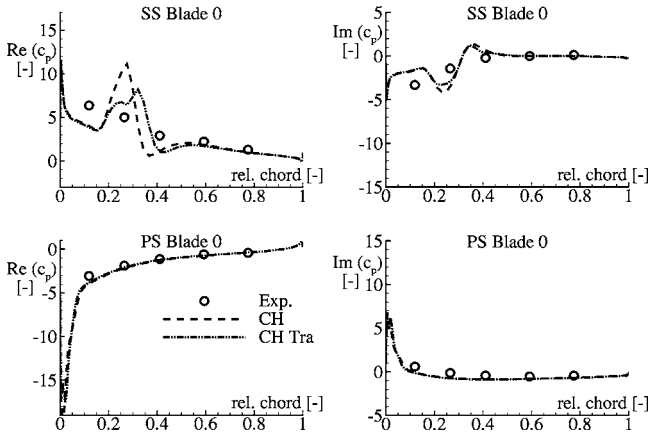

Fig. 10 3D unsteady computations for 0 deg incidence: real and imaginary parts of the first harmonic of the unsteady pressure coefficient on the oscillating blade

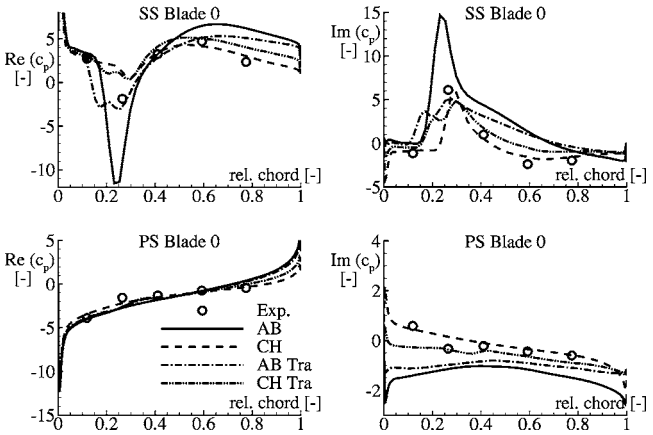

Fig. 11 2D unsteady computations for 4 deg incidence: real and imaginary parts of the first harmonic of the unsteady pressure coefficient on the oscillating blade

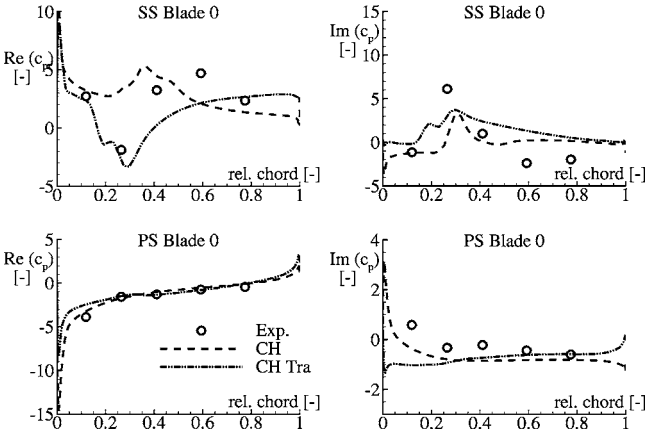

Fig. 12 3D unsteady computations for 4 deg incidence: real and imaginary parts of the first harmonic of the unsteady pressure coefficient on the oscillating blade

shock impulse. To the authors surprise, the imaginary part predicted with the 2D fully turbulent computations with the model of CH agrees excellently with the measurements, although the shock strength is clearly overpredicted and the shock location is calculated too far downstream in the corresponding steady computation. The same trend is found for the 3D fully turbulent calculation, but quantitatively, the computed imaginary part agrees less well with the experiment. The real part also is in good agreement with the experimental values in the 2D calculation, except in shock region where it is underpredicted, while in the 3D fully turbulent calculation greater deviations from the measured values can be found. The 2D transitional calculation with the model of CH is very similar to the fully turbulent regarding both real and imaginary part. The real part predicted by the transitional calculation with the model of AB agrees better with the experiment especially in the shock region. It also predicts the shock impulse well regarding the imaginary part, but overpredicts the imaginary part downstream of the shock. Similar results can be found for the 3D transitional computation with the model of CH.

Except for the 3D calculation with the model of CH, the predicted global aerodynamic work on the oscillating blade is positive for all models (Table 4). This shows that the blade motion is excited by the unsteady aerodynamic forces acting on it. In the 2D computations, the highest excitation is calculated by the fully turbulent computation with the model of AB. This is clearly due to the strong shock impulse. It is almost twice as high as for the transitional computation with the model of AB. With the model of CH, the predicted aerodynamic work is very similar for the fully turbulent and the transitional computation. It is again smaller by a factor of about 2 than for the transitional computation with the model of AB. This is due mainly to the stabilizing values toward the leading edge on both suction and pressure side. This stabilizing effect is even greater in the 3D fully turbulent calculation. It is present on the whole blade span (not shown here). Despite the strong shock in the steady calculation, the excitation through the shock impulse is weaker. Both effects result in a strong overall damping of the oscillating blade. In contrast to that, the excitation through the shock impulse is greater in the 3D transitional calculation. Furthermore, the imaginary part toward the leading edge on the pressure side shows a destabilizing effect, resulting in a strong overall excitation of the oscillating blade.

Table 4 Four degree incidence: aerodynamic work per oscillation cycle

	AB	CH	AB TRA	CH TRA
2D	0.048 mJ	0.0012 mJ	0.027 mJ	0.014 mJ
3D	—	−0.126 mJ	—	0.302 mJ

These results show that the prediction of the aerodynamic damping can depend on the applied model. While all 2D computations and the 3D transitional computation with the model of CH predict an aerodynamic excitation in the 4 deg incidence case, the 3D fully turbulent computation with the model of CH predicts an aerodynamic damping and is thus a fundamentally different aeroelastic behavior.

Conclusions

Steady and unsteady two-dimensional and three-dimensional computations have been carried out for a linear transonic compressor cascade at two operating points including near-stall conditions. Different turbulence models and additional algebraic transition models have been applied in order to accurately predict the flow phenomena and pressure distributions.

With respect to the steady computations, the calculation of the transitional flow phenomena and the pressure distributions can clearly be improved when additional algebraic transition models are applied. Most computational results agree qualitatively and quantitatively well with the experimental data. However, for the three-dimensional computations at near-stall conditions, there still is potential for improvement regarding the prediction of the highly complex flow patterns including the sidewall separations.

For the flutter computations, the improvements due to the additional use of algebraic transition models are not as obvious as they are for the steady computations. But tendencies are captured very well for almost all computations and the 2D computations also partly agree quantitatively well with the experimental results even at near stall conditions. The 3D computations for the case at near stall conditions also show that the prediction of the aerodynamic damping can be dependent on the applied model. The changing impact of the unsteady aerodynamic forces on the oscillating blade—damping for the case with 0 deg incidence and excitation for the case with 4 deg incidence—is captured in the 2D computations for all models and in the 3D transitional computation. The 3D fully turbulent computation, however, predicts a damping and thus a fundamentally different aeroelastic behavior at near-stall conditions.

Nomenclature

A = dimensionless amplitude
c_f = shear stress coefficient $(=\tau_w/(\rho(u_\infty^2/2))$
$\tilde{c}_p(x,t)$ = unsteady pressure coefficient $(=\tilde{p}(x,t)/(A(\bar{p}_{t,\infty}-\bar{p}_\infty)))$
k = turbulent kinetic energy
n = turbulent spot production rate
$\hat{n},N$ = dimensionless turbulent spot production rate
N_{BL} = number of nodes within the boundary layer
p = pressure
Re = Reynolds number
t = time
Tu = turbulence intensity
u = velocity
x,y,z = Cartesian coordinates
y^+ = dimensionless wall distance
α = spot spreading half-angle, yaw angle
γ = intermittency function
ε = turbulent dissipation rate
θ = momentum thickness
λ_θ = pressure gradient parameter $(=(\theta^2/\nu)du/dx)$
μ = viscosity
μ_t = turbulent viscosity
ρ = density

σ = turbulent spot propagation parameter
$\tau_w = \mu \partial u / \partial y$ = wall shear stress

Subscripts

s = separation
t = turbulent
tr = transition onset
w = wall
∞ = freestream

Superscripts

$\sim$ = fluctuation
$\star$ = modified
$-$ = time-average

Appendix: Transition Model Parameters

From [30], Eq. (3):

$$\alpha = 4 + \frac{22.14}{0.79 + 2.72\exp(47.63\lambda_\theta)} \tag{A1}$$

$$\sigma = 0.03 + \frac{0.37}{0.48 + 3\exp(52.9\lambda_\theta)} \tag{A2}$$

$$N = 0.86 \times 10^{-3}\exp[-0.564\ln(Tu)]f(Tu,\lambda_{\theta_{tr}}) \text{ with } N = n\frac{\sigma\theta^3}{\nu} \tag{A3}$$

$$\text{and } f(Tu,\lambda_{\theta_{tr}}) = \begin{cases} \exp[+2.134\ln(Tu)\lambda_{\theta_{tr}} - 59.23\lambda_{\theta_{tr}}] & (\lambda_{\theta_{tr}} \leqslant 0) \\ \exp[-10\lambda_{\theta_{tr}}^{0.5}] & (\lambda_{\theta_{tr}} > 0) \end{cases}$$

From [31], Eq. (2):

$$\hat{n}\sigma = \frac{1}{40}\mathrm{Re}_{x,\mathrm{tr}}^{-1.34} \text{ with } \hat{n} = n\frac{\nu^2}{u_\infty^3} \tag{A4}$$

From [34], Eq. (6)

$$f(\lambda_\theta) = 6.91 + \begin{cases} 12.75\lambda_\theta + 63.64(\lambda_\theta)^2 & (\lambda_\theta \leqslant 0) \\ 2.48\lambda_{\delta_2} - 12.27(\lambda_\theta)^2 & (\lambda_\theta > 0) \end{cases} \tag{A5}$$

References

[1] Whitehead, D., and Grant, R., 1980, "Force and Moment Coefficients for High Deflection Cascades," *Proceedings of the 2nd International Symposium on Aeroelasticity in Turbomachines*, P. Suter, ed., Juris-Verlag, Zurich, pp. 85–128.

[2] Montgomery, M., and Verdon, J., 1994, "CA Linearized Unsteady Euler Analysis for Turbomachinery Blade Rows Using an Implicit Wave-Split Scheme," *Proceedings of the 7th International Symposium on Unsteady Aerodynamics, Aeroacoustics and Aeroelasticity in Turbomachines and Propellers*, Y. Tanida and M. Namba, eds., Vol. 7, pp. 143–160.

[3] Clark, W., and Hall, K., 1995, "A Numerical Model of the Onset of Stall Flutter in Cascades," J. Comput. Phys., **53**, pp. 1–11.

[4] He, L., and Denton, J., 1993, "Three-Dimensional Time-Marching Inviscid and Viscous Solutions for Unsteady Flows Around Vibrating Blades," ASME Paper No. 93-GT-92.

[5] Eguchi, T., and Wiedermann, A., 1994, "Numerical Analysis of Unstalled and Stalled Flutter Using a Navier-Stokes Code with Deforming Meshes," *Proceedings of the 7th International Symposium on Unsteady Aerodynamics, Aeroacoustics and Aeroelasticity in Turbomachines and Propellers*, Y. Tanida and M. Namba, eds., Vol. 7, pp. 237–254.

[6] Abhari, R., and Giles, M., 1995, "A Navier Stokes Analysis of Airfoils in Oscillating Transonic Cascades for the Prediction of Aerodynamic Damping," in *Momentum Transfer in Boundary Layers*, McGraw-Hill, New York, pp. 1–10.

[7] Grüber, B., and Carstens, V., 1996, "Computation of the Unsteady Transonic Flow in Harmonically Oscillating Turbine Cascades Taking into Account Viscous Effects," ASME Paper No. 96-GT-338.

[8] Weber, S., Benetschik, H., Peitsch, D., and Gallus, H., 1997, "A Numerical Approach to Unstalled and Stalled Flutter Phenomena in Turbomachinery Cascades," ASME Paper No. 97-GT-102.

[9] Höhn, W., and Fransson, T., 1997, "Flutter Analysis of Two-Dimensional Viscous Subsonic and Transonic Flow in Turbomachines Using the Advection Upstream Splitting Method (AUSM)," *Proceedings of the 8th International Symposium on Unsteady Aerodynamics, Aeroacoustics and Aeroelasticity in Turbomachines and Propellers*, T. Fransson, ed., Vol. 8, pp. 195–210.

[10] Gerolymos, G., Vallet, I., Bölcs, A., and Ott, P., 1996, "Computation of Unsteady Three-Dimensional Transonic Nozzle Flows Using k-ϵ Turbulence Closure," AIAA J., **34**(7), pp. 1331–1340.

[11] Ekaterinaris, J., and Platzer, M., 1994, "Progress in the Analysis of Blade Stall Flutter," *Proceedings of the 7th International Symposium on Unsteady Aerodynamics, Aeroacoustics and Aeroelasticity in Turbomachines and Propellers*, Y. Tanida and M. Namba, eds., Vol. 7, pp. 287–302.

[12] Brouillet, B., Benetschik, H., Volmar, T., Gallus, H., and Niehuis, R., 1999, "3D Navier-Stokes Simulation of a Transonic Flutter Cascade Near Stall Conditions," in *Proceedings of the International Gas Turbine Congress*, Kobe, Japan, T. Tamaru, ed., The Organizing Commitee IGTC, Gas Turbine Society of Japan, Vol. 1, pp. 511–518.

[13] Savill, A., 1995, "A Summary Report on the Cost ERCOFTAC Transition SIG Project Evaluating Turbulence Models for Predicting Transition," ERCOFTAC Bulletin, **24**, pp. 57-–61.

[14] Müller, M., Gallus, H., and Niehuis, R., 2000, "A Study on Models to Simulate Boundary Layer Transition in Turbomachinery Flows," ASME Paper 2000-GT-274.

[15] Eulitz, F., 2000, "Modeling and Simulation of Transition Phenomena in Unsteady Turbomachinery Flow," *Proceedings of the 9th International Symposium on Unsteady Aerodynamics, Aeroacoustics and Aeroelasticity of Turbomachines*, P. Ferrand and S. Aubert, eds., Vol. 9, pp. 332–337.

[16] Menter, F. R., Langtry, R. B., Likki, S. R., Suzen, Y. B., Huang, P. G., and Vlker, S., 2004, "A Correlation-Based Transition Model Using Local Variables: Part II -Test Cases and Industrial Applications," ASME Paper No. GT-2004–53454.

[17] Praisner, T. J., Grover, E. A., Rice, M. J., and Clark, J. P., 2004, "Predicting Transition in Turbomachinery: Part II-Model Validation and Benchmarking," ASME Paper No. GT-2004–53454.

[18] Emmons, H., 1951, "The Laminar-Turbulent Transition in a Boundary Layer-Part I," J. Aerosp. Sci., **18**(7), pp. 490–498.

[19] Thermann, H., Müller, M., and Niehuis, R., 2001, "Numerical Simulation of the Boundary Layer Transition in Turbomachinery Flows," ASME Paper No. 2001-GT-475.

[20] Benetschik, H., Lohmann, A., Lücke, J., and Gallus, H., 1996, "Inviscid and Viscous Analysis of Three-Dimensional Turbomachinery Flows Using an Implicit Upwind Algorithm," AIAA Paper No. 96–2556.

[21] Roe, P., 1981, "Approximate Riemann Solvers, Parameter Vectors and Difference Schemes," J. Comput. Phys., **43**, pp. 357–372.

[22] van Leer, B., 1979, "Towards the Ultimate Conservative Difference Scheme v. a Second-order Sequel to Godunov," J. Comput. Phys., **32**, pp. 101–136.

[23] Chakravarthy, S., 1988, "High Resolution Upwind Formulations for the Navier-Stokes Equations," Von Karman Institute for Fluid Dynamics-Lecture Series, No. 5, Rhode Saint Genese, Belgium, pp. 1–105.

[24] Abid, R., 1993, "Evaluation of Two-Equation Turbulence Models for Predicting Transitional Flows," Int. J. Eng. Sci., **31**(6), pp. 831–840.

[25] Chien, K., 1982, "Prediction of Channel and Boundary-Layer Flows with a Low-Reynolds-Number-Turbulence Model," AIAA J., **20**(1), pp. 33–38.

[26] Moore, J., and Moore, J., 1999, "Realizability in Turbulence Modelling for Turbomachinery CFD," ASME Paper No. 99-GT-24.

[27] Durbin, P., 1991, "Near-Wall Turbulence Closure Modelling Without Damping Functions," Theor. Comput. Fluid Dyn., **3**(1), pp. 1–13.

[28] Narasimha, R., 1957, "On the Distribution of Intermittency in the Transition Region of a Boundary Layer," J. Aerosp. Sci., **24**(9), pp. 711–712.

[29] Chen, K., and Thyson, N., 1971, "Extension of Emmons' Spot Theory to Flows on Blunt Bodies," AIAA J., **9**(5), pp. 821–825.

[30] Solomon, W., Walker, G., and Gostelow, J., 1996, "Transition Length Prediction for Flows with Rapidly Changing Pressure Gradients," ASME J. Turbomach., **118**(4), pp. 744–751.

[31] Walker, G., Subroto, P., and Platzer, M., 1988, "Transition Modelling Effects on Viscous/Inviscid Interaction Analysis of Low Reynolds Number Airfoil Flows Involving Laminar Separation Bubbles," ASME Paper No. 88-GT-32.

[32] Michelassi, V., and Martelli, F., 1998, "Numerical Simulation of Unsteady Stator-Rotor Interaction in Brite-Turbine Stage," *Blade Row Interference Effects in Axial Turbomachinery Stages*, C. H. Sieverding, ed., Vol. 2, von Karman Institute for Fluid Dynamics, Rhode Saint Genese, Belgium.

[33] Mayle, R., 1991, "The Role of Laminar-Turbulent Transition in Gas Turbine Engines," ASME J. Turbomach., **113**, pp. 509–537.

[34] Sieger, K., Schiele, R., Kaufmann, F., Wittig, S., and Rodi, W., 1995, "A Two-Layer Turbulence Model for the Calculation of Transitional Boundary-Layers," ERCOFTAC Bulletin, **24**, pp. 21–25.

[35] Ellenberger, K., and Gallus, H., 1999, "Experimental Investigations of Stall Flutter in a Transonic Cascade," ASME Paper No. 99-GT-409.

[36] Schreiber, H., and Starken, H., 1981, "On the Definition of the Axial Velocity Density Ratio in Theoretical and Experimental Cascade Investigations," *Symposium on Measuring Techniques for Transonic and Supersonic Flows in Cascades and Turbomachines*, Lyon, France.

Secondary Flows and Loss Caused by Blade Row Interaction in a Turbine Stage

Graham Pullan
Whittle Laboratory,
University of Cambridge,
Cambridge CB3 0DY, UK
e-mail: gp10006@eng.cam.ac.uk

A study of the three-dimensional stator-rotor interaction in a turbine stage is presented. Experimental data reveal vortices downstream of the rotor which are stationary in the absolute frame—indicating that they are caused by the stator exit flowfield. Evidence of the rotor hub passage vortices is seen, but additional vortical structures away from the endwalls, which would not be present if the rotor were tested in isolation, are also identified. An unsteady computation of the rotor row is performed using the measured stator exit flowfield as the inlet boundary condition. The strength and location of the vortices at rotor exit are predicted. A formation mechanism is proposed whereby stator wake fluid with steep spanwise gradients of absolute total pressure is responsible for all but one of the rotor exit vortices. This mechanism is then verified computationally using a passive-scalar tracking technique. The predicted loss generation through the rotor row is then presented and a comparison made with a steady calculation where the inlet flow has been mixed out to pitchwise uniformity. The loss produced in the steady simulation, even allowing for the mixing loss at inlet, is 10% *less than that produced in the unsteady simulation. This difference highlights the importance of the time-accurate calculation as a tool of the turbomachine designer.* [DOI: 10.1115/1.2182001]

1 Introduction

The classical theories of secondary flow, as developed by Squire and Winter [1], Hawthorne [2], and Smith [3] describe how vorticity with a component perpendicular to the streamwise direction (but still contained in the asisymmetric streamsurface) upstream of a blade row can be rotated within the row to create streamwise vorticity at exit. Although such inlet vorticity is usually concentrated within the endwall boundary layers of the machine, this need not always be the case, and the theory is certainly not restricted to these regions. The classical theory is, however, concerned with steady (axisymmetric) inlet flow and is therefore strictly applicable only to isolated blade rows, to stages with large inter-row gaps, or to the circumferentially uniform state found downstream of mixing-planes in steady numerical simulations.

The features present in the exit flowfield of a blade row, such as wakes and streamwise vortices, will eventually mix out and so generate loss (Denton [4]). The amount of entropy produced during this process is dependent upon the environment in which the mixing takes place. For compressors, it has been found that the stretching of the wake within the next blade row reduces its velocity deficit, so that the loss generated by mixing the wake within the row is less than if it had mixed out upstream of the row (Smith [5], Valkov and Tan [6]). In turbines, the situation is less clear since the wake will be first compressed as it impinges near the leading edge of the downstream blade, and then bowed and stretched as it convects through the passage. This process is further complicated when the effects of reduced wake temperatures caused by cooling techniques are included (Rose and Harvey [7]). These works [4–7] concentrate on the loss generated when structures formed by an upstream blade row (wakes and vortices) mix out within the following row. The present work focuses on the structures that form within the downstream row *as a result* of the exit flowfield of the upstream row, and examines the implications for loss generation. Turbomachine designers can only hope to capture such effects with unsteady flow solvers, but it is steady-state calculations which form the bulk of today's routine aerodynamic design work.

In this paper, the flow through a low-speed research turbine is studied. Experimental results are first presented which show several vortices at rotor exit which must be caused by interaction with the stator exit flow. Unsteady computations are then used to verify a proposed mechanism for the formation of these vortices and to identify which regions of the stator wake are responsible. Finally, a comparison is made between the loss generated within the rotor as predicted by unsteady and steady numerical simulations.

2 Experimental Method

The experimental data presented in this paper were acquired in the low-speed (M_2=0.25) axial flow turbine first described by Pullan et al. [8]. Figure 1 illustrates the very low aspect ratio (0.63) of the stator blades compared to the more conventional rotor. An additional feature of the turbine is the significant radius change through the machine (r_{3mid}=1.2r_{1mid}) with the casing endwall in particular at a high flare angle. The stator row comprises 26 blades, the rotor row 126, and the rotor tip diameter is 1.1 m. The row of inlet guide vanes upstream of the stators contains 87 thin, very low turning, blades which set up the required inlet swirl distribution.

Figure 1 also shows the measurement planes available for area traverses. In this paper, five-hole pneumatic probe data at stator exit (plane 2) and hotwire data at rotor exit (plane 3) are presented. The measurement grid at stator exit comprised 41 spanwise points from 2.4% span to 97.6% span, and 41 pitchwise points covering one stator pitch; at rotor exit, 41 spanwise stations were again used, from 3.4% span to 99.0% span, but 74 points were employed over one stator pitch. The measurement points at both traverse planes were uniformly spaced. For flow angle, the five-hole probe has an uncertainty of $\pm 0.3^{\circ}$, and for total pressure the probe is accurate to ±1% of the local dynamic head. The chosen hotwire probe used a single wire slanted at 45°. Measure-

Contributed by the International Gas Turbine Institute (IGTI) of ASME for publication in the JOURNAL OF ENGINEERING FOR GAS TURBINES AND POWER. Paper presented at the International Gas Turbaine and Aeroengine Congress and Exhibition, Vienna, Austria, June 13, 20004–June 17, 2004, Paper No. GT2004-53743. Manuscript received by IGTI October 1, 2003; final manuscript received March 1, 2004. IGTI Review Chair: A. J. Strazisar.

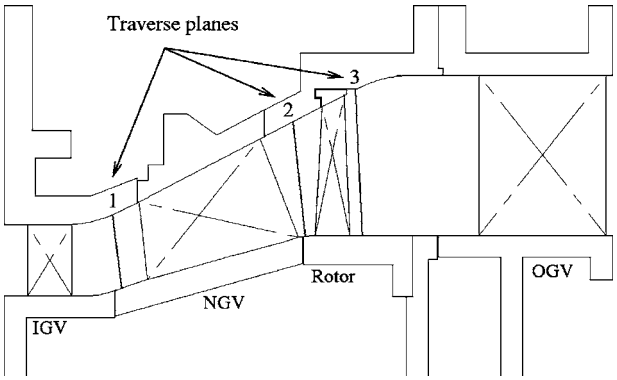

Fig. 1 Meridional view of research turbine, showing traverse planes

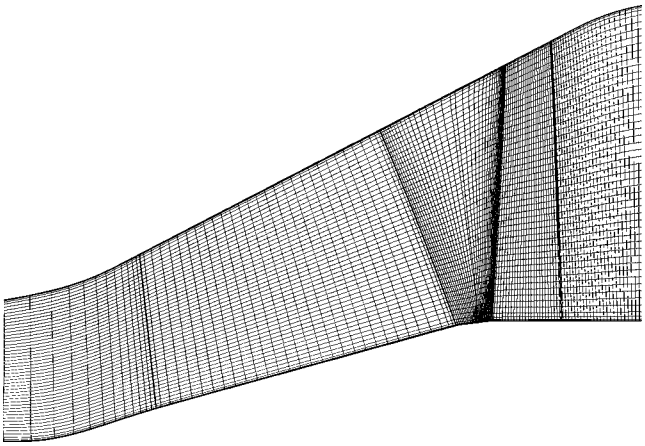

Fig. 2 CFD mesh, meridional view (every second node shown)

ments were taken with the probe rotated about its own axis to eight different positions and the three velocity components were extracted using the method described by Koroumaru et al. [9] and Goto [10]. The hotwire probe has a flow angle uncertainty of $\pm 0.3^{\circ}$ in yaw and $\pm 2.2^{\circ}$ in pitch (Goto [10]). Logging was performed at 62.5 kHz (30 points per rotor passing period) and the data were ensemble averaged over 100 rotor revolutions.

3 Computational Method

The simulations reported in this paper, both steady and unsteady, were performed using Denton's solver, UNSTREST, described by Pullan and Denton [11]. UNSTREST is a development of Denton's widely used steady flow solver, MULTIP (Denton [12]), and solves the flow through a sector of a turbomachine including multiple blade passages and blade rows. The code can be run either in steady mode, with mixing-planes between blade rows, or in unsteady mode with the options of uniform explicit timestep, time-consistent multigrid (He and Denton [13]), or dual time stepping (Jameson [14], Pullan and Denton [11]) available to the user.

UNSTREST solves for five primary flow variables (ρ, ρE, ρV_x, $\rho r V_\theta$, ρV_r) using the "Scree" scheme described in Denton [15]. If R_n is the flux residual at iteration n, and R_{n-1} is that of the previous iteration, then the primary variable f is updated using

$$f_{n+1} = f_n + (2R_n - R_{n-1})\Delta t \tag{1}$$

This algorithm is simple, fast, and requires very low levels of artificial viscosity to maintain stability. Turbulence is modeled using a mixing length approach with wall functions for the surface skin friction (based on Denton [12]). At the inlet boundary, p_0, T_0, yaw, and pitch angles are prescribed. At the exit, the options of fixed static pressure or nonreflecting boundary conditions are available. Transition can be predicted using the simple Baldwin–Lomax method (Baldwin and Lomax [16]), but all boundary layers in the current work were set to be fully turbulent.

Two computational domains were used: One for the full stage, and one for the rotor row alone. Figures 2 and 3 show meridional and blade-to-blade views of the computational mesh for the stage calculation; for clarity, only every second node is shown. The mismatch in airfoil size between stator and rotor is evident in Fig. 3. The grid is of a structured, sheared H-mesh type,with the circumferentially running grid lines constrained to lie at a constant x-ordinate. The actual blade count of 26:126 is modeled in UNSTREST as 26:130 to give the 1:5 ratio seen in Fig. 3. The stator mesh used $118 \times 49 \times 97$ points in the axial, pitchwise, and spanwise directions, respectively. The rotor mesh employed $134 \times 25 \times 97$ points in each passage. The total node count for the unsteady stage simulation was therefore 2.2 million. Dual time stepping was used in the unsteady simulations with 240 outer iterations needed for the rotor to move across the stator pitch. This method gave a speed-up of approximately 5 compared with the uniform timestep explicit scheme.

4 Experimental Results

4.1 Stator Exit. Figures 4 and 5 show measured contours of meridional yaw angle and stagnation pressure at the stator exit traverse plane; the white bands at the upper and lower boundaries of the plots indicate the regions not covered by the probe traverse.

The high turning very low aspect ratio stator generates a flowfield dominated by secondary flow structures. Noting that vortices appear on plots of yaw angle as a series of circumferential contours (the solid-body core) sandwiched above and below by concentric closed contours (the free vortex outer), as described by Binder and Romey [17], Fig. 4 reveals several vortical features. The casing passage vortex, labeled "B", has swept down the suction-surface and exits the blade close to the hub passage vortex, "A". An additional, intense vortex, "C", rotating in the opposite sense to the casing passage vortex, is evident at 75% span. This "shed vortex" forms immediately downstream of the trailing

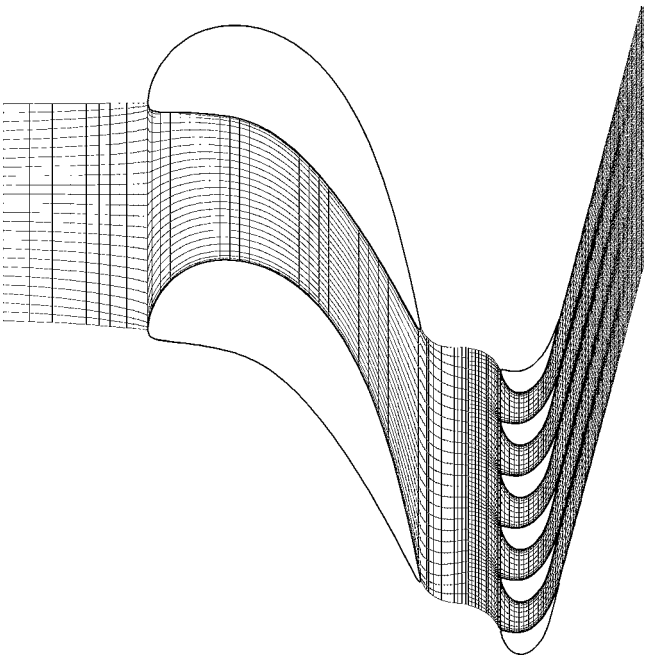

Fig. 3 CFD mesh, circumferential view (every second node shown)

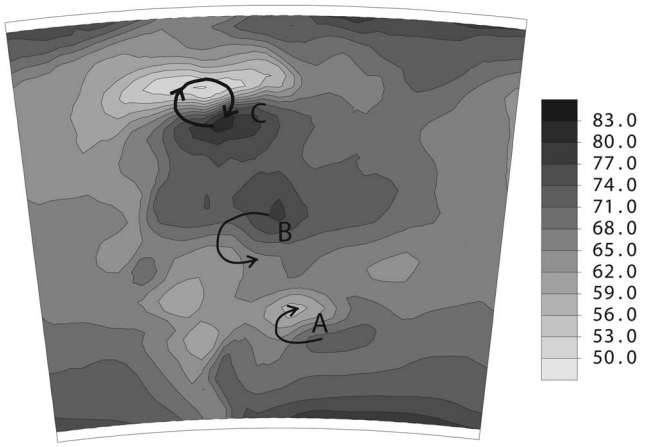

Fig. 4 Measured stator exit meridional yaw angle (degrees)

edge as the shear layer, caused by the spanwise flows pitching strongly inward on the suction-surface and outward on the pressure surface meet, rolls up; the formation of this structure is described in detail by Pullan et al. [8].

The hub and casing passage vortices squeeze the suction-surface boundary layer that grows from the leading edge into a small zone of high loss, the "loss core", Fig. 5. The rotation of the wake in the upper passage caused by the shed vortex is also evident.

4.2 Rotor Exit. The time-averaged relative yaw angle at the rotor exit traverse plane is shown in Fig. 6. This plot, in common with all the time-averaged plots in this paper, has been time-averaged in the *absolute* frame of reference. In the presence of a pitchwise uniform inlet flow, such as that downstream of a mixing-plane in a steady-flow numerical simulation, the contours in Fig. 6 would be purely circumferential. The stator exit flowfield, however, is certainly not pitchwise uniform so that discrete features are seen in Fig. 6 which are periodic on the stator pitch. Although the figure shows time-averaged data, the instantaneous plots (not shown) look very similar with the structures visible in Fig. 6 modulated slightly as the rotor passages move across the measurement window.

At location "D" in Fig. 6, there is strong overturning of the flow at the hub and underturning at 15% span. This is indicative of the rotor hub secondary flows. As a rotor passage sweeps across the measurement window, its hub passage vortex varies greatly in

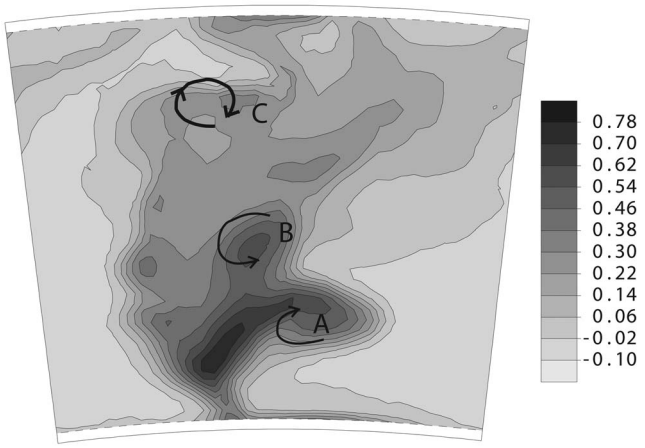

Fig. 5 Measured stator exit stagnation pressure $(\overline{\overline{p_{01}}} - p_0)/\rho U_{mid}^2$

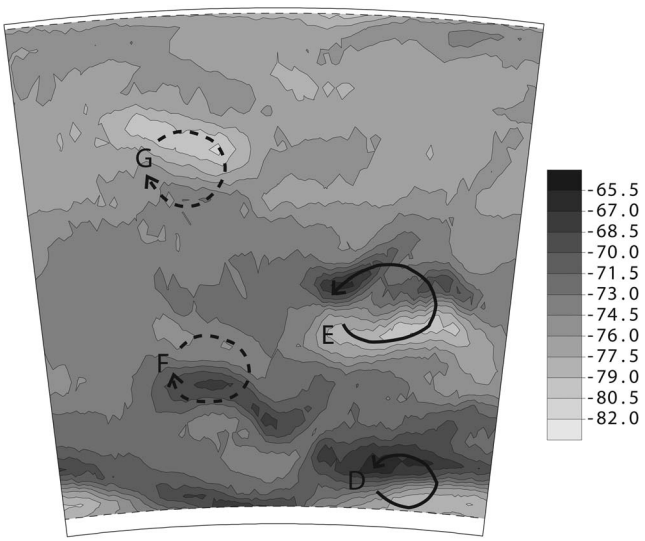

Fig. 6 Measured time-averaged rotor exit relative yaw angle (degrees)

strength in response to the pitchwise nonuniform rotor inlet flow. Figure 6 shows that this vortex is strongest at "D", but it is hardly discernible near the mid-pitch of the plot. No signature of a casing passage vortex is apparent. This is due to a combination of two factors: The casing boundary layer at turbine inlet is swept up in the stator casing passage vortex and a new, thin boundary layer forms; some of this thin boundary layer is then bled off upstream of the rotor by the overshroud leakage flow and so does not enter the row itself.

Three additional features are highlighted in Fig. 6. A vortical structure, or closely coupled pair of structures, is identified at "E" and is of comparable strength to the strongest hub passage vortex location at "D". Weaker features are evident at "F" and "G".

The formation of these structures will be discussed in detail in this paper. For that analysis, it is more convenient to consider the time-averaged *absolute* yaw angle, Fig. 7. The same features are identified in this plot.

The pitchwise variation of the rotor hub passage vortex strength, D, and the additional secondary flows at E, F, and G

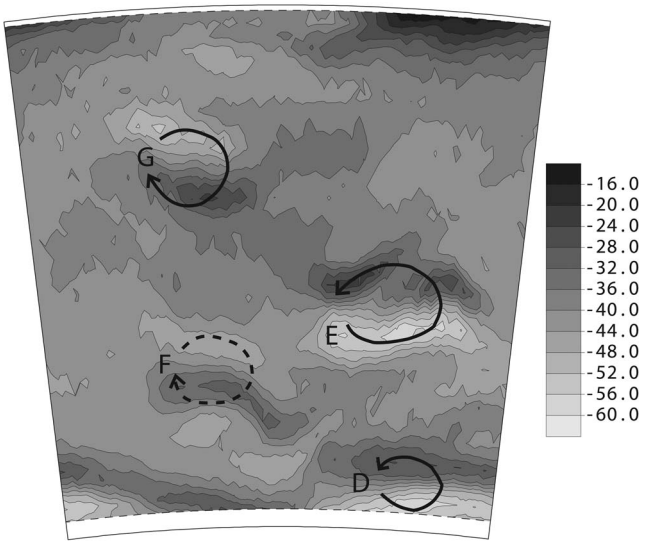

Fig. 7 Measured time-averaged rotor exit absolute yaw angle (degrees)

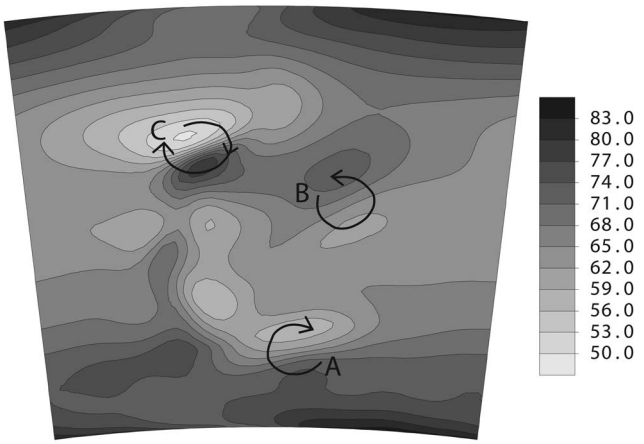

Fig. 8 Predicted stator exit meridional yaw angle (degrees)

must all be caused by the nonuniform stator exit flowfield. Numerical simulations are now used to ascertain which parts of the stator wake are responsible for which features, and to assess their impact on rotor loss production.

5 Computational Results

5.1 Unsteady Stage Simulation

5.1.1 Stator Exit. The simulation results at stator exit are shown in Figs. 8 and 9. When comparisons are made with the measured data, although there is agreement in terms of the overall wake structure, significant discrepancies are evident in the detail. Pullan et al. [8] noted that the shed vortex, C, is difficult to simulate accurately and, although the size and strength of the feature are reproduced, it is predicted to occur too far from the casing (65% span instead of the measured 75% span). The formation of the shed vortex is dependent upon the shear layer of streamwise vorticity shed from the trailing edge of the stator and hence on the casing passage vortex. In the measurements, the casing passage vortex B is approximately mid-way between the shed vortex and the hub passage vortex (Figs. 4 and 5), but it has not penetrated far enough toward the hub in the calculation. With such differences between the actual and simulated stator exit flowfield, discrepancies between the measured and predicted rotor exit flowfield are assured.

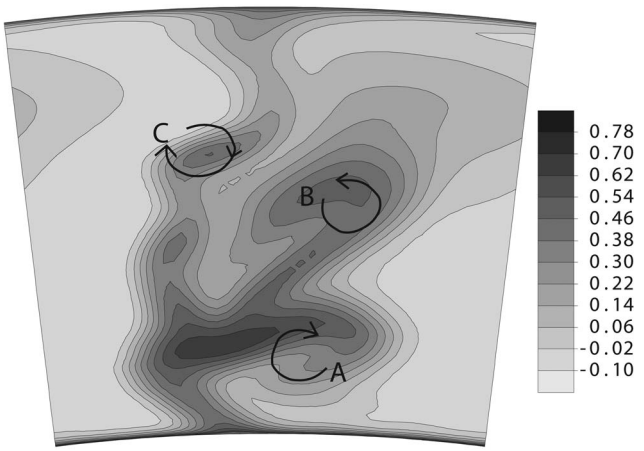

Fig. 9 Predicted stator exit stagnation pressure $(\overline{\overline{p_{01}}} - p_0)/\rho U_{mid}^2$

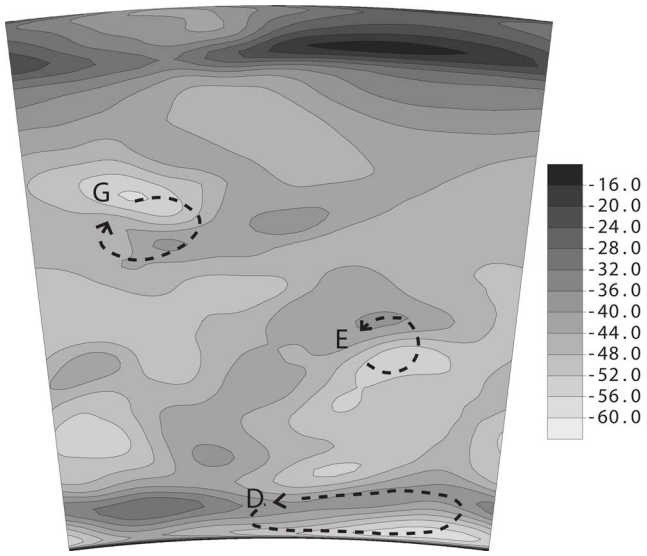

Fig. 10 Calculated time-averaged rotor exit absolute yaw angle (degrees)—stage simulation

5.1.2 Rotor Exit. The predicted time-averaged absolute yaw angle contours at rotor exit are shown in Fig. 10. The agreement between this plot and the measurement data in Fig. 7 is poor. The rotor hub passage vortex strength is more constant with circumferential position than was observed in the experiment. The vortical structure at E, although present, is far weaker than that measured and the vortex observed at F in the experiment is not discernible in the numerical result. The feature, G, is reproduced but it is predicted to occur closer to the hub (58% span) than was measured (72% span).

5.1.3 Unsteady Rotor-Only Simulation. Since the purpose of this work is to understand the mechanisms of formation, and the implications for loss generation, of the vortical structures measured at rotor exit, a more accurate prediction of the flowfield than that shown in Fig. 10 was required. The approach taken was to model the rotor row alone, and to impose the experimentally measured stator exit flowfield as the inlet boundary condition. During the calculation, the inlet boundary condition moves circumferentially relative to the rotor mesh to generate the unsteady solution. The grid used was identical to that employed for the rotor in the stage simulation, with $134 \times 25 \times 97$ points used in the axial, pitchwise, and spanwise directions for each of the five rotor passages of the domain. Figure 1 shows that the distance between traverse plane 2 and the rotor leading edge varies from $1.3c_{mrot}$ at the tip to $0.3c_{mrot}$ at the hub. However, the influence of the rotor potential field at traverse plane 2 is weak (root-mean square of pressure fluctuations in stationary frame $<1.5\%$ of $\overline{\overline{p_{02}}} - \overline{\overline{p_2}}$) so the imposition of the inlet boundary conditions in the rotor-only unsteady simulation can be done with confidence.

The time-averaged rotor exit absolute yaw angle, as obtained from the rotor only simulation, is presented in Fig. 11. The agreement between this result and the measured data is significantly better than that achieved with the unsteady stage simulation, indicating the sensitivity of the vortical structures to the stator exit flowfield. The variation with circumferential position of the rotor hub passage vortex is well reproduced, D, as is the feature at E and the weaker one at G. Feature F in Fig. 7 is not clearly identifiable in Fig. 11, but additional vortical structures are evident between D and E.

Figure 12 shows pitchwise averaged time-averaged distributions of rotor exit absolute yaw angle. The rotor-only curve follows the fluctuations of the experimental results more closely than the stage simulation but, below 80% span, both predicted results

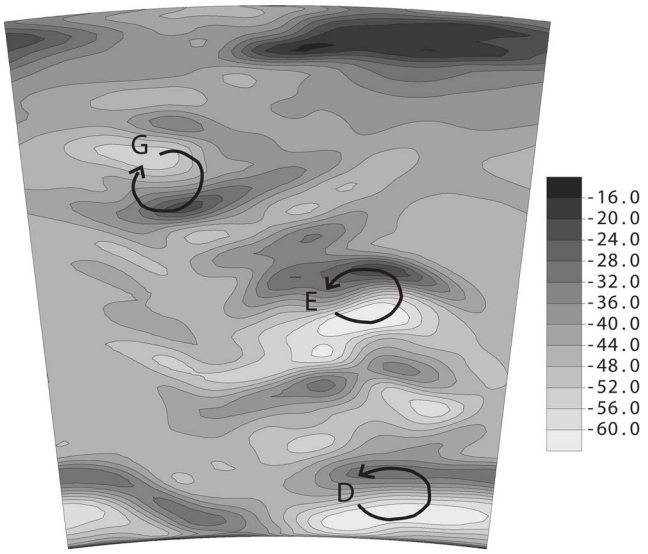

Fig. 11 Calculated time-averaged rotor exit absolute yaw angle (degrees)—rotor only simulation

are overturned as compared to the measurements. This can be partially explained by the pitch reduction, caused by using a 130-blade rotor in the simulations compared to the actual blade count of 126, but it is felt that this difference ($\approx 3\%$) is insufficient to account for all of the discrepancy. Close to the casing, the calculations show the over-turning and under-turning associated with the rotor casing passage vortex, the absence of which in the experimental data has already been discussed; the calculations do not model the over-shroud leakage flow and hence the full casing boundary layer enters the rotor and generates stronger secondary flow.

5.1.4 Formation Mechanisms. To aid the discussion of the mechanisms of formation of the vortical features identified in the preceding sections, a new coordinate system is introduced, as shown in Fig. 13. The direction ξ is aligned with the "primary flow." The primary flow is defined from a least-squares quadratic

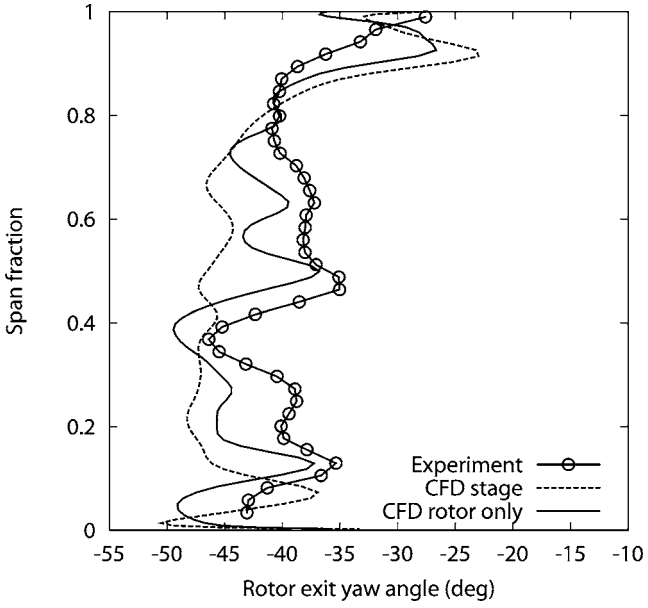

Fig. 12 Measured and predicted time-averaged (pitchwise averaged) rotor exit absolute yaw angle

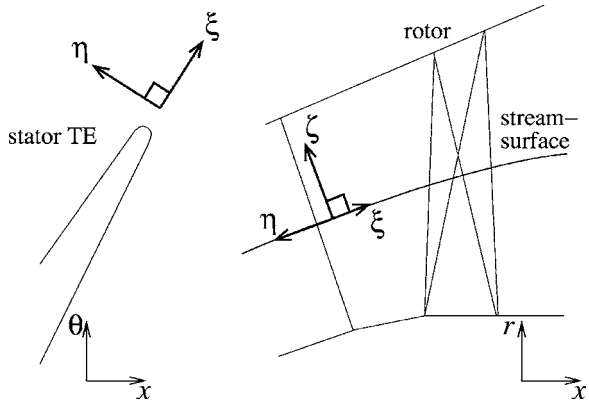

Fig. 13 Coordinate system definition

fit to the pitchwise averaged time-averaged absolute yaw and pitch angles obtained from the rotor-only simulation. The direction η lies in the plane of this stream-surface and is perpendicular to ξ; ζ is perpendicular to both ξ and η.

Classical secondary flow theory is concerned with steady inlet flow. In the rotating reference frame, the component of inlet vorticity which is rotated toward the (relative) streamwise direction at exit is $\omega_{\eta'}$—the component of the absolute vorticity perpendicular to the relative flow direction (Horlock and Lakshminarayana [18]). The flow under consideration here, however, is not pitchwise uniform at stator exit and so is unsteady in the rotating frame. To produce a steady rotor inlet flow, the stator exit flowfield could be mixed out to pitchwise uniformity, as is done in a steady flow mixing-plane calculation, but then the discrete features seen in the absolute frame at rotor exit could not be predicted.

An alternative approach is to always consider the flow in the absolute frame. The effect of the rotor is produced by a body force which is axisymmetric but free to vary radially. This simplification is particularly applicable here since the rotor blade pitch is much smaller than that of the stator blade. The body force results from the requirement to turn the flow. However, the blade pressure forces, which are responsible for the body force, vary on a length-scale based on the blade pitch, whereas the momentum of the fluid can change on a much shorter length-scale, e.g. through a wake. This results in the "three-dimensional relief" effect, described by Wadia and Beacher [19], which means that the body force is not determined by the flow on the local stream-surface alone but by an average over some spanwise extent. Flow which has a higher momentum than this average will therefore be under-turned and that with a lower momentum over-turned. Viewed in this way, any gradient of absolute total pressure (momentum) perpendicular to the axisymmetric stream-surfaces at rotor inlet will lead to the formation of the vortical structures seen at rotor exit. Figure 14 illustrates this process schematically. The particle paths at the top and bottom of the figure are one stator pitch apart and show the path followed by a particle with an "average" total pressure. The particle with a high total pressure is at a radius greater than that with the low total pressure (like at the top of the loss core at stator exit); the former is under-turned and the latter over-turned by the axisymmetric body force and a vortex results.

Using the Euler equation for this steady flow,

$$(\mathbf{V}\cdot\nabla)\mathbf{V} = -\frac{\nabla p}{\rho} \tag{2}$$

and the vector identity

$$(\mathbf{V}\cdot\nabla)\mathbf{V} \equiv \nabla\frac{1}{2}V^2 - \mathbf{V}\times\boldsymbol{\omega} \tag{3}$$

leads to, for incompressible, inviscid flow:

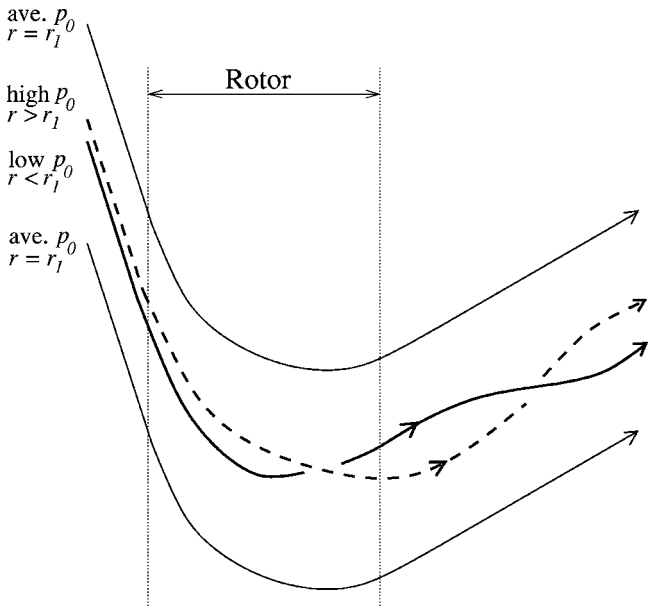

Fig. 14 Schematic of vortex formation mechanism

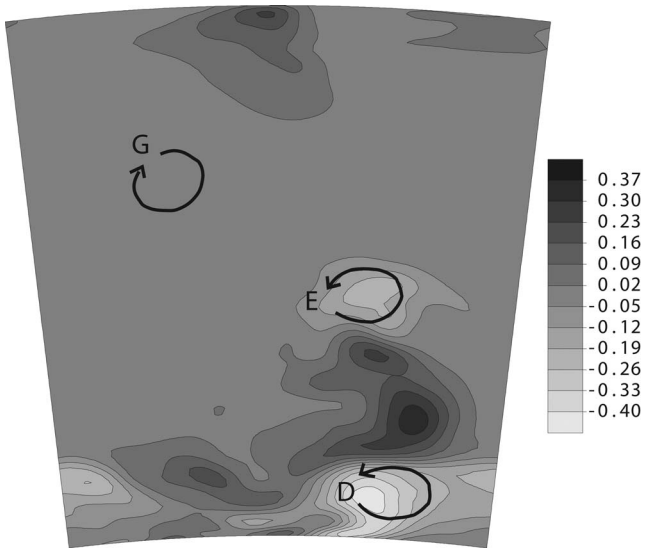

Fig. 16 Time-averaged passive scalar contours at rotor exit

$$\mathbf{V} \times \boldsymbol{\omega} = \frac{\nabla p_0}{\rho} \tag{4}$$

Equation (4) shows that the gradient in total pressure perpendicular to the stream-surface can be obtained from:

$$\frac{1}{\rho}\frac{\partial p_0}{\partial \zeta} = v_\xi \omega_\eta - v_\eta \omega_\xi \approx v_\xi \omega_\eta \tag{5}$$

where the approximation in Eq. (5) can be made since the component of velocity perpendicular to the primary flow, v_η is small by definition. Figure 15 shows contours of the component of the absolute vorticity in the direction perpendicular to the primary flow, ω_η, at stator exit, as calculated from the inlet of the rotor-only simulation. The vorticity in the plot has been nondimensionalised according to

$$\omega_\eta^* = \omega_\eta \frac{c_{xrot}}{4\pi V_{xrot}} \tag{6}$$

where c_{xrot} and V_{xrot} are the mid-height rotor axial chord and axial velocity. The thick white contours at $\omega_\eta^* = \pm 0.35$ in Fig. 15 were used to identify regions of the rotor inlet flowfield which were then tracked through the calculation using the passive scalar technique employed by Pullan and Denton [11]. The passive scalar, an additional primary variable, was initially set to zero throughout the domain, but all nodes at the inlet plane with $\omega_\eta^* \leqslant -0.35$ were assigned a passive scalar of −1 and all those with $\omega_\eta^* \geqslant +0.35$ were prescribed a passive scalar of +1. The time-averaged passive scalar contours at rotor exit are shown in Fig. 16, with the vortex annotation of Fig. 11 superimposed. The correlation between the locations of passive scalar and of vortical structures indicates that the formation mechanism described above *is* responsible for the features at D and E and also for the additional vortices seen between D and E in Fig. 11.

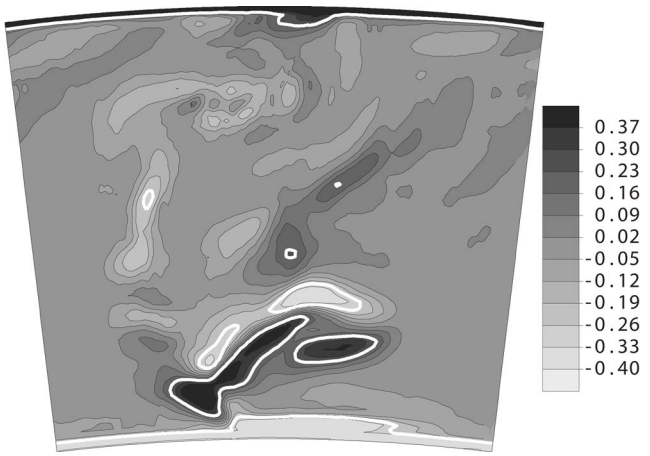

Fig. 15 Nondimensional component of absolute vorticity in η direction, stator exit, ω_η^*

The vortex at G in Fig. 11 is generated by a different mechanism. It is produced by the convection of the strong streamwise vorticity, ω_ξ, contained in the shed vortex, labelled C in Fig. 4. The rotation of this vorticity will happen in the absolute frame as a result of the axisymmetric body force described above. The streamwise vorticity contained in G is therefore not created in the rotor, it is simply transported.

5.2 Loss Generation. Figure 17 shows the variation in lost isentropic efficiency with axial distance for two calculations: The rotor-only unsteady simulation and a rotor-only steady calculation, where the inlet flow has been mixed out to pitchwise uniformity. The mixing process is identical to that which occurs at mixing-planes in steady multirow calculations (Denton [12]): At each radius the total fluxes of mass, momentum, and energy are conserved and the mixed out properties are set to be uniform with circumferential position. The mixing loss associated with this process is the cause of the difference between the two curves at the inlet boundary. Two additional points are marked in Fig. 17. These correspond to the state reached when the flow has been mixed out to pitchwise uniformity at the exit of the computational domain. The lost efficiency has been normalized by the total lost efficiency for the unsteady calculation.

Data taken from the curves of Fig. 17 are given in Table 1.It is apparent that the total loss generated in the steady calculation is 10% less than that generated in the unsteady simulation. Although the steady calculation suffers a loss penalty at inlet due to the mixing process, by the trailing edge of the blade the loss production in the unsteady simulation has overtaken the steady curve. The additional loss produced within the row in the unsteady calculation as compared with the steady is caused by three factors:

(1) The mixing out of the inlet flow.

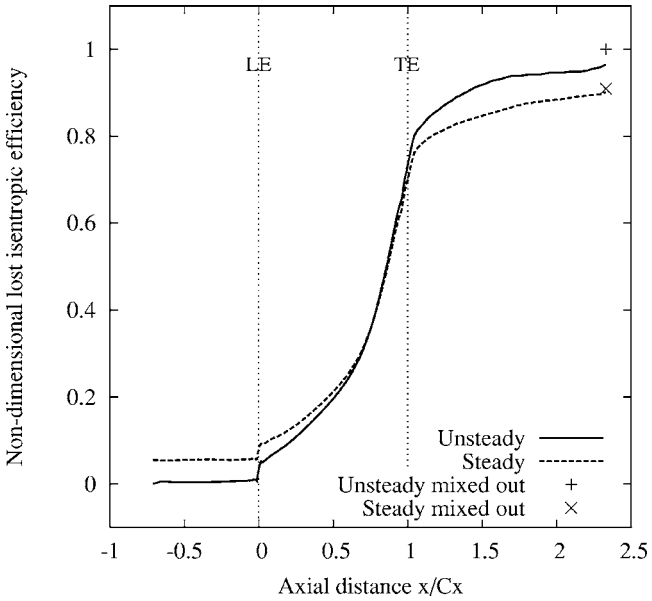

Fig. 17 Generation of loss through the rotor-only computational domain

(2) The unsteady interaction of the inlet flow with the blade row boundary layers.
(3) The mixing associated with the rotor secondary flows over and above that of the rotor secondary flows in the steady calculation.

These three mechanisms occur simultaneously and are extremely difficult to separate and quantify individually. Each of them is now discussed:

The loss created during the mixing of a wake with velocity deficit ΔV is proportional to ΔV^2 (Denton [4]). Figure 18 shows a schematic of the convection of a stator wake through a rotor row. At the leading edge of the rotor, the wake is compressed so that, by Kelvin's circulation theorem, the velocity deficit must increase, and with it the rate of entropy production due to mixing. The wake is then chopped, bowed, and stretched as it passes through the rotor, causing the velocity deficit to decrease and so the entropy production rate reduces. The converse occurs when streamwise vorticity, ω_{ξ}, enters the rotor: the mixing losses reduce as the vortex is compressed near the leading and increase as it is stretched through the passage. With some factors tending to increase entropy production and some reduce it, we cannot be certain whether mixing out the inlet flow *within* the rotor will generate more loss overall than if we had mixed it out *upstream* of the blade row. However, Fig. 17 suggests that, in the present case, more loss is produced when the mixing occurs within the row.

The loss generated by the unsteady interaction of the rotor inlet flow with the blade boundary layers is likely to be small provided

Table 1 Breakdown of loss generation for unsteady and steady rotor only simulations

	Unsteady	Steady
Mixing loss at inlet plane	0.000	0.055
Loss from inlet to trailing edge	0.733	0.644
Loss from trailing edge to exit	0.231	0.201
Mixing loss at exit plane	0.036	0.008
Total	1.000	0.908

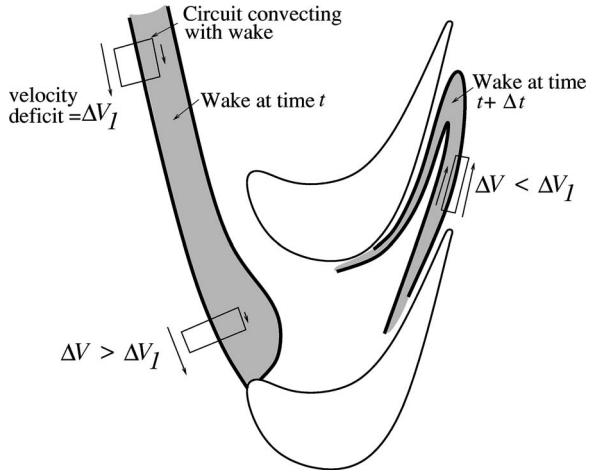

Fig. 18 Schematic of stator wake convection through rotor row

that: Boundary layer transition is not affected (all boundary layers in the simulations are fully turbulent); and significant boundary layer separation is not triggered (this has not been observed).

We now consider the vortical structures generated in the rotor as a result of the stator exit flow, in general, and the loss core in particular. The mixed-out stator exit flowfield used as the inlet to the steady calculation still contains vorticity perpendicular to the relative flow direction, $\omega_{\eta'}$, and will therefore generate secondary flows within the rotor. The circumferentially uniform mixed out inlet flow creates vortices simultaneously and equally in all passages of the rotor. The real stator wake enters each rotor passage in turn as they move by. Since the pitchwise uniform inlet flow distributes the velocity deficit of the loss core over the full stator pitch, the vorticity associated with it is reduced. Therefore, in the steady calculation the strength of each vortex generated is weaker than those produced when the real loss core passes through the rotor row. Since the mixing loss is proportional to the square of the velocity perturbations across the secondary vortices, there will be more entropy generated by the mixing of the secondary flows in the unsteady calculation than in the steady simulation. This is in agreement with Fig. 17.

Table 1 shows that 6% points of the 10% difference in loss generation between the steady and unsteady calculations occurs downstream of the rotor trailing edge, with half of this produced when the flow is mixed out at the exit of the domain. The above discussion of the mixing of secondary flows within the passage also applies to those structures downstream of the rotor and so we expect the unsteady calculation to create more loss than the steady. At the exit plane, the flow in the steady calculation is almost pitchwise uniform and there is only a small additional loss when it is mixed out. The vortices of the unsteady simulation are stronger and more widely spaced circumferentially (being periodic on a stator pitch, not on a rotor pitch) and persist to the exit boundary where they contribute significant loss as they are mixed out.

6 Conclusions

The following conclusions can be drawn from this work:

(1) Vortices downstream of the rotor in a turbine stage have been identified which are caused by the exit flowfield of the stator.
(2) Regions of the stator wake with steep gradients of absolute total pressure normal to the axisymmetric streamsurface of the primary flow have been shown to form the vortices at rotor exit.

(3) In unsteady numerical simulations, the formation of these vortices was found to be extremely sensitive to the predicted total pressure gradients at stator exit.
(4) A steady-state rotor calculation was performed by mixing out the stator exit flow to pitchwise uniformity, as is done in mixing-plane calculations. The steady simulation generated 10% less loss than the unsteady simulation. The turbomachine designer should not, therefore, rely on mixing-plane calculations alone for the analysis of such machines.

Acknowledgment

The author would like to thank John Denton of the Whittle Laboratory for the many helpful and interesting discussions concerning this work. In addition, the author is grateful to Eric Curtis and Nick Hooper, also of the Whittle Laboratory, for their assistance with the experimental work. The author is funded by Rolls-Royce plc and the Department for Trade and Industry (UK).

Nomenclature

c = chord
E = specific total energy $= e + 1/2\,V^2$
e = specific internal energy
M = Mach number
p = pressure
r = radius
s = blade pitch
T = temperature
$U(U_{mid})$ = blade speed (at rotor mid-height)
x = axial ordinate
α = yaw angle
ρ = density
$\bar{f}$ = passage averaged f
$\mathbf{V}$ (V) = velocity vector (scalar)
$\boldsymbol{\omega}(\omega)$ = vorticity vector (scalar)

Subscripts

$x(xrot)$ = axial (of rotor)
$m(mrot)$ = meridional (of rotor)
ξ = flow direction
η = $\perp$ to flow direction, on stream-surface
ζ = $\perp$ to flow direction, $\perp$ to stream-surface
0 = stagnation
1, 2, 3 = stator inlet, stator exit, rotor exit

References

[1] Squire, H. B., and Winter, K. G., 1951, "The Secondary Flow in a Cascade of Airfoils in a Nonuniform Stream," J. Aerosp. Sci. **18**, pp. 271–277.
[2] Hawthorne, W. R., 1955, "Rotational Flow Through Cascades, Part I: The Components of Vorticity," J. Mech. and App. Math., **8**, pp. 266–279.
[3] Smith, L. H., 1955, "Secondary Flow in Axial-Flow Turbomachinery," Trans. ASME **77**, p. 1065.
[4] Denton, J., 1993, "Loss Mechanisms in Turbomachines," ASME J. Turbomach., **115**, pp. 621–656.
[5] Smith, L. H., 1966, "Wake Dispersion in Turbomachines," ASME J. Basic Eng., **88**, pp. 688–690.
[6] Valkov, T. V., and Tan, C. S., 1999, "Effect of Upstream Rotor Vortical Distribances on the Time-Averaged Performance of Axial Compressor Stators, Part I," ASME J. Turbomach., **121**, pp. 428–435.
[7] Rose, M. G., and Harvey, N. W., 2000, "Turbomachinery Wakes: Differential Work and Mixing Losses," ASME J. Turbomach., **122**, pp. 68–77.
[8] Pullan, G., Denton, J. D., and Dunkley, M. J., 2003, "An Experimental and Computational Study of the Formation of a Streamwise Shed Vortex in a Turbine Stage," ASME J. Turbomach., **125**, pp. 291–297.
[9] Koroumaru, M., Inoue, M., Higaki, T., Abd-Elkhalek, F. A. E., and Ikui, T., 1982, "Measurement of Three-Dimensional Flow Field Behind and Impeller by means of Periodic Multisampling with a Slanted Hotwire," JSME, **25**.
[10] Goto, A., 1991, "Three-Dimensional Flow and Mixing in an Axial Flow Compressor with Different Rotor Tip Clearances," *ASME* 91-GT-89.
[11] Pullan, G., and Denton, J. D., 2003, "Numerical Simulations of Vortex-Turbine Blade Interaction," 5th Euro. Conf. on Turbomachinery, Prague, pp. 1049–1059.
[12] Denton, J. D., 1992, "The Calculation of Three Dimensional Viscous Flow Through Multistage Turbomachines," ASME J. Turbomach., **114**, pp. 18–26.
[13] He, L., and Denton, J. D., 1994, "3D Time Marching Inviscid and Viscous Solutions for Unsteady Flows around Vibrating Blades," ASME J. Turbomach., **116**, pp. 469–476.
[14] Jameson, A., 1991, "Time Dependent Calculations Using Multigrid, with Applications to Unsteady flows Past Airfoils and Wings," *AIAA 91-1596*.
[15] Denton, J. D., 2002, "The Effects of Lean and Sweep on Transonic Fan Performance," *TASK Quarterly* Jan 2002, pp. 7–23.
[16] Baldwin, B. S., and Lomax, H., 1978, "Thin Layer Approximation and Algebraic Model for Seperated Turbulent Flows," *AIAA 78–257*.
[17] Binder, R., and Romey, A., 1983, "Secondary Flow Effects and Mixing of the Wake Behind a Turbine Stator," ASME J. Eng. Power, **105**, pp. 40–46.
[18] Horlock, J. H., and Lakshminarayana, B., 1973, "Secondary Flows: Theory, Experiment, and Application in Turbomachinery Aerodynamics," Annu. Rev. Fluid Mech., **5**, pp. 247–249.
[19] Wadia, A., and Beacher, B. F., 1990, "Three-Dimensional Relief in Turbomachinery Blading," ASME J. Turbomach., **112**, pp. 587–598.

Improving the Performance of a Turbine With Low Aspect Ratio Stators by Aft-Loading

Graham Pullan
e-mail: gp10006@eng.cam.ac.uk

John Denton

Eric Curtis

Whittle Laboratory,
University of Cambridge,
Cambridge CB3 0DY, UK

Experimental data and numerical simulations are presented from a research turbine with low aspect ratio nozzle guide vanes (NGVs). The combined effects of mechanical and aerodynamic constraints on the NGV create very strong secondary flows. This paper describes three designs of NGV that have been tested in the turbine, using the same rotor row in each case. NGV 2 used three-dimensional design techniques in an attempt to improve the performance of the datum NGV 1 blade, but succeeded only in creating an intense vortex shed from the trailing edge (as previously reported) and lowering the measured stage efficiency by 1.1% points. NGV 3 was produced to avoid the "shed vortex" while adopting a highly aft-loaded surface pressure distribution to reduce the influence of the secondary flows. The stage with NGV 3 had an efficiency 0.5% points greater than that with NGV 1. Detailed comparisons between experiment and computations, including predicted entropy generation rates, are used to highlight the areas where the loss reduction has occurred and hence to quantify the effects of employing highly aft-loaded NGVs. [DOI: 10.1115/1.2182000]

1 Introduction

Each blade row that a turbomachinery aerodynamicist designs inevitably involves tradeoffs between a number of factors: efficiency, off-design performance, mechanical integrity, life, etc. However, the turbine under consideration in the present work is significantly compromised by the requirement, in the real application, that its nozzle guide vanes (NGVs) must shield components from the hot gas stream that need to reach the center of the gas turbine. This dictates the thickness of the NGVs, hence their chord and hence their low aspect ratio, see Fig. 1. Given these constraints, the designer must produce a stage with the highest possible aerodynamic efficiency.

The high turning ($\approx$100 deg) low aspect ratio ($\approx$0.6) NGVs create a highly three-dimensional flow that is dominated by secondary flows. This flowfield has been described by Pullan et al. [1] who compared a datum stator design, NGV 1, with a more three-dimensional stator, NGV 2. The design philosophy behind NGV 2 was to eliminate endwall overturning by reducing the exit metal angle of the NGV at the hub and casing and increasing the metal angle in the loss core. However, the shear layer of streamwise vorticity shed from the trailing edge of NGV 2 was observed to roll up into an intense vortex that had not been predicted by CFD in the design process and had not been seen in the exit flow of NGV 1. The interaction of the measured NGV 2 wake with the downstream rotor was modeled with steady and unsteady CFD by Pullan [2].

This paper introduces a third NGV designed with a different philosophy: aft-loading. The aim is to reduce the impact of the secondary flows by delaying their driving force, the cross-passage pressure gradient, until as far back in the passage as possible. Surprisingly, although there is some published work on the effect of loading distribution on profile loss (e.g., Howell et al. [3] and Corriveau and Sjolander [4]), there is little in the open literature on the influence of loading distribution on turbine secondary flows. Weiss and Fottner [5] performed linear cascade tests on two turbine profiles, one fore-loaded and one aft-loaded. They found that the passage vortex liftoff line penetrated farther up the span from the endwall in the fore-loaded case. Although the losses were similar at the exit plane, the mixed-out losses were found to be greater for the fore-loaded cascade. Benner et al. [6] studied two cascades of turbine blades: A baseline aerofoil and a modified profile with a larger leading edge radius. The authors found that the modified blade produced a smaller and weaker passage vortex than the baseline case. They attribute this effect to the more aft-loaded pressure distribution of the blade with the larger leading edge radius. Recently, nonaxisymmetric endwall contouring has been used to reduce the secondary kinetic energy associated with endwall flows in linear cascades [7] and in real turbine design [8]. It is noteworthy that this treatment is found to aft-load the blade close to the endwalls.

The present study examines the performance of the turbine stage fitted with aft-loaded NGVs in the context of the performance of the turbine with both NGV 1 and NGV 2 installed. The lost efficency in each blade row is calculated from the measured data. Unsteady CFD predictions are then made for each stage, providing the opportunity to examine the accuracy of loss predictions when systematic geometry changes are made. Further, entropy generation rates are extracted from the computations to analyse how much loss is generated in different areas of the turbine. This "loss audit" is found to be a useful tool in assessing the implications on turbine performance of changes in blade design.

2 Turbine Test Facility

A meridional view of the turbine studied in this investigation is shown in Fig. 1. The experimental facility, first reported in Pullan et al. [1], is large scale (r_{tip}=1.1 m) and low speed (M_2=0.25). The NGV Reynolds number, based on true chord, is 7.95×10^5, and that of the rotor is 1.65×10^5. The rotor is shrouded and is sealed against the upstream axial face of the shroud with a running clearance of 0.6 mm (0.5% of span). The size of the rig allows good spatial resolution to be obtained with five-hole pneumatic probes (diameter 2.05 mm) at traverse planes located downstream of the inlet guide vane, NGV, and rotor blade rows. Unsteady data, not presented here, at rotor exit may also be acquired using single-slant hotwire and fast response pressure transducer probes.

Contributed by the International Gas Turbine Institute (IGTI) of ASME for publication in the JOURNAL OF TURBOMACHINERY. Paper presented at the ASME Turbo Expo 2005: Land, Sea and Air, Reno, NV, June 6, 2005–June 9, 2005, Paper No. GT2005-68548. Manuscript received October 1, 2003; final manuscript received March 1, 2004. IGTI Review Chair: K. C. Hall.

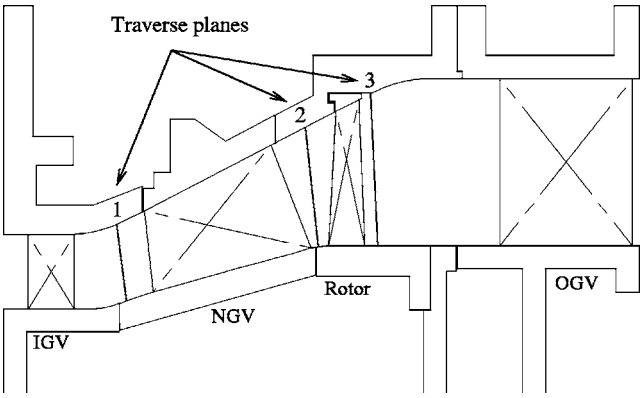

Fig. 1 Meridional view of the research turbine

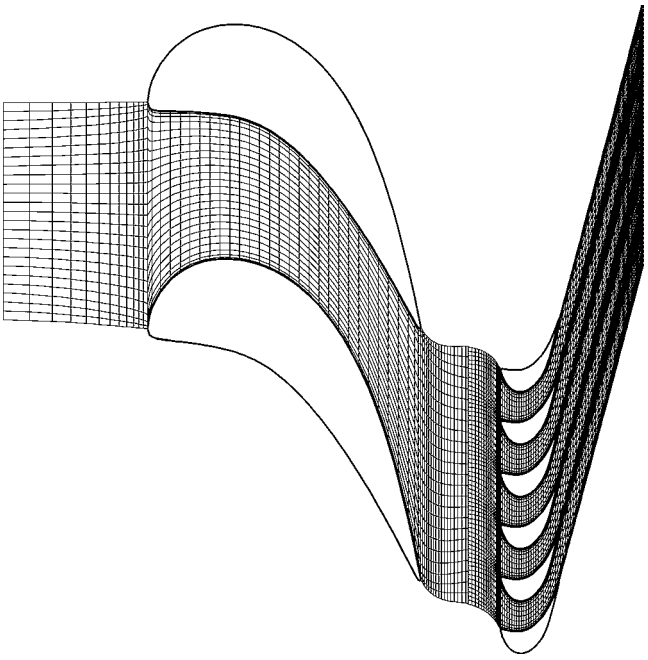

Fig. 2 Computational mesh, circumferential view, NGV 2, (every second point shown)

The efficiency data reported in this paper were obtained from measurements of brake power output, massflow, inlet total temperature, and total pressure at the inlet and exit of the stage. Power output is obtained from a load-cell on the eddy-current dynamometer. The turbine massflow is evaluated from a calibrated inlet contraction. Inlet and exit total pressures are obtained from ten pitot probes which are at different radial heights and arranged around the whole circumference at positions verniered with respect to the NGV pitch. During an efficiency test, these probes are traversed circumferentially (by rotation of the NGV row) so that averaged p_{01} and p_{02} can be obtained. Efficiency data are recorded over a range of flow coefficients but blade Reynolds numbers are held approximately constant by maintaining a fixed nondimensional mass flow and varying the blade speed. Experience with the turbine over nearly ten years of testing and many configurations has shown that the measured efficiency is repeatable to within approximately 0.2% points.

3 Computational Method

The computational results shown in this paper were obtained using the multiblock Reynolds-averaged Navier–Stokes solver, TBLOCK, by John Denton. Although previously unreported, TBLOCK's lineage can be traced through Denton's three-dimensional steady [9,10] turbomachine flow solvers which are highly developed and widely used in both industry and research institutions. TBLOCK solves the flow through a number of structured blocks which may be connected to each other by a range of different boundary conditions: Contiguous nodes, noncontiguous nodes, periodic, mixing-planes for steady calculations, or sliding interface planes for unsteady calculations. The code was conceived to cater for shrouds, leakage paths, bleed slots, and other "real geometry" features of turbomachines and so is highly versatile. Indeed, the code can be easily applied to geometries not associated with turbomachinery.

TBLOCK uses the explicit "scree" algorithm [11] with spatially variable time-steps and three levels of multigrid to accelerate convergence. In time-accurate mode, the semi-implicit dual time-stepping approach is used in which the solution at a particular instant in time is obtained by converging a modified set of equations toward a steady-state in "pseudo-time" [12]. In this mode, a sector of the machine with equal circumferential extent in each blade row must be solved. Turbulence is modeled using a mixing length approach with wall functions used to obtain the surface skin friction. Although this turbulence model is much simpler than most others, experience has shown it to give realistic results for a very wide range of turbomachinery applications (for example, Gbadebo et al. [13]). Transition can be specified at prescribed locations on the solid surfaces. For the calculations presented in this paper, all boundary layers were set to be fully turbulent. This assumption is felt to be justified because of the high turbulence levels expected in the turbine. In addition, the extent of any regions of laminar flow in the rotor row (lowest Reynolds number) in this complex, three-dimensional unsteady, environment is not known.

TBLOCK can be run in parallel on many processors. Domain decomposition is done on a block basis with different numbers of blocks assigned to different processors. Load balancing can be achieved by solving approximately the same number of nodes on each CPU. Communication between processors is handled by the MPI message passing library. The code is written so that a single processor only ever handles the blocks that are allocated to it and so very large domains can be tackled.

The calculations presented in this paper are unsteady and were performed using one NGV passage and five rotor passages. To allow both rows to occupy the same sector of the machine, the rotor pitch had to be reduced by 3%. The shroud leakage path was not modeled. The computational grids in both rows were of the sheared H-mesh type, see Fig. 2. In each blade row, 49 nodes cover one blade pitch and 65 nodes are used over the span. The NGV row uses 120 nodes in the axial direction, while 136 were used in the rotor. The total number of nodes was, therefore, approximately 2.5 million. These grid densities are similar to those which would be used in a routine three-dimensional steady calculation as part of a modern design process. Similar levels of mesh refinement, using Denton's UNSTREST solver, have been successfully validated against data from this turbine [1,2]. The solutions were obtained by running for 25 rotor passing periods, using 48 physical time-steps to discretise each period. 40 iterations in pseudo-time were needed to reach convergence at each time-step. The run time was 19 h when six processors were used on three dual Pentium 2.8 GHz machines.

4 NGV 3 Design

Figure 3 shows a photograph of the three NGV designs tested in the research turbine. Each NGV performs the same duty, producing the same deflection and passing the same massflow at the same pressure drop. From the visible tip profiles alone, the aft-loaded profile of NGV 3 is apparent. Aspects of the design of NGV 3 are now discussed.

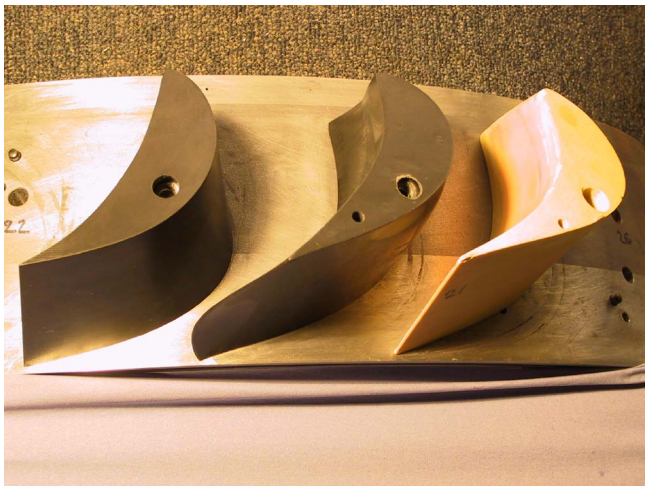

Fig. 3 Photograph of (from left) NGV 3, NGV 2, and NGV 1

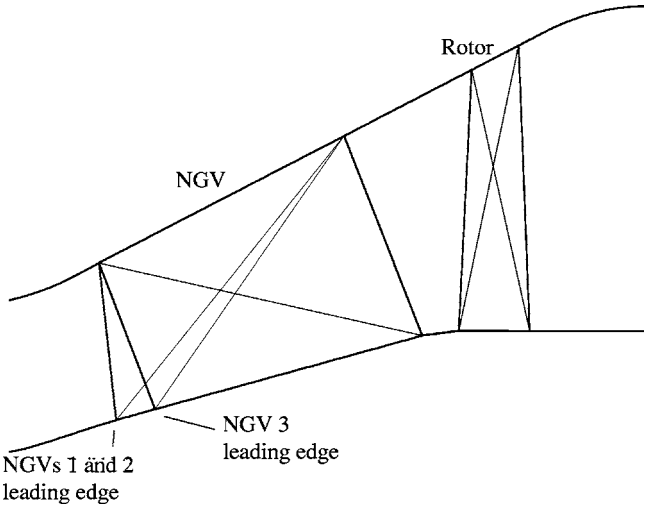

Fig. 5 NGV 3 leading edge location

Figure 4 presents a comparison of the profile of each NGV at mid-span. In order to create the aft-loaded pressure distribution of NGV 3, much of the turning is delayed until downstream of 40% chord. Beyond this point, the high surface curvatures of NGV 3 are clear. NGV 3 is seen to have the greatest thickness-to-chord ratio of the three designs and this allowed a small modification to the meridional view of the stator, Fig. 5. It was found that the required thickness could be achieved even when the chord at the hub was reduced so as to make the leading edge slightly more orthogonal to the stream-surfaces at turbine inlet.

Midspan surface pressure distributions for the three NGV designs are shown in Fig. 6. The aft-loading of NGV 3 relative to both NGV 1 and NGV 2 is immediately evident. As well as delaying the peak-suction to 80% of axial chord, care was also taken to sustain a high pressure-surface pressure as close to the trailing edge as possible. At this radial location, a local zone of reverse curvature on the pressure-surface of NGV 2 leads to a loss of lift after 93% of axial chord; this effect does not extend over the entire span.

As an alternative way of illustrating the difference in the loading distribution of NGV 3 as compared to NGV 1 and NGV 2, Fig. 7 shows the angular momentum of the flow, mass-averaged over the passage, as a function of meridional distance. The delay in the turning of the flow in NGV 3 and the similarity of NGV 1 and NGV 2 is apparent.

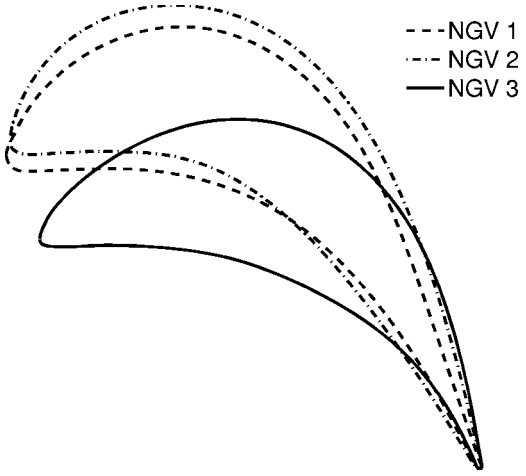

Fig. 4 NGV midspan blade profiles

Aside from aft-loading, the avoidance of the intense vortex shed from the trailing edge of NGV 2 was also important in the design of NGV 3. Development of the three-dimensional steady flow solver used in the design process [9] meant that much greater accuracy in the prediction of the NGV 2 vortex was possible than had been achieved during the design of NGV 2. In addition, Pullan et al. [1] observed that if the pitchwise averaged exit flow angle distribution varies so as to oppose the rollup of the stream-

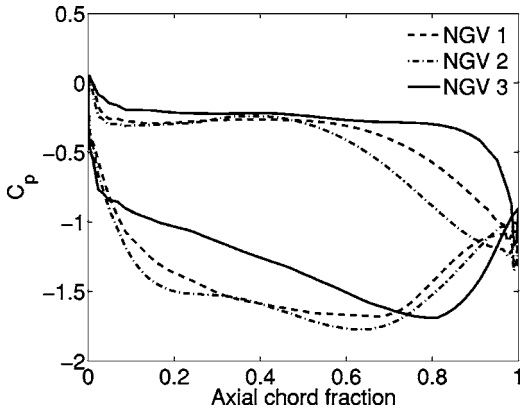

Fig. 6 NGV mid-span surface pressure

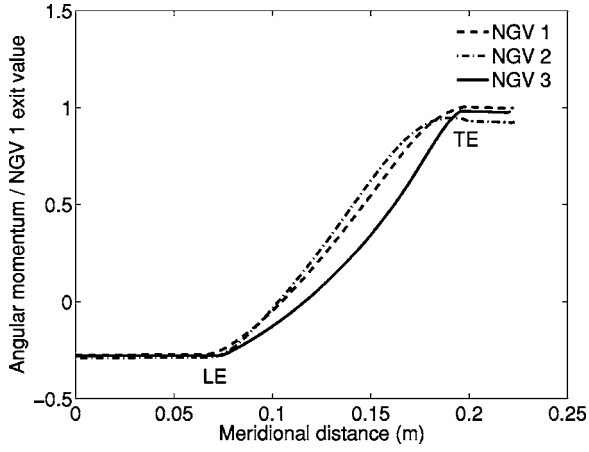

Fig. 7 Angular momentum through three NGV designs

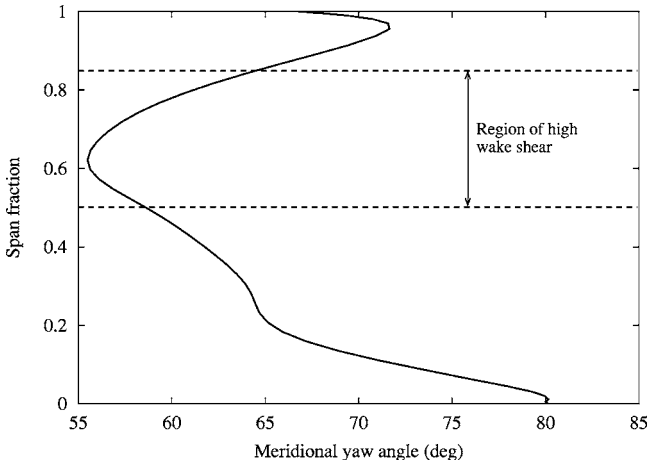

Fig. 8 Predicted meridional yaw angle distribution, NGV 3

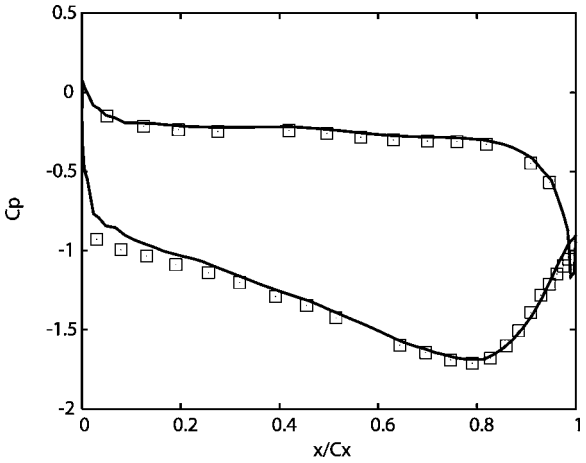

Fig. 9 Measured and predicted midspan surface pressures, NGV 3 (solid line=CFD) $c_p=(p-p_{01})/\rho U^2_{mid}$

wise vorticity shed from the trailing edge, then the shed vortex does not form. This "rule" had been developed from NGV 1 and NGV 2 data and is now applied to NGV 3. Figure 8 shows the flow angle distribution immediately downstream of the trailing edge of NGV 3. The zone where the vorticity in the trailing vortex sheet is most intense is identified as being from 50% to 85% span. For most of this region, the flow angle is increasing with radius and this has been found to delay the rollup of the sheet into a vortex.

5 Results

5.1 Flowfield. Figure 9 shows a comparison of the measured and predicted surface pressure distributions on NGV 3 at midspan. As should be expected, the level of agreement is very good. Close to the leading edge, the predicted suction-surface pressure is higher than the measured values. This is thought to be due to a small discrepancy in the incidence of the NGV.

To illustrate the severity of the secondary flows, the surface flow visualization photographs of the NGV 3 and NGV 2 suction-surfaces are first compared, Fig. 10. The lift-off lines corresponding to the legs of the horseshoe vortex at the casing (suction-side leg = "B", pressure-side leg = "A") and hub (suction-side leg = "C", pressure-side leg = "D") are identified where possible. The flow pitching inward from the casing in NGV 2 does so at an approximately constant pitch angle, whereas in NGV 3, the pitch angle increases sharply close to the trailing edge. This is consistent with the weaker cross-passage pressure gradient in the early part of NGV 3 which increases to a maximum at 80% chord, as compared to the more uniform loading distribution of NGV 2. The secondary flows at the hub, however, appear similar in both NGVs. The penetration of the hub endwall fluid up the suction-surface is, in parts, greater for NGV 3 than NGV 2. This may be caused by the weaker radial pressure gradient in the forward part of NGV 3 as a result of the reduced swirl velocity in this area caused by the delay in the turning of the flow. In NGV 2, the counter-rotating hub and casing passage vortices scrape the suction-surface boundary layer off the blade at a location closer to

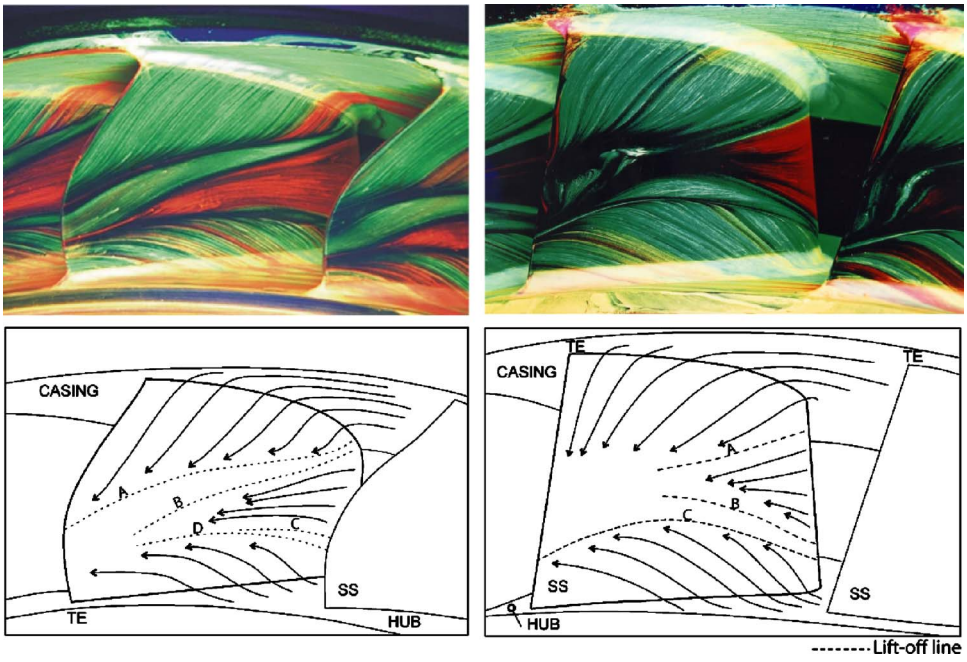

Fig. 10 NGV oil and dye surface flow visualization, NGV 2 (left) and NGV 3

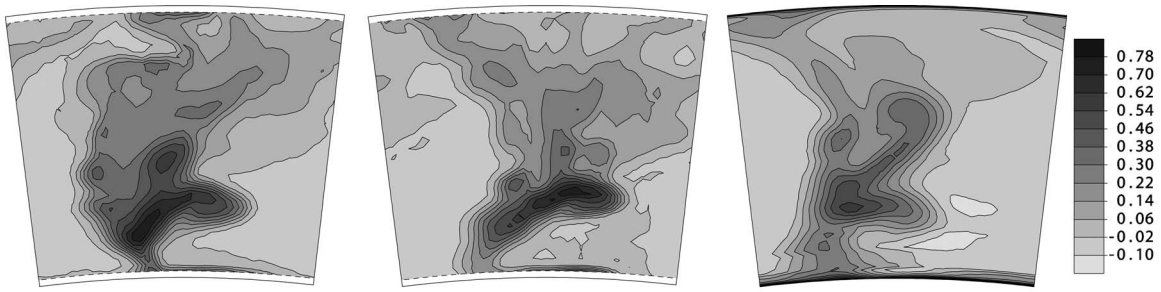

Fig. 11 NGV exit total pressure coefficient, $(p01-p02)/\rho U_{mid}^2$

the hub than is the case for NGV 3.

At NGV exit, area traverses of total pressure coefficient (Fig. 11) and meridional yaw angle (Fig. 12) are presented. Figure 11 shows the loss core, which contains most of the NGV suction surface boundary layer, is indeed farther from the hub in NGV 3 than NGV 2. The exit flow angle distribution of NGV 3, with higher turning at the endwalls than at mid-span, creates the bowed wake shape. The overall structure of the wake is captured by the CFD prediction for NGV 3, but the peak loss is lower than that measured. Figure 12 shows the intense vortex at 75% span downstream of NGV 2, and, as predicted, no such feature is present in the traverse of NGV 3. The agreement between simulation and measurement is good, except that the zone of underturning in the center of the measurement window is further inboard in reality than in the CFD.

5.2 Loss. The agreement between the measured and predicted flowfields has been found to be satisfactory. Attention is now directed to the more difficult problem of the accurate prediction of loss generation. The isentropic efficiency is calculated from experimental data using the following equation:

$$\eta = \frac{P_b}{\dot{m} c_p T_{01}(1 - r_p)} \tag{1}$$

where $r_p = (p_{03}/p_{01})^{\gamma-1/\gamma}$, and P_b is the brake power output. In what follows, the brake power is taken to be the total power developed by the turbine because it has been estimated that windage and bearing losses account for a reduction in power output of less than 0.25%.

The variation in measured efficiency with flow coefficient for the three turbine geometries is shown in Fig. 13. Over most of the range of operating conditions tested, the stage fitted with NGV 3 blades achieves the highest efficiency. At the design point, the NGV 3 stage efficiency is 0.5% points greater than the NGV 1 stage and 1.5% points greater than the NGV 2 stage.

From the efficiency data alone, it is not possible to see whether the changes in performance are due to differing levels of NGV loss, rotor loss, or both. Using data from efficiency measurements in conjunction with traverse data at NGV exit, it is possible to divide the losses into those occurring within the NGV row, and those occurring within the rotor row. The total change in specific entropy across the stage is given by

$$s_3 - s_1 = c_p \ln\left(\frac{T_{03}}{T_{01}}\right) - R \ln\left(\frac{p_{03}}{p_{01}}\right) \tag{2}$$

Since $\eta = (T_{01} - T_{03})/(T_{01} - T_{03s})$, where T_{03s} is the exit temperature reached had the expansion been isentropic, Eq. (2) can be written as

$$s_3 - s_1 = c_p \ln(1 - \eta(1 - r_p)) - R \ln\left(\frac{p_{03}}{p_{01}}\right) \tag{3}$$

and the change in specific entropy across the NGV row alone is given by

$$s_2 - s_1 = -R \ln\left(\frac{p_{02}}{p_{01}}\right) \tag{4}$$

These entropy changes can then be converted into efficiency penalties by evaluating the lost work as a fraction of the isentropic work:

$$\Delta\eta = \frac{\Delta s T_{03}}{c_p T_{01}(1 - r_p)} \tag{5}$$

$$= \frac{\Delta s[1 - \eta(1 - r_p)]}{c_p(1 - r_p)} \tag{6}$$

where Δs refers to the entropy change in the appropriate blade row (i.e., $s_2 - s_1$ or $s_3 - s_2$), and $\Delta\eta$ is the reduction in isentropic efficiency occurring in that region.

The efficiency lost in the NGV and rotor rows can also be evaluated from CFD. Here, the time-averaged and mass-averaged quantities of entropy, and total temperature are used:

$$\Delta\eta = \frac{\Delta s T_{03}}{c_p(T_{01} - T_{03}) + \Delta s_{\text{stage}} T_{03}} \tag{7}$$

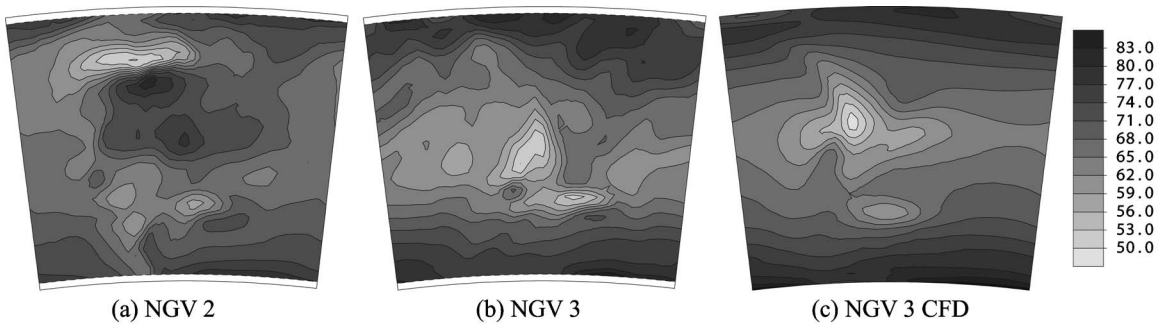

Fig. 12 NGV exit meridional yaw angle (deg)

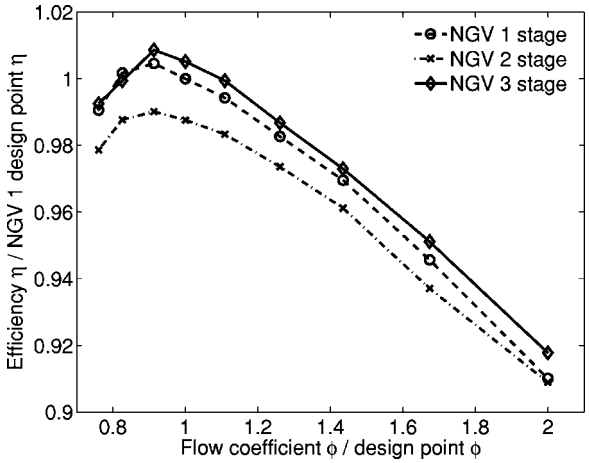

Fig. 13 Measured efficiency of all stages

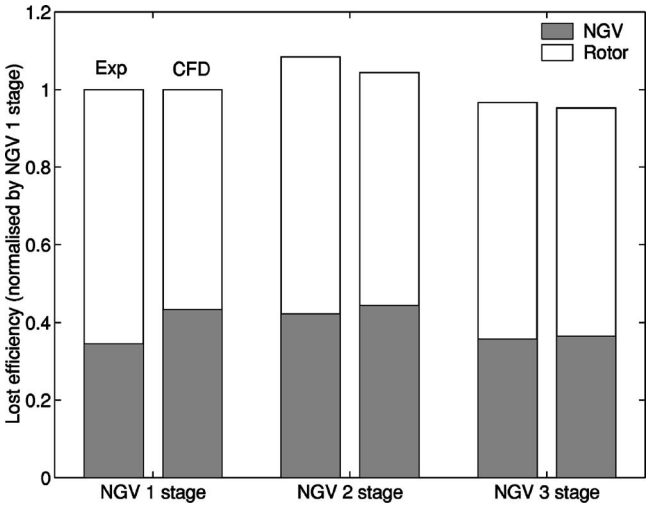

Fig. 14 Comparison of NGV and rotor loss, measured and predicted

where Δs_{stage} is the entropy rise across the stage, $s_3 - s_1$.

The stage efficiency predicted in the simulation is very close indeed to the measured value, being always less than 1% point higher. This discrepancy is to be expected because any tip leakage flow, sealed as much as possible in the experiment, is not modeled, and a correction for windage is not made. However, to compare the measured and predicted lost efficiency split between the two blade rows, the values are divided by the measured and predicted lost efficiency for the NGV 1 stage. The data are presented in Table 1 and in Fig. 14. It can be seen that the variation of stage loss between the three turbines is well predicted. In addition, the proportion of loss occurring within the NGV row also shows good agreement, particularly for the stages fitted with NGV 2 and NGV 3. It is interesting to note that significantly more loss is produced in the rotor row than in the stator row. This is despite the design being closely 50% reaction and the low aspect ratio of the stators. The reasons for this are discussed later.

Figure 15 shows the predicted lost efficiency as a function of meridional distance through the turbine. These curves were obtained by summing the entropy flux through each axial plane at each time-step over one rotor passing period. The total entropy flux was then divided by the associated total mass flux to obtain the mass-averaged time-averaged specific entropy at each plane. An increase in the rate of entropy production is seen in NGV 3 close to the trailing edge where the isentropic blade surface velocities, and cross-passage pressure gradient, are greatest.

The analysis of predicted loss need not be restricted to the blade row level. It is possible to perform an audit of the loss generated in different areas of the blade row by evaluating the entropy generation rates predicted by the CFD code [14–16]. The entropy generation rate per unit volume, $\dot{s}_{\text{gen}}$, can be evaluated using the following equation:

Table 1 Measured and calculated row efficiency losses

		Experiment	CFD
NGV 1 stage	NGV	0.35	0.43
	Rotor	0.66	0.57
	Stage	1.	1.
NGV 2 stage	NGV	0.42	0.44
	Rotor	0.66	0.60
	Stage	1.08	1.04
NGV 3 stage	NGV	0.36	0.36
	Rotor	0.61	0.59
	Stage	0.97	0.95

$$\dot{s}_{\text{gen}} = \frac{1}{T}\tau_{ik}\frac{\partial V_i}{\partial x_k} + \frac{\lambda}{T^2}\frac{\partial T}{\partial x_i}\frac{\partial T}{\partial x_i} \tag{8}$$

The first term on the r.h.s. of Eq. (8) can be rewritten so that

$$\dot{s}_{\text{gen}} = \frac{1}{T}\left(\frac{\partial \tau_{ik} V_i}{\partial x_k} - V_i\frac{\partial \tau_{ik}}{\partial x_k}\right) + \frac{\lambda}{T^2}\frac{\partial T}{\partial x_i}\frac{\partial T}{\partial x_i} \tag{9}$$

Using a finite volume approach, the entropy generation per unit volume in a particular cell of volume Δ_{vol} is

$$\dot{s}_{\text{gen}} = \frac{1}{T\Delta_{\text{vol}}}\left(\underbrace{\sum \tau_{ik}V_iA_k}_{\dot{W}_{\text{visc}}} - \underbrace{V_i\sum \tau_{ik}A_k}_{\dot{W}_{\text{mech}}}\right) + \frac{\lambda}{T^2\Delta_{\text{vol}}}\left(\sum TA_i\right)^2 \tag{10}$$

In Eq. (10), the summations are performed over the faces of the cell. $\dot{W}_{\text{visc}}$ is identified as the total viscous work done on the faces of the cell. $\dot{W}_{\text{mech}}$ is the useful mechanical work done by the viscous body force acting on the cell.

To ascertain where the entropy is generated, the NGV and rotor computational grids are arbitrarily divided into eight regions: Hub, tip, upstream of the leading edge, downstream of the trailing edge, suction-surface, pressure-surface, passage, and base zones. These areas are illustrated for NGV 3 in Fig. 16. The hub and tip zones include *all* cells within 4.5% of span of the respective endwalls. The upstream zone covers cells upstream of a plane 5% of

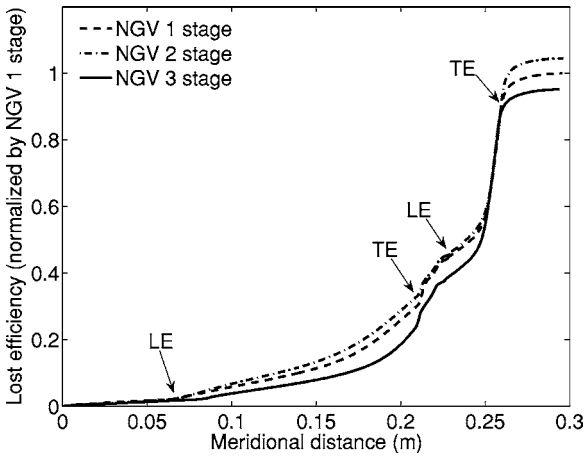

Fig. 15 Predicted lost efficiency curves

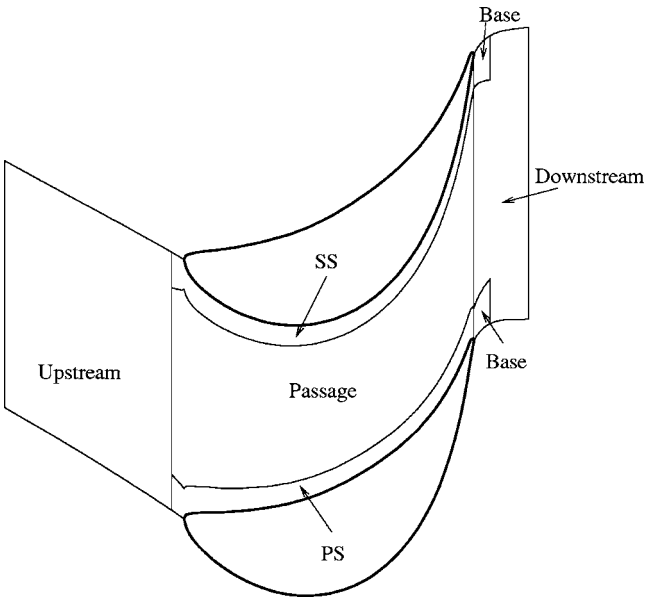

Fig. 16 Zones for loss audit, NGV 3

chord ahead of the leading edge. The suction-surface and pressure-surface zones extend 11.5% of the blade pitch away from the blade surfaces, and 5% of axial chord upstream of the leading edge. The passage zone covers the remaining cells from 5% upstream of the leading edge to the trailing edge. The base region is defined from the trailing edge plane to 5% of axial chord downstream of the blade and within 11.5% of pitch from the mesh periodic boundary. The definition of the base region in this way is a somewhat crude attempt to separate the sudden entropy increase immediately downstream of the trailing edge (see Fig. 15) from that occurring in the remainder of the downstream zone.

The loss audit for the three NGV designs is presented in Fig. 17. The reduction in total lost efficiency predicted for NGV 3 is immediately apparent. Close inspection reveals that the loss reduction occurs in four areas: Hub, tip, and both blade surfaces. In these zones, NGV 3 generates 76% of the entropy produced in the same regions by NGV 2. This result suggests that aft-loading is contributing to an improved performance in these regions. The hub and tip zones are affected less by the cross-passage endwall flow in NGV 3, since this is delayed until closer to the exit of the blade. The isentropic suction-surface velocities were not increased by aft-loading (Fig. 6), so increased losses are not anticipated in this zone. Perhaps the most surprising decrease occurs in the pressure-surface region. Here, the principal factors must be the reduced influence of secondary flow and the reduced isentropic

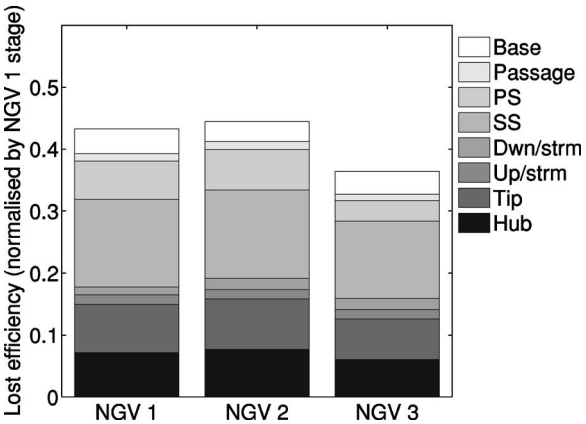

Fig. 17 Loss audit for the three NGVs

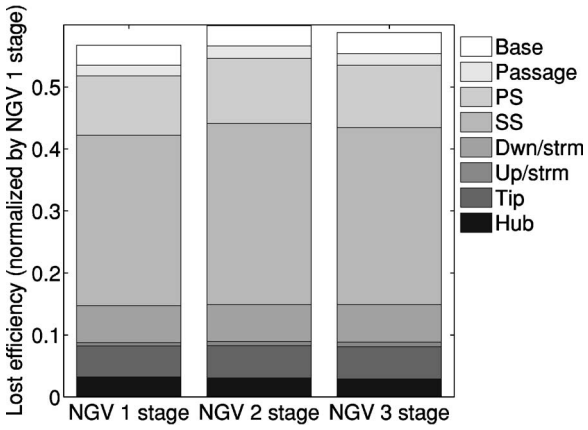

Fig. 18 Loss audit for rotor

pressure surface velocity.

The same zones are used to perform a loss audit for the rotor row, Fig. 18. The time-averaged entropy generation rates are used to evaluate the contributions from each region. The loss predicted to occur in the rotor row is similar when each of the three NGV designs is employed. It is noticeable that the blade surface boundary layers generate more loss than those of the NGV, and it is this that makes the rotor produce more loss then the stator. This is due to a combination of factors: The reduced Reynolds number of the rotor blade; and a higher suction-surface peak isentropic velocity.

The entropy generation rates are available at each physical time-step. In Fig. 19, the rotor loss audit has been performed for *one* rotor passage as it sweeps across the exit flowfield of NGV 3. The loss contributions have been calculated by assuming, at each instant in time, that all the rotor passages contain the same flow as

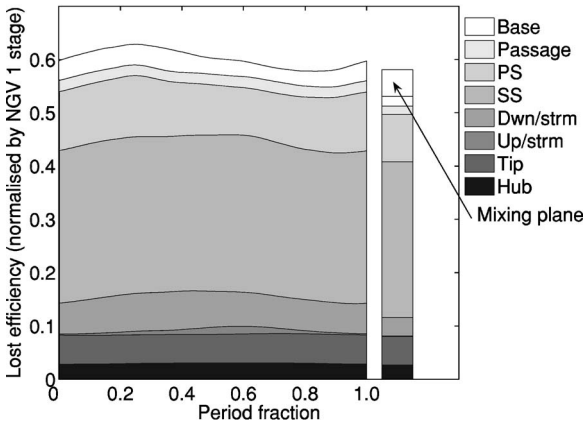

Fig. 19 Time variation of rotor loss generation, by zone, NGV 3 stage

Table 2 Peak-to-peak loss fluctuations as fraction of time-averaged rotor loss, NGV 3 stage

Zone	$\frac{(\Delta\eta_{max}-\Delta\eta_{min})_{zone}}{(\Delta\eta)_{rotor}}$
Hub	0.004
Tip	0.003
Upstream	0.021
Downstream	0.027
Suction-surface	0.023
Pressure-surface	0.043
Passage	0.004
Base	0.026
All zones	0.083

Table 3 Fraction of rotor loss (NGV 3 stage) predicted by unsteady (time-averaged) and steady CFD, by zone

Zone	Fraction of time-averaged rotor loss		
	Unsteady	Steady	Difference
Hub	0.050	0.045	−0.005
Tip	0.090	0.089	−0.001
Upstream	0.012	0.001	−0.011
Downstream	0.107	0.058	−0.049
Suction-surface	0.481	0.486	0.005
Pressure-surface	0.170	0.147	−0.023
Passage	0.034	0.026	−0.008
Base	0.057	0.030	−0.026
Mixing plane	(0.)	0.084	0.084
Total	1.000	0.965	−0.035

the one being tracked.

Table 2 presents the unsteadiness of the loss generated in each zone (the peak-to-peak fluctuation), normalized by the time-averaged loss of the whole rotor domain. Note that, due to phase differences, the unsteadiness of the sum of all the zones is not equal to the sum of the fluctuations in each zone. It can be seen that comparatively high values of unsteadiness occur in the suction-surface, base, upstream, downstream and, in particular, pressure-surface zones.

As a comparison, Fig. 19 also shows the loss predicted to be generated in the different zones by a steady flow calculation performed using the same CFD code. With the inclusion of the loss generated at the mixing-plane, the total loss predicted by the unsteady and steady simulations agree closely, see Table 3. However, there are significant differences in the entropy generated in the individual zones. As would be expected, the zones in which the passing of the rotor through the NGV wake results in large fluctuations in loss production generally exhibit the greatest discrepancy between the loss predicted by steady and unsteady CFD.

6 Conclusions

Comparisons have been made between the performance of a turbine fitted with three different NGV designs: Two mid-loaded and one aft-loaded. The stage fitted with the aft-loaded design achieved the highest efficiency, 0.5% points greater than the best of the mid-loaded NGVs.

The low aspect ratio, high turning NGVs cause extremely strong secondary flows. The exit flowfield, and in particular the position of the loss core, is modified by the aft-loaded design.

Unsteady CFD calculations have been used to simulate the flow in the stage fitted with each NGV design. Particular attention is paid to the accuracy of the loss predictions. It is shown that both the proportion of loss occurring in each blade row, and the trends between different NGV geometries are captured by the CFD.

Finally, predicted entropy generation rates have been used to ascertain the amount of loss produced in distinct regions of the turbine. It is found that the entropy produced on the endwalls and blade surfaces of the rear-loaded blade is only 76% of that generated in the same areas by one of the mid-loaded NGVs. In addition, the time-varying loss occurring in one rotor passage as it sweeps through the NGV wake is extracted. The peak-to-peak fluctuation is approximately 8% of the time-averaged value, with the greatest unsteadiness found on the blade pressure surface. The importance of entropy generation rates as a useful tool of the turbomachine designer is illustrated.

Acknowledgement

The authors are thankful for the assistance of Nick Hooper, of the Whittle Laboratory, in the operation, maintenance and modification of the experimental facility. The contributions of Simon Gallimore, of Rolls-Royce plc, and David Macmanus and Chez Hall, both formerly of Rolls-Royce plc, are also gratefully acknowledged.

Nomenclature

c_p = specific heat at constant pressure
$\dot{m}$ = mass flowrate
p = pressure
r = radius
r_p = pressure ratio function $=(p_{03}/p_{01})^{\gamma-1/\gamma}$
s = specific entropy
x = distance
A = area (of cell face)
M = Mach number
P_b = brake power
T = temperature
U = blade speed
V = velocity
γ = ratio of specific heats
η = isentropic efficiency
λ = thermal conductivity
τ = shear stress

Subscripts

0 = total
1 = stage inlet
2 = NGV exit
3 = stage exit
mid = midspan

References

[1] Pullan, G., Denton, J. D., and Dunkley, M. J., 2003, "An Experimental and Computational Study of the Formation of a Streamwise Shed Vortex in a Turbine Stage," ASME J. Turbomach., **125**, pp. 291–297.
[2] Pullan, G., 2004, "Secondary Flows and Loss Caused by Blade Row Interaction in a Turbine Stage," ASME Paper No. GT2004-53743.
[3] Howell, R. J., Ramesh, O. N., Hodson, H. P., Harvey, N. W., and Schulte, V., 2001, "High Lift and Aft-Loaded Profiles for Low-Pressure Turbines," ASME J. Turbomach., **123**, pp. 181–188.
[4] Corriveau, D., and Sjolander, S. A., 2004, "Influence of Loading Distribution on the Performance of Transonic High Pressure Turbine Blades," ASME J. Turbomach., **126**, pp. 288–296.
[5] Weiss, A. P., and Fottner, L., 1995, "The Influence of Load Distribution on Secondary Flow in Straight Turbine Cascades," ASME J. Turbomach., **117**, pp. 113–141.
[6] Benner, M. W., Sjolander, S. A., and Moustapha, S. H., 2004, "The Influence of Leading-Edge Geometry on Secondary Losses in a Turbine Cascade at the Design Incidence," ASME J. Turbomach., **126**, pp. 277–287.
[7] Hartland, J. C., Gregory-Smith, D. G., Harvey, N. W., and Rose, M. G., 2000, "Nonaxisymmetric Turbine End Wall Design. Part II—Experimental Validation," ASME J. Turbomach., **122**, pp. 286–293.
[8] Brennan, G., Harvey, N. W., Rose, M. G., Fomison, N., and Taylor, M. D., 2003, "Improving the Efficiency of the Trent 500-HP Turbine Using Nonaxisymmetric End Walls. Part I—Turbine Design," ASME J. Turbomach., **125**, pp. 497–504.
[9] Denton, J. D., 1992, "The Calculation of Three-Dimensional Viscous Flow Through Multistage Turbomachines," ASME J. Turbomach., **114**.
[10] Pullan, G., and Denton, J. D., 2003, "Numerical Simulations of Vortex-Turbine Blade Interaction," In 5th Euro. Turbo. Conf., pp. 1049–1059.
[11] Denton, J. D., 2002, "The Effects of Lean and Sweep on Transonic Fan Performance," TASK Q., **6**, pp. 7–23.
[12] Jameson, A., 1991, "Time Dependent Calculations Using Multigrid, with Applications to Unsteady Flows Past Airfoils and Wings," AIAA J., Paper No. AIAA 91–1596.
[13] Gbadebo, S. A., Cumpsty, N. A., and Hynes, T. P., 2004, "Three-Dimensional Separations in Axial Flow Compressors," ASME Paper No. GT2004-53617.
[14] Moore, J., and Moore, J. G., 1983, "Entropy Production Rates from Viscous Flow Calculations. Part 1—A Turbulent Boundary Layer Flow," ASME Paper No. 83-GT-70.
[15] Moore, J., and Moore, J. G., 1983, "Entropy Production Rates from Viscous Flow Calculations. Part 2—Flow in a Rectangular Elbow," ASME Paper No. 83-GT-71.
[16] Dawes, W. N., 1987, "Application of a Three-Dimensional Viscous Compressible Flow Solver to a High-Speed Centrifugal Compressor Rotor - Secondary Flow and Loss Generation," IMechE Paper No. C261/87.

B. Zoppé
Laboratoire des Ecoulements Géophysiques Industriels,
B.P. 53,
38041 Grenoble Cédex 9, France

C. Pellone
Centre National de la Recherche Scientifique,
Grenoble, France

T. Maitre
Institut National Polytechnique
Grenoble, France

P. Leroy
ALSTOM Power Hydro,
B.P. 75,
38041 Grenoble, France

Flow Analysis Inside a Pelton Turbine Bucket[1]

The aim of this work is to provide a detailed experimental and numerical analysis of the flow in a fixed bucket of a Pelton turbine. The head, jet incidence, and flow rate have been varied to cover a wide range of the turbine functioning points. The experimental analysis provides measurements of pressure and torque as well as flow visualization. The numerical analysis is performed with the FLUENT code using the two-phase flow volume of fluid method. The results present a good consistency with experimental data. In particular, the pressure distribution is very well predicted for the whole range of the studied parameters. A detailed analysis of torque and thrust allows evaluating the losses due to the edge and the cutout of the bucket. These results give insight into the benefit we can expect of steady flow calculations through the optimization process of the design of Pelton turbines. [DOI: 10.1115/1.2184350]

1 Introduction

Up to now, Pelton turbines have been designed using experimental techniques and semi-empirical methods. The reason is that the flow in the bucket is unsteady, separated from air by an unknown free surface (two-phase flow), and developed within moving boundaries. These features concern mainly the ideal "first-order" inviscid flow field involved in loss mechanisms, such as bucket back splashing or jet interference. The prediction of this flow represents a great challenge for numerical modeling. A second group of difficulties deals with the actual flow. We mention, for instance, the enlargement or atomization of the jet and water layers, the secondary flow field at the injector outlet, the wake effect behind the injector nozzle, the gravity deviation of the water, etc. These phenomena, depending on Froude, Weber, and Reynolds numbers, are intimately linked to loss mechanisms in the turbine. They also depend on the turbine design. Though they are of second order compared to the first-order aforementioned flow, their understanding is necessary to improve the efficiency predictions, particularly in the case of model to prototype transposition laws.

Nowadays, the performance of computers allows numerical investigations of the flow in both fixed and rotating parts of the Pelton turbine. Concerning the internal viscous flow in the upstream guiding pipes, Reynolds average Navier-Stokes (RANS) approach has proved its relevance. As an example, we note that the calculations precisely predicted the secondary velocity field at the outlet of the injector [1]. Concerning the external flow in the bucket, much work has been performed during the last few years using two kinds of sheet description.

- The first one uses discrete distribution of particles, spherical pellets, or strips to discretize the water sheet. The corresponding methods have been applied for a two-dimensional (2D) fixed and rotating flat plate [2] and for three-dimensional (3D) rotating buckets [3–5]. In these methods, no grid is needed and the air flow is not calculated.
- The second corresponds to more classical grid-based computational fluid dynamics (CFD) approaches using a free-surface tracking method (generally, the well-known volume of fluid VOF method). Steady buckets were calculated by several authors [6–10]. Rotating buckets were also modeled with different levels of approximations. Some calculations were performed on a fixed grid with a moving jet at the inlet [6,11]. In this case, only one bucket is considered and the cutting of the jet inlet by the following bucket is not modeled. Other calculations are performed with a stationary grid zone (stator) containing the jet inlet and a rotating zone (rotor) containing the buckets. The sliding mesh technique allows connecting the two regions. Mack and Moser [12] Mach et al. [13], and Zoppé [14] considered three adjacent buckets. This approach provides the conditions in the middle bucket that are common to all revolving buckets. The only limitation seems to appear at a high number of injectors (4–6), where jet interference phenomena occurs [15]. By assuming a periodic flow between two successive injectors, Perrig et al. [16] avoids this limitation. It is noted that only Mack compared calculated pressure with experimental time-dependent pressure signals.

It is noted that much work has been done in the field of bucket flow modeling, but very few of them are compared to experimental measurements. For example, only Kvicinsky [11] compared the calculated pressure distribution to experimental data. For this reason, the object of this work is to perform RANS modeling of a steady bucket compared to global and local measurements for a significant range of functioning parameters. Vizualizations were also planned to support a better understanding of the flow. A second object of the work is to use numerical modeling to quantify the different causes of thrust loss in the bucket separately. The results, presented at the end of this paper, are used to provide insight into the benefit we can expect of steady-state flow calculations through the global process of Pelton design optimization.

2 Experimental Study

The experimental study was conducted in the laboratories of Alstom Power Hydro (Grenoble, France). The bucket, characteristic of a Pelton turbine, is placed in the uniform flow created by a cylindrical jet. This study mainly provides a cartography of pressures inside the bucket and total forces values on the bucket. The bucket is placed at various incidence angles; several jet diameters and head heights are used.

2.1 Test Implementation. The testing rig is schematized in Fig. 1. A centrifugal pump, driven by a variable speed 250 KW

[1]The bucket geometry is partially provided due to confidentiality.

Contributed by the Turbomachinery Division of ASME for publication in the JOURNAL OF TURBOMACHINERY. Manuscript received November 16, 2004; final manuscript received January 9, 2006. Review conducted by R. L. Davis.

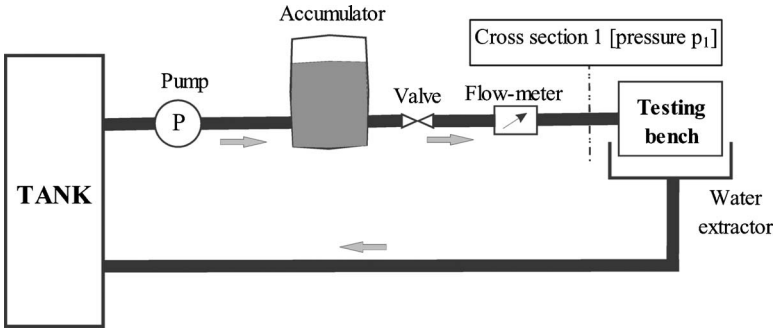

Fig. 1 Diagram of the testing rig

powered motor, supplies the test bench by means of a 200 mm dia pipe. For a given series of tests, the speed of rotation of the pump is maintained constant. The flow rate inside the pipe is measured by means of two flowmeters: an electromagnetic flowmeter (Krohne) and a magnehelic gage (Brooks). The measurement of the first allows the verification of the second. In order to adjust the jet diameter, an orifice is placed at the pipe outlet.

The static head, corresponding to the pressure difference between the interior of the pipe and the atmosphere is measured by means of two differential pressure sensors Rosemount DP27 and E22 located just upstream from the testing bench. The pressure and velocity upstream of the orifice are designated by p_1 and U_1 (cross section 1 on Fig. 1). The atmospheric pressure and the jet outlet velocity are designated by p_{atm} and U. The net head $H_n = U^2/2g$ (g=9.81 m/s^2 is the gravitational acceleration), the static head $H_s=(p_1-p_{\text{atm}})/\rho g$ (ρ=998 kg/m^3 is the water density) and the dynamical head $H_d=U_1^2/2g$ are simply connected by the Bernoulli relation $H_n=H_s+H_d$.

The measurement of the flow rate Q gives the velocity U_1 (so H_d), the measurement of p_1 gives the static head H_s, which leads to the H_n value and thus provides an experimental measurement of the jet velocity U. The adjustment of H_n is ensured using the two valves.

A photograph of the test bench is presented in Fig. 2. It consists of the steel frame, the water jet intake, the water sheet extractors, the water jet extractor (for safety), and the instrumented bucket. In order to limit the flow disturbances related to the singularities of the testing rig (elbows, valves, etc), the bench is placed at the end of a rectilinear pipe, 3.5 m long.

The water sheet extractors are curved pipes of a rectangular cross section. They make it possible to direct the water sheets flowing out the bucket toward the collecting container located under the test area. The extractors position is adjusted according to the bucket incidence. The quantity of water that these elements must direct is significant; in fact, protection was added in order to reduce the splashes near the measurement zone and the backflows on the jet.

The orifice ϕ_d diameter, narrows the water jet to a minimum value of D. One designates by $S=\pi D^2/4$ the cross section of the jet upstream of the bucket. The jet must be minimally disturbed and spoiled by the contact of its free surface with the air. With this intention, a convergent nozzle is placed at the pipe outlet, which allows reducing the jet length between the orifice and the bucket.

The bucket, made out of bronze, L_a=150 mm wide, is furnished with a handle, allowing it to be attached (via two axes) to the test bench frame (Fig. 3). The first axis (point Ω on Fig. 4(a)), located at the arm end, serves as the rotation axis for the entire wheel. The bucket rotation in reference to this axis defines the α incidence angle between the bucket and the jet. The second axis (measurement axis of the moment M) maintains the incidence angle. The bucket edge (hatched surface drawn on the Fig. 4(b)) is situated in the xoy plane named z_0 plane. The yoz plane, perpendicular to the z_0 plane, is the symmetry plane of the bucket containing the bucket "splitter." The projection of the splitter on the oy-axis gives the AB segment, 103 mm long. A direct orthonormal reference frame $oxyz$ is defined, having for origin the middle point O of the AB segment. The xoz plane is called the "reference plane." In order to have a progressive jet inlet flow, the bucket is truncated in the vicinity of point A. This zone constitutes the "cutout" of the bucket. The zone close to point B constitutes the

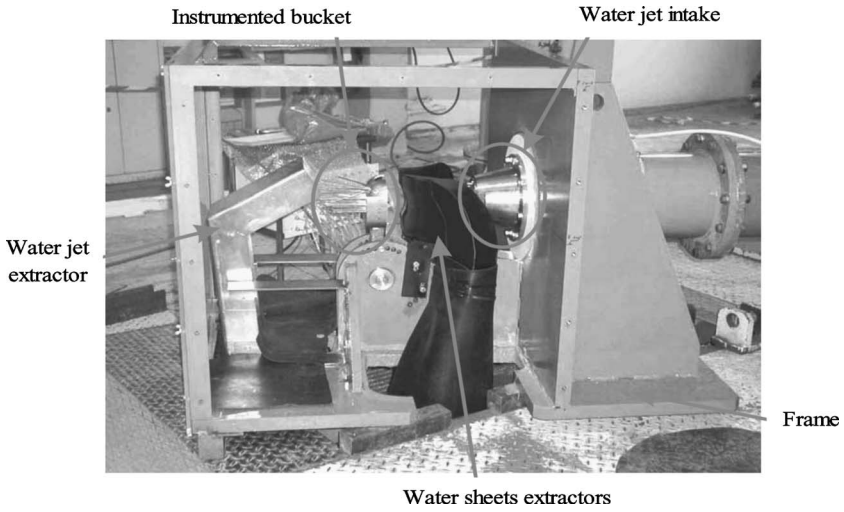

Fig. 2 Testing bench

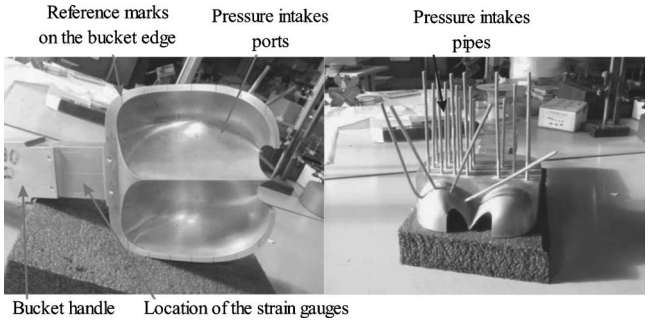

Fig. 3 Bucket experimental devices

"back part" of the bucket.

Three nondimensional numbers are classically used in the study of the flows within a Pelton turbine:

- The Reynolds number $\mathrm{Re}=\rho UD/\mu$, with μ water molecular viscosity equal to 1.002×10^{-3} kg/(m s). This number represents the ratio of the inertia forces with respect to the viscosity forces.

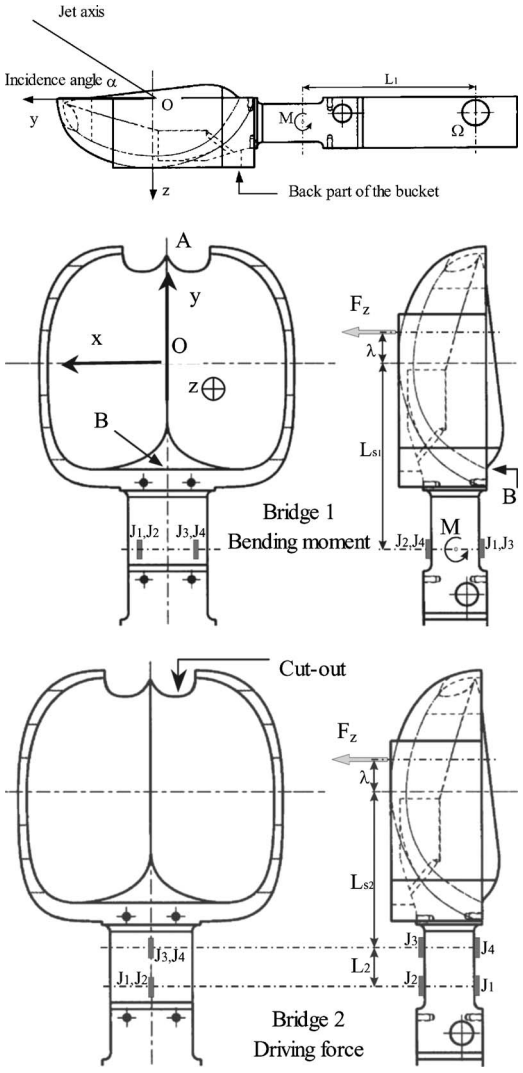

Fig. 4 Schematic views of the bucket

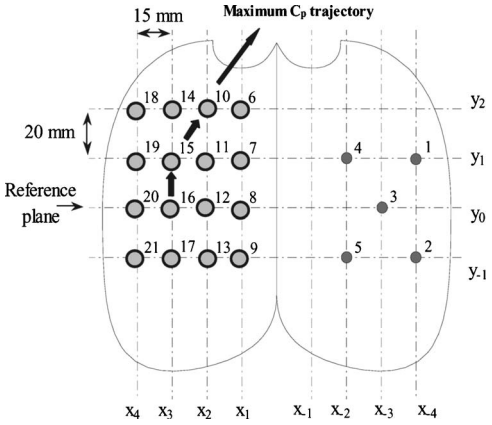

Fig. 5 Location of the pressure intakes

- The Froude number $\mathrm{Fr}=U/\sqrt{gL_a}$. This number represents the ratio of the inertia forces with respect to the gravitational forces.
- The Weber number $\mathrm{We}=\rho U^2L_a/\gamma$, with γ water surface tension equal to 0.074 N/m. This number represents the ratio of the inertia forces with respect to the surface tension forces.

2.2 Pressure Measurement. The pressure p_i is measured in 21 points of the wetted surface (inner surface) of the bucket arranged as indicated in Fig. 5. The five numbered pressure intakes 1–5, located on the right half of the bucket, are the symmetrical ones of the five corresponding measurement points of the left part. These five measurement points are used to ensure the jet-centering control and the flow symmetry with respect to the bucket splitter. The intakes are placed at the points of a regular orthogonal network; the x-axis spacing is of 15 mm and the y-axis spacing of 20 mm.

To work these pressure intakes, the bucket is bored orthogonally on its surface. Fine pipes are welded on to the external surface in front of each orifice (Fig. 3); each tube is connected to the pressure transducer. Measurements of pressure are carried out using a double multiplexer (Scannivalve DSS, 24 channels) connected to a differential pressure transducer (Rosemount DP27). The instrument (Scannivalve) makes it possible to measure the pressure at the 21 points using a single pressure transducer. It operates as a barrel that connects the sensor with the pressure intakes, one after another. This device, requiring only one calibration, provides homogeneous measurement uncertainties. $H_i=(p_i-p_{\mathrm{atm}})/(1/2)\rho U^2$ designates the measured relative pressure at point of index i, the unit of measurement being the water column meter (mCE).

2.3 Thrust and Torque Measurement. Measurements relate to the driving force Pelton F_z (force creating the engine torque) and the bending moment M_w with respect to the wheel axis (Fig. 4). The F_z force is the component, perpendicular to the bucket handle, of the jet force exerted on the bucket. The force and the moment are measured using eight strain gages mounted on the bucket handle (Figs. 4(*b*) and 4(*c*)). In order to increase the handle deformations, the gage region is intentionally weakened. Bridge 1 (Fig. 4(*b*)), made up of four unidirectional gages, measures the bending moment M. Bridge 2 (Fig. 4(*c*)), made up of four semiconductor gages assembled in a differential manner between two cross sections, measures the driving force F_z. The assembly per pair of gages, located on each side of the handle, allows one to eliminate by cancellation the deformations interference due to, for instance, dilation, radial force, or torsion. The measurement error, thus, comes primarily from the gage calibration and amplification

Table 1 Measured magnitudes

Magnitudes	Instrumentation	Relative uncertainty
Flow-rate Q	Electromagnetic flow-meter or turbine flow-meter	± 0,4%
Static head H_s	Differential pressure transducer	± 0,2%
Pressure H_i	Differential pressure transducer + Scanivalve	± 0,2%
Driving force F_z and Bending moment M	Strain gages	± 2,0%

quality. The use of semiconductor gages provides, for bridge 2, a relative error comparable to that of bridge 1 and equal to ±2% (Table 1).

From F_z and M measurements, one deduces the moment M_w and the shift λ (distance between the origin of force and the reference plane) by the relations:

$$M_w = M + F_z L_1 = F_z(\lambda + L_{S1} + L_1) \quad (1)$$

$L_1 = 122$ mm is the distance between the axis of the moment M and the rotation axis. $L_{S1} = 121.7$ mm is the distance between the axis of the moment M and the reference plane. The Pelton diameter is then defined by $D_P = 2(L_{S1} + L_1) = 487.5$ mm.

2.4 Experimental Tests. Table 1 indicates the relative uncertainties recorded for the measurements of the flow rate, static head, pressure, driving force, and the moment. The net head H_n, the orifice diameter ϕ_d, and the incidence α are the three varying parameters.

Four diameters of the orifice were used: $\phi_d = 38.1$ mm, 50.1 mm, 56.0 mm, and 61.5 mm. The incidence α varies from 60 deg to 120 deg in 10 deg steps. The three chosen net heads are $H_n = 30$ m, 40 m, and 50 m. The corresponding velocities have the respective values: $U = 24.26$ m/s, 28.01 m/s, and 31.32 m/s. For each couple of values (orifice diameter-incidence), Table 2 indicates the tested net heads, the total number of tests being 56. Table 3 indicates the mean volume flow rate measured (liters per second) for the three net heads and the four diameters of the orifice. Because of the jet contraction, the orifice ϕ_d is higher than the jet diameter D. The jet diameter, flow rate, and net head are bound by the relation $D = \sqrt{4Q/\pi\sqrt{2gH_n}}$. For the whole of the tests (Table 3), the Reynolds number Re is included in values 3.6×10^6 to 4.7×10^6. In consideration of high values of the Reynolds number, the contraction coefficient of the jet is constant; consequently, for a fixed value of the orifice diameter (or jet diameter) the ratio $Q/\sqrt{H_n}$ remains the same one. The values of the diameter D are obtained with a relative error of 2.5%. The usual nondimensional magnitude D^* indicated in Table 3 is defined by $D^* = L_d/D$.

Table 2 H_n head values. Total of 56 tests

α deg	ϕ_d=38.1 mm	ϕ_d=50.1,1 mm	ϕ_d=56 mm	ϕ_d=61.5 mm
60 deg		30–50 m	30–50 m	30–50 m
70 deg		30–50 m	30–50 m	30–50 m
80 deg	30 - 40 - 50 m	30–40–50 m	30–40–50 m	30–40–50 m
90 deg	30 - 40 - 50 m	30–40–50 m	30–40–50 m	30–40–50 m
100 deg	30 - 50 m	30–50 m	30–50 m	30–50 m
110 deg		30–50 m	30–50 m	30–50 m
120 deg		30–50 m	30–50 m	30–50 m

Table 3 Mean volume flow rate Q, inlet velocity U, Reynolds number R_e

D^*	ϕ_d (mm)	H_n=30 m Q (l/s)	H_n=40 m Q (l/s)	H_n=50 m Q (l/s)
5.07	38.1	16.7	19.3	21.5
3.84	50.1	29.1	33.6	37.5
3.44	56.0	36.2	41.8	46.8
3.13	61.5	43.8	50.5	56.5
Inlet velocity U		24.3 m/s	28.0 m/s	31.3 m/s
Reynolds number R_e		3.6×10^6	4.2×10^6	4.7×10^6

2.5 Flow Visualization (Fig. 6). The photographs are taken with a numerical camera provided with a flash. A droplets fog is always present in the enclosure. It is accentuated when the head or the jet diameter increases. No particular effect of the head on the flow in the bucket was noted. For this reason, the photographs were made in the case of a slight head, so one reaches the maximum quality.

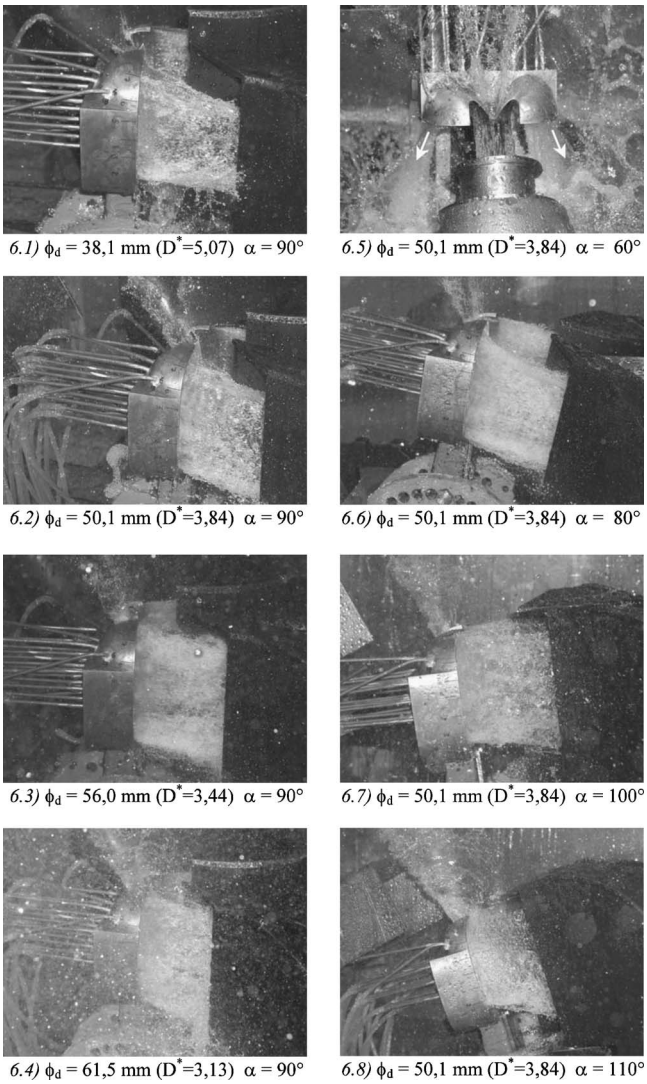

Fig. 6 Different side and top views of the sheets of water

The first panel of Fig. 6 presents the flow obtained with an orifice of 38.1 mm and an incidence of 90 deg. After jet impact in the bucket occurs, the flow at the exit of the bucket turns into a sheet. These sheets of water appear of a white and opaque color, typical of an air-water mixture. Furthermore, downstream the bucket, the sheets of water break up in droplets. At the bucket exit, the streamlines deviation angles are more significant at the ends (back part and cutout) than in the vicinity of the reference plane. This phenomenon involves the contraction of the sheets downstream the bucket. The fifth panel of Fig. 6 (ϕ_d=50.1 mm and α=60 deg) presents a top view of the flow, the white arrows indicating the various directions of the sheet of water at exit of bucket. The various photographs of Fig. 6 highlight the water quantities leaving by the cutout. This phenomenon was observed in the various configurations obtained while varying the orifice diameter and the incidence angle. Images one to four in Fig. 6 correspond to different jet diameters for an incidence fixed at 90 deg. The fluid enters entirely in the bucket. It is observed that the cutout leakage flow rate increases with the diameter.

Images five to eight in Fig. 6 correspond to different angles of incidence for an orifice diameter ϕ_d fixed at 50.1 mm. Let us note that, for incidence α=60 deg, all of the jet does not enter into the bucket. The part of the jet that does not come into the bucket is expelled outside the Pelton wheel. Beyond 80 deg, the jet enters entirely into the bucket. A part of the jet, strongly increasing with the incidence, leaves the bucket by the cutout while having covered only a small distance inside it. In all cases, a leakage flow rate is noted at the cutout.

2.6 Net Head Effect on Pressure. The pressure coefficient is given by $C_p=(p-p_{\text{atm}}/(1/2)\rho U^2)=H_i/H_n$. For the 16 pressure intakes (points 6–21), the measurement of the pressure coefficient was realized for each of the three net heads. No significant variation of the pressure coefficient is noted with the net head. As an example, for a jet diameter D^*=3.44 and an incidence angle of 90 deg, the maximum relative gap is $<$0.1%. As a result, in the following, the results are presented only for H_n=30 m.

2.7 Symmetry Checking. The symmetry of the flow relative to the *yoz* plane was checked for the paired numbered points: (1,19), (2,21), (3,16), (4,11), and (5,13). The measurements show that, for the incidence angle of value 90 deg, the pressures symmetry is realized. For these five points, the maximum relative gap is $<$0.8%.

3 Numerical Study

The numerical study was conducted in the laboratory of LEGI (Grenoble, France). The software used is FLUENT. The Navier-Stokes solver solves the mean equations of turbulence (RANS).

To represent the two-phase flows, there are Eulerian methods and Lagrangian methods [17]. The first consists of assuming each phase as continuous. Information between phases is carried by interface conditions. The second assumes that one of the phases (water) disperses itself in the other (air). Within the framework of this study, the Eulerian methods are well adapted. The free surface is then modeled using a multifluid model or a homogeneous two-phase model or a volume of fluid (VOF) method. The multifluid model is a complete and precise model but requires much computing time. The homogeneous model is rather used for flows where one of the phases is uniformly distributed in the other, such as the flows with bubbles. Under the present configuration the VOF method is completely appropriate [18]. It consists of representing the fluid volume by the water volume fraction χ. The value of χ is 1 when the cell is filled with water and 0 when the cell is empty. The determination of χ requires an additional equation, thus, the advection equation of the fluid. The free surface is the set of points for which the volume fraction is equal to χ_0, χ_0 being included in values 0 to 1.

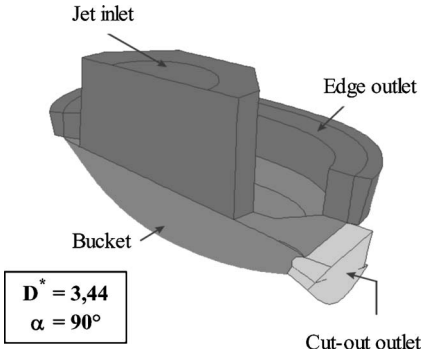

Fig. 7 Diagram of the calculation blocks

The studied cases correspond to seven jet diameters with an incidence fixed at α=90 deg and to seven incidences with a jet diameter fixed at D^*=3.44. The range of diameters used at the time of the experimental study was supplemented by three additional ones: D^*=5.91, 4.39, 2.90. The incidences are identical to the experimental ones.

3.1 Numerical Modeling. A preliminary study was initially performed concerning the 2D and 3D jets impact on a flat plate. The major objective was to evaluate the abilities of the FLUENT VOF model. The numerical results were compared to analytical results for the 2D and experimental results for the 3D. The comparisons with regard to the sheet of water thickness and the pressure are excellent [14].

3.1.1 Discretization. The simulation of the flow in the bucket requires the setting of the control volume, the boundary conditions, and the 3D mesh. Because of the flow symmetry relative to *yoz* plane, only the space of a half bucket geometry is considered. Figure 7 illustrates the composition of the control volume. It consists of four parts: the jet inlet domain, the bucket, the edge, and the cutout. This partition makes it possible to modify only the jet inlet domain when incidence is changed. The inlet domain is built in order to include all of the jet whatever the diameter value. For each case, the jet inlet face is taken parallel to the reference plane. Consequently, the jet inlet border is a half circle for α=90 deg and a half ellipse for the other incidences. This face is located at 50 mm above the reference plane. The outlet region of the bucket edge is 20 mm high above z_0 plane (red zone in Fig. 7).

The boundary conditions are a zero velocity condition on the bottom and the edge of the bucket, a symmetry condition on the faces belonging to the symmetry plane, a uniform velocity condition on the jet inlet face, and a constant pressure condition for all the faces in contact with the air.

The mesh construction required a preliminary study in order to determine the type and the density of cells to be used. A maximum 3 mm size of the cells stabilizes the results in comparison to the refinement of the mesh. Table 4 shows that, for a number of cells higher than 180,000, the thrust and torque become insensitive with the cell numbers. For all the treated cases, a number of cells approximately equal to 300,000 corresponds to the criterion of the maximum size as well as the numerical stability.

The cells constituting the hybrid mesh are hexahedral, tetrahe-

Table 4 Numerical stability test

Cells number	Thrust F_z (N)	Torque M_w (Nm)
37,500	1178	289
94,500	1188	291
183,000	1189	293
342,000	1189	293

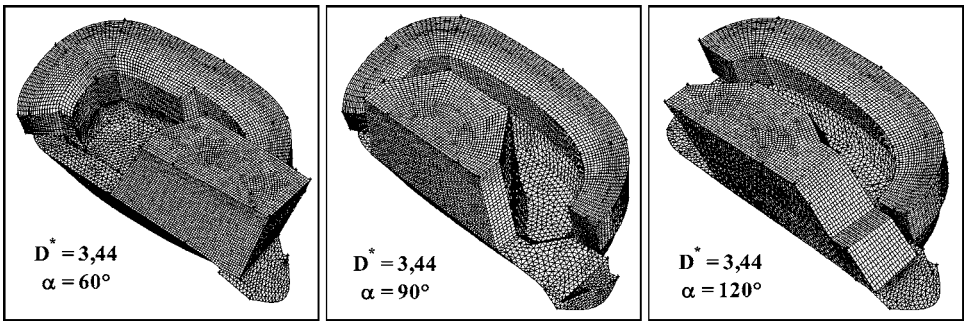

Fig. 8 View of the meshes

dral, or pyramidal in shape. The pyramidal cells allow the connection between domains meshed with the two other types of cells. The jet inlet face is paved in a nonstructured way with quadrilaterals. The inlet domain mesh (blue block) is built using the Cooper method. The domain relative to the cutout outlet is meshed with tetrahedrons. Figure 8 illustrates the meshes obtained for a fixed diameter for three cases of incidence.

3.1.2 Calculation Parameters. The Navier-Stokes equations are discretized by a finite volumes method. The discretization scheme used to model the fluid advection is of the second order, upstream centered. The free surfaces are characterized by the volume fraction value $\chi_0=0.5$. The PLIC method (piecewise linear interface calculation) [19] is used for the geometrical reconstruction of the interface. Turbulence is taken into account using the k-ε standard model with wall functions. On the jet inlet face the k and ε values are expressed according to the mean characteristics of the flow, namely, turbulence intensity and characteristic length. The turbulence intensity is taken equal to 5% and the characteristic length to the jet diameter value.

A 3D boundary layer calculation [20] carried out on the bucket with a 90 deg jet incidence highlights that the viscosity forces are very weak compared to the inertia forces. Compared to the $2\rho QU$ value of the ideal force, the three components of the viscous force have the following values: 0.26% on the x-axis, 0.02% on the y-axis, and −0.3% on the z-axis. Considering these values, in a first stage, a laminar calculation has been performed. In this case, numerical instabilities occur. These instabilities do not originate from the near-wall region but are due to the strong velocity gradients close to the interface (air entrainment due to the water motion). The use of a turbulence model considerably reduces these gradients and, thus, stabilizes the calculation. Consequently, the modeling of the boundary layer and the refinement of the grid near the wall are not really necessary. The values of the dimensionless near wall distance Y^+ are between 250 and 600, and the minimum value of the velocity at the first node of the wall is ~13 m/s compared to the 25 m/s value of the jet velocity. It is significant to note that, for the mesh used, FLUENT calculation gives viscous forces about those given by the 3D boundary layer calculation, namely: 1% on the x-axis, 0.04% on the y-axis, and 0.4% on the z-axis. Finally, the resolution of the viscous flow is not optimal, but it is of no importance because the viscous effects are very weak. This is confirmed by the good comparison between the numerical and experimental pressures (see Fig. 14).

Carried-out calculations are unsteadily converging toward a steady state. Time integration is performed using the implicit Euler method of the second order. The two numerical criteria of convergence are the stabilization of the force exerted by the jet on the bucket and the equality of the inflow and outflow values. It takes ~35 h of time consumption (bi-processor PC AMD Athlon 2000+) to perform the 4500 time steps required to insure the convergence.

The present experimental configurations allow neglecting the force of gravity compared to the force of pressure. Indeed, according to Table 3, minimum velocity of the jet is ~24 m/s, which gives a minimum Froude number of 24. In the same way, the surface tension effects are neglected (the minimum Weber number is equal to 1.2×10^6).

3.2 Numerical Results and Comparison

3.2.1 Fixed Angle of Incidence (α=90 deg). Figure 9 shows the free surface in the case of three experimental jet diameters. Inside the bucket, the wetted surface increases with the jet diameter. The thickness of the outgoing sheet of water (at the bucket edge level) increases back and forwards except for the largest diameter ($D^*=3.13$), for which the sheet of water is thinner in the reference plane area than at the bucket ends. No water leakage flow through the cut-out is noted except for the case where $D^*=3.13$. For the three studied diameters, the experimental tests reveal a low leakage at the cutout outlet (Fig. 6).

In the reference plane, Fig. 10 shows the water thickness. Inside the bucket, the water thickness e, measured according to the bucket normal, is defined as the distance from a point of the bucket surface to the free face. This distance nondimensionalized with respect to the bucket width is given by: $e^*=e/L_a$. The nondimensional curvilinear abscissa s^* is worth 0 for the splitter point and 1 for the edge point. For the lowest jet diameters the water thickness decreases regularly inside the bucket. A water accumulation around the common value $s^*=0.60$ appears only when D^*

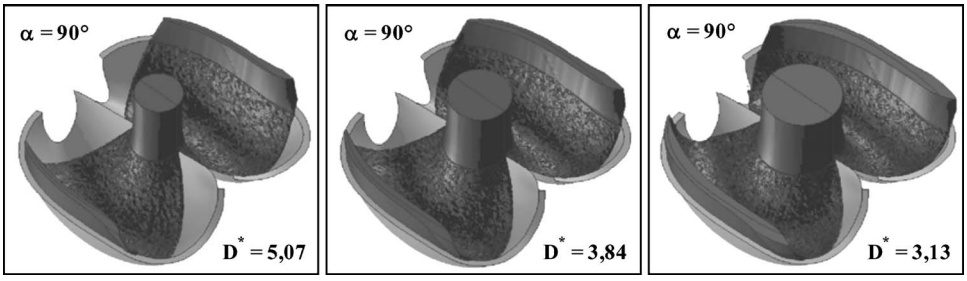

Fig. 9 Free surface of the jet

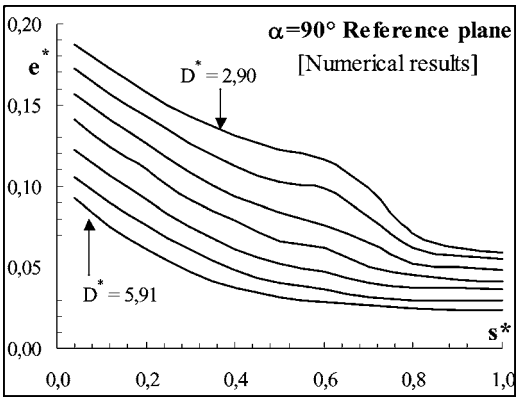

Fig. 10 Thickness of the sheet of water in the reference plane

<3.84. It is characterized by a stage that becomes more and more clear as the jet diameter increases. This phenomenon is related to the overpressure in the bucket bottom, which causes a velocity reduction in the sheet of water core and consequently increases its thickness.

Figure 11 illustrates a cartography of the pressure coefficient C_p (on the left) and of the water volume fraction χ (on the right). The three presented cases correspond to the three cases of Fig. 9. The zone having the strongest pressures ($C_p \sim 0.9$) is located in the bucket bottom and shifted toward the edge. This zone extends when the jet diameter increases. That is in agreement with the pressure effects (on the sheet of water thickness) as previously commented.

3.2.2 Fixed Diameter ($D^*=3.44$). Figure 12 illustrates the water distribution inside the bucket for three incidences. For $\alpha=60$ deg, water spreads out over most of the inner surface and concentrates on the back edge at the bucket exit. Part of the jet does not penetrate inside the bucket: the corresponding water quantity does not act on the bucket. For $\alpha=90$ deg, the sheet of water extends toward the cutout edge and becomes thinner. The entire jet enters the bucket and the entire sheet of water is contained in the bucket. For $\alpha=120$ deg, the sheet of water is particularly wide along the bucket edge. A significant part of the jet goes out of the cutout, which implies, for this case, a significant loss of force.

The experimental views in Fig. 6 confirm, qualitatively, to the preceding numerical results. One, however, notes in this figure that, whatever the diameter and incidence, there is always a quantity of more or less significant water that vacates through the

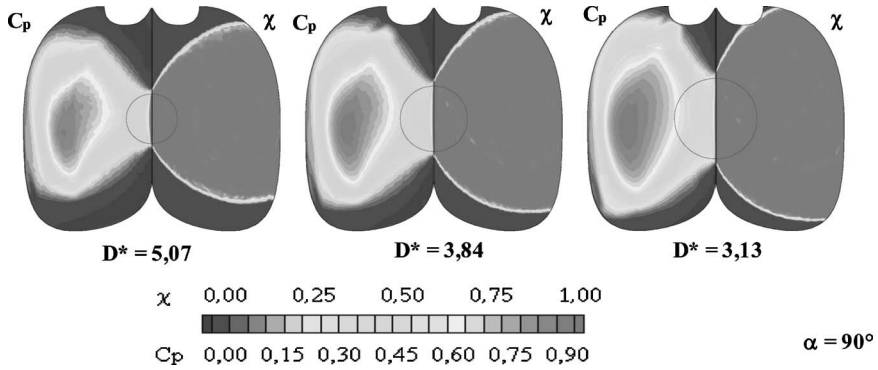

Fig. 11 Pressure coefficient and water volume fraction

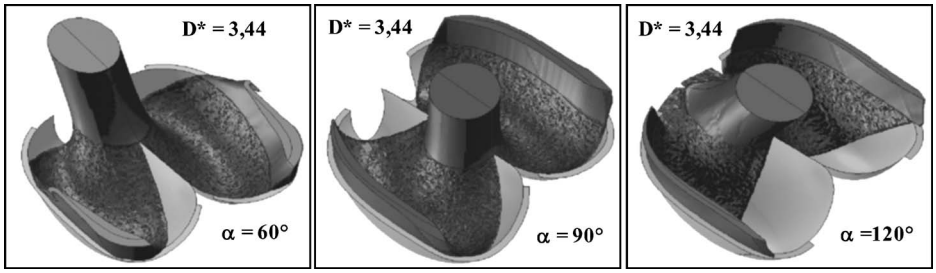

Fig. 12 Free surface of the jet

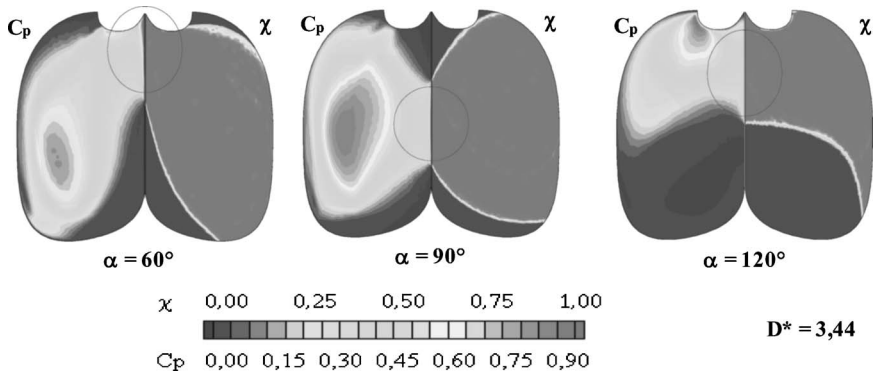

Fig. 13 Pressure coefficient and water volume fraction

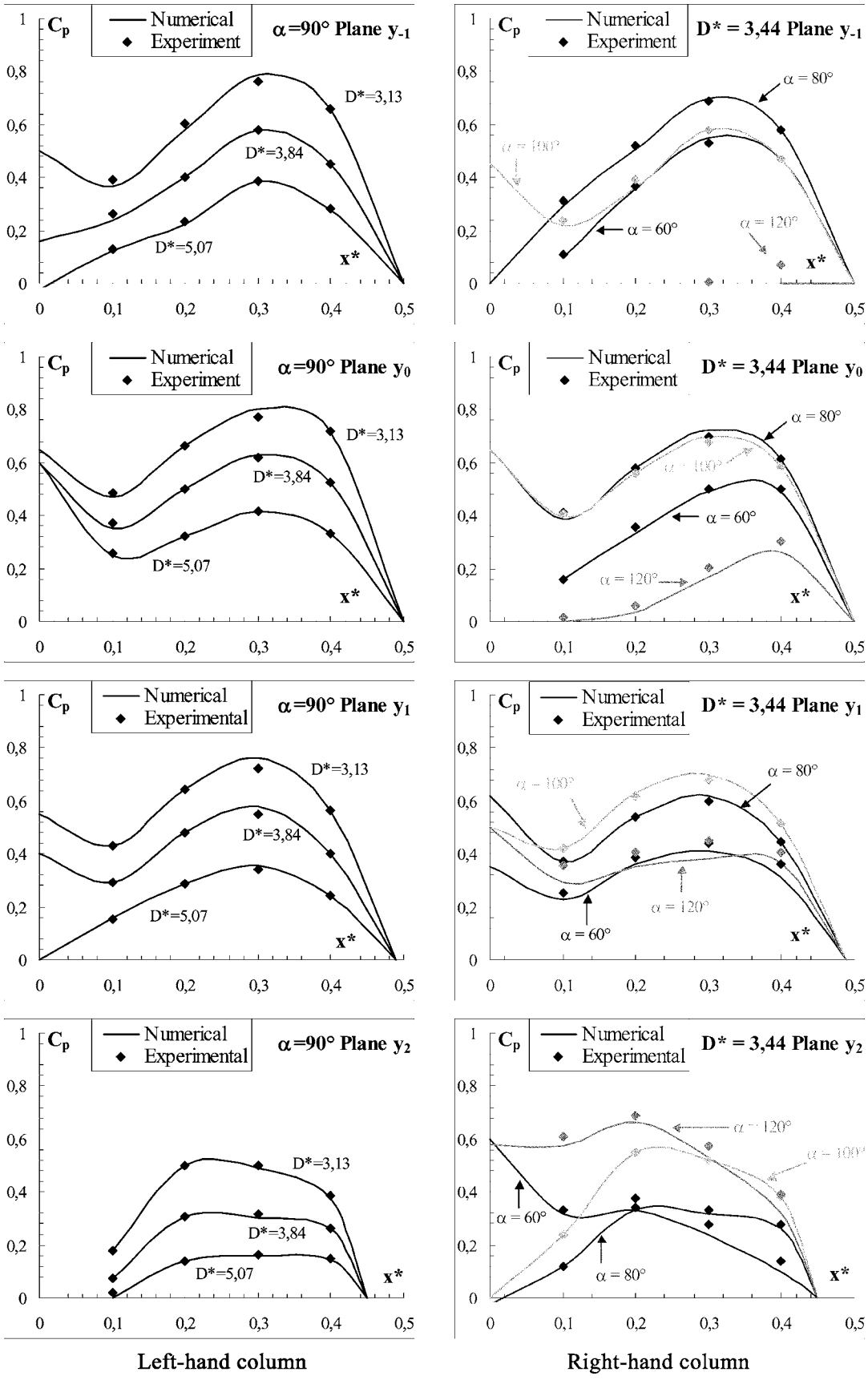

Fig. 14 Pressure coefficient: numerical and experimental results

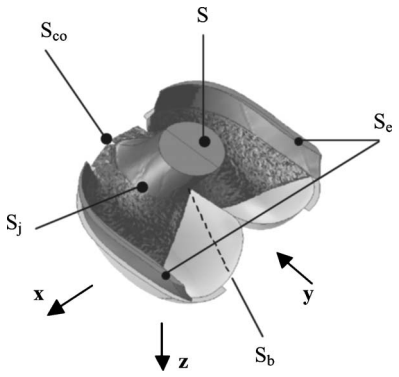

Fig. 15 Schematic view of the boundary surfaces

cutout.

Figure 13 represents the pressure field corresponding to the three previous cases. One notes, in conformity with the experimental results, the displacement of the overpressure zone toward the cutout when the incidence increases. Under the case of the 120 deg incidence, a significant nonwetted zone is localized near the rear of the bucket.

3.2.3 Comparison of the Measured and Calculated Magnitudes. Figure 14 presents the experimental and numerical pressure coefficients in the planes y_{-1}, y_0, y_1, and y_2 indicated on Fig. 5. The four figures in the left-hand column are related to the case of incidence $\alpha=90$ deg. Each figure presents the three jet diameter values: $D^*=3.13$, 3.84, and 5.07. The four figures of the right-hand column are related to the case of jet diameter $D^*=3.44$. Each figure presents four incidence values: $\alpha=60$ deg, 80 deg, 100 deg, and 120 deg. The experimental points and the corresponding numerical curves have the same color.

The agreement of the results with numerical calculations is very good. However, small deviations appear for the points of planes y_1 and y_2 under the case of the two extreme incidences 60 deg and 120 deg. These are the two incidences for which a nonnegligible quantity of fluid goes out through the cutout and for which the flow undergoes the most significant change of direction close to the cutout.

With the incidence fixed at 90 deg (curves on the left side), it is clear that the pressure increases with the diameter. In the planes y_{-1}, y_0, and y_1, the maximum pressure is around the nondimensional abscissa $x^*=0.3$ and in the plane y_2 around $x^*=0.2$. These points are situated in the deepest zone of the bucket. In each plane, no shape variation of the curves is noted by changing the diameter. In the plane y_2, the noted pressure deficit comes from the proximity of the cutout.

Concerning the total force, the momentum theorem is applied to the closed fluid domain illustrated in Fig. 15. This domain consists of the following boundary surfaces:

- the crosssection S of the jet inlet.
- the free surface S_j of the jet.
- the wetted surface S_b located inside the bucket.
- the surface S_e, obtained by the intersection of the sheet of water and a plane parallel with the z_0 plane. This section is located at an external vicinity of the bucket edge.
- the surface S_{co}, obtained by the intersection of the sheet of water and a plane perpendicular to the unit vector $\boldsymbol{n}$. The vector $\boldsymbol{n}$ is directed outside the domain and contained in the symmetry plane (yoz plane). The direction $\boldsymbol{n}$ is selected so that all of the water exiting through the cutout crosses the plane. In almost all configurations, the choice of the direction $\boldsymbol{n}$ parallel with the direction $\boldsymbol{y}$ is sufficient to ensure the previous condition. This section is located at an external vicinity of the cutout.

When projecting on the z-axis—examining the force exerted by the bucket interior on the fluid—one obtains the expression for the Pelton driving force

$$F_z = \rho QU \sin\alpha + \int\int_{S_e} \rho V_z^2 dS + \int\int_{S_{co}} \rho V_n^2 dS \tag{2}$$

$Q=US$ is the flow rate through a jet section. V_z and V_n, respectively, indicate the velocity components according to the z-axis and direction $\boldsymbol{n}$. The maximum force is obtained for the ideal case. This case corresponds to a bucket that would force the streamlines, at exit, to be perpendicular to the z_0 plane and without velocity loss. In fact, the exit velocity on surface S_e is equal to U, which gives the following maximum force:

$$F_{z\max} = \rho QU(1+\sin\alpha) = \frac{\pi}{2}\rho g D^2 H_n (1+\sin\alpha) \tag{3}$$

The nondimensional driving force is defined by $F_z^*=F_z/F_{z\max}$. In order to give a practical evaluation of the loss of force on an actual bucket compared to an ideal bucket, one introduces the relative loss of thrust $\Delta F_z^*=(F_{z\max}-F_z)/F_{z\max}=1-F_z^*$. This equation represents the relative difference between the force generated by the flow and that which this flow, in the ideal case, would have produced. By using the relation (2) the relative loss of thrust is written as the sum of the loss due to the edge and the loss due to the cutout

$$\Delta F_z^* = [\Delta F_z^*]_{\text{Edge}} + [\Delta F_z^*]_{\text{Cutout}} \tag{4}$$

$$[\Delta F_z^*]_{\text{Edge}} = \frac{-1}{S(1+\sin\alpha)} \int\int_{S_e} \frac{V_z}{U}\left(1+\frac{V_z}{U}\right) dS \tag{5}$$

$$[\Delta F_z^*]_{\text{Cutout}} = \frac{1}{S(1+\sin\alpha)} \int\int_{S_{co}} \frac{V_n}{U}\left(1+\frac{V_z}{U}\right) dS \tag{6}$$

In a similar way, the moment M_w relative to the wheel axis is nondimensionalized with respect to the value $M_{w\max}$ corresponding to the ideal case. In this case, the shift λ is taken equal to zero, which provides $M_{w\max}=(D_P/2)F_{z\max}$. The moment relative to the measurement axis is defined by $M^*=M/M_{w\max}$.

Figures 16(*a*) and 17(*a*) present respectively the torque M^* and the thrust F_z^* versus the incidence angle of the bucket for a medium jet size $D^*=3.44$. A good agreement between the numerical and experimental results is noted. It is observed that the maximum thrust is obtained at 90 deg and maximum torque at 110 deg. This is due to the maximum pressure displacement toward the cutout when incidence exceeds 90 deg (cf. Sec. 2.2, Fig. 5).

Below 80 deg, the experimental torque and thrust decrease regularly, although numerical ones present a plateau and then decrease strongly. These discrepancies can be explained as following. Between 70 deg and 80 deg, the numerical calculation underestimates the leakage flow exiting the cutout. This is highlighted by Fig. 18. Consequently, the thrust and torque experimental losses due to the cutout leakage flow are higher than the corresponding numerical losses. In this case, the strong curvature of streamlines and the water sheet thinness are difficult to model.

Let us note that, above 80 deg, when the incidence increases, these differences tend toward zero in spite of the growth of the cutout leakage flow. In this case, the sheets of water that leave the cutout become increasingly thick and have increasingly small curvatures. Thus, numerical calculation provides a very good approximation of the actual flow.

Below 70 deg, the previous experimental analysis shows that a part of the jet does not enter in the bucket (Fig. 6) and flows close to its rear. This flow, probably creates a low-pressure zone that contributes to a torque and thrust increase. This effect has been demonstrated on rotating bucket calculations by Zoppé [14] and Mack [13]. Because the rear zone is not considered in the present

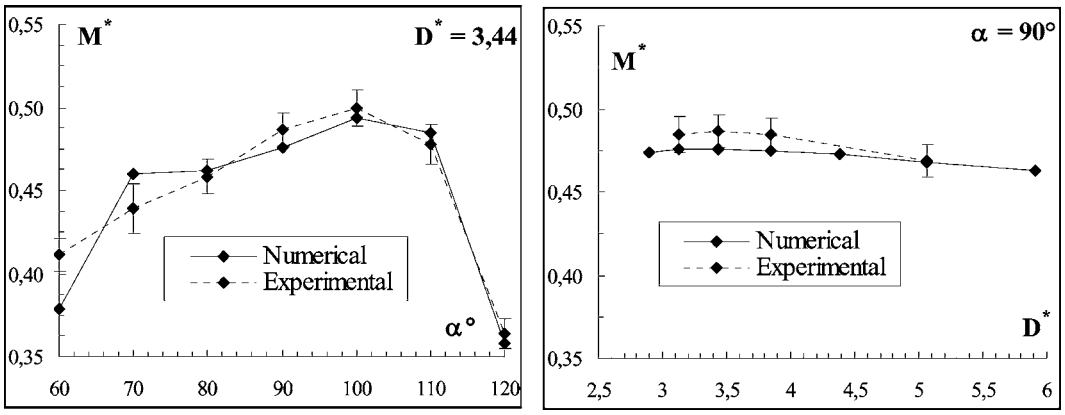

Fig. 16 Total torque

modeling, this mechanism is not predicted. Thus, the torque and thrust values provided by calculation are smaller than the experimental ones.

Figures 16(*b*) and 17(*b*) show torque and thrust variations versus the jet size D^* for a jet incidence $\alpha=90$ deg. Numerical and experimental values fit very well. Both the torque and thrust values are maximum near $D^*=3.44$. This value matches approximately the optimum jet size of the corresponding Pelton turbine.

Figures 19(*a*) and 19(*b*) show the deficit of thrust (compared to an ideal bucket) for the jet size and incidence variations, respectively. On each figure, the contributions of the edge and the cutout (relation (4)) are presented. In Fig. 19(*a*), the edge loss presents a minimum equal to 0.06 at the 100 deg value of incidence and never exceeds 0.105. The cutout loss begins below 80 deg and above 90 deg, and increases strongly. This behavior confirms the previous analysis on the flow-rate loss close to the cutout.

In Fig. 19(*b*), at the 90 deg fixed α value, the cutout losses occur only for the large jet diameters though they always exist in the experiments (see Fig. 6). The edge losses decrease with D^*. For the smaller jets (higher D^*), this decrease is attributed to an increase of the outlet mean velocity at the edge. This is a typical viscous effect [14].

For the larger jets ($D^*<3.44$), the edge loss becomes nearly constant. This last tendency is explained by the kinematic deviation of the fluid compared to the edge bucket. In order to evaluate this deviation, one considers, in projection in the reference plane, the angle between the velocity vector and the plane tangential to the bucket surface at the edge. In the case of the largest jet ($D^*=2,9$), numerical calculation provides a deviation angle value of

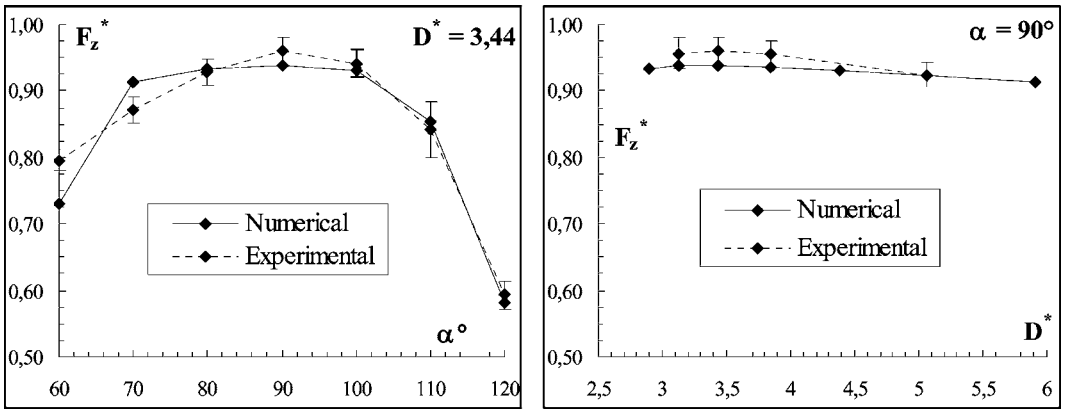

Fig. 17 Total thrust

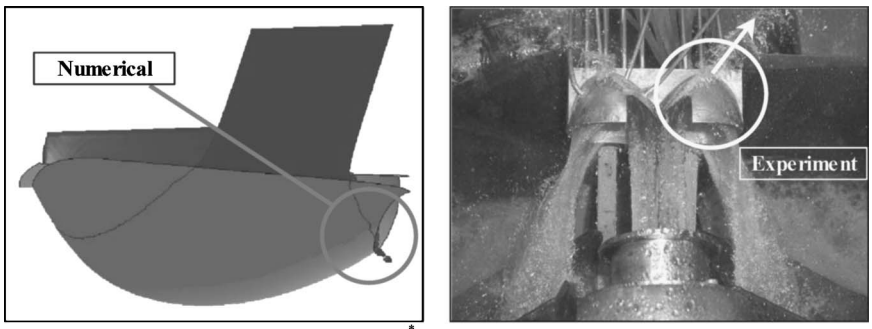

Fig. 18 Cut-out leakage flow rate

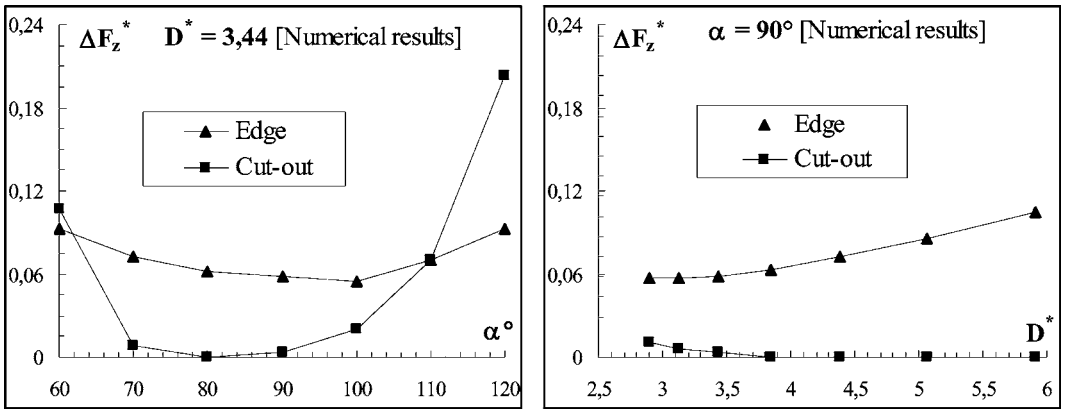

Fig. 19 Edge and cut-out losses

~2 deg everywhere on the edge except for the bucket ends. Using the relation (5) in the 2D configuration case, this deviation angle gives an increase of 0.01 on the edge loss $[\Delta F_z^*]_{\text{Edge}}$.

Figure 20 represents the graph of four nondimensional magnitudes $F_{z\text{num}}^*$, $F_{z\text{exp}}^*$, F_{zv}^*, η_P, versus D^*. The first two correspond to the previous forces obtained, respectively, by the calculation and the experiment. The η_P magnitude indicates the Pelton turbine efficiency.

The nondimensional force $F_{zv}^*=1-\Delta F_{zv}/F_{z\max}$ is obtained by keeping only the contribution ΔF_{zv} of the viscous effects to the total loss. Assuming that the boundary layer is little disturbed by the D^* variation and that the wetted surface variation remains weak, ΔF_{zv} is constant and not varying with D^*. Keeping $F_{z\max}$ proportional to D^2 (relation (3)), one obtains a relative viscous loss proportional to D^{*2} and thus $F_{zv}^*=1-KD^{*2}$. On the assumption that, at point P_0 ($D^*=5.07$), the losses are only of viscous origin, we have $F_{zv}^*(P_0)=F_{z\text{exp}}^*(P_0)$. This relation determines the coefficient K. It is noteworthy that the second experimental point (corresponding to $D^*=3.84$) isexactly on the curve F_{zv}^*. This point separates the inertial zone from the viscous zone. With regard to the inertial zone, the experimental force $F_{z\text{exp}}^*$ decreases more quickly than F_{zv}^*, indicating that the inertial losses become nonnegligible. They consist of losses due to the cutout leakage flow as well as losses due to the streamlines deviation at the bucket edge exit.

The efficiency curve of the Pelton turbine was translated so that the experimental point P_0 belongs to it. It is similar to the curve of the experimental force $F_{z\text{exp}}^*$, in particular, with a maximum in the same area. This similarity occurs owing to the fact that, in the case of a moving bucket, the maximum of thrust is obtained when the jet is approximately perpendicular to the bucket. Finally, it is noted that the curve of the calculated force $F_{z\text{num}}^*$ presents also a maximum at the same point but with weaker gradients. That comes owing to the fact that the losses estimation is not precise enough. In practice, it is difficult to reduce the viscous losses. In fact, the maximum of thrust is limited by the curve F_{zv}^*.

Consequently, if one wants to reduce the losses by a change of design of the fixed bucket, the zone of action to be considered can be only in the inertial zone. In the case of the nominal point ($D^*=3.44$), the maximum gain of thrust is ~1%. This gain quickly increases in the case of larger jets: for example, it is ~3% when $D^*=3.1$.

In consideration of the previous analysis, the results relative to the fixed bucket provide a first approximation of what one could gain on the efficiency of a Pelton turbine.

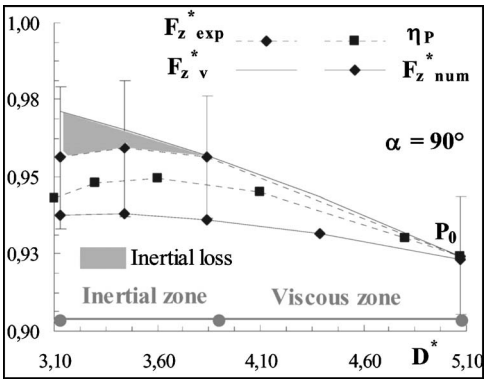

Fig. 20 Non-dimensional forces and Pelton turbine efficiency

4 Conclusion

The experimental and numerical studies of the flow inside a Pelton turbine bucket under fixed configuration were carried out. Three heads, four jet diameters, and seven bucket incidences were studied in order to cover the range of the operating parameters of a rotating bucket.

The main results of the experimental study are as follows:

- The various tested heads lead to the same pressure distribution on the bucket. Moreover, not any particular influence of the head on the jet trajectory inside the bucket was noted.
- In all the cases of varying incidence and diameter, a leakage flow through the cutout is found. This flow rapidly increases with the jet diameter and the bucket incidence.
- The pressure force origin is located near the reference plane except for high incidences for which it moves toward the cutout.

The numerical modeling quality is demonstrated by the low relative difference between the calculated pressures and the measured pressures. It is confirmed by the results regarding the total of all forces. The only difference relates to the flow rate loss through the cutout. The numerical process underestimates this leakage flow rate. The analysis of the losses of force due to the edge and the cutout reveals the following points:

- The losses due to edge slightly vary with the incidence and decrease with the jet diameter.
- The losses due to cutout are lower than those due to edge except at extreme incidences, at which they become dominating.

The variation in losses according to the jet diameter highlights an inertial zone (large diameters) and a viscous zone (small diam-

eters). In the inertial zone, the analysis shows that one can gain from 1% to 3% on the bucket thrust.

The analogy between the Pelton turbine efficiency and the force on the fixed bucket shows that one can carry out part of the optimization of the rotating bucket using analysis performed on the fixed bucket (edge and cutout). The rotating bucket optimization requires further study relating to the following phenomena: unsteady feeding, centrifugal and Coriolis forces, back splashing, and interference of the sheets of water.

Nomenclature

C_p = pressure coefficient
D = jet diameter (m)
D_p = Pelton diameter (m)
F_z = Pelton driving force (N)
$F_{z\max}$ = Pelton driving force for an ideal bucket (N)
g = Gravitational acceleration (m/s^2)
H_d = dynamical head (m)
H_n = net head (m)
H_s = static head (m)
L_a = bucket width (m)
L_{S1} = distance between the measurement axis of M and the reference plane (m)
L_1 = distance between the measurement axis of M and the Pelton wheel axis (m)
M_w = moment of force F_z relative to the Pelton wheel axis (Nm)
M = moment of force F_z relative to the measurement axis (Nm)
$M_{w\max}$ = moment M_w for an ideal bucket (Nm)
p = pressure (Pa)
p_{atm} = atmospheric pressure (Pa)
Q = jet cross section flow rate (m^3/s)
S = cross section of the narrowed jet (m^2)
U = jet velocity (m/s)
Ox = x-axis perpendicular to the plane of symmetry (m)
Oy = y-axis perpendicular to the reference plane (m)
Oz = z-axis perpendicular to the edge plane (m)
s = curvilinear abscissa in the reference plane (m)
y_p = near-wall distance (m)
α = incidence angle (deg)
ϕ_d = orifice diameter (m)
μ = water molecular viscosity (Kg/(m s))
ρ = water density (Kg/m^3)
u_τ = shear velocity (m/s)
χ = water volume fraction
$D^*=L_a/D$ = nondimensional magnitude of the jet diameter
$F_z^*=F_z/F_{z\max}$ = nondimensional driving force
$M^*=M/M_{w\max}$ = nondimensional moment of force
$x^*=x/L_a$ = nondimensional abscissa
$y^*=y/L_a$ = nondimensional ordinate
$z^*=z/L_a$ = nondimensional z value
s^* = nondimensional curvilinear abscissa
$Y^+=\rho y_p u_\tau/\mu$ = dimensionless near-wall distance
$\text{Re}=\rho UD/\mu$ = Reynolds number
$\text{Fr}=U/\sqrt{gL_a}$ = Froude number

References

[1] Parkison, E., Garcin, H., Bissel, C., Muggli, F., and Braune, A., 2002, "Description of Pelton Flow Patterns With Computational Flow Simulations," Symposium Hydropower, Turkey, Nov 4–7, 2002.
[2] Nakanishi, Y., Kubota, T., and Shin, T., 2002, "Numerical Simulation of Flows on Pelton Buckets by Particle Method: Flow on a Stationary/Rotating Flat Plate," *Proceedings of 21th IAHR Symposium*, Lausanne, Sept. 9–12.
[3] Agarwal, A. K., Harwani, L. K., and Ramanthan, S. M., 2004, "Custom Design of Pelton Turbine Runners by Numerical Analysis," *Proceedings of 22th IAHR Symposium*, Stockholm, June 29–July 2.
[4] Kubota, T., Jinjong, X., Masuda, J., and Nakanishi, Y, 1998, "Numerical Analysis of Free Water Sheet Flow of Pelton Buckets," *Proceedings of 19th IAHR Symposium*, Singapore, pp. 316–329.
[5] Liu, J., Han, F., Kubota, T., and Masuda, J., 2002, "Effect of Free Jet Enlargement on the Bucket Flow in Pelton Turbine," *Proceedings of 21th IAHR Symposium*, Lausanne, Sept. 9–12.
[6] Hana, M., 1999, "Numerical Analysis of Non-Stationary Free Surface Flow in a Pelton Bucket," Ph.D. thesis, Norwegian University of Science and Technology.
[7] Janetzky, B., Göde, E., Ruprecht, A., Keck, H., and Schärer, C., 1998, "Numerical Simulation of the Flow in a Pelton Bucket," *Proceedings of 19th IAHR Symposium*, Singapore, pp. 276–283.
[8] Avellan, F., Dupont, Ph., Kvicinsky, S, Chapuis, L., Parkinson, E., and Vullioud, G., 1998, "Flow Calculations in Pelton turbines—Part 2: Free Surface Flows," *Proceedings of 19th IAHR Symposium*, Singapore, pp. 294–305.
[9] Kvicinsky, S., Kueny, J. L., and Avellan, F., 2002, "Numerical and Experimental Analysis of Free Surface Flow in a 3D Nonrotating Pelton Bucket," *Proceedings of 9th International Symposium on Transport Phenomena and Dynamics of Rotating Machinery*, Honolulu, Feb. 10–14.
[10] Traversaz, M., Leroy, P., Zoppé, B., and Maitre, T., 2002, "Numerical Study of Pelton Bucket Flow: Comparison of FLUENT and CFX Results," *Proceedings of 21th IAHR Symposium*, Lausanne, Sept. 9–12.
[11] Kvicinsky, S., 2002, "Méthode d'Analyse des Écoulements 3D à Surface Libre: Application aux Turbines Pelton," Thèse No. 2526, Ecole Polytechnique Fédérale de Lausanne.
[12] Mack, R., and Moser, W., 2002, "Numerical Investigation of the Flow in a Pelton Turbine," *Proceedings of 21th IAHR Symposium*, Lausanne, Sept 9–12.
[13] Mack, R., Aschenbrenner, T., Rohne, W., and Farhat, M., 2004, "Validation of Bucket Flow Simulation Using Dynamic Pressure Measurements," *Proceedings of 22th IAHR Symposium*, Stockholm, June 29–July 2.
[14] Zoppé, B., 2004, "Simulation Numérique et Analyse de l'Écoulement dans les Augets des Turbines Pelton," Thèse, Institut National Polytechnique de Grenoble, France.
[15] Kubota, T., 1989, "Observation of Jet Interference in 6-Nozzle Pelton Turbine," J. Hydraul. Res., **27**(6), pp. 753–767.
[16] Perrig, A., Farhat, M., Avellan, F., Parkison, E., Garcin, H., Bissel, C., Valle, M., and Favre, J., 2004, "Numerical Flow Analysis in a Pelton Turbine Bucket," *Proceedings of 22th IAHR Symposium*, Stockholm, June 29–July 2.
[17] Ishii, M., 1975, *Thermo Fluid Dynamic—Theory of Two-Phase Flow*, Collection Direction Etudes Recherches Electrécité de France, Eyrolles.
[18] Hirt, C. W., and Nichols, B. D., 1981, "Volume of Fluid Method for the Dynamics of Free Boundaries," J. Comput. Phys., **39**(1), pp. 201–225.
[19] Youngs, D. L., 1982, "Time Dependent Multi-Material Flow With Large Fluid Distorsion," *Numerical Methods for Fluid Dynamics*, Academic Press, New York.
[20] Cousteix, J., 1986, "Three-Dimensional and Unsteady Boundary Layer Computation," Annu. Rev. Fluid Mech., **18**, pp. 173–196.

Fei Qin

Liming Chen

School of Mechanical Engineering
and Applied Electronics Technology,
Beijing University of Technology,
Beijing 100022,
P.R.C.

Ying Li
China Huanqiu Contracting
and Engineering Corporation,
Beijing 100029,
P.R.C.

Xiaofeng Zhang
China Continuous Casting Technology
Engineering Co.Ltd,
Beijing 100081,
P.R.C.

Fundamental Frequencies of Turbine Blades With Geometry Mismatch in Fir-Tree Attachments

Geometry mismatch in a turbine blade root, which arose in manufacturing process or caused by wearing out during service, leads to contact conditions changed in fir-tree attachments. As a result, shifting of the fundamental frequencies and redistribution of stress in the blade base possibly cause failure of the blade. A three-dimensional finite element model of a blade and its fir-tree attachments have been constructed and analyzed by taking into account contact nonlinearity in the attachments and large deformation effect of the blade. The geometry mismatch was introduced into the finite element model by defining gaps between two contact surfaces in the attachments. The influence of gap configuration and gap size on contact and fundamental frequencies was investigated. Results showed that gap configuration has significant influence on fundamental frequencies of the blade, especially on its bending modes. Gap size has little influence on the frequencies but significant influence on the contact status and thus changes stress distribution in the attachments. The results also suggest that modeling contact behavior in fir-tree attachments is necessary to obtain more accurate fundamental frequencies.
[DOI: 10.1115/1.2187523]

1 Introduction

Failure of the blade is one kind of severe accident causing the turbine to shut down in power plants and in other turbine used industries. Among those various factors which lead a blade to failure, resonance of working blades is regarded as the most important [1]. Generally the dangerous resonant vibration should be avoided by tuning in design stage of a blade based on accurate computation of its fundamental frequencies. Therefore accurate computation of the fundamental frequencies is critical. Nowadays, the finite element method (FEM) is widely used for this kind of work. When FEM is used, there are two main factors playing dominant roles in the computation accuracy. The first is that the finite element model must be as exact as possible to model geometry and mechanical behaviors of all kinds of members attached to the blade, such as shroud, wire, etc. The second is the modeling of a blade root.

There are several techniques to model the blade root. Usually a cantilever beam model in which the blade is completely fixed at its root is used to evaluate frequencies. This model is very simple but usually overestimates the stiffness of the blade and thus produces higher frequencies. Actually blades are secured to disk via contacting between blade roots and disk grooves. For example, fir-tree blade root shown in Fig. 1 is often used in steam turbines. The blade and the disk are assembled or joined as fir-tree attachments. Therefore the constraint at the blade root is not completely rigid because contact behavior exists in the attachments and the blade and disk are all deformable. In order to obtain more realistic frequency, engineers need to modify the frequency from the cantilever beam model by multipling a coefficient determined according to their experiences or some experimental results [2]. Even though the FEM is used, the blade base is often cut off for simplicity and then completely fixed constraints are applied to the cutting section. One improvement is to replace the completely rigid constraints by spring-like supports which have compliance coefficients of actual blade roots [3,4]. However, the compliance coefficients are difficult to find in engineering.

A more realistic way to compute frequencies of a blade is to take into account the contact behavior in the attachments directly. This technique has such advantages as being realistic, being able to model contact directly, and does not need one to determine the compliance coefficients. The technique also provides the possibility to model geometry mismatch in the attachments. Manufacturing geometry mismatch does exist in blade roots or disk grooves. It has influence on the fundamental frequencies of the blade because it changes the contact status. Besides, after a period of service, wear and tear also results in geometry mismatch in the attachments and changes the contact condition, and thus shifts blade frequencies from those designed ones. This situation is dangerous because the shifted frequencies might fall into resonant. Reference [5] investigated the influence of this kind of geometry mismatch on static stress. Sinclair et al. [6] looked into the contact stress in dovetail attachments and provide a detailed discussion on the effect of contact element size. However, up to the present time we have not found any report about the influence of attachment geometry mismatch on fundamental frequencies of blades.

In this research, a numerical computation method for blade fundamental frequency and contact algorithm are presented first. After that, a three-dimensional finite element model of a real blade and its fir-tree attachments are constructed. Contact nonlinear behavior in the attachments and nonlinear behavior from large deformation of the blade are included in the finite element model. Geometry mismatch is introduced into the model by assigning gaps to the contact surfaces. Four gap configurations and four gap sizes are implemented to investigate influence of geometry mismatch on fundamental frequencies. Finally some conclusions are drawn.

2 Fundamental Frequency Computation of a Blade

2.1 Equations for Free Vibration of a Blade. After discreting a blade using three-dimensional finite elements, its free vibration equation of the numerical model can be written as

$$\mathbf{M}\ddot{\mathbf{u}} + \mathbf{K}\mathbf{u} = 0 \tag{1}$$

where $\mathbf{M}$ is mass matrix, $\mathbf{K}$ the stiffness matrix, and $\mathbf{u}$ the node displacement vector. Solving this eigenvalue problem, the funda-

Contributed by the Turbomachinery Division of ASME for publication in the JOURNAL OF TURBOMACHINERY. Manuscript received September 19, 2005; final manuscript received February 6, 2006. Review conducted by M. Montgomery.

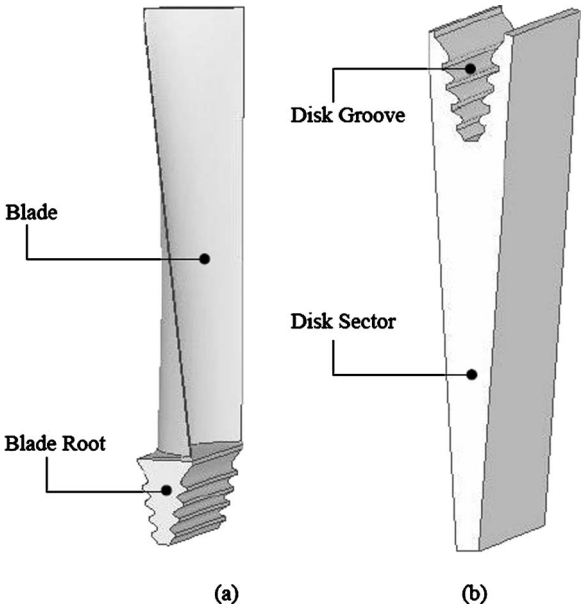

Fig. 1 3-D geometric models of (*a*) steam turbine blade with fir-tree root and (*b*) one sector of a disk

mental frequencies and mode shapes of the blade can be obtained.

For rotating blade, its stiffness increases with increasing rotating speed due to centrifugal effect, which is called centrifugal stiffness effect. As a result, the frequencies calculated from Eq. (1) vary with the speed. Moreover, long skewed blades used in end stages of a steam turbine undergo large deformation under the centrifugal loads so that nonlinear deformation behavior arises. In order to take into account the centrifugal stiffness effect and the large deformation, a nonlinear static analysis of the blade must be carried out first to find the final equilibrium state and its stiffness matrix $\mathbf{K}$ in Eq. (1) prior to solving Eq. (1). The equation used for the nonlinear static computation is [7]

$$(\mathbf{K}_0 + \mathbf{K}_{\mathrm{NL}} - \mathbf{K}_c)\mathbf{u} = \mathbf{Q}_c - \mathbf{F}_N \tag{2}$$

where $\mathbf{K}_0$ is the initial stiffness matrix of the model, $\mathbf{Q}_c$ the inertia load vector, $\mathbf{F}_N$ the contact force vector which will be described in detail in the following section, $\mathbf{K}_c$ the stiffness by the centrifugal stiffness effect, $\mathbf{K}_{\mathrm{NL}}$ the stiffness due to the large deformation, which can be computed by

$$\mathbf{K}_{\mathrm{NL}} = \frac{\partial^2 V_{\mathrm{NL}}}{\partial \mathbf{u} \partial \mathbf{u}} \tag{3}$$

where V_{NL} is the strain energy calculated by taking into account the large deformation effect.

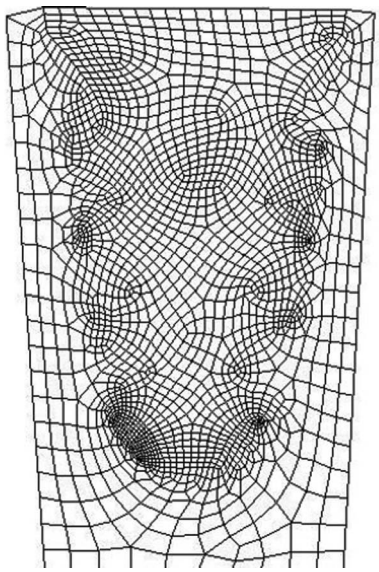

Fig. 2 Finite element mesh of the fir-tree attachments, in which fine elements are placed around the contact surfaces

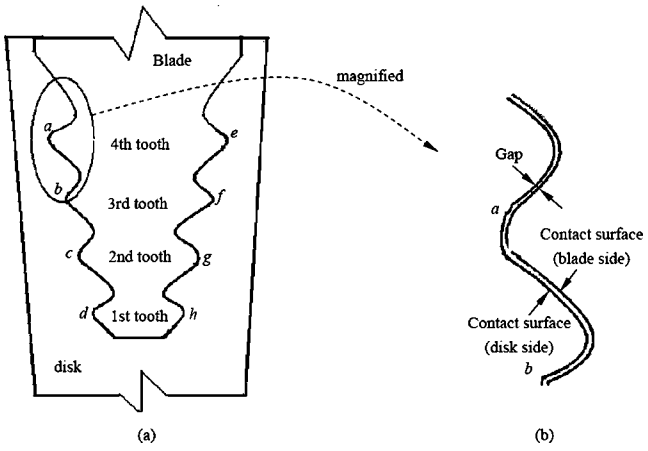

Fig. 3 Sketches of (*a*) fir-tree attachments and (*b*) definition of the gap. Some points are tagged as *a*, *b*, ..., *h* in order to observe contact status in the attachments.

2.2 Contact Algorithm for Fir-tree Attachments. In order to investigate the influence of geometry mismatch on the frequencies, contact behavior in fir-tree attachments must be modeled. There are several contact algorithms within the context of the finite element method such as the penalty function method [8], the Lagrange multiplier method [9], and the augmented Lagrange method [10].

The penalty function method introduces the contact condition, which is stated as the contacted bodies cannot penetrate each other, into its equation as a penalty. When the penalty function method is used, it is helpful to reduce the penetration if greater contact stiffness is used but this might lead to an ill-conditioned equation system and result in convergency difficulty and cause high frequency oscillation of the contact force [8].

The Lagrange multiplier method introduces the contact conditions directly into the variational function and hence additional equations are added to guarantee no penetration between the contact bodies. Introducing the multiplier causes the system stiffness matrix asymmetry, and this needs more iteration time to converge than the penalty function method.

The augmented Lagrange method is one kind of penalty function method but with penetration controlling. In order to satisfy the contact condition the method exerts properly defined forces normal to the contact surface to make the penetration limited in a specific tolerance. The contact force is defined as

Table 1 Definition of gap configurations

	Gap for each tooth (mm)				
	Tooth number				
Gap configuration	First	Second	Third	Fourth	Upper the fourth tooth
I	0	0.05	0.05	0.05	0.05
II	0	0	0.05	0.05	0.05
III	0	0	0	0.05	0.05
IV	0	0	0	0	0.05
Zero gap	0	0	0	0	0

Table 2 Frequencies under different mesh densities

Mesh density	Number of elements	Frequencies (Hz)				
		First	Second	Third	Fourth	Fifth
Coarse	9401	130.03	248.60	424.05	496.30	535.06
Medium	17,261	129.43	246.79	422.88	494.02	533.79
Fine	35,272	129.01	245.66	422.72	493.35	532.59

$$\mathbf{F}_N = \min(0, \mathbf{K}_N \mathbf{g} + \boldsymbol{\lambda}_N^{(i+1)}) \tag{4}$$

where $\mathbf{K}_N$ is a specific contact stiffness of the contact elements, i.e., the penalty factor, g is the penetration, $\lambda_N^{(i+1)}$ is the Lagrange multiplier for $(i+1)$th iteration, which can be found by

$$\boldsymbol{\lambda}_N^{(i+1)} = \begin{cases} \boldsymbol{\lambda}_N^{(i)} + \alpha \mathbf{K}_N \mathbf{g} & |\mathbf{g}| \geqslant \varepsilon \\ \boldsymbol{\lambda}_N^{(i)} & |\mathbf{g}| < \varepsilon \end{cases} \tag{5}$$

where ε is a specific penetration tolerance, α is an inner calculated factor, usually $\alpha < 1$.

After iterating a specific time, if the penetration is still greater than ε, the contact stiffness of each contact element will be augmented through the Lagrange multiplier. This procedure is repeated until the penetration is less than ε. The algorithm can be described in more detailed as following five steps

(a) $\mathbf{K}_N$ is given, and $\lambda_N^{(1)} = \lambda_N^{(0)} + \alpha \mathbf{K}_N \mathbf{g}$;
(b) $\lambda_N^{(i+1)}$ is obtained by Eq. (5)
(c) Find $\mathbf{F}_N$ by Eq. (4);
(d) Obtain $\mathbf{u}$ by solving Eq. (2);
(e) If $|\mathbf{g}(\mathbf{u})| < \varepsilon$, end the iteration otherwise repeat steps (b) to (e).

When the iteration is accomplished, the contact pressure was obtained, the final equilibrium state of the blade and the contact status in the attachments can be determined by solving Eq. (2). Substituting the stiffness matrix $\mathbf{K}$ of the final equilibrium state into Eq. (1) and solving the eigenvalue problem, the fundamental frequencies and mode shapes of the blade will be obtained.

3 The Finite Element Model for Fir-tree Attachments

3.1 FEM Model. A real steam turbine blade and a sector of disk being modeled and analyzed are shown in Figs. 1(*a*) and 1(*b*). The fir-tree root blade has a height of 660 mm and has four root teeth.

Young's modulus and Poission's ratio of the blade and disk are 200 GPa and 0.22, respectively. Density of the blade material is 7800 kg/m^3 and service rotational speed of the turbine is 3000 rpm.

Part finite element mesh of the fir-tree attachments is shown in Fig. 2. In the FEM model zero displacement constraints were applied to the bottom, left and right sides of the disk. For the blade, only the back side of its first tooth was constrained by zero displacement in the axial direction of the turbine. Brick 8-node elements were used to model the blade and the disk. In the current study, linear elasticity behavior is presumed for the whole model. Surface to surface contact elements were defined in all contact surfaces in the attachments.

3.2 Gap Definition. In this research geometry mismatch in the fir-tree attachments is characterized by gaps between the contact surfaces of blade and disk, as shown in Fig. 3. According to Ref. [5] a gap of 0.05 mm was assigned but it might occur in a different spot of the contact surface in the attachments. Four different gap configurations labeled as I, II, III, and IV in Table 1 were investigated. As shown in Table 1, for gap configuration I, except for the first tooth, all other contact surface in the attachments is assigned a gap of 0.05 mm. Configuration II is defined as that the first two teeth are assigned zero gaps while the other 0.05 mm. Similarly defined configurations III and IV can also be found in Table 1. Assigning zero gaps to all contact surfaces defines the configuration zero-gap in Table 1.

Eight points are picked up as observing points. They are labeled $a, b, \ldots, h$ in order to describe the contact status conveniently, as shown in Fig. 3.

3.3 Mesh Density Check. In order to check influence of mesh density on the computed frequencies, three different mesh densities (coarse, medium, and fine) and their outputs are listed in Table 2. Gap configuration I was used for all three mesh cases. The coarse, medium, and fine mesh have 9401, 17,261 and 35,275 brick 8-node elements, respectively. Comparison in Table 2 shows that the first five fundamental frequencies are not so sensitive to the finite element mesh. However the computation of the fine mesh has taken three times more CPU time than the medium mesh. For this reason in the following computation the medium mesh was used for all.

4 Result Discussions

4.1 Frequencies under Different Gap Configurations. The computed contact status for the four different gap configurations was listed in Table 3 where code "0" denotes not contacted and "1" denotes contacted. For configurations I and II, there are three points not contacted while for configuration IV, all points are contacted. From configurations I to IV the contact status varied from partial contacted to full.

Once the contact status was obtained by the nonlinear static analysis as described in Sec. 2.2, frequencies of the blade were calculated for all four gap configurations. For the sake of comparison, frequencies of the same blade but for two different blade root models were computed too. One model is tagged as "fixed" in

Table 3 Contact status under different gap configuration "1" = contacted, "0" = not contacted

Gap configuration	Observing points							
	a	*b*	*c*	*d*	*e*	*f*	*g*	*h*
I	1	0	0	1	1	0	1	1
II	0	0	1	1	1	0	1	1
III	0	1	1	1	0	1	1	1
IV	1	1	1	1	1	1	1	1

Table 4 Frequencies for different models and gap configuration (Hz)

	Root model		Gap configuration			
Frequency	Fixed	Zero-Gap	I	II	III	IV
First	161.83	158.54	129.43	144.26	151.49	155.03
Second	303.73	288.43	246.79	263.87	275.63	281.54
Third	502.61	431.05	422.88	427.65	429.24	430.59
Fourth	612.13	501.23	494.02	496.53	498.65	499.23
Fifth	733.32	639.01	533.79	593.20	624.22	633.66

Table 4 in which the root is fixed completely like the cantilever beam model. The other model is labeled as "zero-gap" in which the contact in the attachments was modeled but the gaps for all contact surfaces were assigned to be zero values. That is, for this model the gap configuration zero-gap listed in Table 1 was used.

All the computed first five order frequencies are listed in Table 4. The results indicate that the most used "fixed" model produced the highest fundamental frequencies among all the root models and the gap configurations. Comparing with the zero-gap model, its first and second frequencies are 2.1% and 5.3% higher while the third and fourth frequencies are more than 15% higher. This suggests that in the computation of fundamental frequencies fixing a blade at its root is much less accurate for third and higher order frequencies.

For gap configurations I–IV, all the calculated frequencies are lower than that of the zero-gap model. Figure 4 shows frequency changes of the four gap configurations compared with the zero-gap model. Here the frequency change Δf is defined as

$$\Delta f^{(i)} = \frac{f^{(i)}_{(\text{gap})} - f^{(i)}_{\text{Zero-Gap}}}{f^{(i)}_{\text{Zero-Gap}}} \times 100 \tag{6}$$

where $f^{(i)}_{(\text{gap})}$ is the ith order frequency of gap configuration I, II, III, or IV, $f^{(i)}_{\text{zero-gap}}$ is the ith order frequency of the zero-gap model.

As shown in Fig. 4, Δf has a significant trend that becomes less and less as the gap configuration changes from I to IV. The first, second, and fifth order frequencies are more sensitive to the gap configuration than the third and fourthones. Checking their mode shapes found that the first mode is a tangential bending vibration mode, the second is axial bending, the third is bending-twisting, the fourth is twisting and the fifth is another axial bending mode. It indicates that the geometry mismatch in the attachments affects bending vibration modes more than twisting modes.

Table 5 lists the results of cases where at one time only one of the four teeth has non-zero gap. Those gap configurations have little influence on the frequencies.

4.2 Influence of Gap Size. Taking the gap configuration III as an example, four different gap sizes—0.05, 0.10, 0.15, and 0.20 mm—were modeled to investigate their influence on contact status and frequencies. Table 6 lists the contact status for different gap sizes. The results show that with the increase of gap size, the contact status changes from complete contacted to partial contacted. Table 7 indicates that the gap size has little influence on frequencies.

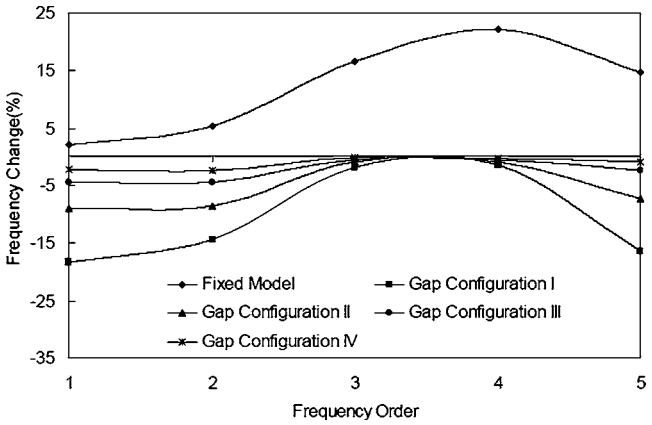

Fig. 4 Frequency change Δf (in percentage) compared with the zero-gap model

5 Conclusions

Influence of geometry mismatch in fir-tree attachments on fundamental frequencies was investigated by 3-D finite element contact analyses. Frequencies for various gap configurations and gap sizes were computed and compared with the fixed blade model and the zero-gap model. Some conclusions drawn include the following.

(1) The more spots where the mismatch exists, the greater the influence on the frequencies. Within this research, for the

Table 5 Frequencies with single tooth gap (Hz)

	Tooth number with the non-zero gap			
Frequency	1	2	3	4
First	156.33	157.46	157.56	157.58
Second	284.90	286.32	286.43	286.54
Third	430.22	430.81	430.88	430.90
Fourth	500.45	500.78	500.84	500.86
Fifth	633.67	636.34	636.62	636.63

Table 6 Influence of gap size on contact status "1"=contacted, "0"=not contacted

	Observing points							
Gap size (mm)	*a*	*b*	*c*	*d*	*e*	*f*	*g*	*h*
0.05	1	1	1	1	1	1	1	1
0.10	0	1	1	1	1	1	1	1
0.15	0	1	1	1	1	1	1	1
0.20	0	1	1	1	0	1	1	1

Table 7 Frequencies under different gap sizes (Hz)

	Gap size (mm)			
Frequency	0.05	0.10	0.15	0.20
First	151.49	151.52	151.52	151.54
Second	275.63	275.65	275.66	275.67
Third	429.24	429.26	429.31	429.33
Fourth	498.65	498.68	498.68	498.68
Fifth	624.22	624.24	624.27	624.27

gap configuration I, its first order frequency is 18% lower than that of the zero-gap model in which there is no geometry mismatch.

(2) The mismatch affects bending vibration modes more than twisting modes.
(3) If the mismatch takes place only at one tooth of a blade, it has little influence on the frequencies. The mismatch size has insignificant influence on the frequencies.
(4) Simply fixing a blade at its root produces inaccurate fundamental frequencies, especially for higher order modes. It is necessary to model the contact behavior in fir-tree attachments if more accurate frequencies are needed.

References

[1] Rao, A. D., 1993, "A Feasibility and Assessment Study for FT4000 Humid Air Turbine (HAT)," EPRI RP-3251–05.
[2] Huang, B. H., Bai, Yu, and Niu, W. D., 2001, *The Theory and Structure of Steam Turbine*, China Electricity Press, Beijing (in Chinese).
[3] Ye, S. J., and Yan, H. Q., 1988, "Vibration Analysis of Gas Turbine Blades with Considering Root Flexibility," Power Eng. J., **6**, pp. 33–38.
[4] Xiao, J. F., and Zhu, B. T., 1999, "Sensitivity Study of Blade Vibration Characteristics to the Boundary Condition of Blade Root," Thermal Power Generation (in Chinese), **26**, pp. 29–32.
[5] Ma, A. X., Wang, S. M., and Lu, W. L., 2001, "The Study of Contact Problem of the Turbine Blade Contacting System by Mismatches." Mechanical Science and Technology (in Chinese), **20**, pp. 369–370.
[6] Sinclair, G. B., Cormier, N. G., Griffin, J. H., and Meda, G., 2002, "Contact Stress in Dovetail Attachments: Finite Element Modeling," ASME J. Eng. Gas Turbines Power, **124**, pp. 182–189.
[7] Wriggers, P., and Vu, V. T., 1990, "Stein E. Finite Element Formulation of Large Deformation Impact-Contact Problems With Friction," Comput. Struct., **37**, pp. 319–331.
[8] Sano, N. A., 1986, "A Penalty Function Type of Virtual Work Principle for Impact Contact Problem of Two Bodies," Bull. JSME, **29**, pp. 3701–3709.
[9] Hughes, T. J., Taylor, R. L., Sackman, J. L., Curnier, A., and Kanoknukulchai, W., 1976, "A Finite Element Method for a Class of Contact-Impact Problems," Comput. Methods Appl. Mech. Eng., **8**, pp. 249–276.
[10] Jiang, L., and Robert, J. R., 1988, "Combined Lagrangian Multiplier and Penalty Function Finite Element Technique for Elastic Impact Analysis," Comput. Struct., **30**, pp. 1219–1229.

Separation and Transition Control on an Aft-Loaded Ultra-High-Lift LP Turbine Blade at Low Reynolds Numbers: Low-Speed Investigation

Xue Feng Zhang[1]
e-mail: george.zhang@pwc.ca

Maria Vera

Howard Hodson

Whittle Laboratory,
University of Cambridge,
Madingley Road,
Cambridge CB3 0DY, UK

Neil Harvey
Compression Systems,
Rolls-Royce plc,
Mail Code PCF-2,
P.O. Box 31,
Derby DE24 8BJ, UK

An experimental study was conducted to improve the performance of an aft-loaded ultra-high-lift low-pressure turbine blade known as U2 at low Reynolds numbers. This was achieved by manipulation of the laminar-turbulent transition process on the suction surface. The U2 profile was designed to meet the targets of reduced cost, weight and fuel burn of aircraft engines. The studies were conducted on both low-speed and high-speed experimental facilities under the unsteady flow conditions with upstream passing wakes. The current paper presents the low-speed investigation results. On the smooth suction surface, the incoming wakes are not strong enough to suppress the separation bubble due to the strong adverse pressure gradient on the suction surface and the low wake passing frequency, which allows the separation between the wakes more time to re-establish. Therefore, the profile losses of this ultra-high-lift blade are not as low as conventional or high-lift blades at low Reynolds numbers even in unsteady flows. Two different types of passive separation control devices, i.e., surface trips and air jets, were investigated to further improve the blade performance. The measurement results show that the profile losses can be further reduced to the levels similar to those of the high-lift and conventional blades due to the aft-loaded nature of this ultra-high-lift blade. Detailed surveys of the blade surface boundary layer developments showed that the loss reduction was due to the suppression of the separation underneath the wakes, the effect of the strengthened calmed region and the smaller separation bubble between wakes.
[DOI: 10.1115/1.2187524]

Introduction

In modern high bypass ratio engines the LP turbine can account for as much as one-third of total engine weight. Given its importance in such machines, much research work has focused on reducing aerofoil count (increasing lift coefficient) while trying to mitigate any loss of performance. The latter arises because there is a strong trade-off between LP turbine efficiency and engine fuel burn. See Harvey et al. [1] and Ashpis [2].

The work described in this paper lies within one strand of LP turbine aerodynamic research—namely how to increase the lift coefficients of subsonic blading with conventional levels of stage aerodynamic loading. However, it should be noted that there are other significant branches of activity in the overall LP turbine field. Vazquez et al. [3] describe an extensive study of high stage loading LP turbines, which result from reducing the numbers of stages relative to conventional machines. Taking this one step further, Malzacher et al. [4] present results from testing of their high speed LP turbine. This is for an engine application in which a geared fan allows significantly higher LP shaft speeds, relative to conventional, giving low stage loadings—the resulting blading is low turning, transonic and low Reynolds number.

Turning back to "high lift" (but otherwise conventional) subsonic LP turbine blading, Hourmouziadis [5] was the first to describe in detail the issues around their design. He showed that a primary element is the behavior of laminar separation bubbles on the suction surface—inevitable for blading with high levels of back surface diffusion at low Reynolds numbers. Subsequent to this the overwhelmingly important discovery has been that the key to achieving good aerodynamic performance in the engine is the control of boundary layer separation and transition on these aerofoil surfaces in the *unsteady* environment. Seminal research in this area includes that of Halstead et al. [6] and Schulte and Hodson [7].

A useful overview of the topic of wake-blade interaction is given by Hodson [8]. The wake shed from the upstream blade row behaves as a negative jet in the downstream blade row. Near the suction surface, it has an accelerating front part and a decelerating rear part with the highest turbulence occurring in the wake center. As the wakes convect through the blade passage, they impinge on the blade suction surface and induce boundary layer transition in a bypass mode. The wake-induced turbulent region, as well as the calmed region that follows it, suppress the separation bubble. The calmed region, which is laminar-like in nature, is mainly responsible for the loss reduction. The understanding of this unsteady flow behavior has been incorporated into the design of a family of high-lift and ultra-high-lift profiles, see Curtis et al. [9], Schulte and Hodson [10], Howell et al. [11], and Brunner et al. [12]. These have been used in the BR715 series of LP turbines, Haselbach et al. [13].

Further increases in the blade lift such as that of the so-called ultra-high-lift blades (with the aim of reducing cost, weight and fuel burn) result in a higher adverse pressure gradient on the blade suction surface. The incoming wakes may not be strong enough to suppress the large separation bubble, especially at low Reynolds

[1]Current address: Turbine Aerodynamics, Pratt & Whitney, Canada.

Contributed by the International Gas Turbine Institute (IGTI) of ASME for publication in the JOURNAL OF TURBOMACHINERY. Paper presented at the ASME Turbo Expo 2005: Land, Sea and Air, Reno, NV, June 6–9, 2005, Paper No. GT2005-68892. Manuscript received October 1, 2004; final manuscript received February 1, 2005. IGTI Review Chair: K. C. Hall.

numbers. Haselbach et al. [13] showed that the performance of their ultra-high-lift blades were more Reynolds number dependent. They reported a 0.5% efficiency drop for an ultra-high-lift LP turbine blade at high altitude, although it had a performance that was similar to a high-lift blade at sea level. Research continues into wake-blade interaction at very high levels of back surface diffusion, such as that of Schobeiri [14] and Houtermans [15]. Even so, it increasingly appears that to apply ultra-high lift LP turbine blades successfully at low Reynolds numbers requires additional loss reduction mechanisms other than "simply" wake-blade interaction.

Several studies of separation control for use in LP turbines have been reported recently, active as well as passive. Recent examples of active systems include Bons et al. [16], Sondergaard [17], and Volino [18] who used steady and pulsed air jets to control the separation on the suction surface of a high-lift LP turbine blade. McAuliffe and Sjolander [19] concluded that active flow control was only useful when the baseline (non-flow control) aerofoil is stalled. Passive systems were also studied by Volino [20], who successfully employed 2-D rectangular trip wires with different heights to control the boundary layer separation and transition on an LP turbine blade over a wide range of Reynolds numbers. Lake et al. [21] and Sieverding et al. [22] also studied the possibility of loss reduction by different surface elements, such as trip wires and dimples. Byerley et al. [23] investigated the use of Guerney flaps but found that they increased losses at engine representative Reynolds numbers. However, all these studies were conducted in steady flow.

The work reported in this paper has focused on the use of passive means of enhancing the beneficial effects of wake passing. It follows on from the first such study of the effects of surface roughness under unsteady flow conditions by Ramesh et al. [24], who tested the effect of distributed roughness on the total pressure losses on the ultra-high-lift profile U2 with upstream unsteady wakes. They showed that a strip of sand-grain roughness could bring about a substantial reduction in the total pressure loss under the unsteady flow conditions. The loss reduction came from the larger extent of the calmed region and the smaller separation bubble between wakes.

Zhang and Hodson [25] conducted an extensive parametric study of the type, size, and location of surface trips on an ultra-high-lift LP turbine blade known as T106C in both steady and unsteady flows. They concluded that the combined effects of the surface trips and the unsteady wakes could further reduce the profile losses of the ultra-high-lift LP turbine blade. The optimum surface trip does not induce transition immediately but hastens the transition process in the separated shear layer underneath the wakes and between them. The earlier boundary layer transition helped to reduce the separation bubble between the passing wakes. The smaller separation underneath the passing wake prevents the formation of the wake's negative jet induced rollup vortex and also reduces the high loss caused by the wake induced separated boundary layer transition on the ultra-high-lift blade. The loss reduction occurred in spite of the negative effects of having a larger turbulent-wetted area due to the earlier transition between wakes. Therefore, to minimize losses, they also recommended that the ultra-high-lift LP turbine blades should be aft-loaded.

The object of the current study is to improve the performance of the aft-loaded ultra-high-lift LP turbine blade U2 in unsteady flow at low Reynolds numbers by using different passive boundary layer control methods including surface trips and air jets and to further understand the flow physical mechanisms involved.

Experimental Facilities and Techniques

The study was conducted in a low-speed linear cascade with a moving bar system. A schematic of the linear cascade test rig is shown in Fig. 1. The linear cascade contains six U2 blades, which were designed by Howell et al. [11]. The high-speed version of this profile has a lift coefficient of 1.22. In order to match the velocity (Mach number) ratio across the high and low speed cascade and therefore the normalized isentropic velocity (Mach number) distributions, the inlet angle of the low-speed profile is reduced (Vera et al. [26]). The parameters of the bar-passing cascade facility are presented in Table 1.

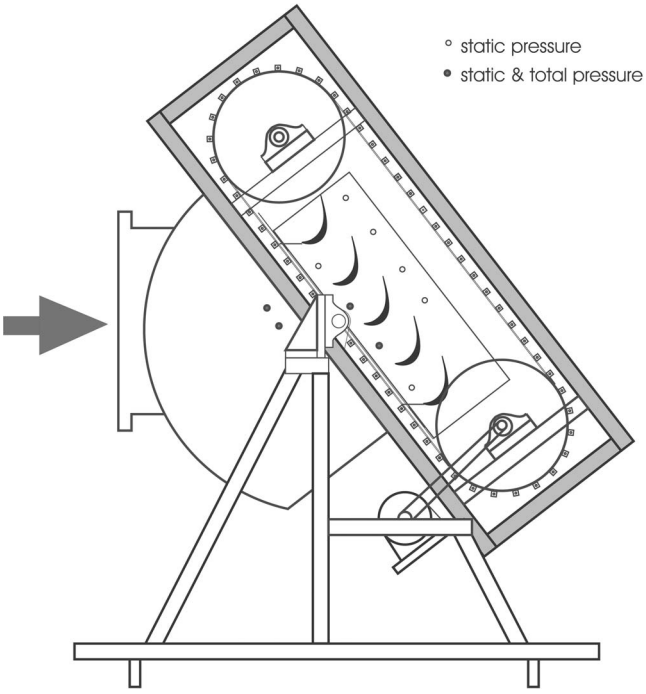

Fig. 1 Schematic of U2 cascade with moving bars

The U2 blade is an aft-loaded profile with a pitch to axial chord ratio of 1.16 and a Zweifel lift coefficient (Z_w) of 1.22. The diffusion factor, $D_v=(V_{\max}-V_{2is})/V_{2is}$, is about 0.4. The tested Reynolds numbers based on the blade chord (C) and the isentropic exit velocity (V_{2is}) covered a range between 100,000 and 210,000. The residual freestream turbulence intensity at the inlet to the test section is 0.5%. To create more realistic LP turbine conditions, the freestream turbulence intensity can be increased to 4.0% by placing a bi-planar, cylindrical rod, turbulence grid in the inlet to the test section.

Moving bars with a diameter of 2.05 mm were used to generate the upstream passing wakes. A flow coefficient ($\phi=V_{1x}/U_{\text{bar}}$) of 0.75 was chosen to be representative of a repeating stage of the U2 profile. The bar pitch can be changed to achieve different reduced frequencies ($f_r=U_{\text{bar}}/s^*_{\text{bar}}C/V_{2is}$). In the current study, the

Table 1 U2 bar-passing linear cascade details

Chord (C)	[mm]	136.0
Axial Chord (C_x)	[mm]	117.8
Blade pitch (s)	[mm]	136.3
Suction surface length (S_0)	[mm]	189.0
Design inlet flow angle (α_1)	[°]	30.46
Design exit flow angle (α_2)	[°]	62.86
Zweifel coefficient (Z_w)		1.22
Bar diameter (d_{bar})	[mm]	2.05
Axial distance: Bars to LE (d)	[mm]	70.0
Bar pitch (s_{bar})	[mm]	189.6
Flow coefficient (ϕ)		0.75
Reduced frequency (f_r)		0.45 & 0.9

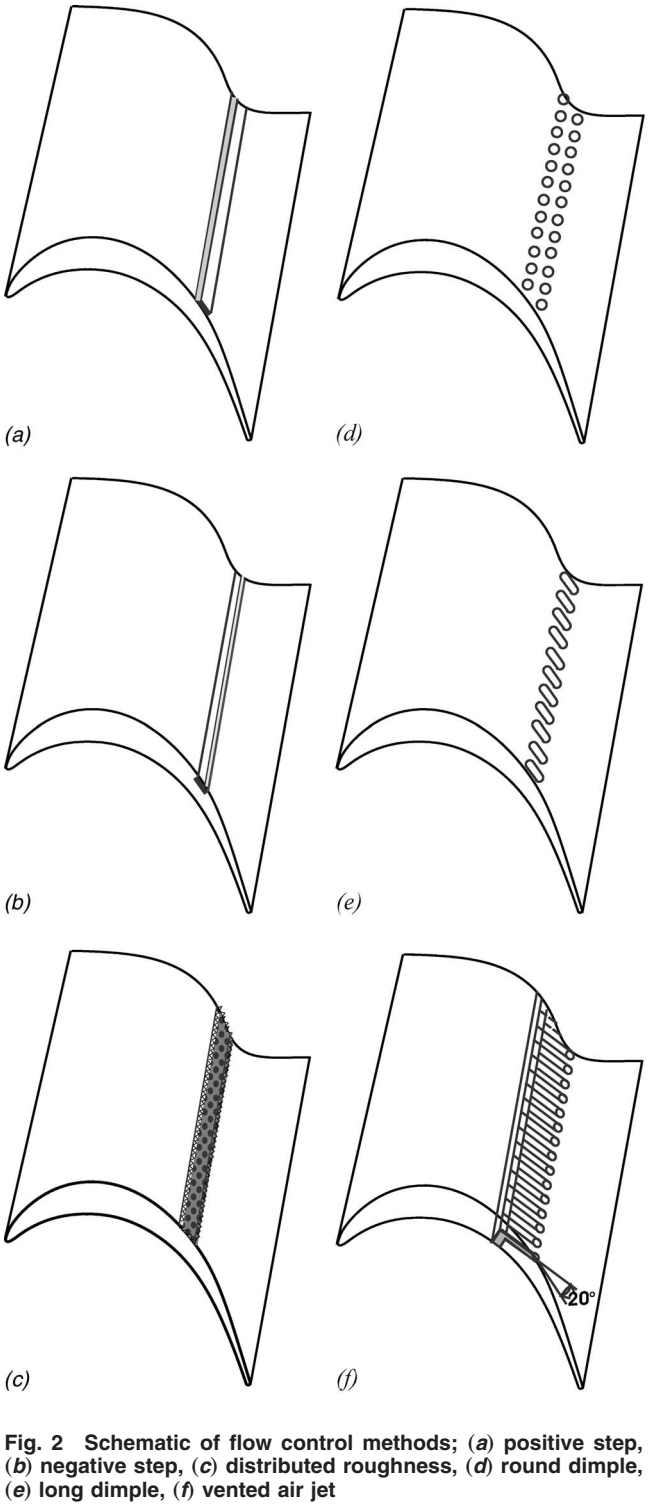

Fig. 2 Schematic of flow control methods; (*a*) positive step, (*b*) negative step, (*c*) distributed roughness, (*d*) round dimple, (*e*) long dimple, (*f*) vented air jet

reduced frequencies of 0.45 and 0.9 were used. In this paper, the discussion is focused on $f_r=0.45$ except where specified differently.

Two different types of separation control methods are used in the current study. They are surface trips and the vented air jets as shown schematically in Fig. 2. The surface trips include positive (i.e., raised) rectangular step, negative (i.e., recessed) rectangular step, distributed roughness, two rows of round-hole dimples and one row of long-hole dimples. The parameters of the flow control devices are presented in Table 2. The location of surface trips, which is with reference to the trailing edge of the surface treatment, is at 64% S_0, i.e., the mid-way between the suction velocity peak and the separation point based on the results of a parametric study by Zhang and Hodson [25].

Table 2 Parameters of flow control devices

	Height k (mm)	k/S_0 (%)	Diameter or width (mm)	Pitch (mm)	Ref. Code
Positive step	0.26	0.14	5.7		SS26
Positive step	0.17	0.09	5.7		SS17
Negative step	−0.26	0.14	5.7		SS-26
Distributed roughness			9.5		#120
Round dimple	−0.29	0.15	5.7	11.4	RD29
Long dimple	−0.29	0.15	5.7	11.4	LD29
Vented hole			1.1	3	Air jet

The positive step was mounted on the blade suction surface by using thin double-sided tape. The height (k) listed in Table 1 includes the tape thickness. The negative straight rectangular step was achieved by covering the rest of the suction surface with plastic sheet of an appropriate thickness. The distributed roughness was produced by gluing #120 graded aluminum oxide grains directly to the blade surface rather than using sand paper to avoid the additional effect due to the thickness of the paper. The round dimples have two rows of round holes with diameter of 5.7 mm and pitch of 11.4 mm. The pitch of the two rows is 11.4 mm and the two rows of holes were half-pitch staggered. The long dimple was produced by connecting two streamwise round holes, which have diameter of 5.7 mm and pitch of 11.4 mm, with straight lines. The pitch of the long dimples is 11.4 mm.

A schematic of the vented blade is shown in Fig. 2(*f*). The air was vented from the blade pressure side to the suction side to control the boundary layer development. The exit-holes, with a diameter of 1.1 mm, were located at 64% S_0 with a pitch of 3 mm. An injection angle of 20° was used in order to minimize the jet mixing loss. A 4 mm wide slot was cut at 50% S_0 on the pressure surface to meet the holes drilled from the suction surface and was used to supply the air. At this location on the pressure surface, the isentropic velocity is very low.

The time mean blade surface static pressure distributions were measured by using a Scanivalve system. The surface static pressure coefficient, C_p, is defined as the ratio of the local dynamic head to the isentropic exit dynamic head, i.e.

$$C_p = \frac{P_{01} - P_s}{P_{01} - P_{s2}} = \left(\frac{V}{V_{2\text{is}}}\right)^2 \tag{1}$$

where P_{01} is the inlet total pressure, P_{s2} is the exit static pressure, and P_s is the measured surface static pressure. V and $V_{2\text{is}}$ are the measured local isentropic surface velocity and isentropic exit velocity, respectively.

A constant temperature anemometry system was used for hot-wire measurements. The boundary layer was surveyed by a Dantec single-wire 55P15 boundary layer probe. The hot-wire was calibrated in accordance with a modified form of King's law. The effects of the ambient temperature drift were taken into account using the correction of Bearman [27]. Hot-wire traverses were performed normal to the blade surface. In order to account for the influence of the surface proximity on the cooling of the heated wire, the Cox correction [28] was applied to the measured data.

The profile loss coefficients of the linear cascade were determined from a series of Pitots placed upstream of the bars and the Neptune probe traverses that were conducted at $0.5C_x$ downstream of the blade trailing edge. The profile loss values given here include the measured loss and the mixing loss. In the case of unsteady flow conditions, the change in stagnation pressure across the moving bars is subtracted from the total loss to give the profile losses (Schulte and Hodson [10]).

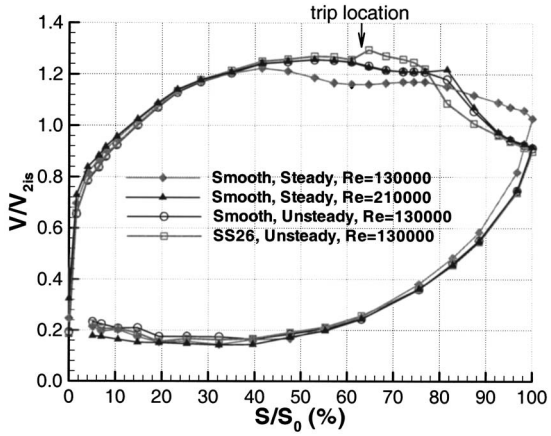

Fig. 3 Surface velocity distributions at Tu=0.5%

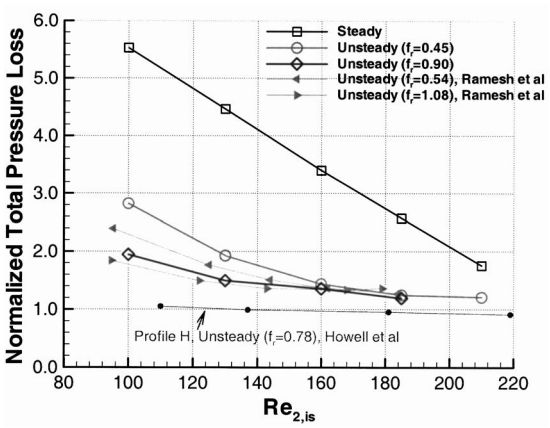

Fig. 4 Total pressure loss coefficients on smooth surface, Tu=0.5%

Results and Discussions

Smooth Surface. To provide a reference, the boundary layer development on the smooth suction surface of the ultra-high-lift LP turbine blade U2 was studied first. The surface velocity distributions were measured at several different Reynolds numbers between 100,000 and 210,000. Figure 3 presents selected measurement results at Tu=0.5%. In the steady flow, i.e., without unsteady passing wakes, the boundary layer on the suction surface separates from the blade surface due to the large deceleration on the rear part of the blade. At low Reynolds numbers (such as that at Re=130,000), the separated boundary layer failed to reattach before the blade trailing edge. The effect of the open separation bubble is to globally change the surface velocity distribution on the suction surface. Only at Reynolds number above 185,000 does the separated boundary layer reattach before the blade trailing edge. At Re=210,000, the suction peak occurs at around 57% S_0 and the boundary layer separates at about 70% S_0. Although the total diffusion on the aft portion of the suction surface is large on this ultra-high-lift blade, the local pressure just after the suction velocity peak changes gradually.

The time-mean surface velocity distribution under unsteady flow conditions at Re=130,000 is also presented in the figure. The periodic passing wakes force the separated boundary layer to reattach before the blade trailing edge. The time-mean separation point occurs at about 70% S_0 and reattachment occurs round 93% S_0. The open separation in the steady flow is turned into an unsteady closed separation bubble by the periodic wake passing. Nevertheless, the effect of time-mean separation bubble is still large on the surface velocity distribution of this ultra-high-lift blade.

Figure 4 presents the total pressure loss coefficients under different flow conditions. The loss coefficients are made nondimensional by the loss of an high-lift profile H reported by Howell et al. [29] at Re=130,000 with unsteady inflow (f_r =0.78). Two sets of data from Ramesh et al. [24] are also plotted in the figure. In the case of steady flow, the large separation on the suction surface results in high profile losses especially at low Reynolds numbers. The passing wakes in the unsteady flow help to reduce the profile losses significantly at the low Reynolds numbers. The benefit from the unsteady wakes at high Reynolds numbers is not as much as that at low Reynolds numbers since the separation is not that large in the steady flow at high Reynolds numbers. Increasing the wake passing frequency (f_r=0.54, 0.9, and 1.08) can further reduce the profile losses at low Reynolds numbers. This is because the low wake passing frequency allows the separation more time to reestablish before the next wake arrival. The measured losses at different reduced frequencies cross at about Re=160,000. At higher Reynolds numbers, increasing the wake passing frequency will cause more losses. This agrees well with the observation of Schulte and Hodson [10], who suggested that there was an optimum wake passing frequency for each flow condition. This is especially true at low Reynolds numbers where the impact of the wakes is greatest.

To study the boundary layer developments on the smooth suction surface, hot-wire boundary layer measurements were conducted at Re=130,000 under unsteady flow conditions with f_r =0.45. Figure 5 presents raw velocity traces at Y_n=0.2 mm at selected streamwise locations. The abscissa is the time normalized by the wake passing period and the ordinate is arbitrary but the scale is constant for all traces. The center of the wake, which travels at the local freestream velocity, is indicated as line A in the figure. The leading edge and trailing edge of the wake, which are defined as the peak and valley caused by the negative jet behavior of the wake in the freestream velocity (see later and also in Fig. 12), are indicated as line L and line T. Another two velocity trajectories line B and line C, which correspond to 50% and 30% of the freestream velocity, respectively, are also plotted in the figure.

The variations in the raw velocity traces show that the wake turbulence induced transition first occurs shortly downstream of the time-mean separation point at 71% S_0, indicated by the spikes occurring after the wake center, where the highest turbulence in the wake is. The wake turbulence induced transitional or turbulent region is followed by the calmed region, which is indicated by the relaxing signal. The calmed region breaks down into turbulent

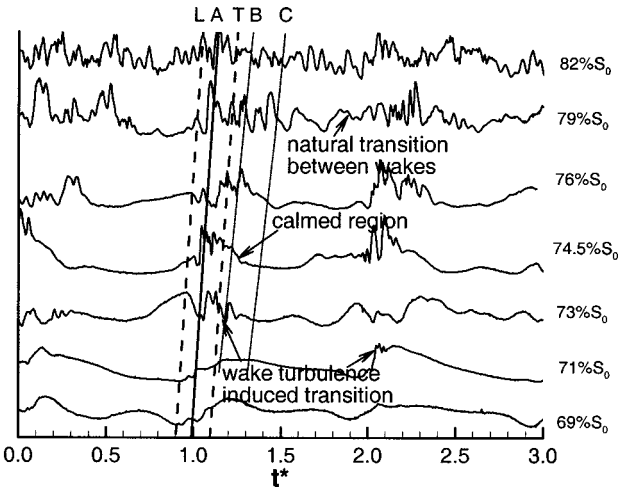

Fig. 5 Raw velocity traces at Y_n=0.2 mm on smooth surface, Re=130,000, Tu=0.5%

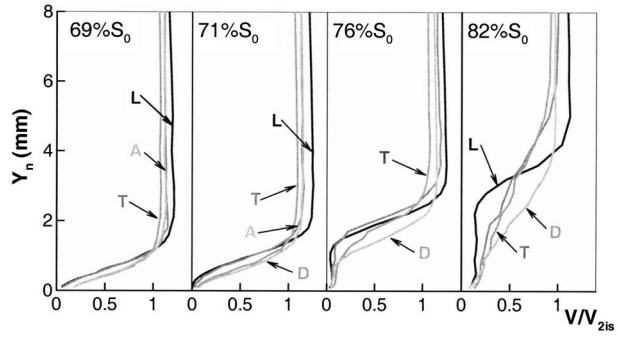

Fig. 6 Normalized velocity profiles on smooth surface at Re =130,000, Tu=0.5%

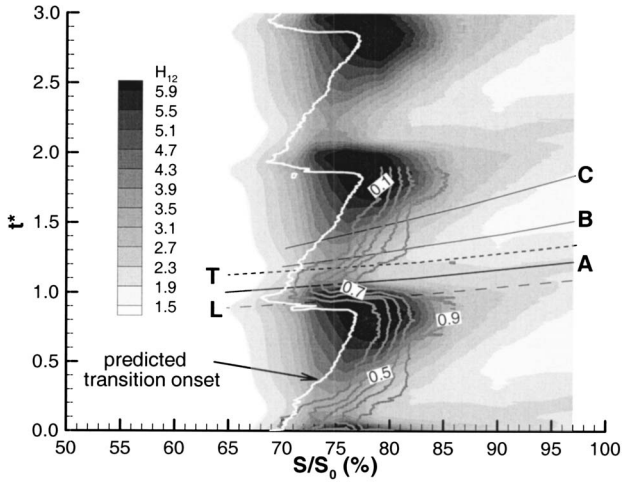

Fig. 7 Shape factor H_{12} (solid contour) and intermittency (contour lines) on smooth surface at Re=130,000, Tu=0.5%

flow further downstream at 76% S_0. The calmed region only exists for a short distance due to the strong adverse pressure gradient. This agrees with the observation by Zhang and Hodson [25] on another ultra-high-lift blade known as T106C. The natural transition of the separated boundary layer between wakes occurs at 79% S_0 indicated by the spikes in the raw signal before the leading edge of the wakes. This is downstream of the transition onset location in the calmed region. The onset of boundary layer transition will be further discussed below.

The ensemble-averaged boundary layer velocity profiles, which are normalized by the isentropic exit velocity V_{2is}, are presented at selected streamwise locations in Fig. 6. At each location, profiles at selected instants (t^*) are indicated by letters, which are consistent with those in Fig. 5. Profiles L, A, and T are those at the wake's leading edge, center, and trailing edge respectively. Profile D occurs midway between line B and line C in Fig. 5, i.e., in the calming affected region. The wake's negative jet behavior can be clearly identified in the freestream at all locations. The wake has an accelerating leading edge (profile L) and a decelerating trailing edge (profile T).

Figure 6 shows that the boundary layer at 69% S_0 is attached and that the magnitude of velocity variation in the boundary layer is smaller than that in the freestream. The velocity profiles at 71% S_0 show that the boundary layer at this location only separates for a part of the whole wake passing period. Although the highest turbulence in the freestream occurs at the center of the wakes, profile A, which corresponds to the wake's center, is still separated. On the other hand, profile T, which is at the wake's trailing edge, is attached. This agrees well with the observation in Fig. 5 that the wake induced transition lags behind the wake's center. Profile D occurs in the calmed region. It is also attached. Due to the strong adverse pressure gradient on this ultra-high-lift blade, the boundary layer at 76% S_0 separates during the whole wake passing period, even in the wake-induced turbulent region and the calming affected region. This only occurs on ultra-high-lift blades and is partly responsible for the high level of loss on this profile at low Reynolds numbers (discussed later). At 82% S_0 the boundary layer in the wake-induced turbulent region and calming affected region reattaches to the blade surface (see profiles T and D), while the rest of the boundary layer is still separated. The maximum boundary layer displacement occurs before the arrival of the wake center such as the profile L.

Figure 7 presents the distance-time (s-t) diagrams of the shape factor H_{12} (solid contour plot) and the calculated intermittency (contoured lines). The labeled lines in the figure are copied from Fig. 5. The shape factor shows the periodic change of the separation bubble on the suction surface in both length and height associated with the wake passing. The wake-induced transitional or turbulent region (between line A and line B) and the calmed region (between line B and line C) largely reduce the size of the separation bubble. However the separation is not completely suppressed although the separation point is delayed. The separation between wakes starts to re-grow after the trailing edge of the calmed region (line C) slowly until the arrival of the next wake.

The intermittency has been calculated from the hot-wire measurement data using the routine of Gostelow and Thomas [30]. This uses the velocity gradient ($\partial V/\partial t$) with a high-pass filter and a smoothing window to take into account the calmed region. The intermittency contours in Fig. 7 shows that the wake induces boundary layer transition around the time-mean separation point (71% S_0). Due to the high turbulence in the wake, the wake induces bypass transition, which is rapid. The calmed region's effect of delaying the boundary layer transition can be seen between line B and line C. However, the calmed region starts transition at 76% S_0 due to the strong adverse pressure gradient on this blade. Due to the low turbulence in the freestream, the onset of transition in the separated shear layer between wakes occurs further downstream. The slow transition process suggests that this is in a natural transition mode.

There is no evidence in the raw velocity traces in Fig. 5 and in the shape factor data of Fig. 7 to show that the wake's negative jet induced one or more roll-up vortices as reported in Stieger and Hodson [31] and Zhang and Hodson [25] on the T106 series blades. This is because on the U2 blade, the wake turbulence induced transition occurs shortly after the separation onset location. Therefore, the roll-up vortex mechanism related to the interaction between the wake's negative jet and the separated boundary layer does not have time/distance to develop.

Zhang and Hodson [32] argued that whether or not wake-induced transition occurs around the separation point was determined by the local Re_θ, which was directly related to the local normalized surface velocity gradient. On the U2 blade, the Re_θ at the separation point is about 250. In the case of their T106C ultra-high-lift blade, the strong local adverse pressure gradient caused by the sharp local deceleration after the suction velocity peak forced the laminar boundary layer to separate at a local Re_θ of 185 before it could develop further. Due to the low receptivity of the laminar boundary layer at separation, the wake turbulence could not induce transition close to separation, which allowed the formation of a roll-up vortex. Therefore, to avoid the formation of the roll-up vortex, the deceleration after the suction side velocity peak of the highly loaded profiles should be changed gradually to achieve a value of Re_θ of around 250 at the separation onset location. Then, the wake turbulence can induce transition around separation and the roll-up mechanism no longer exists.

Figure 7 also presents the predicted transition onset by using Drela's modified version [33] of Abu-Ghannam and Shaw [34] correlation

$$\mathrm{Re}_{\theta s}(H_{12}, n_{\mathrm{crit}}) = 155 + 89.0\left[0.25\tanh\left(\frac{10}{H_{12}-1} - 5.5\right) + 1\right] \times (n_{\mathrm{crit}})^{1.25} \quad (2)$$

where n_{crit} was based on a modified Mack correlation [35] due to Solomon et al. [36] to allow for higher turbulence levels

$$n_{\mathrm{crit}} = -8.43 - 2.4\ln[0.027\tanh(\mathrm{Tu}/2.7)] \quad (3)$$

The onset of the wake-induced transition is well predicted by the correlation except in the front part of the wake between line L and line A, where the largest separation bubble occurs. The transition onsets in the calmed region and the separated region between wakes are also over-predicted. This may be because in these regions, the boundary layer undergoes transition after separation and the correlation in Eq. (2) does not work well to predict the transition with such strong adverse pressure gradient as on this ultra-high-lift blade. Furthermore, the calmed region has a fuller and more stable profile. By using the measured values of H_{12}, the correlation does take the calming effect into account. However, despite this the transition onset is still predicted too early.

Surface Trips. Although the unsteady wakes can periodically reduce the size of the separation bubble on the smooth suction surface of U2 blades and consequently reduce the profile losses, the profile losses are still high compared to those of conventional and high-lift LP turbine blades, especially at low Reynolds numbers. This is due to the large suction side deceleration and the low wake passing frequency. Therefore, another separation control device is required to further reduce the profile losses. As recommend by Zhang and Hodson [25], the positive straight step, which has a height of 0.14% of the suction surface length was investigated first. The straight step is 0.26 mm high and is designated SS26.

The isentropic surface velocity distributions with surface trip SS26 at Re=130,000 under steady and unsteady flow conditions are also presented in Fig. 3. As indicated in the figure, the surface trip was placed at 64% S_0, i.e., at the midway between the suction peak and the separation onset location. Under steady flow conditions, there is no difference in the surface velocity distribution with and without surface trip. This is because the surface trip is located in the open separation bubble. Under unsteady flow conditions, the surface trip changes the surface velocity distribution locally. However, the hot-wire boundary layer measurement results show that the time-mean separation point is not changed by the surface trip. Compared to that on the smooth surface, the reattachment point with surface trip moves about 10% S_0 upstream resulting in a smaller separation bubble.

The total pressure loss coefficients presented in Fig. 8 show that in steady flow, since the surface strip is covered by the open separation bubble at low Reynolds numbers, it has no effect on the boundary layer development. At higher Reynolds numbers, the surface trip can reduce the size of the separation bubble and consequently reduces the profile losses. Under unsteady flow conditions, the combined effects of the surface trip SS26 and the unsteady wakes can further reduce the blade profile losses in the whole range of the tested Reynolds numbers (i.e., from 100,000 to 210,000). The benefit comes from both the unsteady wakes and the surface trip. The profile loss level on this ultra-high-lift blade with the combined effects of unsteady wakes and surface trip is comparable to that of the high-lift profile H from Howell et al. [29]. However, the U2 profile was designed to reduce the number of the blades in the blade-row by approximately 15% relative to the profile H.

The total pressure loss coefficients at elevated freestream turbulence intensity, Tu=4.0%, in the unsteady flow conditions with and without surface trip SS17 are plotted in Fig. 8 too. The straight step SS17 is the optimum one in this flow condition and

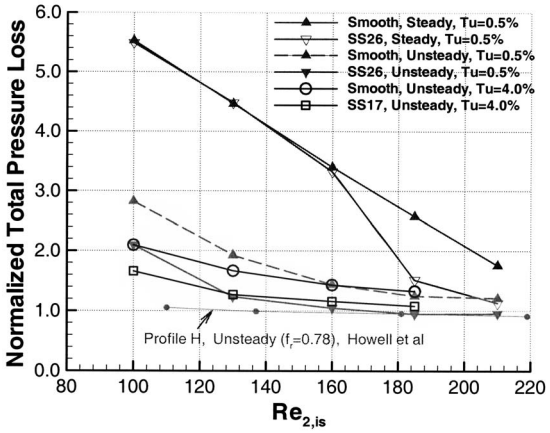

Fig. 8 Total pressure loss coefficients with positive rectangular steps SS26 and SS17

has a height of 0.17 mm. On the smooth surface, the elevated turbulence in the freestream enhances the boundary layer transition process and results in lower profile losses at lower Reynolds numbers. The loss coefficients with low and high freestream turbulence cross at Re=185,000. There is no benefit from the elevated freestream turbulence at Reynolds number higher than this. The surface trip SS17 can further reduce the profile loss at all tested Reynolds numbers. Although the profile losses at high Reynolds numbers are larger than those in low freestream turbulence flow, the blade performance is even better at low Reynolds number. This is very important for LP turbine blades in small aircraft engines working at high altitude.

The boundary layer on the suction surface with the surface trip SS26 in unsteady flow at Re=130,000 and Tu=0.5% was surveyed using hot-wire traverses to investigate the loss reduction mechanisms. Selected raw velocity traces at Y_n=0.2 mm at different streamwise locations are presented in Fig. 9. Due to the disturbances generated by the trailing edge of the surface trip, the wake turbulence induces transition before the time-mean separation onset location at 70% S_0. This can be seen in the raw traces at 67% S_0 and 69% S_0. Since the surface trip SS26 only hastens the transition process underneath the wakes and between them rather induces boundary layer transition immediately after itself, the calmed region still exists after the wake induced transitional or turbulent region. The earlier wake induced transition (in space) caused by the surface trip results in a wider (in time) wake-induced turbulent region and calmed region at the time-mean

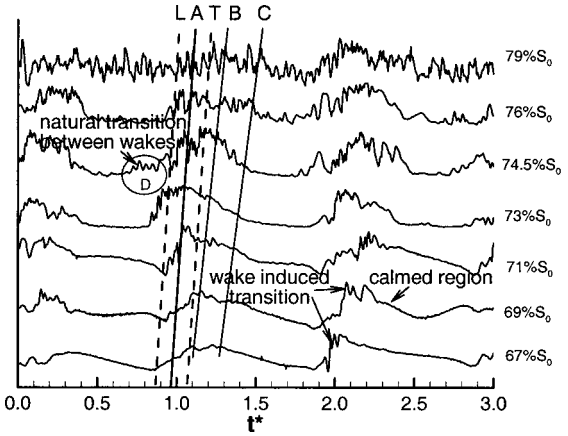

Fig. 9 Raw velocity traces at Y_n=0.2 mm with surface trip SS26 at Re=130,000, Tu=0.5%

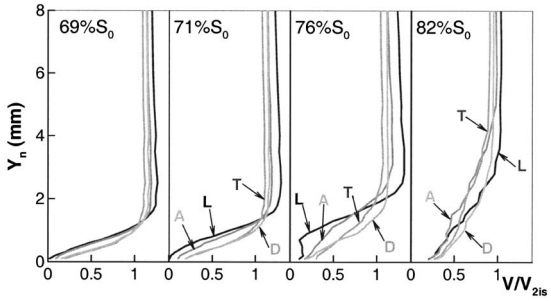

Fig. 10 Normalized velocity profiles with surface trip SS26 at Re=130,000, Tu=0.5%

separation region, which can prevent the boundary layer separation for more time and further reduce the profile losses. At 71% S_0, the turbulence in the front part of the wake (between L and A) is strong enough to induce boundary layer transition due to the disturbance after the surface trip. The calmed region breaks down at 73% S_0. Also, the transition of the separated flow between wakes occurs at about 74.5% S_0, which is 5% S_0 upstream of the location on the smooth surface.

The normalized ensemble-averaged boundary layer velocity profiles at selected streamwise locations are presented in Fig. 10. At 69% S_0, the velocity profiles are similar to those on the smooth surface at the same location although the raw traces show that the wakes start to induce transition at this location. Due to the earlier wake-induced transition caused by the surface trip, the profiles T and D, which are in the wake-induced turbulent region and the calmed region, respectively, are attached at 71% S_0. However, the boundary layer between the wakes, such as profile L, separates from the blade surface. At 76% S_0, where the maximum displacement of the time-mean separation occurs, the profiles L and A are separated but the displacements are much smaller than those on the smooth surface. The boundary layer in the wake-induced turbulent region and the calmed region is still attached. The boundary layer at 82% S_0 is attached during the whole wake passing period. Therefore, due to the effects of the surface trip, the wake-induced turbulent region and the calmed region completely suppress the separation.

The distance-time (s-t) diagrams of the shape factor H_{12} and the calculated intermittency with the surface trip SS26 at Re =130,000 under the unsteady flow conditions are presented in Fig. 11. The shape factor H_{12} clearly shows that in the whole wake passing period, both the length and the height of the separation bubble are reduced compared to those on the smooth surface shown in Fig. 7. The intermittency shows that the wake-induced transition starts upstream of the time-mean separation onset location because of the disturbances generated by the surface trip. However, the transition length does not seem to have changed. Due to the earlier (in space) wake-induced transition, the wake-induced turbulent region (between line A and line B) and the following calmed region (between line B and line C) completely prevent the separation. The separation starts to re-establish after the trailing edge of the calmed region and then remains almost constant until the arrival of the next wake. With the surface trip, the separated flow transition between wakes occurs much earlier than that on the smooth surface.

It is interesting to note that there is a well-defined frequency between the wake passing events in the region labeled D in Fig. 11. This frequency is double the calculated frequency of the most amplified Tollmein-Schlichting frequency (based on a correlation by Walker [37]) before the surface trip. This frequency can be detected in the raw velocity traces even earlier at 74.5% S_0. This suggests the transition in the separated shear layer between wakes is dominated by the Tollmein-Schlichting mechanism, which is amplified by the surface trip. Since the shape factor presented in

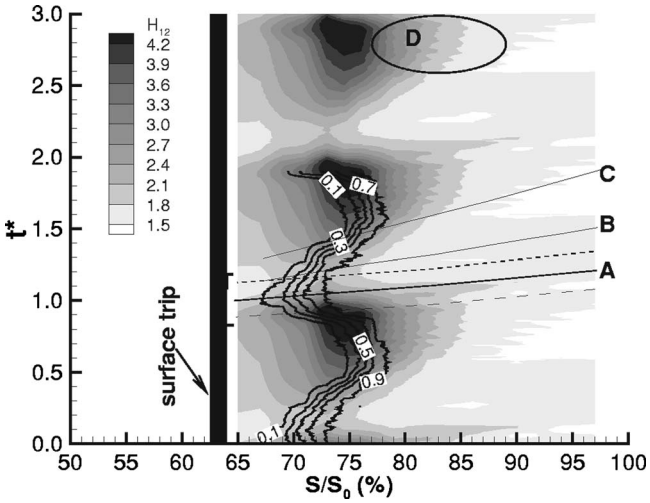

Fig. 11 Shape factor H_{12} (solid contour) and intermittency (contour lines) with surface trip SS26 at Re=130,000, Tu =0.5%

Fig. 11 is based on the ensemble-averaged data, the occurrence of the well-defined frequency means that the periodic passing wakes are controlling the phase at which the Tollmein-Schlichting wave appears in the separated shear layer. Stieger and Hodson [38] observed the same phenomenon on a flat plate, which was subjected to the same pressure distribution as that on the suction surface of a highly loaded LP turbine blade known as T106A. However, there is no such well-defined frequency appearing in the shape factor on the smooth surface of this ultra-high-lift blade shown in Fig. 7. This may imply that the wakes can only control the phase of the Tollmein-Schlichting waves when, in combination with the trips, the transition induced by the wakes is properly phase-locked. This in turn implies that a threshold of disturbances must be passed before this can occur.

The variations in time of the momentum thickness θ at the blade trailing edge on the smooth surface and with the surface trip SS26 at Re=130,000 under the unsteady flow conditions are presented in Fig. 12. An ensemble averaged freestream velocity trace is also plotted at the bottom of the figure to indicate the location of the wake. The variation of the momentum thickness at the trailing edge in one wake passing period shows the effects of the wake-induced turbulent region (between A and B), the calming-effected region (between B and C) and natural transition of the

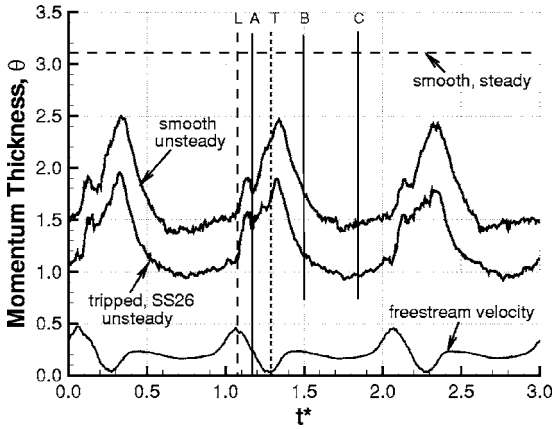

Fig. 12 Trailing edge momentum thickness with/ without surface trip SS26 at Re=130,000, Tu=0.5%

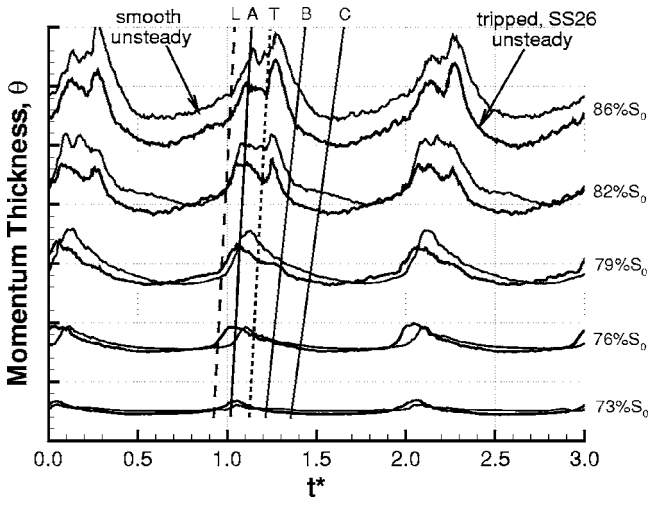

Fig. 13 Momentum thickness at selected locations with/without surface trip SS26 at Re=130,000, Tu=0.5%

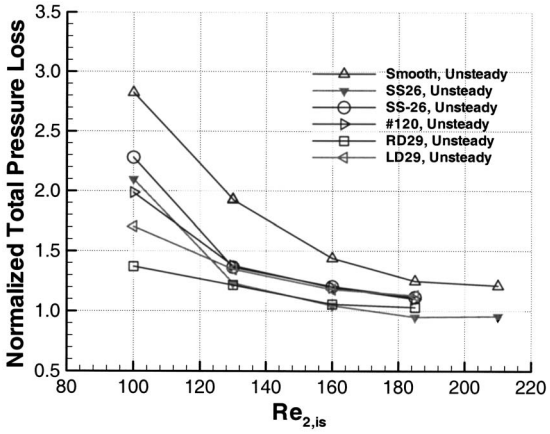

Fig. 14 Total pressure loss coefficients with different surface trips at Tu=0.5% in unsteady flow

separated boundary layer between wakes (after C) consecutively.

On the smooth surface, the wake induced turbulent region has a high level of momentum thickness. This is because the wake-induced transitional or turbulent flow still separates due to the strong adverse pressure gradient. Although the calmed region only exists for a short distance on this ultra-high-lift blade, its beneficial effects on the profile loss are still significant. The region between B and C, which is affected by the calming, has lower momentum thickness, which is one of the most important characters of the calmed region and accounts for the major loss reduction. After C, the momentum thickness increases slowly due to the re-establishing of the separation bubble after the calmed region. Compared to the measured result in steady flow, where the boundary layer fails to reattach before the blade trailing edge, the momentum thickness at the trailing edge was reduced significantly by the passing wakes. Therefore, on the smooth surface, the loss reduction under the unsteady flow condition results from the fact that the wake forces the separation reattach before the blade trailing edge and the beneficial effect of the calmed region.

As shown in Fig. 12, the trailing edge momentum thickness with surface trip SS26 is lower than that on the smooth surface during the whole wake passing period. This is the reason for the reduction in the blade profile losses. The disturbances after the surface trip SS26 allow the wake to induce the boundary layer transition earlier and completely suppress the separation underneath the wake. Therefore, the momentum thickness in the wake-induced turbulent region between A and B decreases. The wider (in time) and stronger calmed region following the earlier wake induced transition reduces the momentum thickness between B and C. The surface trip hastens the separated boundary layer transition between wakes and results in a lower momentum thickness. Due to the aft-loaded nature of this blade, the positive effect from the earlier transition between wakes is larger than the negative effect caused by the larger turbulent-wetted area. Therefore, the loss reduction with the combined effects of the surface trip SS26 and unsteady wakes comes from the suppression of the separation underneath the wake, the wider calming-effected region due to the earlier (in space) wake induced transition and the further reduced separation bubble between passing wakes.

The variations in time of the momentum thickness at selected streamwise locations with and without the surface trip SS26 are presented in Fig. 13 to show its development on the suction surface. The ordinate is arbitrary but the scale is constant for all cases. At 73% S_0 and 76% S_0, the momentum thickness in the wake-induced transitional region between A and B with surface trip SS26 is slightly higher than that on the smooth surface due to the earlier wake-induced transition caused by the additional disturbance generated by the surface trip. There is a clear phase shift between the two signals in this region. This is because with the surface trip, the turbulence in the front part of the wake is able to induce transition as indicated in the raw velocity traces in Fig. 9. At 79% S_0, the momentum thickness in the wake-induced transitional region on the smooth surface becomes higher than that with surface trip. This is because on the smooth surface the flow in the wake-induced transitional region still separated while, with surface trip, the boundary layer underneath the wake has already became turbulent and therefore attached. However, with surface trip SS26 the momentum thickness in the separated boundary layer between wakes is higher than that on the smooth surface. This is because the surface trip enhanced the separated boundary layer transition process between wakes. The growth rate of the momentum thickness in the wake-induced turbulent regions on the smooth surface is larger than that with surface trip, which results even larger difference in θ at 82% S_0. At this streamwise location, the calming effect after the wake-induced turbulent region with the surface trip is more significant. The momentum thickness in the separated boundary layer between wakes on the smooth surface increases to the similar level as that with surface trip due to the natural transition between wakes. At 86% S_0, the momentum thickness in the separated boundary layer between wakes on the smooth surface becomes higher than that with surface trip. Since the transition processes in the boundary layer have almost completed at 86% S_0 in both cases, the variations of the momentum thickness at this streamwise location have similar shapes as those at the blade trailing edge, as shown in Fig. 12. However, compared to that at the blade trailing edge, the difference in θ between the two cases is amplified along the streamwise distance. Therefore, the difference in the momentum thickness variations at the blade trailing edge resulted from the different transition processes in the two cases.

Figure 14 presents the total pressure loss coefficients with different types of surface trips in unsteady flow with Tu=0.5%. The geometries and the parameters of these surface trips are shown in Fig. 2 and Table 2. The negative step SS-26 cannot reduce the profile losses as efficiently as the positive step SS26 does at all Reynolds numbers. However, increasing the depth of the negative step to 0.29 mm results in profile losses similar to those produced by SS26. This is the reason why the depth of the dimples was chosen to be 0.29 mm. The round dimples shown in Fig. 2(*d*) produce more benefit at the lowest Reynolds numbers but a larger penalty at higher Reynolds numbers. Different configurations of round dimples, such as one row at different streamwise locations and two rows without stagger, were tested. The one shown in Fig. 2(*d*) works the best. The long dimples and the distributed rough-

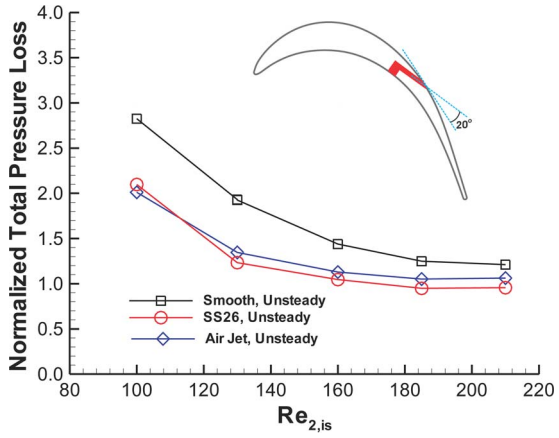

Fig. 15 Total pressure loss coefficients with air jets at Tu =0.5% in unsteady flow

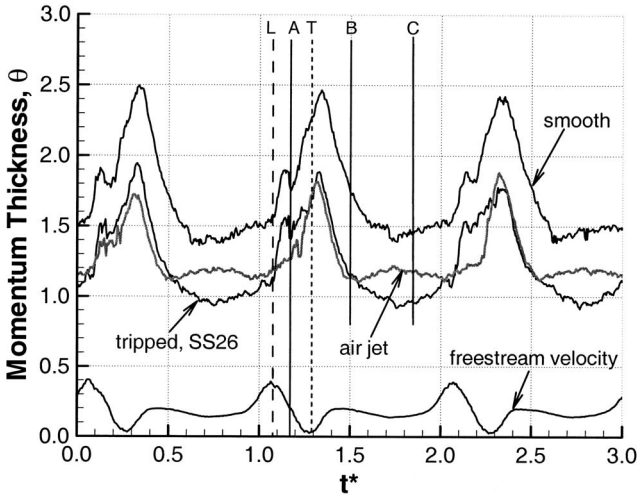

Fig. 16 Trailing edge momentum thickness on vented blade at Re=130,000, Tu=0.5%

ness produce similar profile losses, which are higher than those from SS26 at all tested Reynolds numbers. The loss coefficients with distributed roughness from Ramesh et al. [24] were lower than the current results at low Reynolds numbers but higher at high Reynolds numbers. This suggests that the roughness used in their test was higher than the current one. This may be caused by the double-sided tape used in their tests to place the roughness elements, which increased the height and worked like a step.

Air Jets. Following the work of Bons et al. [16], air jets vented from the blade pressure side were used to control the suction surface boundary layer development on the ultra-high-lift blade U2. The measured total pressure loss coefficients with the effects of the vented air under unsteady flow conditions are presented in Fig. 15. Although the air jets can effectively reduce the profile losses of the ultra-high-lift blade compared to the smooth surface, the total pressure loss coefficients with the air jets are still higher than those with surface trip SS26 at all tested Reynolds numbers.

The boundary layer development on the suction surface of the vented blade was studied by conducting hot-wire traverses at two different spanwise locations. One was directly after the vented hole and the other was midway between the vented holes. The results show that due to the small injection angle, the air jet remains within the boundary layer and the maximum velocity of the jet is about 60% of the local freestream velocity. The boundary layer became turbulent soon after the row of vented holes. There was no boundary layer separation on the suction surface during the whole wake passing period.

The variation in time of the momentum thickness at the blade trailing edge is shown in Fig. 16. The momentum thickness in the region between A and B on the vented blade is almost the same as that with surface trip SS26. However, between B and C, the momentum thickness on the vented blade is higher than that with SS26. This is because after the vented hole, the boundary layer becomes turbulent very quickly. Thus there is no calmed region following the unsteady passing wake. Therefore, there is no benefit from the calmed region in the unsteady conditions. This explains why the losses for the vented blade are higher than that with surface trip SS26. This also agrees with the observation by Zhang and Hodson [25] that the optimum surface trip only hastens the boundary layer transition procedure underneath the wakes and between them and doest not induce transition immediately after itself. Otherwise, the beneficial effects of the calmed region resulting from the unsteady wake induced transition will be absent.

Further Discussion. The low-speed results presented here show that the combined effects of the unsteady wakes and the surface trip can be used to improve the performance of the ultra-high-lift LP turbine blade. Zhang and Hodson [25] pointed out that the optimum location of the surface trip is midway between the blade suction peak and the separation onset location. Upstream of the suction peak, the acceleration prevents the surface roughness from inducing transition whereas downstream of the point of separation, the roughness can no longer affect the onset of the transition. Thus, only the roughness located within the region where the optimum occurs might affect the separated boundary layer transition. Vera et al. [26] suggested that controlling the amount of surface finishing of the turbine blade could be used to replace the surface trips. In addition, a reduction in manufacturing costs might be achieved.

Vera et al. [39] examine the effects of the surface trip and different surface finishings on a high-speed version of the U2 blade at $M_3=0.64$. More detail of the experimental facilities and results can be found in the paper. Figure 17 presents the measured total pressure loss coefficients with a trip wire and two different surface finishings (barrelled and as-cast) under unsteady flow conditions. They are indicated as sf1, sf4, and sf5, respectively, in their paper. The trip wire used in the high-speed test has the same relative height (k/S_0) and was placed at the same streamwise location (S/S_0) as the straight step SS26 used in low-speed test. The measured loss coefficients with trip wire in high-speed agree well

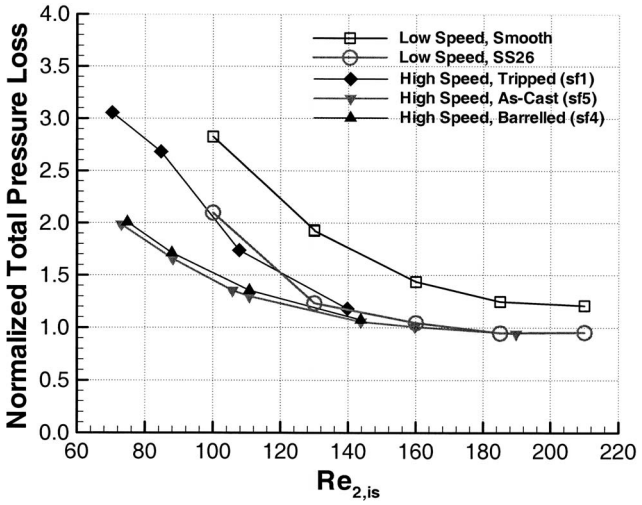

Fig. 17 Total pressure loss coefficients at high speed (M =0.65) in unsteady flow

with the results with SS26 in low-speed. This indicates that the low-speed observations are valid in the high-speed subsonic flow as well.

The barrelled surface and the as-cast surface produce the similar level of profile losses as those of the surface trips at Reynolds number higher than 130,000. The blade performance with rough surface finishes are even better at Reynolds numbers lower than this. This is because the surface trip was optimized for the design condition (i.e., at Re=130,000). While on the rough finishing blades, the flow can "choose" the optimum trip elements by themselves. Zhang and Hodson [25] also showed that although the height of the surface trip significantly affected the boundary layer developments, there was still a relatively wide range of the trip heights, which resulted in the minimum level of losses in the unsteady flow. Therefore, as long as the height of the surface finishes is controlled in this specified range, they will produce similar beneficial effects. This could be very important if the blade surface condition changes after a long period of operation.

Conclusions

The performance of the ultra-high-lift LP turbine blade can be further improved by using surface trips to control the boundary layer separation and transition in the unsteady flow conditions, especially at low Reynolds numbers. The benefit comes from the suppression of the separation underneath the wakes, the effect of the strengthened calmed region, and the smaller separation bubble between wakes. This is because the surface trips hasten the boundary layer transition process both underneath the wakes and between them. Although the calmed region only exists for a short time on the ultra-high-lift blade, its beneficial effects still last to the blade trailing edge. Since the effects of the calmed region after the unsteady wake induced transition is one of the main sources of the loss reduction, any separation control device that will prevent the formation of the calmed region, such as air jets, should be avoided. Furthermore, control of the surface finish during production can be used to achieve beneficial effects similar to those of the surface trip [39].

The profile loss of this ultra-high-lift LP turbine blade can be reduced to a similar level as those of high-lift and conventional profiles. This is because the aft-loaded nature of this blade minimizes the additional losses caused by the earlier occurrence of the boundary layer transition due to the surface trips. Therefore, to reduce the profile losses as much as possible in the unsteady flow condition with the surface trip, the blade should be aft-loaded to reduce the turbulent-wetted area. Furthermore, the deceleration after the suction velocity peak should change gradually. This allows the laminar boundary layer to develop before separation to give $\mathrm{Re}_\theta = 250$ at the separation point, so that the wakes can induce transition around the time-mean separation onset location to avoid the wake induced separated boundary layer transition an the formation of the wake's negative jet induced rollup vortex.

Acknowledgment

This work has been carried out with the support of Rolls-Royce plc. The authors would like to thank them for their support and permission to publish this paper. The valuable help of Richard Thomas and Maciek Opoka of the Whittle Laboratory is also gratefully acknowledged.

Nomenclature

C = blade chord
C_p = surface static pressure coefficient
C_x = blade axial chord
f_r = reduced frequency, $f_r = U_{\mathrm{bar}}/s^*_{\mathrm{bar}} C/V_{2\mathrm{is}}$
H_{12} = boundary layer shape factor
k = height of surface trip
M_3 = Mach number at the mixed-out condition
$\mathrm{Re}_{2,\mathrm{is}}$ = Reynolds number based on C and $V_{2\mathrm{is}}$
Re_θ = Reynolds number based on θ and local freestream velocity
RMS = root mean square
S = distance along suction surface
S_0 = suction surface length
s_{bar} = moving bar pitch
t^* = time normalized by wake-passing period
Tu = turbulence intensity
U_{bar} = bar moving velocity
V_{1x} = axial inlet velocity
$V_{2\mathrm{is}}$ = isentropic exit velocity
Y_n = surface normal coordinate
Z_w = Zweifel lift coefficient
$\alpha_{1,2}$ = inlet and outlet flow angle, respectively
δ^* = boundary layer displacement thickness
ϕ = flow coefficient, $\phi = V_{1x}/U_{\mathrm{bar}}$
γ = intermittency
θ = boundary layer momentum thickness

References

[1] Harvey, N. W., Schulte, V. S., Howell, R. J., and Hodson, H. P., 1999, "The Role of Research in the Aerodynamic Design of an Advanced Low pressure Turbine," 3rd European Conference on Turbomachinery, I MechE, London, March 1999.
[2] Ashpis, D., 1997, "Low Pressure Turbine Flow Physics Program," Minnowbrook II, Workshop on Boundary Layer Transition in Turbomachines, Syracuse University.
[3] Vázquez, R., Cadrecha, D., and Torre, D., 2003, "High Stage Loading Low Pressure Turbines. A New Proposal for an Efficiency Chart," ASME Paper No. GT2003-38374.
[4] Malzacher, F. J., Gier, J., and Lippi, F., 2003, "Aerodesign and Testing of an Aero-Mechanically Highly Loaded LP Turbine," ASME Paper No. GT2003-38338.
[5] Hourmouziadis, J., 1989, "Aerodynamic Design of Low Pressure Turbines," AGARD Lecture Series, 167.
[6] Halstead, D. E., Wisler, D. C., Okiishi, T. H., Walker, G. J., Hodson, H. P., and Shin, H. W., 1997, "Boundary Layer Development in Axial Compressors and Turbines. Parts 1–4," ASME J. Turbomach., **119**.
[7] Schulte, V., and Hodson, H. P., 1994, "Wake Separation Bubble Interaction in Low Pressure Turbines," Paper No. AIAA-94-2931.
[8] Hodson, H. P., 1998, "Blade Row Interactions in Low Pressure Turbines," VKI Lecture Series 1998–02, Blade Row Interference Effects in Axial Flow Turbomachinery Stages.
[9] Curtis, E. M., Hodson, H. P., Banieghbal, M. R., Denton, J. D., Howell, R. J., and Harvey, N. W., 1997, "Development of Blade Profiles for Low-Pressure Turbine Applications," ASME J. Turbomach., **119**, pp. 531–538.
[10] Schulte, V., and Hodson, H. P., 1998, "Unsteady Wake-Induced Boundary Layer Transition in High Lift LP Turbines," ASME J. Turbomach., **120**.
[11] Howell, R. J., Hodson, H. P., Schulte, V., Schiffer, H. P., Haselbach, F., and Harvey, N. W., 2001, "Boundary Layer Development in the BR710 and BR715 LP Turbines-The Implementation of High Lift and Ultra High Lift Concepts," ASME Paper No. 2001-GT-0441.
[12] Brunner, S., Fottner, L., and Schiffer, H.-P., 2000, "Comparison of Two Highly Loaded Low Pressure Turbine Cascades under the Influence of Wake-Induced Transition," ASME Paper No. 2000-GT-268.
[13] Haselbach, F., Schiffer, H. P., Horsman, M., Dressen, S., Harvey, N., and Read, S., 2001, "The Application of Ultra High Blading in the BR715 LP Turbine," ASME Paper No. 2001-GT-0436.
[14] Schobeiri, M. T., Öztürk, B., and Ashpis, D. E., 2003, "On the Physics of Flow Separation along a Low Pressure Turbine Blade under Unsteady Flow Conditions," ASME Paper No. GT2003-38917.
[15] Houtermans, R., Coton, T., and Arts, T., 2003, "Aerodynamic Performance of a Very High Lift LP Turbine Blade with Emphasis on Separation Prediction," ASME Paper No. GT2003–38802.
[16] Bons, J. P., Sondergaard, R., and Rivir, R. B., 2001, "Turbine Separation Control Using Pulsed Vortex Generator Jets," ASME J. Turbomach., **123**(2), pp. 198–206.
[17] Sondergaard, R., Bons, J. P., Sucher, M., and Rivir, R. B., 2002, "Reducing Low-Pressure Turbine Stage Blade Count using Vortex Generator Jet Separation Control," ASME Paper No. GT-2002-30602.
[18] Volino, R. J., 2003, "Separation Control on Low-Pressure Turbine Airfoils Using Synthetic Vortex Generator Jets," ASME Paper No. GT-2003-38729.
[19] McAuliffe, B. R., and Sjolander, S. A., 2004, "Active Flow Control Using Steady Blowing for a Low-Pressure Turbine Cascade," ASME J. Turbomach., **126**(4), pp. 560–569.
[20] Volino, R. J., 2003, "Passive Flow Control on Low-Pressure Turbine Airfoils," ASME Paper No. GT2003-38728.
[21] Lake, J. P., King, P. I., and Rivir, R. B., 2000, "Low Reynolds Number Loss Reduction on Turbine Blades With Dimples and V-Grooves," Paper No. AIAA 00-0738.

[22] Sieverding, C. H., Bagnera, C., Boege, A. C., Cordero Anton, J. A., and Luere, V., 2004, "Investigation of the Effectiveness of Various Types of Boundary Layer Transition Elements of Low Reynolds Number Turbine Bladings," ASME Paper No. GT2004-54103.
[23] Byerley, A. R., Stormer, O., Baughn, J. W., Simon, T. W., Van Treuren, K. W., and List, J., 2002, "Using Guerney Flaps to Control Laminar Separation on Linear Cascade Blades," ASME Paper No. GT-2002-30662.
[24] Ramesh, O. N., Hodson, H. P., and Harvey, N. W., 2001, "Separation Control in Ultra-High Lift Aerofoils by Unsteadiness and Surface Roughness," ISABE.
[25] Zhang, X. F., and Hodson, H. P., 2004, "The Combined Effects of Surface Trips and Unsteady Wakes on Boundary Layer Development of an Ultra-High-Lift LP Turbine Blade," ASME J. Turbomach., **127**(3), pp. 479–488.
[26] Vera, M., Hodson, H. P., and Vazquez, R., 2004, "The Effects of Roughness and Unsteadiness on a High Speed Highly Loaded Low-Pressure Turbine Blade," ASME J. Turbomach., **127**(4), pp. 747–754.
[27] Bearman, P. W., 1971, "Correction for the Effect of Ambient Temperature Drift on Hotwire Measurements in Incompressible Flow," DISA Information, No. 11, pp. 25–30.
[28] Cox, R. N., "Wall Neighborhood Measurements in Turbulent Boundary Layers Using Hot-Wire Anemometer," A.R.C. Report 19101, Feb. 1957.
[29] Howell, R. J., Ramesh, O. N., Hodson, H. P., Harvey, N. W., and Schulte, V., 2001, "High Lift and Aft Loaded Profiles for Low Pressure Turbines," ASME J. Turbomach., **123**, pp. 181–188.
[30] Gostelow, J. P., and Thomas, R. L., 2003, "Response of a Laminar Separation Bubble to an Impinging Wake," ASME Paper No. GT2003-38972.
[31] Stieger, R. D., and Hodson, H. P., 2004, "The Transition Mechanism of Highly-Loaded LP Turbine Blades," ASME J. Turbomach., **126**(4), pp. 536–543.
[32] Zhang, X. F., Hodson, H. P., and Harvey, N. W., 2005, "Unsteady Boundary Layer Study on Ultra-High-Lift Low Pressure Turbine Blades," IMechE J. Power Energy, Part A, **218**(6), pp. 451–460.
[33] Drela, M., 1995, "MISES Implementation of Modified Abu-Ghannam/Shaw Transition Criterion," MISES Code Documentation, MIT.
[34] Abu-Ghannam, B. J., and Shaw, R., 1980, "Natural Transition of Boundary layer—the Effects of Pressure gradient and Flow History," J. Mech. Eng. Sci., **22**(5), pp. 213–228.
[35] Mack, L. M., 1977, "Transition and Laminar Instability," Jet Propulsion Laboratory Publication 77–15, Pasadena, CA.
[36] Solomon, W. J., Walker, G. J., and Hughes, J. D., 1999, "Periodic Transition on an Axial Compressor Stator: Incidence and Colocking Effects: Part II—Transition Onset Predictions," ASME J. Turbomach., **121**(3), pp. 408–415.
[37] Walker, G. J., 1989, "Transitional Flow on Axial Turbomachine Blading," AIAA J., **27**, pp. 595–602.
[38] Stieger, R. D., and Hodson, H. P., 2003, "Unsteady Dissipation Measurements on a Flat Plate Subject to Wake Passing," 5th European Turbomachinery Conference.
[39] Vera, M., Zhang, X. F., Hodson, H. P., and Harvey, N. W., 2005, "Separation Control on an Aft-Loaded Ultra-High-Lift LP Turbine Blade at Low Reynolds Numbers: High-Speed Validation," ASME Paper No. GT2005–68893.

On Vortex Formation in the Wake Flows of Transonic Turbine Blades and Oscillating Airfoils

J. P. Gostelow
Department of Engineering,
University of Leicester,
University Road,
Leicester LE1 7RH, UK

M. F. Platzer
AeroHydro R&T Associates,
3070 Hermitage Road,
Pebble Beach, CA 93953

W. E. Carscallen
Institute for Aerospace Research,
National Research Council of Canada,
Ottawa, ON K1A OR6,
Canada

This paper demonstrates similarities between the vortex shedding from blunt trailing-edge transonic turbine nozzle blades and from oscillating airfoils and bluff bodies. Under subsonic conditions the turbine nozzle cascade shed wake vortices in a conventional von Kármán vortex street. This was linked with a depressed base pressure and associated energy separation in the wake. Under transonic conditions a variety of different shedding configurations was observed with vortices shedding and pairing in several different ways. Similarities are addressed between the observed structures and those from vortex shedding in some other physical situations, such as the vortex wakes shed from cylinders and airfoils in sinusoidal heaving motion in low-speed flow. The established field of vortex-induced vibration has provided a developed classification scheme for the phenomena observed. The paper has brought together three previously independent fields of investigation and, by showing that the three are essentially related, has provided the basis for a new synthesis. [DOI: 10.1115/1.2184354]

Introduction

Vortex shedding from bodies, such as circular cylinders, airfoils, and the blades of turbomachines, is experienced frequently and is of ongoing research interest. Vorticity is rarely shed from a surface continuously. Periodic components in the shear layers are amplified until nonlinear effects prescribe time delays resulting in the shedding of discrete vortices. Behind a bluff body, this most commonly takes the form of the von Kármán vortex street. The overall structure of the resulting wake is relatively simple and the kinematics is well understood, although the detailed formation of the street and its development in all dimensions is much less obvious.

It has been found that not all vortex shedding into a wake takes the form of a classical von Kármán vortex street, with its relatively periodic and predictable modes. Different boundary conditions and dynamic regimes can result in shedding modes that are not of this form. A wide range of alternative modes has been identified under varying circumstances, and these have sufficient commonality that a degree of classification has proved both possible and useful.

This paper brings together results from three, completely independently conducted, fields of investigation involving vortex shedding. The purpose of the paper is to investigate whether and how the somewhat similar manifestations of vortex shedding are related. This investigation is performed with a view to improving the predictive capability for the various vortex-shedding modes.

The first of these is the relatively well-developed field of vortex-induced vibrations of bodies and structures. This has found extensive application in civil engineering work, such as oil risers and tubular structural members. The circular cylinder in cross-flow, with its induced oscillations due to vortex shedding, is the body most commonly investigated [1].

The second field is research undertaken on oscillating airfoils [2]. This has relevance to a range of problems, such as flutter of aircraft wings, helicopter, and turbomachinery blades. It is also relevant to the biohydrodynamics of aquatic animals, birds, and insects—a field that is currently being pursued vigorously because of its application to micro air vehicles [3].

The third field is the finding of anomalous vortex-shedding patterns behind blunt trailing-edge turbine blades at transonic speeds [4]. This area of activity arises from problems uncovered during the development of highly loaded turbine stages and is of ongoing interest in understanding and predicting flows around blading and the resulting losses.

Turbine blades with a blunt trailing edge are known to shed a von Kármán vortex street [5], resulting in a loss penalty. This penalty is considerably larger than would result from a backward-facing step of similar proportions and has been quantified [6,7]. The magnitude of the discrepancy was unexplained until fast schlieren photography came into use for observing flows in cascades of blades. When fast schlierens are taken of the flow over blunt trailing-edge turbine blades, a von Kármán vortex street is usually observed [8], often with associated sound waves propagating upstream. Among other damaging effects, this creates a considerable increase in base drag at subsonic speeds. Other adverse effects include high-frequency sound propagation, vibrational effects, local high heat transfer to or from the blade, and energy separation into hot and cold regions. The existence of a vortex street, often with close-coupled oscillating shock waves, makes flow-field computation challenging.

The discovery of anomalous vortex-shedding patterns in the course of work on transonic turbine blading has prompted an investigation of the circumstances under which such phenomena might occur. This investigation has resulted in the identification of two other sets of circumstances resulting in similar patterns and this has provided an insight into the physics of vortex shedding.

Vortex Formation in the Wake of an Oscillating Cylinder

In 1988, Williamson and Roshko produced a definitive work on the vortex-induced vibration of a circular cylinder [1]. They demonstrated that when a body oscillates in a freestream it can synchronize the vortex formation frequency with that of the body motion. A map of wake structure was produced in the amplitude-wavelength plane, defining the body trajectory. Below a critical wavelength, pairs of like-sign rotating vortices coalesced, forming a classical von Kármán vortex street. Beyond this wavelength,

Contributed by the International Gas Turbine Institute (IGTI) of ASME for publication in the JOURNAL OF TURBOMACHINERY. Manuscript received October 1, 2004; final manuscript received February 1, 2005. IGTI Review Chair: K. C. Hall. Paper presented at the ASME Turbo Expo 2005: Land, Sea and Air, Reno, NV, June 6–9, 2005, Paper No. GT2005-69128.

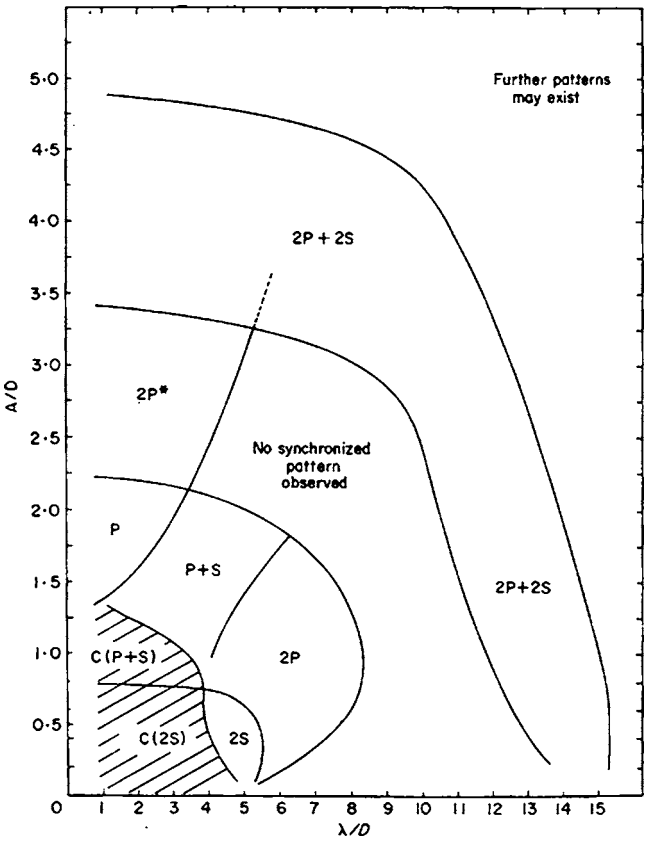

Fig. 1 Map of vortex synchronization regions in the wavelength-amplitude plane [1]

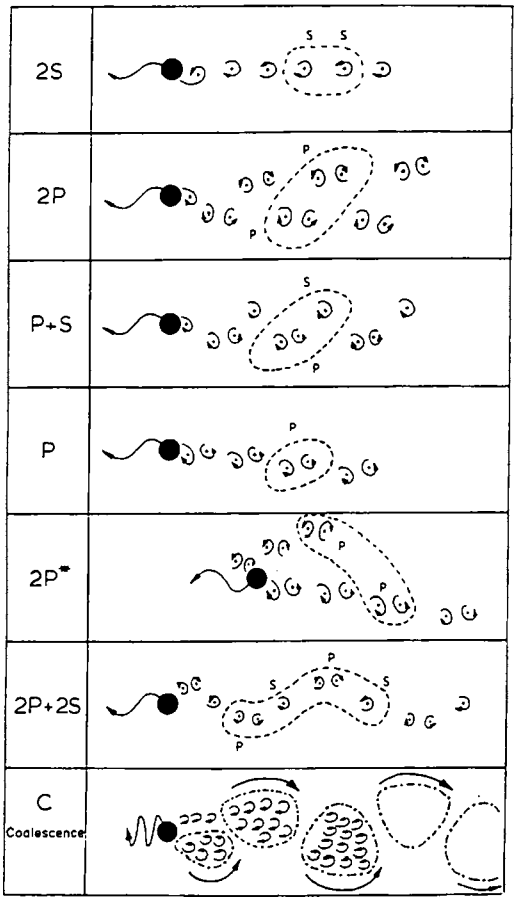

Fig. 2 Sketches of the corresponding vortex-shedding patterns identified by Williamson and Roshko [1]

like-sign vortices convected away from each other and each of them paired with an opposite-sign vortex. The resulting wake comprised a system of vortex pairs with a tendency to convect away from the wake centerline. According to the location on the map, different vortex configurations were found in the wake.

This description established the contemporary view of the field of vortex-induced vibrations. The paradigmic cross-flow over a circular cylinder has proved a powerful focus, and many authors have contributed both experimental and computational work that has confirmed the original map and reinforced the model. Over the last two decades, there has been a push to explore very low mass and damping and the present standing of the field has been reviewed by Williamson and Govardhan [9]. The work has been assisted by the availability of new computational and experimental techniques. New vortex wake modes have been discovered and placed in the context of the map of vortex modes compiled from forced vibration studies; some of these caused free vibration.

The aforementioned investigations have all been oriented toward the problem of bodies, usually circular cylinders, undergoing vortex-induced vibration. This problem is a different one from those discussed in the subsequent two sections of this paper. Nevertheless, it does provide a good conceptual framework and a coherent body of knowledge that can be applied to interpreting vortex shedding from airfoils and turbine blades. In particular, the map of vortex-shedding modes is proving very useful in interpreting flows around airfoils and validating the flow patterns observed computationally in their wakes.

The map of wake behavior in the wavelength-amplitude plane is reproduced in its high-amplitude version in Fig. 1. A version was also presented in Ref. [1] for a lower range of amplitudes and wavelengths giving more information on vortex modes at low amplitudes and wavelengths. Williamson and Roshko also provided a schematic representation of the different wake structures, which is given in Fig. 2. The dashed line encircles the vortices contained in one complete shedding cycle.

The notation adopted by the vortex-induced vibration fraternity is that the S mode consists of single vortices being shed and P indicates that vortices are shed in pairs. $P+S$ means a pattern in which, in each cycle, a vortex pair and a single vortex are shed. The conventional von Kármán vortex street is represented by $2S$. $2P$ implies the formation of vortex pairs that convect laterally outward from the wake centerline, and the $P+S$ mode is an asymmetric version of the $2P$ mode in which the cylinder sheds a pair and a single vortex each cycle. $C(2S)$ and $C(P+S)$ represent the occurrence of the $2S$ and $P+S$ modes near the cylinder. These smaller vortices coalesce rapidly into the larger scale structure. Regions marked P and $2P^*$ refer to vortex modes described as "single pair" and "double pair," respectively. Mode P is a wake comprising a set of vortex pairs convecting downstream but also laterally to one side, taking on the appearance of a jet rather than a wake. Mode $2P^*$ is similar to $2P$ except that the vortex pairs in one of the half cycles convect away from the front of the body. In this case, the convection of each pair is in the downstream direction, creating a jet. Earlier work by King [10] on cantilevered cylinders had associated streamwise oscillation with modes of the $2P^*$ type.

The authors have, for some time, been engaged in both experimental and computational work in the fields of plunging airfoils and transonic turbine blade wake flows. In both of these situations, they have been observing wake vortex configurations that appear to be very similar to those of Williamson and Roshko [1]. It has therefore proved instructive to reinterpret their observations in the light of the established Williamson and Roshko scheme.

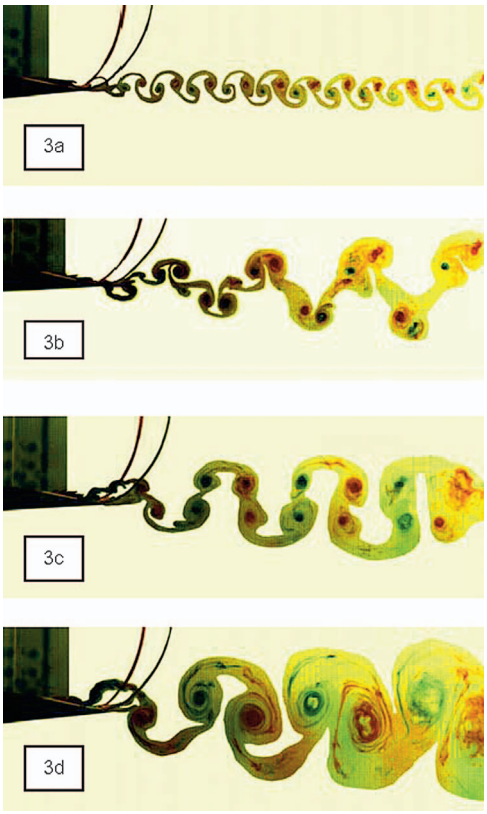

Fig. 3 Vortex patterns [2] for a NACA 0012 airfoil, oscillated in plunge, for a freestream velocity of ~0.2 m/s and a frequency of 2.5 Hz: (*a*) no oscillation, (*b*) *kh*=0.1 (*c*) *kh*=0.2, and (*d*) *kh* =0.4

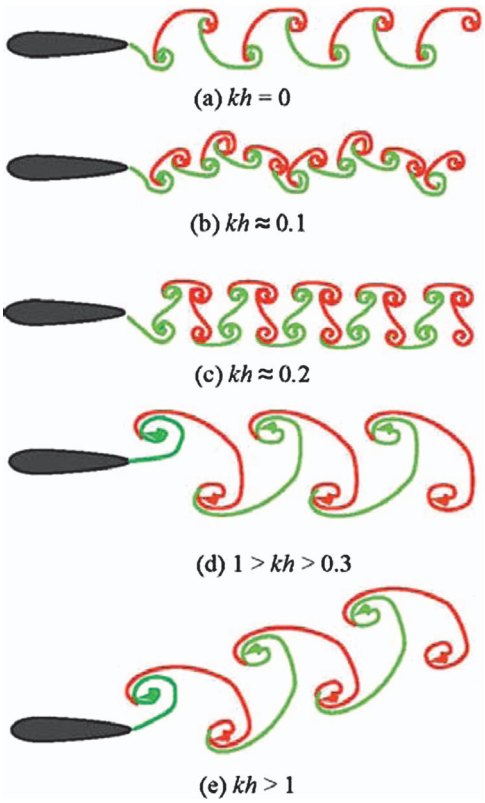

Fig. 4 Sketches [2] of the wake of a plunging airfoil for various values of *kh*

Vortex Shedding From Oscillating Airfoils

Lai and Platzer [2] performed water tunnel tests of a NACA 0012 airfoil that was oscillated sinusoidally in plunge. Using dye flow visualization, they explored the change in vortex pattern shed from the trailing edge as a function of frequency and amplitude of oscillation. The tunnel speed was varied to cover a Reynolds number range (based on airfoil chord) from 500 to 21,000. As expected, the stationary airfoil was found to shed a von Kármán vortex street where the upper row of vortices rotates clockwise and the lower row counterclockwise, as shown in Fig. 3(*a*). However, as soon as the airfoil is oscillated, the shedding process changes. For the cases shown in Figs. 3(*b*)–3(*d*), the tunnel speed and frequency of oscillation were kept constant at 0.2 m/s and 2.5 Hz, respectively, but the amplitude was increased to values of the nondimensional plunge velocity *kh* (maximum plunge velocity divided by the freestream velocity) covering the range $0.1 < kh < 0.8$. It is seen from Figs. 3(*b*) and 3(*c*) that, at $kh = 0.1$ and 0.2, two same-sign vortices are shed per half cycle. At *kh* values of 0.4, and higher, a "reverse" von Kármán vortex street is shed such that the upper row vortices are counterclockwise and the lower row vortices are clockwise as shown in Fig. 3(*d*). The type of vortex street shown in Fig. 3(*d*) is thrust producing. Indeed, Jones et al. [11] have shown that measurements of the time-averaged velocity distribution downstream of the trailing edge yield a jet profile rather than a wake. This thrust is entirely a result of the vortex structure.

It is important to note that the switch from the drag-producing von Kármán vortex street to the thrust-producing "reverse" von Kármán vortex street cannot occur abruptly. Rather the vortex shedding needs to transition through the stages shown in Figs. 3(*b*) and 3(*c*). These stages are sketched in Fig. 4, again taken from Ref. [2]. This change in wake structure has also been observed by Triantafyllou et al. [12], Kadlec and Davis [13], Ohashi and Ishikawa [14], and Koochesfahani [15].

In a very recent study, Young and Lai [16] analyzed the flow visualization results of Lai and Platzer [2] by means of Navier-Stokes computations. Their results are shown in Figs. 5(*a*) and 5(*b*) and may be compared to the cases shown in Figs. 3(*b*) and 3(*c*). It is seen that the agreement is remarkably good. Young and Lai also provided close-up computational details about the flow near the trailing edge, revealing regions of separated flow on either or both sides of the airfoil, which effectively create a blunt trailing edge. The bluntness of the trailing edge varies throughout the oscillation cycle and also varies with oscillation frequency,

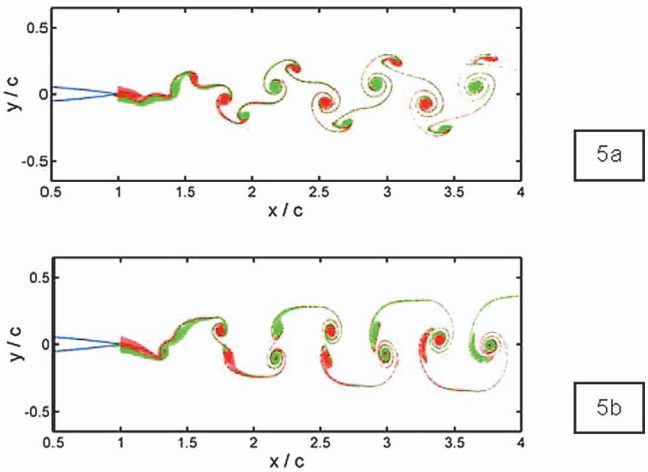

Fig. 5 Numerical results of Young and Lai [16]: (*a*) *kh*=0.1 and (*b*) *kh*=0.16

amplitude, and Reynolds number. It is significant, however, that the separated flow regions at the trailing edge effectively create a blunt trailing edge, which causes vortex shedding with a certain natural frequency. Young and Lai suggested that the interaction between this natural vortex-shedding mode and the vortex shedding caused by the airfoil oscillation is the origin of the vortex pairing shown in Figs. 3(*b*) and 3(*c*). They also note that the observed vortex shedding cannot simply be classified by the nondimensional plunge velocity *kh*, as was done in the visualizations of Lai and Platzer [2]. Instead, the phenomena depend separately on frequency and amplitude because the separated flow region has a more dominant influence at small plunge amplitude than at large amplitude. This explains differences between the laminar and turbulent flow calculations at small amplitudes and high frequencies, whereas similar vortex-shedding patterns were obtained at high amplitudes and lower frequencies. Most importantly, the calculations of Young and Lai confirm that the observed change from the drag-producing von Kármán vortex street to the thrust-producing "reverse" von Kármán vortex street occurs through the more complicated vortex configuration of Fig. 3(*b*) and the vortex pairing configuration of Fig. 3(*c*), which represents the neutral thrust condition.

It is therefore of great interest to note that the vortex wake shed by an oscillating cylinder reveals a similar behavior. Williamson and Roshko [1] identified several vortex-shedding modes from oscillating cylinders as a function of frequency and amplitude of oscillation. Most notably, they found the same vortex-pairing mode as shown in Fig. 4(*c*), which they called the 2*P* vortex-pairing mode. This similarity between the shedding from a "sharp-edged" airfoil and a rounded configuration, such as a cylinder, is not surprising any longer after realizing that the airfoil generates its own blunt trailing edge. As the amplitude and frequency exceeds certain critical values, Williamson and Roshko also identified the asymmetric shedding mode shown in Fig. 4(*e*), which creates a jet flow. The wake in Fig. 4(*e*) is bistable, its direction depending on the starting conditions.

Change in Vortex Shedding Due to Flow Oscillations. References [9–16] provide clear evidence that the vortex shedding from oscillating airfoils and cylinders is dramatically affected by the body oscillation. The question arises whether similar effects have been observed in cases of a stationary body in an oscillating flow. In the following sections, the authors will demonstrate that the basic physics remains unchanged and that, therefore, similar effects can be expected. This similarity was observed by DeTemple [17]. He introduced oscillations into the low-speed flow around a stationary cylinder by subjecting the flow to sound waves. He observed that the acoustically induced flow oscillations changed the conventional von Kármán vortex street into the type of shedding with vortex pairing described above for oscillating airfoils or cylinders.

Vortex Shedding Behind Turbine Blades at Transonic Speeds

In 1989, Carscallen and Oosthuizen [18] published a previously unpublished finding, from the work of Williamson and Moustapha [19], which showed that total temperature traverses taken downstream of an annular turbine nozzle cascade indicated a significant nonuniform distribution of total temperature. This result was unexpected as the inlet flow was at room temperature, with a uniform upstream total temperature profile. The total temperature probes had been calibrated over the range of anticipated stator exit Mach numbers, and the flow of air through the stator blade row was assumed to be adiabatic.

Planar Cascade Testing. To elucidate the causes of the total temperature anomaly, testing in a purpose-designed transonic planar cascade was initiated. The two-dimensional nozzle tested had a chord of 175.3 mm (4.3 times engine size) and a solidity of 1.19. The nozzle aspect ratio was 0.64, turning angle 76 deg and design exit Mach number 1.2. The blades had a circular trailing edge with a diameter of 6.35 mm.

The goals of the research program in the planar cascade were to reproduce the previously observed redistribution of wake total temperature and to study the effect of secondary flows on local heat transfer coefficients at representative engine Mach and Reynolds numbers. These goals were subsequently expanded to investigate the existence of any von Kármán vortex street and the extent of vortex shedding in the vane wakes in an attempt to establish whether the energy separation effects predicted by Kurosaka et al. [20] were the cause of the total temperature discrepancies.

This research has confirmed that over the subsonic Mach number range, a von Kármán vortex street was shed continuously from the nozzle blades. Associated with the vortex shedding was a thermo-acoustic effect, which was particularly strong at high subsonic speeds. On a time-averaged basis, the stagnation temperature on the wake centerline was 20°C lower than for the incoming fluid and the stagnation temperature at the edges of the wake was significantly higher than that of the incoming fluid. It was demonstrated [21] that this was a manifestation of the Eckert-Weise effect [22]. This is a thermoacoustic effect in which the vortex cores emerge colder than the surrounding fluid and are associated with hot spots at the edge of the wake. On a time-averaged basis, this results in a substantial total temperature redistribution. Because similar temperature redistributions were observed in the planar and annular cascades, it is surmised that the vortex-shedding effects described in this paper are equally applicable to annular cascades. The effects described here are thus likely to be present in rotating machines.

In the subsonic flow regime, the presence of a stable von Kármán vortex street led to high wake losses due to the depression of the base pressure while the redistribution of total temperature was caused by the combined pumping action of the vortices. The strength of the von Kármán vortices, the energy redistribution, and the base pressure reduction phenomena increased with increasing subsonic Mach number.

As the transonic regime was traversed, the von Kármán vortex street still occurred but only as one of a number of different and relatively transitory vortex-shedding patterns. As the discharge Mach number became supersonic, the trailing edge shocks became oblique. The origin of the vortices appeared to migrate downstream to the nodal point formed by the shocks and the confluence of the two trailing edge shear layers. In transonic flows the coherent structures in the wake became unstable, less von Kármán-like, and occurred less frequently. This was accompanied by a significant recovery of base pressure.

Vortex-Shedding Modes. Figure 6 is a schlieren photograph of the exit flow field for $Ma=0.81$ and is typical of those acquired over this Mach number range. The top of the photograph shows the suction surface of a blade with the leading edge to the right hand side. The trailing edge of the adjacent blade is shown midway up the right hand side of the photograph. The flow is from right to left. A conventional von Kármán vortex street originates from the trailing edge. These vortices are two-dimensional along the span except near the end walls where they interact with the boundary layers. Acoustic waves are seen propagating upstream.

Figure 7, at $Ma=0.97$, is representative of the flow field in the range of $0.9<Ma<1.0$, in which the von Kármán vortex street is shed on a continuous basis. In this photograph, the boundary layers that separated from just upstream of the trailing edge are seen to extend in a nominally parallel fashion downstream of the blade for a distance of approximately one-half of a trailing edge diameter. At this point, the separated shear layers interact with the acoustic waves, which are piling up to form a normal shock wave. A sequence of photographs, not shown here, reveals that this interaction is very dynamic in nature. Although the von Kármán

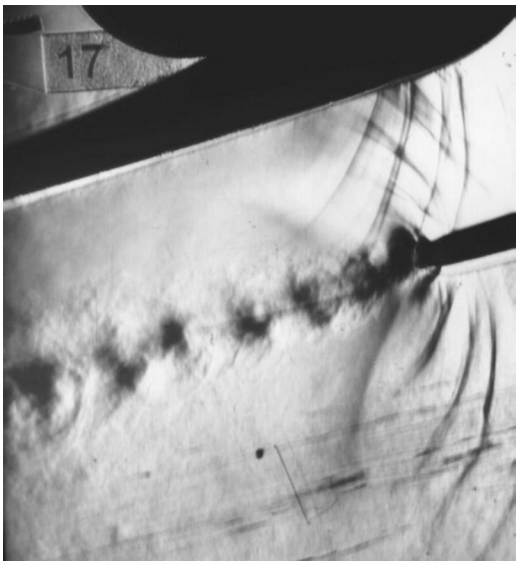

Fig. 6 Von Kármán vortex shedding at Ma=0.8

vortex street is readily apparent and originates downstream of the junction of the shear layer and acoustic waves, occasional anomalous shedding modes are observed.

At transonic speeds, the vortex street was incubated at the confluence of the two separating shear layers and was not always of the conventional von Kármán kind. For some of the time, vortices are shed simultaneously from the two sides of the wake, rather than alternately. Other modes were observed in which vortices are shed in pairs from each side. The transient vortex patterns at transonic speeds are intermingled with wake flows in which no coherent structures exist. Since the passage shock behavior is determined by the vortex-shedding mode, this anomalous behavior could have consequences for predicting the shock position, blade loading and dynamics. None of these additional transonic speed modes are explained by conventional stability theory.

Previously available evidence had suggested that only freestream disturbances were effective in provoking vortex-shedding instability. In the present example, the visible existence and fixed location of acoustic waves precludes such a path for antisymmetric upstream traveling pressure waves. This has the

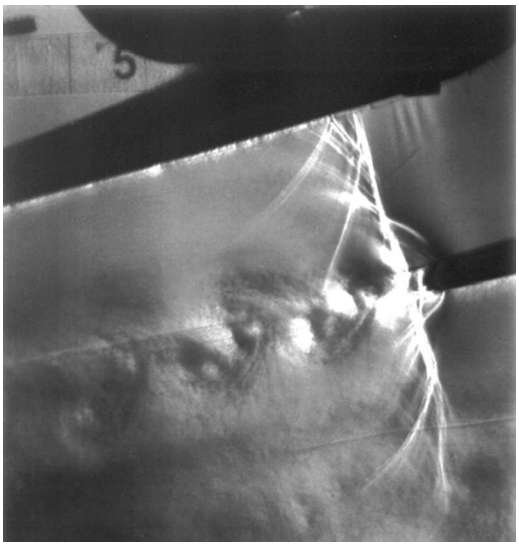

Fig. 7 Von Kármán vortex shedding at Ma=0.97

effect of reducing the lateral distance between incipient vortices to the relatively short wake width at the downstream shock location. Nevertheless, it is plausible that significant free shear layer instabilities are propagated downstream through a Kelvin-Helmholtz (K-H) mechanism. This possibility was corroborated computationally by Brooksbank [23] using a time-accurate Euler code. Figure 8 gives a prediction of the density field in the trailing-edge region of the transonic cascade.

Figures 9–11 are all taken at an isentropic exit Mach number of 1.07. The shock systems and their reflections from the suction surface of the adjacent vane are seen to be very unstable in both physical structure and location. Lambda shocks are apparent in only two of the photographs indicating the unstable nature of the suction surface sonic zone. The shock-wave reflections from the suction surface are seen to interact with the vortex wake and either reflect off individual vortices as shock waves or pass through the wake. In Fig. 9, the vortex wake is classical von Kármán (180 deg out of phase), whereas in Fig. 10 the vortices are shed in phase. A new form of the vortex street is shown in Fig. 11 where the vortices are seen to shed but in a configuration described as "doublets." These vortex doublets appear to be a stable configuration as they do not merge and coalesce as they propagate within the wake.

A detailed survey of schlieren photographs revealed the existence of these patterns over a Mach number range from 0.97 to 1.2. The probability of their occurrence was investigated by Carscallen et al. [24] at the design pressure ratio of 2.3 (Ma=1.16) by analyzing 170, 35 mm schlieren photographs taken over a period of 35 min. A picture was categorized as "No Definable Pattern" if it did not correspond to any identified pattern type; this was the situation for 35.5% of the time. Von Kármán vortices vortices and a subset identified as "leaning von Kármán vortices" occurred for 46.5% of the time. "Doublets" occurred for 4% of the time and "Couples" for 3% of the time. For 1.5% of the time there was a "hybrid" mode with two vortices shed on one side for every one on the other side.

Discussion and Synthesis

It is clear that similar configurations of vortex shedding are being observed in the three fields of investigation. The case of vortex-induced vibration in the shedding about a circular cylinder, and the case of vortices shed from an oscillating airfoil, are occurring in incompressible flows but with the possibility of a driving force feeding the oscillation. The case of the transonic turbine cascade is different in that the blading is fixed with no possibility of a fluctuating force being exerted by movement of a body. There are, however, strong oscillations in the flow and it is argued that the pressure field associated with the trailing-edge shocks is exerting the fluctuating lateral force, which is essential for the vortex-shedding process at transonic speeds.

It is also clear that the classification provided by Williamson and Roshko [1] has the potential to be useful not only for the field of vortex-induced vibration but also to classify problems involving oscillating airfoils and even turbine blades at transonic speed that do not include moving or oscillating boundaries. It has already been suggested that the $2P$ pairing mode is evident in the oscillating airfoil results. In the context of the transonic turbine blading, it is suggested that the "couples" observed in the transonic cascade tests are a form of $2P$ or $2P^*$ wake behavior and that the doublets reflect $2P$ and $P+S$ behavior; the "hybrid" patterns are of the $P+S$ type.

The occurrence of similar changes in vortex shedding in the blunt trailing-edge transonic turbine blades described above suggests that this phenomenon is caused by self-excited flow oscillations. For example, Mabey [25] observed oscillations in the flow over biconvex airfoils at freestream Mach numbers between 0.82 and 0.86. These oscillations were caused by the interaction between the weak shocks generated in this Mach number range on both the lower and upper airfoil surface and the boundary layer.

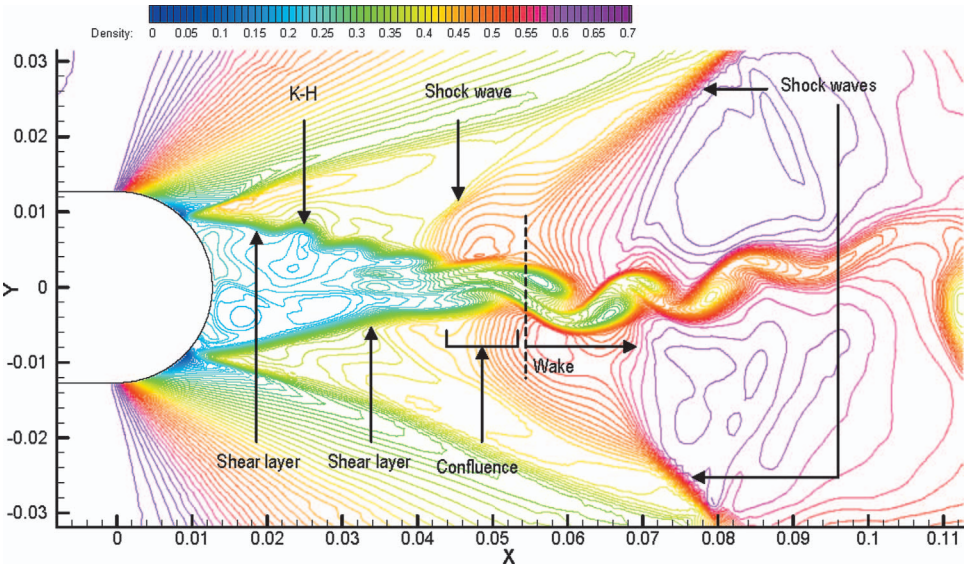

Fig. 8 Prediction of the instantaneous flow-field (density contours) downstream of a turbine blade [23]

The shocks were sufficiently strong to separate the boundary layer and started to oscillate on alternative surfaces due to the periodic formation and collapse of the separation bubble, which formed downstream of the shock. For Mach numbers below 0.82, the effect was absent because of the absence of a transonic shock. At Mach numbers above 0.86, on the other hand, the flow became steady again because the flow separation extended from the shock to the trailing edge. Hence, this type of self-induced flow oscillation is likely to occur (and has been observed also on advanced supercritical airfoils) in a specific but relatively narrow Mach number range.

The above considerations suggest that the observed changes in vortex shedding from the blunt trailing edges of the transonic cascade in the Mach number range between 0.97 and 1.2 are caused by a similar self-induced oscillation mechanism. As shown in Figs. 9–11, shocks are generated at the confluence of the shear layers and the shocks interact with the shear layers in a manner similar to the mechanism described by Mabey [25] for the biconvex airfoil. Findings, from schlieren visualization, computational work, and separate hydraulic analogy experiments have shown the shock-wave/wake-interaction structure at the confluence of the shear layers to be particularly dynamic and mobile. As a result an oscillatory flow is set up that causes the observed changes in vortex shedding. It is likely that this effect can occur only in a narrow Mach number range because, as for the airfoil, the shocks may not exceed a certain strength. However, too little is known about this type of interaction and the available flow visualizations do not allow more specific statements.

Losses are directly affected by vortex shedding behavior through the reduction in base pressure, which results when the vortex street is shed [26,27]. Sieverding and Heinemann [8] experimentally confirmed that the base pressure was independent of the state of the boundary layers if vortex shedding was present. In the transonic turbine cascade at $Ma > 1.0$, the Strouhal number was found to be 0.24 for the von Kármán vortex street, when based on the diameter of the nodal point formed by the confluence

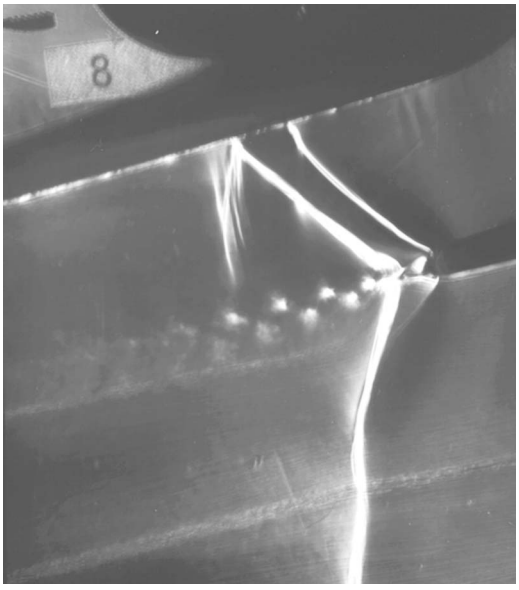

Fig. 9 Von Kármán vortex shedding at Ma=1.07

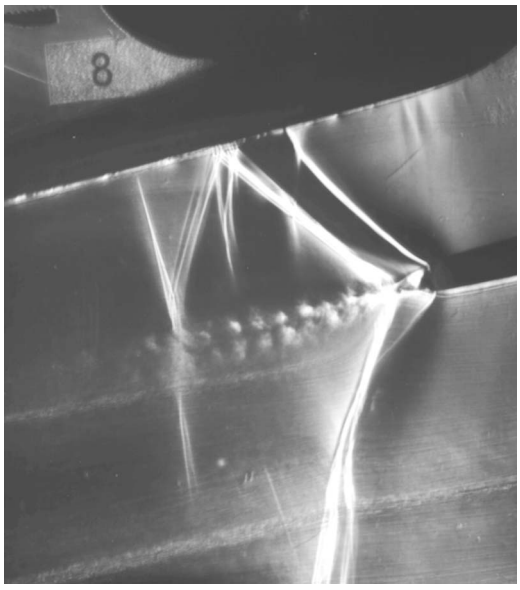

Fig. 10 Shedding of couples at Ma=1.07

Fig. 11 Shedding of doublets at Ma=1.07

of the trailing-edge shear layers and trailing-edge shock waves. The base pressure recovered significantly in transonic flows, where the vortex street changed its character. The anomalous vortex-shedding patterns were therefore associated with a reduction in loss.

The characteristics and stability of vortex streets in unforced subsonic flows have been studied by Rosenhead [28], Ehrhardt [29], and Sun [30]. There is clearly scope for similar stability analysis of a more general class of compressible flows with periodic forcing.

Conclusions

The authors have demonstrated a strong similarity between the vortex wakes shed from cylinders and airfoils in sinusoidal heaving motion in low-speed flow and the wakes shed from a turbine nozzle cascade in transonic flow. The tests of Williamson and Roshko [1] on oscillating cylinders and Lai and Platzer [2] on oscillating airfoils show that the structure of the von Kármán vortex street, which forms downstream of stationary cylinders and airfoils in low Reynolds number incompressible flow may change to one comprising different arrangements of vortices when the body oscillates. The changed vortical wake structure depends on the amplitude and frequency of the heaving oscillations. Williamson and Roshko, and Lai and Platzer, have discussed the mechanism leading to these changes in a vortex wake. More recently, Young and Lai [16] succeeded in predicting this phenomenon by means of Navier-Stokes calculations. The mechanism causing this changed vortex shedding is therefore now fairly well documented and understood for oscillating cylinders and airfoils in low-speed flow.

Cascade tests carried out by Carscallen and Gostelow [4] established that strong vortex shedding occurred over the entire range of discharge Mach numbers. At subsonic Mach numbers, the vortices were shed in a classical von Kármán vortex street. This resulted in a base pressure reduction causing high wake losses. At Mach numbers above unity, the von Kármán vortex street was found to be but one of a number of transient, yet distinct, shedding patterns. These modes of vortex-shedding were characterized as classical von Kármán couples, hybrid, and doublets. Broadly corresponding designations from the field of vortex-induced vibration were identified in terms of the $2S$, $2P$, $2P^*$, and $P+S$ definitions.

The occurrence of similar changes in vortex shedding from transonic cascades suggests that the existence of an oscillating body is not a fundamental requirement. The wake instability can be caused by an oscillating flow mechanism. As shown by Mabey [25], among others, shock-induced transonic flow oscillations could also change the modes of vortex shedding. The transonic cascade schlieren photographs showed that the interaction between the base flow shear layers and the shock waves, which form at Mach numbers between 0.97 and 1.2, are the likely mechanism causing the changes in observed vortex-shedding patterns.

Insofar as the structure of the wake is concerned, this paper has brought together three previously unrelated fields of investigation and, by showing that the three are essentially related, has provided the basis for a new synthesis. The next step would be to provide an integrated theory for this broader field of wake vortex formation.

Acknowledgment

This paper is dedicated to the memory of our dear friend and colleague, Professor Gallus. The authors are appreciative of the support of the National Research Council of Canada. Professor Platzer acknowledges the support of AFOSR.

Nomenclature

A = amplitude of oscillation
D = diameter
f = frequency
kh = nondimensional plunge velocity $=2\pi fA/V$
h = nondimensional amplitude of oscillation
Ma = isentropic exit Mach number
V = velocity
x = streamwise distance
y = lateral distance
λ = wavelength

References

[1] Williamson, C. H. K., and Roshko, A., 1988, "Vortex Formation in the Wake of an Oscillating Cylinder," J. Fluids Struct., **2**, pp. 355–381.
[2] Lai, J. C. S., and Platzer, M. F., 1999, "Jet Characteristics of a Plunging Airfoil," AIAA J., **37**(12), pp. 1529–1537.
[3] Shyy, W., Berg, M., and Ljungqvist, D., 1999, "Flapping and Flexible Wings for Biological and Micro Air Vehicles," Prog. Aerosp. Sci., **35**, pp. 455–505.
[4] Carscallen, W. E., and Gostelow, J. P., 1994, "Observations of Vortex Shedding in the Wake From Transonic Turbine Nozzle Vanes," Proc. ISROMAC-5, Kaanapali, HI, pp. 153–169.
[5] Lawaczek, O., and Heinemann, H-J., 1975, "Von Kármán Vortex Streets in the Wakes of Subsonic and Transonic Cascades," AGARD CP-177.
[6] Deych, M. E., Fillipov, G. A., and Lazarev, L. YA., 1965, *Atlas of Axial Turbine Cascade Characteristics*, Mash. Publ. House, Moscow.
[7] Craig, H. R. M., and Cox, H. J. A., 1971, "Performance Estimation of Axial Flow Turbines," Proc. Inst. Mech. Eng., **185**, pp. 32–71.
[8] Sieverding, C. H., and Heinemann, H., 1989, "The Influence of Boundary Layer State on Vortex Shedding From Flat Plates and Turbine Cascades," ASME Paper No. 89-GT-296.
[9] Williamson, C. H. K., and Govardhan, R., 2004, "Vortex-Induced Vibrations," Annu. Rev. Fluid Mech., **36**, pp. 413–55.
[10] King, R., 1974, "Vortex-Excited Oscillations of a Circular Cylinder in Steady Currents," Offshore Technol. Conf., Paper No. OTC 1948.
[11] Jones, K. D., Dohring, C. M., and Platzer, M. F., 1998, "Experimental and Computational Investigation of the Knoller-Betz Effect," AIAA J., **36**(7), pp. 1240–1246.
[12] Triantafyllou, G. S., Triantafyllou, M. S., and Grosenbaugh, M. A., 1993, "Optimal Thrust Development in Oscillating Foils With Application to Fish Propulsion," J. Fluids Struct., **7**, pp. 205–224.
[13] Kadlec, R. A., and Davis, S. S., 1996, "Visualization of Quasiperiodic Flows," AIAA J., **17**(11), pp. 1164–1169.
[14] Ohashi, H., and Ishikawa, N., 1972, "Visualization Study of a Flow Near the Trailing Edge of an Oscillating Airfoil," Bull. JSME, **15**, pp. 840–845.
[15] Koochesfahani, M. M., 1989, "Vortical Patterns in the Wake of an Oscillating Airfoil," AIAA J., **27**(9), pp. 1200–1205.
[16] Young, J., and Lai, J. C. S., 2004, "Oscillation Frequency and Amplitude Effects on the Wake of a Plunging Airfoil," AIAA J., **42**(10), pp. 2042–2052.
[17] DeTemple, E., 1987, "Zur Phänomenologie Karmanscher Wirbelstrassen in durch Schall überlagerter Strömung," Mitteilungen aus dem Max Planck Institut für Strömungsforschung, Gottingen, Nr. 84.
[18] Carscallen, W. E., and Oosthuizen, P. H., 1989, "The Effect of Secondary Flow

on the Redistribution of the Total Temperature Field Downstream of a Stationary Turbine Cascade," AGARD-CP-469, pp. 27-1–27-18.
[19] Williamson, R. G., and Moustapha, S. H., 1986, "Annular Cascade Testing of Turbine Nozzles at High Exit Mach Numbers," ASME J. Fluids Eng., **108**, pp. 313–320.
[20] Kurosaka, M., Gertz, J. B., Graham, J. E., Goodman, J. R., Sundaram, P., Riner, W. C., Kuroda, H., and Hankey, W. L., 1987, "Energy Separation in a Vortex Street," J. Fluid Mech., **178**, pp. 1–29.
[21] Carscallen, W. E., Currie, T. C., Hogg, S. I., and Gostelow, J. P., 1999, "Measurement and Computation of Energy Separation in the Vortical Wake Flow of a Turbine Nozzle Cascade," ASME J. Turbomach., **121**, pp. 703–708.
[22] Eckert, E. R. G., 1986, "Energy Separation in Fluid Streams," Int. Commun. Heat Mass Transfer, **13**, pp. 127–143.
[23] Brooksbank, E. J., 2001, "A Numerical Investigation of Time Resolved Flows Around Turbine Blades," Ph.D. thesis, University of Leicester.
[24] Carscallen, W. E., Fleige, H. U., and Gostelow, J. P., 1996, "Transonic Turbine Vane Wake Flows," ASME Paper No. 96-GT-419.
[25] Mabey, D. G., 1989, "Physical Phenomena Associated With Unsteady Transonic Flows," *Unsteady Transonic Aerodynamics* (Progress in Astronautics and Aeronautics, Vol. 120), Chap. 1.
[26] Roshko, A., 1955, "On the Wake and Drag of Bluff Bodies," J. Aeronaut. Sci., **22**, pp. 124–132.
[27] Motallebi, F., 1988, "Base Pressure in Transonic Speeds a Comparison Between Theory and Experiment," ASME Paper No. 88-GT-132.
[28] Rosenhead, L., 1953, "Vortex Systems in Wakes," Adv. Appl. Mech., **3**, pp. 185–195.
[29] Ehrhardt, G., 1979, *Stabilität Zweireihiger Straßen Geradliniger und Kreisförmiger Wirbel*, Fortschr.-Ber. VDI-Z, Reihe, 7, No. 49. VDI-Verlag, Düsseldorf.
[30] Sun, Y. C., 1983, "The Existence of the Kármán Vortex Streets of Unequal Vortex Strengths and the Possible Forms of Wake Flow Behind Bluff Bodies," Forsch. DFVLR, Köln.

Aerodynamic Losses of a Cambered Turbine Vane: Influences of Surface Roughness and Freestream Turbulence Intensity

Qiang Zhang

Phillip M. Ligrani[1]

Convective Heat Transfer Laboratory,
Department of Mechanical Engineering,
University of Utah,
Salt Lake City, UT 84112-9208

The effects of surface roughness and freestream turbulence level on the aerodynamic performance of a turbine vane are experimentally investigated. Wake profiles are measured with three different freestream turbulence intensity levels (1.1%, 5.4%, and 7.7%) at two different locations downstream of the test vane trailing edge (1 and 0.25 axial chord lengths). Chord Reynolds number based on exit flow conditions is 0.9×10^6. *The Mach number distribution and the test vane configuration both match arrangements employed in an industrial application. Four combered vanes with different surface roughness levels are employed in this study. Effects of surface roughness on the vane pressure side on the profile losses are relatively small compared to suction side roughness. Overall effects of turbulence on local wake deficits of total pressure, Mach number, and kinetic energy are almost negligible in most parts of the wake produced by the smooth test vane, except that higher freestream losses are present at higher turbulence intensity levels. Profiles produced by test vanes with rough surfaces show apparent lower peak values in the center of the wake. Integrated aerodynamic losses and area-averaged loss coefficient* Y_A *are also presented and compared to results from other research groups.*
[DOI: 10.1115/1.2185125]

Introduction

To characterize the randomly distributed nature of surface roughness, the use of equivalent sand-grain roughness size k_s has been widely accepted by many researchers. It was first proposed and utilized by Nikuradse [1] and Schlichting [2]. This quantity represents the size of sand grains, which give the same skin friction coefficients in internal passages as the roughness being evaluated. This measure of roughness size continues to be used widely in empirical correlation equations (which are based on experimental data) to represent rough surface behavior, and for closure models employed in a variety of numerical prediction codes. Later reevaluation and additional advances in the use of equivalent sand-grain roughness are made by many researchers, including Coleman et al. [3], Sigal and Danberg [4,5], Van Rij et al. [6], and Zhang et al. [7].

Recently, the effect of surface roughness on turbomachinery flow behavior has received increased attention due to ongoing needs to improve turbomachinery performance and efficiency. Valuable information is provided by publications from several research groups, including Bammert and Sandstede [8,9], Kind et al. [10], Bogard et al. [11], Abuaf et al. [12], and Leipold et al. [13]. A comprehensive review of these research works is given by Zhang et al. [14], who investigate the effects of surface roughness on the aerodynamic performance of symmetric airfoils with different inlet turbulence intensity levels in subsonic flows. According to these authors, surface roughness alters the boundary development over the turbine airfoils, increases profile losses, and significantly decreases turbine efficiency. Combined effects of surface roughness, freestream turbulence, and Reynolds number on heat transfer and laminar-turbulent transition are investigated by Stripf et al. [15]. Their results show a strong influence of roughness on the onset of transition even for the smallest roughness Reynolds numbers. Roberts and Yaras [16] also present experimental results showing that transition inception location remains sensitive to surface roughness with increasing freestream turbulence. Boyle and Senyitko [17] compare total pressure losses for smooth and rough vanes over a range of Reynolds and Mach numbers for three turbulence levels. Their work concentrates on loss differences between the rough and smooth vanes, and on approaches to predicting surface roughness effects. They indicate that, at high Reynolds numbers, roughness nearly doubles loss levels compared to ones that exist for the lowest Reynolds number employed. Yun et al. [18] present measurements as well as a mean line analysis of turbine efficiency reduction due to blade surface roughness. In another study, Zhang et al. [19] present experimental data on wake turbulence structure also measured downstream of symmetric airfoils with different surface roughness and inlet turbulence intensity levels. These authors indicate that all wake profile quantities broaden and vortex shedding frequencies decrease as either the level of surface roughness or the mainstream turbulence intensity increases.

Of the investigations that study the effects of augmented freestream turbulence levels, Gregory-Smith and Cleak [20] show that the mean flow field is not significantly affected by inlet turbulence intensity levels as high as 5%. Boyle et al. [21] provide turbine vane aerodynamic data over Reynolds numbers from 1.5×10^4 to 3.3×10^6 made at midspan locations downstream of a linear cascade with inlet turbulence intensity levels as high as 10%. In a study of aerodynamic losses downstream of subsonic turbine airfoil with no film cooling, Ames and Plesniak [22] demonstrate important connections between wake growth and the level of freestream turbulence. Wake mixing and eddy diffusivity magnitudes, in particular, are altered by different levels of

[1]To whom correspondence should be addressed.

Contributed by the Aeromechanics Committee of ASME for publication in the JOURNAL OF TURBOMACHINERY. Manuscript received January 20, 2006; final manuscript received January 23, 2006. Review conducted by D. Wisler.

freestream turbulence. Jouini et al. [23] present detailed measurements of midspan aerodynamic performance characteristics of a turbine cascade at off-design conditions. Measurements of blade loading, exit flow angles, and trailing edge base pressures at different exit Mach numbers, ranging from 0.5 to 1.2, show that profile losses are closely related to base pressure behavior. Radomsky and Thole [24] present measurements of time-averaged velocity components and Reynolds stresses along a turbine stator vane at elevated freestream turbulence levels. As the freestream turbulence level increases, transition occurs farther upstream on the suction side, with increased velocity fluctuations near the pressure side. Boyle et al. [25] provide aerodynamic data for a linear turbine vane cascade, including surface pressure distributions and aerodynamic losses for different Reynolds numbers, Mach numbers, and levels of inlet turbulence.

Zhang and Ligrani [26] investigate the effects of surface roughness, freestream Mach number, and turbulence intensity on the aerodynamic performance of turbine airfoils. Their data show that magnitudes of integrated aerodynamic losses (IAL) change by a much larger amount as either the freestream Mach number or turbulence intensity are altered, when the airfoil is roughened (compared to smooth airfoil results). Note that investigations by Zhang et al. [14,19] and Zhang and Ligrani [26] employ symmetric airfoils with no camber, surrounded by flows without significant turning.

The present investigation employs a cambered turbine vane that produces substantial flow turning and matches a vane configuration employed in an industrial application. Considered are the effects of surface roughness on aerodynamic losses downstream of the vane for three different inlet turbulence intensity levels. Vane geometry and Mach number distribution match flow conditions in an industrial application. One smooth vane is employed, along with two other vanes with three-dimensional irregular roughness distributed uniformly over entire vane surfaces. A fourth vane is also employed with roughness of different sizes distributed over the vane surface (i.e., a variable rough surface-)whose arrangement is based on observations of roughened turbine vanes from industrial applications. A mesh grid and cross bars are used to augment the magnitudes of longitudinal turbulence intensity at the inlet of the test section. Wake profile data are presented for two different locations downstream of the vane trailing edge that illustrate the influences of varying freestream turbulence intensity level and vane surface roughness on local aerodynamic losses, local Mach numbers, local kinetic energy, integrated aerodynamics losses (IAL), and area-averaged loss coefficients. Analyses and comparisons of results from other recent investigations are also discussed. As such, the present data provide unique and useful information to designers of turbomachinery components and to individuals developing models for computational fluid dynamics (CFD) predictions. To the authors' knowledge, no similar study is reported in the archival literature.

Experimental Apparatus and Procedures

Transonic Wind Tunnel. The University of Utah Transonic Wind Tunnel (TWT) is used for this study. It produces Mach numbers, pressure variations, Reynolds numbers, passage mass flow rates, and scaled physical dimensions that match values along airfoils in operating aeroengines and in gas turbines used for utility power generation. Detailed descriptions are provided by Jackson et al. [27] and Furukawa and Ligrani [28]. A Gardner-Denver Co. Model No. RL-1155-CB compressor is used to pressurize the array of eight tanks whose total capacity volume is 11.9 m^3. A VanAir VAS93039 Model No. D16-5 Deliquescent desiccant dryer, a Pall Corp. 5EHG-4882-207 oil filter, and two Permanent Filter Corp. Model No. 13846 particulate filters are located just downstream of the compressor to remove particulates and moisture from the air. A Fisher pressure regulator with a 6 $\times$4 EWT design sliding gate valve, a Fisher type 667 diaphragm actuator, a 3582 series valve positioner, and a Powers 535 1/4 DIN process controller are used to regulate the pressure in the test section as the storage tanks discharge. A plenum tank, a 30.48 cm i.d. pipe, a circular-to-square transition duct, a nozzle, and the test section then follow. The test section is connected to a large 92.71 cm$\times$91.44 cm$\times$91.44 cm plenum with a square plastic flange at its outlet. The plenum diffuses high-speed air from the test section exit into a reservoir of low-velocity air. This plenum is then connected to two ducts, which are subsequently connected to the atmosphere.

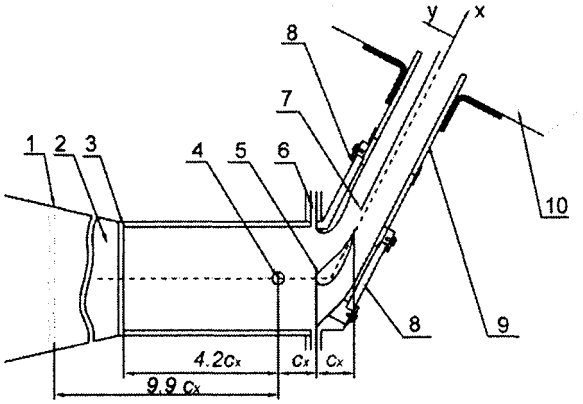

1. Bar Grid Position 2. Nozzle 3. Fine Mesh Grid Position
4. Inlet Pressure Probe and Thermocouple
5. Test Blade 6. Bleeding System
7. Exit Pressure Probe and Thermocouple
8. Zinc-Selenide Window 9. Tailboard 10. Exit Plenum

Fig. 1 Schematic diagram of the test section

Test Section. The present test section is designed to match Reynolds numbers, Mach numbers, pressure gradients, passage mass flow rates, boundary layer development, streamline curvature, airfoil camber, and physical dimensions of turbine vanes in operating industrial engines. A schematic diagram of the test section with the cambered vane is shown in Fig. 1. The inlet of the test section is 12.70 cm$\times$12.70 cm. The side and bottom walls of the test section are made of steel, and top wall is made up of acrylic. As shown in Fig. 1, two zinc-selenide windows are also placed on both of the sidewalls, so that the entire airfoil surface is accessible to optical, surface temperature measurement schemes, such as infrared thermography.

Appropriate cascade flow conditions are maintained, in part, by a pair of adjustable bleed, ducts which are located on the two sidewalls, as shown in Fig. 1. The flow rate of each bleed duct is regulated using an adjustable ball valve. Following these, the test section walls have the same pressure-side and suction-side contours as the test vane. The exit area and exit flow direction from the cascade test section can be altered by changing the angles of the two exit tailboards, which are also shown in Fig. 1. Thus, (i) changing the total pressure at the test section inlet using the pressure-regulator/sliding-gate valve arrangement, (ii) changing the angular positions of the two tailboards, and (iii) adjusting the ball valves of the bleeding system are employed to alter the Mach number distribution along the vane in the test section, for a particular vane and test section configuration. By adjusting these items, appropriate Mach number distributions along the test vane are obtained, which are discussed later in the paper. Experimental parameters for the operating conditions employed in this study are tabulated in Table 1.

Test Vanes and Surface Roughness. Table 2 gives geometric parameters of the test vanes. The coordinates of this test vane profile were provided by personnel at Pratt and Whitney Canada Corporation, along with appropriate operating conditions that are used in industrial environments.

Table 1 Experimental operating conditions

Exit Mach number M_{ex}	0.65
Exit Reynolds number[a]	0.9×10^6
Inlet Reynolds number[a]	0.4×10^6
Inlet Mach number	0.23
Inlet total pressure	106 kPa
Inlet turbulence intensity	1.1%, 5.4%, 7.7%
Inlet turbulence length scale	–2.7 mm 4.7 mm
Inlet relative humidity	15–20%

[a]Based on true chord length.

Four different vanes, all with the same exterior dimensions but with different surface roughness characteristics, are used. One vane has a smooth surface, two other vanes have uniform rough surfaces, and one vane has variable roughness on the pressure side. The roughness applied simulates the actual roughness that develops on operating turbine airfoils, over long operating times, due to particulate deposition and to spallation of thermal barrier coatings (TBCs). The roughness is applied by bonding nickel particles, manufactured by Praxair Surface Technologies Inc., to the test vane surfaces. The approach employed is described by Zhang and Ligrani [26]. With this technique, the same exterior dimensions to the surfaces of all four test vanes are obtained, regardless of whether their surfaces are smooth or rough.

A schematic diagram of test turbine vane with uniform rough surfaces is shown in Fig. 2(*a*). The vane with the uniform smaller-sized roughness elements has Praxair T1166F particles, which range in size from 20 μm to 53 μm. The vane with the uniform larger-sized roughness elements has Praxair NI-914 particles, which range in size from 40 μm to 200 μm. The vane with variable roughness is shown in Fig. 2(*b*). Four types of different nickel-based powders are used on the pressure side of a test vane, while the suction side is left smooth. Detailed information regarding the nickel powders and surface coverage for the variable rough vane is given in Table 3.

The arrangement of variable rough surface is based on observations of roughened turbine vanes from industrial applications. From these observations, the suction side is more or less uniform in roughness and remains at or very close to the "as-cast" condition, even after very long operating times. Pressure-side roughness, on the other hand, is more variable. Local roughness magnitudes are often the same on the suction side as near the pressure-side leading edge. Local roughness sizes then vary linearly to the full roughness size, which are typically reached at about 40% of the distance along the pressure surface. Thus, differences in surface roughness characteristics between the suction and pressure sides can be very significant due to the different flow and operating conditions encountered that sometimes cause more particulate deposition and spallation on the suction-side surface. There is also a considerable scatter in the roughness patterns both in qualitative and quantitative terms that are present on vanes and blades from operating engines. The configuration of variable roughness investigated here is one typical configuration, as shown by the data presented in Fig. 2(*b*) and in Table 3.

Pressure and Temperature Measurements. As tests are conducted, Validyne Model DP15-46 pressure transducers (with diaphragms rated at either 34.5 kPa or 344.7 kPa) and calibrated copper-constantan thermocouples are used to sense pressures and temperatures at different locations throughout the facility. Signals from the pressure transducers are processed by Celesco Model CD10D carrier demodulators. All pressure-transducer measurement circuits are calibrated using a Wallace and Tiernan FA145 bourdon tube pressure gage as a standard. A United Sensor PLC-8-KL pitot-probe with an attached, calibrated Watlow standard type-K copper-constantan thermocouple, and a five-hole conical-tipped pressure probe (cone angle 15 deg), also with a similar Watlow thermocouple, are used to sense total pressure, static pressure, and recovery temperature at the inlet and exit of the test section, respectively, during each blowdown. Mach numbers, sonic velocities, total temperatures, and static temperatures are determined from these data. The five-hole probe has a tip that is 1.27 mm in diameter and a stem that is 3.18 mm in diameter. Each port has a diameter of 0.25 mm. The overall response time of the pressure-measuring system is ~0.2 s. The conical probe is aligned using two yaw ports placed on either side of the probe. The alignment using the two yaw ports is implemented at one location at the start of each traverse. The probe is located downstream of the vane such that the position in the streamwise direction is adjustable. As a blowdown is underway, it is traversed to different pitchwise locations using a two-axis traversing sled with two Superior Electric M092-FF-206 synchronous stepper motors, connected to a Superior Electric Model SS2000I programmable motion controller and a Superior Electric Model SS2000D6 driver. Commands for the operation of the motion controller are provided by LABVIEW 7.0 software and pass though a serial port after they originate in a Dell Precision 530 PC workstation. Each profile is measured through the wake from $-y/cx$ locations to $+y/cx$ locations and then repeated as the probe is traversed in the opposite direction. The resulting data are subsequently averaged at

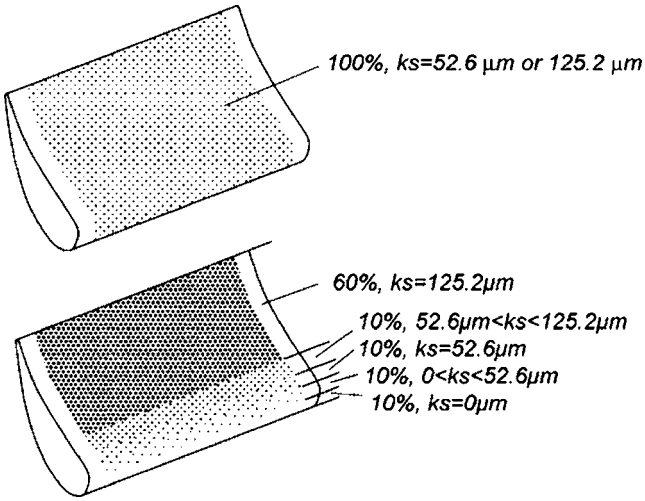

Fig. 2 Test section vanes with rough surfaces: (*a*) Vane with uniform roughness and (*b*) vane with variable roughness on pressure side

Table 2 Test vane geometric parameters

True chord c	7.27 cm
Axial chord cx	4.85 cm
Pitch p	6.35 cm
Span	12.7 cm
Flow turning angle	62.75 deg

Table 3 Nickel-based powders used on the test vane with variable surface roughness on the pressure side

Percentage of the surface distance on the PS Side (starting from LE) (%)	Powder name	Size (μm)
0–10		0
10–20	NI-105	5–45
20–30	T1166F	20–53
30–40	NI-107	45–106
40–100	NI-914	40–200

each wake measurement location. Note that measurements are obtained at five or six pitchwise locations during each blowdown test, and thus, multiple blowdown tests are required to obtain a complete profile spanning an entire vane pitch.

Voltages from the carrier demodulators and thermocouples are read sequentially using Hewlett-Packard HP44222T and HP44222A relay multiplexer card assemblies, installed in a Hewlett-Packard HP3497A low-speed Data Acquisition/Control Unit. This system provides thermocouple compensation electronically such that voltages for type-T thermocouples are given relative to 0 °C. The voltage outputs from this unit are acquired by the Dell Precision 530 PC workstation through its USB port, using LABVIEW 7.0 software and a GPIB-USB-B adaptor made by National Instruments.

Augmenting Mainstream Flow Turbulence Levels. Three different arrangements are used at the inlet of the test section to produce three different levels of mainstream turbulence intensity: (i) no grid or bars, (ii) fine mesh grid, and (iii) cross bars. The fine mesh grid consists of an array of four square rods arranged horizontally and four square rods arranged vertically. Each rod is spaced 25.4 mm from adjacent rods and is 6.5 mm on each side. The open area amounts to 48% of the inlet area. The cross-bar device consists of two parallel bars, where each is 25.4 mm in width, with 25.4 mm spacing from the adjacent bar and 25.4 mm spacing from the top and bottom walls of the inlet duct. The open area amounts to 60% of the inlet area. Note that the installation positions for fine mesh grid and bar grid are different due to considerations of inlet uniformity (see Fig. 1).

Longitudinal Turbulence Intensity Measurements. A single, horizontal-type platinum-plated tungsten hot-wire sensor, with a diameter of 12.7 μm and a length of 2.54 mm, is employed to measure the time varying longitudinal component of velocity at the inlet of the test section (one axial chord length upstream of the test vane leading edge). The time-averaged longitudinal velocity and the longitudinal turbulence intensity are then determined from these measurements. The measurement location is one axial chord length upstream of the vane leading edge. The hot-wire probe is driven by a Disa 55M10 constant-temperature hot-wire anemometer bridge with an overheat ratio of 1.6. The analog signal from this bridge is then processed using a Dantec 56N20 signal conditioner with a low-pass, anti-aliasing filter set to 100 kHz. The time-varying output voltage signal is then sampled at a 200 kHz rate using a DATEL PCI441D I/O board installed in the Dell Precision 530 PC workstation. During each measurement, 2×10^6 voltage values are sampled over a time period of 10 s. Data are acquired using LABVIEW 7.0 software and then processed further using MATLAB 6.1 software. The entire measurement system, including the hot-wire sensor, is calibrated in the freestream of the TWT. A Kiel-type pressure probe, wall static taps, and a copper-constantan thermocouple are used to measure and determine the total pressure, static pressure, recovery temperature, and velocity at the inlet of the test section as the calibration is conducted.

Experimental Uncertainties. Uncertainty estimates are based on 95% confidence levels and determined using procedures described by Kline and McClintock [29] and by Moffat [30]. Mach number uncertainty is 0.005. Uncertainty magnitudes of stagnation and static temperatures are 0.5 °C. Pressure uncertainty is 0.25 kPa. Uncertainties of C_p, $M_e/M_{e,\infty}$ and KE are 0.0013 (0.07), 0.0023 (0.96), and 0.03 (0.90), respectively, where typical nominal values of these quantities are given in parenthesis. IAL uncertainty is 0.04 N/cm (0.800 N/cm). Magnitudes of IAL, determined from replicate runs, are always within IAL uncertainty ranges. Note that uncertainty range bars would not be visible (or would be nearly invisible) if these are added to data points in the figures.

TWT Qualifying Flow Characteristics. During each blowdown test, the total pressure, Reynolds number, and turbulence level at the test-section inlet are maintained in a continuous and steady fashion for 45 s long time intervals. Such characteristics are not only due to the TWT design, but also to the excellent performance characteristics of the TWT mainstream air pressure regulator and its controller. Additional detailed information is provided by Jackson [31]. During each blowdown test, the inlet total pressure at the inlet of the test section Poi (one axial chord length upstream of the vane leading edge) is maintained constant for each experimental condition examined at 106 kPa. Corresponding exit freestream Mach number, measured one axial chord length downstream of the airfoil trailing edge, is about 0.65, and chord Reynolds number (based on exit flow conditions) is 0.9×10^6. Experimental operating conditions employed in this study are shown in Table 1. Table 1 also gives three different magnitudes of the inlet longitudinal turbulence intensity level and length scale. Here, turbulence intensity is defined as the ratio of the root mean square of the longitudinal fluctuation velocity component divided by the local streamwise mean component of velocity. The autocorrelation function is integrated with respect to the time lag to obtain the longitudinal integral time scale. This quantity is then multiplied by the mean velocity to get the longitudinal integral length scale, which is a representative of the largest eddies in the turbulent flow field.

Inlet uniformity measurements are conducted at five different pitchwise locations at the inlet of the test section (one axial chord length upstream of the test vane, as shown in Fig. 1). With no turbulence grid employed, the total pressure and static pressure show excellent spatial uniformity at this location, varying by $<0.5\%$ of mean values. With the fine mesh grid and bar grid, the total pressure and static pressure generally vary $<0.6\%$ of mean values. Note that the bar grid is installed further away from the leading edge of the vane compared to the position of the fine mesh grid, as shown in Fig. 1. This maintains acceptable levels of uniformity in the flow as it approaches the vane.

To verify experimental data obtained and procedures employed, a comparison is made to results from Ames and Plesniak [22]. To do this, a total loss coefficient ω is determined, which is defined using

$$\omega = \frac{p_{oi} - p_{oe}}{p_{oi} - p_{se}} \tag{1}$$

The Ames and Plesniak data are taken ~ 0.3 axial chord lengths downstream of a smooth vane with $M_{ex}=0.27$. The vane used by Ames and Plesniak [22] is two times the size of vanes from present study and has an exit angle of 72.4 deg, compared to an exit angle of 62.75 deg for the present investigation. The present data used for comparison are obtained for exit Mach number of 0.35 at a measurement location of 0.25 axial chord lengths downstream of the trailing edge of a smooth vane. Figure 3 shows that the two sets of data have similar magnitudes and similar qualitative distributions. The lower turning angle is believed to be one factor that results in the slightly lower loss in the present study. The small quantitative differences are also due to slightly different vane configurations, flow conditions, and measurement locations relative to the vane trailing edges. Overall, the agreement between the two data sets provides verification of procedures and results from the present study.

Experimental Results and Discussion

Roughness Characterization. Magnitudes of equivalent sand-grain roughness are determined for all surfaces under investigation using procedures described by Van Rij et al. [6]. The first step in this process is determination of detailed surface contour coordinates using a Wyko high-resolution optical surface profilometer. Figure 4(*a*) shows an enlarged image of a portion of the test rough surface, which is comprised of nickel powder T1166F, obtained from such optical profilometry data. The image of a rough surface from the pressure side of a turbine vane from a utility power

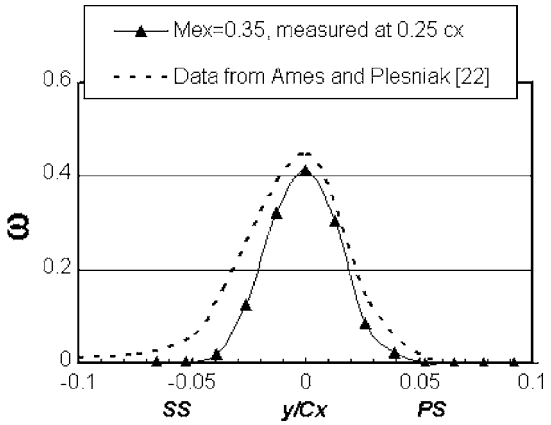

Fig. 3 Comparison of smooth vane wake total pressure loss coefficient profile with similar data from Ames and Plesniak [22]

engine is shown in Fig. 4(*b*). This particular sample is obtained from a location on the surface that is located close to the trailing edge area, which is roughened due to surface particulate deposition. The qualitative and quantitative similarity of the two images is apparent, including the distributions, irregularity, nonuniformity, and three-dimensional nature of the roughness elements. Equivalent sand grain roughness size of this real turbine vane surface is ~62.3 μm, which is close to 52.59 μm, the size for the test surface with nickel powder T1166F. Table 4 also shows the similarity of other surface roughness statistics from the utility power engine turbine vane to test surfaces comprised of nickel powders T1166F and NI-914.

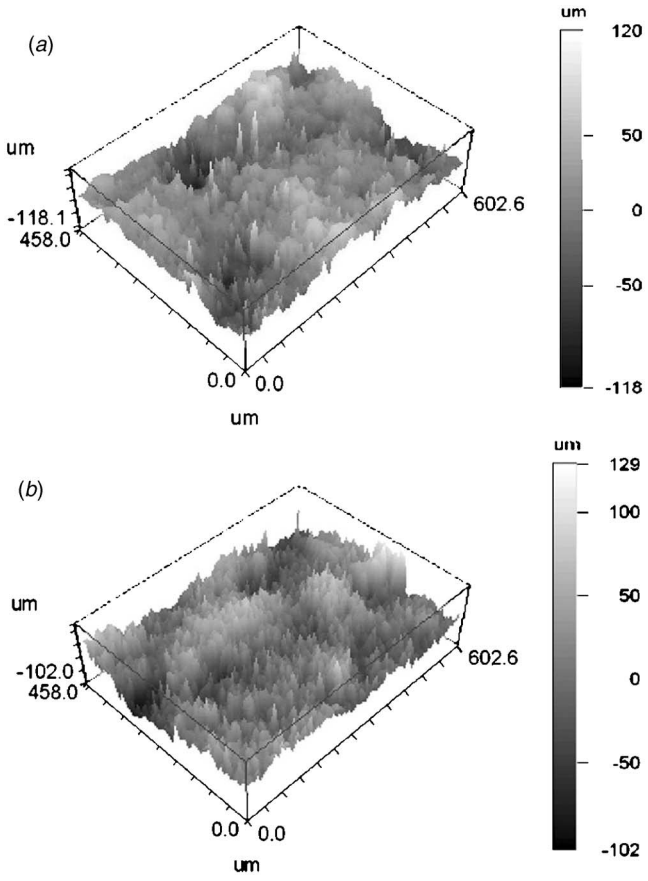

Fig. 4 Three-dimensional Wyko profilometry traces of portions of the rough surfaces: (*a*) Simulated rough surface with small-sized roughness elements and (*b*) rough surface from the pressure side of a turbine vane with particulate deposition from a utility power engine

The second step in the procedure is numerical determination of a modified version of the Sigal and Danberg roughness parameter Λ_s [4–6]. According to van Rij et al. [6], the modified version of Λ_s is defined using

$$\Lambda_s = \left(\frac{S}{S_f}\right)\left(\frac{S_f}{S_s}\right)^{-1.6} \tag{2}$$

where S is the reference area, or the area of the smooth base surface before adding on the roughness, S_f is the total frontal area over the rough surface, and S_s is the windward wetted surface area of all of the roughness elements on the surface. S/S_f is then a roughness density parameter, and S_f/S_s is a roughness shape parameter.

In the third part of the procedure, with Λ_s known, the ratio of equivalent sand-grain roughness size to mean roughness height, k_s/k, is determined using a correlation for three-dimensional, irregular roughness with irregular geometry and arrangement. According to van Rij et al. [6], k_s/k is given by

$$\frac{k_S}{k} = \begin{cases} 1.584 \times 10^{-5}\Lambda_S^{5.683} & \Lambda_S \leqslant 7.842 \\ 1.802\Lambda_S^{0.0304} & 7.842 \leqslant \Lambda_S \leqslant 28.12 \\ 255.5\Lambda_S^{-1.454} & 28.12 \leqslant \Lambda_S \end{cases} \tag{3}$$

The mean roughness height k is estimated as the distance between the maximum point of the ensemble average of all of the roughness peaks in any roughness sample and a base height. Determination of this base location is based on analytic procedures, which are also given by Van Rij et al. [6].

With this approach, magnitudes of equivalent sand-grain roughness size for the three-dimensional, irregular roughness of the present study are determined. Resulting values are given in Table 4, where each is based on an average of measurements from eight separate profilometry scans of each surface.

Mach Number Distributions. Figure 5 shows the Mach number distribution along the turbine vane pressure side and along the vane suction side for the present operating condition, which is produced by setting a certain stagnation pressure at the test-section inlet using the TWT mainstream air pressure regulator. Note that the exact same positions of the tailboards and the same flow settings on the bleeding system (shown in Fig. 1) are used for each blowdown test and each experimental condition investigated. The data shown in Fig. 5 are based on measurements of total pressure at the test-section inlet and vane midspan static pressures. These are measured using two different airfoils, which are constructed especially for this task: (i) a smooth vane ($k_s/cx=0$) and (ii) a vane with uniform small-sized roughness ($k_s/cx=0.00108$). Each of these vanes has five pressure taps on the pressure side and five pressure taps on the suction side, as well as one pressure tap located on the leading edge at the vane midspan. Figure 5 shows that the Mach number distributions on pressure and suction sides are in excellent agreement with data obtained from an operating industrial engine (which are based on an analytic solution provided by a gas turbine company). This Mach number distribution briefly enters the transonic region on the vane suction side and is subsonic on the pressure side. Compressible flow analysis is used to calculate Mach number distributions. Note that an adverse pressure gradient is present on the suction side for $Bx/cx>0.90$. As a result, a diffusion flow field and possibly earlier flow separation are expected to occur near the suction-side trailing edge. The flow acceleration and relatively low Mach numbers present on the pressure side produce thinning of the turbulent boundary layers accompanied by suppression of boundary layer turbulence.

Figure 5 also shows that the Mach number distributions for the roughened vane with $k_s/cx=0.00108$ and the smooth vane are in

Table 4 Characteristics of rough surfaces investigated

Surface	Λ_s	k_s/k	k (μm)	k_s (μm)	k_s/cx
Smooth	3020.7	0.0026	3.50	0.0094	0
Rough surface with nickel powder T1166F	20.1	1.889	27.92	52.59	0.00108
Rough surface with nickel powder NI-914	15.4	1.959	64.03	125.19	0.00258
Variable rough surface	See Fig. 2(*b*)				
Turbine vane from a utility power engine	43.5	1.641	40.82	62.30	0.00129

excellent agreement for the experimental condition. This means that; (i) the roughness has little effect on the airfoil Mach number and surface static pressure distributions and (ii) the contour shapes of the smooth vane and uniformly roughened vane with $k_s/cx = 0.00108$ are the same. This first result is consistent with data from Bammert and Sandstede [9], Kind et al. [10], Boyle and Senyitko [17], and Sitaram et al. [32] who show that roughness has only small effects on the turbine airfoil surface static pressure distributions. Note that the trailing edge area is not accessible for measurement because static pressure tap tubes cannot be installed in the portion of the vane with such a small trailing edge diameter.

Local Aerodynamic Performance. Figures 6–10 present local aerodynamic performance data in the wake for different surface roughness conditions and magnitudes of mainflow turbulence intensity. To provide an appropriate standard of comparison, each profile is measured over one complete exit pitch spacing (which is the effective pitch spacing that would exist between adjacent vanes). The inlet total pressure and vane Mach number distribution are kept constant as different vanes are employed.

Figure 6 shows normalized profiles of local total pressure losses coefficient C_p measured one axial chord length downstream of the test vane for Tu=1.1% (with no turbulence generator installed). Data are given for a smooth vane, a vane with uniform small-sized

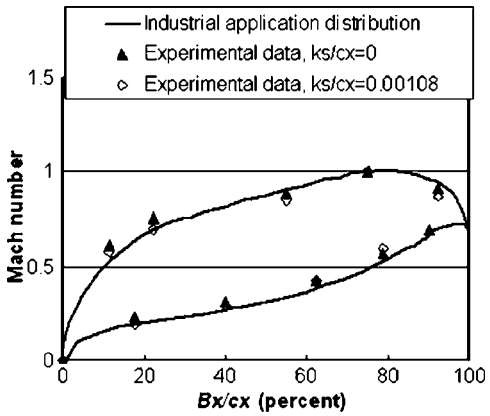

Fig. 5 Mach number distributions along the test vane

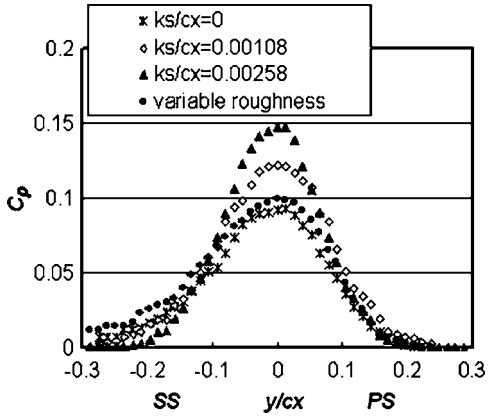

Fig. 6 Normalized local total pressure loss profiles measured one axial chord length downstream of the test vane with various surface roughness for Tu=1.1%

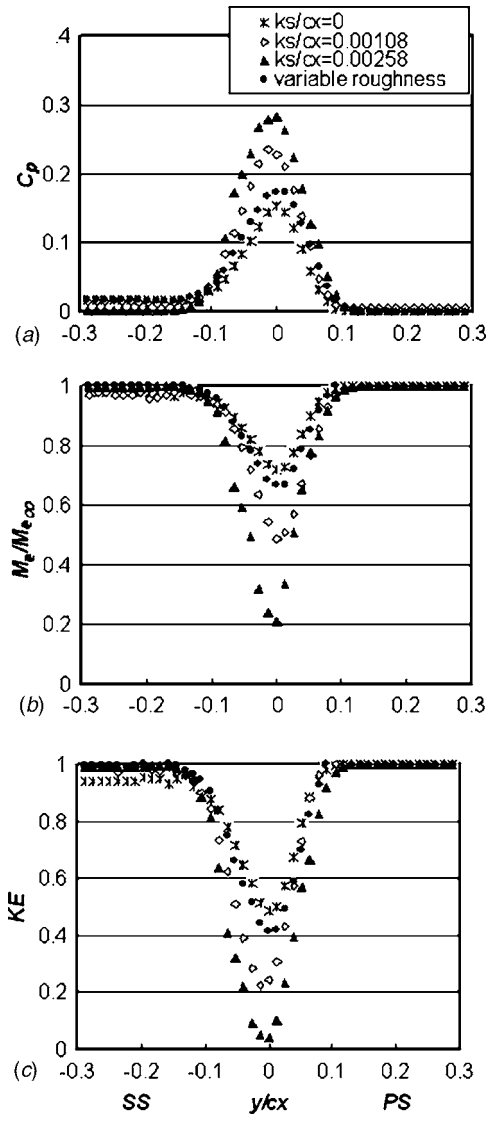

Fig. 7 Profiles measured 0.25 axial chord length downstream of the test vane with various surface roughness for Tu=5.4%: (*a*) Normalized local total pressure losses, (*b*) normalized local Mach numbers, and (*c*) normalized local kinetic energy

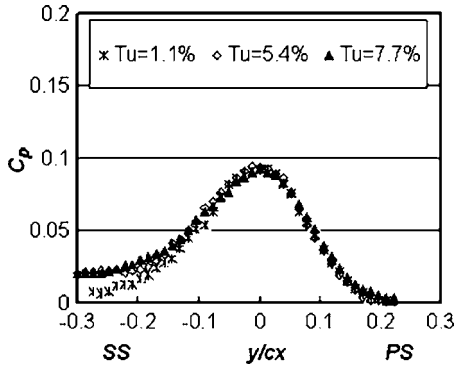

Fig. 8 Normalized local total pressure losses. Profiles measured with different turbulence intensity levels one axial chord length downstream of the test vane with a smooth surface.

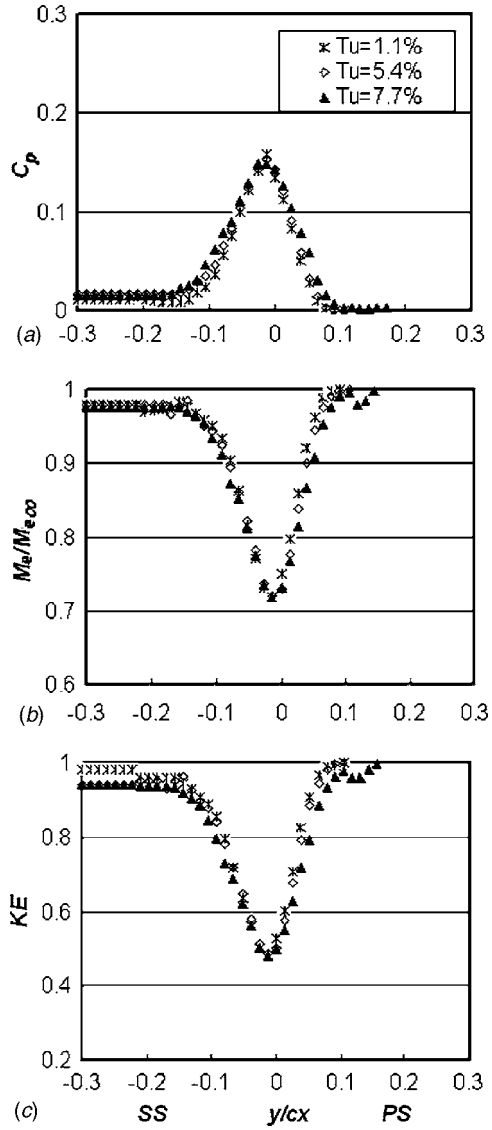

Fig. 9 Profiles measured at 0.25 axial chord length downstream of the test vane with a smooth surface: (*a*) Normalized local total pressure losses, (*b*) normalized local Mach numbers, and (*c*) normalized local kinetic energy

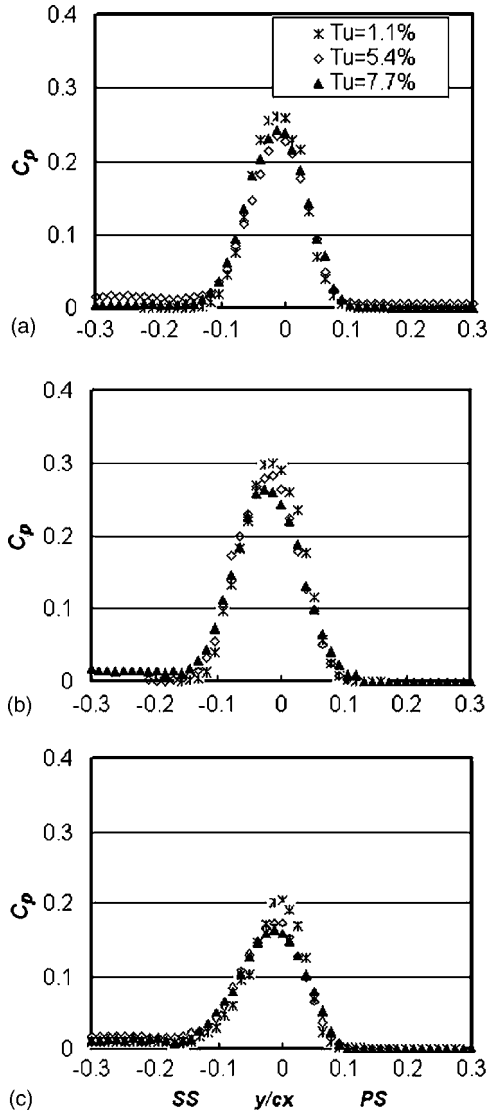

Fig. 10 Normalized local total pressure losses profiles measured 0.25 axial chord length downstream of the test vane: (*a*) $k_s/cx=0.00108$, (*b*) $k_s/cx=0.00258$, and (*c*) variable roughness

roughness ($k_s/cx=0.00108$), a vane with uniform large-sized roughness ($k_s/cx=0.00258$), and a vane with variable roughness. Figure 6 shows that, as k_s/cx increases, total pressure losses increase at each y/cx location within the wake. Similar data and observations are described by Zhang and Ligrani [26], Zhang et al. [14], Kind et al. [10], and Boyle and Senyitko [17]. Generally, broader wakes with increased roughness size are due to different boundary layer development with increasing roughness (earlier laminar-turbulent transition, augmented mixing and turbulent transport in the boundary layers, thicker boundary layers at trailing edges), and increased turbulent diffusion within the wake.

Compared to the symmetric C_p profiles obtained by Zhang and Ligrani [26], the asymmetry of the wake profiles from the present study can be observed in Fig. 6. Suction-side wakes (at negative y/cx) are thicker than the pressure-side wakes (at positive y/cx). This is mostly due to different growth and development of boundary layers on the suction and pressure sides of the vane. On the suction side, where local freestream velocities are higher, the diffusing flow field toward the aft end of the suction side is a significant contributor to the thick boundary layer near the trailing edge, which also gives thicker wake immediately downstream of the trailing edge. On the pressure side, boundary layer thickness is

usually much smaller than on the suction side because of relatively low surface Mach numbers and continuous flow acceleration. Bammert and Sandstede [9] report data showing the boundary layer on the suction side is considerably thicker than on the pressure side. Also according to Bammert and Sandstede [9], wake profile losses from turbine blades and vanes are due more to suction-side events by a factor 2.5–3.5 times compared to events originating near the pressure side. Some other research groups find that differences in momentum losses between the suction surface and the pressure surface events can be even larger. Here, one important reason why the pressure surface has a lower roughness effect is that k_s^+, the roughness Reynolds number, is lower due to the relatively lower local Reynolds number.

Figure 6 also includes measurements made downstream of the vane with variable roughness shown in Fig. 2(*b*). In most cases, variable surface roughness profile points in Fig. 6 lie slightly above the profile measured with a smooth vane ($k_s/cx=0$). Thus, the variable roughness placed on the vane pressure side increases total pressure losses only by small amounts, compared to those produced by uniform roughness on both pressure and suction sides. Thus, roughness on the vane pressure side has relatively smaller effects on the profile losses. Similar conclusions are given by Kind et al. [10], whose study employs turbine blades with roughness placed at various locations on the suction- and pressure-side surfaces. Note that the suction-side wake profile on Fig. 6 at $y/cx<0$ is also widened somewhat for the vane with variable roughness; even this vane has a smooth suction side. This is connected to different rates of boundary layer development as different levels of roughness are encountered along the vane pressure surface, which gives different magnitudes of boundary layer mixing and losses, and a different wake initial condition near the vane trailing edge, compared to vanes with uniformly roughened surfaces.

Figure 7 shows effects of surface roughness on normalized local total pressure losses C_p, normalized local Mach numbers $M_e/M_{e,\infty}$ and normalized local kinetic energy KE. These data are measured in the wake 0.25 axial chord lengths downstream of vanes for Tu=5.4% (with fine grid installed). Note that C_p, $M_e/M_{e,\infty}$, and KE are not independent of each other since they are all derived from pressure measurements. The different profiles provide information on local wake deficits of total pressure, Mach number, and kinetic energy, which all increase at each y/cx location within the wake as k_s/cx increases. Compared to the results in Fig. 7(*a*), the profile in Fig. 6 (measured one axial chord length downstream of the vane) are broader (i.e., spread over a wider range of y/cx), with lower peak values. This is mostly a result of transverse turbulent diffusion of streamwise momentum as the wake advects from 0.25 to 1 axial chord length downstream. Figure 7 and 6 additionally show that increased thickening of the wake is present as surface roughness size becomes larger. This is especially apparent and more substantial within the wake at negative y/cx values, or downstream of the suction sides of the vanes. In contrast, the effects of surface roughness are less apparent for positive y/cx values, or downstream of the pressure sides of the vanes. This is partially due to the different growth of boundary layers on the pressure and suction sides for different amounts of surface roughness.

Figure 8 present results that illustrate the effects of different inlet freestream turbulence levels on wake loss profiles downstream of a smooth vane. Results from the present study are presented for Tu magnitudes of 1.1%, 5.4%, and 7.7% for one axial chord length downstream of the test vane. As shown in Fig. 8, these C_p profiles are generally not sensitive to changes of the inlet turbulence intensity level for most of the wake. Also note that freestream turbulence effects are partially evident in the wake area for $y/cx<-0.15$ with higher C_p losses as turbulence intensity level increases. Similar suction-side freestream losses caused by higher turbulence intensity are also reported by Ames and Plesniak [22].

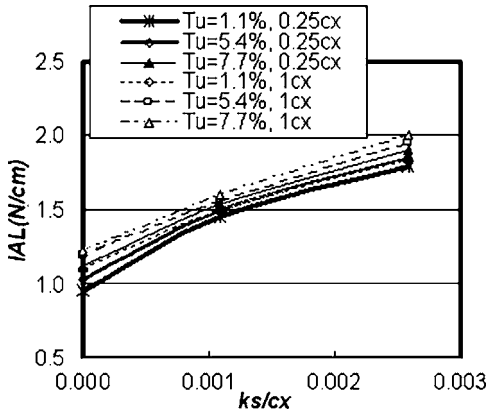

Fig. 11 Comparison of IAL as dependent on normalized equivalent sand-grain roughness size for different inlet turbulence intensity levels, as measured at two different locations downstream of the test vane trailing edge (1 and 0.25 axial chord lengths)

Figures 9(*a*)–9(*c*) show normalized local total pressure losses C_p, normalized local Mach numbers $M_e/M_{e,\infty}$, and normalized local kinetic energy KE measured 0.25 axial chord lengths downstream of the smooth test vane for various turbulence intensity levels. These wake profiles are less altered by the traverse turbulence diffusion of streamwise momentum than profiles measured further downstream. Effects of turbulence intensity levels on local deficits of total pressure, Mach number, and kinetic energy are almost negligible throughout the wake, except for locations downstream of the suction side where $y/cx<-0.1$.

Figures 10(*a*)–10(*c*) show C_p data obtained with small-sized roughness ($k_s/cx=.00108$), big-sized roughness ($k_s/cx=.00258$), and variable roughness along the vane surface at 0.25 axial chord length downstream of the test vane. Compared to Fig. 9(*a*), data in Figs. 10(*a*)–10(*c*) show trends that are similar to ones described by Zhang and Ligrani [26] and Ames and Plesniak [22]. In particular, lower peak values in the center of the wake and slight broadening of wake profiles are present at higher inlet turbulence intensity levels. This is consistent with Zhang and Ligrani [26] who suggest that thicker rough surface boundary layers are somewhat more sensitive to changes of freestream turbulence level than thinner boundary layers that develop over a smooth surface. From the data presented in Figs. 6–10, it is apparent that effects of inlet turbulence intensity on wakes are relatively small compared with the more substantial influences of surface roughness.

Integrated Aerodynamic Losses

Dimensional magnitudes of integrated aerodynamic loss (IAL) are determined by integrating profiles of $(P_{oi}-P_{oe})$ with respect to y in the transverse flow direction across the wake for one single vane spacing, from $-p/2$ to $p/2$.

$$\mathrm{IAL}=\int_{-p/2}^{p/2}(p_{oi}-p_{oe})dy \tag{4}$$

In the present study, IAL magnitudes are mostly the result of two phenomena: (i) the losses resulting from formation of the boundary layers along the vane surfaces and (ii) the flow separation, recirculation zone, and wake mixing losses that are initially present just downstream of the vanes.

IAL magnitudes presented in Fig. 11 are determined from profiles that are measured at two different locations downstream of the test vane trailing edge (1 and 0.25 axial chord lengths). The overall trends of the data in this figure illustrate the dominating influences of the surface roughness (as characterized by normalized equivalent sand-grain roughness size) on aerodynamic losses

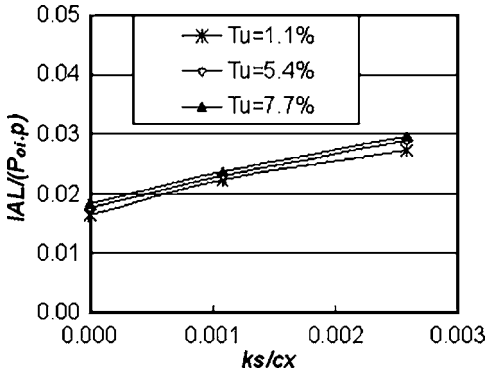

Fig. 12 Comparison of normalized IAL as dependent on normalized equivalent sand-grain roughness size for different inlet turbulence intensity levels obtained one axial length downstream of the turbine vane

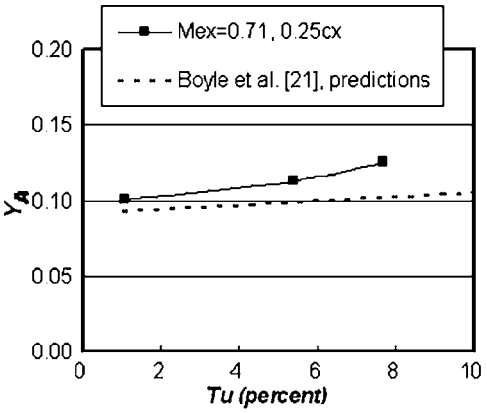

Fig. 13 Comparison of area averaged loss coefficients measured in normal planes 0.25*cx* downstream of the vane, with predictions from Boyle et al. [21]

and the weaker dependence of these losses on inlet freestream turbulence intensity level. As shown in Fig. 11, IAL magnitudes increase only slightly with increasing turbulence intensity level. Comparisons of IAL data from two different wake locations indicate that overall magnitudes of total pressure deficits and momentum deficits do not change greatly as the wake is advected in the streamwise direction because not much mean streamwise momentum is converted into turbulence by local shear and turbulence production.

IAL data, obtained from profiles that are measured one axial chord length downstream of the turbine vane, are normalized using the test section passage pitch p and test section inlet stagnation pressure P_{oi} in Fig. 12. Here, normalized IAL magnitudes increase almost linearly as k_s/cx increases for each magnitude of turbulence intensity.

Boyle et al. [21] employ an area averaged loss coefficient Y_A in their analysis, which is defined using an equation of the form

$$Y_A = \frac{P_{oi} - P_{oe,A}}{P_{oi} - P_{se,A}} \tag{5}$$

Here, $P_{oe,A}$ and $P_{se,A}$ are area averaged exist total pressure and static pressure, respectively. These are determined using equations given by

$$P_{oe,A} = \int_{-p/2}^{p/2} P_{oe} d(y/p) \tag{6}$$

and

$$P_{se,A} = \int_{-p/2}^{p/2} P_{se} d(y/p) \tag{7}$$

respectively.

Boyle et al. [21] employ vanes with 4.445 cm axial chord length and an ~80 deg flow turning angle for their numerical predictions. Their data are based on measurements made in an axial plane located 0.29 axial chord length downstream of their vane trailing edge. Figure 13 shows comparison of their data with results from the present study over a range of turbulence intensity levels, which are measured in normal planes 0.25*cx* downstream of the smooth vane. Here, $M_{ex}=0.7$ and $\mathrm{Re}=1\times10^6$ for Boyle et al. [21] compared to $M_{ex}=0.71$ and $\mathrm{Re}=0.95\times10^6$ for the present study. These data sets indicate that slightly higher Y_A losses are generally observed as higher inlet turbulence intensity levels are present. This is consistent with results from Gregory-Smith and Cleak [20] and Ames and Plesniak [22]. Predicted values by Boyle et al. [21] are slightly lower than the present experimental results, but differences are relatively small and trends are generally consistent. Note that some differences between the present results and those from Boyle et al. [21] are due to difference in flow turning and other experimental conditions. In addition, different wake traversing procedures are employed: profiles from the present study are measured in planes that are oriented normal to the backflow direction; wake data from Boyle et al. [21] are given for axial planes.

Summary and Conclusions

The effects of surface roughness and freestream turbulence level on the aerodynamic performance of a turbine vane are experimentally investigated. Wake profiles are measured with three different freestream turbulence intensity levels (1.1%, 5.4%, and 7.7%) at two different locations downstream of the test vane trailing edge (1 and 0.25 axial chord length). The Mach number distribution and the test vane configuration both match arrangements employed in an industrial application. Four vanes with different surface roughness are employed in this study: (i) smooth, (ii) small-sized roughness, ($k_s/cx=0.00108$), (ii) big-sized roughness, ($k_s/cx=0.00258$), and (iv) variable rough surface only on the pressure side. All four vanes have the same shape and exterior dimensions. The nonuniform, irregular, three-dimensional roughness on the tested vanes is employed to match the roughness that exists on operating turbine vanes and blades subject to extended operating times with significant particulate deposition on the surfaces. This is verified by detailed three-dimensional optical profilometry traces and rough surface statistics (such as equivalent sandgrain roughness size), which are similar for the roughness from a power engine turbine blade and the test surfaces employed in this study.

Local wake deficits of total pressure, Mach number, and kinetic energy all increase at each y/cx location within the wake as k_s/cx increases. Asymmetry is present in all the wake profiles measured downstream of the turbine vane. Suction-side wakes (at negative y/cx) are thicker than the pressure-side wakes (at positive y/cx) due to different growth and development of boundary layers on the suction and pressure sides. This is partially a result of diffusion near the aft end of the airfoil suction side, which may be leading to a locally augmented region of flow separation. The effects of surface roughness are then much less apparent for pressure-side wakes at positive y/cx. Total pressure losses from variable roughness on the pressure side are only slightly higher than losses produced by smooth vanes and, generally, less than losses caused by uniform roughness on both pressure and suction sides.

For a smooth test vane, increasing freestream turbulence intensity has negligible effects on the wake shape and structure while increasing integrated freestream losses. Wake profiles form test vanes with rough surfaces show lower peak values in the center of

the wake and slightly broadening wake profiles at higher inlet turbulence intensity levels. This indicates that thicker rough surface boundary layers are more sensitive to changes of freestream turbulence level than thinner boundary layers that develop over smooth surfaces.

The effect of inlet turbulence intensity on wakes is relatively small compared to the substantial effect of surface roughness. This is additionally illustrated by integrated aerodynamic losses (IAL) data since normalized IAL magnitudes increase almost linearly as ks/cx increases, whereas IAL changes are very small as Tu increases.

Acknowledgment

The research reported in this paper was sponsored by the National Science Foundation (NSF Grant No. CTS-0086011). Dr. Stefan Thynell and Dr. Richard Smith were the NSF program monitors. The authors also acknowledge Mike Blair of Pratt & Whitney Corporation, Dr. Hee-Koo Moon of Solar Turbines Inc., Edward North, Ihor Diakunchak of Siemens-Westinghouse Corp., and Dr. Sri Sreekanth and Dr. Ricardo Trindade from Pratt & Whitney-Canada Corporation for guidance and suggestions on this research effort.

Nomenclature

Bx = linear distance measured along the axial chord from vane leading edge
c = true chord length
cx = axial chord length
C_p = local total pressure coefficient, $(P_{oi}-P_{oe})/P_{oi}$
M_e = exit local Mach number in the wake
M_{ex} = exit freestream Mach number measured 0.25 cx downstream of the vane trailing edge
$M_{e,\infty}$ = exit free-stream Mach number
k = roughness height
KE = normalized local kinetic energy, $(P_{oe}-P_{se})/(P_{oe}-P_{se})_\infty$
k_s = equivalent sand-grain roughness
k_s^+ = roughness Reynolds number, or normalized sand-grain roughness size, $k_s^+=k_sV_\tau/\nu$, where V_τ is friction velocity and υ is kinetic viscosity
p = effective passage pitch
P_o = stagnation pressure
P_{oe} = exit local stagnation pressure
$P_{oe,m}$ = mass averaged exit stagnation pressure
$P_{oe,\infty}$ = exit freestream stagnation pressure
$P_{oe,A}$ = area averaged exit total pressure
P_{se} = exit local static pressure
$P_{se,A}$ = area averaged static pressure
P_{oi} = inlet stagnation pressure
PS = pressure side
s = blade surface length from leading edge of the vane
S = rough surface flat reference area
S_f = total roughness frontal area
S_s = total roughness windward wetted surface area
SS = suction side
Tu = Turbulence intensity
u = exit local streamwise velocity
U_∞ = freestream velocity over the vane surface
ν = kinetic viscosity
x = linear distance along vane centerline from leading edge of the vane
y = normal coordinate measured from vane centerline
Y_A = area averaged loss coefficient used by Boyle et al. [21]
Λ_s = Sigal and Danberg [4,5] roughness parameter
ω = total pressure loss coefficient used by Ames and Plesniak [22], $(P_{oi}-P_{oe})/(P_{oi}-P_{se})$
ρ = exit local density

Subscripts

A = area
e = exit
∞ = freestream

References

[1] Nikuradse, J., 1933, "Laws of Flow in Rough Pipes," NACA TM 1292, National Advisory Committee on Aeronautics.
[2] Schlichting, H., 1936, "Experimental Investigation of the Problem of Surface Roughness," NACA TM-832, National Advisory Committee on Aeronautics.
[3] Coleman, H. W., Hodge, B. K., and Taylor, R. P., 1984, "A Re-evaluation of Schlichting's Surface Roughness Experiment," ASME J. Fluids Eng., **106**, pp. 60–65.
[4] Sigal, A., and Danberg, J. E., 1990, "New Correlation of Roughness Density Effect on Turbulent Boundary Layer," AIAA J., **28**(3), pp. 554–556.
[5] Sigal, A., and Danberg, J. E., 1988, "Analysis of Turbulent Boundary Layer Over Roughness Surface With Application to Projectile Aerodynamics," Army Ballistic Research Lab, Aberdeen Proving Grounds MD, Technical Report No. BRL-TR-2977.
[6] Van Rij, J. A., Belnap, B. J., and Ligrani, P. M., 2002, "Analysis and Experiments on Three-Dimensional, Irregular Surface Roughness," ASME J. Fluids Eng., **124**, pp. 1–7.
[7] Zhang, Q., Lee, S. W., and Ligrani, P. M., 2003, "Determination of Rough-Surface Skin Friction Coefficients From Wake Profile Measurements," Exp. Fluids, **35**, pp. 627–635.
[8] Bammert, K., and Sandstede, H., 1975, "Influence of Manufacturing Tolerances and Surface Roughness of Blades on the Performance of Turbines," ASME Paper No. 75-GT-35.
[9] Bammert, K., and Sandstede, H., 1980, "Measurements of the Boundary Layer Development Along a Turbine Blade With Rough Surfaces," ASME J. Eng. Power, **102**, pp. 978–983.
[10] Kind, R. J., Serjak, P. J., and Abbott, M. W. P., 1996, "Measurements and Prediction of The Effects of Surface Roughness on Profile Losses and Deviation in a Turbine Cascade," ASME Paper No. 95-GT-203.
[11] Bogard, D. G., Schmidt, D. L., and Tabbita, M., 1998, "Characterization and Laboratory Simulation of Turbine Airfoil Surface Roughness and Associated Heat Transfer," ASME J. Turbomach., **120**, pp. 337–342.
[12] Abuaf, N., Bunker, R. S., and Lee, C. P., 1998, "Effects of Surface Roughness on Heat Transfer and Aerodynamics Performance of Turbine Airfoils," ASME J. Turbomach., **120**, pp. 522–529.
[13] Leipold, R., Boese, M., and Fottner, L., 2000, "The influence of Technical Surface Roughness Caused by Precision Forging on the Flow Around a Highly Loaded Compressor Cascade," ASME J. Turbomach., **122**, pp. 416–425.
[14] Zhang, Q., Lee, S. W., and Ligrani, P. M., 2004, "Effects of Surface Roughness and Turbulence Intensity on the Aerodynamic Losses Produced by the Suction Surface of a Simulated Turbine Airfoil," ASME J. Fluids Eng., **126**, pp. 257–265.
[15] Stripf, M., Schulz, A., and Wittig, S., 2004, "Surface Roughness Effects on External Heat Transfer of a HP Turbine Vane," ASME Paper No. GT2004-53114.
[16] Roberts, S. K., and Yaras, M. I., 2004, "Boundary-Layer Transition over Rough Surfaces With Elevated Freestream Turbulence," ASME Paper No. GT2004-53668.
[17] Boyle, R. J., and Senyitko, R. G., 2003, "Measurements and Predictions of Surface Roughness Effects on Turbine Vane Aerodynamics," ASME Paper No. GT-2003-38580.
[18] Yun, Y. I., Park, I. Y., and Song, S. J., 2004, "Performance Degradation Due to Blade Surface Roughness in a Single-Stage Axial Turbine," ASME Paper No. GT2004-53094.
[19] Zhang, Q., Lee, S. W., and Ligrani, P. M., 2004, "Effect of Surface Roughness and Freestream Turbulence on the Wake Turbulence Structure of a Symmetric Airfoil," Phys. Fluids, **16**, pp. 2044–2053.
[20] Geogory-Smith, D. G., and Cleak, J. G. E., 1992, "Secondary Flow Measurements in a Turbine Cascade With High Inlet Turbulence," ASME J. Turbomach., **114**, pp. 173–183.
[21] Boyle, R. J., Luci, B. L., Verhoff, V. G., Camperchioli, W. P., and La, H., 1998, "Aerodynamics of a Transitioning Turbine Stator Over a Range of Reynolds Numbers," ASME Paper No. 98-GT-285.
[22] Ames, F. E., and Plesniak, M. W., 1997, "The Influence of Large-Scale, High Intensity Turbulence on Vane Aerodynamics Losses, Wake Growth, and the Exit Turbulence Parameters," ASME J. Turbomach., **119**, pp. 182–192.
[23] Jouini, D. B. M., Sjolander, S. A., and Moustapha, S. H., 2001, "Aerodynamic Performance of a Transonic Turbine Cascade at Off-Design Conditions," ASME J. Turbomach., **123**, pp. 510–518.
[24] Radomsky, R. W., and Thole, K. A., 2002, "Detailed Boundary Layer Measurements on a Turbine Stator Vane at Elevated Freestream Turbulence Levels," ASME J. Turbomach., **124**, pp. 107–118.

[25] Boyle, R. J., Lucci, B. L., and Senyitko, R. G., 2002, "Aerodynamics Performance and Turbulence Measurements in a Turbine Vane Cascade," ASME Paper No. GT-2002-30434.
[26] Zhang, Q., and Ligrani, P. M., 2004, "Effects of Mach Number and Surface Roughness on the Aerodynamic Losses of a Symmetric Transonic Turbine Airfoil," J. Propul. Power, **20**, pp. 1117–1125.
[27] Jackson, D. J., Lee, K. L., Ligrani, P. M., and Johnson, P. D., 2000, "Transonic Aerodynamics Losses Due to Turbine Airfoil, Suction Surface Film Cooling," ASME J. Turbomach., **122**, pp. 317–326.
[28] Furukawa, T., and Ligrani, P. M., 2002, "Transonic Film Cooling Effectiveness From Shaped Holes on a Simulated Turbine Airfoil," J. Thermophys. Heat Transfer, **16**, pp. 228–237.
[29] Kline, S. J., and McClintock, F. A., 1953, "Describing Uncertainties in Single Sample Experiments," Mech. Eng. (Am. Soc. Mech. Eng.), **75**, pp. 3–8.
[30] Moffat, R. J., 1988, "Describing the Uncertainties in Experimental Results," Exp. Therm. Fluid Sci., **1**, pp. 3–17.
[31] Jackson, D. J., "Aerodynamic Mixing Losses and Discharge Coefficients Due to Film Cooling From a Symmetric Turbine Airfoil in Transonic Flow," M.S. thesis, Department of Mechanical Engineering, University of Utah.
[32] Sitaram, N., Govardhan, M., and Murali Krishna, V. T., 1999, "Loss Reduction by Means of Two-Dimensional Roughness Elements on the Suction Surface of a Linear Turbine Rotor Cascade," Flow, Turbul. Combust., **62**, pp. 227–248.

Degradation of Film Cooling Performance on a Turbine Vane Suction Side due to Surface Roughness

James L. Rutledge[1]
David Robertson[2]
David G. Bogard

University of Texas at Austin,
Austin, TX

After an extended period of operation, the surfaces of turbine airfoils become extremely rough due to deposition, spallation, and erosion. The rough airfoil surfaces will cause film cooling performance degradation due to effects on adiabatic effectiveness and heat transfer coefficients. In this study, the individual and combined effects of roughness upstream and downstream of a row of film cooling holes on the suction side of a turbine vane have been determined. Adiabatic effectiveness and heat transfer coefficients were measured for a range of mainstream turbulence levels and with and without showerhead blowing. Using these parameters, the ultimate film cooling performance was quantified in terms of net heat flux reduction. The dominant effect of roughness was a doubling of the heat transfer coefficients. Maximum adiabatic effectiveness levels were also decreased significantly. Relative to a film cooled smooth surface, a film cooled rough surface was found to increase the heat flux to the surface by 30%–70%. [DOI: 10.1115/1.2185674]

Introduction

New turbine stage components are typically run for several years before extensive maintenance is required. During that period, surface roughness will increase due to deposition, spallation, and erosion [1,2]. A rough airfoil surface will cause film cooling performance degradation due to early boundary layer transition, thickening of the boundary layer, and increased turbulent mixing in the boundary layer. The roughness affects both the adiabatic effectiveness and the heat transfer coefficient. Several previous studies have evaluated the effects of roughness on film cooling of flat surfaces, but there has been very limited research on airfoil models. In this study, a simulated nozzle guide vane was used and effects of roughness upstream and downstream of a row of suction side film cooling holes was compared to smooth surface performance.

Effects of surface roughness on adiabatic effectiveness for film cooling using a row of holes on a flat surface have been studied by Goldstein et al. [3] and Schmidt et al. [4]. Schmidt et al. [4] also measured changes in heat transfer coefficient due to coolant injection with a rough surface. Roughness elements for the Goldstein et al. study were as large as $0.5D$, where D was the coolant hole diameter. For the Schmidt et al. study the roughness consisted of an array of conical elements with a maximum roughness element height of $0.4D$ and an equivalent sandgrain roughness of $\mathrm{Re}_k \approx 100$. Roughness downstream of the coolant holes was found to have a small effect on laterally averaged adiabatic effectiveness, i.e., less than 10% decrease for low momentum ratios and less than 5% increase for high momentum flux ratios. While roughness caused a 50% increase in heat transfer coefficient, coolant injection did not cause a significant change in heat transfer coefficient except within $10D$ of the hole where less than a 10% decrease occurred at low momentum flux ratio, and less than a 10% increase occurred for high momentum flux ratio.

Guo et al. [5] performed a limited study of the effects of surface roughness on a fully film cooled simulated vane. A transient testing technique was used that yielded data in the leading edge and forward part of the vane. They found that the minimal roughness used increased h by nearly a factor of 2 in the downstream regions of the vane, which may be due to transitioning from laminar to turbulent flow initiated by the roughness. They also concluded that adiabatic effectiveness was only slightly affected by the roughness in the region of interest of this paper.

Bogard et al. [6] used the current simulated turbine vane test facility to determine roughness effects on adiabatic effectiveness performance of the vane suction side film cooling. A large decrease in adiabatic effectiveness was found due to roughness upstream of the cooling holes. This was speculated to be due to boundary layer thickening caused by the surface roughness. Since this previous study did not include heat transfer coefficients, the effects of roughness on the net heat flux reduction could not be determined.

For the current study, adiabatic effectiveness distributions were measured for a wider range of conditions than previously tested. In these tests low and high mainstream turbulence levels were used, and tests were conducted with and without concurrent showerhead cooling. Furthermore, heat transfer coefficients were measured using a constant heat flux foil downstream of the coolant holes. Adiabatic effectiveness and heat transfer coefficients results were combined to determine the effect of roughness on the net heat flux reduction.

Experimental Facilities and Procedures

Tests were conducted in a closed loop wind tunnel driven by a 50 hp adjustable speed fan. The test section shown in Fig. 1 consisted of a simulated three-vane linear cascade. The vane geometry replicated an actual engine geometry scaled up nine times. The center vane was the test vane and is shown in Fig. 2. The outer wall was adjusted to achieve a nondimensional pressure distribution around the vane that matched an inviscid CFD simulation of the actual engine geometry and conditions. The cascade inlet velocity was 5.8 m/s and the exit velocity was 32 m/s, yielding an exit Reynolds number of 1.06×10^6 (based on a true chord length of $C=594$ mm) to match realistic engine conditions. A removable passive turbulence generator 50 cm upstream of the vane cascade consisted of 12 rods with outside diameter of 3.8 cm and pitched 8.5 cm apart. With the turbulence generator installed,

[1]Currently with the U.S. Air Force.
[2]Currently with Florida Turbine Technology.

Contributed by the International Gas Turbine Institute (IGTI) of ASME for publication in the JOURNAL OF TURBOMACHINERY. Manuscript received October 1, 2004; final manuscript received February 1, 2005. Assoc. Editor: K. C. Hall.

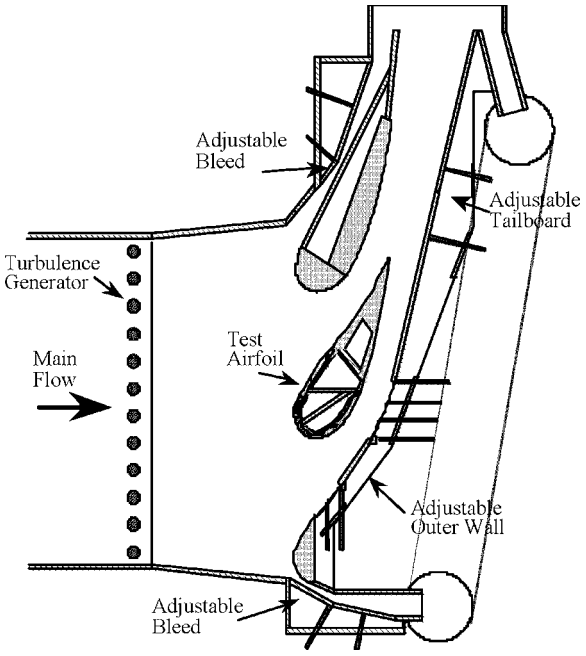

Fig. 1 Schematic of the simulated turbine vane test section

the turbulence at 0.18 C upstream of the test vane's leading edge was determined to be $Tu_\infty=21\%$ with $\Lambda_f/C=0.069$. Without the turbulence generator installed, the turbulence was $Tu_\infty=3.5\%$ with $\Lambda_f/C=0.074$. The relatively high "low" mainstream turbulence condition was due to a simulated hot streak generator that was installed in the facility but not used in this study.

The vane was constructed of a low conductivity polyurethane foam, $k=0.48$ W/m K, to facilitate the measurement of adiabatic wall temperature and to minimize conduction losses for heat transfer tests. The vane's showerhead region consisted of six rows of film cooling holes with a streamwise angle of 90 deg and an injection angle of 25 deg. The first row of suction side coolant holes downstream of the showerhead was located at $s/C=0.208$, had an injection angle of 56 deg, and oriented streamwise. All film cooling holes were cylindrical and had a diameter of 4.11 mm. The area studied was between this first row of suction side coolant holes and the second row, located at $s/C=0.367$. Since the showerhead plenum was fed independently of the suction side plenum, measurements could be made with or without the showerhead, and a range of suction side blowing ratios could be achieved while keeping the showerhead blowing at $M_{sh}=1.6$, an optimum showerhead blowing ratio described by Cutbirth and Bogard [7]. The showerhead region was covered with tape during nonuse. Table 1 summarizes the experimental conditions.

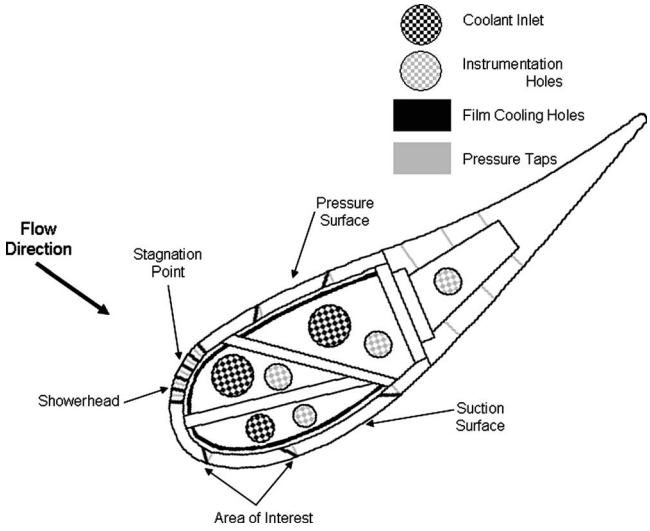

Fig. 2 Schematic of test vane details

Table 1 Test conditions

True chord length	59.4 cm
Span	54.9 cm
Pitch	45.7 cm
Inlet velocity	5.8 m/s
Exit Reynolds number	1.06×10^6
High freestream	Tu=21%
Turbulence at inlet	$\Lambda_f=4.1$ cm
Low freestream	Tu=5.2%
Turbulence at inlet	$\Lambda_f=4.4$ cm
Showerhead blowing Ratio (when in use)	$M_{sh}=1.6$
Film cooling hole Diameter	4.11 mm
Density ratio (ρ_c/ρ_∞)	1.6 (for η) 1.0 (for h)

The roughness design used in this study was the same as used by Bogard et al. [6]. It consisted of an array of 4 mm diameter cones with 1 mm height pitched 4.3 mm. This roughness configuration was estimated to have an equivalent sandgrain roughness height of 0.5 mm [6] resulting in a roughness Reynolds number of $Re_k\approx50$. The roughness was selected to represent a typical turbine roughness (see the data of Bons et al. [1] and Bogard et al. [2]).

Spatial heat transfer coefficient data were obtained by application of a uniform heat flux and measuring the temperature distribution via infrared thermography (a FLIR ThermaCAM P20 infrared camera calibrated in situ using type E thermocouples). The thermocouple data were acquired using a National Instruments Data Acquisition system (NI DAQ). LabVIEW software was written to compute parameters in real time and write the data to disk.

The uniform heat flux was applied using electrical heating of a stainless steel foil attached to the surface of the vane. The electrical heat flux was determined by measuring the voltage drop across the heat flux plate and the current through the heat flux plate. A rough heat flux plate had the roughness array stamped in it and was 0.002 in. thick. The smooth heat flux plate was necessarily 0.004 in. thick in order to provide the structural rigidity required to maintain a smooth surface. Lateral heat conduction was determined to be negligible. A one-dimensional heat conduction model (utilizing the known surface and interior boundary conditions and thermal conductivity of the vane material) was used to correct the surface heat flux for conduction into the substrate. At most, 5% of the electrical heat flux was lost due to conduction. A numerical model demonstrated that two-dimensional conduction issues were only significant at the edges of the heat flux plate. Heat transfer due to radiation was also subtracted from the total heat flux in order to determine the convective heat flux. The maximum heat loss due to radiation was typically 9% of the electrical heat flux. The convective heat transfer coefficient was determined through the following equation:

$$h=\frac{q''_{\text{electrical}}-q''_{\text{radiation}}-q''_{\text{conduction}}}{T_s-T_{\text{aw}}} \tag{1}$$

Although roughness was at times placed upstream of the first row of suction side coolant holes, the heat flux was only applied in the region downstream of the coolant holes. If the heat flux were applied upstream as well, the jets would displace the existing thermal boundary layer, thus initiating a new thermal boundary layer. Since the purpose of this study was to isolate the hydrody-

namic effects of film cooling on heat transfer, a heated starting length was not used upstream of the injection.

Adiabatic effectiveness was determined from surface temperature measurements made using infrared thermography similar to the heat transfer measurements. Adiabatic effectiveness, η, was determined using the following equation:

$$\eta \equiv \frac{T_\infty - T_{\text{aw}}}{T_\infty - T_c} \tag{2}$$

A density ratio of DR=1.6 for the coolant was achieved using liquid nitrogen to cool the air in a secondary loop that was then used as the coolant of the test vane. A range of suction side blowing ratios was tested from $M=0.3$ to 1.4. Tests were conducted with and without showerhead cooling. When the showerhead cooling was in operation, only one blowing ratio was used, $M_{\text{sh}}=1.6$, which was the optimum blowing ratio for the showerhead [7].

A density ratio of DR=1.0 was used for the heat transfer experiments. Although heat transfer tests could be performed with higher density coolant, the uncertainty in h for these measurements was prohibitively large because of a high sensitivity to the precise values of the surface temperatures. Consequently, for heat transfer experiments, the coolant temperature was maintained within 0.2 K of the mainstream temperature.

Although the vane was constructed of low thermal conductivity foam, conduction through the wall of the vane caused the measured surface temperatures to be slightly lower than what they would have been with a truly adiabatic surface. Radiation effects were found to be negligible during adiabatic effectiveness tests. The effect of conduction was corrected with a one-dimensional conduction model as described by Robertson [8]. By blocking the flow of coolant to the film cooling holes in the view of the IR camera, and allowing the other holes to flow freely, the decrease in surface temperature due to conduction was measured directly. This wall temperature without film cooling, normalized in terms of adiabatic effectiveness, was designated η_0. The following equation was used to correct the other measurements for conduction:

$$\eta = \frac{\eta_{\text{measured}} - \eta_0}{1 - \eta_0} \tag{3}$$

A concept known as "net heat flux reduction" has been used as a way of predicting the percentage reduction in local heat flux on an actual vane [9]. The net heat flux reduction is given by

$$\Delta q_r \equiv 1 - \frac{q_f''}{q_0''} = 1 - \frac{h_f(T_{\text{aw}} - T_w)}{h_0(T_\infty - T_w)} = 1 - \frac{h_f}{h_0}\left(1 - \frac{\eta}{\phi}\right) \tag{4}$$

where ϕ is defined as follows:

$$\phi = \frac{T_\infty - T_s}{T_\infty - T_c} \tag{5}$$

where T_s is the surface "metal" temperature for the actual airfoil. Based on expected values for ϕ given in the literature, a value of $\phi=0.6$ was presumed for this analysis [9].

A negative net heat flux reduction indicates a net heat flux increase. For the purposes of this study, we have modified Eq. (4) to provide a technique for predicting the net change in heat load due to roughness. In order to emphasize the fact that roughness increases the heat load, the effect is presented simply as the quantity, $q_{f,\text{rough}}/q_{f,\text{smooth}}$, given by

$$\frac{q''_{f,\text{rough}}}{q''_{f,\text{smooth}}} = \frac{h_{f,\text{rough}}(T_{\text{aw,rough}} - T_w)}{h_{f,\text{smooth}}(T_{\text{aw,smooth}} - T_w)} = \frac{h_{f,\text{rough}}(\eta_{\text{rough}} - \phi)}{h_{f,\text{smooth}}(\eta_{\text{smooth}} - \phi)} \tag{6}$$

Combining low density ratio heat transfer data with high density ratio adiabatic effectiveness data requires selection of a blowing parameter that aligns the measurements. In the absence of definitive data that suggests which of blowing ratio, momentum flux ratio, or velocity ratio is best suited for the task, blowing ratio was selected for this study. Furthermore, it will be shown that $\bar{h}$ is relatively insensitive to the 26% or 60% change in M required to match the momentum flux ratio or velocity ratio, respectively.

In addition to the heat transfer and adiabatic effectiveness measurements, a hot wire anemometer was used to make velocity measurements. An A.A. Lab Systems Ltd. AN-1003 Hot Wire/Hot Film Anemometry System was employed, and the same NI DAQ hardware was used for the data acquisition.

Uncertainty

Precision uncertainties in the hot wire measurements were determined to be ±0.5% of mean velocities and ±3% for turbulence intensities. The uncertainty in surface temperature was the main source of uncertainty for both η and h. Typical infrared camera calibrations resulted in an uncertainty of $\delta T = \pm 0.5$ K for the temperature range for h tests and $\delta T = \pm 2.0$ K for the temperature range covering η tests.

Uncertainty in the measurement of the heat transfer coefficients was caused by uncertainty in the heat flux and uncertainty in the temperature measurements. Because the heat transfer coefficient is inversely proportional to the temperature difference between the freestream and the surface temperature, uncertainty in h was extremely high at the leading edge of the heat flux plate due to the small ΔT. However, data are accurate for $x/D > 3$ where the uncertainty is typically approximately 5%, but always less than 7%.

Uncertainty in the measurement of adiabatic effectiveness was influenced by the uncertainty in the infrared measurement (±2.0 K) and the uncertainty in the measurement of the coolant temperature and the mainstream temperature. The uncertainty was calculated to be $\delta\eta = \pm 0.02$ for all values of η. This value was also confirmed experimentally, by repeating an individual test several times during the course of an experiment and also by repeating experiments on different days.

Velocity Profile Results

Hot wire anemometry measurements were made of the flow approaching the coolant holes approximately 2 hole diameters upstream of the row of suction side film holes studied. These measurements were made with various upstream configurations (i.e., high/low mainstream Tu, upstream roughness, etc.). Mean velocity profiles for various conditions are presented in Fig. 3(*a*) and profiles of the turbulence intensity are presented in Fig. 3(*b*). The mean velocity profiles show that the boundary layer thickness increased from $\delta = 0.15D$ to $\delta = 0.45D$ due to roughness upstream of the coolant holes. Increased levels of mainstream turbulence and showerhead blowing had little effect on the boundary layer thickness. Similarly, surface roughness caused a large increase in turbulence intensity that was substantially more than caused by increased levels of mainstream turbulence and showerhead blowing.

Adiabatic Effectiveness Results

In this study a variety of roughness configurations were tested including roughness upstream, roughness downstream, and roughness both upstream and downstream (all rough) of the coolant holes. The all smooth case was also tested as a baseline. All of the roughness conditions were tested under both high and low mainstream turbulence levels. For the purposes of this paper we focus on the comparison between the all smooth and the all rough cases at the high mainstream turbulence level (most representative of actual gas turbines).

A comparison of the results of smooth and all rough with mainstream turbulence and without showerhead cooling can be found in Fig. 4. Roughness caused the spanwise averaged effectiveness to decrease in the low and moderate blowing ratios, and increase in the high blowing ratios. This is consistent with the findings of Bogard et al. [6].

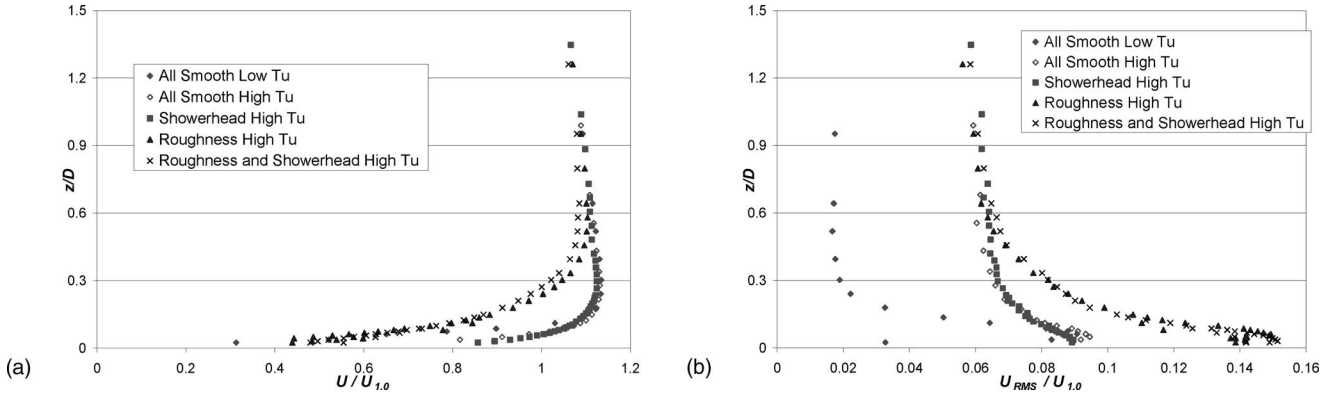

Fig. 3 (*a*) Mean velocity profiles for the indicated conditions. (*b*) rms velocity profiles for the indicated conditions.

A comparison of the area averaged adiabatic effectiveness for all of the roughness configurations with $Tu_\infty = 21\%$ is presented in Fig. 5. Roughness was found to decrease the maximum adiabatic effectiveness, with the largest decrease occurring for the all rough case. Roughness also shifted the blowing ratio at which the highest area averaged adiabatic effectiveness occurred towards higher blowing ratios.

Another interesting finding of this study is illustrated in the comparison of Figs. 4 and 6. With the addition of the showerhead cooling the effect of the roughness is decreased. In other words, in a real gas turbine engine the impact of roughness on the suction side film cooling is mitigated by the presence of the showerhead cooling.

Heat Transfer Results

Heat transfer results at high freestream turbulence and without showerhead cooling are presented in Fig. 7. The heat transfer coefficients start high at $x/D = 1.0$ where the heat flux plate starts due to the unheated starting length. In addition to the film cooled conditions, two no blowing conditions are provided for reference.

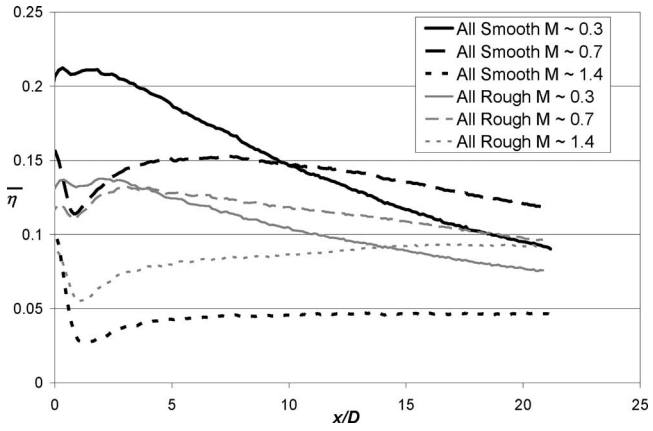

Fig. 4 Spanwise averaged comparison of adiabatic effectiveness. Smooth and all rough under high mainstream Tu

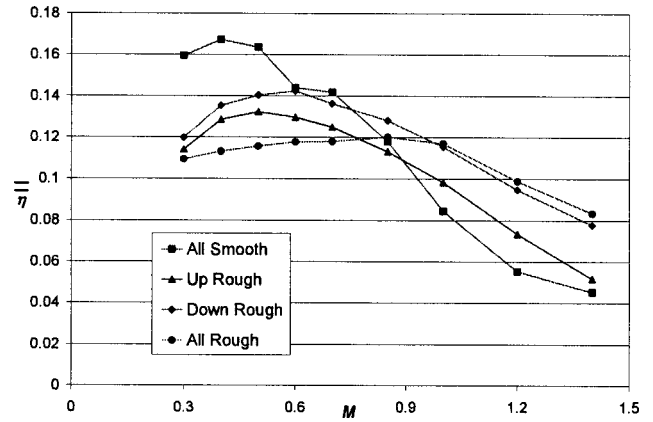

Fig. 5 Area averaged comparison of all of the roughness configurations tests under high mainstream Tu

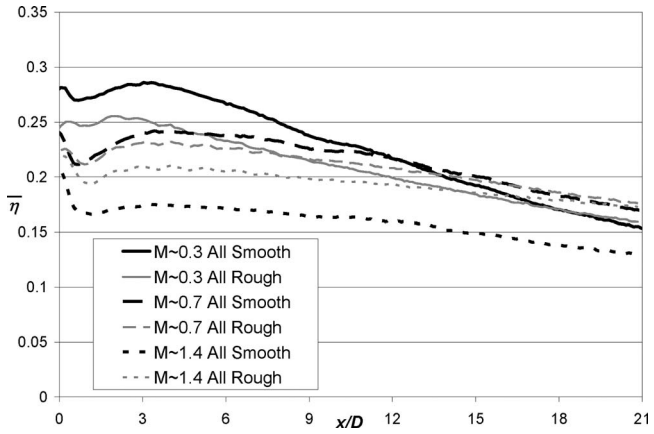

Fig. 6 Spanwise averaged comparison of adiabatic effectiveness with showerhead cooling. Smooth and all rough under high mainstream Tu.

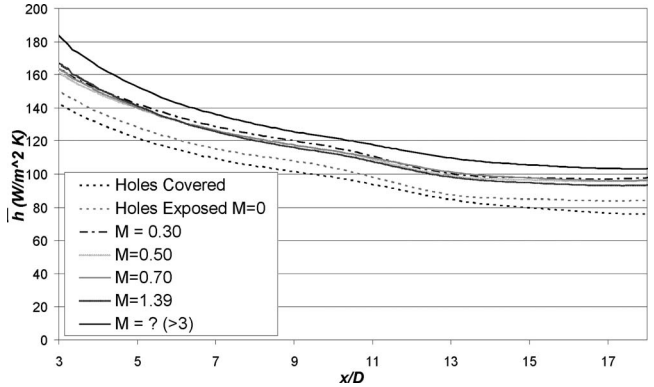

Fig. 7 Spanwise averaged heat transfer coefficients. All smooth, showerhead off, high turbulence.

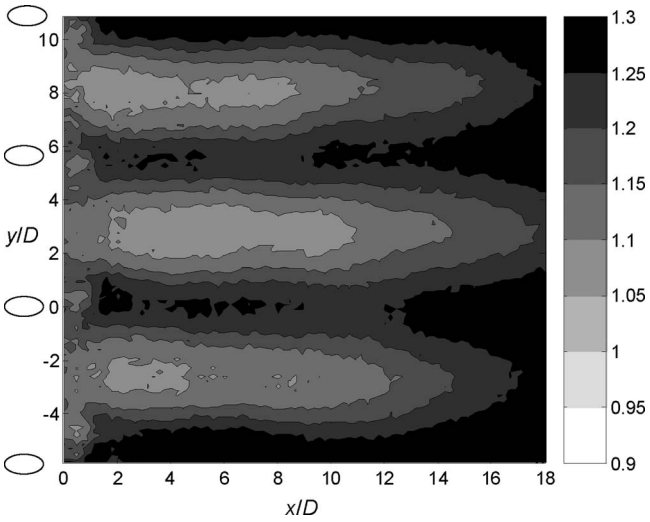

Fig. 8 Heat transfer coefficient augmentation due to blowing at $M=0.7$ (h_f/h_o). All smooth, showerhead off, high turbulence.

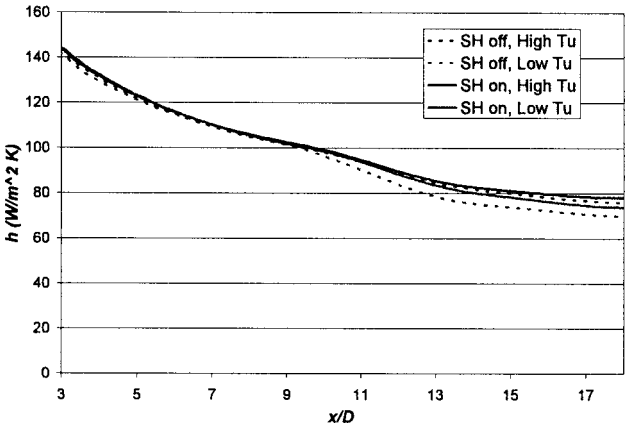

Fig. 10 Effects of turbulence and showerhead cooling on spanwise averaged heat transfer coefficients. All smooth, $M=0$, holes covered.

One of the $M=0$ conditions was a smooth vane without holes, simulated by placing scotch tape over the holes. Simply by exposing the holes, an increase in h was observed. Another increase in h was observed when coolant was ejected out of the holes. The spanwise averaged heat transfer coefficient was insensitive to changes in the blowing ratio that corresponded to the tested range; however, a significant increase in h was observed for a blowing ratio beyond the facility's measurement capabilities designated by $M=?(>3)$. Spatial contours of h_f/h_0, presented in Fig. 8, show that h is increased primarily along the path of the coolant jets downstream of the holes. This suggests that injection of the coolant jet causes an increase in turbulence level, or promotes transitioning of the boundary layer.

Increases in $\bar{h}_f/\bar{h}_0$ for low and high mainstream turbulence levels are displayed in Fig. 9 for a representative position of $x/D=12$. These results show that, for a smooth surface, coolant injection causes a 15%–25% increase in h. The smaller increase for the high turbulence mainstream turbulence case might be attributed to the higher reference heat transfer coefficient for high mainstream turbulence.

The effect of mainstream turbulence and showerhead blowing on $\bar{h}$ with no coolant jets is shown in Fig. 10. Evident from this figure is that increasing the mainstream turbulence or injecting coolant from the showerhead had essentially no effect on the heat transfer coefficient. The small influence of turbulence intensity is not very surprising considering that the *local* turbulence intensity is only $Tu \approx 6\%$ for the high turbulence condition at the location of the holes. Although showerhead cooling showed an increase in $\bar{h}$ by at most 8% at low turbulence and beyond $x/D=12$, this was only marginally greater than the uncertainty of the measurement.

Figure 11 shows the spatial h distribution that occurred at $M=0.7$ with the showerhead off and high turbulence conditions when the region downstream of injection was rough. Aside from the individual roughness elements being quite evident, the interesting observation with the rough surface downstream of injection is that the heat transfer coefficient is lower downstream of the holes than between the holes, which is the opposite of what was observed on the smooth surface. In fact, by comparing rough surface h distributions with and without film cooling, it is evident that the regions downstream of the holes experience a decrease in h due to blowing, but an increase in h between the holes. The lower h downstream of the holes may be attributed to the decrease in velocity downstream of a jet that is evident by the boundary layer measurements. The increase in turbulence intensity due to

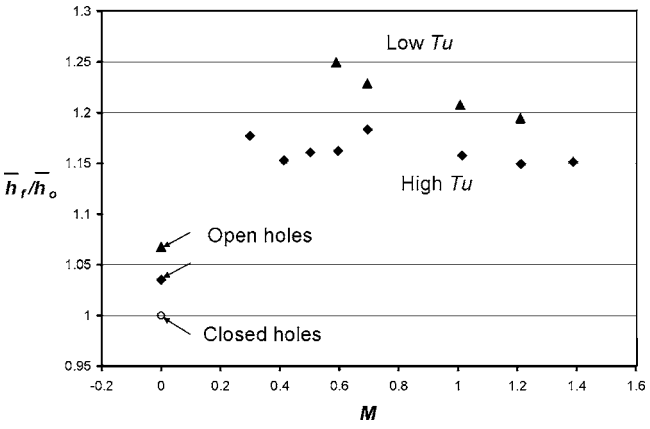

Fig. 9 Effect of suction side film cooling on $\bar{h}$ at $x/D=12$ (all smooth, showerhead off)

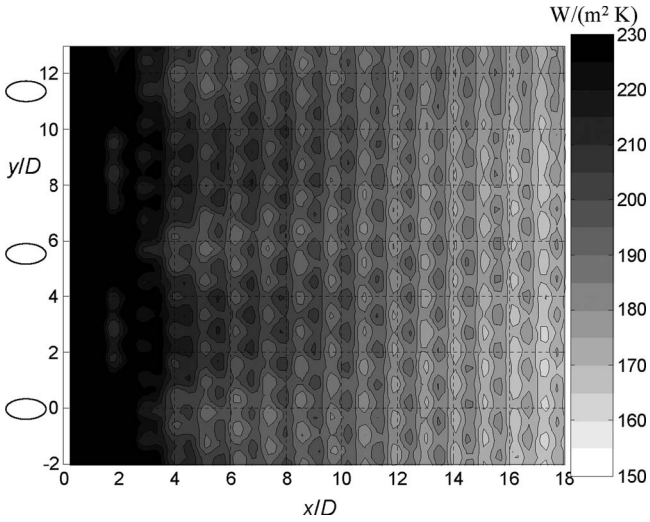

Fig. 11 Heat transfer coefficient distribution, $M=0.7$. Downstream rough, showerhead off, high turbulence.

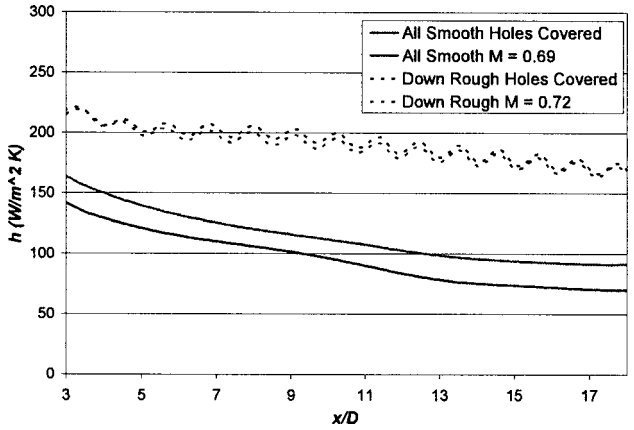

Fig. 12 Influence of downstream roughness on spanwise averaged heat transfer coefficients. Upstream smooth, showerhead off, low turbulence.

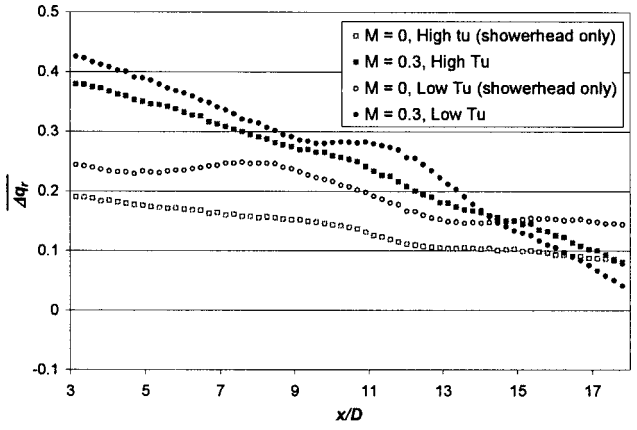

Fig. 14 Net heat flux reduction due to film cooling on a smooth vane with showerhead blowing at $M^*=1.6$

the jet on a rough surface is negligible compared to the reduced interaction with roughness elements due to a lower velocity coolant jet.

Roughness had a substantial effect on h as shown in Fig. 12 for low mainstream turbulence—as much as a doubling of $\bar{h}$, which is consistent with the results of Bogard et al. [2] who used a flat surface test plate. With roughness there was no difference in $\bar{h}$ with coolant injection relative to no coolant injection. Although not shown here, results with high mainstream turbulence levels showed no change in $\bar{h}$ relative to low mainstream turbulence results [10].

Adding roughness upstream of the film cooling holes caused as much as a 10% decrease in h compared to the case with roughness only downstream of the holes. Otherwise the general trends were similar. The lower h values observed with full roughness rather than downstream roughness may be attributed to a thickening of the boundary layer upstream of the coolant holes.

Net Heat Flux Reduction

Net heat flux reduction, Δq_r, due to film cooling on a smooth wall with high mainstream turbulence is shown in Fig. 13(*a*) for the case without showerhead blowing, and in Fig. 13(*b*) for the case with showerhead blowing. Without showerhead blowing, the heat flux was reduced by at most 20% near the holes. For $M=1.4$, the results indicate that the high rate of blowing causes an approximately 10% increase in the heat load. This result indicates that the increase in h due to blowing was not offset by a sufficiently large adiabatic effectiveness. Showerhead cooling causes a significant increase in Δq_r because of increased adiabatic effectiveness combined with virtually no increase in the heat transfer coefficients.

Figure 14 compares the net heat flux reduction due to blowing (with the showerhead) with high and low mainstream turbulence on a smooth vane. This shows that mainstream turbulence had little effect when combined suction side and showerhead blowing was used, but for showerhead blowing alone, high mainstream turbulence caused a reduction in Δq_r. This is because the high turbulence condition caused a decrease in the adiabatic effectiveness for the showerhead alone case.

Net heat flux reductions with rough surfaces and high mainstream turbulence, presented in Fig. 15, show that the combined showerhead and suction side blowing was substantially more than either showerhead or suction side alone, but less than the sum of the two individual effects.

Comparisons of net heat flux reduction due to blowing with low and high mainstream turbulence levels and with rough surfaces are presented in Fig. 16. Here it is seen that net heat flux reduction is considerably more with low Tu. Since the turbulence intensity had little effect on h, the differences in Δq_r are due to the relatively poor adiabatic effectiveness observed at high Tu.

Figure 17 shows how the transition from a completely smooth to a rough vane affects the heat load for several different blowing rates with showerhead cooling. As the surface finish changes from smooth to rough over this region of the vane, the uncooled vane

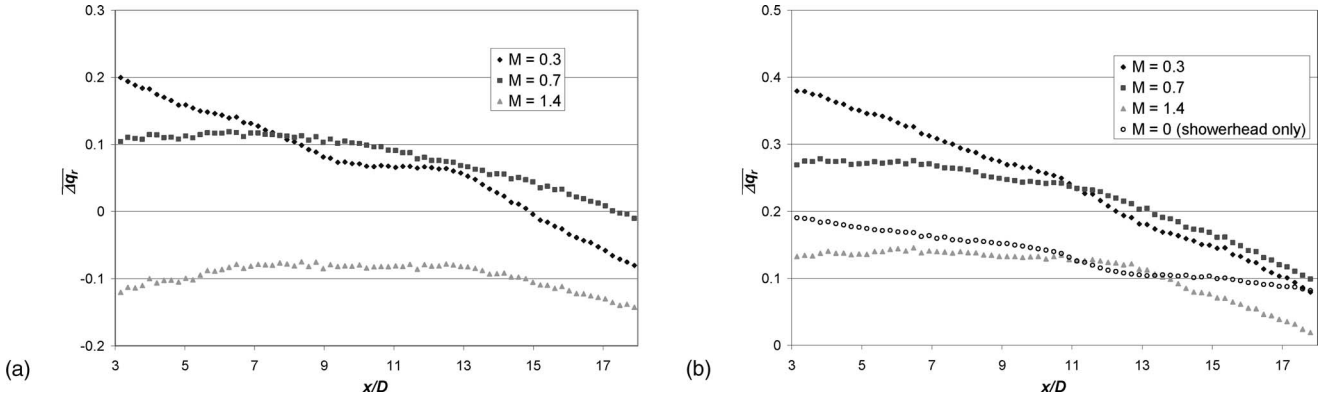

Fig. 13 (*a*). Net heat flux reduction due to adding suction side blowing. All smooth, high turbulence, showerhead off. (*b*) Net heat flux reduction due to adding suction side and showerhead blowing. All smooth, high turbulence, showerhead on for cases with suction side cooling.

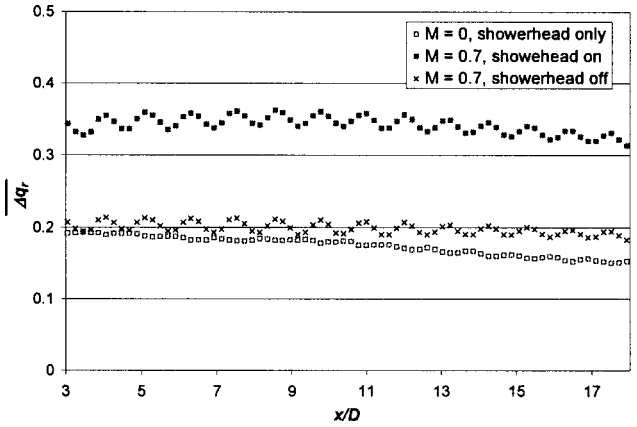

Fig. 15 Net heat flux reduction with and without showerhead injection for rough walls and high turbulence

was found to have a 50%–130% increase in heat load depending on position. Coolant injection from the showerhead alone does little to reduce this effect of surface roughness. However, combined showerhead and suction side coolant injection significantly mitigates the increase in heat load with surface roughness with the maximum increase in heat load being reduced to 70%.

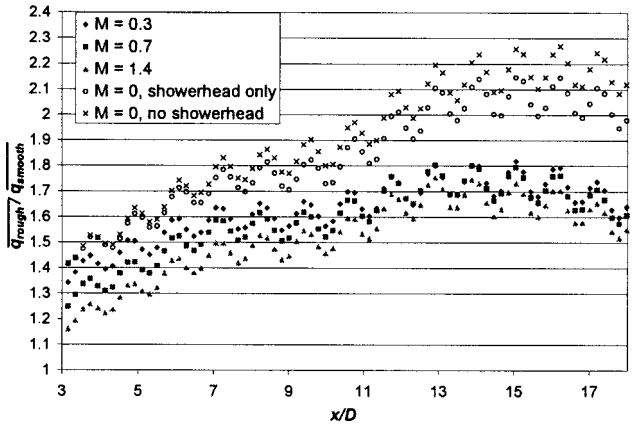

Fig. 16 Net heat flux reduction due to film cooling on a fully rough vane

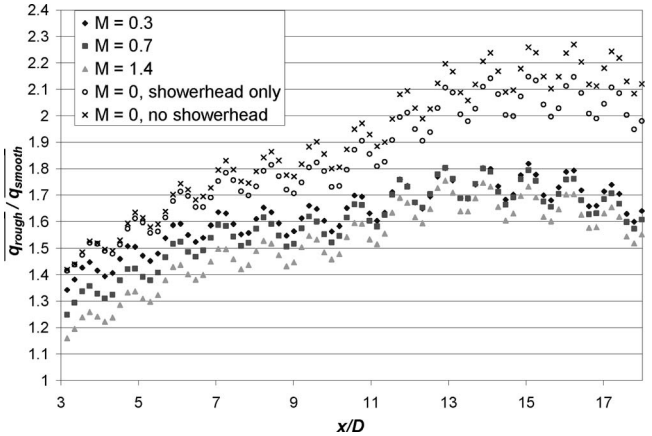

Fig. 17 Heat flux increase due to adding upstream and downstream roughness. High turbulence, showerhead on for cases with suction side cooling.

Conclusions

Adiabatic effectiveness and heat transfer experiments on the suction side of a simulated turbine vane were used to quantify the effects of film cooling and roughness on the net heat flux into the vane. Roughness was generally found to result in decreased adiabatic effectiveness due to the increased mixing within the boundary layer. However, this increased mixing helped bring separated coolant back to the vane surface at extremely high blowing ratios ($M=1.4$). Film cooling jets were found to increase the heat transfer coefficient on a smooth surface 15%–25%, even though there was no heated starting length upstream of the jets. Roughness caused a large ($2\times$) increase in the heat transfer coefficient while making the effects of the jets negligible. Relative to the nonfilm cooled case, benefits of film cooling were found to be greater on a rough vane than on a smooth vane, although the heat flux was found to increase from 30% to 70% as the surface of a fully film cooled vane evolves from smooth to rough.

Acknowledgment

We gratefully acknowledge support for this work provided by the Office of Naval Research through the University of Texas Electric Ship Program directed by Dr. Robert Hebner.

Nomenclature

C = true chord length
DR = density ratio, ρ_c/ρ_∞
D = film cooling hole diameter
h = heat transfer coefficient
M = blowing ratio, $\rho_c U_c/\rho_\infty U_\infty$
q'' = heat flux
Re = Reynolds number, $U_\infty C/\upsilon$
Re_k = roughness Reynolds number, $u_\tau k_s/\nu$
s = streamwise surface distance from the stagnation line
T = temperature
Tu = turbulence intensity, $u_{\mathrm{rms}}/U_{\mathrm{mean}}$
U = streamwise velocity
u = fluctuating velocity
x = streamwise surface distance from the first row of suction side coolant holes
y = spanwise distance along vane
z = distance normal to the vane surface

Greek Symbols

Δq_r = net heat flux reduction
Λ_f = turbulence integral length scale
δ = boundary layer thickness
η = adiabatic effectiveness, $(T_\infty - T_{\mathrm{aw}})/(T_\infty - T_c)$
ν = kinematic viscosity
ρ = density
ϕ = overall effectiveness, $(T_\infty - T_s)/(T_\infty - T_c)$

Subscripts

aw = adiabatic wall
c = coolant
f = with film cooling
o = without film cooling
rms = root mean squared
s = surface
sh = showerhead
w = wall
∞ = mainstream

Superscripts

$\overline{}$ = spanwise averaged
$\overline{\overline{}}$ = area averaged

References

[1] Bons, J. P., Taylor, R., McClain, S., and Rivir, R. B., 2001, "The Many Faces of Turbine Surface Roughness," ASME J. Turbomach., **123**, pp. 739–748.

[2] Bogard, D. G., Schmidt, D. L., and Tabbita, M., 1998, "Characterization and Laboratory Simulation of Turbine Airfoil Surface Roughness and Associated Heat Transfer," ASME J. Turbomach., **120**, pp. 337–342.

[3] Goldstein, R. J., Eckert, E. R. G., Chiang, H. D., and Elovic, E., 1985, "Effect of Surface Roughness on Film Cooling Performance," ASME J. Eng. Gas Turbines Power, **107**, pp. 111–116.

[4] Schmidt, D. L., Sen, B., and Bogard, D. G., 1996, "Effects of Surface Roughness on Film Cooling," ASME Paper No. 96-GT-299.

[5] Guo, S. M., Lai, C. C., Jones, T. V., Oldfield, M. L. G., Lock, G. D., and Rawlinson, A. J., 2000, "Influence of Surface Roughness on Heat Transfer and Effectiveness for a Fully Film Cooled Nozzle Guide Vane Measured by Wide Band Liquid Crystals and Direct Heat Flux Gages," ASME J. Turbomach., **122**, pp. 709–716.

[6] Bogard, D. G., Snook, D., and Kohli, A., 2003, "Rough Surface Effects on Film Cooling of the Suction Side Surface of a Turbine Vane," ASME Paper No. EMECE2003–42061.

[7] Cutbirth, J. M., and Bogard, D. G., 2002, "Thermal Field and Flow Visualization Within the Stagnation Region of a Film Cooled Turbine Vane," ASME J. Turbomach., **124**, pp. 200–206.

[8] Robertson, D. R., 2004, "Roughness Impace on Turbine Vane Suction Side Film Cooling Effectiveness," M. S. thesis, University of Texas at Austin.

[9] Sen, B., Schmidt, D. L., and Bogard, D. G. 1996, "Film Cooling With Compound Angle Holes: Heat Transfer," ASME J. Turbomach., **118**, No. 4, pp. 800–806.

[10] Rutledge, J. L., 2004, "Suction Side Roughness Effects on Film Cooling Heat Transfer on a Turbine Vane," M. S. thesis, University of Texas at Austin.

Calculation of the Expansion Through a Cooled Gas Turbine Stage

Leonardo Torbidoni[1]
Ansaldo Energia,
Via Nicola Lorenzi 8,
16152 Genova,
Italy
e-mail: leonardo.torbidoni@aen.ansaldo.it

J. H. Horlock
Whittle Laboratory,
University of Cambridge,
Madingley Road,
CB3 0DY, UK

*In recent work by the same authors [Torbidoni, L., and Horlock, J. H., 2005, ASME J. Turbomach, **127**, pp. 191–199], a new method for calculating the coolant flow requirements of a high-temperature gas turbine blade was described. It involved consideration of successive chordwise strips of blading; the coolant required in each strip was obtained by detailed study of the heat transfer processes across the wall of the blade and then setting limits on the maximum blade metal temperature. In the present paper, the gas state paths, involving viscous losses, heat transfer, and mixing of the coolant with the mainstream, are determined strip by strip along the whole blade chord for the stator and rotor of the stage and illustrated on an enthalpy-entropy chart. The work output from each rotor strip is obtained together with the losses (entropy creation) through the whole stage. It is then possible to calculate the thermodynamic efficiency for the cooled turbine stage and compare it to that of the uncooled stage. Illustrative calculations are given, a main calculation being based on the mean flow across the blade pitch. But, in a second supplementary calculation, allowance is also made for flow variations across the blade pitch. By comparing these two calculations, it is shown that the mean flow calculation is usually adequate.* [DOI: 10.1115/1.2185123]

1 Introduction

With the purpose of improving gas turbine performance evaluation and providing a simple, flexible, and reliable tool for use in innovative cycle design and stage preliminary design, a new method for evaluating the cooling requirements for a high-temperature gas turbine blade row was presented in a previous paper by the same authors [1]. Details are also reported in [2]. It involved splitting the blade into a number of chordwise blade strips, containing elements $\Delta s dy$ as illustrated in Fig. 1, and the cooling flow for each strip (s=const) was determined by integration from $y=0$ to $y=H$. In order to carry out a full blade calculation, proceeding from strip to strip, knowledge of the local properties of the mainstream gas flow at entry to each strip is needed and the modeling of the cooled expansion through the blade channel is therefore required.

For this purpose, a one-dimensional model (at the mean stage diameter) of the expansion through the stage was initially developed and is detailed here (but a subsequent modification to a simple two-dimensional blade-to-blade method is also described). The basic idea is to evaluate the mainstream gas flow conditions and the velocity triangles at a succession of stations in the chordwise direction, each station representing the exit section of a single strip of the blade and the entering section to the next.

For each blade strip considered, two main branches of calculation can then be recognized:

(i) the blade strip cooling modeling, as already described in [1,2], which is aimed at the evaluation of the cooling requirements for the considered strip; s=const.
(ii) the one-dimensional modeling of the mainstream gas flow expansion through the portion of the blade channel corresponding to the considered blade strip.

Calculation of the mainstream conditions downstream of the blade strip then requires knowledge of the expansion through the portion of blade channel, the heat flux exchanged through the blade strip wall, the film mass flow rate and its mixing with the main gas flow. The evaluation procedure can be then restarted for the next blade strip.

In the case of a rotor blade, the elementary power produced in each portion of blade channel may also be calculated. The expansion process may then be plotted on a specific enthalpy-entropy diagram. The stage efficiency may be determined if required.

2 One-Dimensional Modeling of the Flow Through the Blading

The calculation steps in the one-dimensional modeling of the mainstream gas flow may be listed as follows:

(a) The flow angles (i.e., α, absolute, and β, relative) at the mean stage diameter are prescribed at inlet and at exit from a blade row, and these angles are assumed to vary linearly with the chordwise distance s through the blade channels.

(b) With an overall mass flow specified, it is assumed that the *mean axial velocity* (i.e., the axial velocity $\bar{C}_x$ that would pass the mass flow if the blades were of zero thickness) is assumed to remain constant. A finite prescribed blade thickness can then be assumed in the calculation, and the actual local axial velocity C_x obtained from the continuity equation. A pitchwise mean flow velocity is then obtained as $C_x/\cos\alpha$.

(c) The losses in uncooled flow are first determined from the work of Kacker and Okapuu [3]. It is assumed that all the components of these losses, except those associated with shocks at the leading edge and with trailing edge thickness, vary linearly with the coordinate s through the blades.

(d) When film cooling is applied, the changes in the stagnation enthalpy and temperature of the mainstream gas flow across a single blade strip are to be found, the cooling mass flow required in the strip already being determined by the method described in [1] and detailed in [2]. This change in stagnation enthalpy is partly associated with the heat transferred across the blade strip wall and partly from the subsequent mixing of the two streams, the mainstream gas mass flow increasing in the mixing. Louis et al. [4]

[1]Formerly at TPG, Universitá di Genova, Italy.

Contributed by the International Gas Turbine Institute (IGTI) of ASME for publication in the JOURNAL OF TURBOMACHINARY. Manuscript received by October 1, 2004; final manuscript received February 1, 2005. IGTI Review Chair: K. C. Hall. Paper presented at the ASME Turbo Expo 2005: Land, Sea and Air, Reno, NV, June 6–9, 2005, Paper No. GT2005-68113.

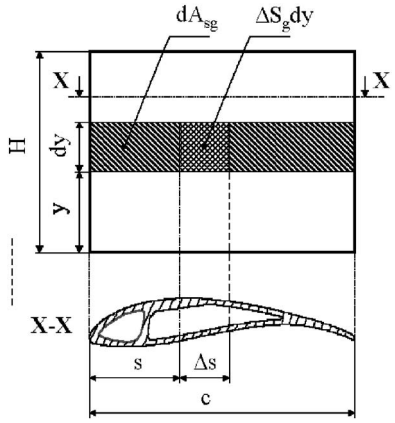

Fig. 1 Element Δsdy for heat transfer through blade surface to coolant

presented a cooled turbine model in which they divided the expansion path into three separate phenomena: uncooled expansion, convective cooling, and mixing with further cooling and losses. We follow the same approach here. Thus, for each elementary portion of blade channel corresponding to a single blade strip, it is possible to break the elementary overall expansion down as follows and as illustrated in the diagram of Fig. 2:

(i) an uncooled expansion at constant mass flow (illustrated as A-B in Fig. 2), where the viscous losses (as they were found from (c) above) are not related to blade cooling;
(ii) a convective heat flux exchange through the blade strip wall from the mainstream mass flow m_g (illustrated as B-C in Fig. 2), where it is assumed that losses are only thermodynamic, not viscous. Using the steady flow energy equation for a semi-perfect gas, together with the knowledge of the (low-speed) coolant mass flow rate Δm_{cl} required to cool the corresponding blade strip and its temperature rise $(T_{0\mathrm{cl,out}}-T_{0\mathrm{cl,in}})$, it then follows that specific stagnation enthalpy drop in the mainstream gas flow is

$$\Delta h_{0,CV} = -(\Delta m_{\mathrm{cl}}/m_g)\bar{c}_{p,\mathrm{cl}}(T_{0\mathrm{cl,out}} - T_{0\mathrm{cl,in}})$$

with

$$\bar{c}_{p,\mathrm{cl}} = \frac{\int_{T_{0\mathrm{cl,in}}}^{T_{0\mathrm{cl,out}}} c_{p,\mathrm{cl}}(T')dT'}{T_{0\mathrm{cl,out}} - T_{0\mathrm{cl,in}}}$$

where $c_{p,\mathrm{cl}}(T')$ indicates the constant pressure specific heat as a function of the coolant temperature and depending on its composition.

(iii) For the third process (illustrated as C-D in Fig. 2), the change in the mainstream gas stagnation specific enthalpy and temperature associated with the mixing is determined for the elementary expansion step by using the steady flow energy equation for semi-perfect gases, together with knowledge of the fraction r_{fc} of the coolant mass flow rate that is discharged from the blade surface for feeding the film layer. Thus,

$$(m_g + r_{fc}\Delta m_{\mathrm{cl}})c_{p,\mathrm{mix}}T_{0\mathrm{mix}} = m_g\bar{c}_{p,g}T_{0g} + r_{fc}\Delta m_{\mathrm{cl}}\bar{c}_{p,\mathrm{cl}}T_{0\mathrm{cl}} \tag{1}$$

with

$$\bar{c}_{p,g} = \frac{\int_{T_{0mix}}^{T_{0g}} c_{p,g}(T')dT'}{T_{0g} - T_{0\mathrm{mix}}} \tag{2}$$

$$\bar{c}_{p,\mathrm{cl}} = \frac{\int_{T_{0\mathrm{cl}}}^{T_{0\mathrm{mix}}} c_{p,\mathrm{cl}}(T')dT'}{T_{0\mathrm{mix}} - T_{0\mathrm{cl}}} \tag{3}$$

$$c_{p,\mathrm{mix}} = \frac{m_g\bar{c}_{p,g} + r_{fc}\Delta m_{\mathrm{cl}}\bar{c}_{p,\mathrm{cl}}}{m_g + r_{fc}\Delta m_{\mathrm{cl}}} \tag{4}$$

where $c_p(T')$ indicates the constant pressure specific heat as a function of the gas temperature and depending on its composition, while subscripts g and cl, respectively, indicate mainstream gas and coolant before mixing and subscript mix denotes the mixed gas flow. From Eqs. (1)–(4), it is then possible to obtain $T_{0\mathrm{mix}}$ and $h_{0\mathrm{mix}}$.

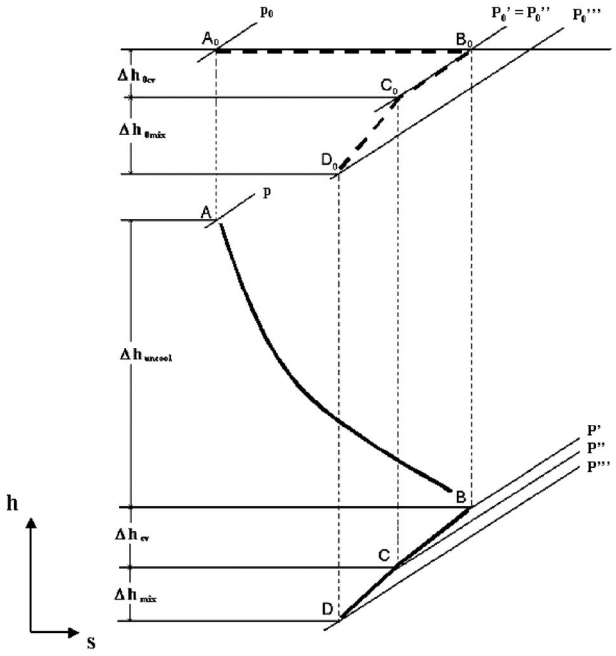

Fig. 2 Diagram showing the elementary *expansion step*, where stagnation (dotted lines) and static (continuous lines) specific enthalpies are plotted versus the specific entropy for the mainstream gas flow. The three major phenomena are depicted in succession: (A-B) uncooled expansion, (B-C) convective heat exchange and (C-D) mixing.

Hartsel's method [5], based on the Shapiro [6] relations for one-dimensional compressible gas flow, is then used to find the change in stagnation pressure Δp_{0g} associated with mixing of the film layer and the mainstream gas at the end of the blade strip:

$$\frac{\Delta p_{0g}}{p_{0g}} = -\frac{\gamma}{2}(\mathrm{Ma}_g)^2_{\mathrm{inj}}\left(\frac{r_{fc}\Delta m_{\mathrm{cl}}}{m_g}\right)\left\{\left(\frac{c_{p,\mathrm{cl}}}{c_{p,g}}\right)\left[\left(\frac{T_{0\mathrm{cl}}}{T_{0g}}\right)_{\mathrm{inj}} - 1\right] + 2\left[1 - \frac{(C_{\mathrm{cl}})_{\mathrm{inj}}}{(C_g)_{\mathrm{inj}}}\cos\alpha_{\mathrm{inj}}\right]\right\} \tag{5}$$

.

The injection velocity of the coolant $(C_{\mathrm{cl}})_{\mathrm{inj}}$ is obtained through the *momentum flux blowing ratio I*. Such a parameter has been used by Young and Wilcock [7] and Wilcock et al. [8], and it is defined by

$$I = \frac{(\rho_{\mathrm{cl}}C^2_{\mathrm{cl}})_{\mathrm{inj}}}{(\rho_g C^2_g)_{\mathrm{inj}}} \tag{6}$$

After elaboration and assuming that the injected fluid enters the mainstream at the local static pressure, Eq. (6) can be also written as

$$I = \frac{\gamma_{cl}(\mathrm{Ma}_{cl})^2_{inj}}{\gamma_g(\mathrm{Ma}_g)^2_{inj}}$$

where $(\mathrm{Ma}_{cl})_{inj}$ is the injection coolant Mach number and $(\mathrm{Ma}_g)_{inj}$ is the local mainstream gas flow Mach number at the injection location. Young and Wilcock [7] gave practical values of the *momentum flux blowing ratio I* in the range 0–1. Once a value of I is prescribed, the injection velocity of the coolant $(C_{cl})_{inj}$ can be obtained from Eq. (6) by means of an iterative calculation that allows the value of coolant density ρ_{cl} to be evaluated, and Δp_{0g} is then obtained from Eq. (5).

(e) After these various processes, the stagnation conditions of the mainstream gas flow downstream of each single blade strip are determined. The local specific static enthalpy in the mainstream is found by subtracting the known local kinetic energy from the specific stagnation enthalpy. The local static pressure is then found from the isentropic relation between the stagnation and static states, and the static density is also obtained. Finally, the local blade height at the end of each blade strip is obtained from the continuity equation and the prescribed axial velocity [2].

(f) The coolant air not used in film cooling is assumed to be discharged at the blade trailing edge (i.e., after the last strip in the downstream direction) and Hartsel's work (i.e., his so-called Totlos method [5]) is again used to determine the changes in the flow properties due to such mixing downstream of the blade.

(g) Within the calculation of each elementary blade strip, the gas physical properties $[c_p, \mu]$ are evaluated from the gas thermodynamic conditions and composition by means of polynomials fitted to tabulated data.

(h) A similar polynomial method is adopted in evaluating the specific entropy of the mainstream flow, as it is described in Sec. 3.

(i) For a *rotating row*, the procedure used for a *stationary row* is followed, but considering relative properties for the flow and relative velocities. Once the *uncooled* expansion at constant mass flow has been evaluated through the elementary portion of the rotor blade channel (as described in step (d)), the *relative* mainstream gas flow conditions and velocities are then known at inlet and at exit section from the considered rotating blade strip. Since the local relative flow angle β is prescribed and the peripheral velocity U at the mean diameter of the rotor is given as input, the *absolute* velocities may be determined together with the *absolute* specific stagnation enthalpy h_{0g}. This allows the elementary specific work L_s exchanged through the elementary portion of the rotor blade channel to be calculated, since $L_s = \Delta h_{0g}$.

(j) The cooling mass flow quantities Δm_{cl} calculated for all the blade strips of width Δs are then summed from $s=0$ to $s=c$, to give the total cooling mass flow required to cool the whole blade $\Sigma \Delta m_{cl}$. Similarly, the total power P exchanged in the whole rotating blade row is given by the sum of the contributions obtained in all the blade strips of the rotor; hence, $P = \Sigma(m_g L_s)$, m_g being the nonconstant mainstream gas mass flow that supplies each blade strip of the rotating blade row (alternatively, for the uncooled stage, the total power is simply obtained from the difference between the entry and exit absolute stagnation enthalpy flux).

3 Entropy Analysis

The procedure presented in Sec. 2 allows the expansion through the cooled blade row to be evaluated by means of a one-dimensional *stepped* approach. The mainstream gas flow local conditions can be evaluated at exit from each of the elementary *expansion steps*. The same level of detail may now be followed in the analysis of the specific entropy variation along the whole expansion.

Now indicating stagnation conditions with T and p, the specific entropy of a semi-perfect gas is given by

$$s - s_{ref} = \int_{T_{ref}}^{T} \frac{c_p(T')}{T'} dT' - \frac{\mathbb{R}}{W} \ln\left(\frac{p}{p_{ref}}\right) \tag{7}$$

where T_{ref} and p_{ref} are, respectively, temperature and pressure of the so-called reference state. The reference state, for which $T_{ref} = 0$ K and $p_{ref} = 1$ bar, is conventionally defined as the state of zero entropy, i.e., $s_{ref} = 0 kJ/kgK$.

The specific entropy s_{mix} of a mixture of semi-perfect gases is given by

$$s_{mix} = \frac{\sum_i (x_i W_i s_i)}{\sum_i (x_i W_i)} \tag{8}$$

where x_i and W_i represent the mol fraction and molecular weight of a component i. From Eqs. (7) and (8) and from Dalton's law, it follows that:

$$s_{mix} = \frac{\sum_i (x_i W_i s_i^*) - \mathbb{R}\sum_i (x_i \ln x_i) - \mathbb{R} \ln p}{\sum_i (x_i W_i)}$$

where

$$s^* = \int_{T_{ref}}^{T} \frac{c_p(T')}{T'} dT'$$

Values of s^* are evaluated from the gas thermodynamic conditions and composition by means of polynomials fitted to tabulated data. Finally, the analysis of the specific entropy variation along the whole expansion can then be obtained.

4 Blade Row and Stage Performance

Film cooling of the first turbine stage is now a standard practice in real engines. As stated before, the cooling flow is totally or partly introduced into the main flow through film injection holes in the blade surface and also from slots in the trailing edge and openings at the blade tips. The main flow and the multiple coolant streams differ in total temperature, total pressure, and chemical composition. Thus, it is necessary to model the working fluids as mixtures of gases.

5 Approximate Flow Conditions on the Pressure and Suction Surfaces

Some preliminary consideration of the flow conditions at the blade pressure and suction surfaces may be obtained at the blade mean diameter by means of an approximate analysis. The one-dimensional analysis described above allows the following pitchwise average properties to be evaluated at the mean blade row diameter:

(i) stagnation enthalpy h_0
(ii) static enthalpy h
(ii) stagnation pressure p_0
(iv) static pressure p
(v) density ρ
(vi) axial velocity C_x for finite prescribed blade profile thickness

while, as stated, the flow angle α through the blading is prescribed, as well as the blade profile thickness t_b.

We now consider the elementary control volume depicted in Fig. 3. The elementary control volume, located at a distance x in axial direction downstream of the blade channel inlet section, is defined by the blade channel surfaces and is dx thick.

Indicating p_p and p_s as the static pressure, respectively, at the pressure and suction blade surfaces, and C_u as the tangential component of the mainstream flow velocity, the tangential momentum equation applied to the shown control volume may be written as

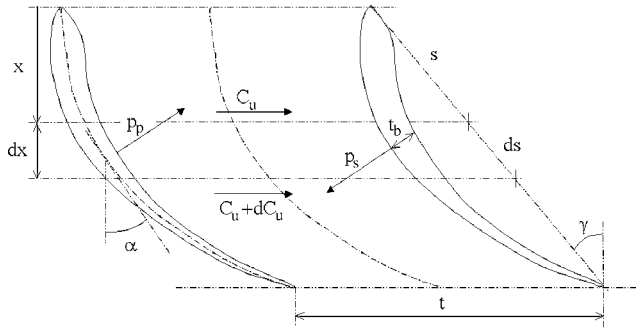

Fig. 3 Schematic of the elementary control volume of the preliminary pressure and suction blade surfaces evaluation

$$(p_p - p_s)\cos\alpha\, ds = \rho C_x \left[t - \left(\frac{t_b}{\cos\alpha} \right) \right] dC_u$$

Since $ds/dx = 1/\cos\gamma$, it follows that

$$(p_p - p_s)\left(\frac{\cos\alpha}{\cos\gamma} \right) = \rho C_x \left[t - \left(\frac{t_b}{\cos\alpha} \right) \right] \frac{d(C_x \tan\alpha)}{dx}$$

and assuming the axial velocity C_x to be almost constant

$$(p_p - p_s) \cong \rho C_x^2 \left[t - \left(\frac{t_b}{\cos\alpha} \right) \right] \left(\frac{1}{\cos\alpha} \right)^3 \left(\frac{d\alpha}{ds} \right)$$

from which the local value of $(p_p - p_s)$ can be calculated. If we now assume that the pitchwise mean pressure p, as calculated by the one-dimensional analysis, is

$$p = \frac{p_p + p_s}{2}$$

then local values of the static pressure at the pressure and suction blade surfaces may be obtained

$$p_p = p + \frac{p_p - p_s}{2}, \quad p_s = p - \frac{p_p - p_s}{2}$$

In order to complete the preliminary evaluation of the gas flow conditions at the pressure and suction blade surfaces, we assume that the local stagnation enthalpy h_0 and pressure p_0, as calculated by the one-dimensional analysis, are uniform in the *blade-to-blade* direction. Applying the isentropic relation between stagnation and static conditions gives local values of the static enthalpy h_p and h_s, respectively, at the pressure and suction blade surfaces

$$h_p = h_0 \left(\frac{p_p}{p_0} \right)^{(\gamma-1)/\gamma}, \quad h_s = h_0 \left(\frac{p_s}{p_0} \right)^{(\gamma-1)/\gamma}$$

In conclusion, local values of velocity C_p and C_s, respectively, at the pressure and suction blade surfaces, are given by

$$C_p = \sqrt{2(h_0 - h_p)}, \quad C_s = \sqrt{2(h_0 - h_s)}$$

For a *rotating row*, a similar procedure can be followed, but now considering relative conditions of the flow and relative velocities.

6 Calculation of the Flow in a Film-Cooled Stage

The new model presented has been applied to the evaluation of an existing high-temperature gas turbine stage (i.e., nozzle plus first rotor). We first briefly describe the selection of the blading.

The *base profile T6*, from data published by Horlock [9], was chosen to define the nozzle and rotor blade profiles. Therefore, together with the ratio of maximum profile thickness on blade chord equal to 0.2, the variation of the blade thickness along the chordwise coordinate s at the mean stage diameter could be obtained. Trailing edge thickness was adopted equal to 0.015 times the blade chord.

The relative flow angles with respect to axial direction at the inlet and outlet sections of the rotor blade row were set at 42 deg and −65 deg at the mean diameter. Since the stage flow coefficient was 0.5, the resulting absolute flow angle at the nozzle outlet section was 71 deg, while at the inlet section it was 0 deg.

The resulting degree of reaction and stage loading coefficient were 0.3 and 1.5, respectively. The Mach number at the exit nozzle was 0.952.

The calculation of the cooling flow requirements for the stage was described in detail in [1] and [2]. We give a brief summary of these calculations in the Appendix.

6.1 Nozzle Flow Calculation. The input data for the calculation of the nozzle, assuming ten blade strips over the nozzle chord, were as shown in Table 1. The resulting total [fractional] cooling flow m_{cl}/m_g is close to 0.06. Figure 4 gives the specific enthalpy-entropy diagram of the mainstream gas flow for the expansion through the nozzle guide vane row, both stagnation and static enthalpy being shown. The uncooled expansion is also shown with entropy increasing steadily through the blade row. There are several interesting features about the cooled expansion depicted in Fig. 4:

Table 1 Input data for the nozzle guide vane row calculation

Nozzle input data			
m_g	140.6 kg/s (at entry section)	α_2	71 deg
		Bi_{bw}	0.25
T_g	1800 K	Bi_{tbc}	0.2
p_g	32 bar	$T_{cl,in}$	829 K
Pr_g	0.72	$T_{bg,max}$	1125 K
K_{comb}	0.15	ΔZ	94.64 [for each strip]
$\bar{C}_x$	194 m/s [i.e. C_x at entry sect.]	$\Delta\alpha_h$	0.0095
		E_h	2
D_m	741 mm	n_p	3
Profile data	T6 profile max thickness/c=0.2	ψ_i	0.8
		ψ_d	2.24
c	60 mm	r_{fc}	1 (0.5 for last strip)
$\sigma = c/p$	1.15		
Stagger angle	36 deg	α_{inj}	20 deg
Values $\Delta Z, c, \Delta a_h, E_h, n_p, \Psi_i, \Psi_d$ lead to		External blade geometry leads to	
d	1.9 mm	Φ_g	2.053
Δn_{ch}	1.764 (for each strip)	Mach number	0.967 (exit from nozzle)

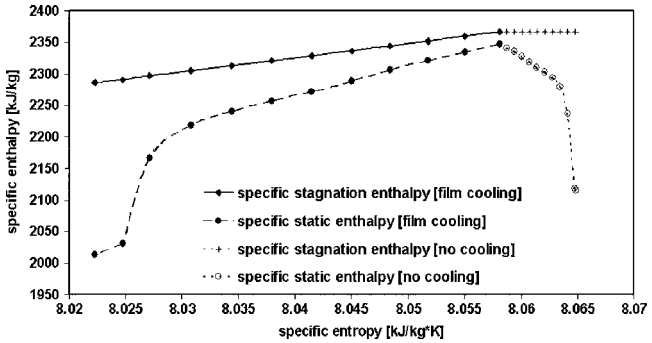

Fig. 4 Enthalpy-entropy diagrams for uncooled and cooled nozzle guide vane row (showing both stagnation and static enthalpy for the mainstream gas flow)

(i) as to be expected, the expansion line heels over to the left, cooling of the mainstream gas being dominant and causing reduction in specific entropy even though there are irreversibilities due to viscous losses, mixing and temperature differences between mainstream and coolant
(ii) the mixing process downstream of the trailing edge leads to similar decreases in stagnation enthalpy and entropy, both associated with low temperature cooling air injected into the mainstream.

Some further details of the nozzle guide vane row calculations are given in Fig. 5, which shows the variation of the stagnation and static pressures through the cooled nozzle. Points on the lines indicate the conditions at the inlet section of each blade strip, except the last point indicating the blade row exit section conditions: the stagnation pressure slightly drops along the blade due to viscous and mixing losses, while static pressure decreases due to expansion. Figure 6 shows the variation of the mainstream flow axial velocity and actual velocity for a finite prescribed blade profile thickness. Points on the lines indicate values at the inlet section of each blade strip, except the last point indicating the blade row exit section: the axial velocity behavior depends on the finite blade thickness, while the actual velocity results from the axial velocity and the prescribed flow angle. Figure 7 shows the contributions to the specific entropy variation due to uncooled expansion, convective heat transfer across the blade wall, mixing, and trailing edge discharge. In particular, Fig. 7 considers each single elementary *expansion step* along the blade chord. The diagram shows that:

(i) Contributions associated with heat exchange, i.e., convective transfer and mixing, are negative.
(ii) The major contribution is due to mixing. Even though the specific entropy production due to mixing losses is positive, an overall decrease in specific entropy associated with a large amount of low temperature cooling air injected into the mainstream is evident.
(iii) The overall balance gives a decreasing specific entropy, this being in accordance with the expansion trend depicted in Fig. 4.

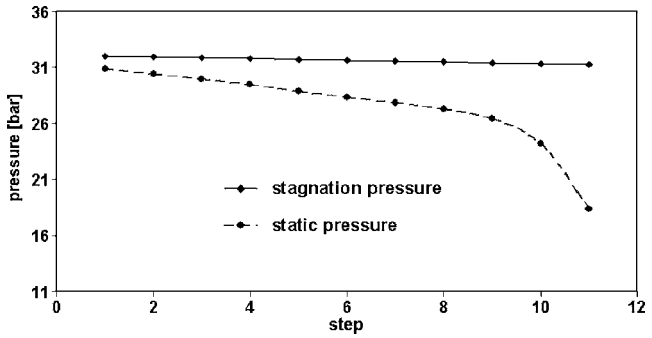

Fig. 5 Mainstream gas flow stagnation and static pressure for ten steps along the cooled nozzle-blade chord

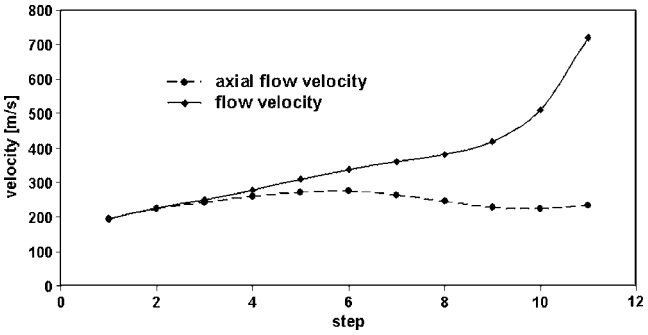

Fig. 6 Mainstream gas flow velocity and axial velocity for ten steps along the cooled nozzle-blade chord

Although the mainstream gas flow specific entropy decreases continuously through the cooled nozzle, the absolute entropy does not. In fact, as it is expected, multiplying the local-specific entropy by the local mass flow gives the increasing value of the absolute entropy shown in Fig. 8, where both the contributions of each *expansion step* and the absolute entropy variation are depicted (the last step considering the trailing edge discharge).

Finally, results of the preliminary calculation about the flow conditions at the blade pressure and suction surfaces are shown in

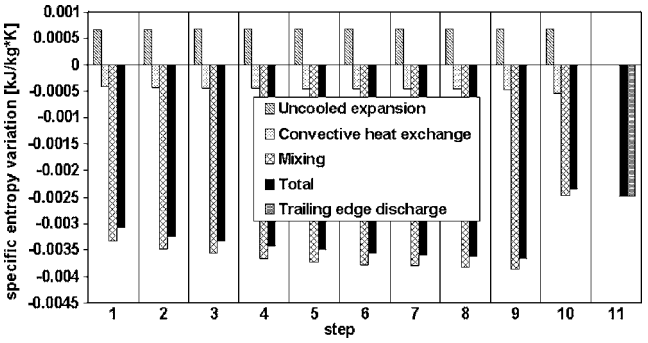

Fig. 7 Specific entropy variation for ten steps along the cooled nozzle-blade chord due to uncooled expansion, convective heat transfer across the blade wall, mixing, and trailing-edge discharge

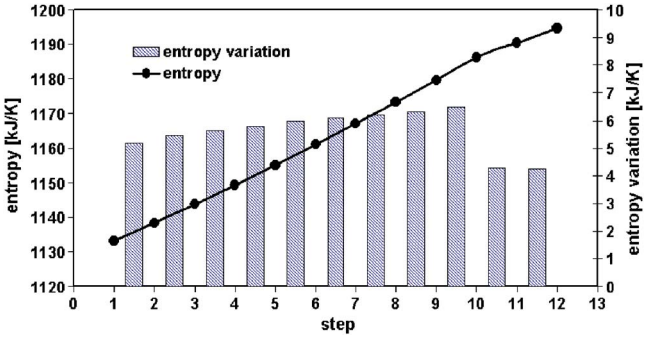

Fig. 8 Entropy and entropy variation for ten steps along the cooled nozzle-blade chord (last column refers to trailing edge discharge)

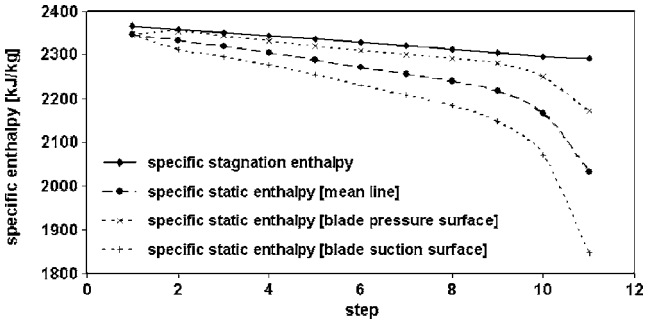

Fig. 9 Stagnation and static enthalpy for ten steps along the cooled nozzle-blade chord (showing enthalpy at the mean blade channel line and at the blade pressure and suction surfaces for the mainstream gas flow)

Figs. 9 and 10. Figure 9 gives the variations of the stagnation and static enthalpies along the nozzle chord, and Fig. 10 shows the variations of the velocities. Points on the lines indicate values at the inlet section of each blade strip, except the last point indicating the blade row exit section.

6.2 Rotor Flow Calculation. For the rotating blade row, a similar analysis to that for the nozzle guide vane row has been carried out, now considering relative conditions of the flow and relative velocities. However, only the major results will be presented here.

The data in Table 2 give the input database for the calculation of the rotating row. The input gas properties are now derived from the nozzle output, and they are automatically calculated by the code. We still assume ten blade strips over the rotor chord. The resulting total [fractional] cooling flow m_{cl}/m_g is close to 0.052.

Results of the rotor calculation are given in Fig. 11, which gives the specific relative enthalpy-entropy diagram for the expansion through the rotating row, both stagnation and static relative enthalpy being shown. The uncooled expansion is also shown with entropy increasing steadily through the blade row. As for the nozzle, the expansion line heels over to the left.

6.3 Comparison Between Stepped and Whole Blade Chord Approaches. After completion of the stepped calculations above, assuming ten blade strips over the chord of each of the two blade rows, a comparative analysis considering a *single strip* for each "whole blade chord" was carried out for the gas turbine stage.

Results are given in Figs. 12 and 13. Figure 12 gives the specific enthalpy-entropy diagram for the expansion through the cooled nozzle guide vane row, both stagnation and static enthalpy being shown. The expansion lines evaluated by the stepped approach are those of Fig. 4, while the expansion lines evaluated by the whole blade chord approach have been overwritten on the diagram (shown as linear between inlet and exit), for comparison. Similarly, the expansion lines through the cooled rotor blade row depicted in Fig. 13 and evaluated by the stepped approach are the same as in Fig. 11, while the expansion lines evaluated by the whole blade chord approach have been overwritten on the same diagram, which now considers relative flow stagnation conditions. From the two diagrams it is clear that the local flow conditions for the two rows are indeed differently evaluated by the two approaches, as to be expected. Moreover, such a difference is more evident for the rotor, for which the mainstream gas entry conditions result from the nozzle calculations. This means that the difference in the expansion evaluation from the two approaches is expected to increase for the downstream stages.

It may also be noted that large changes in properties occur toward the end of the blades. This is because of the assumption that α varies linearly through the blading; consequently, large changes of $\tan\alpha$ occur there, i.e., the blade is heavily "rear loaded." An assumption of linearity for $\tan\alpha$ rather than α will remedy this.

With the full details of the flow through the stage thus determined, it is possible to calculate its thermodynamic efficiency. The actual power output was calculated as 36.165 MW, and following Hartsel [5], this was divided by the power developed in separate isentropic expansions of the mainstream and the two

Table 2 Input data for the rotating blade row calculation

Rotor input data			
m_g	From nozzle calcs.	β_2	42 deg
T_g	From nozzle calcs.	β_3	−65 deg
p_g	From nozzle calcs.	Bi_{bw}	0.25
Pr_g	From nozzle calcs.	Bi_{tbc}	0.2
K_{comb}	0.10	$T_{cl,in}$	829 K (absolute) 773 K (relative)
$\bar{C}_x$	194 m/s [i.e. C_x at entry sect.]	$T_{bg,max}$	1025 K
		ΔZ	50.48 (for each strip)
D_m	741 mm	$\Delta\alpha_h$	0.0095
Profile data	T6 profile max thickness/c=0.2	E_h	2
		n_p	3
c	27 mm	ψ_i	0.8
$\sigma=c/t$	1.08	ψ_d	2.24
Stagger angle	−11 deg	r_{fc}	1 (0.5 for last strip)
N	166.7 rps	α_{inj}	20 deg
Values $\Delta Z, c, \Delta a_h, E_h, n_p, \Psi_i, \Psi_d$ lead to		External blade geometry leads to	
d	1.48 mm	Φ_g	2.053
Δn_{ch}	0.619 (for each strip)	Peripheral velocity	388 m/s (at the mean diameter)

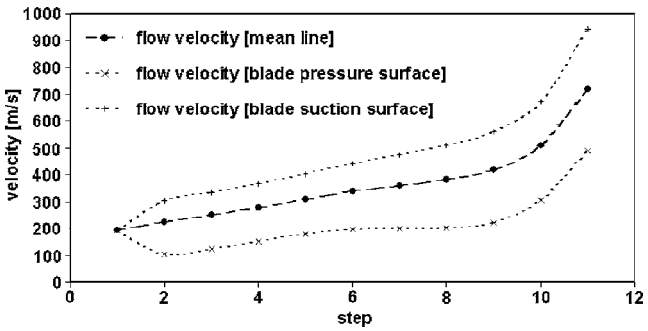

Fig. 10 Mainstream gas flow velocity for ten steps along the cooled nozzle-blade chord (showing velocity at the mean blade channel line and at the blade pressure and suction surfaces).

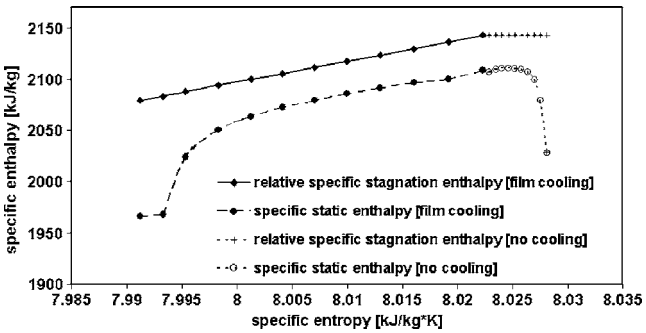

Fig. 11 Enthalpy-entropy diagrams for uncooled and cooled rotating rows (showing both relative stagnation and static enthalpy for the mainstream gas flow)

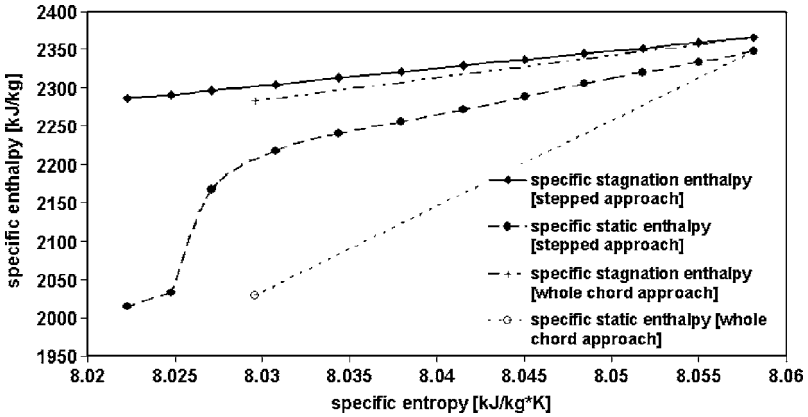

Fig. 12 Enthalpy-entropy diagrams for cooled nozzle guide vane row (showing both stagnation and static enthalpy for the mainstream gas flow). Expansion evaluated by the stepped approach is the same as in Fig. 4. Expansion evaluated by the whole-blade-chord approach is overwritten on the diagram, for comparison.

cooling flows, to give Hartsel's stage efficiency as 90.84%. A calculation of the efficiency with zero cooling flow gave an uncooled efficiency of 91.60%, so there is but a small loss in efficiency from the introduction of cooling.

There are other interpretations of the form of cooled stage efficiency in the literature. Estimates were made of these alternative efficiencies, but they are not given here. They form the subject of later papers.

7 Conclusions

A new method of evaluating the expansion through a cooled gas turbine stage has been presented in this paper; it is based on the one-dimensional analysis of the mainstream gas flow expansion through the blading and it involves a stepped approach. It provides a method of calculating the detailed flow through a cooled turbine stage, the blade cooling modeling already being presented in a previous work of the same authors.

Because of its simplicity and flexibility, it is hoped that the new method will represent a useful tool for the innovative gas-turbine-based cycle design and for the preliminary blade design. However, the full potential of the code lies in its ability to respond to variation of input data (e.g., heat transfer coefficients, blade internal geometry, etc.) along the blade chord and when nonconventional fluids and operating conditions have to be considered.

These features have yet to be exploited and will be the subject of the future work (which should lead to the optimum distribution of the cooling flow with chordwise distance s, and may enable the total cooling flow to be minimised). The new method presented should then give more reliable evaluations than the semi-empirical methods, particularly for the study of innovative cycles. It does not attempt to give the full detail that a comprehensive cfd calculation could give, but its simplicity and speed should enable it to be used in preliminary design.

Acknowledgment

The authors wish to thank the Thermochemical Power Group of the University of Genoa, Italy, for funding the first author in the project. Authors also thank Professor Aristide Massardo. His technical contributions were of major assistance, particularly in the selection of the project and the development of the program. The authors are grateful to Professor John B. Young for giving them access to his recent work on the concept of efficiency for a cooled turbine cascade. The authors are also grateful to Professor R.

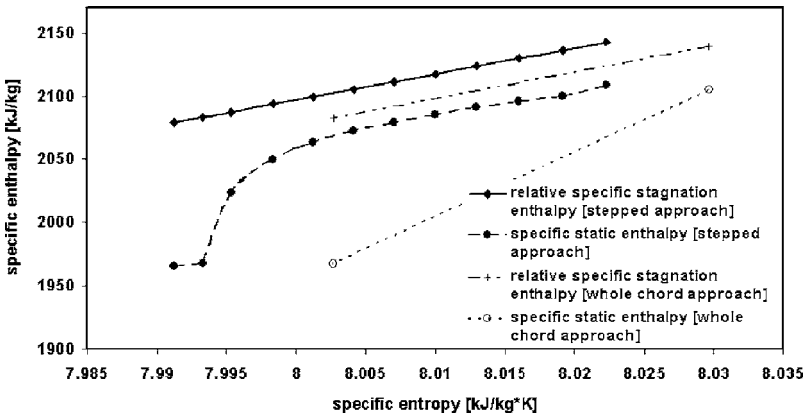

Fig. 13 Enthalpy-entropy diagrams for cooled rotating row (showing both relative stagnation and static enthalpy for the mainstream gas flow). Expansion evaluated by the stepped approach is the same as in Fig. 11. Expansion evaluated by the whole-blade-chord approach is overwritten on the diagram, for comparison.

Singh and Professor P. Pilidis for the help and for the provision of facilities at Cranfield University, UK.

Nomenclature

A = area
A_g = for cross-sectional area of gas flow (single-blade channel)
$A_{g,s}$ = for wetted heat transfer areas of gas flow (single blade)
Bi = Biot number
C = flow velocity
c = chord
c_p = specific heat at constant pressure
d = cooling channel hydraulic diameter, also elementary difference
D_m = mean diameter of blading
E_h = parameter that considers increased surface of cooling channels due to turbulence promoters
h = specific enthalpy
I = momentum flux blowing ratio
K_{comb} = combustor pattern factor
K_{cool} = $\text{St}_g(c_{p,g}/c_{p,\text{cl}})(A_{g,s}/A_g)$
L_s = specific work
m = mass flow rate (for a single-blade channel or blade, when not specified)
Ma = Mach number
N = rotational speed
n_{ch} = number of cooling channels inside the blade
n_p = number of cooling channel passes
P = power
p = pressure
p_{ch} = cooling channel perimeter
Pr = Prandtl number
R = gas constant
$\mathbb{R}$ = universal gas constant
r_{fc} = fraction of the coolant flow used for film cooling
s = coordinate along chord line, also specific entropy
St = Stanton number
T = temperature
t = blade row pitch or spacing
t_b = blade profile thickness
U = peripheral rotor velocity
W = molecular weight
w^+ = nondimensional mass flow rate
x = axial coordinate, also mol fraction
Z = blade cooling system technology level parameter

Greek

α = absolute flow angle (measured from axial direction), film injection angle (plus subscript-inj)
α_h = ratio, (empty blade cross-sectional area)/c^2
β = relative flow angle
γ = ratio between the constant pressure and the constant volume specific heats, also blade row stagger angle
Δ = referring to blade "strip," also arithmetic difference
ε_0 = cooling effectiveness
η = efficiency
η_{ad} = adiabatic wall film effectiveness
$\eta_{c,\text{ext}}$ = cooling efficiency referred to the maximum external blade temperature
μ = dynamic viscosity
ρ = density
σ = c/t blade row solidity
Φ = ratio, wetted blade perimeter on blade chord
Ψ_d = $p_{\text{ch}}/\pi d$ shape parameter for coolant channels
ψ_i = heat transfer interference parameter

Subscripts

0 = stagnation condition
2 = exit from stationary blade row
3 = exit from rotating blade row
ad = referring to film effectiveness
b = blade
bw = blade wall
cl = coolant, cooling side
ch = referring to coolant channels
CV = referring to convective heat exchange
ext = external
g = gas, gas side
i = referring to mixture component i, also coolant stream i
in = inlet
inj = injection
int = internal
max = maximum
mix = referring to mixed flow, also mixture
out = outlet
p = referring to blade pressure surface
ref = referring to *reference state*
s = referring to blade suction surface, also surface
tbc = referring to thermal barrier coating
u = referring to tangential direction
x = axial

Superscripts

- = mean or average (gas properties, etc.)
$'$ = as defined in the text

The parameter s^* appears in complex equation and is as defined in the text.

Appendix: Cooling Flow Calculations

As explained in [1] and amplified in [2], two major parameters had to be provided as input for the calculation of the coolant flow: the so-called cooling system technology level parameter referred to the single blade strip ΔZ, and the ratio $\Delta\alpha_h$ referred to the single blade strip and defined as

$$\Delta\alpha_h = \frac{\text{empty blade strip cross-sectional area}}{c^2}$$

with c the whole blade chord. Theses parameters may be written as [1,2]

$$\Delta Z = \Psi_i \Delta\alpha_h^{0.2} n_p^{0.8} E_h \left(\frac{c}{d}\right)^{1.2} \tag{A1}$$

$$\Delta\alpha_h = \Delta n_{ch} n_p \left[0.25 \Psi_d \pi \left(\frac{d}{c}\right)^2\right] \tag{A2}$$

Thus, for a cooled turbine blade of given chord c, the method of calculation involves choosing values of ΔZ and $\Delta\alpha_h$, the number of passes for the internal flow n_p, and the interference and enhancement factors for heat transfer, Ψ_i and E_h, respectively. A value of the product $(\Psi_d \Delta n_{\text{ch}})$ is then implied by these choices, and this, in turn, means that the number of channels for the blade strip Δn_{ch} is determined once a particular shape for cooling channels has been chosen, e.g., ellipses with $\Psi_d = 2.24$.

The input data for the calculation of the nozzle and the rotor were as in Tables 1 and 2, respectively. Ten blade strips over the blade chord were assumed for both the nozzle and the rotor. In particular $\Delta\alpha_h = 0.0095$ and $\Delta Z = 94.64$ were chosen for all the strips of the nozzle, while $\Delta\alpha_h = 0.0095$ and $\Delta Z = 50.48$ for all the

strips of the rotor. Considering ten strips, it follows from Eq. (A2) that the corresponding α_h for the whole blade (with $n_{ch}=10 \times \Delta n_{ch}$) is

$$\alpha_h = 10 \times \Delta\alpha_h = 0.095$$

for both the nozzle and the rotor, which, in turn, means the ratio:

$$\frac{\text{empty whole blade cross-sectional area}}{\text{whole blade cross-sectional area}} \cong 0.8,$$

and

$$(\text{whole blade cross-sectional area})/c^2 \cong 0.119;$$

while, according to Eqs. (A1) and (A2)

$$\frac{Z}{\Delta Z} = \left(\frac{\alpha_h}{\Delta\alpha_h}\right)^{0.2}$$

and the corresponding Z for the whole blade is

$$Z = \Delta Z\left(\frac{\alpha_h}{\Delta\alpha_h}\right)^{0.2} = 94.64 \times 10^{0.2} \cong 150$$

and

$$Z = \Delta Z\left(\frac{\alpha_h}{\Delta\alpha_h}\right)^{0.2} = 50.48 \times 10^{0.2} \cong 80$$

for nozzle and rotor, respectively.

Tables 1 and 2 give the values of ΔZ, $\Delta\alpha_h$, E_h, n_p, Ψ_i, Ψ_d and α_{inj}, which were taken as constant for all the blade strips; while the fraction r_{fc} of the coolant flow used for film cooling was unity (i.e., full film) for all the strips except the last one, for which $r_{fc}=0.5$ in a way to let some coolant to be discharged through the trailing edge slot in the nozzle and through both the trailing edge slot and the openings at the blade tip in the rotor (in the rotor, the coolant flow discharged at the blade tip is assumed to be 0.25 times the coolant flow discharged through the trailing edge). That was done for simplicity for the present work.

Nevertheless all those parameters may be set in input as varying from one blade strip to the next, this giving an increased flexibility to the model. The maximum allowable metal blade temperature $T_{bg,max}$ was set equal to 1125 K for the nozzle, and equal to 1025 K for the rotor.

Moreover, the leakage losses have been dropped for simplicity in the present calculation, although they are accounted in the final code as described in point (c) of Sec. 2.

A.1 Comparison of Cooling Flow Calculation With a Semi-Empirical Approach. Finally, we may compare the cooling flow calculation for the nozzle guide vane row cooling with that obtained using the semi-empirical "mean flow" method of Wilcock et al. [8], which leads to the three basic equations

$$\frac{m_{cl}}{m_g} = K_{cool} w^+$$

$$(1 + Bi_{tbc})w^+ = \frac{\varepsilon_0}{\eta_{c,ext}(1-\varepsilon_0)} - \eta_{ad}\left[\frac{1}{\eta_{c,ext}(1-\varepsilon_0)} - 1\right],$$

$$\eta_{c,ext} = \frac{\eta_{c,int}}{1 + w^+ \eta_{c,int} Bi_{bw}}.$$

Those authors chose values of the parameters K_{cool}, $\eta_{c,ext}$, and η_{ad} based on practical engine experience and obtained coolant fractional flows in line with such practice. The results of the new code gave the following values of the parameters for the example of the turbine nozzle guide vanes:

$$K_{cool} = 0.01921, \quad \eta_{c,ext} = 0.456, \quad \eta_{ad} = 0.320$$

Substitution of these values into the equations above, together with the cooling effectiveness ε_0 and the Biot numbers resulting from the input data, gave a coolant mass flow fraction of $m_{cl}/m_g=0.0604$, compared to $m_{cl}/m_g=0.0590$ resulting from the code, with a difference of $<1.7\%$. This served to validate the code, the small remaining difference in the coolant mass flow fraction probably resulting from the different assumptions on blade wall metal temperature, which is assumed to be constant in [8] but is allowed to vary along the span in the new code.

It should however be noted that these values of m_{cl}/m_g are low compared to those obtained in [8], where, in particular, a much higher value of K_{cool} was employed in order to obtain coolant mass flows comparable to those used in real engines.

References

[1] Torbidoni, L., and Horlock, J. H., 2005, "A New Method to Calculate the Coolant Requirements of a High Temperature Gas Turbine Blade," ASME J. Turbomach. **127**, pp. 191–199.

[2] Torbidoni, L., 2004, "A New Method to Evaluate the Performance of a High Temperature Gas Turbine Stage," Ph.D. thesis, University of Genoa, Italy.

[3] Kacker, S. C., and Okapuu, U., 1982, "A Mean Line Prediction Method for Axial Flow Turbine Efficiency," ASME J. Eng. Power, **112**, pp. 104, 111–119.

[4] Louis, J. F., Hiaroka, K., and El-Masri, M. A., 1983, "A Comparative Study of the Influence of Different Means of Cooling on Gas Turbine Performance," ASME Paper No. 83-GT-180.

[5] Hartsel, J. E., 1972, "Prediction of Effects of Mass-Transfer Cooling on the Blade-Row Efficiency of Turbine Airfoils," AIAA Paper No. AIAA-72–11.

[6] Shapiro, A., 1953, *The Dynamics and Thermodynamics of Compressible Fluid Flow*, Ronald Press, New York, Vol. I, pp. 219–231.

[7] Young, J. B., and Wilcock, R. C., 2002, "Modelling the Air-Cooled Gas Turbine: Part 2-Coolant Flows and Losses," ASME J. Turbomach., **124**, pp. 214–221.

[8] Wilcock, R. C., Young, J. B., and Horlock, J. H., 2004, "The Effect of Turbine Blade Cooling on the Cycle Efficiency of Gas Turbine Power Plants," ASME J. Eng. Gas Turbines Power **127**, pp. 109–120.

[9] Horlock, J. H., 1973, *Axial Flow Turbines*, Krieger, Melbourne, FL.

Effect of Jet Pulsation and Duty Cycle on Film Cooling From a Single Jet on a Leading Edge Model

Srinath V. Ekkad[1]
Mem. ASME
Mechanical Engineering Department,
Louisiana State University,
Baton Rouge, LA 70803
e-mail: ekkad@me.lsu.edu

Shichuan Ou

Richard B. Rivir

U.S. Air Force Research Laboratory,
Wright-Patterson AFB, OH 45433

The effect of jet pulsation and duty cycle on film effectiveness and heat transfer was investigated on a film hole located on the circular leading edge of a blunt body. A transient infrared technique was used to measure both heat transfer coefficients and film effectiveness from a single test. Detailed Frossling number and film effectiveness distributions were obtained for all flow conditions. Jet pulsing frequencies of 5 Hz, 10 Hz, and 20 Hz have been studied. The effect of duty cycle created by the valve opening and closing times was also set at different levels of 10%, 25%, 50%, and 75% of designated 100% fully open condition for different blowing ratios from 0.25 to 2.0. The combination of pulse frequency and duty cycle was investigated for different blowing ratios on a single leading edge hole located at 22 deg from geometric leading edge. Results indicate that higher effectiveness and lower heat transfer coefficients are obtained at the reduced blowing ratios, which result from reduced duty cycles. The effect of varying the pulsing frequency from 5 Hz to 20 Hz is not discernable beyond the level of experimental uncertainty. Effective blowing ratio due to lowering of the duty cycle at a given blowing ratio seems to play a more important role in combination with pulsing, which provides improved cooling effectiveness at lower heat transfer coefficients.
[DOI: 10.1115/1.2185122]

Introduction

Film cooling has been used to protect the surface and allow higher turbine inlet temperatures to be used that increase the thermal efficiency of the Brayton cycle. Typically, 20–25% of high pressure compressor air is used for cooling high-performance turbine engines. The reduction of the percentage of high-pressure air used for cooling increases the flow available for combustion with a proportional increase in thrust. Film cooling techniques that promote attached flows and are stable in the boundary layer in the presence of curvature and pressure gradients have the possibility of improving the downstream film effectiveness and reducing heat transfer coefficient. Film cooling techniques, which can excite or couple existing flow instabilities, can in some cases inhibit the normal high mixing rates by extending life times of naturally occurring vortical structures. Pulsed film cooling is investigated using the transient IR technique to demonstrate the reduction of film cooling flow without sacrificing effectiveness performance or increasing of the heat transfer.

Studies on flow control of separated low-pressure turbine flows used pulsed jets. Lake et al. [1,2] and Bons et al. [3], Sondergaard et al. [4], and Bons et al. [5] utilize the introduction of longitudinal vortices to reattach separated flows. Bons et al. [5] investigated vortex generator jets injected at 90 deg skew to the primary flow. Reduction of the control flow down to a duty cycle of 1% still affected reattachment of the separated flow. These pulsed control flows with a reduced duty cycle flow showed the capability to significantly modify the near wall boundary layer with reattachment of the separated flow long after the injected pulse was convected off the airfoil. It is suggested that longitudinal vortices would entrain outer-layer/freestream fluid at higher temperatures resulting in higher values of the heat transfer coefficient as a result of the increased temperature gradients. Although the study itself never conducted any heat transfer measurements, the expected heat transfer correlation with strong curvature and pressure gradients in these pulsed flows were found to be significantly different.

Pulsed vortex generator jet techniques have been successfully employed in flow control for low Reynolds number flows in low-pressure turbine cascades [6–8]. In this application, pulsed vortex generator jets (VGJs) are introduced at 90 deg skew and 30 deg inclined to the oncoming primary flow. The intent was to reattach a separated flow by introducing a long-lived starting vortex into the flow. Pulsing of these VGJs at duty cycles down to 1% has proved effective in reattaching these massively separated flows in a low-pressure turbine cascade. The duty cycle of 1% represents a very large control authority $\rho_c U_c / \rho_\infty U_\infty \sim 5 \times 10^{-5}$. The focus is to introduce and control structures that will remain stable and effective in flows with large curvatures and pressure gradients, such as occur on turbine blading. These structures are postulated to provide an improved stable layer of film for cooling purposes that may inhibit mixing or also lower heat transfer—and this has proven to be the case as will be documented Although the exact physical mechanisms are still being defined, there are very clear advantages to the use of pulsed flows and their associated starting vortices for control of wall flows, turbine film cooling flows, and many other flows. The possibility of reducing the duty cycle and actual film flow rate significantly without losing film effectiveness can contribute significant improvements in turbine performance.

There have been a few studies that have addressed bulk flow pulsations [9–12]. The pulsation was created by the periodic rotation of an array of six shutter blades. The shutter blades, which were placed across the span of the wind tunnel test section and driven by a DC motor and a timing belt, caused the mainstream pulsation and subsequent coolant pulsation. However, in the present study, the coolant jet pulsation was controlled by the opening and closing time settings and the mainstream was remained unchanged. The characteristics of experimental conditions

[1]To whom correspondence should be addressed.

Contributed by the Turbomachinery Division of ASME for publication in the JOURNAL OF TURBOMACHINERY. Manuscript received January 4, 2005; final manuscript received January 25, 2006. Review conducted by T. Arts.

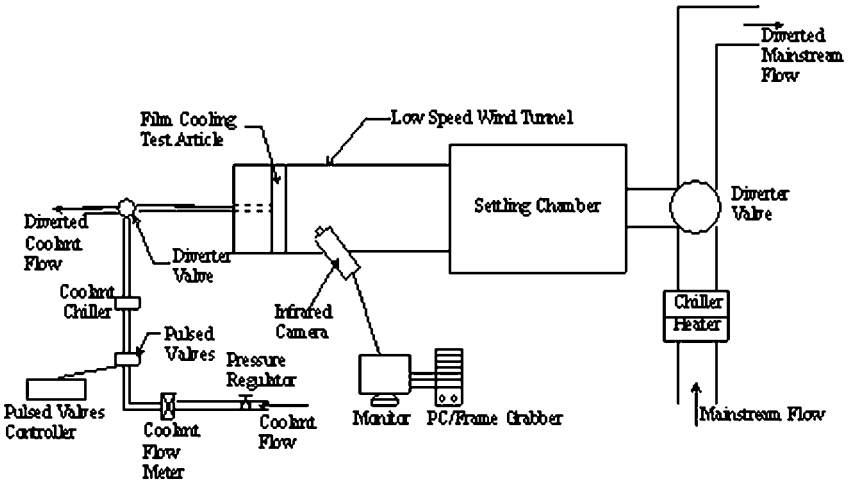

Fig. 1 Schematic of test facility

were significantly different. In the present study, the presence of starting and stopping vortices due to the pulsation of film cooling jets is not present in the study of bulk pulsation effects on constant film cooling jets. The advantages of this new technique include:

1. reduced film cooling flow
2. increased film effectiveness
3. reduced heat transfer
4. possible combination with flow control objectives to achieve increased blade loading

Currently, the basic measurements of h and η are only accurate to ±8–10%. At 1100°C, this is an error of 110°C in the expected hot section part. An error of only 27.78°C (50°F) results in a loss of a factor of two in part lifetime. Improved accuracy of heat transfer coefficient h and film effectiveness η is needed in basic heat transfer and film cooling measurements. The measurements of h and η in this paper will illustrate a transient IR technique, which can improve the accuracy of h and η measurements. Vedula and Metzger [13] proposed simultaneous measurements of the heat transfer coefficient and film effectiveness from a single test using a transient liquid-crystal technique for the three-temperature film cooling problem. This proved to be impractical with transient liquid crystals due to the small temperature differences. Two tests are typically used to make these measurements.

In the present study, a transient infrared thermography technique is used for obtaining both heat transfer coefficient and film effectiveness from a single test. The transient IR technique is based on the two-equation, single test proposed by Vedula and Metzger [13] and was demonstrated successfully by Ekkad et al. [14]. In this test, two images with surface temperature distributions are captured at two different times during the transient test. The test is typical of a transient liquid-crystal technique experiment wherein the test surface at ambient is suddenly exposed to a hot mainstream and cold coolant jet. The surface temperature response is captured by the IR camera at different time instants during the transient test. Simultaneous η and h distributions are investigated and presented, at the leading edge, for pulsed duty cycles from 100% to 10%, at nominal pulse blowing ratios of 0.5, 0.75, 1.0, 1.5, and 2.0. Pulse frequencies of 5 Hz and 10 Hz were investigated. The freestream Reynolds number based on the leading edge diameter was 60,000.

There have been several studies in the recent years that have used IR thermography techniques for heat transfer coefficient and film effectiveness measurements. Most of these studies either measured film effectiveness with adiabatic wall with steady-state conditions or measured heat transfer coefficient with steady-state conditions and constant wall heat flux surface. There are no studies that have used the IR technique for simultaneous determination of film effectiveness and heat transfer coefficients in transient mode. This is the first study to use the advantages of IR technique for simultaneous film cooling measurements although Licu et al. [15] used a technique with wideband liquid crystals to measure both h and η in a single test.

Test Facility

Figure 1 shows the facility used for the present study. The facility consists of a low-speed wind tunnel with a 76.2 cm dia, settling chamber and 30.5 cm dia solenoid valve to switch the temperature-controlled mainstream flow from a bypass loop to the test section. A temperature-controlled coolant loop provides the coolant flow to the film hole. Mainstream and coolant flow loops have a capacity of both heating and cooling. The coolant flow is provided from shop air and passes through an air filter, pressure regulator, heat exchanger, and Rotameter to measure the flow rate. It then separately enters two pulse valves controlled by an IOTA ONE pulse driver system (controller). The pulse driver system controls valves to synchronously open and close over a continuously variable pulse length and duty cycle. Duty cycle (percent) is defined as the valve open time with respect to valve open time plus time. The pulsed coolant flow exits through a 0.635 cm solenoid valve to switch the flow from bypass to the film hole. There is no heating for the coolant as the test is run with a cold coolant. The test surface is a half cylinder with a diameter of 8.89 cm and height of 36.4 cm joined by a flat afterbody made of Plexiglas™ to meet the required semi-infinite solid assumption for the transient test.

Figure 2 shows the opened out view of the leading edge of the bluff body. The original test surface had several holes, and for this study, only a single hole was used and the others were plugged from inside and outside to ensure coolant flow only through the chosen single hole. The chosen single film hole located at 21.5 deg from true leading edge is used for this study due to the flow rate limited by the pulse valves. All the other film holes are blocked from inside and outside of the test model. The film hole is angled 20 deg to the surface in the spanwise direction and 90 deg in the streamwise direction. The hole is 4.76 mm dia and located approximately at the midspan of the test chamber. The hole to leading edge diameter ratio (d/D) is 0.054 and hole length to hole diameter ratio (L/d) is 11.69.

The surface temperature is obtained with an infrared thermography system—FLIR ThermaCAM SC3000. The system provides a high-quality, nonintrusive method for obtaining thermal data for analysis. The system has a quantum well infrared photon (QWIP)

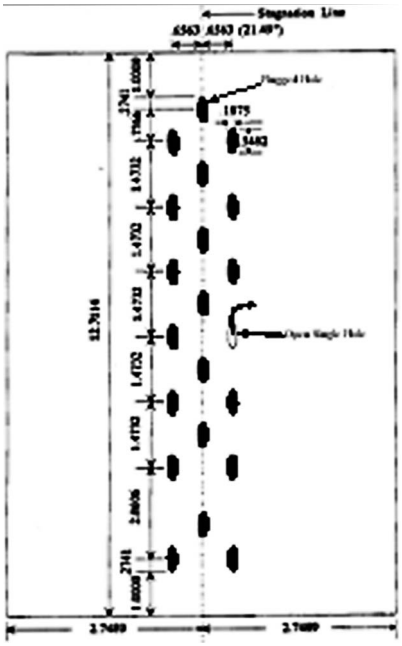

Fig. 2 Illustration of the opened out view of the leading edge test model with open hole and plugged hole locations

detector, which receives and records the thermal electromagnetic radiation between 8 μm and 9 μm in a 320×240 pixel field. The system is cooled internally down to 70 K with a Stirling cycle. The system has several temperature ranges between 20°C and 1500°C. It can be extended up to 2000°C with optional filters. The stated system accuracy is ±2% of the chosen measurement range or ±2°C (±2 K), whichever is larger. A temperature range of −20–80°C with an accuracy of ±2°C (or ±2 K) is used for this study. The system calibration is conducted using a thermocouple placed on the black painted test surface to act as the benchmark. This thermocouple is used to estimate the emissivity of the test surface. The emissivity of the black painted test when viewed through a calcium fluoride window is 0.96.

Procedure

A thermocouple is attached to the test surface with aluminum tape. The thermocouple is located outside the measurement domain to prevent from interference caused by the aluminum tape. The test surface is then sprayed with black flat paint to increase the emissivity like a perfect blackbody with a known emissivity of unity. The IR camera is focused on the test surface (typically, covers slightly larger than the region of interest and the thermocouple). Prior to the actual thermal measurements, calibration of the entire thermography system and the IR signal is required. The test surface is then heated with the hot air supplied by the blower through the mainstream heater. The temperatures of thermocouples are monitored until steady state is reached. The temperature measured by the thermocouple is then compared to that measured by the IR system. The factors required for an accurate IR measurement to compensate for the effects of several different sources of radiation include the distance between the test surface and the front lens of camera, the relative humidity, and the background temperature. Multiple temperature calibrations compensate for all other emitting sources of radiation within view of test article. A number of temperatures are used to establish the corrective value of emissivity. To calibrate the surface emissivity, the IR temperatures at the thermocouple beads are obtained from the real-time thermal image and compared to the indicated thermocouple temperatures. The surface emissivity is then adjusted and determined until the IR temperature matches the thermocouple

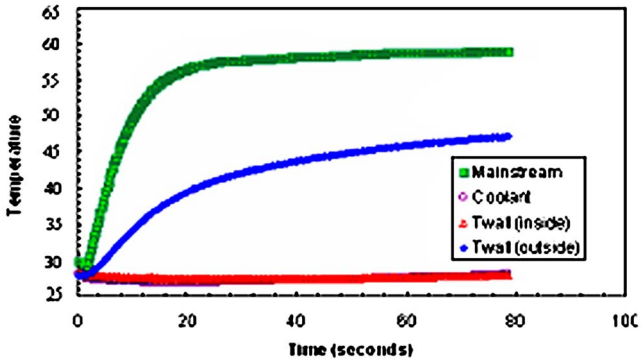

Fig. 3 Temperature response of different thermocouples in degrees celsius

temperature within 0.1°C. The surface emissivity with a black flat paint is, typically, in the range of 0.93–0.97. A thermocouple placed in the mainstream, 31 cm upstream of the film hole, is used to measure the mainstream temperature. Another thermocouple placed in the coolant chamber adjacent to the film hole is used to measure the coolant temperature. Before the transient test is initiated, the mainstream flow is diverted away from the test section and heated to a desired temperature. The coolant flow is also diverted away from the test section but is maintained at ambient temperature. Once the mainstream reaches the desired temperature, the IR camera is triggered to take images at the same time the mainstream and coolant flows are routed into the test section. The mainstream and coolant temperatures are also recorded at the same instant. The thermal images are converted to temperatures at different instants of time.

Typically, the mainstream temperature increases from the initial temperature to set temperature during the first 15–20 s and then steadies as shown in Fig. 3. The coolant temperature is, however, maintained at the initial temperature. The wall temperature monitored by the thermocouple used for emissivity estimation rises as the outside surface is heated during the transient test at a more gradual rate than mainstream temperature. The inside wall temperature is unaffected by the heating on the opposite side confirming the usage of the semi-infinite solid assumption. The test surface was modeled as a semi-infinite solid medium imposed by a sudden transient heating. The entire solid medium was initially at a uniform temperature before the transient test. During the transient heating test, each point on the surface will respond with different temperature at different time due to different heat transfer coefficient. Faster time of temperature change in response to the prescribed temperature during the transient test will produce higher heat transfer coefficient and vice versa. The basic heat conduction equations with boundary conditions defining the system are shown below

$$k\frac{\partial^2 T}{\partial y^2} = \rho C_p \frac{\partial T}{\partial t} \tag{1a}$$

$$-k\frac{\partial T}{\partial y}\bigg|_{y=0} = h(T_r - T_w) \tag{1b}$$

$$T|_{y=\infty} = T_i \tag{1c}$$

$$T|_{t=0} = T_i \tag{1d}$$

where T_r is the reference temperature or the main flow temperature (which could be the film temperature in a film cooling situation), T_w is the prescribed wall condition (color-change) temperature, and T_i is the initial temperature of the test surface before the transient. Applying the prescribed boundary conditions and initial conditions to the problem and solving for the wall temperature

response with time at $y=0$ produces a solution of the form

$$\frac{T_w - T_i}{T_\infty - T_i} = 1 - \exp\left(\frac{h^2 \alpha t}{k^2}\right) \operatorname{erfc}\left(\frac{h\sqrt{\alpha t}}{k}\right) \tag{2}$$

where h is the unknown quantity in the equation with T_w is the wall temperature at time t after the initiation of the transient test and T_∞ as the freestream temperature. The material properties, α (0.1076×10^{-6} m^2/s) and k (0.187 W/m K) dictate the applicability of the semi-infinite solid solution. The wall temperature response is measured at every point on the test surface, and the Eq. (2) is used to calculate the local heat transfer coefficient. Equation (2) assumes that the oncoming mainstream flow imposes a step change in air temperature on the surface, which is not true in the transient experiment. Therefore, Eq. (2) was modified to represent the response of the changing mainstream temperature. The mainstream temperature rise is simulated as a superposed set of elemental steps using the Duhamel's superposition theorem. Metzger and Larson [16] showed that the wall temperature response can be represented as

$$T_w - T_i = \sum_{j=1}^{N} U(t - \tau_j) \Delta T_\infty \tag{3}$$

where

$$U(t - \tau_j) = 1 - \exp\left[\frac{h^2}{k^2}\alpha(t - \tau_j)\right] \operatorname{erfc}\left[\frac{h}{k}\sqrt{\alpha(t - \tau_j)}\right] \tag{4}$$

The superposition is imposed by measuring the mainstream temperature (T_∞) variation with time (τ) during the transient test. The step changes are then input into the above solution to obtain the unknown heat transfer coefficient.

In film cooling situations, the basic convective heat load equation is modified to include the film temperature based on the definition of the local heat flux. The equation becomes

$$\frac{T_w - T_i}{T_f - T_i} = 1 - \exp\left(\frac{h_f^2 \alpha t}{k^2}\right) \operatorname{erfc}\left(\frac{h_f\sqrt{\alpha t}}{k}\right) \tag{5}$$

where T_f is the local film temperature and is a function of the local mixing between the mainstream and coolant jet near the surface.

Vedula and Metzger [13] presented a method wherein two color-change times can be obtained from a single transient test at every location. If during the transient, the liquid-crystal coating indicates one surface temperature (T_{w1}) at time t_1 and another surface temperature (T_{w2}) at time t_2. Basically, two events are measured at every point leading to the solution of both h_f and T_f from the simultaneous solution of

$$\begin{aligned} \frac{T_{w1} - T_i}{T_f - T_i} &= 1 - \exp\left(\frac{h_f^2 \alpha t_1}{k^2}\right) \operatorname{erfc}\left(\frac{h_f\sqrt{\alpha t_1}}{k}\right) \\ \frac{T_{w2} - T_i}{T_f - T_i} &= 1 - \exp\left(\frac{h_f^2 \alpha t_1}{k^2}\right) \operatorname{erfc}\left(\frac{h_f\sqrt{\alpha t_2}}{k}\right) \end{aligned} \tag{6}$$

In the proposed transient test, the mainstream will be heated and the coolant supply will be cold or similar to room temperature. The Duhamel's superposition theorem will be applied to the mainstream temperature response as the coolant will be at a constant temperature through the experiment. However, due to inherent difficulties of determining two events far apart so that the uncertainty can be reduced, this technique has never been applied to solve for both the unknowns from a single transient test. To avoid the difficulties associated with the single transient test, Vedula and Metzger [13] suggested two different tests with the same flow conditions but different coolant temperatures measuring the indication of the same color-change temperature. They ran two tests with one that had mainstream and coolant running at about the same temperatures and another test that had the mainstream hot and the coolant at room temperature. Since they did not have a true step change in air temperatures for both mainstream and coolant, they applied the superposition integration for both temperatures. Also, they defined film effectiveness (η) as

$$\eta = \frac{T_f - T_\infty}{T_c - T_\infty} \tag{7}$$

where T_f represents the film temperature, which is the same as adiabatic wall temperature as there is no heat transfer into the wall during the transient test. Several studies have used this technique [8–10] to obtain film cooling measurements for different surface geometries. Ekkad et al. [17] and Du et al. [18] used a transient cooling technique to eliminate the use of superposition integration for the mainstream and coolant temperatures but they still needed two different tests to obtain both heat transfer coefficient and film effectiveness at every point on the surface.

The mainstream temperature, coolant temperature, and surface temperature distributions from the IR images are used to calculate the local heat transfer coefficient and film effectiveness at each pixel of the IR image. To calculate heat transfer coefficient and film effectiveness distributions, two images are required. The first image is typically around 15–20 s after the initiation of the test and the second image around 60–70 s after the test initiation.

Uncertainty in the calculation comes from measurement of initial, mainstream, and coolant temperatures. Estimated uncertainty in initial and wall temperature (ΔT_i) is ±1.1 °C, mainstream temperature (ΔT_∞) is ±1.1 °C, and coolant temperature (ΔT_c) is ±1.1 °C. The camera frame rate is 60 Hz resulting in a time error of ±0.016 s, and the test surface property uncertainty is estimated at ±3%. The resulting average uncertainty using the methodology proposed by Kline and McClintock [19] for heat transfer coefficient and film effectiveness is ±4.5% and ±7.0%, respectively. However, uncertainty for local film effectiveness depends on the local value. Uncertainty for effectiveness measurements is ±0.05. Uncertainty in the vicinity of the hole is affected by the presence of two-dimensional (2D) conduction and will be significantly higher than the average uncertainty with values around ±15%.

Results and Discussion

Experiments were performed at a mainstream velocity of 12.63 m/s, which represents a flow Reynolds number of 60,000 based on leading edge diameter. Six different coolant-to-mainstream blowing ratios were studied ranging from 0.25 to 2.0 for a single hole on the leading edge surface to evaluate the experimental technique. Frequencies of 5 Hz, 10 Hz, and 20 Hz were studied. Different duty cycle conditions were simulated by varying the open and shut settings to obtain 100% (almost), 75%, 50%, and 25%. The duty cycle setting produces lower average flow compared to the fully open setting (or continuous flow).

Figure 4 shows the effect of blowing ratio on spanwise averaged Frossling number ($\mathrm{Nu}/\mathrm{Re}^{0.5}$) distributions for the unpulsed jet. Since there is a single hole, the spanwise region encompasses about 1.5 distances between the holes. At low blowing ratios, there is no enhancement downstream of injection due to low mixing and attached jets. The Frossling numbers are around 1.2 downstream of the hole for $M=0.25$. As blowing ratio increases, the region downstream of the hole sees the highest enhancement due to jet-mainstream interactions. Further downstream, the values decreases as jet dissipates into the mainstream. The Frossling solution [20] for a cylinder in cross-flow is shown for comparison. This result is for a cylinder without film holes. For a circular leading edge with low free-stream turbulence, Frossling numbers at stagnation point are around 1.0 and decrease downstream until about 80 deg from stagnation point, during which transition occurs. As stated before, the film hole is located at 21.5 deg from leading edge stagnation point which is well within the laminar

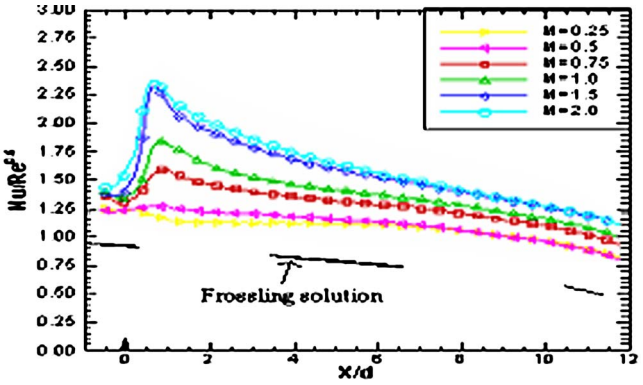

Fig. 4 Effect of blowing ratio on spanwise-averaged Nusselt number distribution for an unpulsed jet

boundary layer region. Film injection is orthogonal to the mainstream region resulting in a strong lateral velocity. As film injection rate (or blowing rate) increases, the jet tends to resist the mainstream strongly and pushes upward. The jet-mainstream interaction also increases with increasing blowing ratio resulting in local turbulence behind the hole as shown by the high heat transfer region for higher blowing ratios. The Frossling numbers are around 1.25 for $M=0.25$ and as high as 2.5 for $M=2.0$.

Figure 5 shows the effect of blowing ratio on spanwise averaged film effectiveness distributions for the unpulsed jet. Lower blowing ratios produced attached jets downstream of the hole creating very high effectiveness and subsequently reducing downstream. Higher blowing ratios produce stronger jets that tend to lift off along the hole direction. The higher effectiveness region is along the hole direction and decreases downstream. This is the reason spanwise averaging shows higher effectiveness downstream of the hole for low blowing ratios. The jets get pushed downstream for low-velocity jets, whereas higher-velocity jets mover farther laterally before losing the momentum and get pushed downstream. For low blowing ratios, the jet does not possess a strong lateral momentum along the hole direction and gets pushed to the downstream edge, resulting in high effectiveness values just downstream of the hole. The jet effect begins to decrease downstream due to reduced coverage. As blowing ratio increases, the lateral momentum of the jet becomes stronger and the high film effectiveness region moves to the top of the hole location in the direction of the hole exit. Also for higher blowing ratio, jet liftoff occurs resulting in lower effectiveness just downstream. Highest effectiveness coverage appears to occur between blowing ratios of 0.5 and 1.0.

The effect of pulsing frequency and duty cycle was studied for each of the chosen continuous blowing ratios. Figure 6 shows the effect of pulsing frequency and duty cycle on span-averaged

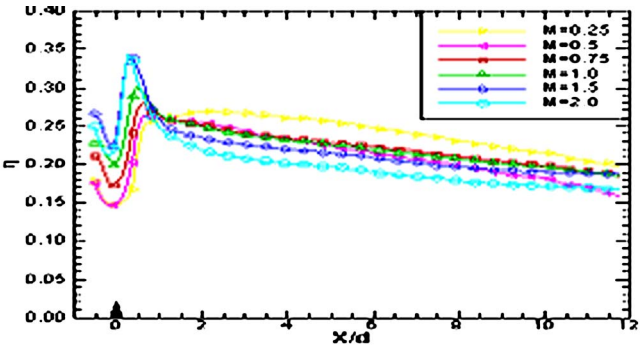

Fig. 5 Effect of blowing ratio on spanwise-averaged film effectiveness distribution for an unpulsed jet

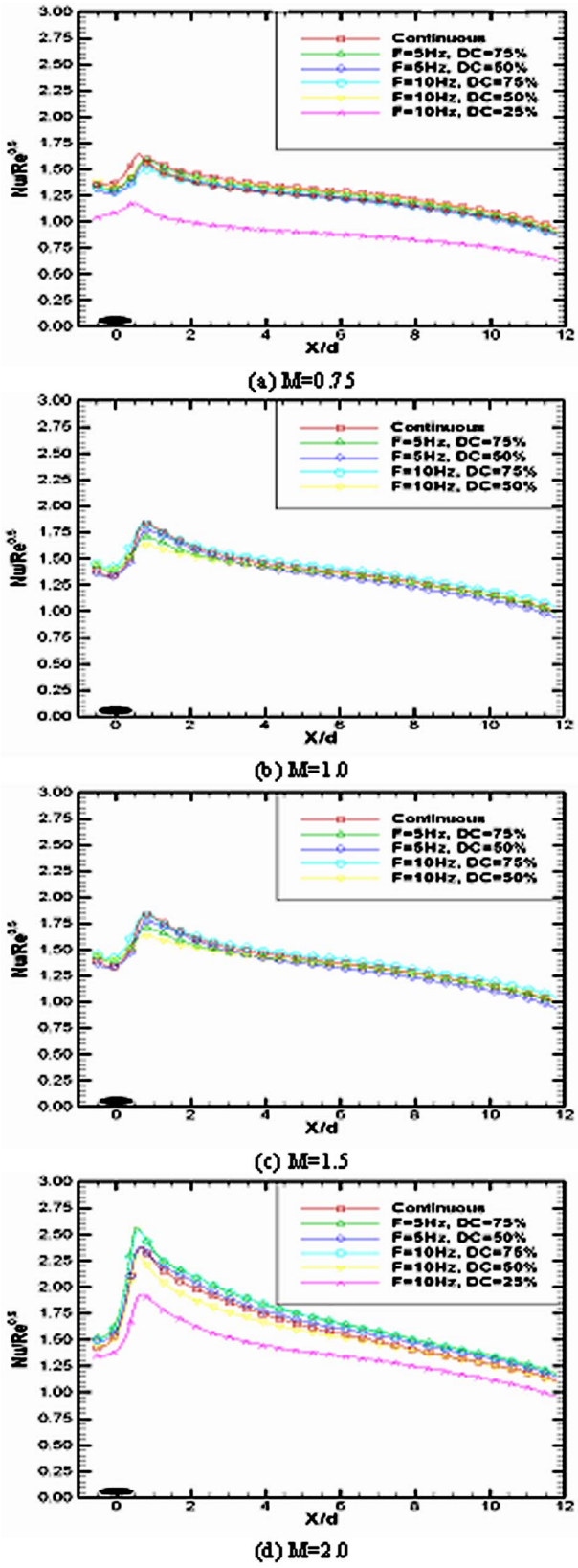

Fig. 6 Effect of pulsing frequency and duty cycle on Frossling number distributions

Frossling number distributions at each continuous blowing ratio of $M=0.75$, 1.0, 1.5, and 2.0. At a low blowing ratio of $M=0.75$, the pulsing frequency and duty cycle have no effect on the Frossling number compared to the continuous blowing. As the duty cycle is

reduced to 25%, the time-average blowing ratio becomes <0.2 with very little heat transfer enhancement. There is local enhancement near the hole but downstream the effect completely vanishes. For $M=1.0$, the pulsing frequency and duty cycle have little effect with small variations downstream of the hole. A low duty cycle was not tested for this blowing ratio. For $M=1.5$, three different pulsing frequencies of 5 Hz, 10 Hz, and 20 Hz were tested for DC=50%. There is almost negligible effect of the pulsing frequency on the Frossling number. It appears that the level of pulsing is not as much as a factor as the duty cycle setting. A duty cycle setting of 25% produces low heat transfer coefficients than the other cases for $M=1.5$. However, further decreasing the duty cycle setting to 10% radically reduces the Frossling numbers due to significantly reduced coolant injection compared to the continuous blowing condition. At $M=2.0$, decreasing duty cycle gradually drops the level of Frossling number after injection location. A duty cycle of 25% produces a 40% reduction in Frossling numbers. Overall, it appears that duty cycle and pulsing frequency have very little effect on Frossling numbers for DC higher than 50% for all blowing ratios.

Figure 7 presents the effect of pulsing frequency and duty cycle on span-averaged film cooling effectiveness compared to continuous blowing conditions. At a low blowing ratio 0.75, the pulsing frequency and duty cycle effect is almost negligible. At the low blowing ratio, the effectiveness is already significantly high, resulting in very little effect of pulsations. At $M=1.0$, the pulsing appears to cause some effect in increasing the film effectiveness immediately downstream of injection. A blowing ratio of 1.0 in this case indicates equal momentum of the mainstream and coolant jet in the vicinity of the hole. There is some possibility of local jet liftoff that may be affected by pulsations and thus a better cooling protection is produced by pulsating jets. Pulsing appears to produce lower liftoff as will be evident at higher blowing ratios of 1.5 and 2.0. At $M=1.5$, a lower duty cycle of 25% clearly produces the highest film effectiveness. But further reduction in duty cycle to 10% causes drastic reduction in film effectiveness. At 25%, it appears that the coolant flow rate and the momentum ratio is sufficient to produce an effective film but at 10% there is very little coolant flow coming out of the holes with enough momentum to produce an effective film. This coincides with the Frossling number distributions for the same conditions in Fig. 6(*c*). At $M=2.0$, the continuous blowing rate effectiveness is lower than all the 10 Hz, 50% DC case. The pulsed jet conditions with 25% duty cycle produces the highest effectiveness. It appears that the reduction of actual blowing ratio to a lower effective blowing ratio produces desired results. Overall the pulsing effect produce slightly lower heat transfer coefficients and higher film effectiveness than the continuous pulsed 100% duty cycle.

Using the duty cycle and averaging the flow rate during several 100 cycles, an average jet blowing ratio can be determined. Figures 8 and 9 are presented to compare the performance of the pulsed/continuous films based on the average blowing ratio. When a pulsed case is switched from the continuous blowing condition, coolant flow rate is fluctuating between two extreme values (minimum and maximum). The effective (average) blowing ratio is calculated based on the average flow rate of these two extreme values in addition to measuring the exit velocity characteristics of the pulsed jet at different pulsing frequencies and duty cycle settings.

Figure 8 compares the Frossling number distributions for different effective blowing ratios. Four different blowing ratios are examined, $M=0.25$, 0.5, 1.0, and 1.5. Results show that the heat transfer coefficients are lower for the continuous jets compared to pulsed blowing even at the effective blowing ratio. At $M=0.5$, the differences between pulsed and unpulsed jets are significant, but the differences decrease at higher effective blowing ratios.

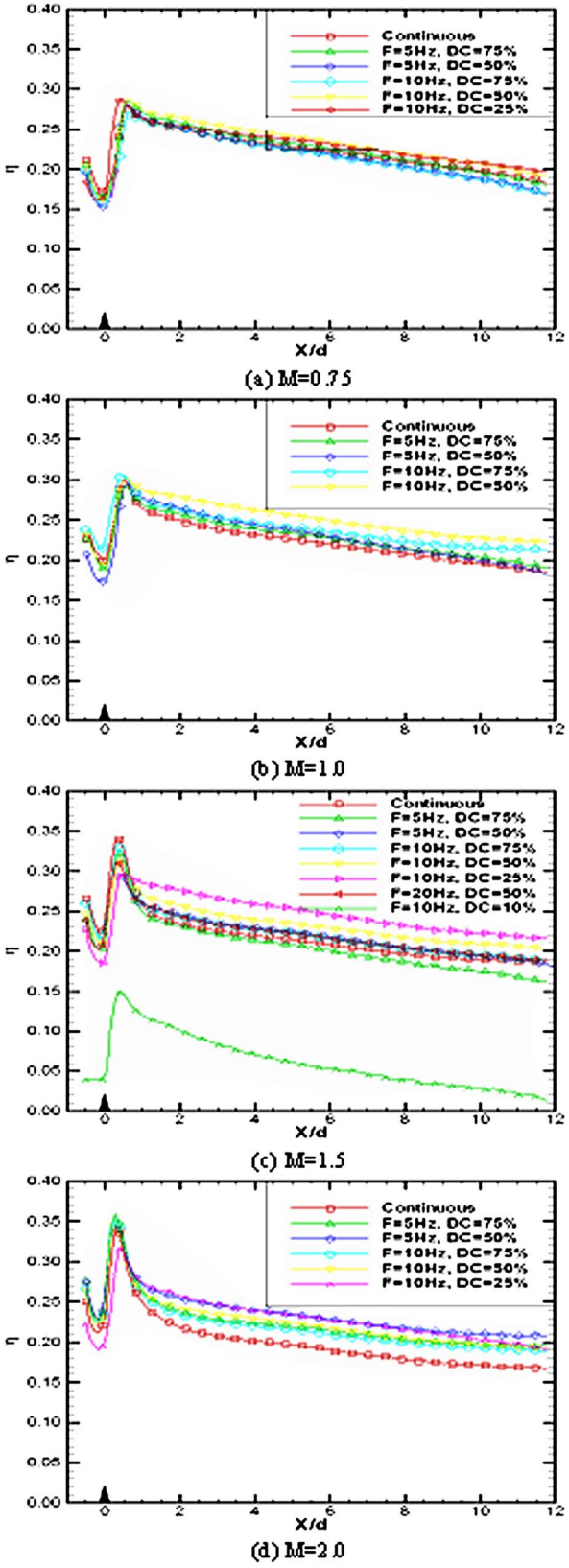

Fig. 7 Effect of pulsing frequency and duty cycle on film effectiveness distributions

Overall, it appears that the pulsed jets provide a slight increase in heattransfer coefficients compared to the continuous jets at a similar reference velocity.

Figure 9 compares the film effectiveness distributions for

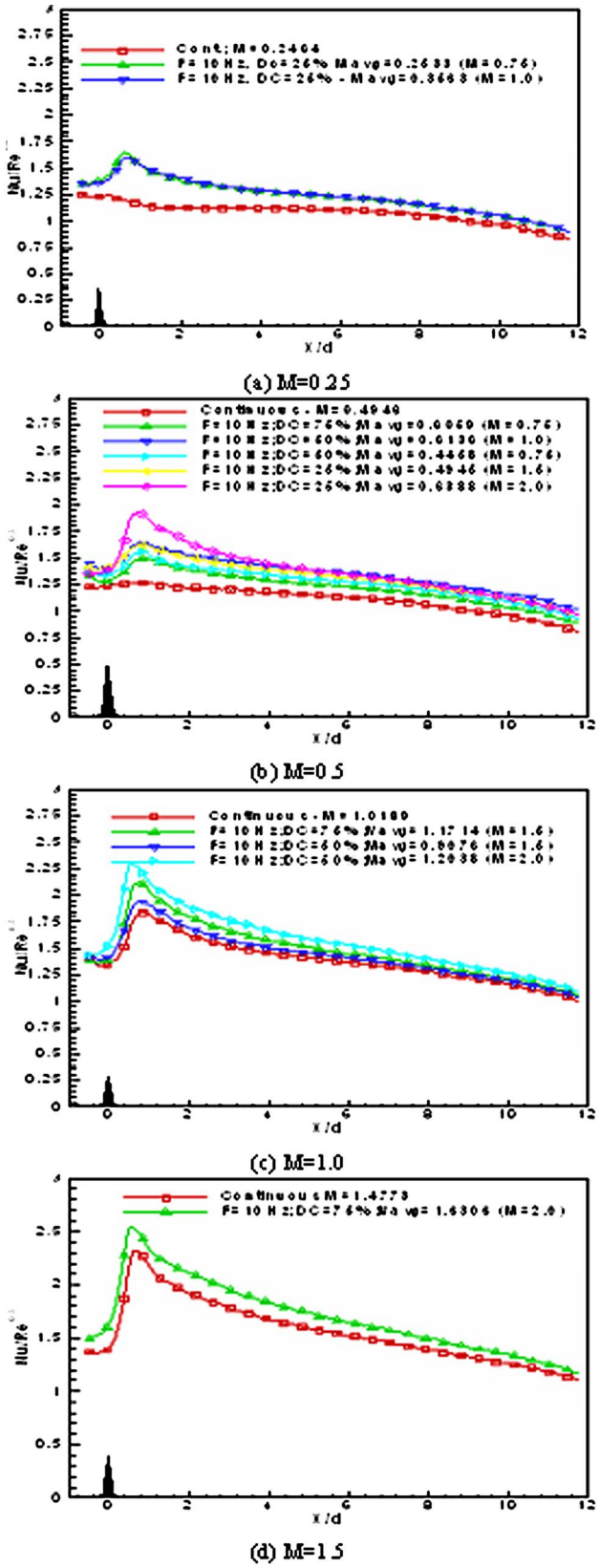

Fig. 8 Effect of pulsing frequency on Nusselt number for a particular effective blowing ratio

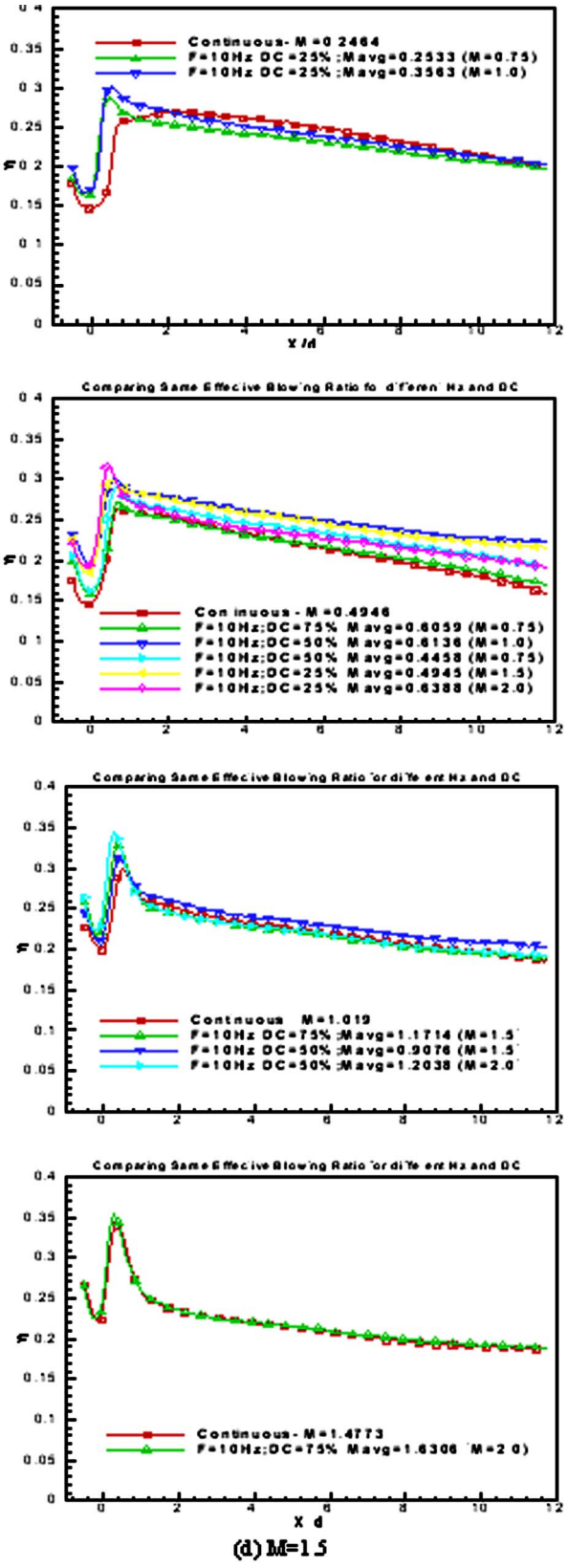

Fig. 9 Effect of pulsing frequency on film effectiveness for a particular effective blowing ratio

different effective blowing ratios. Again, at high and low blowing ratios, there is negligible effect of pulsing. At an average $M=0.5$ continuous reference blowing velocity, it does appear that pulsing enhances film effectiveness. Pulsing overall may cause the jet to spread more on the surface and provide similar or higher effectiveness. Pulsing a higher momentum jet will produce a lower momentum pulsed jet resulting in better spreading and overall better film effectiveness.

Varying frequency between 5 Hz and 20 Hz did not provide any significant differences in heat transfer coefficient and film effectiveness. The duty cycle effect is compared only for a pulsing frequency of 10 Hz. Typically, the duty cycle effect is to reduce total mass flow and thus reduce the average blowing ratio compared to the continuous flow. It appears that the pulsing and duty cycle effect is to reduce the time-averaged blowing ratio. However, the pulsed jet at the time-averaged blowing ratio produces higher effectiveness than the continuous blowing condition. This result clearly shows that the pulsed jet produces relatively better results than the continuous blowing jet.

Conclusions

A comprehensive study was conducted to study the effect of jet pulsation and duty cycle on heat transfer over a leading edge model with film cooling through an injection hole. Detailed film cooling measurements were obtained using a transient infrared technique. The results show that pulsing the jets provides positive results with higher film effectiveness and slightly lower heat transfer coefficients compared to a continuous jet. The pulsed jet with different duty cycle conditions simulate jets with lower average jet momentum with respect to the mainstream resulting in lower lift-off and more spreading on the test surface. This directly indicates the higher effectiveness and reduced heat load. The pulsed frequency itself is not a factor as long as the jet is pulsed. However, there is a duty cycle condition beyond which the coolant flow reduces significantly causing no effect of injection. This study is the first to focus on the effect of pulsed jets on film cooling showing promising results.

Nomenclature

c_p = specific heat (kJ/kg K)
d = film hole diameter (m)
DC = duty cycle (%)=valve open time/(valve open time+close time)
F = pulsing frequency (Hz)=1/(valve open time +close time)
h = local heat transfer coefficient without film injection (W/m^2 K)
h_f = local heat transfer coefficient with film injection (W/m^2 K)
k = thermal conductivity of test surface (W/m K)
L = length of film hole (m)
M = blowing ratio=$\rho_c V_c/\rho_\infty V_\infty$
M_{avg} = time-averaged blowing ratio for pulsed jets
Nu = Nusselt number based on leading edge diameter d ($=h_f d/k$)
Re = freestream Reynolds number ($V_\infty d/\nu$)
ρ = density of test surface
ρ_c = coolant density (kg/m^3)
ρ_∞ = mainstream density (kg/m^3)
t = time (s)
T_c = coolant temperature (K)
T_f = film temperature (K)
T_i = test surface initial temperature (K)
T_r = reference temperature (K)
T_∞ = mainstream temperature (K)
T_w = local wall temperature (K)
V_c = coolant velocity (m/s)
V_∞ = mainstream velocity (m/s)
x = streamwise distance from leading edge to trailing edge (m)
y = coordinate normal to surface (m)
η = film cooling effectiveness
ν = kinematic viscosity of mainstream (m^2/s)
α = thermal diffusivity (m^2/s)
τ = time step in Duhamels' integration (sec)

References

[1] Lake, J., King, P., and Rivir, R., 1999, "Reduction of Separation Losses on a Turbine Blade with Low Reynolds Numbers," 37th AIAA Aerospace Sciences Meeting, Reno January, AIAA Paper No. AIAA-99-0242.
[2] Lake, J., King, P., and Rivir, R., 2000, "Low Reynolds Number Loss Reduction on Turbine Blades With Dimples and V-Groves," 38th Aerospace Sciences Meeting, Reno, AIAA Paper No. AIAA 2000–0738.
[3] Bons, J., Sondergaard, R., and Rivir, R., 1999, "Control of Low-Pressure Turbine Separation Using Vortex Generator Jets," 37th AIAA Aerospace Sciences Meeting, Reno, AIAA Paper No. AIAA-99–0367, January.
[4] Sondergaard, R., Bons, J., and Rivir, R., 2002, "Control of Low Pressure Turbine Separation Using Vortex Generator Jets," J. Propul. Power, **18**(4), pp. 889–895.
[5] Bons, J. P., Sondergaard, R., and Rivir, R. B., 2002, 'Reducing Low Pressure Turbine Stage Blade Count Using Vortex Generator Jet Separation Control," ASME Turbo Expo 2002, June, ASME Paper No. GT-2002.
[6] Bons, J. P., Sondergaard, R., and Rivir, R. B., 2002, "The Fluid Dynamics of LPT Blade Separation Control Using Pulsed Jets," ASME J. Turbomach., **124**, pp. 77–85.
[7] Rivir, R., Sondergaard, R., Bons, J., and Lake, J., 2000, "Passive and Active Control of Separation in Gas Turbines," AIAA Fluids, Denver, June, AIAA Paper No. 2000–2235.
[8] Bons, J. P., Sondergaard, R., and Rivir, R. B., 2001, "Turbine Separation Control Using Pulsed Vortex Generator Jets," ASME J. Turbomach., **123**, pp. 198–206.
[9] Ligrani, P. M., Gong, R., Cuthrell, J. M., and Lee, J. S., 1996, "Bulk Flow Pulsations and Film Cooling, Part 1: Injectant Behavior," Int. J. Heat Mass Transfer, **39**(11), pp. 2271–2282.
[10] Ligrani, P. M., Gong, R., Cuthrell, J. M., and Lee, J. S., 1996, "Bulk Flow Pulsations and Film Cooling, Part 2: Flow Structure and Film Effectiveness," Int. J. Heat Mass Transfer, **39**(11), pp. 2283–2292.
[11] Jung, I. S., Lee, J. S., and Ligrani, P. M., 2002, "Effects of Bulk Flow Pulsations on Film Cooling With Compound Angle Holes: Heat Transfer Coefficient Ratio and Heat Flux Ratio," ASME J. Turbomach., **124**, pp. 142–151.
[12] Seo, H. J., Lee, J. S., and Ligrani, P. M., 1998, "The Effect of Injection Hole Length on Film Cooling With Bulk Flow Pulsations," Int. J. Heat Mass Transfer, **41**, pp. 3515–3528.
[13] Vedula, R. P., and Metzger, D. E., 1991, "A Method for the Simultaneous Determination of Local Effectiveness and Heat Transfer Distributions in a Three Temperature Convective Situations," ASME Paper No. 91-GT-345.
[14] Ekkad, S. V., Ou, S., and Rivir, R. B., 2004, "A Transient Infrared Thermogrpahy Method for Simultaneous Film Cooling Effectiveness and Heat Transfer Coefficient Measurements From a Single Test," ASME J. Turbomach., **126**, pp. 597–603.
[15] Licu, D. N., Findlay, M. J., Gartshore, I. S., and Salcudean, M., 2000, "Transient Heat Transfer Measurements Using a Single Wide-Band Liquid Crystal Test," ASME J. Turbomach., **122**, pp. 546–552.
[16] Metzger, D. E., and Larson, D. E., 1986, "Use of Melting Point Surface Coatings for Local Convective Heat Transfer Measurements in Rectangular Channel Flows With 90-Deg. Turns," ASME J. Heat Transfer, **108**, pp. 48–54.
[17] Ekkad, S. V., Du, H., and Han, J. C., 1998, "Detailed Film Cooling Measurements on a Cylindrical Leading Edge Model: Effect of Free-stream Turbulence and Density Ratio," ASME J. Turbomach., **120**, pp. 779–807.
[18] Du, H., Han, J. C., and Ekkad, S. V., 1998, "Effect of Unsteady Wake on Detailed Heat Transfer Coefficient and Film Effectiveness Distributions for a Gas Turbine Blade," ASME J. Turbomach. **120**, pp. 808–817.
[19] Kline, S. J., and McClintock, F. A., 1953, "Describing Uncertainties in Single Sample Experiments," Mech. Eng. (Am. Soc. Mech. Eng.), **75**, pp. 3–8.
[20] Frossling, N., 1958, "Evaporation Heat Transfer and Velocity Distribution in Two-Dimensional and Rotationally Symmetric Boundary Layer," NACA, TM-1432.

Karsten Kusterer
e-mail: kusterer@bub-agema

Torsten Hagedorn

B&B-AGEMA GmbH,
Julicher Strasse 338,
D-52070 Aachen,
Germany

Dieter Bohn
Institute of Steam and Gas Turbines,
Aachen University,
Templergraben 55,
D-52056 Aachen,
Germany
e-mail: post-bohn@idg.rwth-aachen.de

Takao Sugimoto
e-mail: sugimoto_t@khi.co.jp

Ryozo Tanaka

Gas Turbine Research & Development Center,
Kawasaki Heavy Industries, Ltd.,
Akashi 673-8666,
Japan

Improvement of a Film-Cooled Blade by Application of the Conjugate Calculation Technique

The conjugate calculation technique has been used for the three-dimensional thermal load prediction of a film-cooled test blade of a modern gas turbine. Thus, it becomes possible to take into account the interaction of internal flows, external flow, and heat transfer without the prescription of heat transfer coefficients. The numerical models consist of all internal flow passages and cooling hole rows, including shaped holes. Based on the results, deficiencies of the test configuration close to the leading edge region and in the blade tip region have been detected, which lead to hot spots and surface areas of high thermal load. These regions of high thermal load have been confirmed by thermal index paint measurements in good agreement to the conjugate calculation results. Based on the experimental and numerical results, recommendations for the improvement of the blade cooling were derived and an improved blade-cooling configuration has been designed. The conjugate calculation results, as well as new measurement data, show that the changes in the cooling design have been successful with respect to cooling performance. Regions of high thermal load have vanished, and effective cooling is reached for all critical parts of the test blade. [DOI: 10.1115/1.2183314]

Keywords: film cooling, conjugate heat transfer, thermal design process, cooling fluid distribution

Introduction

Cooling configurations for turbine first-stage blades in modern gas turbines consist of complex interior geometries with large number of cooling holes in order to provide cooling air for film-cooling purposes. The aim is to reach a most efficient cooling by using high internal convective cooling and shielding the external surface against the hot gas by means of homogeneous coverage of the surface with a cooling film. Thus, the design of such configurations becomes very complex due to three-dimensional flow phenomena, mixing of cooling fluid and hot gas, and the unknown heat transfer conditions of the external film cooling and the internal convective cooling. Testing of the designed configuration under real hot gas conditions requires significant efforts with respect to the availability of an adequate test facility, experimental time, and money.

Numerical flow simulations can provide additional information on the three-dimensional internal and external flows and, thus, it might be possible to detect deficiencies of a configuration prior to testing. The prediction of the thermal load is the most difficult task and essential for the evaluation of the cooling performance of the designed configuration. Reliable calculation of three-dimensional temperature distributions for the complex cooled blade are of significant importance in order to reduce the number of test runs for a newly designed cooled blade.

Conjugate Calculation Technique. Unfortunately, temperatures on the blade surface and in the blade solid body are highly dependent on local heat transfer and fluid flow interaction at the internal and external surfaces. As in most cases, detailed knowledge of local heat transfer coefficients is not available during the design process, the conjugate flow and heat transfer simulation is a sophisticated attempt to solve this problem.

The conjugate calculation methods are based on a coupled calculation of the fluid flow, heat transfer at solid/fluid boundaries and heat conduction in the solid walls. The basic idea of coupled fluid flow and heat transfer calculation is not a new idea, but it has been the significant increase in calculation capabilities based on new computer technologies, which allowed several research groups in the early 1990s to develop computation codes for 2-D and 3-D conjugate calculation. Thus, a large number of conjugate calculation approaches have been published in recent years. With respect to the application of conjugate calculation methods on blade film cooling, the work of following groups can be mentioned as examples. Heidmann et al. [1] have used the Glenn-HT code for calculation of conjugate heat transfer effects on a realistic film-cooled turbine vane. Within this code, the boundary element method (BEM) by Li and Kassab [2,3] has been implemented. The BEM does not require meshing of the solid region. As described by Rigby and Lepicovsky [4], the Glenn-HT code has also been extended to solve conjugate heat transfer problems by gridding inside the solid and setting the velocities there to zero. Adami et al. [5] have upgraded a finite volume CFD solver by coupling it to a routine solving the Fourier equation in the solid domain. The code has been tested successfully for a transonic NGV, including film cooling of the pressure side. The following additional collection of publications in Refs. [6–12] might be helpful for a good overview on different conjugate calculation approaches and application to gas turbine cooling, but is surely not complete.

In the present paper, the homogeneous conjugate calculation technique in the CHTFLOW solver developed by Bohn et al. [13,14] at Aachen University has been used. The homogeneous method involves the direct coupling of the fluid flow and the solid body

Contributed by the International Gas Turbine Institute (IGTI) of ASME for publication in the JOURNAL OF TURBOMACHINERY. Manuscript received October 1, 2004; final manuscript received February 1, 2005. IGTI Review Chair: K. C. Hall. Paper presented at the ASME Turbo Expo 2005: Land, Sea and Air, Reno, NV, June 6–9, 2005, Paper No. GT2005-68555.

using the same discretization and numerical approach for both zones. Therefore, it is possible to have an interpolation-free crossing of the heat fluxes between the neighboring cell faces. Additional information on the boundary conditions at the blade walls, such as the distribution of the heat transfer coefficient, becomes obsolete, and the wall surface temperatures as well as the temperatures in the blade walls are the direct result of this simulation. The physical domain is divided into separate blocks for the fluid and solid body regions. Full, compressible, two- or three-dimensional Navier-Stokes equations are solved in the fluid blocks. The Fourier equation is solved in the solid body blocks. Coupling of fluid blocks and solid body blocks is achieved via a common wall temperature resulting from the equality of the local heat fluxes passing through the contacting cell faces. The code has been validated and tested for convective cooling and film-cooling configurations. For a precise description of the numerical method and example results, the reader is referred to [15,16].

Improvement of Thermal Design Process. Based on its theoretical approach, the conjugate calculation technique has been identified as a powerful tool for the improvement of the thermal design process with respect to time and cost reduction. Nevertheless, the industrial application of the conjugate calculation within the thermal design process of modern gas turbine blades has not been tested in detail due to the difficulties of handling very complex configurations. Therefore, Kawasaki Heavy Industries has decided in 2002 to start a project together with the Institute of Steam and Gas Turbines of Aachen University, and B&B-AGEMA in order to investigate the ability, effort, and performance of the conjugate calculation technique for thermal load simulation of a realistic cooling configuration of a test blade.

Experimental investigations, including thermal index paint measurements under real hot gas conditions for different operating points, were performed at Akashi R&D Center. All conjugate calculations for the test configuration were done with CHTFLOW solver at B&B-AGEMA in a blind test case. The experimental results had not been provided before the simulation results had been submitted to KHI. The results have been published in [17,18] and with respect to the influence of different operating conditions in [19]. The results have shown that despite a number of simplifications in modeling the geometry itself, dividing up the calculation in two different tasks, and the application of the simple turbulence model [20], the CCT has been able to detect major and minor deficiencies in the original cooling design in agreement with the measurement results. It has been found that the lack of precise inlet boundary conditions for realistic hot gas flow conditions is an important factor for differences in measurement and calculation. Nevertheless, the conjugate calculation technique in its present state has proven to be a valuable tool for the numerical testing of the conventionally designed cooling configuration. In order to continue the successful project, it has been decided in 2003 to design an improved cooling configuration for the test blade based on recommendations from numerical and measurement results. The new configuration has been built and tested again at KHI R&D center in Akashi and a conjugate calculation has been performed for the new configuration at B&B-AGEMA.

The content of the paper is a summary of the main results for the first configuration (CONF A), the recommendations for improvements with respect to the leading-edge cooling, and the results of calculations and measurements for the improved test configuration (CONF B).

Blade-Cooling Configurations

Configuration A (CONF A). An experimental test configuration (CONF A) has been developed in 2001 by Kawasaki Heavy Industries (KHI), LTD., for the film cooling of a first-stage rotor blade of a modern gas turbine [21]. The test configuration has been used to investigate the influence of different operating conditions on the thermal load of the blade. At the blade leading edge,

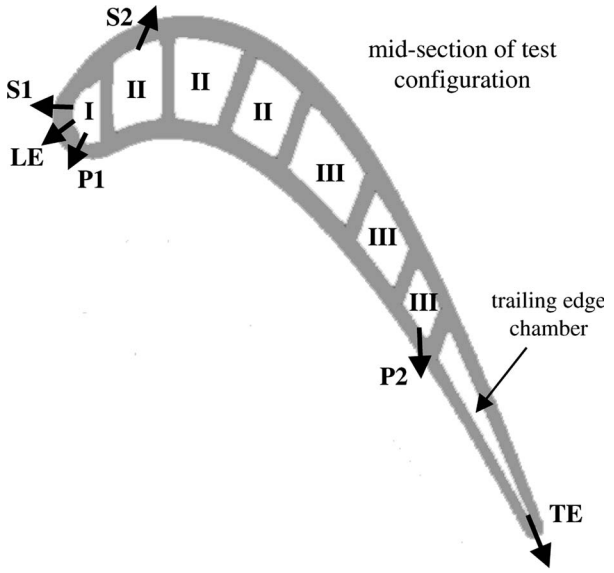

Fig. 1 Film-cooled test blade (CONF A)

the configuration consists of three rows of radially inclined cooling holes (indicated as "P1," "LE," and "S1" in Fig. 1), which are supplied with cooling air by a single cooling channel. Furthermore, the experimental test configuration also includes two rows of shaped holes, one on the suction side (indicated as "S2") and one on the pressure side (indicated as "P2") respectively, supplied by further internal cooling passages as shown in Fig. 1. The leading edge is supplied directly by a separate cooling channel (no. I), whereas the two other channels are typically serpentine shaped (Fig. 2).

The trailing edge chamber is supplied by channel no. III through several crossover holes before the cooling air is ejected through a row of small slots at the trailing edge. To increase the convective heat transfer, the internal walls of the passages are equipped with small squared ribs. Furthermore, a large number of pin-fins are to be found in the trailing edge chamber. The configuration has been analyzed experimentally under hot gas conditions by KHI at Akashi R&D Center. Thermal load has been evaluated by means of thermal index paint measurements.

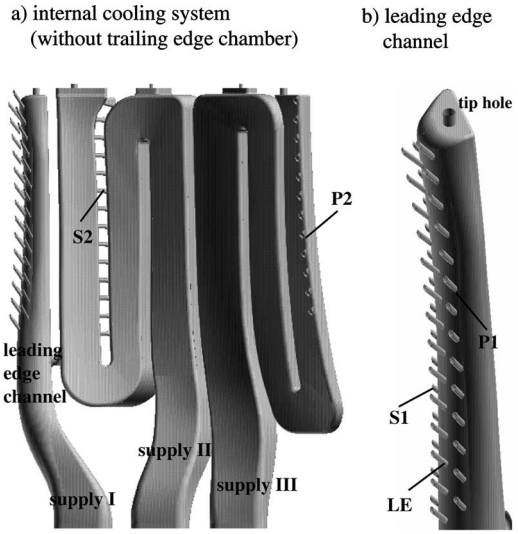

Fig. 2 Internal system of test configuration (CONF A)

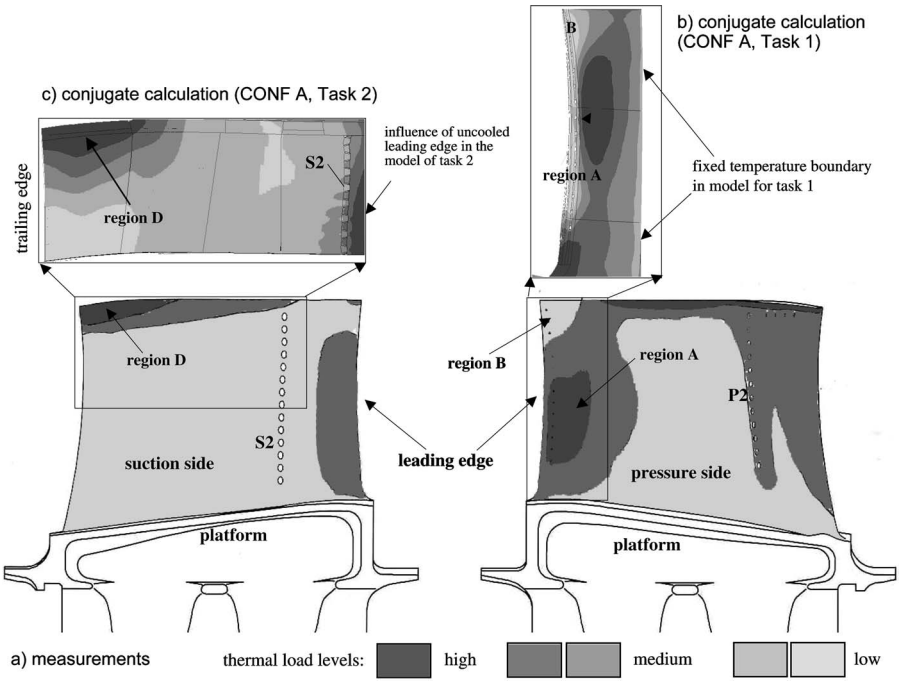

Fig. 3 Thermal index paint measurements and comparison to conjugate calculation results of CONF A

Configuration B (CONF B). Configuration B (CONF B) is the improved test configuration derived from the recommendations based on measurement and conjugate calculation results. Nevertheless, basic features of CONF B are taken from CONF A. The leading edge channel supplies three rows of radially inclined holes. The positions of rows have been shifted slightly and also the exact location of holes has been changed in a way that an improved coverage of the leading edge region is established.

The serpentine-shaped channels have been modified slightly with respect to internal geometry, but basically the internal configuration is similar to CONF A. For CONF B, the position of the S2 row with shaped holes is only changed minimal, but radial inclination angles of the holes have been introduced, whereas CONF A has a streamwise ejection of cooling air. The position of P2 row is changed significantly. The P2 row is now fed directly by the trailing edge chamber with cooling air. Cooling holes have been added to the tip region in order to improve cooling for a high thermal load region as found in the results for CONF A [19].

Knowledge from the improved test blade configuration (CONF B) has been used to solve a thermal load problem of a prototype blade for the L20A engine as reported by KHI [22]. Additional improvements of the prototype blade were achieved by an appropriate incidence angle by coordination of the first-stage reaction and having improved the internal convection cooling as well.

Results

Thermal Load of CONF A. Results for CONF A have been published in [19] and were presented at the ASME Technical Congress 2004 in Vienna. Thus, here only the main results with respect to regions of high thermal load are given in order to show necessity with respect to improvement of CONF A. Additionally, full views of thermal index paint measurement results of the pressure side and the suction side can be provided. Detailed description of the numerical models and simplifications can also be derived from [19].

Figure 3(*a*) shows different thermal load regions for the suction side and the pressure side of CONF A blade based on results from thermal index paint measurements under real operating conditions. As it can be seen for the leading edge part of the pressure side, thermal load is high in a large region marked as region "A." The tip part of the leading edge has lower thermal load (region "B"). The reason for high thermal load is that cooling fluid from row P1 is not distributed along the pressure side, as expected for the investigated operating condition. Only the tip part is covered sufficiently by cooling air and, thus, surface temperatures are lower.

Figure 3(*b*) compares the result of the conjugate calculation for the leading edge part of CONF A (task 1 as described in detail in [19]) with the measurement data. The conjugate model of the fluid part contains the internal leading edge channel flow, ejection through all cooling holes of the three rows of the blade leading edge, and complete 3-D passage flow. With respect to the solid body, coupled heat transfer, and heat conduction calculation, the model is limited to the leading edge region and a fixed temperature condition has been set as an artificial thermal load boundary as marked in Fig. 3(*b*). The result shows that cooling air fails to protect a large part of the pressure side leading edge and, thus, also a region A can be found. Similar to the measurement data, a region B with lower thermal load can also be found. The position of region A is slightly different from measurement data. The influence of different numerical boundary conditions on the calculated thermal load might be the major reason for the differences [19] as precise inlet boundary conditions, in particular radial distribution of total temperature and incidence angle, are not known for the investigated operating point.

A second task for investigation of the thermal load in the blade tip region includes the conjugate calculation of the serpentine-shaped channels II and III, trailing edge chamber, trailing edge ejection, ejection from rows S2 and P2, and full 3-D passage with a detailed model of the blade tip clearance. The solid part is limited to the upper half of the test blade. Figure 3(*c*) shows that high thermal load region "D" is found in the calculation similar to measurement results. The high thermal load in front of row S2 is only because of the uncooled leading edge region in the model and, thus, does not exist in the measurement data.

Recommendations for Improvement. Based on the thermal load results presented for CONF A, the necessity for improvement of internal and external cooling is obvious. Recommendations for

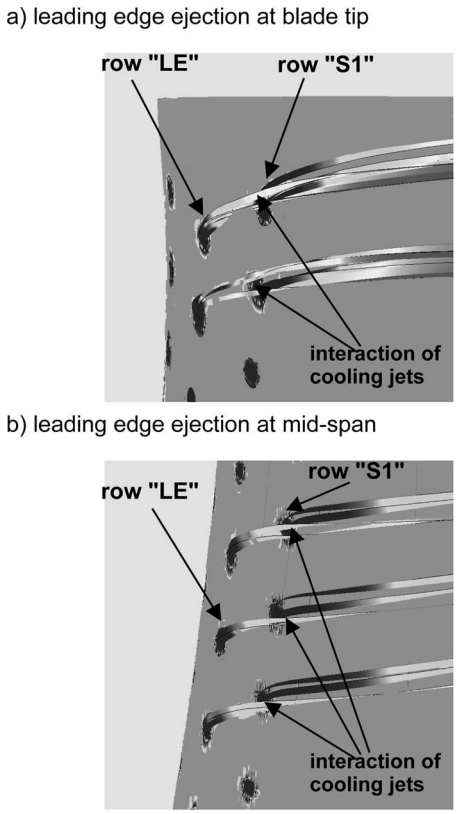

Fig. 4 Interaction of cooling jets

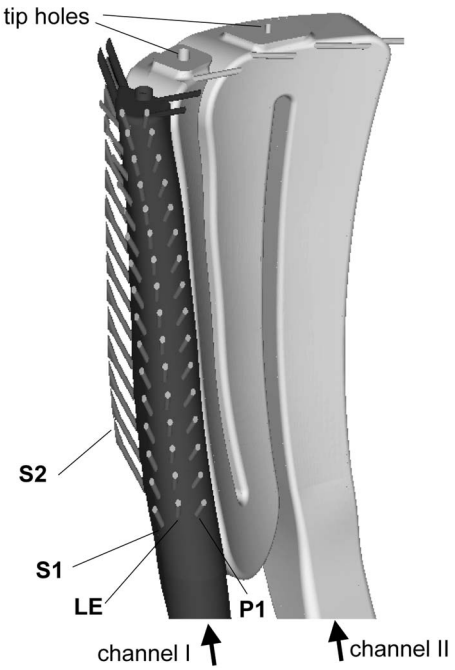

Fig. 5 Part of internal geometry for CONF B

the improvement of the leading edge film cooling are mainly based on shifting the positions of the cooling hole rows. In particular, cooling hole row P2 is moved towards the pressure side in order to realize full protection of the surface by the ejected cooling air. Furthermore, the amount of cooling air ejected from P2 is increased, if the distance to the stagnation line is increased only slightly [23]. Thus, there is also an improvement of the convective cooling by the cooling holes. Furthermore, it has to be taken into account that the stagnation point varies with radial height of the blade. The new position of every single hole of row P1 is found by the equalization of the pressure differences between the hole outlets and the stagnation line at the analyzed radial position. Thus, a homogeneous distribution of the ejected cooling air on the cooling holes of the P1 row can be reached.

The external flow field and flow velocities in the leading edge region are different from expected flow conditions of CONF A. As a result, the visualization of the 3-D cooling jet paths from the conjugate calculation shows a strong interaction of the cooling jets from row LE and row S1. Figure 4(*a*) shows for blade tip region that the cooling jet from LE is guided directly to the position of a neighboring hole from row S1 and suffers from a liftoff effect due to the interaction with the cooling jet from the S1 row. Cooling air and hot gas mix out quickly and direct wall contact is lost. Therefore, the suction side cooling is also less efficient than expected (see region of medium thermal load on suction side view for the leading edge in Fig. 3(*a*)). Figure 4(*b*) shows a similar effect also for cooling jets in the midspan region. In order to improve the film cooling on the suction side, the cooling holes of rows LE and S1 are shifted with respect to the precise radial location in a way that interaction of the cooling jets is most possible avoided.

Further improvements are recommended in order to reach lower thermal load in the blade tip region, in particular for the region D as marked in Fig. 3(*a*). Here, additional cooling holes located directly at the blade tip region should provide cooling air that is joining the tip clearance flow and flowing through the radial gap between blade tip and casing. Thus, hot gas attack in this region is reduced. Further improvements in the internal cooling geometry lead to enhanced convective cooling.

Based on the abovementioned recommendations, a new test configuration has been designed, which is labeled as CONF B.

Thermal Load of CONF B. Figure 5 gives an overview of the internal geometry of the leading edge channel (channel I) and the first serpentine-shaped channel (channel II) of CONF B. Thus it becomes clear, how the cooling holes are supplied. In order to investigate the thermal load, the conjugate calculation has been used again for the leading edge part of CONF B. The model contains now not only the leading edge channel with rows P1, LE, and S1, but also the channel with row S2 of shaped holes as shown in Fig. 5. External passage flow and detailed radial gap flow is also part of the 3-D flow simulation. The solid region contains the blade material surrounding both supply channels and the cooling holes. Thereby, direct coupling of the solid body and the fluid flow regions is established in the leading edge region and the internal and external heat transfer are taken into account during the calculation.

Due to the limitations of the modeling, several effects similar to the investigation presented for task 1 of CONF A analysis [19] have to be taken into account while evaluation of the results:

- Convective cooling effects from the third supply channel are not part of the calculation.
- Surface temperatures and solid body temperatures in the leading edge region will be affected by an adiabatic wall condition at end of solid blade part.
- Enhanced heat transfer of the ribs in the supply channel is not part of the model.
- The blade platform is considered to be adiabatic.

The numerical grid for the model includes more than 3.5×10^6 grid points and calculation is done by a multitask parallel calculation on a LINUX-PC-Cluster with eight processors (Pentium® 4, 2.4 GHz). The boundary conditions for the calculation have been derived from KHI design tool calculations and 3-D CFD stage calculations. For the steady blade calculations, the inlet

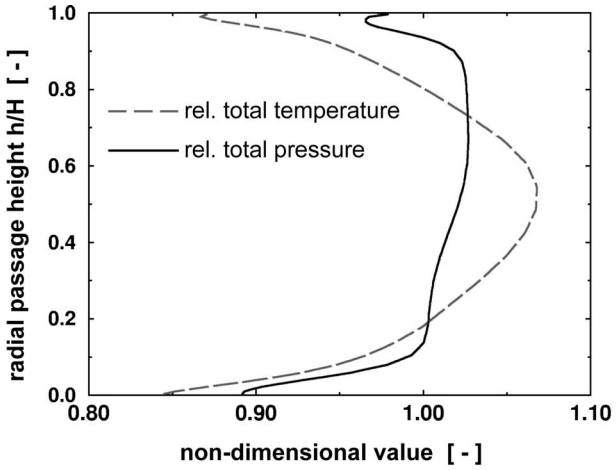

Fig. 6 Radial distribution of nondimensional boundary conditions for blade inlet (CONF B)

boundary conditions are radial distributions of the relative total pressure, relative total temperature, radial flow angle, and relative circumferential flow angle. At the blade outlet, a radial static pressure distribution has been prescribed. Nondimensional radial distributions based on averaged values of the inlet conditions for relative total temperature and relative total pressure are presented in Fig. 6. Thus, it is shown that temperatures in midspan region are approximately 7% higher than averaged value. The boundary conditions for relative total temperature and relative total pressure of the coolant flow were taken from the design data. Regarding the amount of cooling flow, it can be stated that the overall amount is almost the same for CONF B as for CONF A. Nevertheless, due to different positions of rows and single holes, there is a small increase in the cooling flow amount for channel I of CONF B compared to the amount for channel I of CONF A.

An aerothermal calculation with adiabatic blade surfaces has been performed before the conjugate calculation in order to evaluate adiabatic film-cooling effectiveness and adiabatic surface temperatures. Thus, it has been possible to check the performance of the new film-cooling arrangement with respect to redesigned hole positions. Figures 7(*a*)–7(*f*) show the temperature field of the aerothermal calculation in radial cutting planes in the leading edge region for different radial height. Thus, it can be shown that cooling air is distributed from rows LE and S1 (#: hole number) along the suction side as expected and a continuous and homogeneous cooling film is established along the suction side. Cooling air from row P1 is distributed along the pressure side for all radial heights, and thus reduced temperatures in former high thermal load region A can be expected.

Figure 8 proves by stream tube visualization that flow paths of the cooling jets from rows LE and S1 are now established in a way that interaction of the jets from both rows is reduced significantly. This leads to a homogeneous cooling film and is the main reason for the improvement of suction side film-cooling effectiveness.

Thermal load results are provided again by the thermal index paint measurements and the conjugate calculation. The measurement results for CONF B are presented in Fig. 9 for suction side (Fig. 9(*a*)) and pressure side (Fig. 9(*b*)). Thus, it can be seen that for suction side and pressure side in the leading edge region, all areas of high and medium thermal load are vanished. Further improvement for CONF B is also recognizable for the blade tip region. The region of high thermal load has vanished and thermal load is at medium level now. This is found to be acceptable with respect to real operating experience. It can be stated that for both critical regions (leading edge and blade tip), significant reduction of thermal load has been reached. The conjugate calculation,

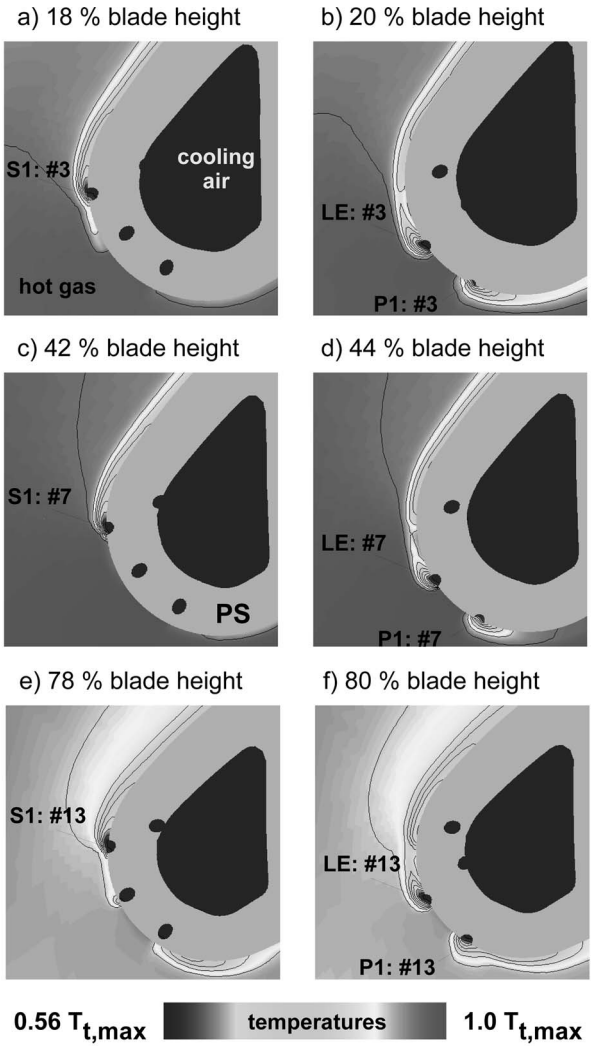

Fig. 7 Fluid temperatures for blade leading edge in radial sections in aerothermal calculation (CONF B)

which has been performed for the blade leading edge part also, shows no hints for further regions of high thermal load (see Figs. 9(*a*) and 9(*b*)). A region of medium level (region P) is found near to the platform of the blade. This is not surprising, as convective

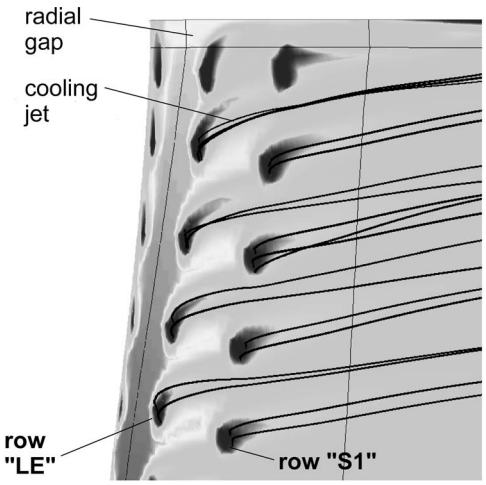

Fig. 8 Stream tube visualization of cooling jets (CONF B)

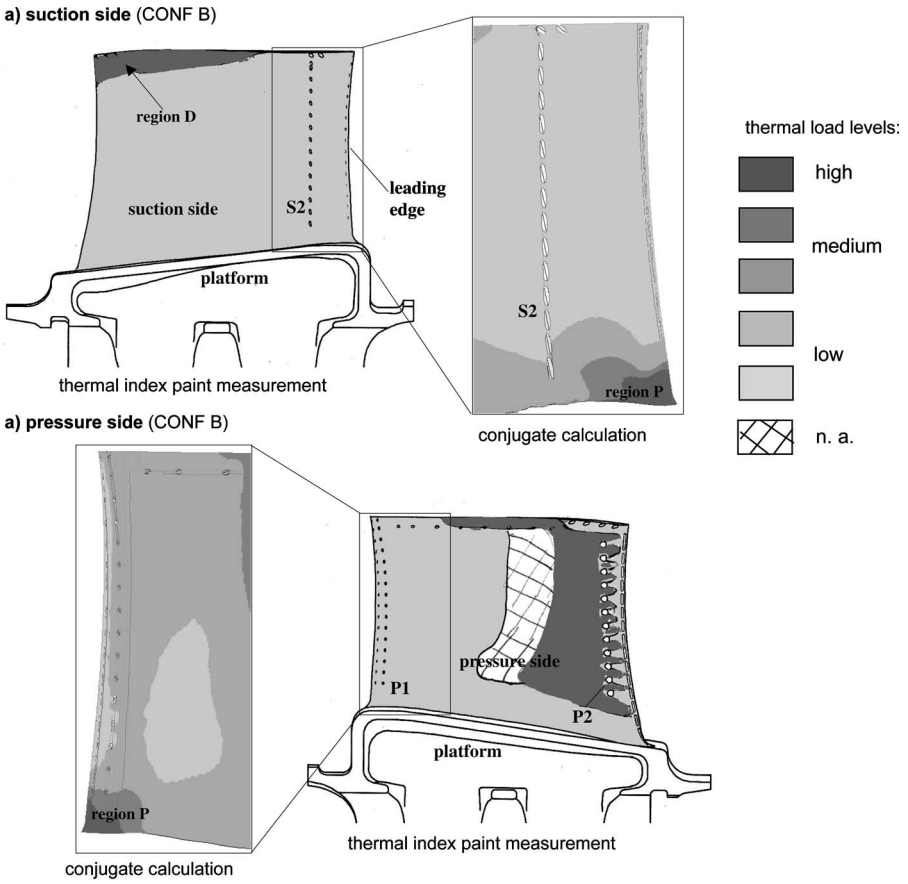

Fig. 9 Thermal index paint measurements and comparison to conjugate calculation results of CONF B

cooling and additional cooling air ejection for the platform is not included in the model. As a result, high temperatures are calculated in this region, which cannot be found under real operating conditions in the measurement data.

Conclusions

A first cooling configuration (CONF A) for a turbine test blade has been investigated by thermal index paint measurement and by application of the conjugate calculation technique with respect to its thermal load. It has been found by measurements and calculations that regions of high thermal load can be detected for the blade leading edge and the blade tip region. Therefore, recommendations, in particular based on the conjugate calculation results, have been given for a redesign of the configuration. Cooling hole rows and positions of the hole outlets at the leading edge have been shifted in a way that a significantly improved protection of the leading edge by the ejected cooling air is reached. Further improvements include additional cooling holes in the tip region and enhanced convective cooling, in particular with respect to the trailing edge chamber. For the redesigned configuration (CONF B) the regions of high and medium level thermal load at the blade leading edge have vanished. This can be proven by further thermal index paint measurements under realistic operating conditions and by the conjugate calculation of CONF B leading edge part. Improvements of the thermal load level can also be realized in the blade tip region.

Despite simplification in modeling the geometry itself, neglecting parts of the internal configuration, and the application of the simple turbulence model, the numerical results are very promising. The conjugate calculation technique in its present state has proven to be a valuable tool for the numerical testing of the cooling configuration. Thus, the number of expensive experimental test runs under real hot gas conditions has been reduced based on the recommendations from analyses with the conjugate calculation tool. The next step will include further improvements in order to reduce the cooling air effort and, thereby increase thermal efficiency for gas turbine application.

Nomenclature

h, H = (m) blade height
T = (K) temperature
y^+ = nondimensional wall coordinate

Subscripts

max = maximum
t = relative total

Abbreviations

CCT = conjugate calculation technique
CFD = computational fluid dynamics
LE = leading edge cooling row
NGV = nozzle guide vane
P1, P2 = pressure side cooling rows
S1, S2 = suction side cooling rows
TE = trailing edge ejection row

References

[1] Heidmann, J. D., Kassab, A. J., Divo, E. A., Rodriguez, F., and Steinthorsson, E., 2003, "Conjugate Heat Transfer Effects on a Realistic Film-Cooled Turbine Vane," ASME Paper No. GT2003-38553.
[2] Li, H., and Kassab, A. J., 1994, "Numerical Prediction of Fluid Flow and Heat Transfer in Turbine Blades with Internal Cooling," AIAA Paper No. 94-2933.
[3] Li, H., and Kassab, A. J., 1994, "A Coupled FVM/BEM Approach to Conju-

gate Heat Transfer in Turbine Blades," AIAA Paper No. 94-1981.
[4] Rigby, D. L., and Lepicovsky, J., 2001, "Conjugate Heat Transfer Analysis of Internally Cooled Configurations," ASME Paper No. 2001-GT-405.
[5] Adami, P., Martelli, F., and Montomoli, F., 2003, "A Finite Volume Method for the Conjugate Heat Transfer in Film Cooling Devices," *Proceedings of the XVI Int. Symposium on Air Breathing Engines*, Paper No. ISABE-2003-1066.
[6] Kao, K.-H., and Liou, M.-S., 1996, "On the Application of Chimera/Unstructured Hybrid Grids for the Conjugate Heat Transfer," ASME Paper No. 96-GT-156.
[7] Han, Z.-X., Dennis, B. H., and Dulikravich, G. S., 2000, "Simultaneous Prediction of External Flow-Field and Temperature in Internally Cooled 3-D Turbine Blade Material," ASME Paper No. 2000-GT-253.
[8] Takahashi, T., Watanabe, K., and Takahashi, T., 2000, "Thermal Conjugate Analysis of a First Stage Blade in a Gas Turbine," ASME Paper No. 2000-GT-251.
[9] York, W. D., and Leylek, J. H., 2003, "Three-Dimensional Conjugate Heat Transfer Simulation of an Internally-Cooled Gas Turbine Vane," ASME Paper No. GT2003-38551.
[10] Imlay, S. T., Soetrisno, M., and Roberts, D. W., 1996, "Coupled Flow and Heat Transfer Analysis Using Hybrid Structured-Unstructured Grids," AIAA Paper No. 96-0622.
[11] Okita, Y., and Yamawaki, S., 2002, "Conjugate Heat Transfer Analysis of Turbine Rotor-Stator System," ASME Paper No. GT-2002-30615.
[12] Facchini, B., Magi, A., and Del Greco, A. S., 2004 "Conjugate Heat Transfer Simulation of a Radially Cooled Gas Turbine Vane," ASME Paper No. GT2004-54213.
[13] Bohn, D., and Bonhoff, B., 1994, "Berechnung der Kühl- und Störwirkung eines filmgekühlten transonisch durchströmten Turbinengitters mit diabaten Wänden," VDI-Bericht **1109**, Germany, pp. 261–275 (in German).
[14] Bohn, D., Bonhoff, B., Schönenborn, H., and Wilhelmi, H., 1995, "Validation of a Numerical Model for the Coupled Simulation of Fluid Flow and Diabatic Walls With Application to Film-Cooled Turbine Blades," VDI-Bericht, Germany, **1186**, pp. 259–272.
[15] Bohn, D., Krüger, U., and Kusterer, K., 2001, "Conjugate Heat Transfer: An Advanced Computational Method for the Cooling Design of Modern Gas Turbine Blades and Vanes," *Heat Transfer in Gas Turbines*, B. Sundén and M. Faghri, eds. WIT Press, Southampton, UK, pp. 58–108.
[16] Bohn, D., and Kusterer, K., 2003, CHTflow, Conjugate Heat Transfer and Flow Simulation Code, Version 3.3, Reference Manual, Institute of Steam and Gas Turbines, B&B-AGEMA, Aachen.
[17] Bohn, D., Kusterer, K., Sugimoto, T., and Tanaka, R., 2003, "Conjugate Analysis of a Test Configuration for a Film-Cooled Blade Under Off-Design Conditions," *Proceedings of the XVI Int. Symposium on Air Breathing Engines*, Paper No. ISABE-2003-1176.
[18] Kusterer, K., Bohn, D., Sugimoto, T., and Tanaka, R., 2003, "Conjugate Heat Transfer Analysis of a Test Configuration for a Film-Cooled Blade," *Proceedings of the 8th International Gas Turbine Conference*, IGTC2003Tokyo TS-083, Tokyo, Japan.
[19] Kusterer, K., Bohn, D., Sugimoto, T., and Tanaka, R., 2004, "Conjugate Calculations for a Film-Cooled Blade Under Different Operating Conditions," ASME Paper No. GT2004-53719.
[20] Baldwin, B. S., and Lomax, H., 1978, "Thin Layer Approximation and Algebraic Model for Separated Turbulent Flows," AIAA Paper No. 78-257.
[21] Sugimoto, T., Nagai, K., Ryu, M., Tanaka, R., Kimura, T., and Nagatomo, T., 2002, "Development of a 20MW-Class High-Efficiency Gas Turbine L20A," ASME Paper No. GT-2002-30255.
[22] Sugimoto, T., Nagai, K., Ryu, M., Tanaka, R., and Kimura, T., 2004, "A Review of L20A Engine Design and Field Operating Experience," ASME Paper No. GT2004-53411.
[23] Bohn, D., Becker, V., and Kusterer, K., 1997, "3-D Conjugate Flow and Heat Transfer Calculations of a Film-Cooled Turbine Guide Vane at Different Operating Conditions," ASME Paper No. 97-GT-23.

Effect of Unheated Starting Lengths on Film Cooling Experiments

Sarah M. Coulthard

Ralph J. Volino
e-mail: volino@usna.edu

Karen A. Flack

Department of Mechanical Engineering,
United States Naval Academy,
Annapolis, Maryland 21402

The effect of an unheated starting length upstream of a row of film cooling holes was studied experimentally to determine its effect on heat transfer coefficients downstream of the holes. Cases with a single row of cylindrical film cooling holes inclined at 35 deg *to the surface of a flat plate were considered at blowing ratios of 0.25, 0.5, 1.0, and 1.5. For each case, experiments were conducted to determine the film-cooling effectiveness and the Stanton number distributions in cases with the surface upstream of the holes heated and unheated. Measurements were made using an infrared camera, thermocouples, and hot and cold-wire anemometry. Ratios were computed of the Stanton number with film cooling* (St_f) *to corresponding Stanton numbers in cases without film cooling* (St_o)*, but the same surface heating conditions. Contours of these ratios were qualitatively the same regardless of the upstream heating conditions, but the ratios were larger for the cases with a heating starting length. Differences were most pronounced just downstream of the holes and for the lower blowing rate cases. Even 12 diameters downstream of the holes, the Stanton number ratios were 10–15% higher with a heated starting length. At higher blowing rates the differences between the heated and unheated starting length cases were not significant. The differences in Stanton number distributions are related to jet flow structures, which vary with blowing rate.* [DOI: 10.1115/1.2184355]

Introduction

Film cooling has been studied extensively in order to provide improved cooling of the airfoils in gas turbine engines and thus increase the life of the airfoils and allow for higher turbine inlet temperatures. Both the film cooling effectiveness and the enhancement of the heat transfer coefficient caused by the film cooling jets are of interest. Many studies have been done using simple flat plate geometries to gain more insight into the physics of the problem. To determine the heat transfer coefficient, surface heaters are typically used to provide a known uniform heat flux at the plate surface. Most of the previous flat plate experimental studies of heat transfer coefficients with film cooling have included an unheated starting length, with heaters only located downstream of the film cooling holes. An unheated starting length will result in a thinner thermal boundary layer and higher heat transfer. It is typically assumed that the ratio, h_f/h_o, of the heat transfer coefficient with film cooling to the heat transfer coefficient in a similar flow without film cooling and the same surface heating will not be greatly affected by the presence of an unheated starting length. Examples of studies with unheated starting lengths include Sen et al. [1] and Schmidt and Bogard [2]. Although it is certainly plausible that an unheated starting length will affect a film cooled and uncooled boundary layer similarly, there is surprisingly little verification of the assumption in the literature. Mayhew et al. [3] conducted experiments in a facility with a heated region upstream of the film cooling holes. They compared their results to data from similar studies with unheated starting lengths and attributed differences observed in heat transfer coefficient ratios to unheated starting length effects. The heat transfer ratios were larger in the heated starting length cases. Mayhew et al. [3] noted that since the thermal boundary layer is thicker in these cases, the film cooling flow may have more of an opportunity to disturb the thermal boundary layer and increase heat transfer. The only known study of unheated starting length effects is by Kelly and Bogard [4]. They considered full coverage film cooling on a flat plate with normal injection, presenting heat transfer coefficient ratios at three streamwise locations downstream of the first row of holes for one of their cases. At $x=2D$, directly downstream of the holes, h_f/h_o was 30% higher with a heated starting length than with an unheated starting length. At $x=4D$ downstream of the holes, the effect was reduced, and by $x=10D$ downstream of the holes the heated and unheated starting length cases were indistinguishable. At the midspan between adjacent holes, the unheated starting length had no effect on h_f/h_o. No experimental results appear to be available in the literature for other geometries.

In the present study, heaters were placed on the surface of a plate upstream, downstream, and between the holes in a single row of film cooling holes. Tests were run with only the downstream heaters on, with the upstream and downstream heaters on, and, finally, with all the heaters on to determine the effect of the earlier start of the thermal boundary layer. The film cooling geometry consisted of a single row of five round holes inclined at 35 deg to the surface and parallel to the streamwise direction. The holes were spaced $3D$ apart, center to center, with a length-to-diameter ratio $L/D=4$. The geometry matches that used by Burd and Simon[5], Gritsch et al. [6], Kohli and Bogard [7], Sinha et al. [8], and Pietrzyk et al. [9]. It is similar to that used by Mayhew et al. [3], who used a 30 deg injection angle. Blowing ratios of 0.25, 0.5, 1.0, and 1.5 were investigated.

Experimental Facilities and Techniques

Experiments were conducted with an open loop subsonic wind tunnel with a test plate attached at the exit and a plenum to supply the film cooling jets. The wind tunnel, shown in Fig. 1, was comprised of six sections: a blower, a diffuser with three screens, a heat exchanger to maintain air nominally at 20°C, a honeycomb, a settling chamber with three screens, and a nozzle with an 8.8 area reduction. The nozzle exit area is 0.38 m × 0.10 m. The exiting mainstream air was uniform in temperature and velocity to within 0.1°C and 1%, respectively. The freestream turbulence intensity at the nozzle exit was 1%. This value is lower than typical intensity levels in an engine, which will depend on the location in

Contributed by the Turbomachinery Division of ASME for publication in the JOURNAL OF TURBOMACHINERY. Manuscript received December 19, 2005; final manuscript received January 16, 2006. Review conducted by D. Wisler.

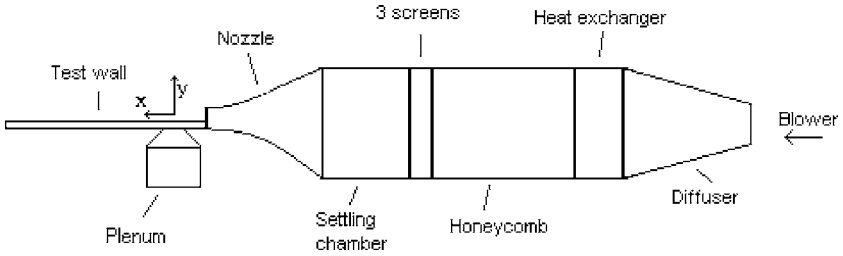

Fig. 1 Wind tunnel configuration

the turbine. Air exiting the nozzle forms a wall jet at $U_\infty=8$ m/s along a flat plate that serves as the test wall. The mainstream velocity remained at 8 m/s 19.5D downstream from the leading edge of the film cooling holes. At this downstream location, the velocity outside the boundary layer was a uniform 8 m/s up to the edge of the free shear layer, which was located 3D above the wall. The freestream unsteadiness level gradually increased in the streamwise direction to 6%. This increase in unsteadiness is due to the growth of the shear layer at the edge of the wall jet. The wall jet configuration is based on the facility of Burd and Simon [5].

The film cooling supply plenum was supplied by a manifold connected to a high-pressure air source. The supply pressure was adjusted to vary the blowing ratio from $B=0.25$ to 1.5. The air passed through small diameter solenoid valves between the manifold and the plenum. The valves were used in a subsequent study of unsteady film cooling. In the present study the valves were fully open. The flow through the valves was choked. For a given supply pressure, the film cooling mass flow remains constant, independent of downstream conditions. The plenum had a finned tube heat exchanger to maintain the temperature of the coolant jets at ~27°C. Warm water at 30°C circulates through multiple tube passes of the heat exchanger. The jet air from the valves passes over the tubes in a cross-flow manner, which causes heat transfer from the hot water in the tubes to the jet flow.

The test wall was constructed of polyurethane foam with a thermal conductivity of 0.03 W/mK. The dimensions are 0.38 m wide, 44 mm thick, and 1.17 m long, with a starting length of 13.3D upstream of the row of film cooling holes. A wall opposite the starting length and side walls along the length of the test wall help limit interaction between the wind tunnel flow and the still air in the room, as shown in Fig. 2. Metal foil heating elements encapsulated in silicon rubber coatings (Minco, Inc.) were placed on the foam surface as shown in Fig. 3. The small heaters between the holes do not completely fill the area between the holes, leaving a small unheated region about 8 mm long in the streamwise direction. The heaters are covered with a 0.79 mm thick black sheet of Formica® laminate to provide a smooth test surface. The heaters provide a heat flux which is uniform to within 1.4%. Any small spatial non-uniformity in the heat flux at the test surface is quantified by examining the local surface temperature in a case with no film cooling and the cooling holes taped over (i.e., simple flow over a flat plate with an unheated starting length). This allows for correction of the local heat flux in all subsequent tests for computation of Stanton numbers. Stanton number ratios are unaffected by the corrections, since the corrections cancel when the ratios are computed. The film cooling geometry consists of a single row of five round holes inclined at 35 deg to the surface and parallel to the streamwise direction. The sharp edged holes have a diameter of $D=19.05$ mm and are spaced 3D apart, center to center, and with a length-to-diameter ratio $L/D=4$. A 1.6 mm thick trip was installed 11D upstream of the leading edge of the film cooling holes to ensure a turbulent boundary layer.The test plate was instrumented with type-E thermocouples of 76.2 μm dia wire. The thermocouples were located between the heaters and Formica, which was attached with an epoxy. Thermocouples were also placed in the film cooling plenum, at the plenum-side end of the outermost film cooling hole, at the wind tunnel exit, on the back of the test plate, in the ambient air, on the wall of the room to measure the surrounding temperature for radiation corrections, and in ice water as a reference. Constant current and constant temperature (hot-wire) anemometry were used to measure flow temperature and velocity, respectively. Boundary layer probes with 1.27 μm dia platinum sensors (TSI model 1261A-P.5) were used for temperature measurements, and boundary layer probes with 3.81 μm dia tungsten sensors (TSI model 1218-T1.5) were used for the velocity. An infrared (IR) camera (FLIR Systems Merlin model) with a Stirling cooled detector was used to measure the surface temperature field of the test wall. The temperature resolution of the camera is 0.05°C. The camera has a 255 $\times$ 318 pixel detector and was positioned such that each pixel corresponded to a 1 mm $\times$ 1 mm area on the test wall. The field of view on the test wall corresponded to 13.4D $\times$ 16.7D. The emissivity of the test wall was determined to be 0.95 through comparison of IR images of the test wall and a surface of known emissivity (black electrical tape) at the same temperature.

The boundary layer 0.8D upstream of film cooling hole leading edge had a momentum thickness Reynolds number of 550 and a shape factor of 1.48. The local skin friction coefficient at this location was $C_f=5.4\times10^{-3}$. With the upstream heaters active, the

Fig. 2 Test wall with side walls

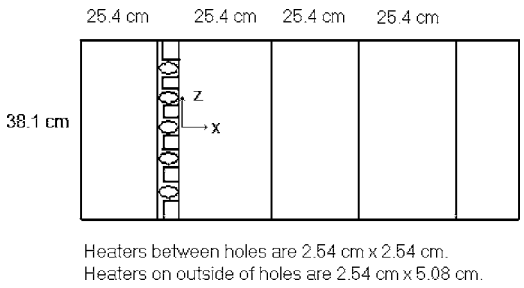

Fig. 3 Heater configuration

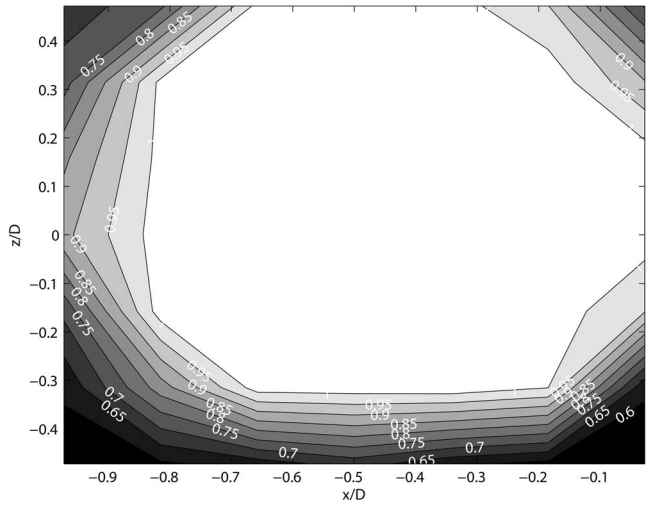

Fig. 4 Dimensionless temperature profile, θ, at exit plane of center hole with $B=0.5$

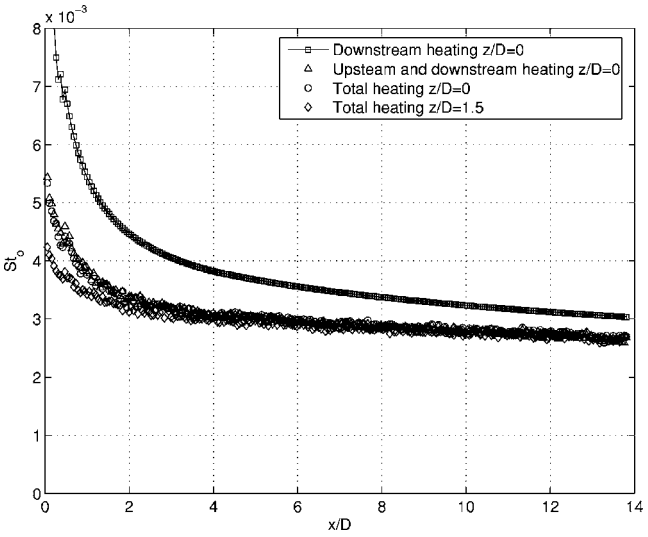

Fig. 6 St_o for various heater configurations

enthalpy thickness Reynolds number $0.8D$ upstream of the holes was 470. The Reynolds number based on hole diameter and mainstream velocity was 10,000.

The film cooling jet flow uniformity was measured by traversing the constant current and hot-wire probes over the hole exit with the main flow in the wind tunnel off. Figure 4 shows the temperature distribution for a jet flow corresponding to blowing ratio $B=0.5$. The jet temperature is clearly very uniform and matches the plenum temperature to within 0.2°C. These results indicate very little cooling of the jet flow as it passes through the hole channel. The temperature distribution was checked for all blowing ratios and found to be uniform in all cases. Figure 5 shows the mean velocity for the jet flow in the $B=0.5$ case. The higher velocity region in the upstream section of the hole was due to the flow of the jet from the plenum through and out of the hole. Burd and Simon [5] discuss jet velocity distribution in similar configurations in more detail. The jet velocities were averaged over the hole exit to determine an average velocity. The jet velocity distribution will no doubt change when the main flow is turned on, but the mean velocity will remain the same since the flow rate is set by the choked mass flow through the upstream solenoid valves. Since the jets are only heated to ~7°C above the mainflow temperature, the density ratio of jets to mainflow is 0.98. Hence the blowing and velocity ratios are essentially equal. The temperature and velocity measurements were compared among the five film cooling holes. The hole to hole variation in temperature was 2% of the jet to mainstream temperature difference and velocity variation was 8% of the mainstream velocity.

The film cooling effectiveness and Stanton number are defined respectively as follows:

$$\eta = \frac{T_{aw} - T_\infty}{T_{\text{jet}} - T_\infty} \tag{1}$$

$$\text{St} = \frac{q''_{\text{conv}}}{\rho c_p U_\infty (T_w - T_{aw})} \tag{2}$$

Tests were conducted at blowing ratios of 0.25, 0.5, 1.0, and 1.5 with the wall heaters off and then again with the three combinations of heaters. The local convective heat flux was computed by subtracting a uniform small (~1% of q''_{conv}) conduction correction for heat flow out the back of the test wall, and a larger local radiation heat flux (~15% of q''_{conv}) from the uniform heat input to the wall heaters. From the data with and without heaters, T_{aw}, η and St were computed for each case.

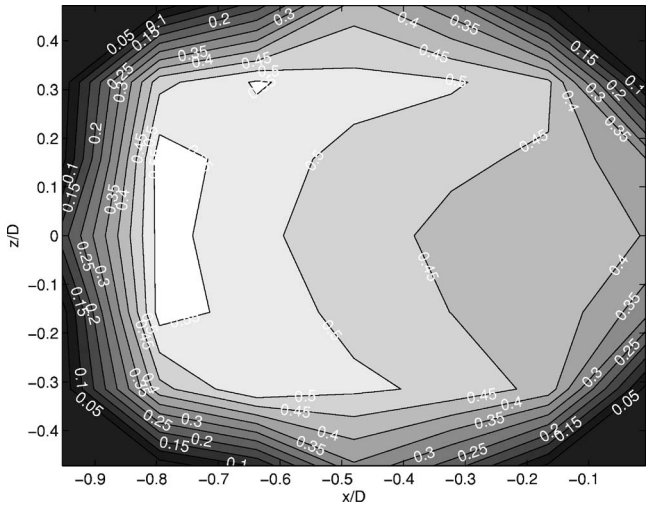

Fig. 5 Dimensionless velocity profile, U_{jet}/U_∞, at exit plane of center hole with $B=0.5$

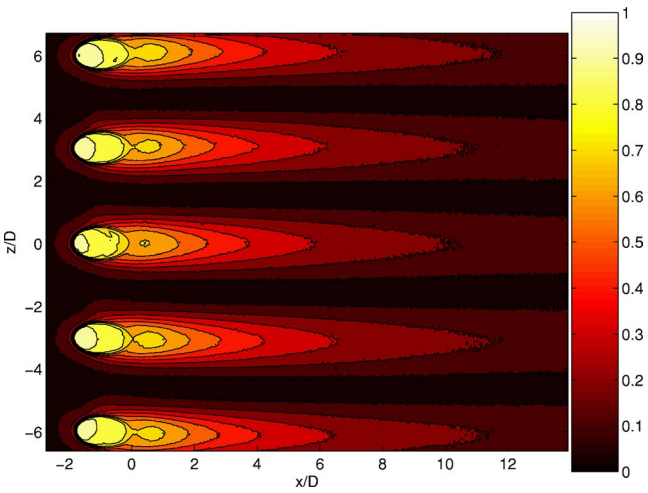

Fig. 7 Film cooling effectiveness contour plot for $B=0.25$

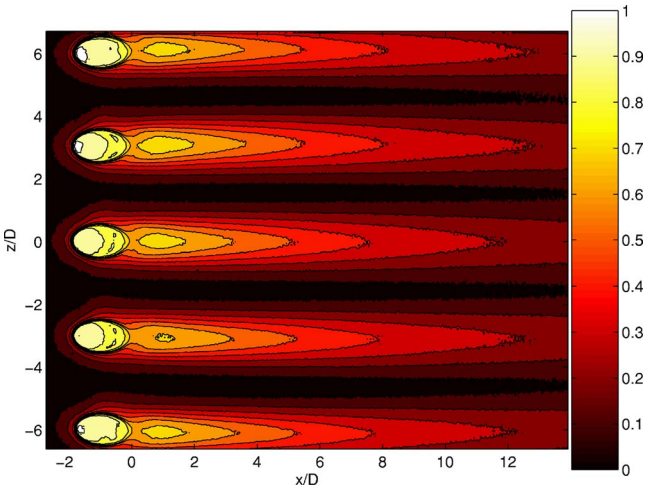

Fig. 8 Film cooling effectiveness contour plot for $B=0.5$

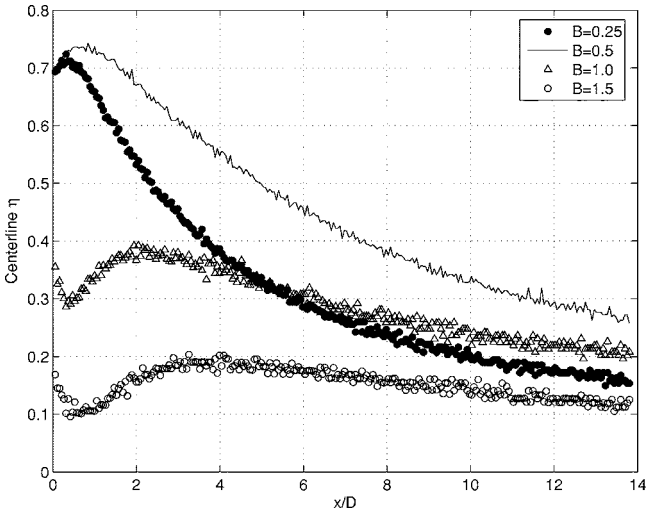

Fig. 10 Centerline, $z/D=0$, film cooling effectiveness

The uncertainty in the measured temperature was 0.2°C, the uncertainty in the measured velocity was 3%, and the uncertainty in the atmospheric pressure was 1%. The uncertainties in the film cooling effectiveness and the Stanton number were determined using standard propagation of error with a 95% confidence interval. The uncertainty in the film cooling effectiveness is 6%, and the uncertainty in the Stanton number is 8%. The uncertainty in the ratio of two Stanton numbers is 11%.

Results

Baseline experiments were performed with no film cooling. For these experiments, the film cooling holes were covered with tape. Stanton number distributions (St_o) were determined for heating downstream of the holes, upstream and downstream of the holes, and at all locations on the test wall. Stanton numbers were also computed using a boundary layer code (TEXSTAN, Crawford and Kays [10]) using a mixing length turbulence model and heat transfer boundary conditions to match the three experimental cases. The calculated and experimental Stanton numbers agreed to within 5%. Figure 6 shows the St_o distributions in the streamwise direction for the case of no film cooling with the three heater combinations. The origin of the coordinate system for the measurements is taken as the trailing edge of the center film cooling hole. At $2D$ downstream of the film cooling holes, the Stanton numbers with an unheated starting length were ~35% higher than with upstream heating. The difference decreased to 14% $13D$ downstream of the holes. The small heaters between the holes had no effect at $z/D=0$, since the tape over the holes is still unheated. St_o is therefore equal for the case with "upstream and downstream heating" (small heaters off) and the case with "total heating" (small heaters on). At $z/D=1.5$, the small heaters have some effect, with St_o about 13% lower for the total heating case at $x/D=1$. The effect of the small heaters was only discernable within $3D$ downstream of the film cooling holes. This was true both with and without film cooling. Hence, the focus of this study is on differences between the cases with only downstream heating and heating upstream and downstream of the holes, regardless of the whether the small heaters are active.

The film cooling effectiveness results agreed with similar studies in the literature. Figures 7–9 are contour plots of the film cooling effectiveness for blowing ratios of $B=0.25$, 0.5, and 1.0. Figure 10 depicts the centerline film cooling effectiveness for blowing ratios of $B=0.25$, 0.5, 1.0, and 1.5. The results for the blowing ratios of $B=0.25$, 0.5, and 1.0 match the results of Sinha et al. [8], the $B=0.5$, 1.0, and 1.5 results match the results of Gritsch et al. [6], and the $B=0.5$ and 1.0 cases match the results of Burd and Simon [5]. The film cooling effectiveness was also averaged in the spanwise direction, as shown in Fig. 11. The two lower blowing ratio cases yield similar results, with high values

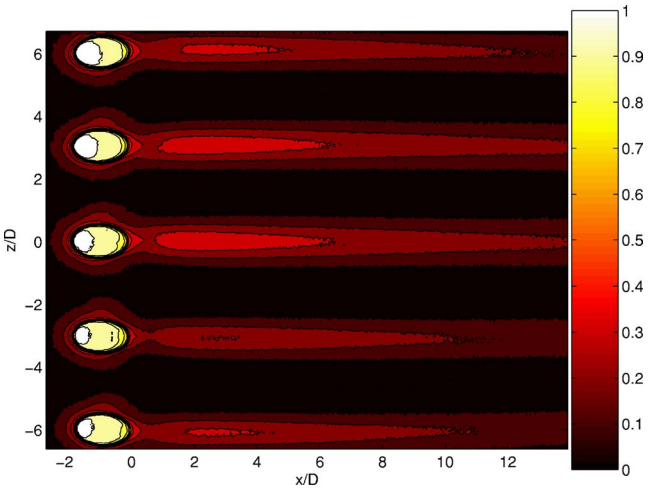

Fig. 9 Film cooling effectiveness contour plot for $B=1.0$

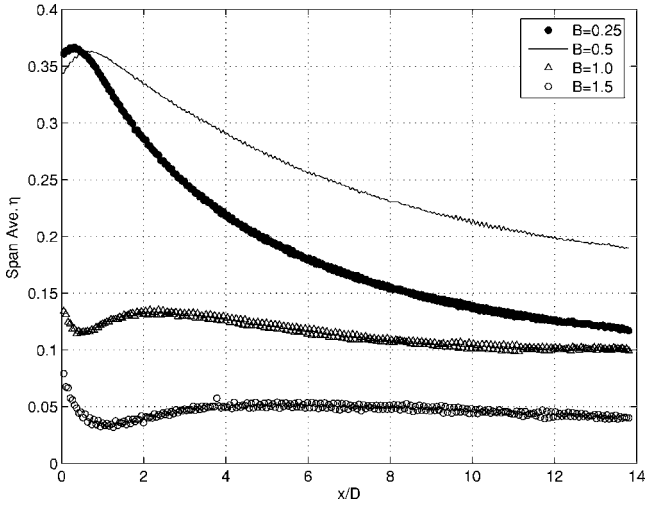

Fig. 11 Spanwise-averaged film cooling effectiveness

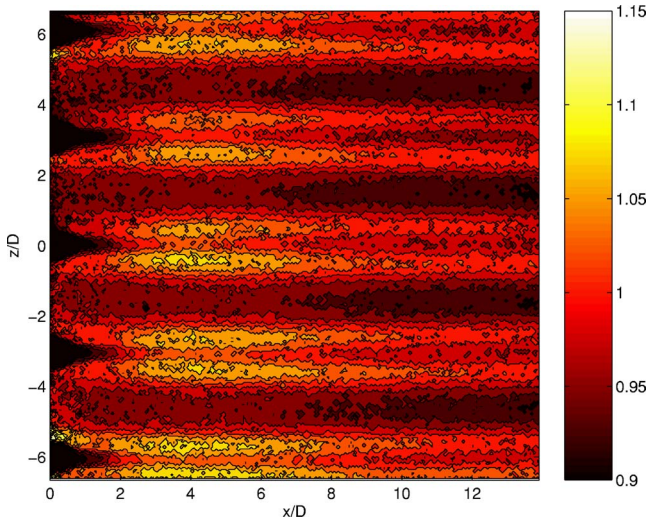

Fig. 12 St_f/St_o for $B=0.25$ with unheated starting length

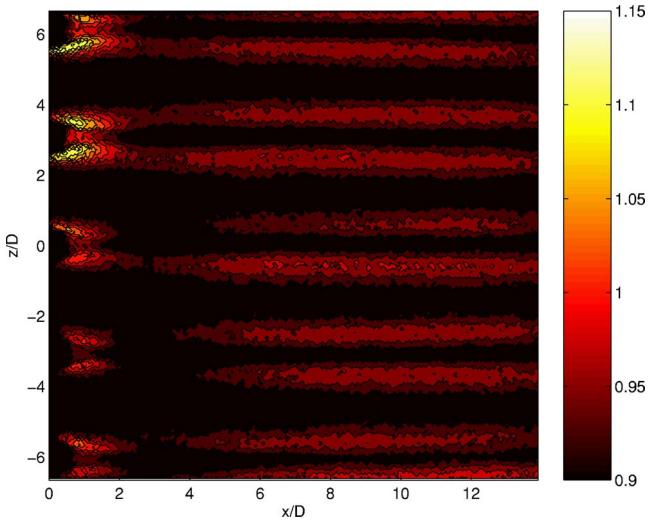

Fig. 14 St_f/St_o for $B=0.5$ with unheated starting length

immediately downstream of the holes. Substantially lower values of the film cooling effectiveness are observed for the two higher blowing ratio cases due to jet liftoff.

Contours of the Stanton number ratio, St_f/St_o, are shown in Figs. 12–19. A few features are clear in these figures and show how the film cooling flow enhances the heat transfer rate. Immediately downstream of the film cooling holes, at x/D between 0 and 1, there are small regions of high St_f/St_o in all cases at $z/D = \pm 0.5$ around each hole. These regions are believed to be caused by the horseshoe vortex, which forms when the main flow boundary layer wraps around the film cooling jet. Another feature is the pair of high St_f/St_o lines, which are symmetric about the centerline of each hole and extend downstream along the surface. As will be explained, these are believed to be caused by the kidney vortices associated with the film cooling jets. Between the high St_f/St_o lines, in the region directly downstream of the center of each hole, St_f/St_o is relatively low. Mayhew et al. [3] also saw these lines of high St_f/St_o and called them "fork tines." Mayhew et al. [3] used a heated wall upstream of their film cooling holes and suggested that since the fork-tine patterns had not been reported in some studies with unheated starting regions, that they might result from differences in the upstream boundary condition. In the present study, however, the tines were apparent in cases with both an unheated and a heated starting length. The hole-to-hole variability apparent in the St_f/St_o distributions is within the experimental uncertainty and can be explained by the hole-to-hole variation in jet velocity noted above.

A heated starting length generally increases the St_f/St_o ratio, as shown in Figs. 12–19. At each blowing ratio, the St_f/St_o patterns are very similar in the unheated (Figs. 12, 14, 16, and 18) and heated (Figs. 13, 15, 17, and 19) cases, but the features are more distinct due to the higher St_f/St_o values with the heated starting length. At the lower blowing ratios, this is particularly apparent downstream of each hole in the region $0 < x/D < 2$. This is illustrated more quantitatively in Figs. 20–31, which show spanwise profiles of St_f/St_o. Figures 20 and 23 show the $B=0.25$ and $B=0.5$ cases at $x/D=1$. Heated starting length cases are shown with the small heaters between the holes both on and off. It is clear that the small heaters have no significant effect. The St_f/St_o ratio is between 20% and 30% greater in the heated starting length cases than in the unheated cases. Kelly and Bogard [4] saw similar results. They noted that the film cooling jet forces the start of a new thermal boundary layer, regardless of the upstream boundary condition. Hence, the St_f values for the heated and unheated starting length cases are about the same. Without film cooling, however, St_o in the present study is ~35% higher with an unheated

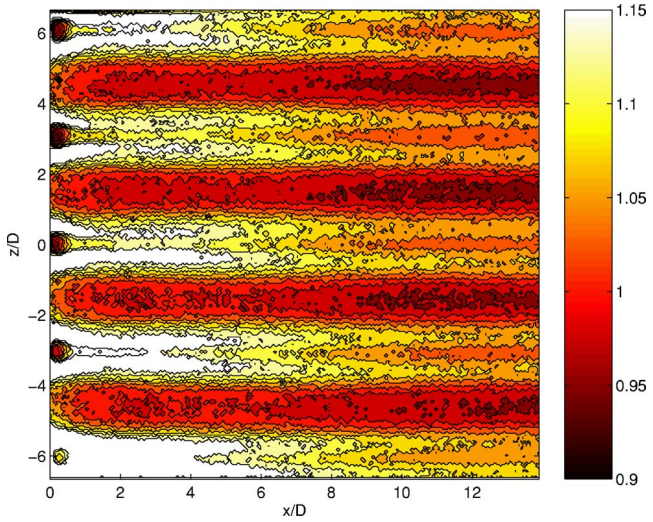

Fig. 13 St_f/St_o for $B=0.25$ with heated starting length

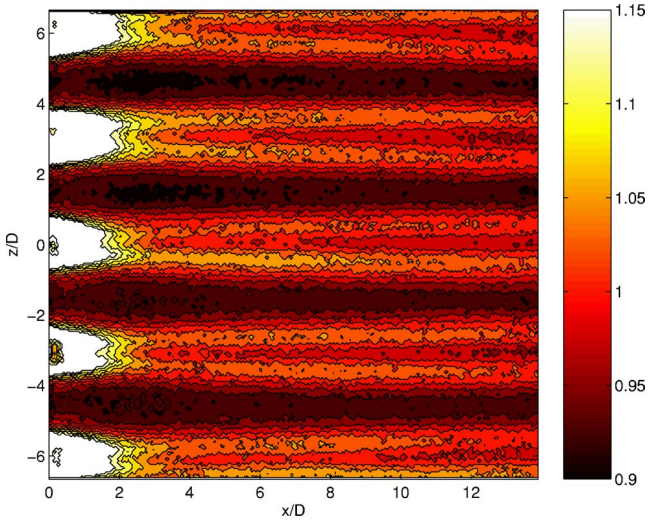

Fig. 15 St_f/St_o for $B=0.5$ with heated starting length

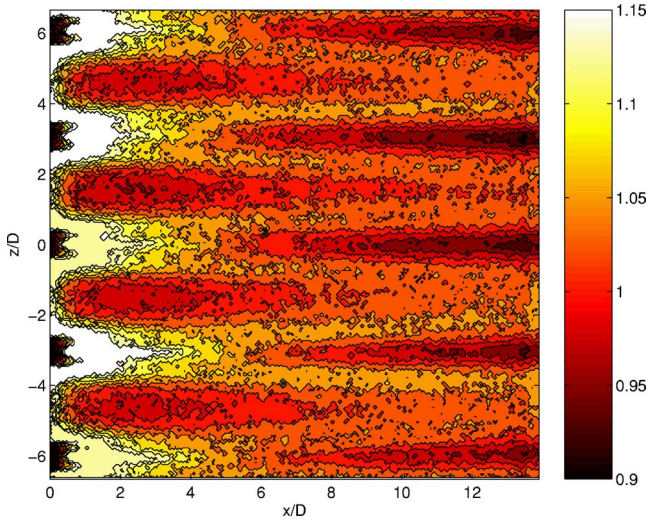

Fig. 16 St_f/St_o for $B=1.0$ with unheated starting length

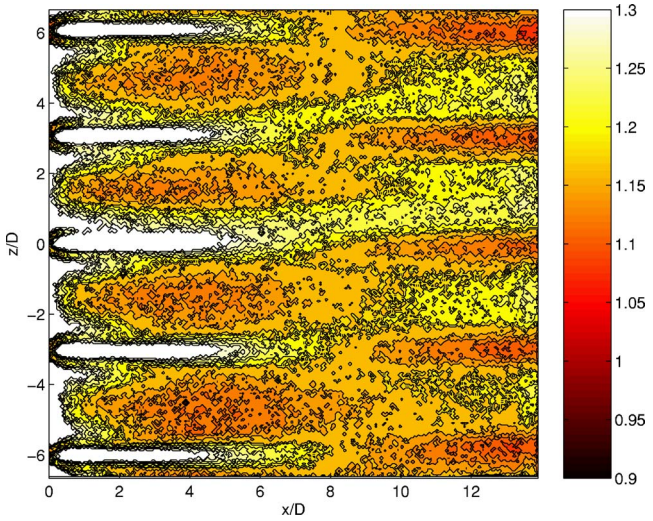

Fig. 18 St_f/St_o for $B=1.5$ with unheated starting length

starting length. This helps explain the high St_f/St_o values. The fork tines are apparent in Figs. 20 and 23 in both the heated and unheated starting length cases as double peaks in the St_f/St_o ratios at $z/D=\pm 0.3$. The tines extend directly downstream in the $B=0.25$ and $B=0.5$ cases. Figures 21 and 23 show spanwise profiles of St_f/St_o at $x/D=6$ and 12, respectively, for the $B=0.25$ case. The difference between the heated and unheated starting length cases is not as strong as was observed upstream, but the St_f/St_o ratio is still $\sim 10\%$ higher for the heated start cases. Note that caution should be exercised before attaching any physical meaning to small 10% differences in St_f/St_o, since they are within the experimental uncertainty. The spacing of the tines increases to $z/D=\pm 0.5$ at $x/D=6$ and remains about the same at $x/D=12$. Figures 24 and 25 show similar results at $x/D=6$ and 12 for the $B=0.5$ case. With $B=0.5$, St_f/St_o is $\sim 10-15\%$ higher in the heated starting length cases at the downstream locations. The tine spacings are about the same for the $B=0.25$ and $B=0.5$ cases. Mayhew et al. [3] showed that the tine spacing remained essentially constant for their $B=0.5$ case. They provide documentation to $x/D=27$.

As the blowing ratio increases, the fork tines spread outward in the spanwise direction, causing the tines of one hole to interfere with and merge with those of the adjacent film cooling holes. This merging occurs at x/D of ~ 13 in the $B=1.0$ case (Figs. 16 and 17) and at x/D of ~ 10 in the $B=1.5$ case (Figs. 18 and 19). Mayhew et al. [3] observed the same merging at these blowing ratios. They noted that the merging results in high heat transfer coefficients at the spanwise positions midway between the film cooling holes and that this could be particularly detrimental since the film cooling effectiveness is lowest at these spanwise positions. Another difference between the high and low blowing ratio cases is a narrow band of high St_f/St_o in the region between the tines, directly downstream of the center of the film cooling holes. This band extends to about $x/D=5$ with $B=1.0$ and to $x/D=7$ with $B=1.5$. The end of the band corresponds to the position where the fork tines begin to spread. The increased blowing ratio lengthens the distance of high heat transfer directly downstream of the holes, and increases the slope of the fork tines during separation. Thus, the tines separate at a further streamwise distance, yet merge at a closer streamwise distance. The behavior described above is true for both the unheated and heated starting length cases.

Figures 26–28 show spanwise profiles of St_f/St_o for a blowing ratio of $B=1.0$. These figures show no significant difference between the unheated and heated starting length cases. The region directly behind the film cooling holes does not exhibit the fork

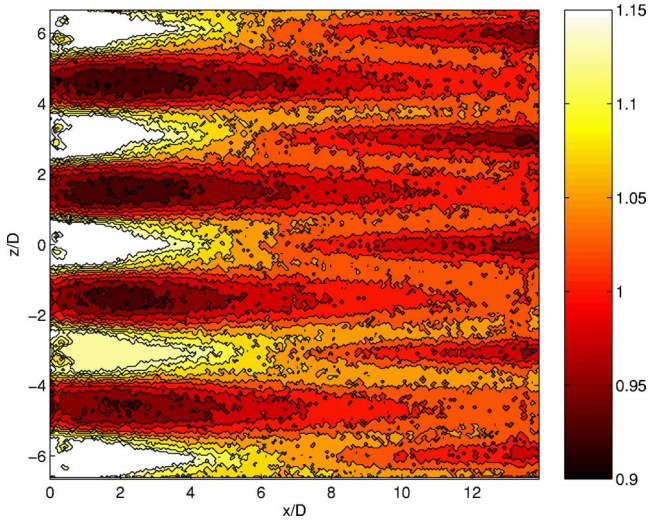

Fig. 17 St_f/St_o for $B=1.0$ with heated starting length

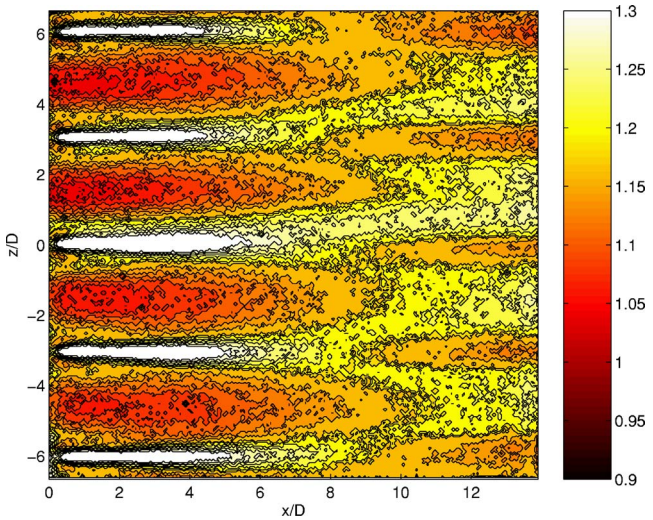

Fig. 19 St_f/St_o for $B=1.5$ with heated starting length

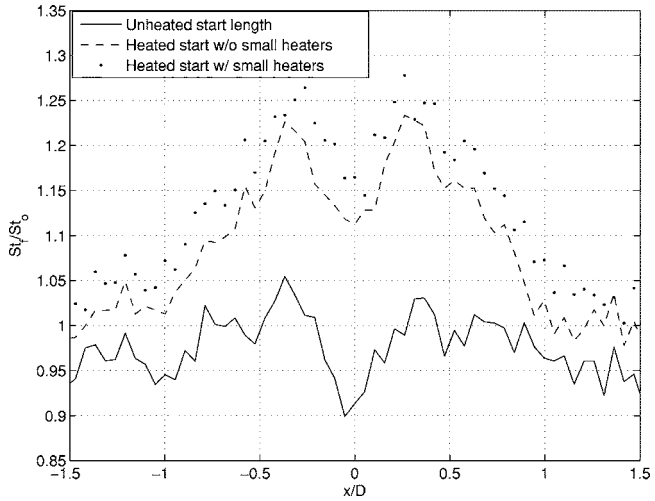

Fig. 20 St_f/St_o for $B=0.25$ at $x/D=1$

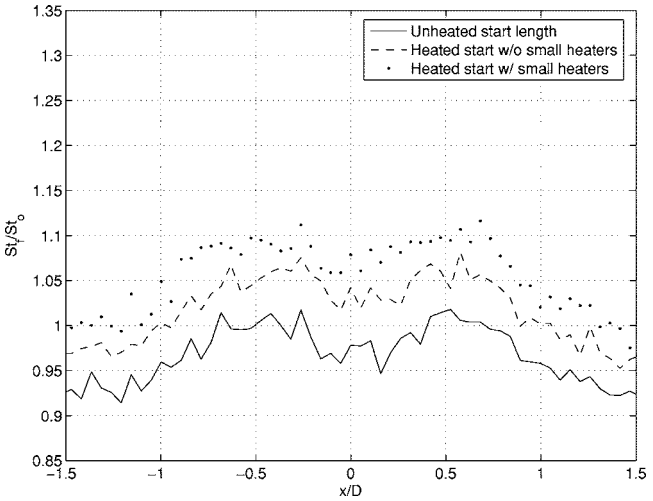

Fig. 22 St_f/St_o for $B=0.25$ at $x/D=12$

tines, as shown in Fig. 26. By $x/D=6$, the fork tines have begun to form, but they are not as clear as at the lower blowing ratios. By $x/D=12$ the tines have joined with the adjacent tines, with peaks at $z/D=\pm 1$. Figures 29–31 show similar behavior at a blowing ratio of $B=1.5$. At $x/D=1$ and $x/D=6$ the fork tines are absent, with a region of high heat transfer downstream of the holes centered at $z/D=0$. By $x/D=12$, heat transfer is lowest at $z/D=0$ and highest at $z/D=\pm 1.5$, where the tines have merged. The St_f/St_o ratio in the unheated starting length case is $\sim 10\%$ higher than in the heated start cases at $B=1.5$ and $x/D=1$. This is inconsistent with the trend observed at lower blowing ratios, but it is a small difference within the uncertainty band and may not have physical significance.

Flow measurements can help explain the heat transfer behavior described above. In the $B=0.25$ and $B=0.5$ cases, the film cooling jets remain near the wall, as evidenced by the high film cooling effectiveness shown in Figs. 7–11 at these blowing ratios. Figures 32–34 show mean temperature contours of the flow in planes at three streamwise positions for the $B=0.5$ case. These contours indicate that the jet fluid is adjacent to the wall, with the core of the jet located at about $y/D=0.25$. At $x/D=3.5$, the width of the core extends from approximately $0.3D$ to $-0.3D$ in the spanwise direction, the same distance between the fork tines shown in Figs. 14, 15, and 23. The core widens slightly in the spanwise direction

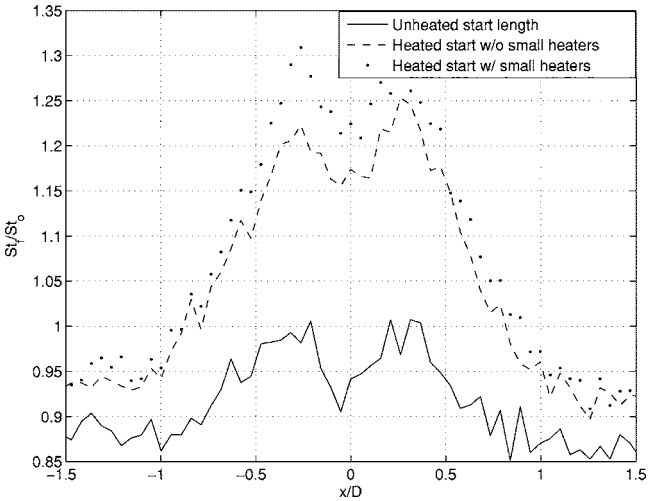

Fig. 23 St_f/St_o for $B=0.5$ at $x/D=1$

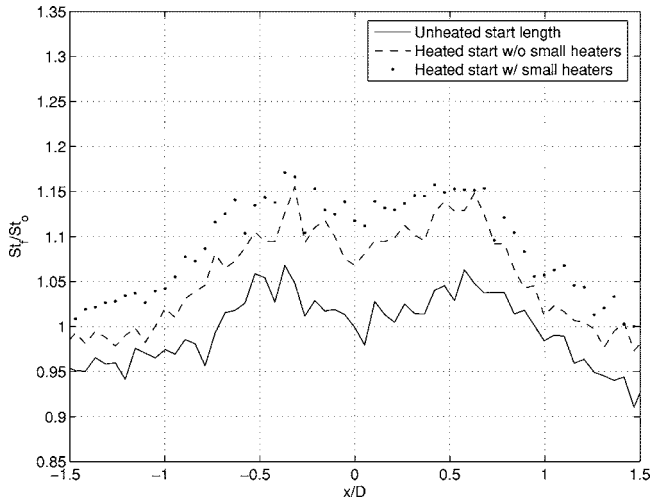

Fig. 21 St_f/St_o for $B=0.25$ at $x/D=6$

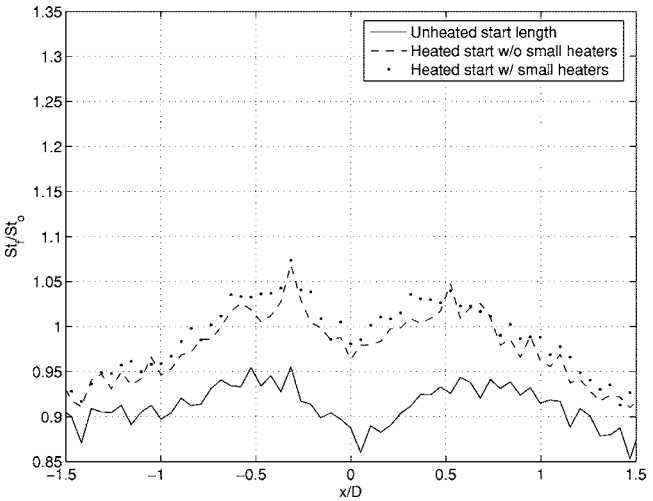

Fig. 24 St_f/St_o for $B=0.5$ at $x/D=6$

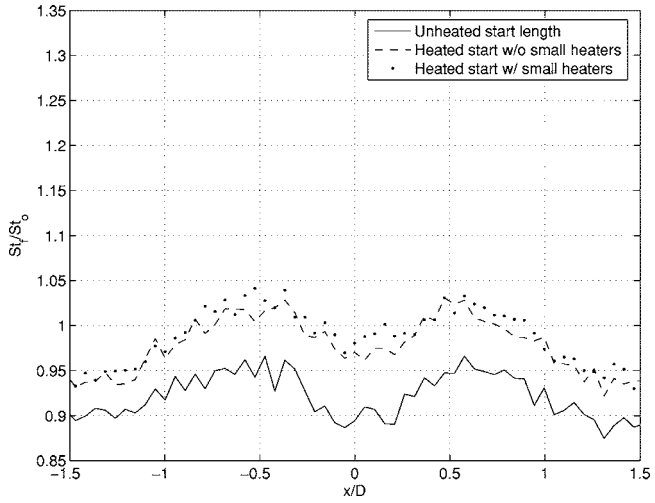

Fig. 25 St$_f$/St$_o$ for B=0.5 at x/D=12

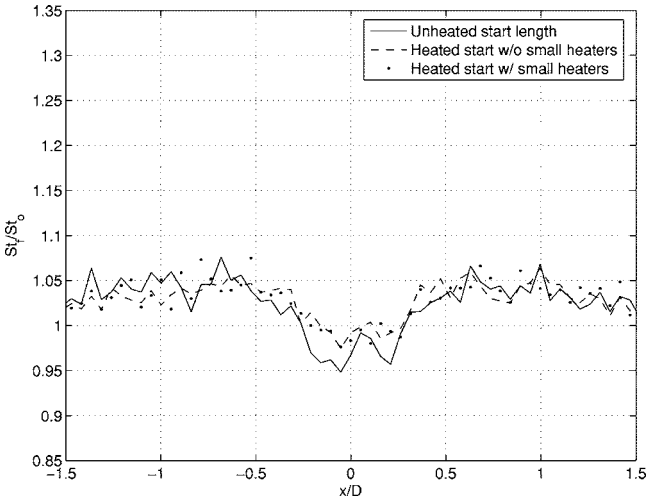

Fig. 28 St$_f$/St$_o$ for B=1.0 at x/D=12

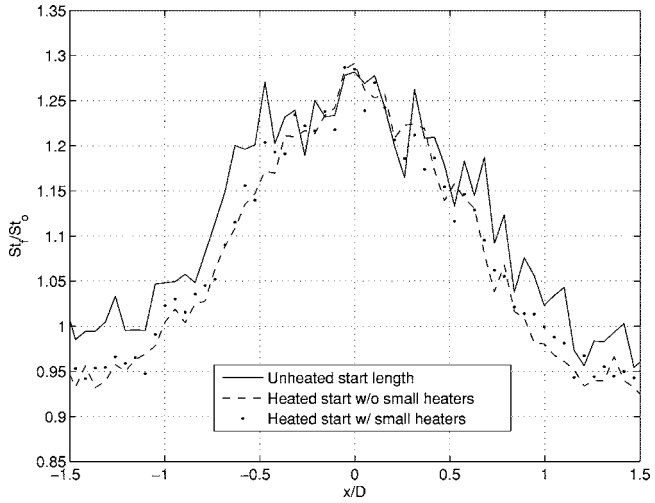

Fig. 26 St$_f$/St$_o$ for B=1.0 at x/D=1

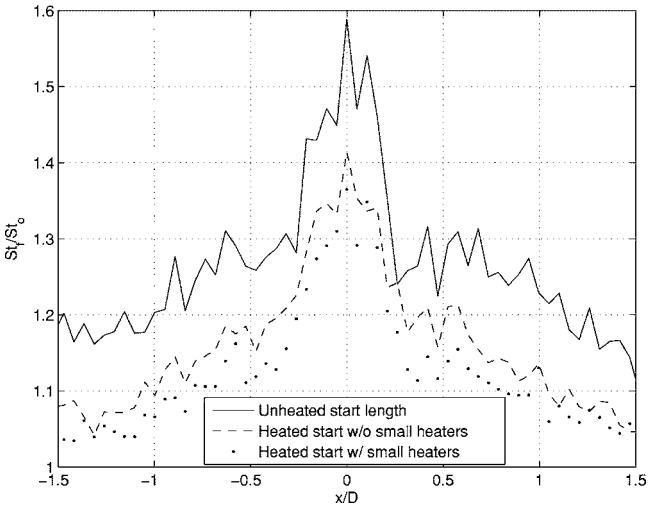

Fig. 29 St$_f$/St$_o$ for B=1.5 at x/D=1 (note scale change for this figure)

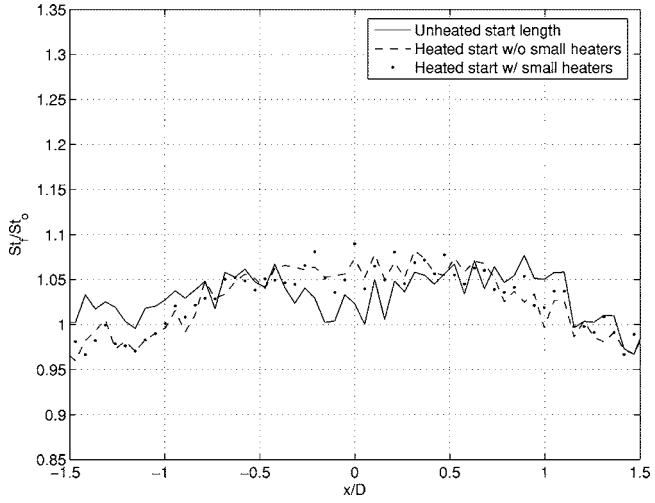

Fig. 27 St$_f$/St$_o$ for B=1.0 at x/D=6

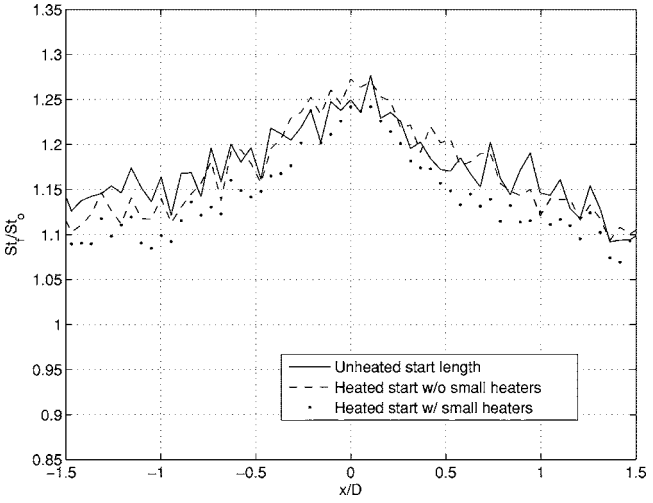

Fig. 30 St$_f$/St$_o$ for B=1.5 at x/D=6

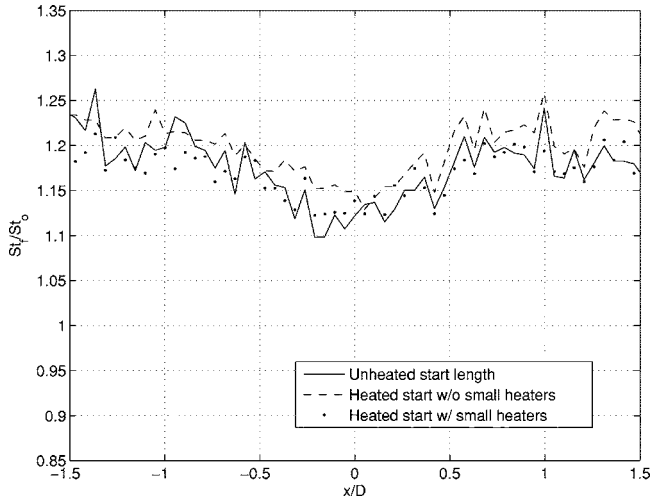

Fig. 31 St_f/St_o for $B=1.5$ at $x/D=12$

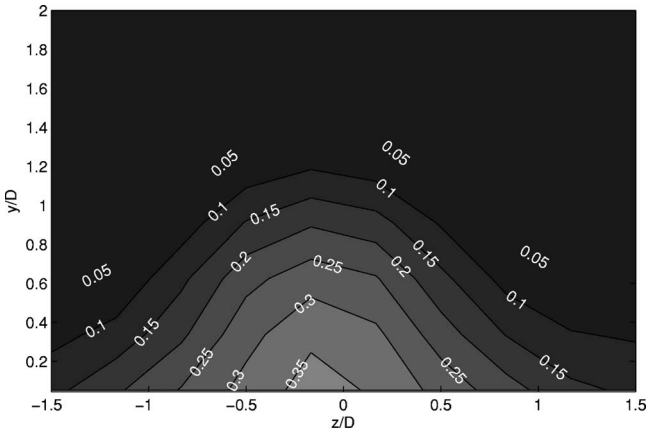

Fig. 34 Temperature, θ, for $B=0.5$ at $x/D=14$

at the downstream locations, in agreement with the separation of the fork tines in Figs. 24 and 25. Film cooling jets are known to contain pairs of kidney-shaped vortices. These vortices include a downwash of fluid around the outer edge of the jet, which would cause fluid to impinge on the wall at about $z/D=\pm 0.3$. This explains the high St_f of the fork tines at these spanwise locations. Fluid would flow upward between the vortices in the center of the jet, and the lack of impinging fluid between the vortices results in the lower heat transfer between the tines along the centerline downstream of the film cooling holes.

For the $B=1.0$ and $B=1.5$ cases, the film cooling jets lift off the wall on exiting the holes. The $B=1.0$ mean temperature contours of Figs. 35–37 indicate that the core of the film cooling jet is considerably farther from the wall than in the $B=0.5$ case. This observation is supported by the lower film cooling effectiveness for the higher blowing rate cases in Figs. 10 and 11. When the jets lift off the wall, the interaction with the main flow likely creates

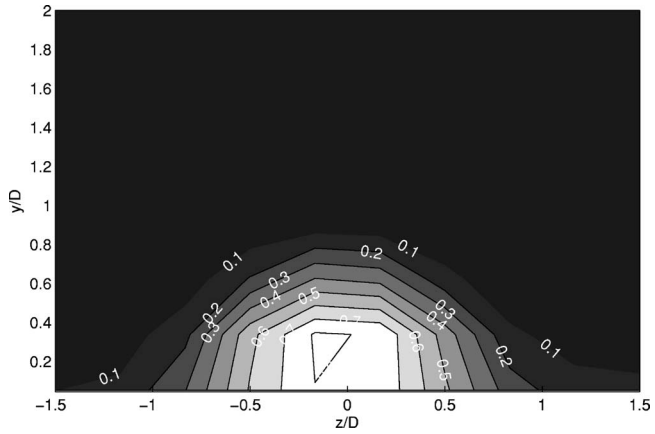

Fig. 32 Temperature, θ, for $B=0.5$ at $x/D=3.5$

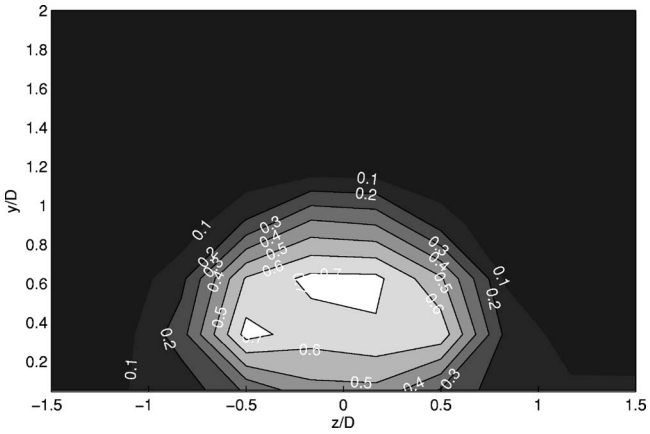

Fig. 35 Temperature, θ, for $B=1.0$ at $x/D=3.5$

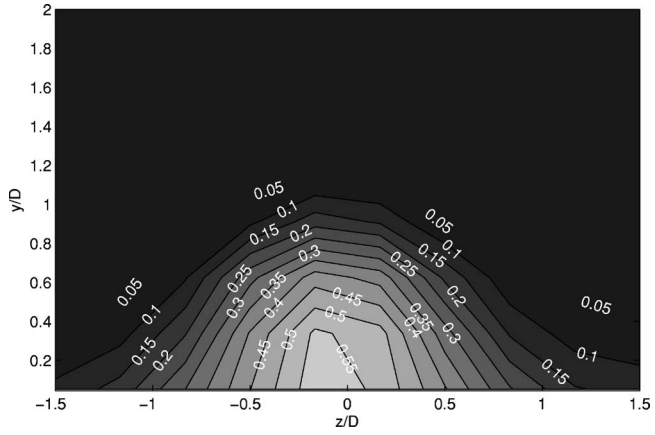

Fig. 33 Temperature, θ, for $B=0.5$ at $x/D=7$

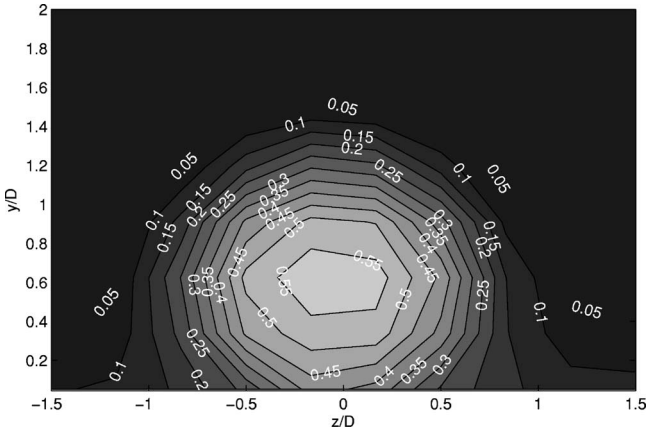

Fig. 36 Temperature, θ, for $B=1.0$ at $x/D=7$

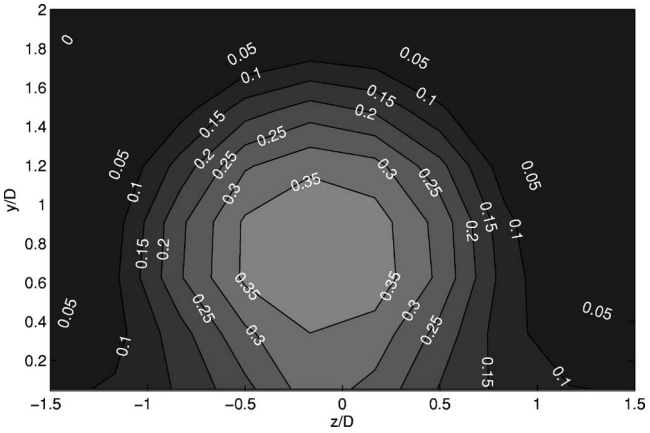

Fig. 37 Temperature, θ, for $B=1.0$ at $x/D=14$

more turbulence than in the lower blowing rate cases. This may explain the region of high heat transfer coefficient directly downstream of the holes in the $B=1.0$ and $B=1.5$ cases. The jet fluid is apparently too far from the wall to produce the fork tine signature immediately downstream of the holes. At these blowing ratios, the jet flow does not reach the test wall until further downstream, at which point the fork tine signature appears.

Conclusions

For the geometry investigated, the effect of an unheated starting length is most pronounced immediately downstream of the cooling holes. Near the holes, Stanton number ratios are as much as 30% higher for the cases with a heated starting length, particularly at the lower blowing ratios. The difference between the heated and unheated starting length cases decreases with downstream distance from the cooling holes, but differences persist even 12 diameters downstream of the holes, where Stanton number ratios can still be 10–15% higher for the heated starting length cases. At higher blowing ratios, no significant differences between the heated and unheated starting length cases were observed. The flow structure is independent of the wall heating and causes surface heat transfer patterns that are similar for the heated and unheated starting length cases. The vortices associated with the film cooling jets appear to produce "fork tined" heat transfer signatures on the wall. Variations in the signatures appear to be caused by jet liftoff at higher blowing ratios.

Acknowledgment

This work was done under the Trident Scholar Program at the U.S. Naval Academy.

Nomenclature

B = $(\rho_{\text{jet}}U_{\text{jet}})/(\rho_\infty U_\infty)$, blowing ratio
C_f = skin friction coefficient
c_p = specific heat at constant pressure
D = film-cooling hole diameter
h = heat transfer coefficient
L = length of film-cooling hole channel
q''_{conv} = convective heat flux
St = Stanton number
T = temperature
U = velocity
x = streamwise coordinate, distance from trailing edge of film-cooling holes
y = normal coordinate, distance from the wall
z = spanwise coordinate, distance from the centerline of the center hole
η = film cooling effectiveness
ρ = density
θ = dimensionless temperature, $(T_{\text{jet}}-T_\infty)/(T_{\text{plenum}}-T_\infty)$

Subscripts

aw = adiabatic wall
conv = convection
f = with film cooling
jet = film cooling jet
o = without film cooling
w = wall
∞ = mainstream

References

[1] Sen, B., Schmidt, D. L., and Bogard, D. G., 1996, "Film Cooling With Compound Angle Holes: Heat Transfer," ASME J. Turbomach., **118**, pp. 800–806.
[2] Schmidt, D. L., and Bogard, D. G., 1996, "Effects of Free-Stream Turbulence and Surface Roughness on Film Cooling," ASME Paper No. 96-GT-462.
[3] Mayhew, J. E., Baughn, J. W., and Byerley, A. R., 2002, "The Effect of Freestream Turbulence on Film Cooling Heat Transfer Coefficient," ASME Paper No. GT-2002-30173.
[4] Kelly, G. B., and Bogard, D. G., 2003, "An Investigation of the Heat Transfer for Full Coverage Film Cooling," ASME Paper No. GT2003-38716.
[5] Burd, S., and Simon, T. W., 2000, "Effects of Hole Length, Supply Plenum Geometry, and Freestream Turbulence on Film Cooling Performance," NASA CR-2000-210336.
[6] Gritsch, M., Schulz, A., and Wittig, S., 1998, Adiabatic Wall Effectiveness Measurements of Film-Cooling Holes With Expanded Exits," ASME J. Turbomach., **120**, pp. 560–567.
[7] Kohli, A., and Bogard, D. G., 1998, "Fluctuating Thermal Field in the Near-Hole Region for Film Cooling Flows," ASME J. Turbomach., **120**, pp. 86–91.
[8] Sinha, A. K., Bogard, D. G., and Crawford, M. E., 1991, "Film Cooling Effectiveness Downstream of a Single Row of Holes With Variable Density Ratio," ASME J. Turbomach., **113**, pp. 442–449.
[9] Pietrzyk, J. R., Bogard, D. G., and Crawford, M. E., 1990, "Effect of Density Ratio on the Hydrodynamics of Film Cooling," ASME J. Turbomach., **112**, pp. 437–443.
[10] Crawford, M. E., and Kays, W. M., 1976, "STAN5—A Program for Numerical Computation of Two-Dimensional Internal and External Boundary Layer Flows," NASA CR 2742.

Journal of Turbomachinery

Technical Brief

Validation of Heat-Flux Predictions on the Outer Air Seal of a Transonic Turbine Blade

John P. Clark

Marc D. Polanka

Matthew Meininger

Air Force Research Laboratory,
Turbine Branch,
Wright Patterson AFB,
OH 45433

Thomas J. Praisner
United Technologies,
Pratt & Whitney,
East Hartford, CT 06108

It is desirable to accurately predict the heat load on turbine hot section components within the design cycle of the engine. Thus, a set of predictions of the heat flux on the blade outer air seal of a transonic turbine is here validated with time-resolved measurements obtained in a single-stage high-pressure turbine rig. Surface pressure measurements were also obtained along the blade outer air seal, and these are also compared to three-dimensional, Reynolds-averaged Navier-Stokes predictions. A region of very high heat flux was predicted as the pressure side of the blade passed a fixed location on the blade outer air seal, but this was not measured in the experiment. The region of high heat flux was associated both with very high harmonics of the blade-passing event and a discrepancy between predicted and measured time-mean heat-flux levels. Further analysis of the predicted heat flux in light of the experimental technique employed in the test revealed that the elevated heat flux associated with passage of the pressure side might be physical. Improvements in the experimental technique are suggested for future efforts.
[DOI: 10.1115/1.2184351]

Contributed by the International Gas Turbine Institute of ASME for publication in the JOURNAL OF TURBOMACHINERY. Manuscript received December 1, 2002; final manuscript received March 1, 2003. Presented at the International Gas Turbine and Aeroengine Congress and Exhibition, Atlanta, GA, June 16–19, 2003, Paper No. GT2003-38916. Review conducted by H. R. Simmons.

Introduction

For future gas turbine engines, it is desirable both to increase performance and to reduce operating costs. Although turbine performance increases are achievable through increases in turbine inlet temperature, this often results in decreased turbine durability. Since designers typically rely on an experience-based approach, there is a durability margin that is built into the design of turbine components. Consequently, component life estimates can either be overpredicted or underpredicted. If part life is greater than predicted, then turbine components are using more than the optimum amount of cooling, and the performance of the overall system is reduced perforce. However, if part life is less than predicted, then the system requires more frequent inspection coupled with possible repairs and/or part replacements. This inevitably results in increased life-cycle costs as well as reduced readiness of the armed forces. The prediction of turbine blade outer air seal (BOAS) region cooling requirements contains an especially significant amount of empiricism. Thus, a better fundamental understanding of the complex flow and thermal environment in this region is critical to improving the predictive capability that will allow minimization of cooling at desired durability and performance levels.

As detailed in the review article of Dunn [1], several researchers have predicted the flow in the near-blade-tip region, over the tip, and on the BOAS, but very few studies that focus on time-resolved predictions are available in the open literature. Most of the previous predictive studies have attempted to replicate time-mean experimental data. For example, Ameri and Bunker [2] performed computations for the flow in a linear cascade typical of a first-stage power generation turbine. This was a simulation of the experiment of Bunker et al. [3] that obtained nearly full surface heat transfer data on flat tips with various edges, three clearances, and two turbulence levels. The simulation compared favorably with the data. Also, Moore et al. [4] studied flat tip region flows from incompressible laminar to turbulent transonic conditions and compared their predictions of flow characteristics and heat transfer to available experimental data. Some have also attempted to predict the flow and heat transfer in full scale, rotating turbine rigs. Metzger et al. [5] performed predictions of the data taken by Dunn et al. [6,7] on the Garrett 731-2 turbine. They showed that a simple model describing the tip flow could be used to predict the time-averaged tip and BOAS heat transfer once the leakage flow rate was estimated. Ameri and Steinthorsson [8] also made predictions of the time-averaged heat transfer of the Dunn et al. [6,7] experiment and showed good agreement with the experimental results. Several recent experimental studies have reported heat transfer and cooling effectiveness in the vicinity of blade tips in cascades [9–11], but perhaps the most relevant investigation to the current study was performed by Chana and Jones [12]. The authors' measurements provided new insights into the blade outer air seal flow, and they revealed high unsteadiness in the tip region both in pressure and in heat transfer. They also suggested that an unsteady oscillation in heat transfer to and from the BOAS exists with each blade passage.

In the present study, a detailed comparison of time-resolved

Table 1 Grid counts used for the 3D RANS simulations

Axial × radial × circumferential grid counts:		
O-Mesh	113 × 33 × 57	113 × 33 × 57[a]
H-Mesh	185 × 33 × 57	169 × 33 × 57

[a]Each blade also had a 57 × 32 × 32 tip-clearance grid

measurements and Reynolds-averaged Navier-Stokes (RANS) predictions of pressure and heat transfer on a blade outer air seal is presented. The measurements were conducted in the Turbine Research Facility (TRF) at Wright-Patterson Air Force Base. All details of the short-duration experimental technique and the transonic turbine are presented in Polanka et al. [13], and further comparisons of data and prediction (e.g., on the blade tip) are given in a companion paper [14]. The turbine represents a modern single-stage high-pressure turbine used for military aircraft application. The blade-tip geometry is flat with a nominal clearance of 0.24 mm (~0.5% of trailing-edge span). For the pressure measurements reported here the method of Kline and McClintock [15] resulted in ±0.45% uncertainty while the turbine total quantities had ±0.15% uncertainty. Furthermore, a jitter analysis as described by Moffat [16] was performed through the heat-flux data-reduction algorithm to obtain the uncertainty in the surface heat transfer. This varied from gage to gage, but did not exceed 4% of the mean levels presented here. What follows is a detailed comparison between the experimental data and a prediction at the turbine design condition.

Computational Methods

Steady-state pressure fields and wall heat fluxes in the single-stage, transonic turbine were predicted using the three-dimensional (3D), Reynolds-averaged Navier-Stokes (RANS) code described collectively by Ni [17,18], Ni and Bogoian [19], and Davis et al. [20]. The code employed a finite volume, cell-centered, Lax-Wendroff [21] method and was accurate to second order in both space and time. Numerical closure was obtained with the high Reynolds number k-ω turbulence model as described by Wilcox [22], and multigrid techniques were used to obtain rapid convergence. Consistent with the experiment, an isothermal boundary condition was imposed on all solid boundaries, and these were also treated as no-slip surfaces. Turbulent flow was assumed throughout, and the inlet boundary layer was allowed to grow over a distance consistent with the inlet flow path of the rig.

Single-stage, steady-state calculations were performed with 44 vanes and 58 blades as per the experiment. For such steady-state calculations, the Ni code employs a mixing-plane approximation to transfer information across the inter-row boundary (see Ni [17]). In this instance, the mixing plane approximation consists of circumferentially averaging the two-dimensional (2D) exit flow field from the vane row and mapping one-dimensional (1D) profiles onto the inlet boundary of the downstream blade row. For these calculations an OH grid topology was employed, and the grid counts used to model each airfoil passage and the tip clearance region are listed in Table 1. These grid counts were consistent with standard work criteria defined by Praisner [23] at Pratt & Whitney (P&W) to capture properly the thermal fields in modern gas turbines. The P&W design viscous grid was defined to produce near surface values of $y^+ < 1$ over all no-slip boundaries as recommended by Dunham and Meauze [24] for use with two-equation turbulence models. Also, the grid gave ~15 grid points in the boundary layer on each airfoil surface.

The 3D steady flowfields predicted by the flow solver were postprocessed to allow for direct comparisons to time-resolved experimental pressure and heat transfer distributions on the blade outer air seal. The majority of the postprocessing was straightforward, but some of it requires clarification. For example, the conclusion of Prasad and Wagner [25] that the time-resolved pressure on the turbine BOAS was consistent with the periodic passing of a flow field that was steady in the blade frame of reference was assumed to be valid. Consequently, it was possible to compare both time-resolved experimental pressures and heat fluxes on the BOAS to the steady-state predictions, as will be shown. Careful attention was paid to the frequency content of the experimental data, and the predicted signals were low-pass filtered to ensure a consistent comparison where appropriate. Finite impulse response (FIR) digital filters were employed to ensure that the phase angles of all fluctuations were preserved over the pass band of the filter. Also, the values of the predicted wall heat flux that were compared to experimental data were calculated via a heat balance applied across the first computational cell in the direction normal to and into the wall, namely,

$$q'' = -k(T_w - T_s)/\Delta n \tag{1}$$

In Eq. (1), the thermal conductivity of air k was evaluated at the film temperature $(T_s + T_w)/2$, and Δn was the distance between the first two grid points adjacent to the wall and normal to it. The driving temperature T_s was the local static temperature, and T_w was the wall temperature.

It should be noted that the computational results presented below are from true predictions of the flow field. That is, a design grid was generated for the single-stage turbine geometry, a set of boundary conditions from a single experiment conducted in the TRF were mapped onto the computational domain, and the flow solver was exercised. The relevant boundary conditions included the measured upstream total pressure (383 kPa) and total temperature (449 K), the downstream static pressure (107 kPa), the wheel speed (7500 rpm), and the time-mean wall temperature over the experimental test window (362 K). The boundary conditions were taken as measured time-average values for 100 ms of the total run time of the experiment. Over that interval, the upstream total quantities, the wheel speed, and the wall temperature on the BOAS varied by <1%, while the downstream static pressure varied 1.3%. The freestream turbulence intensity was taken to be 2%, and that was in keeping with previous measurements in the TRF. The turbulence intensity sets the boundary condition on k, and the boundary condition for ω was set to ensure a turbulent length scale of order 10% of the span at the leading edge of the vane [23]. This investigation focused only on the baseline run described in Polanka et al. [13], where the relevant similarity parameters for the engine are a gas-to-metal temperature ratio of 1.47, a total-to-total pressure ratio of 2.76, a corrected speed of 0.57 (midspan tangential velocity divided by sonic speed at inlet), and an exit Reynolds number based on axial chord of 3.80×10^5.

Results

Figure 1 is a pair of plots giving the predicted distributions of static pressure and wall heat-flux on the BOAS. The local static pressure is normalized by the turbine-inlet total pressure to give an indication of the local absolute Mach number through the turbine blade row while the local wall heat flux is plotted in kilowatts per square meter. The heat flux is plotted in its raw form purposefully: a true physics-based durability design system implies a capability to predict accurately the local cooling requirements of hot section parts. Toward this end, validation is taken here to mean a comparison of predicted and measured raw heat fluxes without invocation of any heat transfer coefficient. Discrete static-pressure measurements were taken with high response, surface-mounted Kulite transducers at the axial stations indicated on Fig. 1, while heat fluxes were measured at equivalent axial locations using button-type thin-film gages as described by Dunn [1] (see also [26]). The characteristics of the specific gages used here were reported by Weaver et al. [27]. The substrate buttons were ~3 mm thick; thus, the semi-infinite assumption employed to reduce the

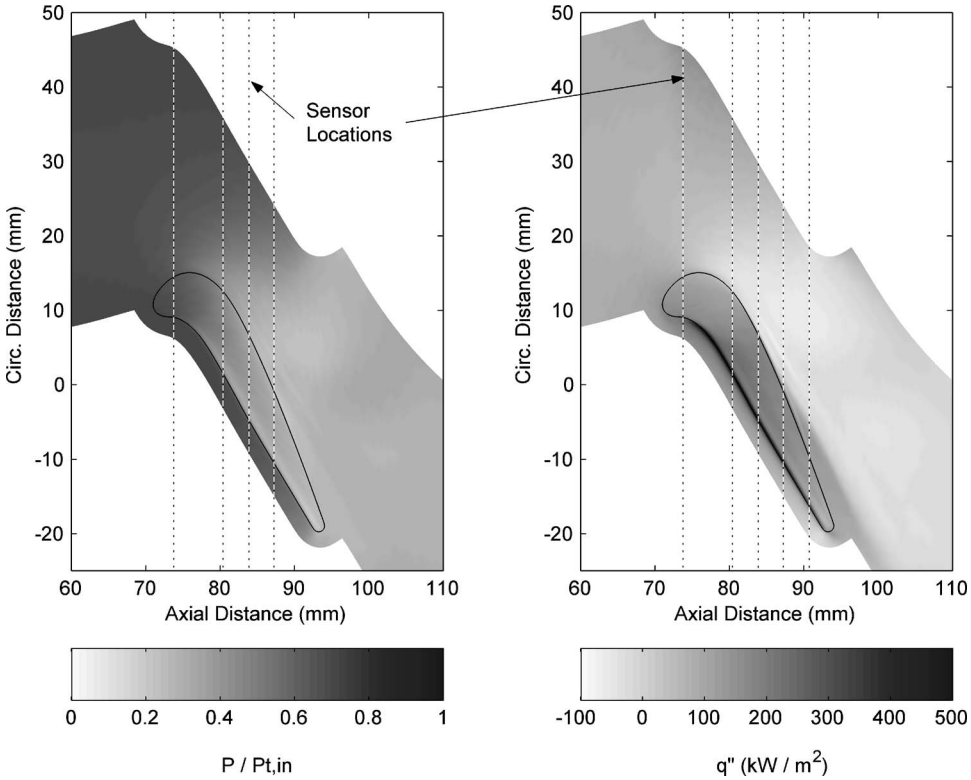

Fig. 1 Predicted BOAS static pressure and heat-flux distributions

heat-flux data was well justified over the experimental time interval studied here (≈1 s after flow start). Also, ohmic heating of the gages by the sensing current applied to them resulted in a very small change in surface temperature (<0.1 K). Again, the flow over the BOAS was considered to be steady in the blade frame of reference. In the stationary frame of reference, a fixed sensor was therefore in an unsteady flow field. Accordingly, the steady RANS predictions in Fig. 1 were translated to the stationary frame of reference for comparison to true time-resolved measurements on the BOAS.

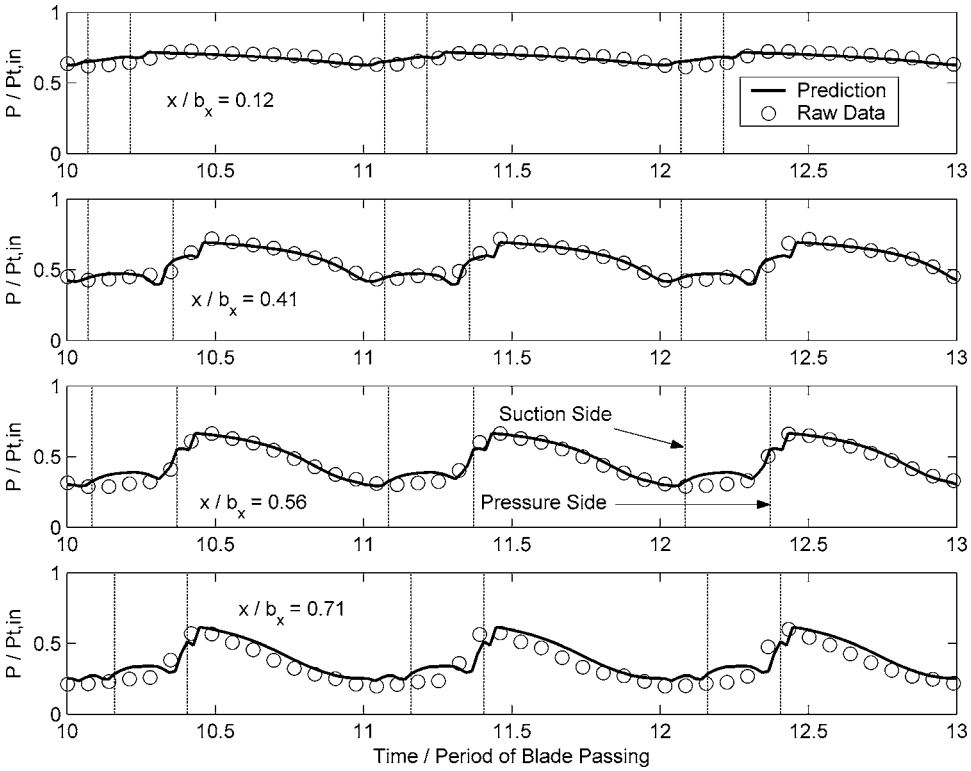

Fig. 2 Comparison of measured and predicted time-resolved static pressures on the BOAS

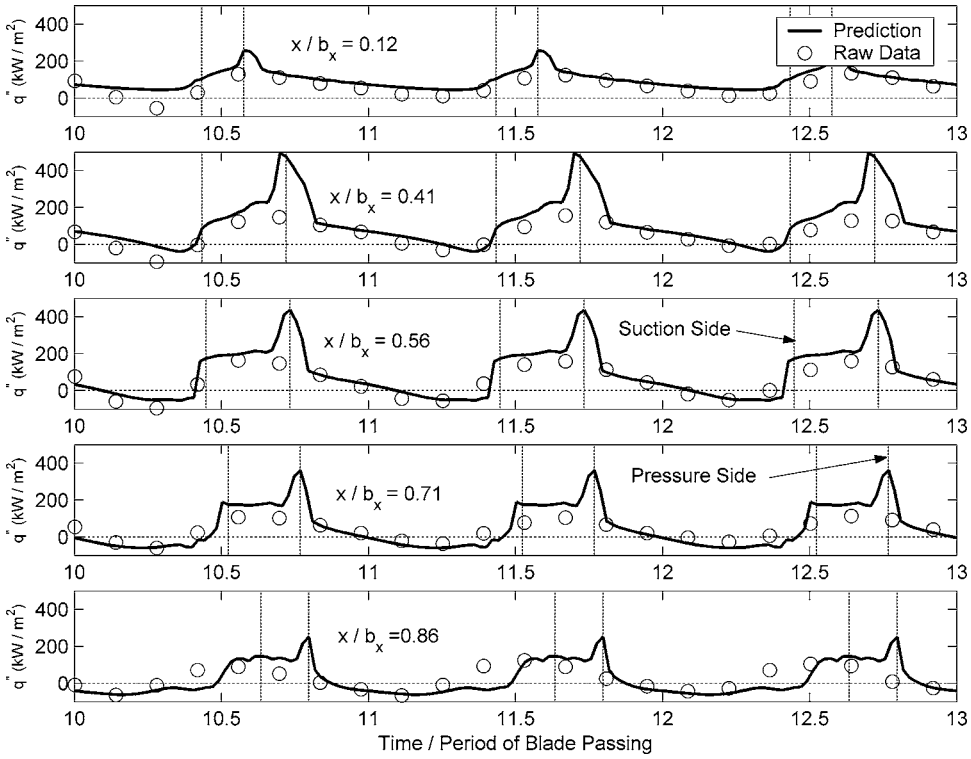

Fig. 3 Comparison of measured and predicted time-resolved heat fluxes on the BOAS

Time-Resolved Pressure. Figure 2 is a plot of the time-resolved pressure for the four BOAS gages as compared to the time-resolved experimental data. Also shown on the figure are the times that the blade pressure and suction surfaces were at each gage location. The prediction and the data compare quite well in terms of the peak-to-peak variation over a blade-passing period and in terms of the DC level (i.e., the time mean). Both the predicted and experimental traces also have a steep rise in level after the passage of the tip pressure side followed by a decrease as the blade passage traversed the sensor. However, the predicted time trace is characterized by an increase in pressure across the tip followed by a decrease as the pressure side of the tip passed over the gage. The experimental data suggest a more constant pressure as the tip passed over the gage. In contrast, the experimental data of Chana and Jones [12] and Prasad and Wagner [25] revealed more of the variation evident in the current prediction.

Time-Resolved Heat Transfer. Although the time-mean BOAS pressure distribution was accurately predicted with the 3D RANS solver, the time-mean heat transfer was substantially overpredicted, as seen in Fig. 3. In the figure, a set of time-resolved heat fluxes on the BOAS for the five thin-film gages used in the experiment is shown. For each gage, both the experimental data and the predictions are plotted. The experimental data were not ensemble averaged in any way before plotting: instead, it is shown as raw data. Therefore, some aperiodicity is evident in the experiment but not in the computation. The ordinate for each plot is heat flux, while the abscissa is time nondimensionalized by the period of blade passing. Again, raw heat-flux levels were plotted purposefully without the benefit of ensemble averaging. This is because the end goal of this study was a validation of calculated heat-flux levels for a given set of boundary conditions. This is a necessary capability if a durability designer is to determine film-cooling requirements for a BOAS during the design cycle. Also plotted on the figure are vertical lines representing the predicted times that the blade tip pressure and suction sides are over the heat-flux gage. Note that, for all gages, the predicted heat flux is a maximum when the blade tip pressure side is over the heat-flux gage, when a very large excursion from the mean level occurs. This makes physical sense because the boundary layer on the BOAS is greatly energized by the tip-clearance flow as it comes over the tip from the pressure side. Thus, the attendant thinning of the boundary layer on the BOAS resulting from this effect should be associated with very high levels of both shear stress and heat flux.

The prediction reveals higher frequency content with each blade passing than was observed in the experiment. To investigate this, discrete Fourier transform (DFT) magnitudes for both the measurement and computation at $x/b_x=0.56$ are shown in Fig. 4. Note that the abscissa of the plot is engine order, which is a frequency normalized by the number of rotor revolutions per second. Since there are 58 turbine blades around the rotor circumference, the first blade passing frequency occurs at engine order 58. The predicted heat-flux variation on the BOAS is derived from the full spatial (and, hence, both temporal and spectral) resolution of the simulation (355 kHz), and very high harmonics of the blade-passing frequency are evident in the plot. Such high harmonics are not typically seen in time-resolved predictions of vane-blade interaction [28], and this is an indication that the validation of the BOAS prediction may require an increase in the bandwidth of heat flux measurements relative to the state of the art.

From inspection of Fig. 3, it is clear that both the peak level of the predicted signals and the time-mean levels are lower in the experiment relative to the prediction. From the point of view of the turbine durability engineer, accurate prediction of the time-mean heat flux is paramount. The mean level of the computation is clearly affected by the frequency content of the signal, and this suggests that very high frequencies must be resolved in experiments to validate the prediction properly. Therefore, it becomes important to determine whether or not the high-frequency components of the predicted signal over the blade tip are truly characteristic of this flow field. In the TRF, time-resolved temperature signals are recorded and subsequently processed into time-resolved heat fluxes by solving the 1D unsteady heat conduction equation. As clearly shown by Oldfield [29], a thin-film gage re-

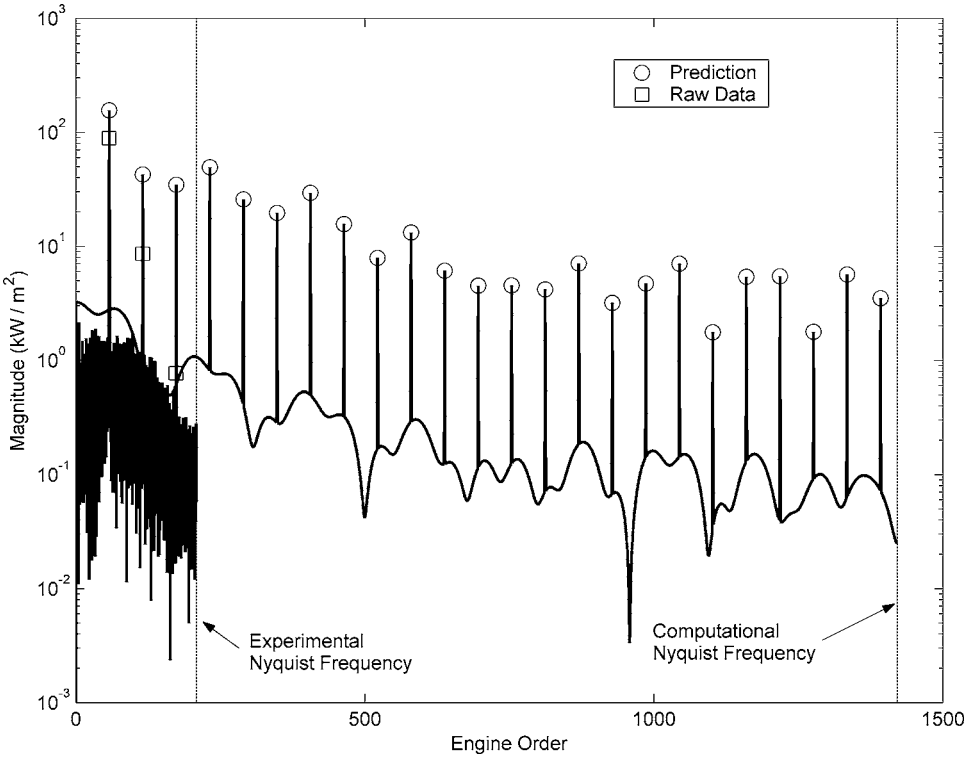

Fig. 4 Comparison of discrete Fourier transform (DFT) magnitudes from the measured and predicted heat flux variations on the BOAS at $x/b_x=0.56$

sponse is frequency dependent, and high frequency fluctuations in heat flux can be lost unless a significant fraction of the A/D input range is used to capture the AC portion of the temperature signal. All the temperature signals obtained for this study were conditioned through DC-coupled amplifiers that had a flat frequency response in the Bessel filter passband prior to digitization. Thus, it is possible that a systematic error in the experiment accounts for both the lack of high-frequency components in the data and the overprediction of the time-mean heat flux on the BOAS.

It is possible to determine the effects of the measurement technique on the frequency content of the BOAS heat flux with some rigor. If one considers the predicted time variation of heat flux to be accurate, it is possible to calculate the predicted time history of the substrate surface temperature that would result from that heat flux by invoking the 1D unsteady heat-conduction equation and solving it numerically. One can then assess the effects of A/D resolution and low-pass filtering on the measured temperature and reconstruct the predicted heat-flux traces that would result from those operations to compare to the true measured variation. This was done, and the results are plotted in Fig. 5 for the thin-film gage at $x/b_x=0.56$. In the topmost panel of the figure, two predicted surface-temperature histories are shown. One temperature history takes the A/D resolution into account (0.0164 K/count at 12 bits of resolution) and the other includes the effect of low-pass filtering at 20 kHz before acquisition. Heat-flux traces are also plotted in the central panel of Fig. 5. The time-history predicted directly by the 3D RANS solver is shown along with the experimental data. Also plotted are heat-flux traces determined by reprocessing the predicted surface-temperature histories via the method of Cook and Felderman [30]. Note that the A/D resolution in temperature is adequate to reproduce the frequency content of the RANS-predicted heat flux, but low-pass filtering the temperature trace before acquisition brings the predicted heat flux into much closer agreement with the actual measurements.

Thus, it is clear that the discrepancies between the experiment and prediction as regards frequency content as well as maximum and mean levels can be a consequence of the measurement system. This is not to say that the RANS solver and the turbulence model used in conjunction with it are perfectly adequate to predict the BOAS heat-transfer variation. However, the results of this exercise do help to explain why the disagreement between measurement and prediction is so large. Furthermore, giving the predictive tool the benefit of the doubt when comparing predictions to experimental results has yielded a means whereby future measurements can be improved. This should aid in closing the gap between experiment and prediction for this complicated flow field.

Note that for some portion of the blade-passing period the measured heat flux on the BOAS is negative, and this is quite inconsistent with what occurs in the engine situation. Negative levels of heat flux are sometimes seen in data derived from wall temperature measurements via the technique of Cook and Felderman [30] as a consequence of the differentiation operation concomitant with the method, but they do not typically persist from blade passing to blade passing as seen here [31]. Thus, the negative heat fluxes here are an indication that the local recovery temperature is less than the wall temperature over that same interval. Although the turbine-inlet temperature (449 K) is elevated relative to the pretest wall temperature (362 K), the upstream total temperature was limited by the tight running clearance (0.24 mm) of the turbine and the need to achieve the design corrected speed of the motor. Since the flow through the rig is diabatic and enthalpy is extracted from the flow by the turbine blade, the local recovery temperature over the BOAS becomes smaller than the local wall temperature for some portion of each blade-passing period. For the same reason, the local static temperature over the BOAS in the laminar sublayer is smaller than the local surface temperature. The heat flux then becomes negative as defined by Eq. (1), and this is representative of heat transfer *from* the BOAS to the freestream during a portion of the blade-passing interval.

Note that this phenomenon occurs in the prediction as well as in the experiment. To show this, a separate adiabatic wall simulation

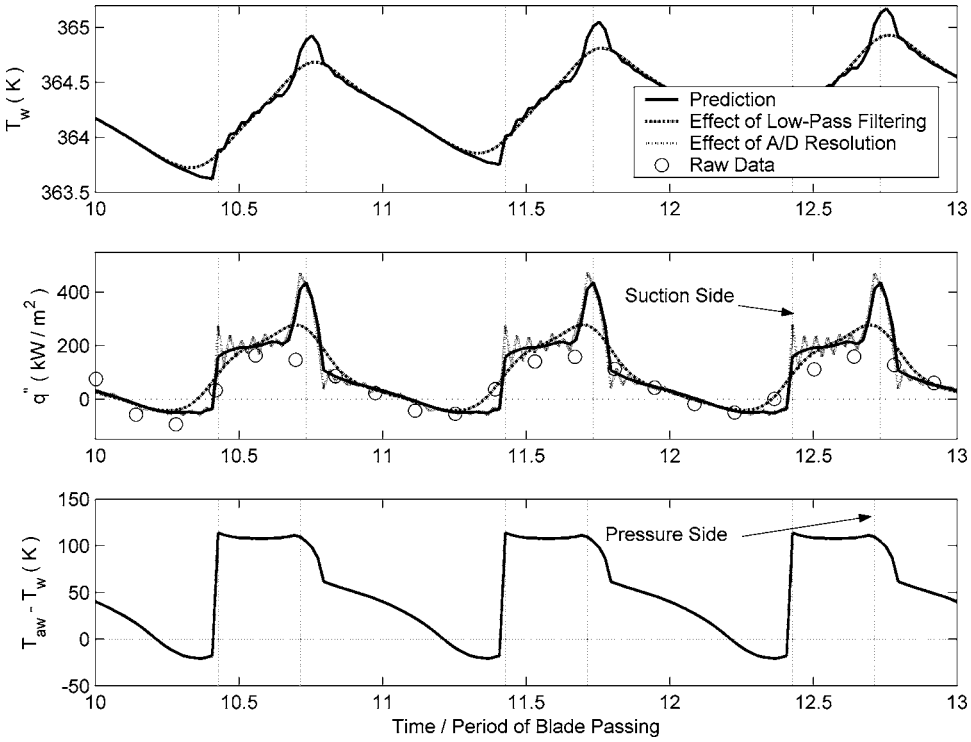

Fig. 5 Assessment of A/D resolution and low-pass filtering on the predicted BOAS surface temperature with attendant effects on the apparent measured wall heat-flux. Also, the time history of the heat-flux driving potential is shown. All signals are for the gage at x/b_x=0.56.

was run in order to determine the driving temperature at the solid boundary. The predicted time history of the heat transfer driving potential over the thin-film gage located at x/b_x=0.56 is shown in the bottom panel of Fig. 5. Here the difference between the local adiabatic wall temperature in the absolute frame of reference and the wall temperature from the isothermal simulation was taken as the driving potential. As shown, negative heat-flux results for both the prediction and the experiment at time windows consistent with the negative predicted driving potential. Again for the BOAS, this was physically realistic given the relatively low turbine-inlet temperature combined with both the diabatic nature of the flow field and the extraction of energy from the flow by the turbine blade.

Conclusions

This work compared experimental data taken on the BOAS of a full-scale, rotating turbine stage to a prediction of the flow field made with a 3D RANS solver. Although differences in magnitude occurred between the prediction and the experimental data, particularly with respect to heat transfer, the general trends were consistent. Also, the predicted time history of heat flux on the BOAS was characterized by very high levels of heat transfer as the pressure side of the blade tip passed over the gages. Consequently, very high frequencies and high-amplitude fluctuations were observed in the predicted signals that were not observed in the experiment. These large-amplitude fluctuations were physically realistic, and processing the predicted time-resolved heat flux in a manner consistent with the experiment revealed that both the peak and the time-mean levels on the BOAS could be as high as was predicted. Thus, instrumentation developments are underway to improve the bandwidth of heat-flux measurements for future tests. Finally, using the results of the predictions, the driving temperature for BOAS heat transfer was investigated. It was shown that the local adiabatic wall temperature of the flow in the vicinity of the BOAS fluctuated with time and can result in a negative heat transfer driving potential (and, hence, heat flux).

Nomenclature

k = thermal conductivity (kW/m K)
n = normal distance from a solid boundary (m)
P = pressure (kPa)
q'' = heat flux (kW/m^2)
T = temperature (K)
x/b_x = fraction of blade axial chord
y^+ = law-of-the-wall variable

Subscripts

aw = adiabatic wall
in = inlet
s = static properties
t = total properties
w = wall

References

[1] Dunn, M. G., 2001, "Convective Heat Transfer and Aerodynamics in Axial Flow Turbines," ASME Paper No. 2001-GT-0506.
[2] Ameri, A. A., and Bunker, R. S., 2000, "Heat Transfer and Flow on the First-Stage Blade Tip of a Power Generation Gas Turbine: Part 2-Simulation Results," ASME J. Turbomach., **122**, pp. 272–277.
[3] Bunker, R. S., Bailey, J. C., and Ameri, A. A., 2000, "Heat Transfer and Flow on the First-Stage Blade Tip of a Power Generation Gas Turbine: Part 1-Experimental Results," ASME J. Turbomach., **122**, pp. 263–271.
[4] Moore, J., Moore, J. G., Henry, G. S., and Chaudhry, U., 1989, "Flow and Heat Transfer in Turbine Tip Gaps," ASME J. Turbomach., **111**, pp. 301–309.
[5] Metzger, D. E., Dunn, M. G., and Hah, C., 1991, "Turbine Tip and BOAS Heat Transfer," ASME J. Turbomach., **113**, pp. 502–507.
[6] Dunn, M. G., Rae, W. J., and Holt, J. L., 1984, "Measurement and Analyses of Heat Flux Data in a Turbine Stage: Part I-Description of Experimental Apparatus and Data Analysis," ASME J. Eng. Gas Turbines Power, **106**, pp. 229–233.
[7] Dunn, M. G., Rae, W. J., and Holt, J. L., 1984, "Measurement and Analyses of Heat Flux Data in a Turbine Stage: Part II-Discussion of Results and Comparison With Predictions," ASME J. Eng. Gas Turbines Power, **106**, pp. 234–240.
[8] Ameri, A. A., and Steinthorsson, E., 1996, "Analysis of Gas Turbine Rotor Blade Tip and BOAS Heat Transfer," ASME Paper No. 96-GT-189.
[9] Christophel, J. R., Couch, E., Thole, K. A., and Cunha, F. J., 2004, "Measured

Adiabatic Effectiveness and Heat Transfer for Blowing From the Tip of a Turbine Blade," ASME Paper No. GT2004-53250.
[10] Nasar, H., Ekkad, S. V., and Bunker, R. S., 2005, "Effect of Tip and Pressure Side Coolant Injection on Heat Transfer Distributions for a Plane and Recessed Tip," ASME Paper No. GT2005-68595.
[11] Mhetras, S., Yang, H., Gao, Z., and Han, J. C., 2005, "Film Cooling Effectiveness on Squealer Rim Walls and Squealer Cavity Floor of a Gas Turbine Blade Tip Using Pressure Sensitive Paint," ASME Paper No. GT2005-68387.
[12] Chana, K. S., and Jones, T. V., 2002, "An Investigation On Turbine Tip and BOAS Heat Transfer," ASME Paper No. GT2002-30554.
[13] Polanka, M. D., Hoying, D. A., Meininger, M., and MacArthur, C. D., 2003, "Turbine Tip and BOAS Heat Transfer and Loading Part A: Parameter Effects Including Reynolds Number, Pressure Ratio and Gas to Metal Temperature Ratio," ASME J. Turbomach., **125**, pp. 97–106.
[14] Polanka, M. D., Clark, J. P., White, A. L., Meininger, M., and Praisner, T. J., 2003, "Turbine Tip and BOAS Heat Transfer and Loading, Part B: Comparisons Between Prediction and Experiment, Including Unsteady Effects," ASME Paper No. GT2003-38916.
[15] Kline, S. J., and McClintock, F. A., 1953, "Describing Uncertainties in Single Sample Experiments," Mech. Eng. (Am. Soc. Mech. Eng.), **75**, pp. 3–8.
[16] Moffat, R. J., 1982, "Contributions to the Theory of Single-Sample Uncertainty Analysis," ASME J. Fluids Eng., **107**, pp. 153–160.
[17] Ni, R. H., 1999, "Advanced Modeling Techniques for New Commercial Engines," XIV ISOABE Conference, Florence, Sept. 5–10.
[18] Ni, R. H., 1982, "A Multiple-Grid Scheme for Solving the Euler Equations," AIAA J., **20**(11), pp. 1565–1571.
[19] Ni, R. H., and Bogoian, J. C., 1989, "Prediction of 3-D Multistage Turbine Flow Field Using a Multiple-Grid Euler Solver," AIAA Paper No. 89-0203.
[20] Davis, R. L., Shang, T., Buteau, J., and Ni, R. H., 1996, "Prediction of 3-D Unsteady Flow in Multi-Stage Turbomachinery Using an Implicit Dual Time-Step Approach," AIAA Paper No. 96-2565.
[21] Lax, P. D., and Wendroff, B., 1964, "Difference Schemes for Hyperbolic Equations With High Order Accuracy," Commun. Pure Appl. Math., **17**, pp. 381–398.
[22] Wilcox, D. C., 1998, *Turbulence Modeling for CFD*, 2nd ed., DCW Industries, Inc., La Canada, CA.
[23] Praisner, T. J., 2001, personal communication.
[24] Dunham, J., and Meauze, G., 1998, "An AGARD Working Group Study of 3D Navier-Stokes Codes Applied to Single Turbomachinery Blade Rows," ASME Paper No. 98-GT-50.
[25] Prasad, A., and Wagner, J. H., 2000, "Unsteady Effects in Turbine Tip Clearance Flows," ASME J. Turbomach., **122**(4), pp. 621–627.
[26] Schultz, D. L., and Jones, T. V., 1973, "Heat Transfer Measurements in Short-Duration Hypersonic Facilities," NATO AGARDOGRAPH 165.
[27] Weaver, M. W., Moselle, J. R., Dunn, M. G., and Guenette, G. R., 1994, "Reduction of Data From Heat-Glux Gauges: A Documentation of the MIT ACQ Code and an Adaption to Single-Sided Gauges," Calspan Report No. 7733-4.
[28] Clark, J. P., and Grover, E. A., 2006, "Assessing Convergence in Predictions of Periodic-Unsteady Flowfields," ASME Paper No. GT2006-90735.
[29] Oldfield, M. L. G., 1988, "Experimental Techniques in Unsteady Flows," Oxford University Engineering, Laboratory Report No. 1843/90.
[30] Cook, W. J., and Felderman, E. J., 1966, "Reduction of Data from Thin-Film Heat-Transfer Gauges: A Concise Numerical Technique," AIAA J., **4**(3), pp. 561–562.
[31] Dunn, M. G., 2005, personal communication.